EPA 903-R-04-004
July 2004

United States
Environmental
Protection Agency

Region III
Chesapeake Bay
Program Office

U.S. Army Corps of Engineers
Engineer Research & Development Center
Environmental Laboratory

US Army Corps
of Engineers®
Engineer Research and
Development Center

The 2002 Chesapeake Bay Eutrophication Model

Carl F. Cerco
Mark R. Noel

July 2004

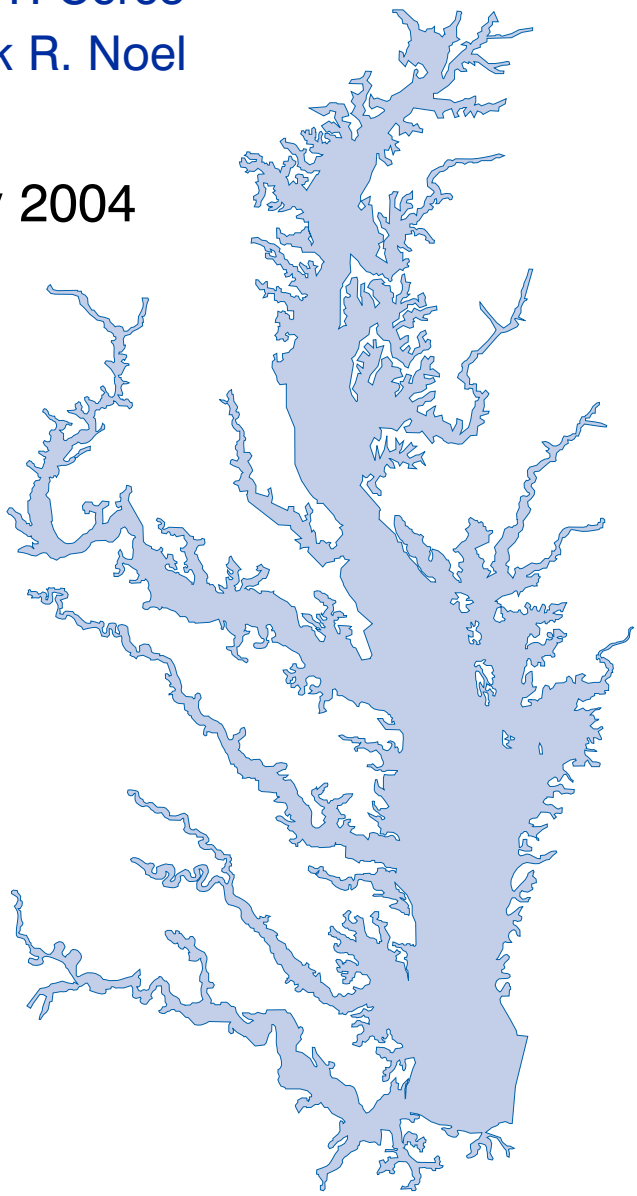

EPA 903-R-04-004
July 2004

The 2002 Chesapeake Bay Eutrophication Model

CARL F. CERCO and **MARK R. NOEL**
U. S. Army Corps of Engineers
Waterways Experiment Station
3909 Halls Ferry Road
Vicksburg, MS 39180

Prepared for: **Chesapeake Bay Program Office**
U.S. Environmental Protection Agency
410 Severn Avenue
Annapolis, MD 21401

This work was accomplished by ERDC through a cooperative agreement with the U.S. Environmental Protection Agency Chesapeake Bay Program Office, which was administered by the Baltimore District U. S. Army Corps of Engineers.

Contents

Executive Summary

Introduction

Deterioration of water quality in Chesapeake Bay and associated losses of living resources have been recognized as a problem for more than twenty years. An order-of-magnitude increase in anoxic volume and a catastrophic decline in submerged aquatic vegetation (SAV) were among the primary problems cited. Two decades later, elimination of anoxia and restoration of SAV remain prime management goals. Models have been employed as tools to guide management since the formation of the first water quality targets. Over time, as management focus has been refined, models have been improved to provide appropriate, up-to-date guidance.

The Chesapeake 2000 Agreement called for a ten-fold increase in biomass of oysters and other filter feeding organisms. At the same time, regulatory forces were shaping the direction of management efforts. Regulatory agencies in Maryland listed the state's portion of Chesapeake Bay as "impaired." The US Environmental Protection Agency added bay waters within Virginia to the impaired list. Settlement of a lawsuit required development of a Total Maximum Daily Load (TMDL) for Virginia waters by 2011. To avoid imposition of an arbitrary TMDL, the Chesapeake 2000 Agreement specified removal of water quality impairments by 2010. Impairments in the bay were defined as low dissolved oxygen, excessive chlorophyll concentration and diminished water clarity. A model recalibration was undertaken, with emphasis on improved accuracy in the computation of the three key indicators.

The Chesapeake Bay Environmental Model Package

Three models are at the heart of the Chesapeake Bay Environmental Model Package (CBEMP). Distributed flows and loads from the watershed are computed with a highly-modified version of the HSPF model. Nutrient and solids loads are computed on a daily basis for 94 sub-watersheds of the 166,000 km^2 Chesapeake

Bay watershed. The CH3D-WES hydrodynamic model computes three-dimensional intra-tidal transport on a grid of 13,000 cells. Computed loads and transport are input to the CE-QUAL-ICM eutrophication model which computes algal biomass, nutrient cycling, and dissolved oxygen, as well as numerous additional constituents and processes. The eutrophication model incorporates a predictive sediment diagenesis component. Ten years, 1985–1994, are simulated continuously using time steps of 5 minutes (hydrodynamic model) and 15 minutes (eutrophication model).

This Report

This report comprises the primary documentation of the eutrophication component of the 2002 CBEMP. We concentrate here on portions of the model that have undergone major revisions and on portions that have not been previously documented. Aspects of the model that proved particularly troublesome are documented for reference against future improvements. We have minimized repetition of previously-reported information and model results. Complete model results are available on a CD-ROM that accompanies this report.

Coupling with the Hydrodynamic Model

CH3D-WES

Hydrodynamic model formulation is based on principles expressed by the equations of motion, conservation of volume, and conservation of mass. Quantities computed by the model include three-dimensional velocities, surface elevation, vertical viscosity and diffusivity, temperature, salinity, and density.

The basic equations of CH3D-WES are solved via the finite-difference method on a grid of discrete cells. The computational grid extends from the heads of tide of major bay tributaries out onto the continental shelf. The grid contains 2961 cells, roughly 4 km^2 in area, in the surface plane. Number of cells in the vertical ranges from one to nineteen. Surface cells are 2.14 m thick at mean tide. Thickness of all sub-surface cells is fixed at 1.53 m. Total number of cells in the grid is 12,920.

Calibration and Verification

The hydrodynamic model was calibrated and verified against a large body of observed tidal elevations, currents, and densities. The calibration process was reviewed by an Expert Panel consisting of three university faculty members. Final approval was obtained from the panel before the hydrodynamic model was used to drive the water quality model.

Linkage to the Water Quality Model

Hydrodynamics for employment in the water quality model were produced for ten years, 1985–1994. Each year was a single, continuous production run. Computed flows, surface elevations, and vertical diffusivities were output at two-hour intervals for use in the water quality model. The algorithms and codes for linking the hydrodynamic and water quality models were developed over a decade ago and have been tested and proved in extensive applications since then. In every model application, the linkage is verified by comparing transport of a conservative

substance computed in each model. For estuarine applications, the transport tests commonly take the form of comparing salinity computed by two models. In the present application, salinity comparisons verify that the hydrodynamic and water quality models are correctly coupled and that transport processes in the two models are virtually identical.

Boundary Conditions

Boundary conditions must be specified at all open edges of the model grid. These include river inflows, lateral flows, and the ocean interface.

Ocean Boundary Conditions

In the first version of the model, the open edge of the model grid was at the entrance to Chesapeake Bay. In the Tributary Refinements phase of model development, the grid was extended beyond the bay mouth, out onto the continental shelf. The primary objective was to ensure that boundary conditions specified at the edge of the grid were beyond the influence of conditions within the bay. The grid extension traded one set of problems for another. Model boundaries were moved from a location with abundant observations to multiple locations at which little information was available. In the present phase of the model study, specification of boundary conditions at the edge of the grid proved especially problematic. The strategy was developed in which conditions observed at the bay mouth were extended to the edges of the grid. Kinetics were disabled outside the bay mouth to prevent substance transformations.

Our Recommendation

Extension of the grid onto the continental shelf had two objectives. The first was to move nutrient boundary conditions to a location beyond the influence of loads within the bay. The second was to allow for coupling with a proposed continental shelf model. The first objective was met, albeit with trade-offs. The proposed shelf model has been postponed indefinitely. The extension of the grid produced enormous difficulties for both the hydrodynamic and water quality modeling teams and did not increase the accuracy of either model. Consequently, we recommend the boundary be restored to the mouth of the bay in future model efforts.

Hydrology and Loads

Hydrology

Major sources of freshwater to the Chesapeake Bay system are the Susquehanna River, to the north, and the Potomac and James Rivers to the west. Of these, the Susquehanna provides by far the largest flow fraction, followed by the Potomac and James. All tributaries exhibit similar seasonal flow patterns. Highest flows occur in winter (December–February) and spring (March–May). Lowest seasonal flows occur in summer (June–August) and fall (September–November) although tropical storms in these seasons can generate enormous flood events.

Loads

Loads to the system include distributed or nonpoint-source loads, point- source loads, atmospheric loads, bank loads, and wetlands loads. Nonpoint-source loads enter the system at tributary fall lines and as runoff below the fall lines. Point-source loads are from industries and municipal wastewater treatment plants. Atmospheric loads are from the atmosphere directly to the water surface. Atmospheric loads to the watershed are incorporated in the distributed loads. Bank loads originate with shoreline erosion. Wetland loads are materials created in and exported from wetlands.

Nonpoint-Source Loads

Nonpoint-source loads are from Phase IV of the EPA Chesapeake Bay Watershed Model. Loads are provided on a daily basis, routed to surface cells on the model grid. Routing is based on local watershed characteristics and on drainage area contributing to the cell.

Largest nitrogen loads, by far, come from the Susquehanna River. Lesser loads enter at the Potomac and James fall lines. Magnitude of nitrogen loading corresponds to relative flows in these tributaries. The greatest phosphorus loads enter at the Susquehanna, Potomac, and James fall lines. Phosphorus loads are not proportional to flows in these tributaries. In 1990, phosphorus load in the Potomac was 70% of the load in the Susquehanna although Potomac flow was 25% of the Susquehanna. Phosphorus load from the James amounted to half the load from the Susquehanna although flow was less than 25% of the Susquehanna. Multiple factors may account for the disparity between flow and load. No doubt watershed characteristics and above-fall-line point-source loadings contribute. A speculation is that a portion of the Susquehanna particulate phosphorus load is retained in the Conowingo reservoir, just upstream of the fall line.

In 1990, the largest solids load was from the Potomac, followed by the Susquehanna and James. The relative importance of the major tributaries varies from year to year, however, depending on occurrence of major storm events. For suspended solids, the Conowingo reservoir acts as a settling basin to remove solids from the Susquehanna before entering the bay. Although solids can be scoured from the Conowingo at high flows, the predominant effect of the reservoir is to diminish Susquehanna solids loads relative to the other major tributaries.

Point-Source Loads

Point-source loads were provided by the EPA Chesapeake Bay Program Office in December 2000. These were based on reports provided by local regulatory agencies. Loads from individual sources were summed into loads to model surface cells and were provided on a monthly basis. Despite the provision of monthly values, loads from Virginia were most often specified on an annual basis while loads from Maryland varied monthly.

Point-source loads are concentrated in urban areas. Major nitrogen loads originate in Northern Virginia/District of Columbia, Richmond Virginia, Baltimore Maryland, and Hampton Roads Virginia. Of these, only loads to the Patapsco show a monotonic decreasing trend. Loads to the upper Potomac and upper James

suggest a decrease after 1990. Point-source nitrogen loads to the Back River and the lower James show no trend.

Point-source phosphorus loads are concentrated in the same urban areas as nitrogen although the relationship by size differs. In 1990, largest loads were from Hampton Roads and Richmond Virginia. Northern Virginia /District of Columbia contributed the least phosphorus load of the major urban centers. The same area showed the least reduction of phosphorus loads over the simulation period, possibly a consequence of load reductions prior to 1985. In the remaining urban areas, point-source phosphorus loads were halved from 1985 to 1994.

Atmospheric Loads

Daily atmospheric loads for each surface cell were computed by the EPA -Chesapeake Bay Program Office and provided in January 2000. Wet deposition of ammonium and nitrate was derived from National Atmospheric Deposition Program observations. Dry deposition of nitrate was derived from wet deposition using ratios calculated by the Regional Acid Deposition Model. Deposition of organic and inorganic phosphorus was specified on a uniform, constant, areal basis derived from published values.

Bank Loads

Bank loads are the solids, carbon, and nutrient loads contributed to the water column through shoreline erosion. Although erosion is episodic, bank loads can be estimated only as long-term averages. The volume of eroded material is commonly quantified from comparison of topographic maps or aerial photos separated by time scales of years. Consequently, the erosion estimates are averaged over periods of years.

Erosion rates for various portions of the system were summarized by the Baltimore District, US Army Corps of Engineers. The summary indicates widespread coverage but no estimates for the tidal fresh portions of the western tributaries, for the Patuxent River, and for major eastern shore embayments. Extensive measures of composition of eroded material are available for the major Virginia tributaries but are sparse or absent elsewhere. In view of the missing coverage and high variance in the observations, we decided to consider bank loading as a spatially and temporally uniform process. We found an erosion rate of 5.7 kg m^{-1} d^{-1} (0.7 ton ft^{-1} yr^{-1}) produced reasonable solids computations in the model.

The spatial distribution of bank loads depends directly on the length of the modeled shoreline. Segments receiving the greatest loads include the lower estuarine Potomac, Tangier Sound, and the tidal fresh portions of the major western tributaries. One characteristic of bank nutrient loads is they are phosphorus-enriched relative to organic matter. The modeled affinity of phosphorus for silt and clay produces a nitrogen-to-phosphorus ratio in modeled loads of 0.5:1 while the characteristic ratio in phytoplankton is 7:1.

Wetlands Loads

Wetlands loads are the sources (or sinks) of oxygen and oxygen-demanding material associated with wetlands that fringe the shore of the bay and tributaries.

These loads are invoked primarily as an aid in calibration of tributary dissolved oxygen. Wetlands areas adjacent to model surface cells were derived via GIS analysis and provided by the EPA Chesapeake Bay Program in November 2001. Loads to each cell were computed as the product of adjacent wetlands area and areal carbon export or oxygen consumption.

A uniform carbon export of 0.3 g C m^{-2} d^{-1} was employed. A uniform oxygen demand of 2 g O_2 m^{-2} d^{-1} was employed. Segments receiving the largest carbon loads and subject to the greatest oxygen consumption include the mid-portion of the bay, Tangier Sound, several Eastern Shore tributaries, the middle and lower James River, the tidal fresh York River, and the York River mouth.

Loading Summary

Loads from all sources were compared by for 1990, a year central to the simulation period. Runoff in this year was moderate in the Susquehanna and James and low in the Potomac.

Nonpoint sources dominated the nitrogen loads except in a few segments adjacent to major urban areas. In these regions, point sources contributed a significant fraction of nitrogen loads. Atmospheric nitrogen loads were significant only in the large, open segments of the mainstem bay and in the lower Potomac. Bank loads were negligibly small throughout.

Nonpoint sources usually comprised the largest fraction of phosphorus loads but were not so predominant as for nitrogen. As with nitrogen, point-source loads were significant in urban areas and atmospheric loads contributed to substantially to large open-water segments. A major contrast with nitrogen was in bank loading which equaled or exceed nonpoint-source phosphorus loads in segments distant from major inflows. These included the eastern embayments and the river-estuarine transition segments of western tributaries.

Nonpoint sources dominate the solids loads in segments adjoining the inflows of the Susquehanna, Potomac, and James. Otherwise, bank loads are the dominant source. For 1990, bank loads contribute more solids, system-wide, than nonpoint sources. Of course, the relative contribution of bank loads depends on annual hydrology. In high-flow years, nonpoint sources may dominate. Still, the summary indicates that control of bank erosion should be included in any solids management plan.

Kinetics

The foundation of CE-QUAL-ICM is the solution to the three-dimensional mass-conservation equation for a control volume. Control volumes correspond to cells on the hydrodynamic model grid. Solution is via a finite-difference scheme using the QUICKEST algorithm in the horizontal plane and a Crank-Nicolson scheme in the vertical direction. Discrete time steps, determined by computational stability requirements, are 15 minutes.

At present, the CE-QUAL-ICM model incorporates 24 state variables in the water column including physical variables, multiple algal groups, two zooplankton groups, and multiple forms of carbon, nitrogen, phosphorus and silica (Table ES-1).

Table ES-1
Water Quality Model State Variables

Temperature	Salinity
Fixed Solids	Freshwater Cyanobacteria
Spring Diatoms	Other (Green) Algae
Microzooplankton	Mesozooplankton
Dissolved Organic Carbon	Labile Particulate Organic Carbon
Refractory Particulate Organic Carbon	Ammonium+Urea
Nitrate+Nitrite	Dissolved Organic Nitrogen
Labile Particulate Organic Nitrogen	Refractory Particulate Organic Nitrogen
Total Phosphate	Dissolved Organic Phosphorus
Labile Particulate Organic Phosphorus	Refractory Particulate Organic Phosphorus
Chemical Oxygen Demand	Dissolved Oxygen
Dissolved Silica	Particulate Biogenic Silica

Algae

Algae are grouped into three model classes: cyanobacteria, spring diatoms, and other green algae. The cyanobacteria distinguished in the model are the bloom-forming species found in the tidal, freshwater Potomac River. Spring diatoms are large phytoplankton that produce an annual bloom in the saline portions of the bay and tributaries. The other green algae represent the mixture that characterizes saline waters during summer and autumn and fresh waters year round.

Zooplankton

Two zooplankton groups are considered: microzooplankton and mesozoo-plankton.

Organic Carbon

Three organic carbon state variables are considered: dissolved, labile particulate, and refractory particulate. Labile and refractory distinctions are based upon the time scale of decomposition. Labile organic carbon decomposes rapidly in the water column or the sediments. Refractory organic carbon decomposes slowly, primarily in the sediments, and may contribute to sediment oxygen demand years after deposition.

Nitrogen

Nitrogen is first divided into available and unavailable fractions. Available refers to employment in algal nutrition. Two available forms are considered: reduced and oxidized nitrogen. Reduced nitrogen includes ammonium and urea. Nitrate and nitrite comprise the oxidized nitrogen pool. Unavailable nitrogen state variables are dissolved organic nitrogen, labile particulate organic nitrogen, and refractory particulate organic nitrogen.

Phosphorus

As with nitrogen, phosphorus is first divided into available and unavailable fractions. Only a single available form, dissolved phosphate, is considered. Three forms of unavailable phosphorus are considered: dissolved organic phosphorus, labile particulate organic phosphorus, and refractory particulate organic phosphorus.

Silica

Silica is divided into two state variables: dissolved silica and particulate biogenic silica. Dissolved silica is available to diatoms while particulate biogenic silica cannot be utilized.

Chemical Oxygen Demand

Chemical oxygen demand is the concentration of reduced substances that are oxidized by abiotic processes. The primary component of chemical oxygen demand is sulfide released from sediments. Oxidation of sulfide to sulfate may remove substantial quantities of dissolved oxygen from the water column.

Dissolved Oxygen

Dissolved oxygen is required for the existence of higher life forms. Oxygen availability determines the distribution of organisms and the flows of energy and nutrients in an ecosystem. Dissolved oxygen is a central component of the water-quality model.

Salinity

Salinity is a conservative tracer that provides verification of the transport component of the model and facilitates examination of conservation of mass. Salinity also influences the dissolved oxygen saturation concentration and may be used in the determination of kinetics constants that differ in saline and fresh water.

Temperature

Temperature is a primary determinant of the rate of biochemical reactions. Reaction rates increase as a function of temperature although extreme temperatures may result in the mortality of organisms and a decrease in kinetics rates.

Fixed Solids

Fixed solids are the mineral fraction of total suspended solids. Solids are considered primarily for their role in light attenuation.

Format of Model-Data Comparisons

The Monitoring Data Base

The water quality model was applied to a ten-year time period, 1985–1994. The monitoring data base maintained by the Chesapeake Bay Program was the principal source of data for model calibration. Observations were collected at 49 stations in the bay and 89 stations in major embayments and tributaries. Sampling was conducted once or twice per month with more frequent sampling from March through October. Samples were collected during daylight hours with no attempt to coincide with tide stage or flow. At each station, salinity, temperature, and dissolved oxygen were measured in situ at one- or two-meter intervals. Samples were collected one meter below the surface and one meter above the bottom for laboratory analyses. At stations showing significant salinity stratification, additional samples were collected above and below the pycnocline. Analyses relevant to this study are listed in Table ES-2. The listed parameters are either analyzed directly or derived from direct analyses.

Comparison with the Model

Time series comparisons of computations and observations were produced at 42 locations. These were selected to provide coverage throughout the system. At least one station was selected within each of the Chesapeake Bay Program Segments represented on the grid. Within the model code, daily-average concentrations were derived from computations at discrete time steps (15 minutes). These were compared to individual observations, at surface and bottom.

The spatial distributions of observed and computed properties were compared in a series of plots along the axes of the bay and major tributaries. Three years were selected for comparisons: 1985, 1990, and 1993. The year 1985 was a low-flow year although the western tributaries were impacted by an enormous flood event in November. Flows in 1990 were characterized as average while major spring runoff occurred in 1993.

Model results and observations were averaged into four seasons:

Winter—December through February

Spring—March through May

Summer—June through August

Fall–September through November

The mean and range of the observations, at surface and bottom, were compared to the average and range of daily-average model results.

The vertical distributions of observed and computed properties were compared at selected stations in the bay and major tributaries. As with the longitudinal comparisons, selection and aggregation were required to produce a manageable volume of information. Comparisons were completed for three years and were subjected to

Table ES-2
Constituents in Model-Data Comparisons

Constituent	Time-Series	Longitudinal	Vertical
Chlorophyll >a=	X	X	
Dissolved Inorganic Nitrogen	X		
Dissolved Inorganic Phosphorus	X	X	
Dissolved Organic Nitrogen	X		
Dissolved Organic Phosphorus	X		
Dissolved Oxygen	X	X	X
Light Attenuation	X	X	
Ammonium	X	X	
Nitrate+Nitrite	X	X	
Particulate Organic Carbon	X	X	
Particulate Organic Nitrogen	X		
Particulate Phosphorus	X		
Salinity	X	X	X
Total Nitrogen	X	X	
Total Organic Carbon	X	X	
Total Phosphorus	X	X	
Total Suspended Solids	X	X	
Temperature	X		X
Dissolved Silica	X	X	

seasonal averaging as previously described. Parameters were limited to the three for which detailed vertical observations were available: temperature, salinity, and dissolved oxygen.

Zooplankton

This chapter details the formulation of zooplankton kinetics in the Chesapeake Bay Environmental Model Package. Two zooplankton groups, microzooplankton and mesozooplankton, were incorporated into the model during the tributary refinements phase.

The present model represents zooplankton biomass within 50% to 100% of observed values. Discrepancies between observations and model certainly indicate

shortcomings in the model. A large portion of the discrepancies, however, must be attributed to observational methodology and to the variance inherent in the populations. A high degree of accuracy is unlikely to be obtained but more realism and, potentially, more accuracy can be added to the model. Suggestions for improvement range from parameter re-evaluation through complete model reformulation.

A basic improvement in the model is to distinguish, through parameter values, freshwater and estuarine zooplankton populations. Differentiation between individual tributaries may also be appropriate. Differentiation of freshwater and saltwater populations is readily justified and this approach will likely prove successful.

Another potential improvement is to add a second mesozooplankton group. One group would represent the winter-spring population; the second group would represent the summer population. No doubt, these two populations exist and can be differentiated. The second group can be readily included and adds realism to the model. The potential quantitative improvement in model computations cannot be foreseen.

The final improvement is the most difficult. Add age structure to the mesozooplankton model. Adults in the present model instantaneously reproduce adults. In the most realistic model, adults would produce eggs. Eggs would hatch into larvae, mature into juveniles and, later, into adults. A model of this sort offers the highest probability of success in representing the time series of observed mesozooplankton. A multi-stage population model requires tremendous resources in programming, calibration, and execution. The additional effort is likely not worthwhile in the present multi-purpose model. The improvement is highly recommended if the present model is employed in an application that focuses largely on zooplankton.

Effects of Predation and Respiration on Primary Production

A basic Nutrient-Phytoplankton-Zooplankton (NPZ) model is used to examine effects of predation and respiration formulations on computed primary production.

Phytoplankton with Respiration Only

The simplest system contains phytoplankton and a nutrient with no predators or predation term. Gross production increases as a function of respiration over much of the range, then declines precipitously as respiration attains roughly 75% of the maximum growth rate. Net production also exhibits a curvilinear relationship to respiration with a peak at roughly 50% of the maximum growth rate. The potential increase in production along with respiration is counter-intuitive. Since biomass declines as respiration increases, a simultaneous decline in production is expected. The key is to realize that production is the product of biomass and the nutrient-limited growth rate. As respiration increases over much of its range, nutrients are released from algal biomass, the nutrient limitation to growth is relaxed, and the product of growth and biomass increases.

Phytoplankton with Zooplankton

A system which includes zooplankton but no higher-order predation terms is examined next. Algal biomass decreases rapidly and approaches zero asymtotically as predation rate is increased from the minimum feasible value. Surprisingly, zooplankton biomass also diminishes as predation rate is increased. The steady state solution indicates maximum biomass occurs at low predation rates in which zooplankton slowly feed on a large algal standing stock. Primary production responds in direct proportion to algal biomass. Maximum production occurs a minimum predation rate. The steady-state solution for the basic parameter set indicates little or no nutrient limitation. Consequently production, the product of nutrient-limited growth and biomass, responds primarily to changes in biomass.

Phytoplankton with Quadratic Predation

Predation by higher trophic levels (other than zooplankton) on phytoplankton is represented by a quadratic term in the algal mass-balance equation. Algal concentration declines as predation rate increases. Despite the decrease in algal biomass, primary production increases as predation is raised from minimum levels. The increase occurs because the nutrient limit to production is relaxed as predation liberates nutrients from algal biomass. Consequently, the product of nutrient-limited growth rate and algal biomass increases despite the decrease in biomass. The increasing trend in production continues until nutrients are no longer limiting. At that point, production declines in proportion to biomass.

Process-Based Primary Production Model

Primary production calculations in the original version of the CBEMP were consistent with characteristics of similar models. Computed production matched or exceeded observed production in the turbidity maximum region, where nutrients are abundant but light is limited. In the middle and lower portions of the bay, where light attenuation is diminished but nutrients are sparse relative to the turbidity maximum, computed production fell short of observed.

Management efforts in the Bay now require investigation of the effects of filter-feeders in reducing eutrophication, so that the amount of production available to these organisms must be represented. At the same time, water quality standards are becoming more stringent such that accurate computations of chlorophyll and nutrient concentrations cannot be ignored. Consequently, the CBEMP must now represent both properties of the system and production rates.

A primary production model is described and compared to three observational data bases: light-saturated carbon fixation, net phytoplankton primary production, and gross phytoplankton primary production. The model successfully reproduces the observations while maintaining realistic calculations of algal carbon, chlorophyll, limiting nutrient, and light attenuation. Computed primary production in light-limited regions is proportional to the algal growth rate. Successful computation of primary production in nutrient-depleted waters depends on the formulation and magnitude of the model predation term. Our quadratic formulation mimics a predator population that is closely coupled to algal biomass and rapidly recycles nutrients from algal biomass to available form.

Suspended Solids and Light Attenuation

Light Attenuation Model

We applied a model that related light attenuation to attenuation from water, from inorganic solids, and from organic solids. Model parameters were determined for each Chesapeake Bay Program Segment represented in the model domain. The result was a model in which background attenuation was highest near the freshwater sources and lowest near the ocean interface. Solids near the fall lines were characterized as having higher attenuation than solids in regions distant from sources in upland watersheds. Our light attenuation model is similar to the model developed as part of the second technical synthesis on submerged aquatic vegetation and water quality. Managers and other users of the two models, ours and "Tech Syn II," should be confident that guidance obtained from the two models will be consistent.

Suspended Solids

The principal suspended solids variable in the CBEMP was inorganic (fixed) suspended solids. Organic solids were derived from particulate carbon variables (phytoplankton, zooplankton, detritus) and added to inorganic solids for comparison to observed total suspended solids.

Aside from loads, the distribution of inorganic solids in the water column was determined by two settling velocities. One represented settling through the water column and the other represented net settling to the bed sediments. Net settling was always less than or equal to settling through the water column. The reduced magnitude of net settling represented the effect of resuspension. The employment of net settling was a primary distinction between our own suspended solids model and a true sediment transport model. Our model included no resuspension mechanism. Once a particle was deposited on the bottom, it remained there.

Recommendations

Our present efforts probably represent the state of the art in use of a water-quality model to guide management of water clarity. We recognize significant improvements in monitoring and modeling are necessary to bring modeling of water clarity up to the levels achieved in modeling nutrient cycling. The most crucial need is for a rigorous, mechanistic three-dimensional sediment transport model. The sediment transport model will accommodate the resuspension process, which is missing in the current representation. Resuspension does not constitute a new source of sediments to the system. Rather, it is a process that returns to the water column sediments that originated in external loads and as internal production. Our current net settling algorithm provides a mechanism to represent the spatial distribution of suspended solids and, especially, features like the classic turbidity maximum. The net settling algorithm is less useful, however, in the prediction of solids responses to load reductions. As currently formulated, our net settling algorithm ensures that load reductions produce reductions in computed sediment concentrations. Resuspension may, however, counter or eliminate benefits gained from load reductions. Consequently, management scenarios run with the present model represent the maximum benefit to be gained from solids load reductions.

Tributary Dissolved Oxygen

Analysis and modeling of tributary dissolved oxygen has largely focused on persistent or intermittent anoxia that occurs in bottom waters near the mouths of four major western tributaries: the York, Rappahannock, Potomac, and Patuxent. A tendency present in the model since the earliest application is the over-prediction of surface dissolved oxygen in the tributaries, especially in the tidal freshwater portions. This performance characteristic was overlooked when attention was focused on bottom waters. During the present study, sponsors noted the discrepancies between computed and observed surface dissolved oxygen concentrations and asked for improved model performance. An extensive number of calibration and sensitivity runs were performed while attempting to improve the model.

Two phenomenon vex the computation of dissolved oxygen in the western tributaries. The first is the computation of excess dissolved oxygen in the tidal fresh portions of the James and Potomac Rivers. The excess dissolved oxygen is the result of an excess of computed production over consumption. We believe the problem lies on the consumption side. Riverine organic carbon loads to the Virginia tributaries are virtually unknown as are point-source carbon loads to all tributaries. In addition, the James and Potomac receive loads from combined-sewer overflows and urban runoff. Improved dissolved oxygen computations require improved information on loading. Ideally, measures of respiration or of biochemical oxygen demand in the water column should also be conducted.

The second vexing process is the occurrence of depressed surface dissolved oxygen in the lower estuaries, notably the York, the Rappahannock, and the Potomac. Our best explanation of the phenomenon is transfer of oxygen demand and/or oxygen-depleted water from the bottom to the surface. The phenomena cannot be represented by simple adjustments vertical mixing, however. The phenomenon requires additional study and may be beyond modeling without process-based field observations.

The York, Rappahannock, and Patuxent Rivers adjoin extensive tidal wetlands which appear to influence water quality. Nutrients, as well as dissolved oxygen, are, no doubt, exchanged between wetlands and channel. To represent the wetlands physically, addition of wetting-and-drying to the hydrodynamic model is required. A wetland biogeochemical module should be added to the water quality model. And, as with so many processes, field investigations may also be necessary.

Modeling Processes at the Sediment-Water Interface

The Sediment Diagenesis Model

The need for a predictive benthic sediment model was revealed in a steady-state model study that preceded Corps' modeling activity. For management purposes, a model was required with two fundamental capabilities:

- Predict effects of management actions on sediment-water exchange processes, and
- Predict time scale for alterations in sediment-water exchange processes.

A sediment model to meet these requirements was created for the initial three-dimensional coupled hydrodynamic-eutrophication model. With some modifications, the initial sediment model is employed in the present CBEMP.

Cumulative distributions were created for the population of Chesapeake Bay sediment-water flux observations and for corresponding computations from the present model. Computed sediment oxygen demand exceeded observed throughout the distribution. Median computed demand exceeded observed by more than 0.5 g m^{-2} d^{-1}. Observed sediment ammonium release exceeded computed throughout the distribution. Median observed release exceeded modeled by 10 mg m^{-2} d^{-1}. A number of explanations can be offered for these results. The excess of sediment oxygen demand may be attributed to computed bottom dissolved oxygen. Computed bottom water dissolved oxygen does not match the lowest observations at all locations. As a result, computed sediment oxygen demand exceeds observed because the model allows consumption of oxygen where no oxygen is present in the bay. The excess of observed over computed ammonium release may indicate more nitrogen should be deposited on the bottom. Or the occasional excess of computed dissolved oxygen may be allowing more nitrification to take place in the modeled sediments than in the observations.

The preponderance of observed and computed sediment-water nitrate fluxes are essentially zero. Half the observed and computed sediment-water phosphate fluxes are less than or effectively zero. In the upper half of the distribution, the observations show a gradual transition to sediment phosphorus release while the model shows a much steeper gradient. Maximum phosphorus releases agree in both model and observations. Observed sediment silica release greatly exceeds modeled. At the median, modeled release is essentially zero while median observed release is 175 mg m^{-2} d^{-1}. Maximum observed release exceeds 600 mg m^{-2} d^{-1} while the maximum modeled release is 100 mg m-2 d^{-1}.

The Benthos Model

For the “Virginia Tributary Refinements” phase of the model activities, a decision was made to initiate direct interactive simulation of three living resource groups: zooplankton, benthos, and SAV. Benthos were included in the model because they are an important food source for crabs, finfish, and other economically and ecologically significant biota. In addition, benthos can exert a substantial influence on water quality through their filtering of overlying water. Benthos within the model were divided into two groups: deposit feeders and filter feeders. The deposit-feeding group represents benthos which live within bottom sediments and feed on deposited material. The filter-feeding group represents benthos which live at the sediment surface and feed by filtering overlying water.

Examination of present model results indicates the computation of filter feeders closely resembles the original application. Computed deposit feeders have, perhaps, increased since the original application. The increase in deposit feeders is interpreted to have negligible impact on model computations. The resemblance of results between the present model and the Tributary Refinements model indicates the activity of the benthos, as originally calibrated, is maintained in the present model.

Benthic Algae

Benthic algae are considered to occupy a thin layer between the water column and benthic sediments. Biomass within the layer is determined by the balance

between production, respiration, and losses to predation. Nutrients from diagenetic sediment production and from the overlying water are both available to the benthic algae.

Computed benthic algal biomass ranges up to 3 g C m^{-2}, in agreement with measures conducted in a variety of systems. The primary determinate of algal density is light. Algal biomass shows an inverse relationship to optical depth (total depth × light attenuation) at the sediment-water interface. No algae are computed above optical depth 5. The highest densities of computed benthic algae are found in shallow water near the mouths of the lower western tributaries, along the lower eastern shore, and in eastern embayments. Lesser densities occur in tidal fresh waters and in other shoal areas.

Submerged Aquatic Vegetation (SAV)

An SAV submodel, which interacted with the main model of the water column and with the sediment diagenesis submodel, was created for the "Virginia Tributary Refinements" phase of the model activities. Three state variables were modeled: shoots (above-ground biomass), roots (below-ground biomass), and epiphytes (attached growth). Three dominant SAV communities, *Vallisneria americana*, *Ruppia maritima*, or *Zostera marina*, were modeled.

When the phytoplankton production relationships and parameters in the present eutrophication model were revised, corresponding changes were made to the epiphyte component of the SAV model. Examination of the SAV component of the model revealed that these changes, and perhaps others, had a substantial, detrimental, effect on computed SAV. Computed epiphytes overwhelmed the vegetation. As a consequence, a re-calibration of the SAV model was completed. We endeavored to bring epiphytes and SAV back into calibration while minimizing revisions to the extensive model parameter suite. Changes were centered on the epiphyte loss terms and on the SAV production-irradiance relationships. The computations in the present model are consistent with, but not identical to, the original application. The original application obeyed light attenuation criteria listed in the first SAV Technical Synthesis. During the re-calibration we verified that the present model remains consistent with these criteria.

Dissolved Phosphate

An excess of computed dissolved phosphate, especially during summer, has been a characteristic of the model since the original phase. While tuning the model to effect an overall reduction in computed dissolved phosphate presents no problem, reducing phosphate in summer while maintaining sufficient phosphate to support the spring phytoplankton bloom is precarious.

We conducted an extensive number of sensitivity runs and process investigations in order to calibrate dissolved phosphate in the present model. The final model calibration incorporates dissolved organic phosphorus mineralization, uptake by sulfide oxidizing bacteria, and precipitation. Introduction of the two uptake mechanisms as well as alterations in multiple parameter values provided a reasonable representation of summer-average phosphate in the surface of the bay, especially during years of dry to moderate hydrology. Considerable excess of computed phosphate remained present in a wet year.

Phosphorus is a limiting nutrient in the mainstem bay in spring while nitrogen is the primary limiting nutrient in summer. Consequently, our rough approach to modeling dissolved phosphate in summer is acceptable. Still, a new phosphorus model seems appropriate, especially for management of freshwater segments where phosphorus is the more important nutrient.

The first step in a new phosphate model is to explicitly recognize phosphate uptake by heterotrophic bacteria. Bacteria do not necessarily have to be incorporated into the model as a state variable. One reviewer suggested relating phosphate uptake to organic carbon respiration, which is a bacterial process.

The second step in an improved phosphorus model is to explicitly differentiate particulate inorganic phosphorus from particulate organic phosphorus through the addition of a particulate inorganic phosphorus state variable.

A third step is to explore the utilization of dissolved organic phosphorus by bacteria and phytoplankton.

A concluding modification is to implement realistic sediment transport processes. No doubt, a distinct particulate inorganic phosphorus form exists and is transported along with the solids with which it is associated. Our ability to simulate solids transport with the present model is limited, however. Consequently, correct representation of total phosphorus is impossible when solids distributions cannot be reproduced.

Statistical Summary of Calibration

The calibration of the model involved the comparison of hundreds of thousands of observations with model results in various formats. Comparisons involved conventional water quality data, process-oriented data, and living-resources observations. The graphical comparisons produced thousands of plots which cannot be assimilated in their entirety. Evaluation of model performance requires statistical and/or graphical summaries of results.

Examination of statistical summaries (Table ES-3) requires a good deal of judgement and interpretation. Generalizations and distinctions are not always possible. One clear pattern is that the model overestimates, on average, surface chlorophyll. The overestimation ranges from less than 1 mg m^{-3} to more than 2 mg m^{-3}. The model consistently underestimates salinity although the mean error is always less than 1 ppt. For all systems except the Potomac, computed mean summer, bottom dissolved oxygen is within 1 g m^{-3} of the observed average. In the Potomac, computed mean summer bottom dissolved oxygen is almost 2 g m^{-3} higher than observed. Careful examination of model results indicates the region of greatest computed excess is in the tidal fresh portion of the river, where observed bottom dissolved oxygen exceeds 5 g m^{-3}. Excessive computed dissolved oxygen, surface and bottom, is a characteristics of the present model in most tidal freshwater regions. Except in the James, the model underestimates mean total phosphorus concentration. Underestimation of total phosphorus has been a characteristic of the model since the earliest application. We originally attributed the shortfall to omission of bankloads. In this version we include bankloads of phosphorus but they are difficult to estimate accurately. The model also omits resuspension of particulate phosphorus and has difficulty reproducing the concentration of particulate phosphorus in the turbidity maximums. In the James, we attribute the excess computed phosphorus to uncertainty in the large point-source and distributed loads to this tributary.

Table ES-2 Statistical Summary of Calibration 1985-1994						
Surface Chlorophyll, ug/L	**Mainstem Bay**	**James**	**York**	**Rappahannock**	**Potomac**	**Patuxent**
Mean Error	-0.53	-2.05	-1.68	-2.55	-1.85	-1.53
Absolute Mean Error	5.01	9.29	4.71	8.22	7.45	8.15
Relative Error	58.4	75.7	60.1	81.4	80.2	65.4
Summer, Bottom Dissolved Oxygen, mg/L	Mainstem Bay	James	York	Rappahannock	Potomac	Patuxent
Mean Error	0.32	-0.09	0.37	0.62	-1.31	-0.92
Absolute Mean Error	1.47	2.43	1.18	1.93	2.13	1.74
Relative Error	35.7	36.6	22.8	35.4	40.5	39.3
Light Attenuation, 1/m	Mainstem Bay	James	York	Rappahannock	Potomac	Patuxent
Mean Error	0.02	-0.21	0.09	-0.17	-0.02	-0.20
Absolute Mean Error	0.36	0.97	0.84	0.89	1.03	0.84
Relative Error	35.3	43.7	41.9	42.3	45.2	38.4
Salinity, ppt	Mainstem Bay	James	York	Rappahannock	Potomac	Patuxent
Mean Error	0.71	0.11	0.95	0.01	0.45	0.16
Absolute Mean Error	1.97	2.01	1.84	1.49	0.97	1.69
Relative Error	11.8	31.2	14.5	18.3	22.5	17.5
Total Nitrogen, mg/L	Mainstem Bay	James	York	Rappahannock	Potomac	Patuxent
Mean Error	0.04	-0.16	0.01	0.14	0.32	-0.13
Absolute Mean Error	0.17	0.42	0.23	0.28	0.61	0.43
Relative Error	24.3	44.6	33.1	33.8	31.9	41.5
Total Phosphorus, mg/L	Mainstem Bay	James	York	Rappahannock	Potomac	Patuxent
Mean Error	0.005	-0.021	0.012	0.001	0.032	0.041
Absolute Mean Error	0.014	0.069	0.036	0.036	0.053	0.047
Relative Error	37.6	63.8	49.2	52.6	58.9	47.6

Examination of relative errors (Table ES-3) indicates that chlorophyll has the greatest error, salinity the least. Relative error in chlorophyll prediction is 60% to 80% while relative error in salinity prediction is 10% to 20%. The chlorophyll error reflects the difficulty in computing this dynamic biological component which can attain unlimited magnitude. In contrast, salinity is purely physical and is bounded at the upper end by oceanic concentration. The remaining components are in the mid-range, 30% to 50%, with total phosphorus, perhaps exhibiting slightly higher relative error. The higher error in phosphorus reflects the aforementioned difficulties in evaluating loads, in simulating resuspension, and in representing particulate phosphorus transport.

The mainstem bay is clearly superior in computations of salinity, total nitrogen, and total phosphorus. The James River stands out as demonstrating the highest

relative error in these components. We partially attribute the greater accuracy in the mainstem to the relatively dense computational grid in this region. An additional, and probably more significant influence, is that the mainstem is dominated by internal processes while the tributaries are strongly influenced by point-source and distributed loads. The point-source loads are incompletely described, especially in the early years of the simulation and in the Virginia tributaries. Below-fall-line distributed loads cannot be measured; they can only be computed by the watershed model. We believe the uncertain loads, discharged into the constrained volumes of the tributaries, are the major reason for higher relative error in the tributaries. The James River stands out in this regard.

1 Introduction

Deterioration of water quality in Chesapeake Bay (Figure 1-1) and associated losses of living resources have been recognized as problems for more than twenty years (Flemer et al. 1983). An order-of-magnitude increase in anoxic volume and a catastrophic decline in submerged aquatic vegetation (SAV) were among the primary problems cited. Two decades later, elimination of anoxia and restoration of SAV remain prime management goals. Models have been employed as tools to guide management since the formation of the first water quality targets. Over time, as management focus has been refined, models have been improved to provide appropriate, up-to-date guidance.

Three models are at the heart of the Chesapeake Bay Environmental Model Package (CBEMP). Distributed flows and loads from the watershed are computed with a highly-modified version of the HSPF model (Bicknell et al. 1996). These flows are input to the CH3D-WES hydrodynamic model (Johnson et al. 1993) which computes three-dimensional intra-tidal transport. Computed loads and transport are input to the CE-QUAL-ICM eutrophication model (Cerco and Cole 1993) which computes algal biomass, nutrient cycling, and dissolved oxygen, as well as numerous additional constituents and processes. The eutrophication model incorporates a predictive sediment diagenesis component (DiToro and Fitzpatrick 1993). The first coupling of these models simulated the period 1984-1986. Emphasis in the model application was on examination of bottom-water anoxia. Results indicated a decision to reduce controllable nutrient input by 40% (Baliles et al. 1987) would reduce anoxic volume by 20%.

Circa 1992, management emphasis shifted from dissolved oxygen, a living-resource indicator, to living resources themselves. In response, the computational grid was refined to emphasize resource-rich areas (Wang and Johnson 2000) and living resources including benthos (Meyers et al. 2000), zooplankton (Cerco and Meyers 2000), and submerged aquatic vegetation (Cerco and Moore 2001) were added to the model. The simulation period was extended from 1985 to 1994.

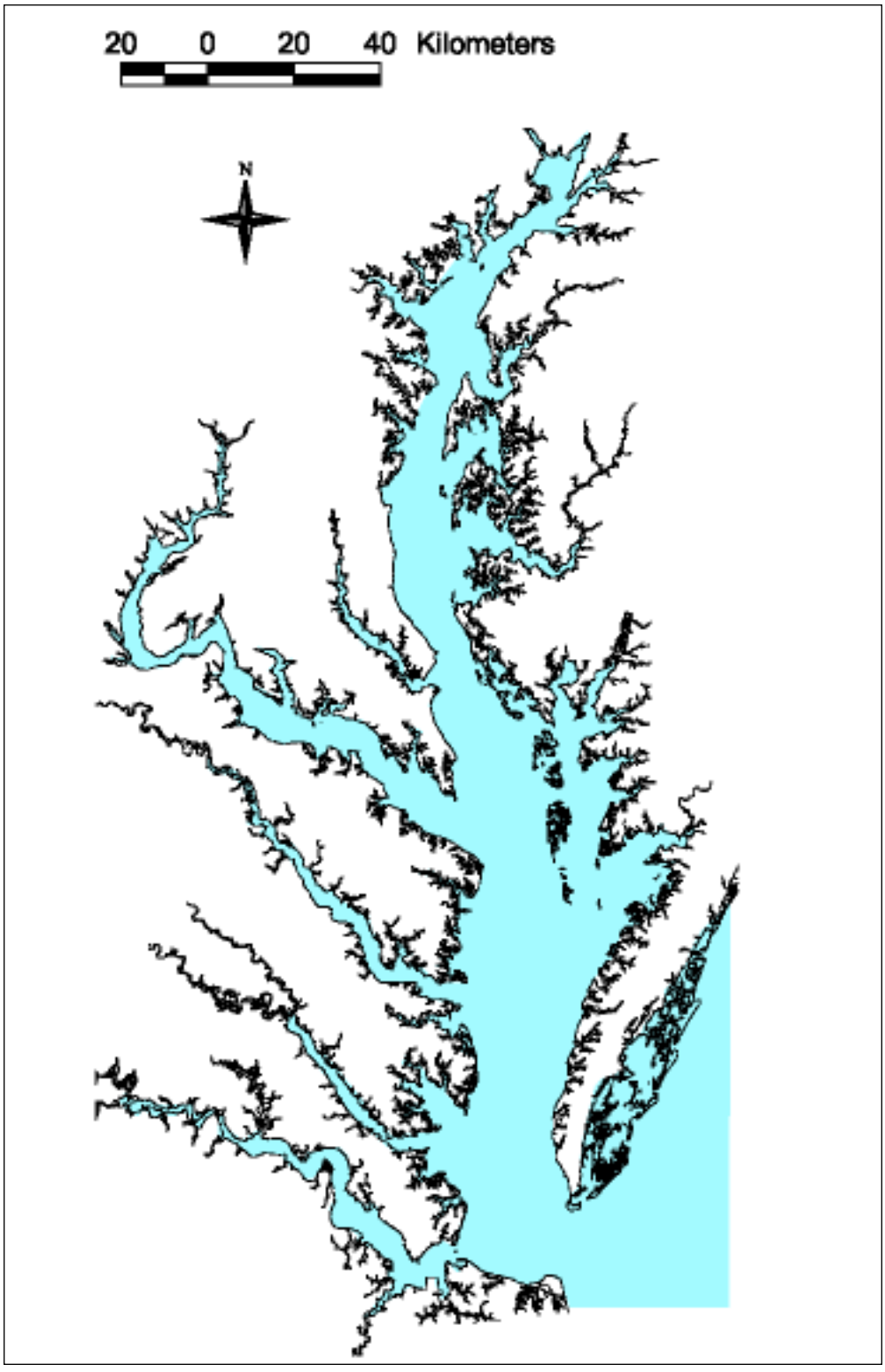

FIGURE 1-1. Chesapeake Bay

During this modeling phase, fixed solids were identified as major components of light attenuation. Reductions in attenuation achieved solely through nutrient controls on phytoplankton could not restore submerged aquatic vegetation system-wide (Cerco and Moore 2001; Cerco et al. 2002).

In keeping with the emphasis on living resources, the Chesapeake 2000 Agreement (Gilmore et al. 2000) called for a ten-fold increase in biomass of oysters and other filter feeding organisms. In response, the computational grid was further refined and plans were made to incorporate new living resources into the model. At the same time, regulatory forces were shaping the direction of management efforts. Regulatory agencies in Maryland listed the state's portion of Chesapeake Bay as "impaired." The US Environmental Protection Agency added bay waters within Virginia to the impaired list. Settlement of a lawsuit required development of a Total Maximum Daily Load (TMDL) for Virginia waters by 2011. To avoid imposition of an arbitrary TMDL, the Chesapeake 2000 Agreement specified removal of water quality impairments by 2010. Impairments in the bay were defined as low dissolved oxygen, excessive chlorophyll concentration and diminished water clarity. Management emphasis shifted from living resources back to living-resource indicators: dissolved oxygen, chlorophyll, and clarity. A model recalibration was undertaken, with emphasis on improved accuracy in the computation of the three key indicators.

The 2002 Chesapeake Bay Environmental Model Package

The framework of the original CBEMP remains intact although the components have been substantially modified and improved over fifteen years. The watershed model is now in Phase 4.3 (Linker et al. 2000). Documentation may be found may be found on the Chesapeake Bay Program web site http://www.chesapeakebay.net/modsc.htm. Nutrient and solids loads are computed on a daily basis for 94 sub-watersheds of the 166,000 km^2 Chesapeake Bay watershed and are routed to individual model cells based on local watershed characteristics and on drainage area contributing to the cell. The hydrodynamic and eutrophication models operate on a grid of 13,000 cells. The grid contains 2,900 surface cells (4 km^2) and employs non-orthogonal curvilinear coordinates in the horizontal plane. Z coordinates are used in the vertical direction which is up to 19 layers deep. Depth of the surface cells is 2.1 m at mean tide and varies as a function of tide, wind, and other forcing functions. Depth of sub-surface cells is fixed at 1.5 m. A band of littoral cells, 2.1 m deep at mean tide, adjoins the shoreline throughout most of the system. Ten years, 1985-1994, are simulated continuously using time steps of 5 minutes (hydrodynamic model) and 15 minutes (eutrophication model).

Expert Panels

Expert review has been part of the model activity since its commencement. For the present study, several "Expert Panels" were assembled to review various aspects of the model application. These teams were:

Hydrodynamics Expert Panel

Dr. Richard Garvine
College of Marine Studies
University of Delaware, Newark DE

Dr. Albert Y. Kuo
Virginia Institute of Marine Science
College of William and Mary, Gloucester Point, VA

Dr. Lawrence P. Sanford
University of Maryland Center for Environmental Science
Horn Point Laboratory, Cambridge MD

Primary Production Expert Panel

Dr. Lawrence W. Harding
University of Maryland Center for Environmental Science
Horn Point Laboratory, Cambridge MD

Dr. Raleigh Hood
University of Maryland Center for Environmental Science
Horn Point Laboratory, Cambridge MD

Dr. W. Michael Kemp
University of Maryland Center for Environmental Science
Horn Point Laboratory, Cambridge MD

Total Maximum Daily Load Expert Panel

Dr. Kevin Farley
Department of Environmental Engineering
Manhattan College, Riverdale NY

Dr. Wu-Seng Lung
Department of Environmental Engineering
University of Virginia, Charlottesville VA

We gratefully acknowledge the advice and assistance provided by our experts. Successful completion of this study would not have been possible without them.

This Report

This report comprises the primary documentation of the eutrophication component of the 2002 CBEMP. The Chesapeake Bay model study has been extensively documented since its earliest stages. We concentrate here on portions of the model that have undergone major revisions and on portions that have not been previously documented. Aspects of the model that proved particularly troublesome are documented for reference against future improvements. We have minimized repetition of previously-reported information and model results. The reader is referred to the Bibliography, below, and to the EPA Chesapeake Bay Program web site, http://www.chesapeakebay.net/modsc.htm, for additional information.

Bibliography

Baliles, G., Schaefer, W., Casey, R., Thomas, L., Barry, M., and Cole, K. (1987). "*Chesapeake Bay Agreement*." United States Environmental Protection Agency Chesapeake Bay Program, Annapolis MD.

Bicknell, B., Imhoff, J., Kittle, J., Donigian, A., Johanson, R., and Barnwell, T. (1996). "Hydrologic simulation program - FORTRAN user's manual for release 11," United States Environmental Protection Agency Environmental Research Laboratory, Athens GA.

Cerco, C., and Cole, T. (1993). "Three-dimensional eutrophication model of Chesapeake Bay," *Journal of Environmental Engineering*, 119(6), 1006-10025.

Cerco, C., and Cole, T. (1994). "Three-dimensional eutrophication model of Chesapeake Bay," Technical Report EL-94-4, US Army Engineer Waterways Experiment Station, Vicksburg, MS.

Cerco, C. (1995a). "Simulation of long-term trends in Chesapeake Bay eutrophication," *Journal of Environmental Engineering*, 121(4), 298-310.

Cerco, C. (1995b). "Response of Chesapeake Bay to nutrient load reductions," *Journal of Environmental Engineering*, 121(8), 549-557.

Cerco, C., and Cole, T. (1995). "User's guide to the CE-QUAL-ICM three-dimensional eutrophication model," Technical Report EL-95-15, US Army Engineer Waterways Experiment Station, Vicksburg, MS.

Cerco, C. (2000). "Phytoplankton kinetics in the Chesapeake Bay model," *Water Quality and Ecosystem Modeling*, 1, 5-49.

Cerco, C., and Meyers, M. (2000). "Tributary refinements to the Chesapeake Bay Model," *Journal of Environmental Engineering*, 126(2), 164-174.

Cerco, C., and Moore, K. (2001). "System-wide submerged aquatic vegetation model for Chesapeake Bay," *Estuaries*, 24(4), 522-534.

Cerco, C., Linker, L., Sweney, J., Shenk, G., and Butt, A. (2002). "Nutrient and solids controls in Virginia's Chesapeake Bay tributaries," *Journal of Water Resources Planning and Management*, 128(3), 179-189.

Cerco, C., Johnson, B., and Wang, H. (2002). "Tributary refinements to the Chesapeake Bay model," ERDC TR-02-4, US Army Engineer Research and Development Center, Vicksburg, MS.

Cerco, C., and Noel, M. (2003). "Managing for water clarity in Chesapeake Bay," *Journal of Environmental Engineering*, in press.

DiToro, D., and Fitzpatrick, J. (1993). “Chesapeake Bay sediment flux model,” Contract Report EL-93-2, US Army Engineer Waterways Experiment Station, Vicksburg, MS.

DiToro, D. (2001). *Sediment Flux Modeling*, John Wiley and Sons, New York.

Flemer, D., Mackiernan, G., Nehlsen, W., and Tippie, V. (1983). “Chesapeake Bay: A profile of environmental change,” U.S. Environmental Protection Agency, Region III, Philadelphia, PA.

Gillmore, J., Glendening, P., Ridge, T., Williams, A., Browner, C., and Bolling, B. (2000). “Chesapeake 2000 Agreement.” United States Environmental Protection Agency Chesapeake Bay Program, Annapolis MD.

HydroQual Inc., (2000). “Development of a suspension feeding and deposit feeding benthos model for Chesapeake Bay,” Project No. USCE0410, HydroQual Inc., Mahwah NJ.

Johnson, B., Heath, R., Hsieh, B., Kim, K., and Butler, L. (1991). “Development and verification of a three-dimensional numerical hydrodynamic, salinity, and temperature model of Chesapeake Bay,” HL-91-7, US Army Engineer Waterways Experiment Station, Vicksburg, MS.

Johnson, B., Kim, K., Heath, R., Hsieh, B., and Butler, L. (1993). “Validation of a three-dimensional hydrodynamic model of Chesapeake Bay,” *Journal of Hydraulic Engineering*, 199(1), 2-20.

Linker, L., Shenk, G., Dennis, R., and Sweeney, J. (2000). “Cross-media models of the Chesapeake Bay watershed and airshed,” *Water Quality and Ecosystem Modeling*, 1(1-4), 91-122.

Meyers, M., DiToro, D., and Lowe, S. (2000). “Coupling suspension feeders to the Chesapeake Bay eutrophication model,” *Water Quality and Ecosystem Modeling*, 1(1-4), 123-140.

Wang, H., and Johnson, B. (2000). “Validation and application of the second-generation three-dimensional hydrodynamic model of Chesapeake Bay,” *Water Quality and Ecosystem Modeling*, 1(1-4), 51-90.

Coupling with the Hydrodynamic Model 2

Introduction

Modeling the physics, chemistry, and biology of the Bay required a package of models. Transport processes were modeled by a three-dimensional hydrodynamic model that operated independently of the water quality model. Transport information from the hydrodynamic model was processed and stored on-line for subsequent use by the water quality model.

The Hydrodynamic Model

CH3D-WES

The CH3D-WES (Computational Hydrodynamics in Three Dimensions—Waterways Experiment Station) hydrodynamic model was a substantially revised version of the CH3D model originally developed by Sheng (1986). Model formulation was based on principles expressed by the equations of motion, conservation of volume, and conservation of mass. Quantities computed by the model included three-dimensional velocities, surface elevation, vertical viscosity and diffusivity, temperature, salinity, and density. Details of the model formulation and initial application to Chesapeake Bay were presented by Johnson et al. (1991).

Computational Grid

The basic equations of CH3D-WES were solved via the finite-difference method. The finite-difference solution algorithm replaced continuous derivatives in the governing differential equations with ratios of discrete quantities. Solutions to the hydrodynamics were obtained using five-minute intervals for the discrete time steps. The spatial continuum of the Bay was divided into a grid of discrete cells. To achieve close conformance of the grid to Bay geometry, cells were represented in curvilinear rather than rectangular coordinates. A z-plane grid was employed in

which the number of vertical layers varied depending on local depth. Velocities were computed on the boundaries between cells. Temperature, salinity, and density were computed at the center of each cell.

The computational grid extended from the heads of tide of major bay tributaries out onto the continental shelf (Figure 2-1). The shelf portion of the grid (30 x 150 km) was sized to capture large-scale circulation features outside the bay mouth. The grid contained 2961 cells, roughly 4 km^2 in area, in the surface plane (Figures 2-1, 2-2). Number of cells in the vertical ranged from one to nineteen (Figure 2-3). The maximum depth was in the shelf portion of the grid. Within the bay, maximum number of layers was seventeen. Surface cells were 2.14 m thick at mean tide. Variations in surface level caused by tides, wind, and other forcings were represented by computed variations in thickness of the surface layer. Thickness of all sub-surface cells was fixed at 1.53 m. Total number of cells in the grid was 12,920.

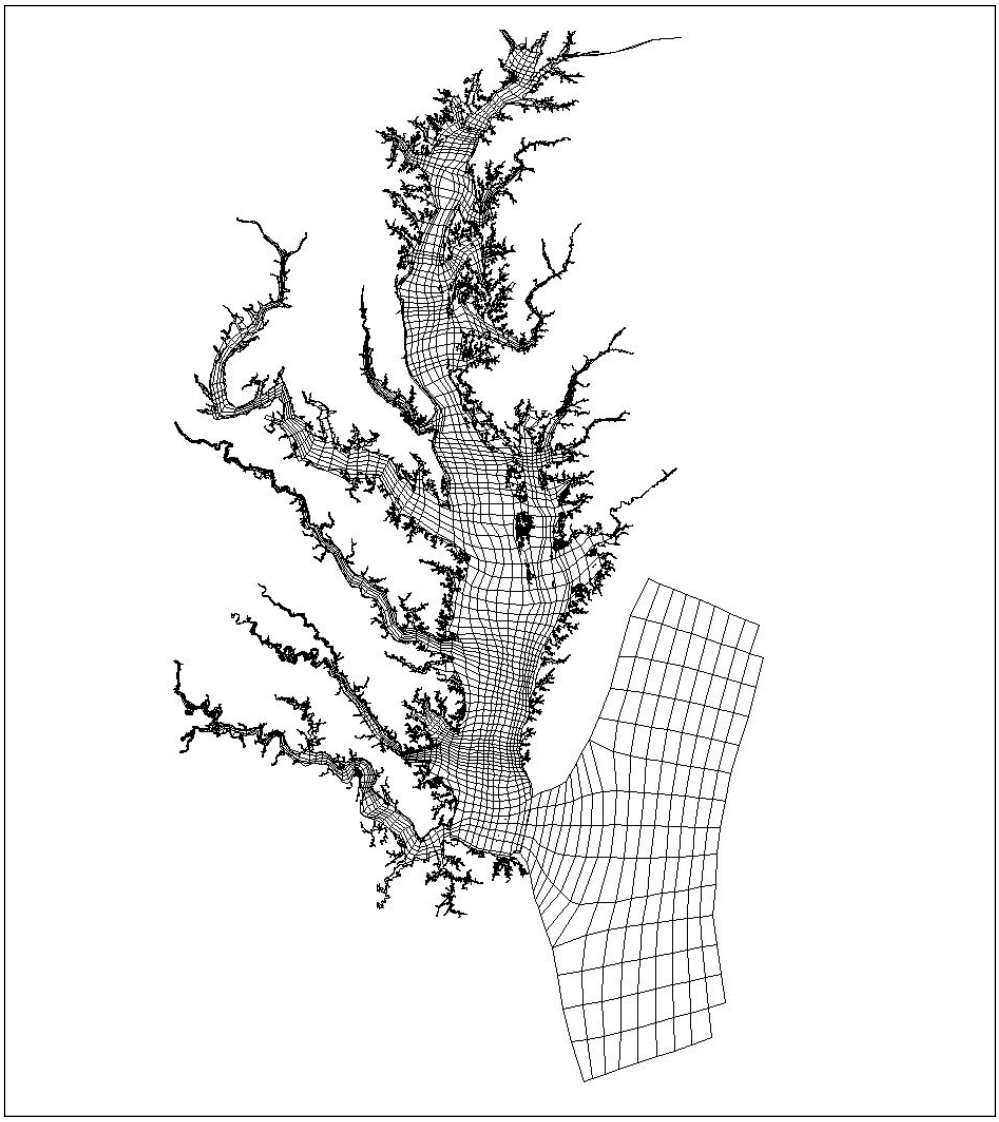

Figure 2-1. The computational grid

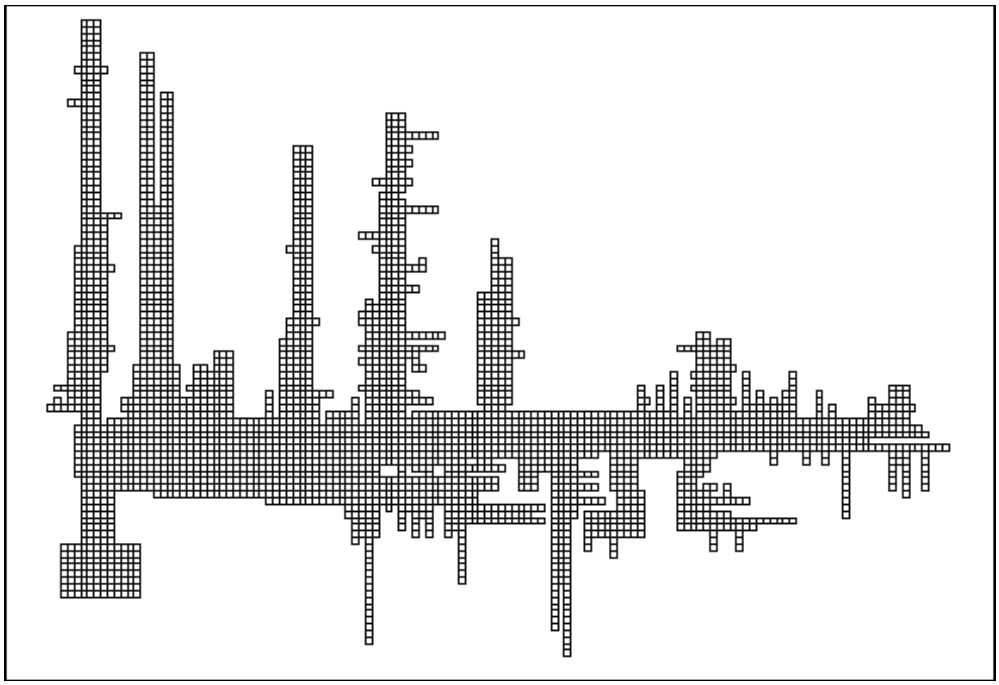

Figure 2-2. The computational grid in transformed coordinates.

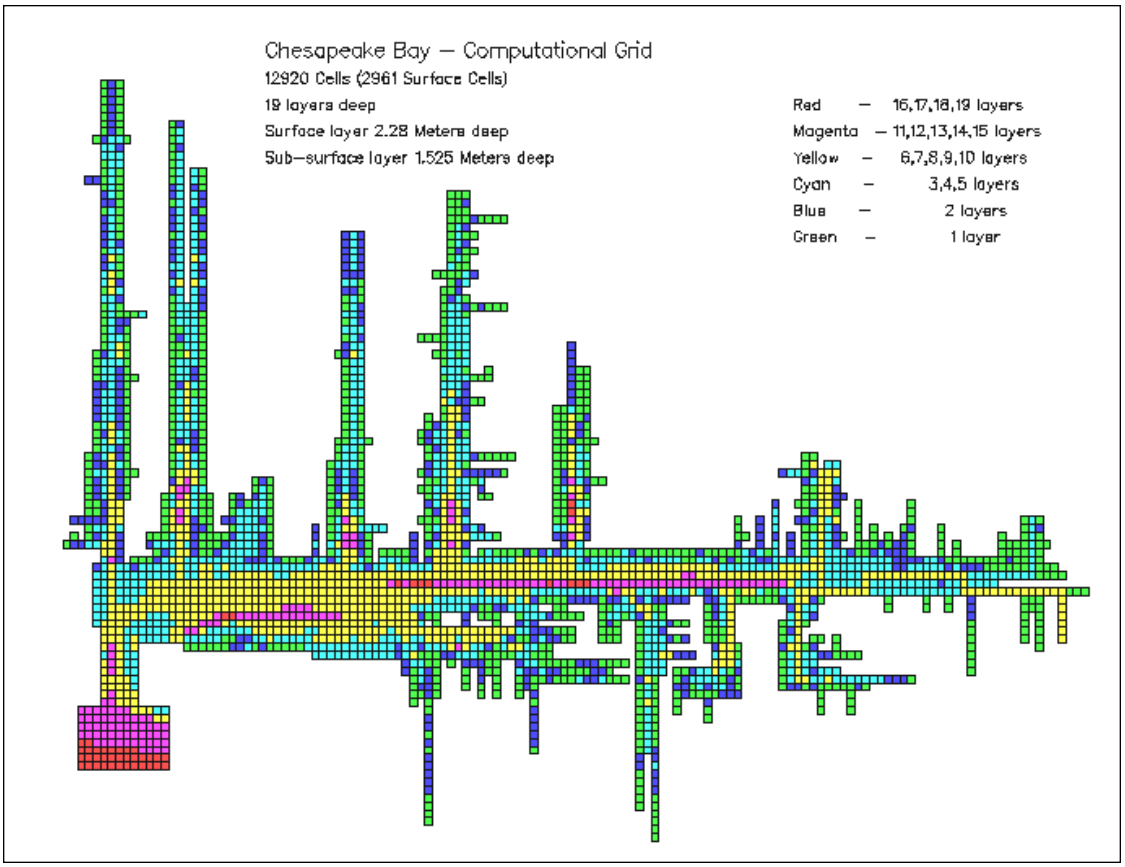

Figure 2-3. Number of cells in water column

Calibration and Verification

The hydrodynamic model was calibrated and verified against a large body of observed tidal elevations, currents, and densities. Details of the calibration procedure were presented by Johnson and Nail (2001).

Linkage to the Water Quality Model

Hydrodynamics for employment in the water quality model were produced for ten years, 1985–1994. Each year was a single, continuous production run. Initial temperature and salinity for the first year were derived from observations. The initial hydrodynamic field was obtained from a five-day spin-up period. Thereafter, initial conditions for each year were taken from conditions computed at the end of the previous year. Consequently, the hydrodynamic simulation was effectively a continuous ten-year run, initialized only once.

Computed flows, surface elevations, and vertical diffusivities were output at two-hour intervals for use in the water quality model. The two-hour hydrodynamics were determined as arithmetic means of hydrodynamics computed on a five-minute basis. The use of intra-tidal hydrodynamics contrasted with the earliest model application (Cerco and Cole 1994) in which Lagrangian-average hydrodynamics were stored at 12.4-hour intervals (Dortch et al. 1992).

The algorithms and codes for linking the hydrodynamic and water quality models were developed over a decade ago (Dortch 1990) and have been tested and proved in extensive applications since then. In every model application, the linkage is verified by comparing transport of a conservative substance computed in each model. For estuarine applications, the transport tests commonly take the form of comparing salinity computed by two models. In the present application, salinity comparisons verify that the hydrodynamic and water quality models are correctly coupled (Figures 2-4, 2-5) and that transport processes in the two models are virtually identical.

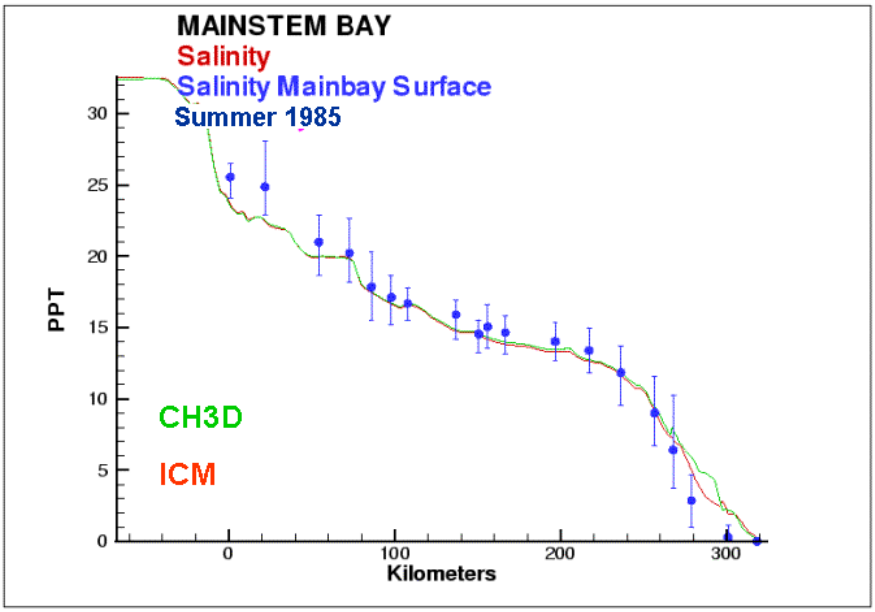

Figure 2-4. Surface salinity along Chesapeake Bay axis computed by hydrodynamic and water quality models.

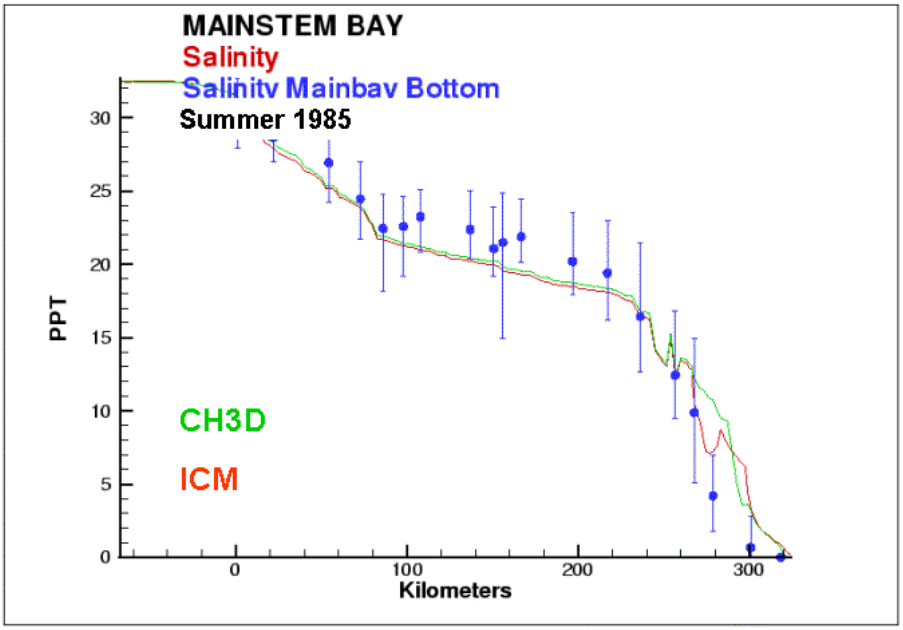

Figure 2-5. Bottom salinity along Chesapeake Bay axis computed by hydrodynamic and water quality models.

Vertical Diffusion

One of the first steps in the present application was the comparison of model results on the new grid with results on the previous grid, used for the Virginia Tributary Refinements (Cerco et al. 2002). Model code, parameters, and loads were identical. Only the grids differed. On the new grid, dissolved oxygen computed at the bottom of the bay differed substantially from computations on the previous grid (Figure 2-6). Origin of the discrepancy was eventually traced to the algorithm used to compute vertical diffusion in the hydrodynamic model. The algorithm was undergoing revision as part of the application to a new grid and a general re-verification of the hydrodynamic model.

Once the importance of the vertical diffusion algorithm was apparent, sensitivity analyses were conducted within both the hydrodynamic and water quality models. The models were run for two years, 1985 and 1986, and assessments were largely based on seasonal-average salinity and dissolved oxygen computations.

Formulation

The hydrodynamic model computed vertical viscosity (or friction) from first principles using a two-equation turbulence closure scheme (Johnson et al. 1991). Vertical diffusivity was determined through the Prandtl number. The Prandtl number is the ratio of turbulent momentum transport to turbulent mass transport. In unstratified water, the Prandtl number is commonly taken as unity. In stratified water, turbulent mass transport is retarded more than momentum transport. A

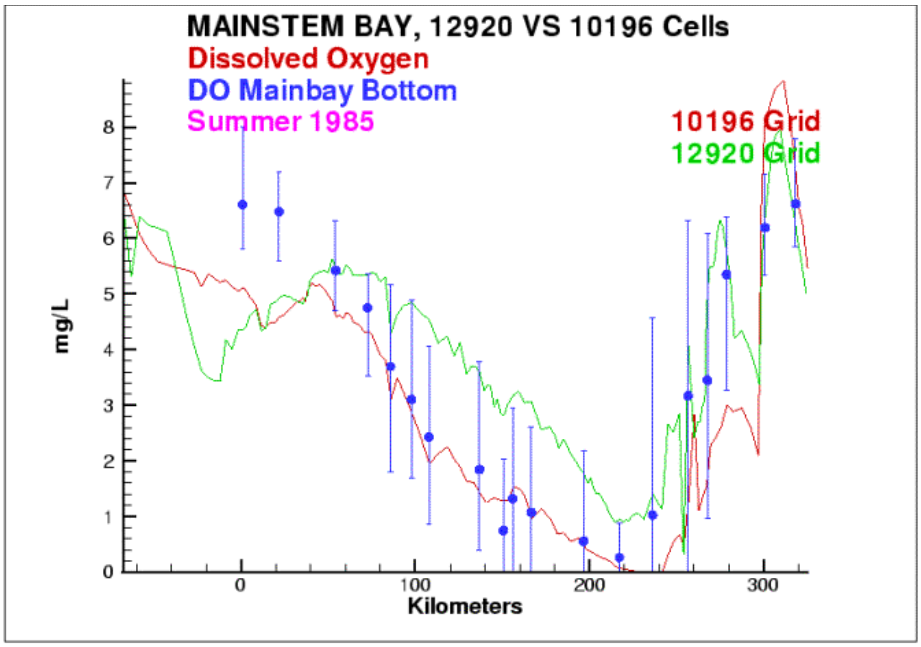

Figure 2-6. Bottom dissolved oxygen computed along bay axis on two grids.

variety of formulations have been proposed to describe the effect of stratification on Prandtl number. Formulations tested in the hydrodynamic model included the Bloss formulation (Bloss et al. 1988):

$$D_Z = \frac{A_Z}{1 + 3 \bullet R_I^2} \tag{2-1}$$

in which:
D_Z = vertical diffusivity ($cm^2\ s^{-1}$)
A_Z = vertical viscosity ($cm^2\ s^{-1}$)
R_I = Richardson number

and the Munk-Anderson relationship (Munk and Anderson 1948):

$$D_Z = A_Z \bullet \frac{(1 + R_I)^{1/2}}{\left(1 + \frac{10}{3} \bullet R_I\right)^{3/2}} \tag{2-2}$$

The Richardson number is defined:

$$R_I = -\frac{g}{\rho} \bullet \frac{\delta\rho\ /\ \delta Z}{(\delta U\ /\ \delta Z)^2} \tag{2-3}$$

in which:
g = gravitational acceleration ($cm^2\ s^{-1}$)
ρ = density of water ($g\ cm^{-3}$)
U = horizontal velocity ($cm\ s^{-1}$)
Z = vertical distance (cm)

The Richardson number represents the ratio of turbulence suppression, via vertical density gradient, to turbulence creation, via velocity shear. For any Richardson number, the Bloss relationship provides lower vertical diffusivity than the Munk-Anderson relationship (Figure 2-7).

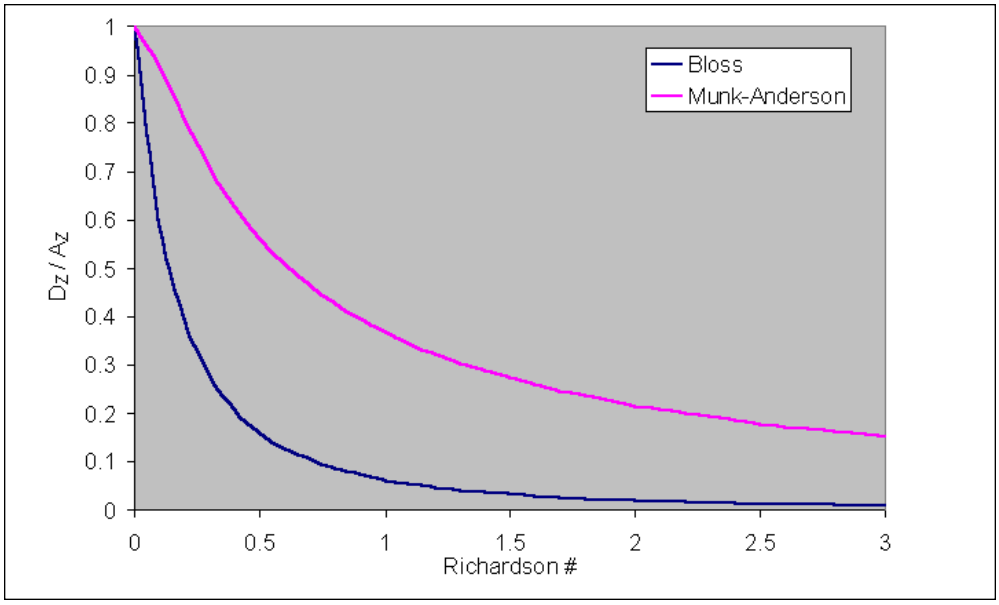

Figure 2-7. The effect of Bloss and Munk-Anderson formulations on vertical diffusivity.

Hydrodynamic Model Results

Within the mainstem of Chesapeake Bay, visual assessment indicated the Bloss relationship provided more favorable salinity computations (Figure 2-8). Salinity computed using the Munk-Anderson relationship averaged 1.5 ppt lower than using the Bloss relationship (Table 2-1). The mean difference between computed and observed salinity was lower for the Bloss relationship although the root-mean-square salinity error computed using the Bloss and Munk- Anderson relationships was equivalent.

Within the tributaries, the difference in computed salinity based on the alternate formulations was difficult to judge. Results suggested the Munk-Anderson relationship provided superior results in the James River (Figure 2-9). Elsewhere, no relationship was clearly superior to the other (Figures 2-10 to 2-13).

Water Quality Model Results

Computed summer bottom dissolved oxygen was universally 1 gm m^{-3} lower using the Bloss relationship versus Munk-Anderson. In the bay (Figure 2-14) and Potomac (Figure 2-18), the Bloss relationship clearly provided superior computations of bottom dissolved oxygen. In the James, the higher dissolved oxygen computations computed by the Munk-Anderson relationship were closer to observed (Figure 2-15). Elsewhere, neither relationship could be judged clearly superior (Figures 2-16, 2-17, 2-19).

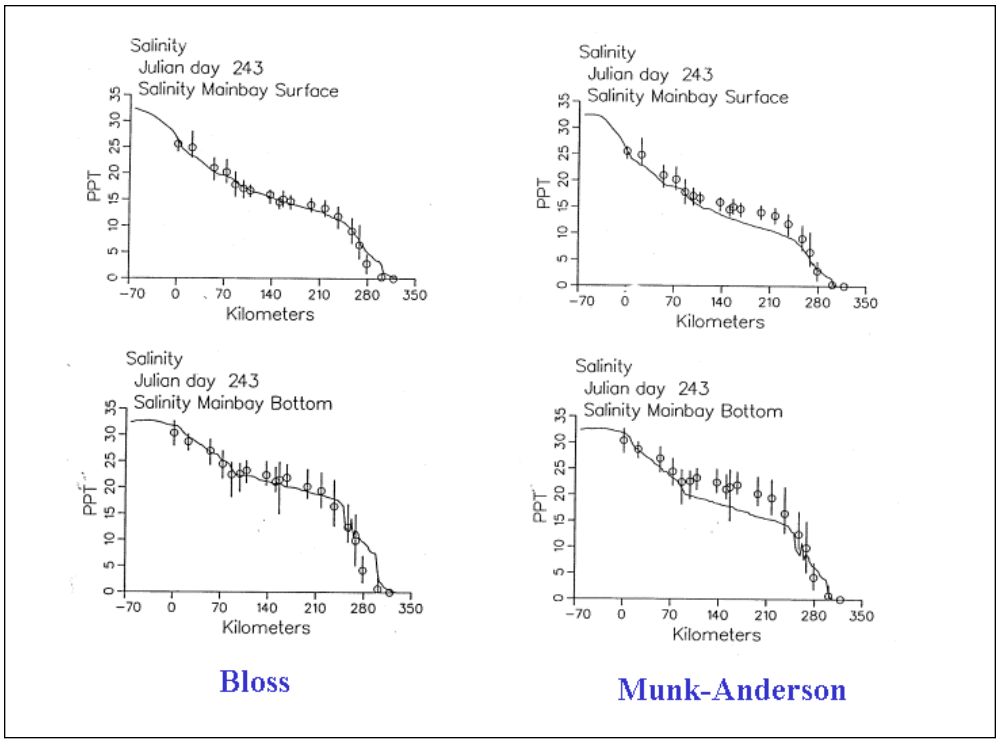

Figure 2-8. Computed salinity along the axis of Chesapeake Bay, summer 1985, for the Bloss (left) and Munk-Anderson (right) relationships.

Table 2-1. Statistical Comparison of Computations on Different Grids and with Different Formulations for Prandtl Number

	Salt, ppt		**DO, mg/L**		**Temperature, C**	
	Mean Error	RMS Error	Mean Error	RMS Error	Mean Error	RMS Error
10,000 cell, VA Trib Refinements	-0.99	2.78	0.005	1.88	0.74	1.93
12,000 cell with Bloss scheme	-0.27	2.78	-0.057	1.97	0.69	1.77
12,000 cell with Munk-Anderson scheme	1.1	2.82	-0.45	1.9	0.67	1.65

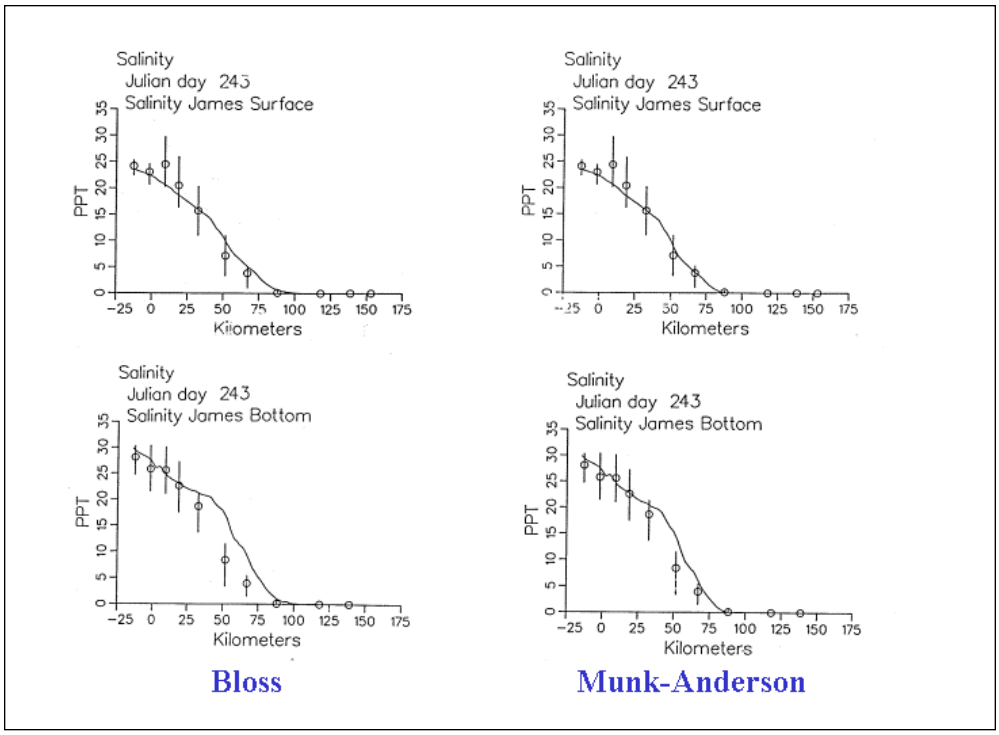

Figure 2-9. Computed salinity along the James River axis, summer 1985, for the Bloss (left) and Munk-Anderson (right) relationships.

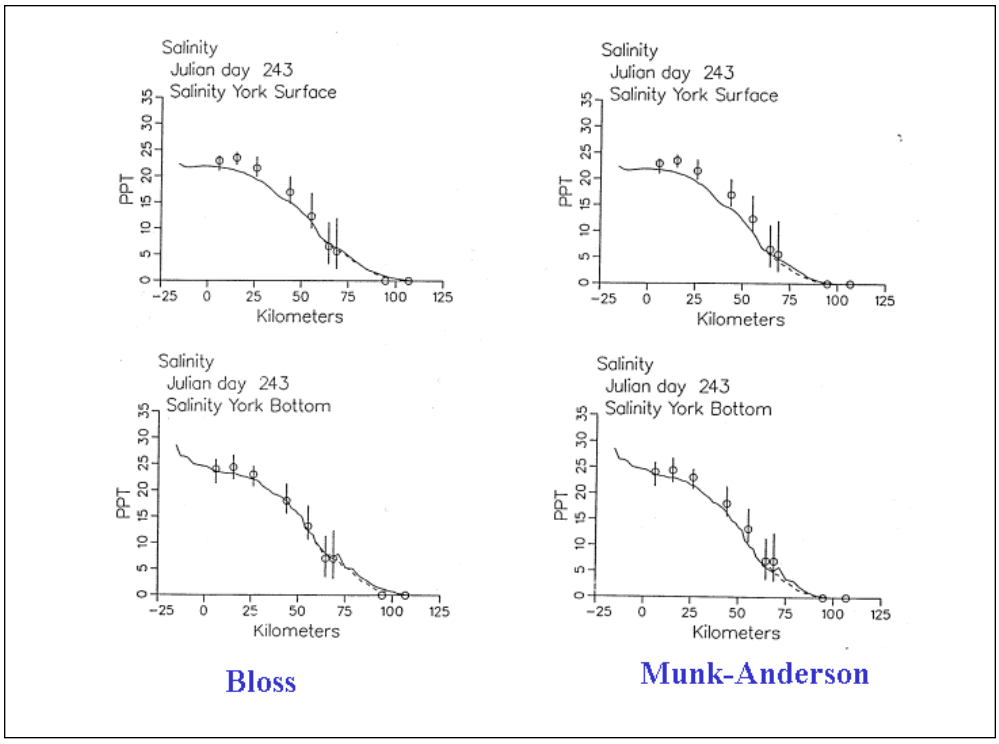

Figure 2-10. Computed salinity along the York River axis, summer 1985, for the Bloss (left) and Munk-Anderson (right) relationships.

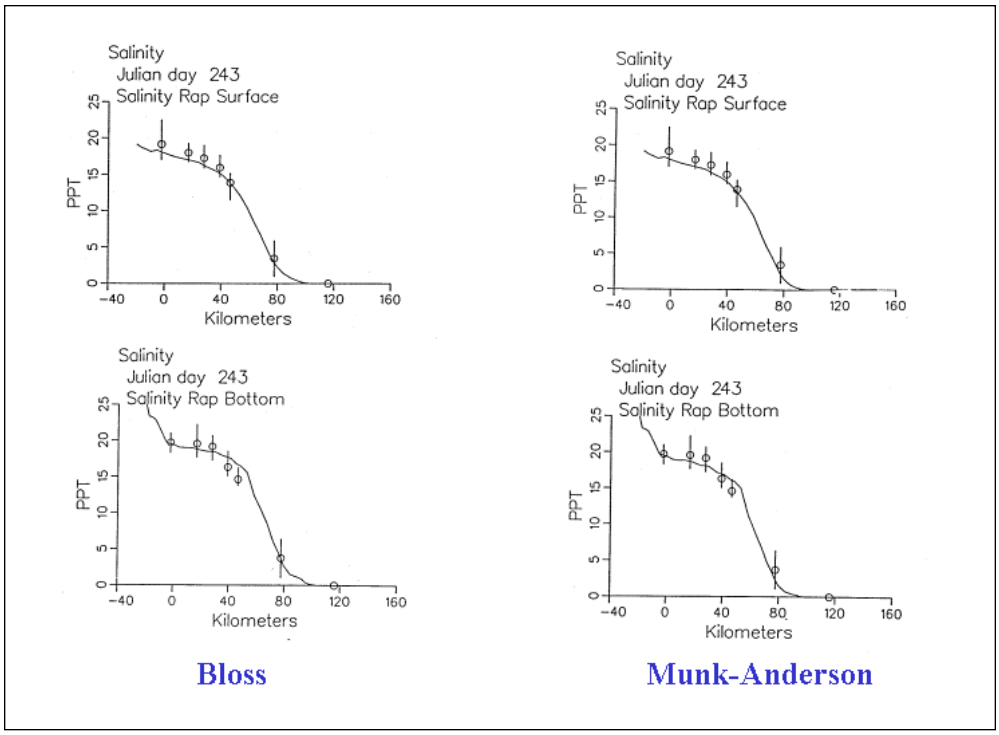

Figure 2-11. Computed salinity along the Rappahannock River axis, summer 1985, for the Bloss (left) and Munk-Anderson (right) relationships.

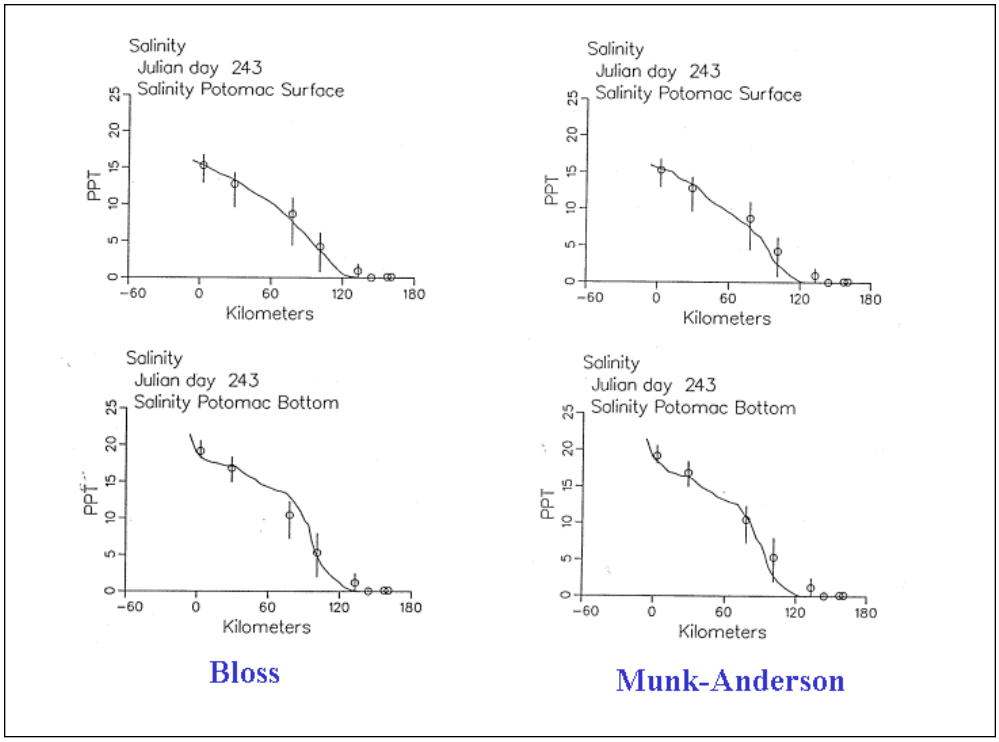

Figure 2-12. Computed salinity along the Potomac River axis, summer 1985, for the Bloss (left) and Munk-Anderson (right) relationships.

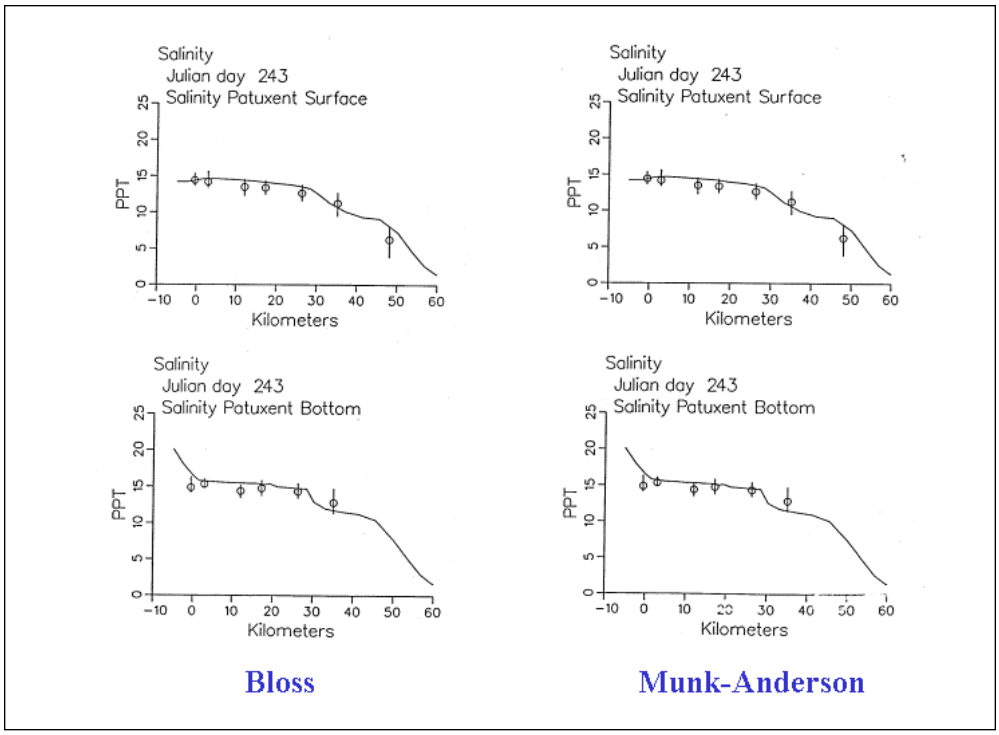

Figure 2-13. Computed salinity along the Patuxent River axis, summer 1985, for the Bloss (left) and Munk-Anderson (right) relationships.

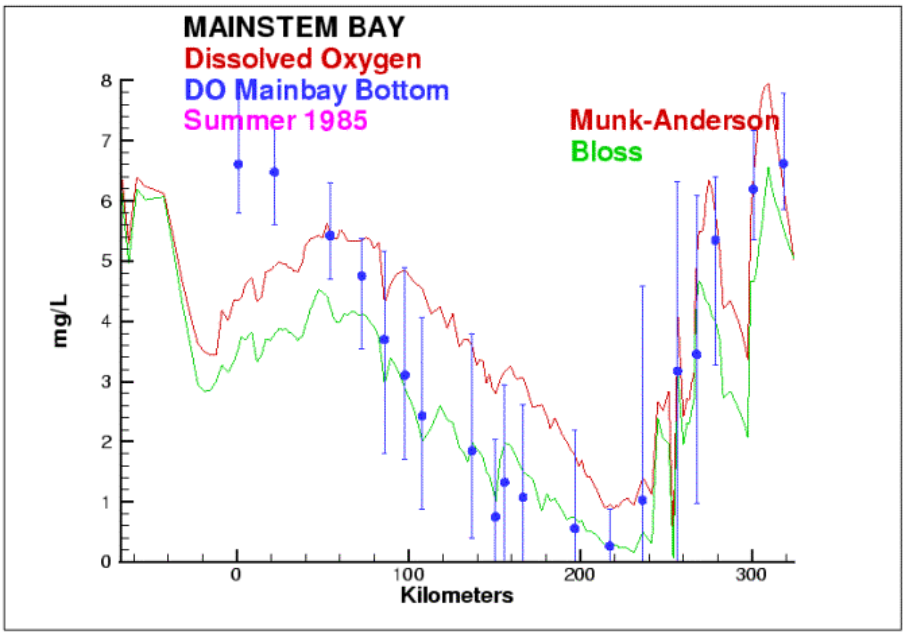

Figure 2-14. Computed bottom dissolved oxygen along the axis of Chesapeake Bay, summer 1985, for the Bloss and Munk-Anderson relationships.

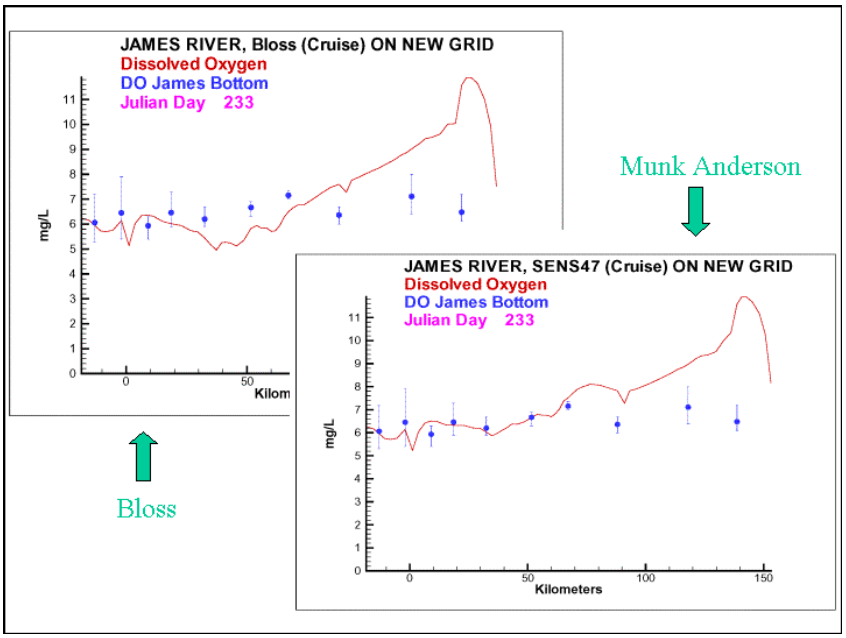

Figure 2-15. Computed bottom dissolved oxygen along the James River axis, summer 1985, for the Bloss (left) and Munk-Anderson (right) relationships.

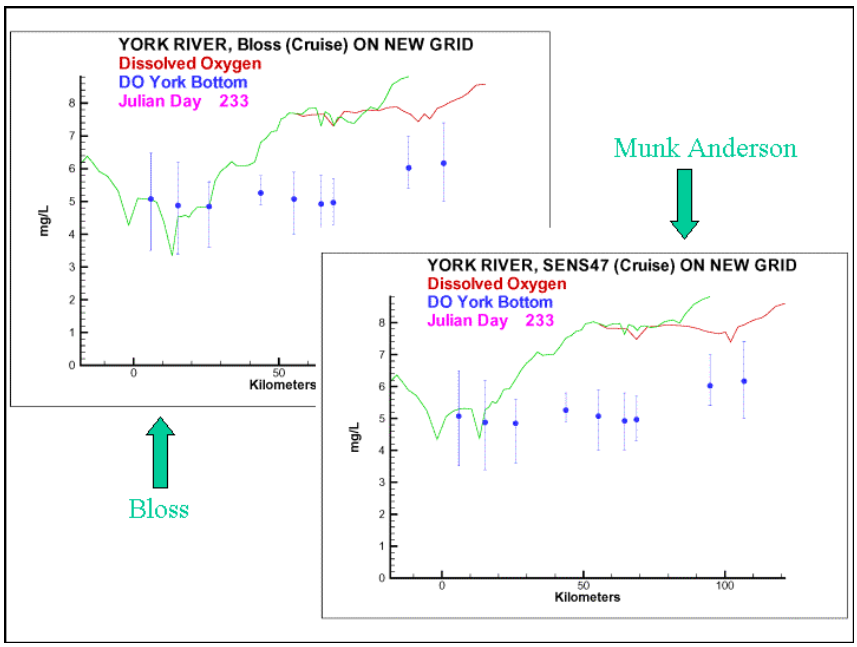

Figure 2-16. Computed bottom dissolved oxygen along the York River axis, summer 1985, for the Bloss (left) and Munk-Anderson (right) relationships.

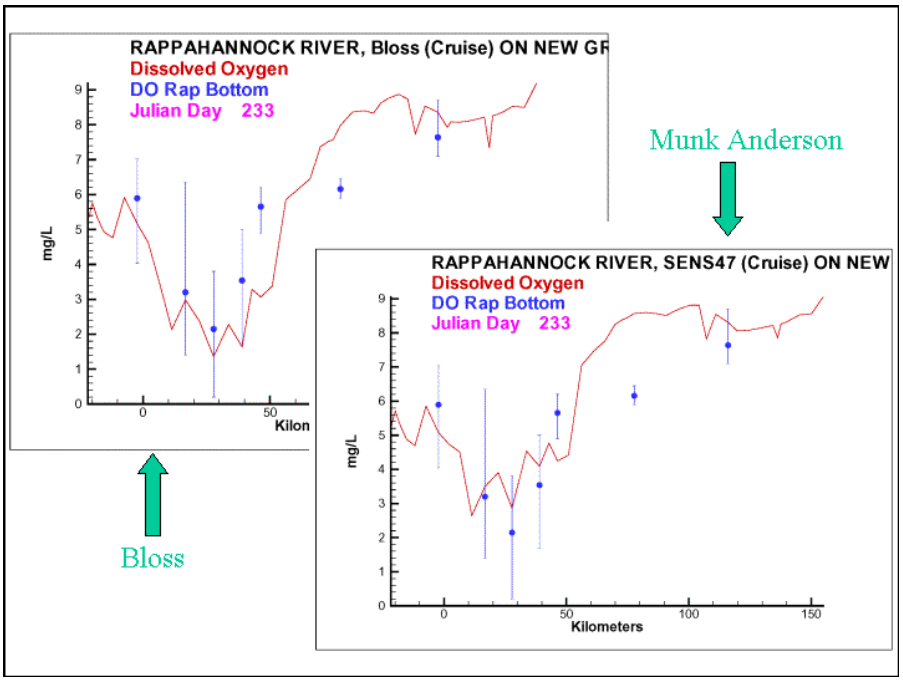

Figure 2-17. Computed bottom dissolved oxygen along the Rappahannock River axis, summer 1985, for the Bloss (left) and Munk-Anderson (right) relationships.

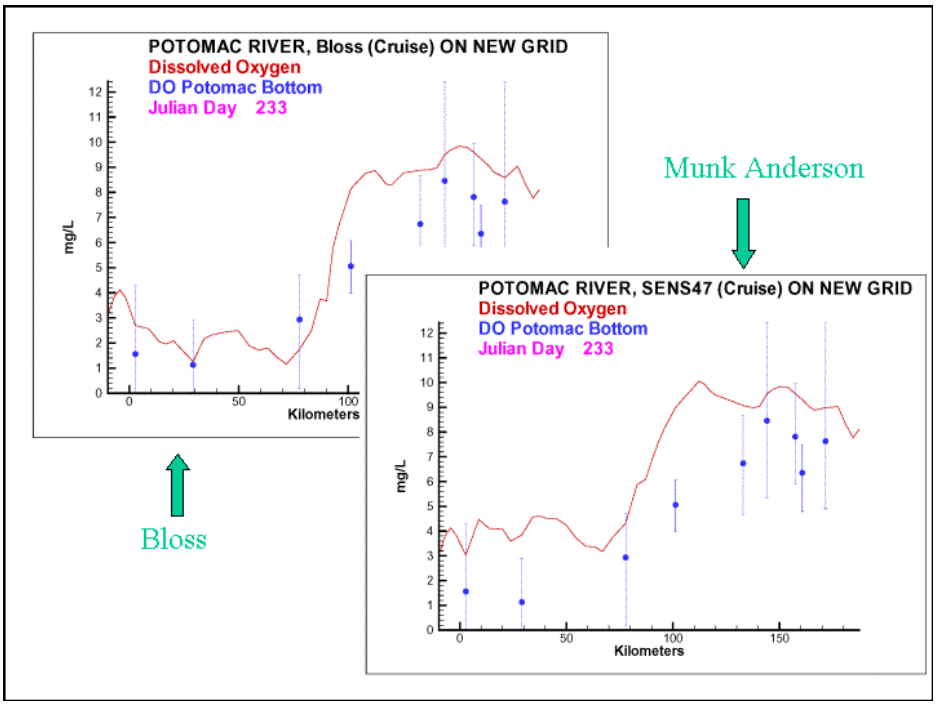

Figure 2-18. Computed bottom dissolved oxygen along the Potomac River axis, summer 1985, for the Bloss (left) and Munk-Anderson (right) relationships.

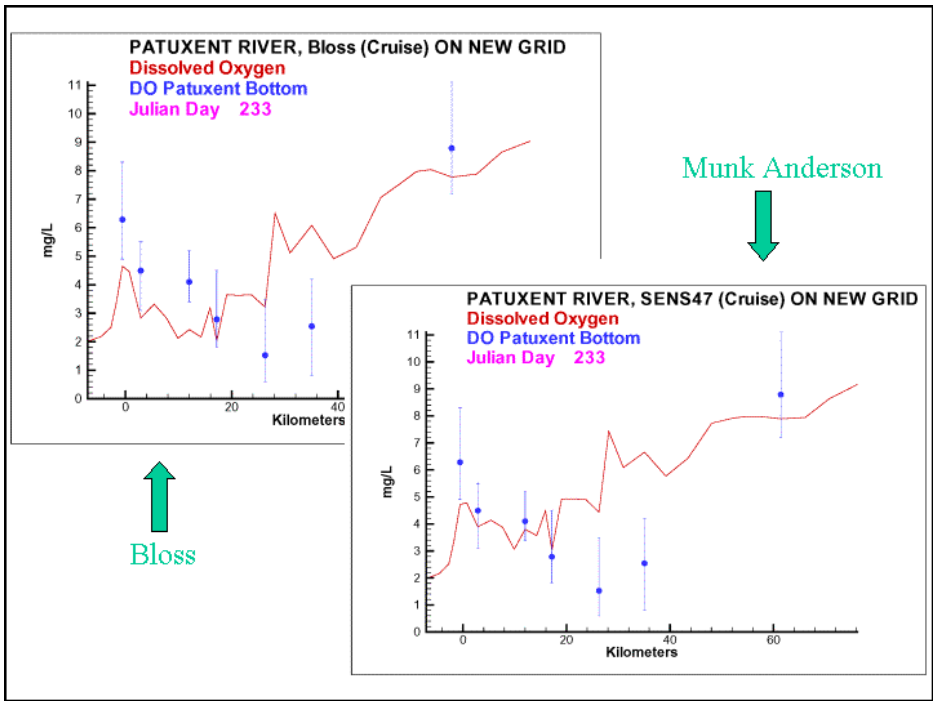

Figure 2-19. Computed bottom dissolved oxygen along the Patuxent River axis, summer 1985, for the Bloss (left) and Munk-Anderson (right) relationships.

The Decision

The model team proposed using a mixed scheme in which the Bloss and Munk-Anderson relationships were applied in the systems for which they provided the best results. The first author's opinion was (and remains) that the use of the mixed scheme was entirely appropriate. The existence of numerous relationships, including Bloss, Munk-Anderson and others, indicates that no one relationship has universal applicability. The Hydrodynamics Expert Panel insisted that the mixed scheme should not be used. The Panel's opinion was that one relationship must be applied system-wide. Their recommendation was accepted and the Bloss scheme was selected for use. This scheme provided the best results in two systems, the mainstem bay and the Potomac, for which computation of bottom-water anoxia was crucial. Since dissolved oxygen was not a management issue in the James, the consequences of employing the Bloss scheme there were considered acceptable.

References

Bloss, S., Lehfeldt, R., and Patterson, J. (1988). "Modeling turbulent transport in stratified estuary," *Journal of Hydraulic Engineering*, 114(9), 1115-1133

Cerco, C., and Cole, T. (1994). "Three-dimensional eutrophication model of Chesapeake Bay," Technical Report El-94-4, US Army Engineer Waterways Experiment Station, Vicksburg MS.

Dortch, M. (1990). "Three-dimensional Lagrangian residual transport computed from an intratidal hydrodynamic model," Technical Report EL-90-11, US Army Engineer Waterways Experiment Station, Vicksburg MS.

Dortch, M., Chapman, R., and Abt, S. (1992). “Application of three-dimensional Lagrangian residual transport,” *Journal of Hydraulic Engineering*, 118(6), 831-848

Johnson, B., Kim, K., Heath, R., and Butler, L. (1991). “Development and verification of a three-dimensional numerical hydrodynamic, salinity and temperature model of Chesapeake Bay,” Technical Report HL-91-7, US Army Engineer Waterways Experiment Station, Vicksburg, MS.

Johnson, B., and Nail, G. (2001). “A 10-year (1985-1994) simulation with a refined three-dimensional numerical hydrodynamic, salinity, and temperature model of Chesapeake Bay and its tributaries,” June 2001 Draft Report, Coastal and Hydraulics Laboratory, US Army Engineer Research and Development Center, Vicksburg MS.

Munk, W., and Anderson, E. (1948). “Notes on the theory of the thermocline,” *Journal of Marine Research*, 7, 276-295.

Sheng, P. (1986). “A three-dimensional mathematical model of coastal, estuarine and lake currents using boundary-fitted grid,” Report 585, ARAP Group of Titan Systems, Princeton NJ.

Boundary Conditions 3

Introduction

Boundary conditions must be specified at all open edges of the model grid. These include river inflows, lateral flows, and the ocean interface. Numerical treatment of all boundary conditions is identical. When flow across a boundary is out of the system, the concentration at the boundary is assigned the value computed at the model cell immediately inside the boundary. When flow across a boundary is into the system, concentration at the boundary is assigned a specified boundary value. Diffusion across the boundary is considered to be zero. The method of assigning boundary concentrations varies with the nature of the boundary.

River Inflows

Loads of carbon, nitrogen, phosphorus, and solids were specified at the river inflows. Consequently, boundary concentrations of these substances were set to zero so that no material entered the system other than the specified loads. Boundary concentrations were required for substances not usually considered in the form of loads. These included temperature, dissolved oxygen, phytoplankton, zooplankton, and silica. Boundary concentrations were specified as monthly values (Tables 3-1–3-7). Determination of the values depended on available observations.

Dissolved oxygen and temperature were based on mean monthly values in the fall-line monitoring program. Zooplankton was not monitored at the river inflows. Boundary conditions were based on nearby in-stream observations or adapted from other rivers when no observations were available. Mean dissolved silica concentrations were based on fall-line observations. Particulate silica concentrations were derived from a 1994 observation program.

Limited chlorophyll observations were obtained from the fall-line data base. These were converted to algal carbon, the model state variable, using a carbon-to-chlorophyll ratio of 30. Phytoplankton in river inflows were assigned to the model

Table 3-1. Boundary Conditions at James and Appomattox Rivers

Month	Temperature, oC	Chlorophyll, ug/L	Micro Zoo, mg C/L	Meso Zoo, mg C/L	Dissolved Oxygen, mg/L	Dissolved Silica, mg Si/L	Particulate Silica, mg Si/L
1	4.8	3	0.01	0.005	13.4	3.4	0.16
2	5.5	3	0.01	0.005	13	3.4	0.26
3	8.8	3	0.01	0.005	11.8	3.4	0.19
4	13.8	3	0.01	0.005	10.4	3.4	0.15
5	19.2	3	0.01	0.005	9.2	3.4	0.18
6	23.5	3	0.01	0.005	8.2	3.4	0.1
7	25.6	3	0.01	0.005	7.5	3.4	0.07
8	25	3	0.01	0.005	7.2	3.4	0.15
9	21.7	3	0.01	0.005	7.7	3.4	0.04
10	16.7	3	0.01	0.005	9	3.4	0.05
11	11.3	3	0.01	0.005	10.8	3.4	0.08
12	7	3	0.01	0.005	12.5	3.4	0.11

Table 3-2. Boundary Conditions at Pamunkey River

Month	Temperature, oC	Chlorophyll, ug/L	Micro Zoo, mg C/L	Meso Zoo, mg C/L	Dissolved Oxygen, mg/L	Dissolved Silica, mg Si/L	Particulate Silica, mg Si/L
1	5	3	0.01	0.005	13.4	4.9	0.19
2	6	3	0.01	0.005	13	4.9	0.26
3	9.2	3	0.01	0.005	11.3	4.9	0.16
4	14	3	0.01	0.005	9.4	4.9	0.14
5	19	3	0.01	0.005	7.8	4.9	0.14
6	22.9	3	0.01	0.005	6.9	4.9	0.15
7	24.6	3	0.01	0.005	6.6	4.9	0.14
8	23.7	3	0.01	0.005	6.6	4.9	0.36
9	20.4	3	0.01	0.005	7	4.9	0.13
10	15.7	3	0.01	0.005	8.1	4.9	0.15
11	10.7	3	0.01	0.005	10	4.9	0.18
12	6.8	3	0.01	0.005	12	4.9	0.19

Table 3-3. Boundary Conditions at Mattaponi River

Month	Temperature, oC	Chlorophyll, ug/L	Micro Zoo, mg C/L	Meso Zoo, mg C/L	Dissolved Oxygen, mg/L	Dissolved Silica, mg Si/L	Particulate Silica, mg Si/L
1	4.2	3	0.01	0.005	12.9	3.64	0.17
2	5.2	3	0.01	0.005	12.4	3.64	0.29
3	8.6	3	0.01	0.005	10.8	3.64	0.14
4	13.6	3	0.01	0.005	9.2	3.64	0.1
5	18.7	3	0.01	0.005	8	3.64	0.07
6	22.7	3	0.01	0.005	7.3	3.64	0.12
7	24.4	3	0.01	0.005	7	3.64	0.04
8	23.4	3	0.01	0.005	6.9	3.64	0.26
9	20	3	0.01	0.005	7.2	3.64	0.12
10	15	3	0.01	0.005	8.3	3.64	0.1
11	9.9	3	0.01	0.005	10.4	3.64	0.12
12	5.9	3	0.01	0.005	11.9	3.64	0.18

Table 3-4. Boundary Conditions at Rappahannock River

Month	Temperature, oC	Chlorophyll, ug/L	Micro Zoo, mg C/L	Meso Zoo, mg C/L	Dissolved Oxygen, mg/L	Dissolved Silica, mg Si/L	Particulate Silica, mg Si/L
1	3.3	3	0.01	0.005	13.3	4.56	0.17
2	4.1	3	0.01	0.005	13	4.56	0.23
3	7.8	3	0.01	0.005	11.9	4.56	0.27
4	13.3	3	0.01	0.005	10.5	4.56	0.27
5	19.2	3	0.01	0.005	9	4.56	0.23
6	23.8	3	0.01	0.005	7.8	4.56	0.17
7	26.1	3	0.01	0.005	7.3	4.56	0.12
8	25.3	3	0.01	0.005	7.6	4.56	0.09
9	21.6	3	0.01	0.005	8.6	4.56	0.08
10	16.1	3	0.01	0.005	10	4.56	0.08
11	10.2	3	0.01	0.005	11.5	4.56	0.09
12	5.5	3	0.01	0.005	12.7	4.56	0.12

Table 3-5. Boundary Conditions at Potomac River

Month	Temperature, oC	Chlorophyll, ug/L	Micro Zoo, mg C/L	Meso Zoo, mg C/L	Dissolved Oxygen, mg/L	Dissolved Silica, mg Si/L	Particulate Silica, mg Si/L
1	2.1	3	0.01	0.005	14.7	2	0.43
2	3.2	3	0.01	0.005	14.4	2	0.64
3	7.3	3	0.01	0.005	13.1	2	0.6
4	13.5	3	0.01	0.005	11.4	2	0.6
5	20	3	0.02	0.01	9.7	2	0.54
6	25.2	3	0.02	0.01	8.5	2	0.47
7	27.6	3	0.04	0.01	8.1	2	0.33
8	26.5	3	0.04	0.01	8.3	2	0.27
9	22.4	3	0.02	0.005	9.1	2	0.23
10	16.2	3	0.01	0.005	10.6	2	0.26
11	9.7	3	0.01	0.005	12.3	2	0.33
12	4.5	3	0.01	0.005	13.8	2	0.41

Table 3-6. Boundary Conditions at Patuxent River

Month	Temperature, oC	Chlorophyll, ug/L	Micro Zoo, mg C/L	Meso Zoo, mg C/L	Dissolved Oxygen, mg/L	Dissolved Silica, mg Si/L	Particulate Silica, mg Si/L
1	3.8	3	0.02	0.01	11.9	3.7	0.65
2	4.6	3	0.02	0.01	12.1	3.7	0.65
3	7.8	3	0.02	0.01	11.1	3.7	0.65
4	12.6	3	0.02	0.01	9.2	3.7	0.65
5	17.7	3	0.05	0.01	7.2	3.7	0.65
6	21.7	3	0.05	0.01	5.7	3.7	0.65
7	23.6	3	0.05	0.01	5	3.7	0.65
8	22.8	3	0.05	0.01	5	3.7	0.65
9	19.6	3	0.05	0.01	5.6	3.7	0.65
10	14.8	3	0.04	0.01	6.7	3.7	0.65
11	9.7	3	0.04	0.01	8.4	3.7	0.65
12	5.7	3	0.02	0.01	10.2	3.7	0.65

Table 3-7. Boundary Conditions at Susquehanna River

Month	Temperature, oC	Chlorophyll, ug/L	Micro Zoo, mg C/L	Meso Zoo, mg C/L	Dissolved Oxygen, mg/L	Dissolved Silica, mg Si/L	Particulate Silica, mg Si/L
1	1.9	5	0	0	14.1	2.2	0.53
2	2.3	5	0	0	14.1	2.14	0.53
3	5.8	5	0.001	0	13.3	1.98	0.54
4	11.7	5	0.004	0.001	11.7	1.8	0.55
5	18.3	5	0.015	0.002	9.4	1.25	0.42
6	23.8	5	0.02	0.002	6.8	1.08	0.4
7	26.9	5	0.016	0.001	4.8	0.94	0.37
8	26.6	5	0.011	0.001	4.1	0.93	0.35
9	23	5	0.01	0.001	5.3	1.22	0.44
10	17.2	5	0.01	0.001	7.7	1.28	0.39
11	10.6	5	0.006	0.001	10.6	1.77	0.49
12	5	5	0.002	0.001	12.8	2.39	0.65

Group 3 (summer, green algae) except at the Potomac River. There, during summer, half the boundary concentration was assigned to model Group 1 (blue-green algae). Special consideration was required due to the model treatment of internal algal nutrients. Within the water quality model, these were quantified implicitly, by ratio to algal carbon. Within the watershed model, these were explicitly quantified as part of the organic nitrogen and phosphorus loads. To keep the algal nutrients from being added to the model twice, once explicitly as organic load and once implicitly by ratio to algal carbon, the implicit algal nutrients were subtracted from the explicit loads. For nitrogen, the quantity removed from each daily organic nitrogen load was:

$$\text{Algal N} = \text{Anc} \bullet \text{B} \bullet \text{Q} \qquad (3\text{-}1)$$

in which
Algal N = nitrogen load associated with algal carbon (g d^{-1})
Anc = algal nitrogen-to-carbon ratio (g N g^{-1} C)
B = algal carbon (g m^{-3})
Q = river inflow (m^3 d^{-1})

An analogous quantity was removed from the organic phosphorus load.

Lateral Inflows

Lateral inflows, determined by the watershed model, entered at model cells adjoining the shoreline. Dissolved oxygen in the lateral flows was at saturation concentration. Temperature was equilibrium temperature. Dissolved and particulate silica were specified at 3.67 and 0.19 g Si m^{-3}, respectively. These were based on system-wide characteristic values for river inflows. Concentrations of all other substances in lateral flows were zero.

Ocean Boundary Conditions

Background

In the first version of the model (Cerco and Cole 1994), the open edge of the model grid was at the entrance to Chesapeake Bay. Boundary concentrations were initially based on an array of Chesapeake Bay Program monitoring stations coincident with the edge of the model grid. Inspection of the short record then available suggested nitrogen and phosphorus concentrations at the mouth were declining in response to load reductions within the bay. A requirement was imposed that the model boundary conditions should respond to conditions within the bay. Consequently, "mass balance" boundary conditions were developed for nitrogen and phosphorus. The mass-balance boundary conditions determined the inflowing concentrations of nitrogen and phosphorus as a weighted sum of outflowing concentrations and concentrations in a hypothetical oceanic reservoir.

The mass-balance boundary conditions were successful but unnecessary. Sensitivity runs (Cerco and Cole 1994) indicated the inflowing nutrient concentrations at the mouth declined by only 5% (phosphorus) to 10% (nitrogen) following load reductions of 90%. Moreover, the apparent reduction in nitrogen concentration at the mouth was attributed to changes in methodology. (The reduction in phosphorus remains unexplained to this day.)

In the Tributary Refinements phase of model development (Cerco et al. 2002), the grid was extended beyond the bay mouth, out onto the continental shelf. The primary objective was to ensure that boundary conditions specified at the edge of the grid were beyond the influence of conditions within the bay. The grid extension traded one set of problems for another. Model boundaries were moved from a location with abundant observations to multiple locations at which little information was available. Surveys conducted from May 1995 to August 1996 provided information on key water quality constituents but detailed boundary conditions for the simulation period, 1985-1994, could not be reconstructed. Boundary conditions for major nitrogen and phosphorus constituents were specified as constant concentrations throughout the simulation period. As a consequence, mean nitrogen and phosphorus concentrations at the mouth of the bay were well represented but the dynamics, especially of nitrogen, were not.

In the present phase of the model study, specification of boundary conditions at the edge of the grid proved especially problematic. During the re-evaluation of the hydrodynamic model and refinement of water quality model kinetics, unpredictable behavior occurred in the portion of the grid outside the bay mouth. Both models were in a transient state of development yet both models were expected to compute dynamics in a region for which no data existed. Circulation and water quality computed at the bay mouth were unsuited for calibration of the models within the bay. For the water quality model, the strategy was developed in which conditions observed at the bay mouth were extended to the edges of the grid. Kinetics were disabled outside the bay mouth to prevent substance transformations. This strategy carried over into the final calibration of the present model.

Assignment

The open boundary of the grid was divided into three faces (Figure 3-1). Observations from the northernmost monitoring station (CB7.4N) were imposed at the northern face. Observations from the central monitoring station (CB7.4) were imposed at the eastern face. Observations from the southernmost monitoring station (CB8.1E) were imposed at the southern face.

Observations at the mouth were conducted once or twice per month. Salinity, temperature, and dissolved oxygen were measured in-situ, at one-meter intervals, from surface to bottom. Samples for laboratory analysis were collected one meter below the surface and one meter off the bottom. At the center station (CB7.4), additional samples were collected above and below the pycnocline. For boundary condition specification, samples were averaged by month and into three layers. The surface mixed layer comprised the upper four model cells (depth < 6.7 m). The pycnocline comprised the next four cells (6.7 m < depth < 12.8 m). The bottom mixed layer comprised all cells below the upper eight (depth > 12.8 m). Missing surface and bottom observations were filled with long-term monthly mean values. Missing pycnocline observations were filled by linear interpolation between surface and bottom.

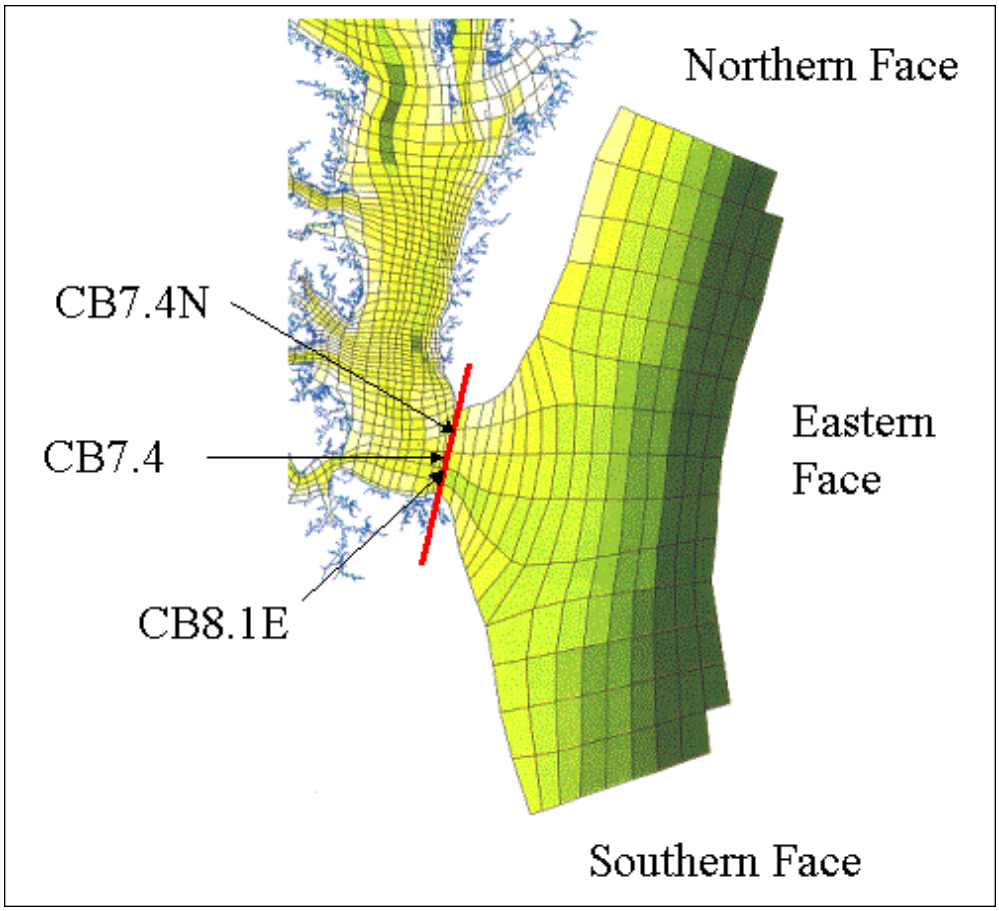

Figure 3-1. The Ocean Boundary Region Including Monitoring Stations, Transect, and Boundary Faces.

Although the principles for assigning boundary conditions were straightforward, refinements to the observations were required and occasional exceptions to the process occurred. Salinity boundary conditions were transferred exactly from the hydrodynamic model (Johnson and Nail 2001) to ensure agreement in salinity computations between the hydrodynamic and water quality models. Long-term mean monthly values of dissolved organic and particulate phosphorus were employed in 1985 and 1986 to overcome apparent analytical errors in the early observations.

The model required specification of algal boundary conditions as carbonaceous biomass. We assumed this biomass comprised 90% of the observed particulate organic carbon. From November through May, phytoplankton at the ocean boundary were assigned to the spring diatom group. In the remaining months, oceanic phytoplankton were assigned to the summer, mixed group.

Observations of organic particulate matter consisted of viable phytoplankton and other organisms as well as detritus. The model state variables were detrital matter. Observations of particulate organic carbon, particulate organic nitrogen, and particulate phosphorus were corrected to remove algal carbon and nutrients. The remaining detrital matter was considered to be 10% labile and 90% refractory.

Regular observations were available for ammonium while the corresponding model state variable represented ammonium plus urea. Observations near the mouth of the bay (Lomas et al. 2002) indicated urea was 0.01 g m^{-3}. This concentration was subtracted from observed dissolved organic nitrogen and added to observed ammonium.

Limited observations were available on which to base boundary conditions for zooplankton and particulate biogenic silica. Microzooplankton were assigned the constant value 0.01 g C m^{-3} while mesozooplankton were varied from 0.002 (winter) to 0.028 (summer) g C m^{-3}. Particulate biogenic silica was assigned the constant value 0.068 g Si m^{-3} and corrected to remove the algal component, leaving only detrital silica.

Results

Net Circulation. Computed net circulation was examined for three years, 1985, 1990, and 1993, at a transect drawn across the mouth of the bay (Figure 3-1). The year 1985 is considered a low-flow year although the western tributaries were affected by a major autumn storm event. Flows in 1990 were moderate. The year 1993 was characterized by high spring runoff followed by a dry summer.

Eulerian- (or arithmetic-) average volumetric flow was computed at each flow face in the grid transect as:

$$\text{Qbar} = \frac{1}{T} \bullet \int_0^T Q \; dt \qquad (3\text{-}2)$$

in which
Qbar = annual average volumetric flow (m^3 s^{-1})
Q = instantaneous volumetric flow (m^3 s^{-1})
t = time (s)
T = averaging interval (one year)

Results (Figures 3-2 to 3-4) conform to expectations. Net flows in the deepest portion of the transect, driven by a longitudinal density gradient, are into the bay. Flows out of the bay are confined to surface waters. Rotational effects tilt the level of no net motion so that flows at the northern side of the transect tend to be into the bay at all depths. A small irregularity occasionally occurs at one depth on the northern side (Figures 3-3, 3-4). We cannot determine if this truly reflects a

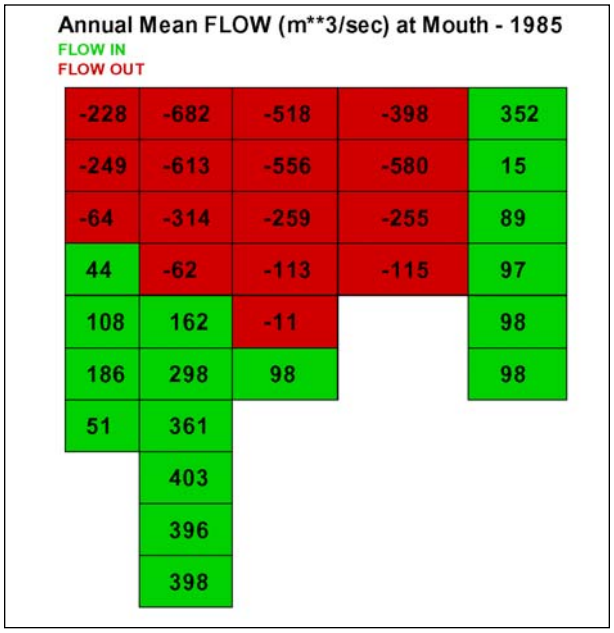

Figure 3-2. Net Volumetric Flows (m^3 s^{-1}) at the Mouth of the Bay for 1985. This view is into the Bay from the Shelf. Positive flows are into the Bay.

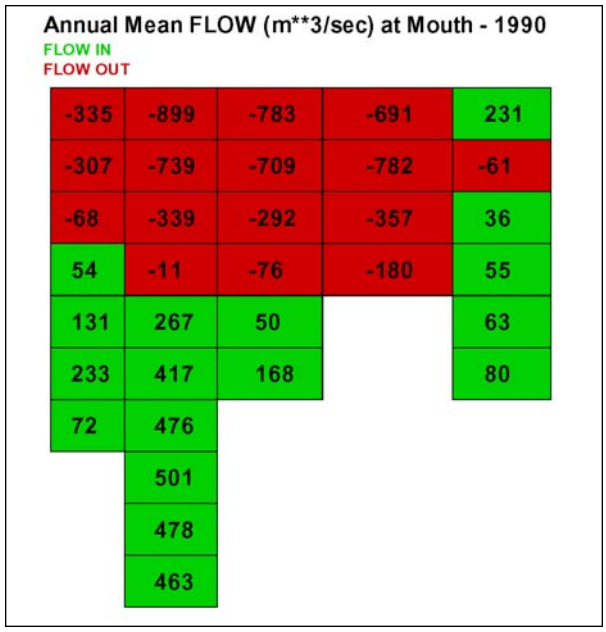

Figure 3-3. Net Volumetric Flows (m^3 s^{-1}) at the Mouth of the Bay for 1990. This view is into the Bay from the Shelf. Positive flows are into the Bay.

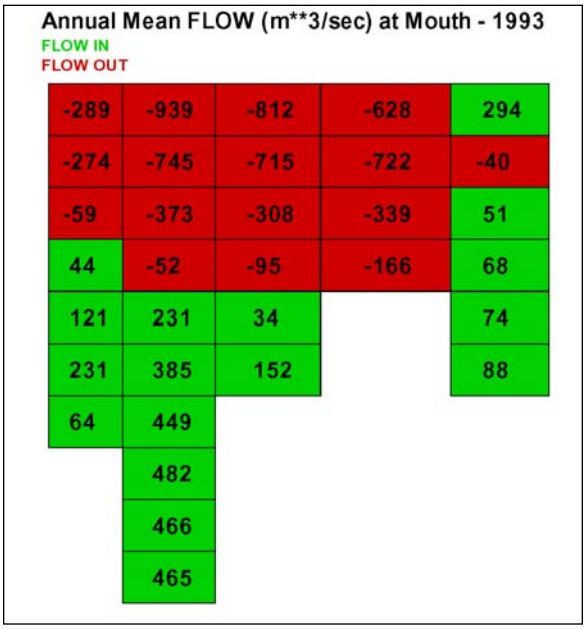

Figure 3-4. Net Volumetric Flows (m^3 s^{-1}) at the Mouth of the Bay for 1993. This view is into the Bay from the Shelf. Positive flows are into the Bay.

complex circulation pattern or if this irregularity is an artifact of the grid and/or boundary conditions. Annual net flows in and out of the bay are roughly 3,000 and 6,000 m^3 s^{-1}, respectively (Table 3-8). The computed flows are in reasonable agreement with net flows, 6,000 to 8,000 m^3 s^{-1}, measured during two months in 1971 (Boicourt 1973).

Table 3-8. Volume and Mass Transport at Bay Mouth

	Flow, m^3 sec^{-1}	DIN, ton d^{-1}	Total N, ton d^{-1}	DIP, ton d^{-1}	Total P, ton d^{-1}
1985					
In	3262	15	89	5.2	10.2
Out	-5025	-54	-202	-4.3	-8.3
Net	-1762	-38	-113	0.9	1.9
1990					
In	3784	17	87	5.5	10.3
Out	-6637	-40	-258	-4.7	-10.3
Net	-2854	-23	-171	0.8	-0.0
1993					
In	3707	15	91	4.1	9.7
Out	-6564	-58	-277	-4.7	-9.5
Net	-2857	-43	-186	-0.5	0.2

Salinity Structure. Annual-mean computed salinity at the mouth (Figures 3-5 to 3-7) is influenced by the effects of density, rotation, and boundary conditions. The rotational effects produce a tilting of the computed pycnocline. In the upper four or five model layers (depth < 7 m), the water on the south side is fresher than water on the north side at the same depth. This phenomenon is apparent in the observations as well. The observations suggest the depth of the computed freshwater plume should be greater than the present representation but a more detailed analysis is required. The apparent disparity in plume depths may be an artifact of comparing averages of discrete observations with continuous model results.

In deeper waters (depth > 7 m), salinity computed on the north side is less than on the south side at the same depth. This phenomenon is also suggested in the observations. The lower-salinity water originates in a plume that hugs the Delmarva peninsula and enters the bay at the northern side of the mouth. Salinity boundary conditions on the northern face, adjacent to the coast, were related to flow in the Delaware River (Cerco et al. 2002) and were lower than elsewhere on the grid perimeter.

Computed Concentrations at Bay Mouth. Selected comparisons of computed and observed concentrations for Station CB8.1E (Figure 3-1) are presented here. This station is in a channel (20 m) on the southern side of the bay mouth. At this location, net flow in the surface water (depth < 7 m) is usually out of the bay while net flow in deeper water is into the bay (Figures 3-2 to 3-4). Complete time series comparisons for all substances and stations across the mouth are included in an appendix to this report.

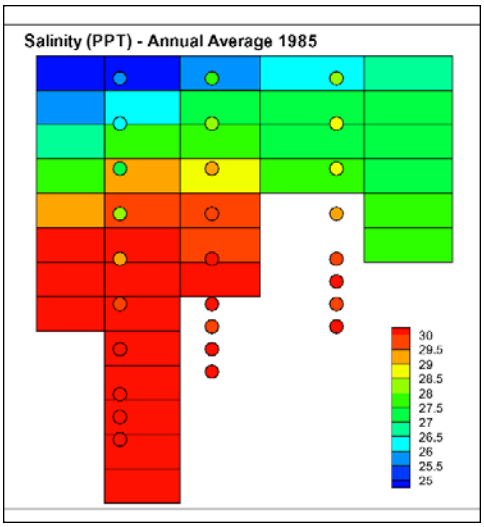

Figure 3-5. Annual-Average Computed and Observed Salinity at the Mouth of the Bay for 1985. This View is into the Bay from the Shelf. Observations (Circles) are Superimposed on Model Values. Bottom observations were collected in deep channels not entirely represented by the model grid.

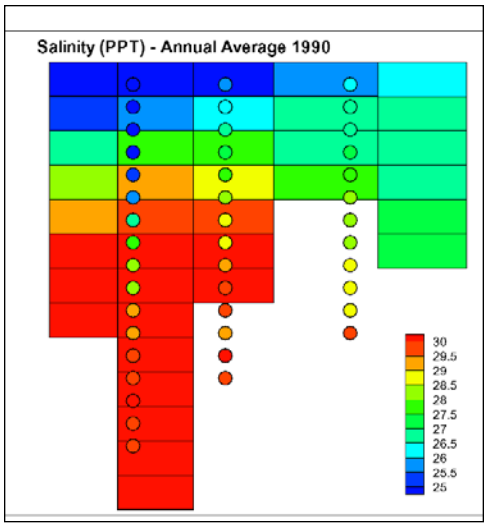

Figure 3-6. Annual-Average Computed and Observed Salinity at the Mouth of the Bay for 1990. This View is into the Bay from the Shelf. Observations (Circles) are Superimposed on Model Values. Bottom observations were collected in deep channels not entirely represented by the model grid.

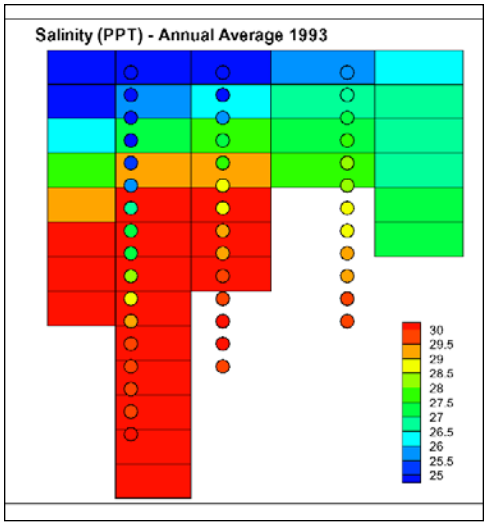

Figure 3-7. Annual-Average Computed and Observed Salinity at the Mouth of the Bay for 1993. This View is into the Bay from the Shelf. Observations (Circles) are Superimposed on Model Values. Bottom observations were collected in deep channels not entirely represented by the model grid.

The time series (Figures 3-8 to 3-29) compare instantaneous observations to daily-average model computations for the surface and bottom samples. While the time series allow the formation of quick judgements for some substances, formation of even qualitative opinions for other substances is difficult. Consequently, statistical summaries (Table 3-9) are provided for key parameters. The summaries are based on one-to-one comparisons of all observations at the three sample stations across the mouth. For each sampling, multiple observations in a single model cell, if any, were averaged and then compared to computations in the same cell, averaged over the sample day.

The summaries show remarkable agreement between observed and modeled salinity at the mouth. The model provides near perfect representation of mean dissolved inorganic phosphorus and is within ten percent of mean observed total phosphorus. Modeled mean total nitrogen at the mouth is high by roughly 20% with the excess split between dissolved inorganic and organic forms. Computed mean silica and chlorophyll at the mouth exceed observed by 50% or more but exact specification of these boundary conditions is not considered critical.

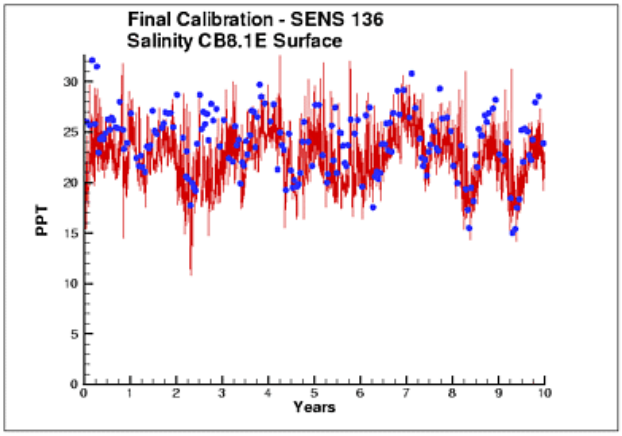

Figure 3-8. Computed and Observed Surface Salinity at Station CB8.1E.

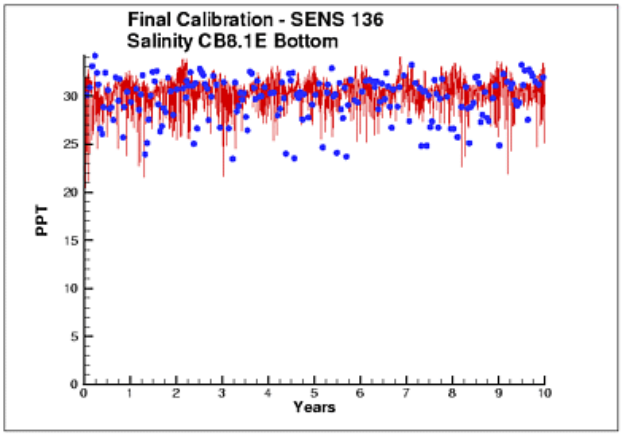

Figure 3-9. Computed and Observed Bottom Salinity at Station CB8.1E.

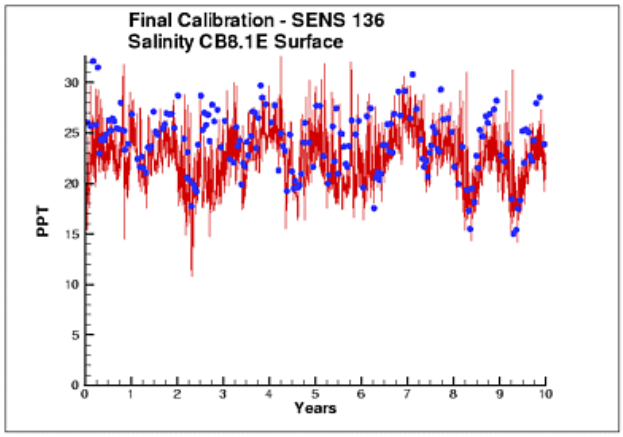

Figure 3-10. Computed and Observed Surface Total Suspended Solids at Station CB8.1E.

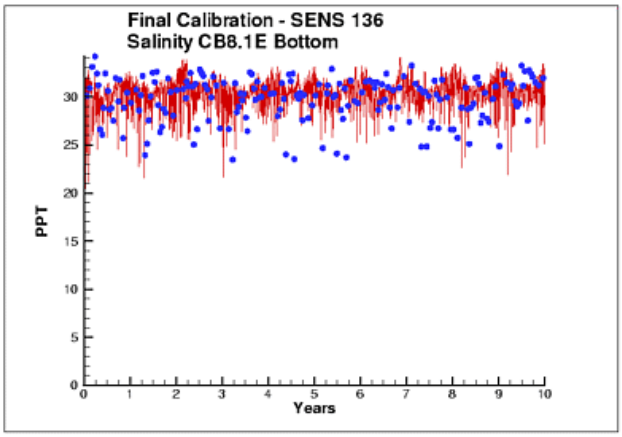

Figure 3-11. Computed and Observed Bottom Total Suspended Solids at Station CB8.1E.

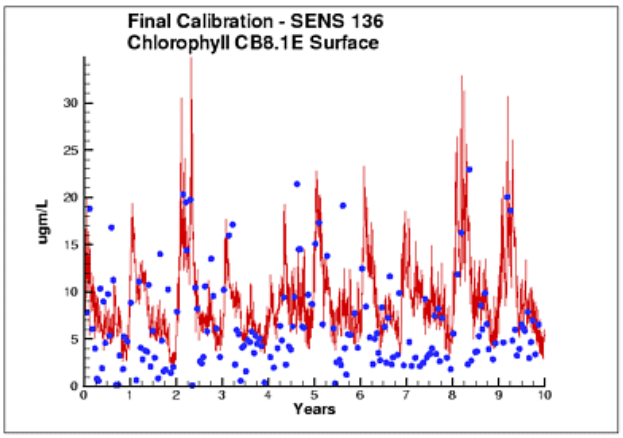

Figure 3-12. Computed and Observed Surface Chlorophyll at Station CB8.1E.

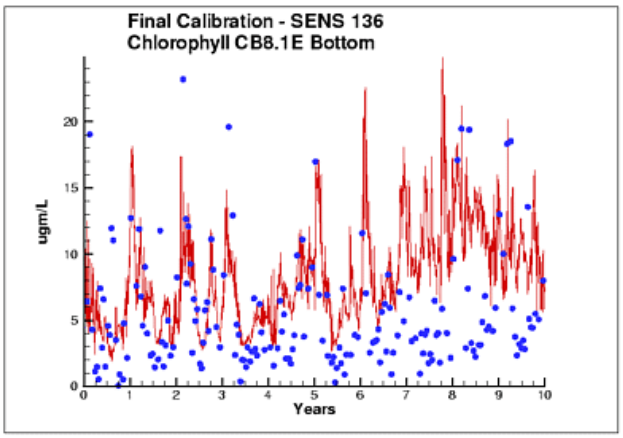

Figure 3-13. Computed and Observed Bottom Chlorophyll at Station CB8.1E.

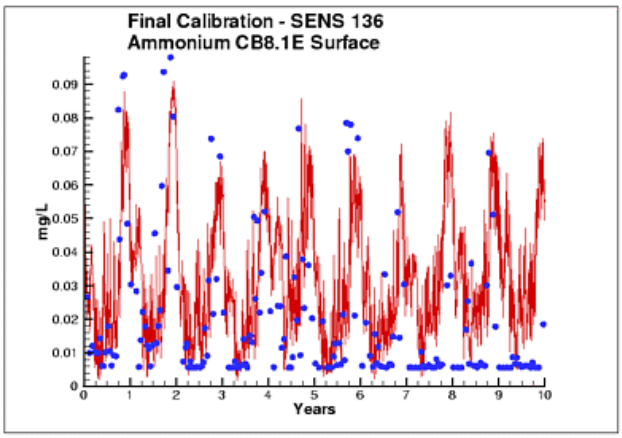

Figure 3-14. Computed and Observed Surface Ammonium at Station CB8.1E.

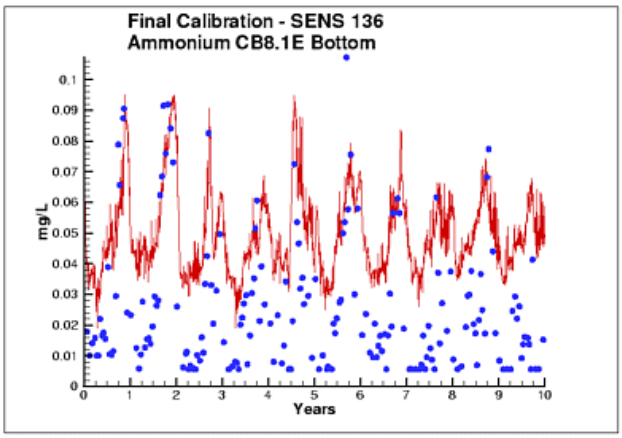

Figure 3-15. Computed and Observed Bottom Ammonium at Station CB8.1E.

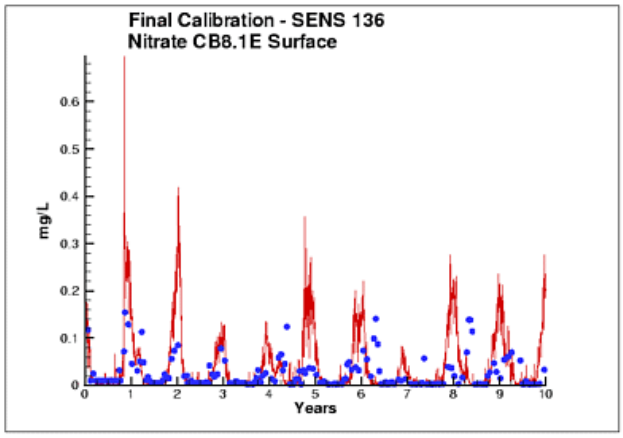

Figure 3-16. Computed and Observed Surface Nitrate at Station CB8.1E.

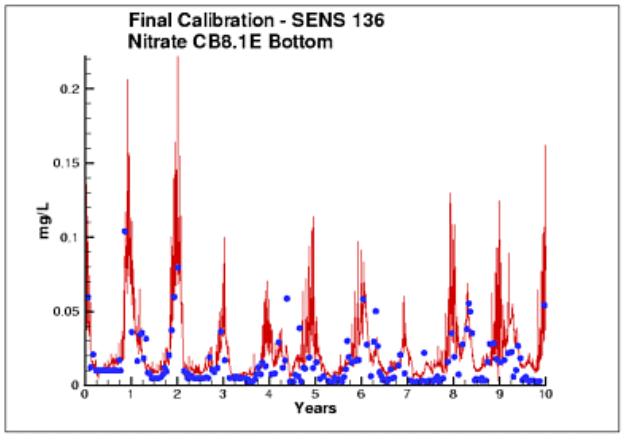

Figure 3-17. Computed and Observed Bottom Nitrate at Station CB8.1E.

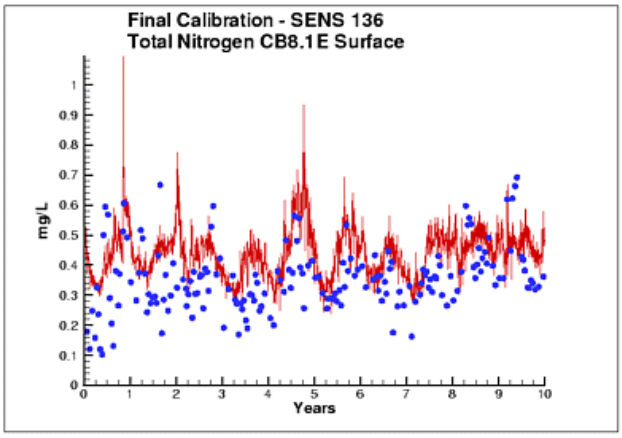

Figure 3-18. Computed and Observed Surface Total Nitrogen at Station CB8.1E.

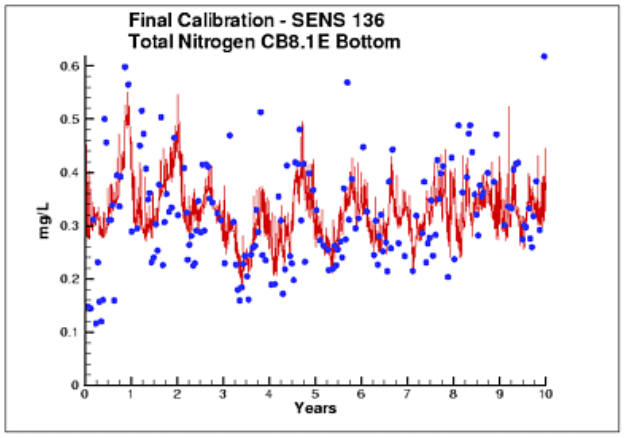

Figure 3-19. Computed and Observed Bottom Total Nitrogen at Station CB8.1E.

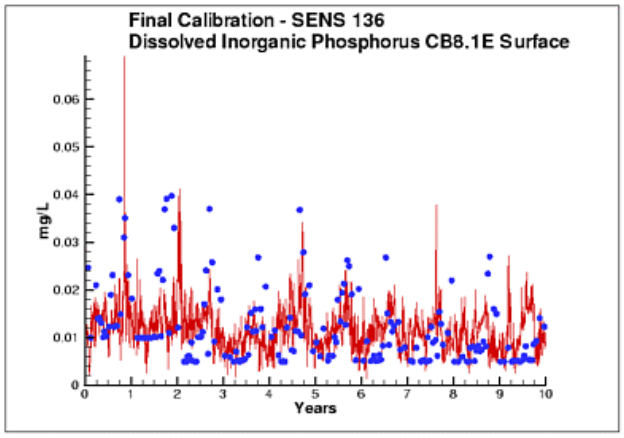

Figure 3-20. Computed and Observed Surface Dissolved Inorganic Phosphorus at Station

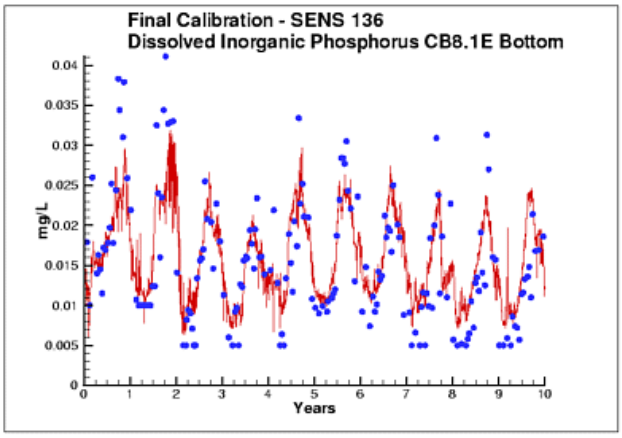

Figure 3-21. Computed and Observed Bottom Dissolved Inorganic Phosphorus at Station

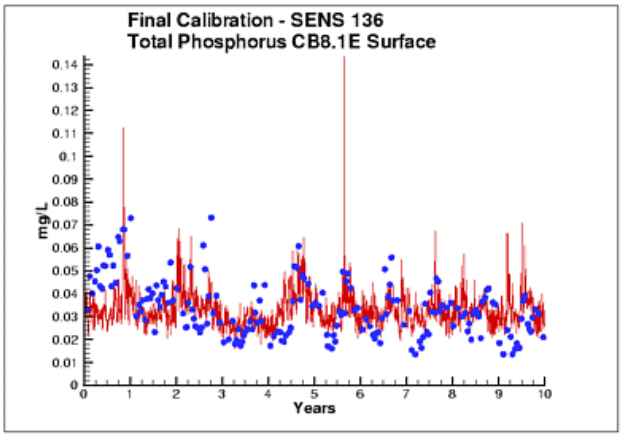

Figure 3-22. Computed and Observed Surface Total Phosphorus at Station CB8.1E.

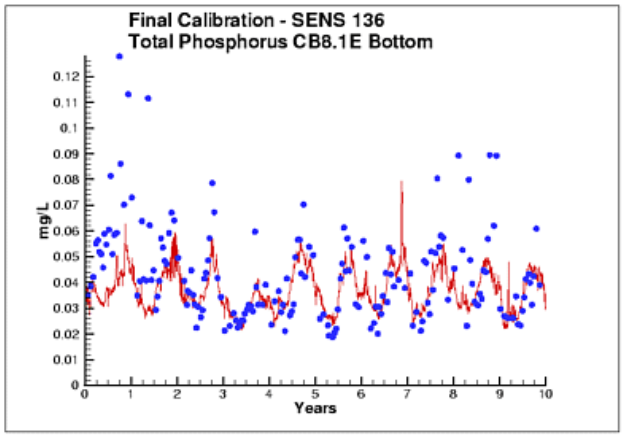

Figure 3-23. Computed and Observed Bottom Total Phosphorus at Station CB8.1E.

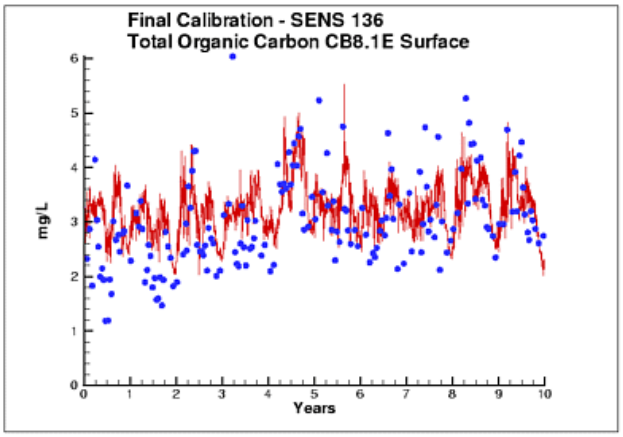

Figure 3-24. Computed and Observed Surface Total Organic Carbon at Station CB8.1E.

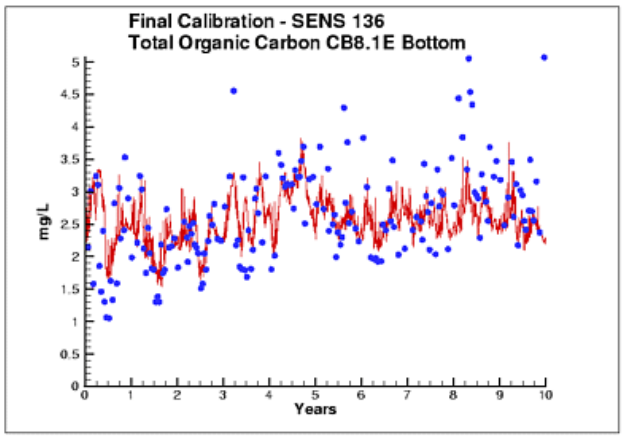

Figure 3-25. Computed and Observed Bottom Total Organic Carbon at Station CB8.1E.

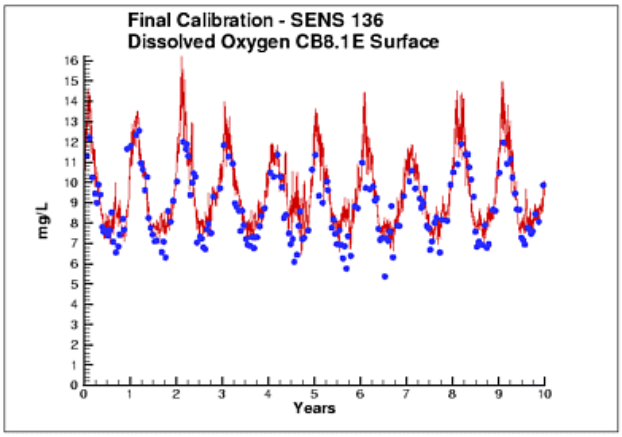

Figure 3-26. Computed and Observed Surface Dissolved Oxygen at Station CB8.1E.

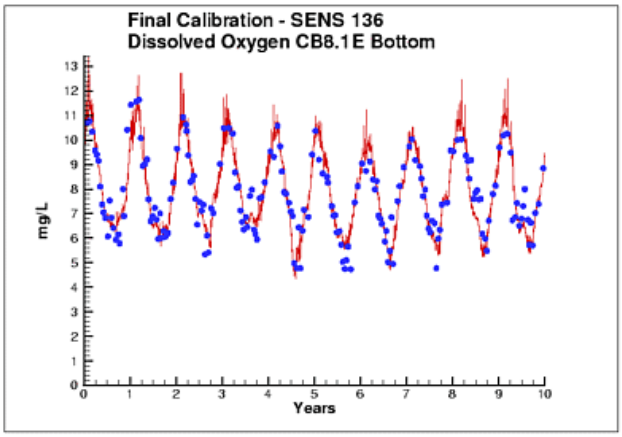

Figure 3-27. Computed and Observed Bottom Dissolved Oxygen at Station CB8.1E.

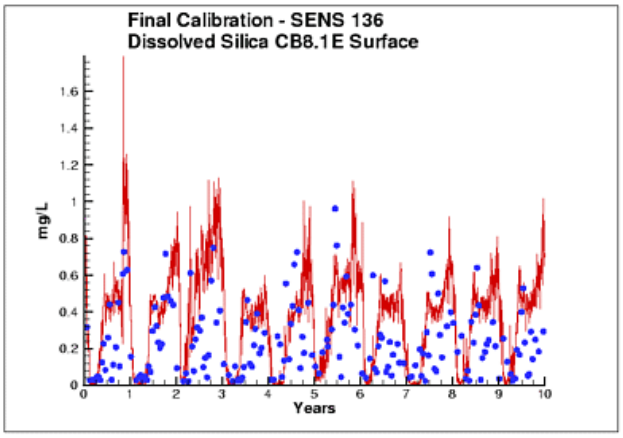

Figure 3-28. Computed and Observed Surface Dissolved Silica at Station CB8.1E.

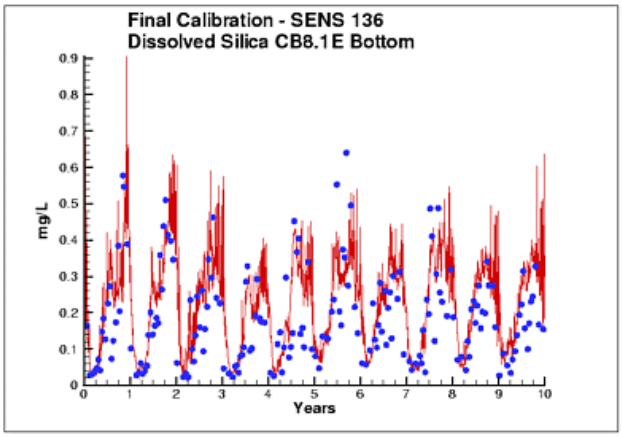

Figure 3-29. Computed and Observed Bottom Dissolved Silica at Station CB8.1E.

Table 3-9. Statistical Summary of Computed and Observed Concentrations at Bay Mouth

Constituent	Number Observations	Observed Mean	Model Mean	Observed Standard Deviation	Model Standard Deviation	Observed Maximum	Model Maximum	Observed Minimum	Model Minimum	Observed Median	Model Median
Dissolved Oxygen, mg/L	3909	8.11	8.20	1.57	1.58	12.80	13.50	3.71	4.40	7.86	7.81
Chlorophyll, ug/L	951	5.08	7.56	4.33	3.04	26.90	20.74	0.00	2.16	3.96	6.93
Dissolved Inorganic Nitrogen, mg/L	983	0.033	0.071	0.036	0.034	0.249	0.189	0.008	0.007	0.016	0.071
Dissolved Inorganic Phosphorus, mg/L	979	0.012	0.012	0.007	0.005	0.042	0.033	0.005	0.002	0.010	0.011
Dissolved Silica, mg/L	994	0.154	0.270	0.145	0.180	0.962	0.928	0.023	-0.016	0.106	0.289
Salinity, ppt	3917	28.3	28.3	3.2	3.2	34.4	34.1	15.0	15.4	28.9	29.1
Total Nitrogen, mg/L	957	0.307	0.363	0.102	0.072	0.717	0.655	0.100	0.176	0.294	0.356
Total Phosphorus, mg/L	972	0.034	0.031	0.016	0.007	0.158	0.066	0.011	0.016	0.031	0.030

Net Transport. Computed net transport of key nutrients at the bay mouth was examined for the same three years as net circulation. Eulerian- (or arithmetic-) average transport of key nutrients was computed for each flow face in the grid transect as:

$$F = \frac{1}{T} \bullet \int_0^T Q \bullet C \; dt \qquad (3\text{-}3)$$

in which:
F = net flux (kg s^{-1})
C = concentration (kg m^{-3})

Results (Table 3-9) indicate the bay exports 90 tons nitrogen per day, largely in dissolved organic form. This quantity agrees closely with the export of 86 tons N d^{-1} computed in the original model (Cerco and Cole 1994) and with an export of 126 tons N d^{-1} estimated by Boynton et al. (1995).

Computed net transport of phosphorus at the bay mouth is into the bay at a mean rate less than 1 ton phosphorus per day (Table 3-9). No form, organic or inorganic predominates. The present import is lower than both the previous model computation, 7.4 tons P d^{-1} (Cerco and Cole 1994), and the estimate based on a system-wide nutrient budget, 11 tons P d^{-1} (Boynton et al. 1995). Explanation for the decreased import may lie in underestimation of phosphorus in water entering the bay through the mouth. While total phosphorus is well represented in an average sense, peak concentrations at the bottom are missed (Figure 3-23). Improved representation of these peaks should result in greater phosphorus transport into the bay.

A Recommendation

Extension of the grid onto the continental shelf had two objectives. The first was to move nutrient boundary conditions to a location beyond the influence of loads within the bay. The second was to allow for coupling with a proposed continental shelf model. The first objective was met, albeit with trade-offs. The proposed shelf model has been postponed indefinitely.

In retrospect, extension of the boundaries to avoid influence of bay loads was unnecessary. From 70% to 85% of the mix of water at the bay mouth originates in the sea rather than in rivers, as evidenced by typical salinities of 25 to 30 ppt. Riverine and point-source loads are attenuated during transport such that a 90% load reduction results in only 5% to 10% concentration changes at the bay mouth (Cerco and Cole 1994). The extension of the grid produced enormous difficulties for both the hydrodynamic and water quality modeling teams and certainly did not increase the accuracy of either model. Consequently, we recommend the boundary be restored to the mouth of the bay in future model efforts.

Grid refinements also produce enormous difficulties. The present boundary condition "works." The grid should not be refined solely to alter the location of the boundaries. If future modeling requires grid changes, however, consideration should be given to restoration of the boundary to the bay mouth.

References

Boicourt, W. (1973). "Circulation of water on the continental shelf from Chesapeake Bay to Cape Hatteras," Ph.D. diss., Johns Hopkins University, Baltimore, MD.

Boynton, W., Garber, J., Summers, R., and Kemp, W. (1995). "Inputs, transformations, and transport of nitrogen and phosphorus in Chesapeake Bay and selected tributaries," *Estuaries*, 18(1B), 285-314.

Cerco, C., and Cole, T. (1994). "Three-dimensional eutrophication model of Chesapeake Bay," Technical Report El-94-4, US Army Engineer Waterways Experiment Station, Vicksburg MS.

Cerco, C., Johnson, B., and Wang, H. (2002). "Tributary refinements to the Chesapeake Bay model," ERDC TR-02-4, US Army Engineer Research and Development Center, Vicksburg MS.

Johnson, B., and Nail, G. (2001). "A 10-year (1985-1994) simulation with a refined three-dimensional numerical hydrodynamic, salinity, and temperature model of Chesapeake Bay and its tributaries," June 2001 Draft Report, Coastal and Hydraulics Laboratory, US Army Engineer Research and Development Center, Vicksburg MS.

Lomas, M., Trice, T., Glibert, P., Bronk, D., and McCarthy, J. (2002). "Temporal and spatial dynamics of urea concentrations in Chesapeake Bay: biological versus physical forcing," *Estuaries*, submitted.

Hydrology and Loads 4

Hydrology

Major sources of freshwater to the Chesapeake Bay system are the Susquehanna River, to the north, and the Potomac and James Rivers to the west (Figure 4-1). Of these, the Susquehanna provides by far the largest flow fraction (64% of total gauged flow) followed by the Potomac (19%) and James (12%). The remaining western-shore tributaries, the York (3%), the Rappahannock (3%) and Patuxent (<1%) contribute only small fractions of the total freshwater to the bay.

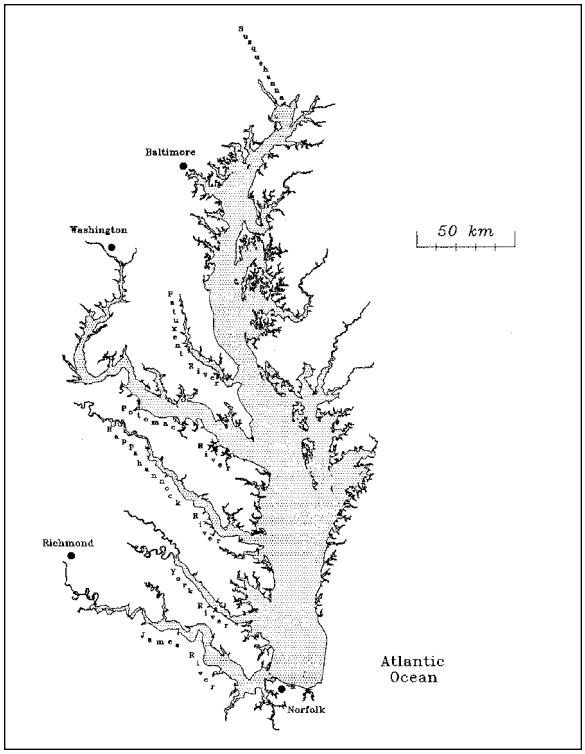

Figure 4-1. Major tributaries of the Chesapeake Bay.

All tributaries exhibit similar seasonal flow patterns. Highest flows occur in winter (December–February) and spring (March–May). Lowest seasonal flows occur in summer (June–August) and fall (September–November) although tropical storms in these seasons can generate enormous flood events.

During the simulation period, the Susquehanna exhibited peak spring flows in 1993 and 1994 (Figure 4-2). The summer of 1994 was also a high-flow season although, by contrast,

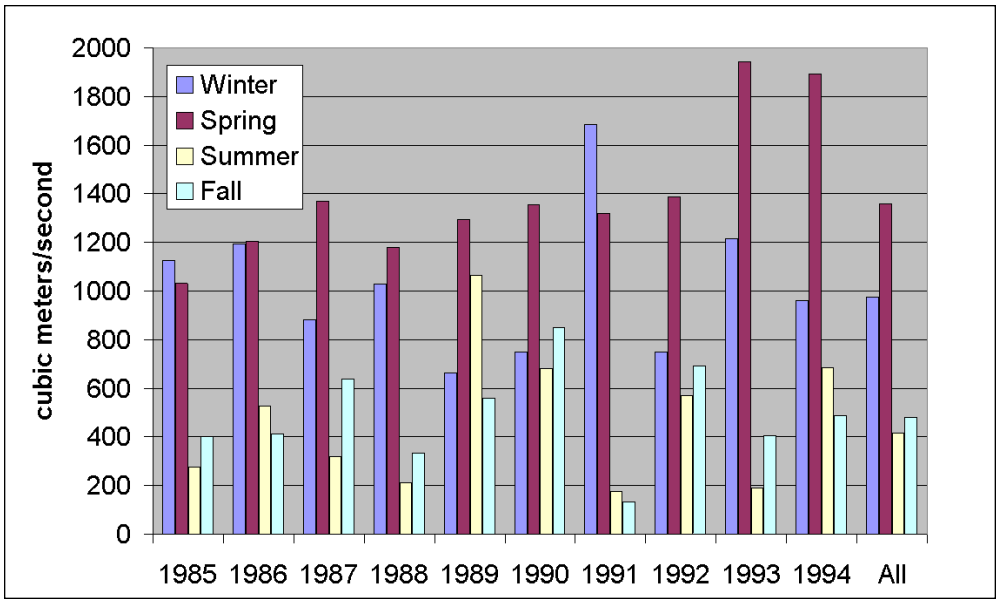

Figure 4-2. Susquehanna River Seasonal Median Flows 1985-1994.

summer of 1993 had below-average flows. The year 1985 was a low-flow year, when all seasons are considered. Other years with extremely dry seasons included 1988 and 1991.

The Potomac (Figure 4-3) and James (Figure 4-4) followed the pattern of high spring flows in 1993 and 1994. The James also exhibited a large spring pulse in 1987 that was not evident in the two other major tributaries. An enormous flood event in November of 1985 influenced the James seasonal median but was "averaged out" of the Potomac flow for that season. Dry seasons in the James included the summers of 1986 and 1988. In the Potomac, the driest seasons were 1986, 1988, and 1991.

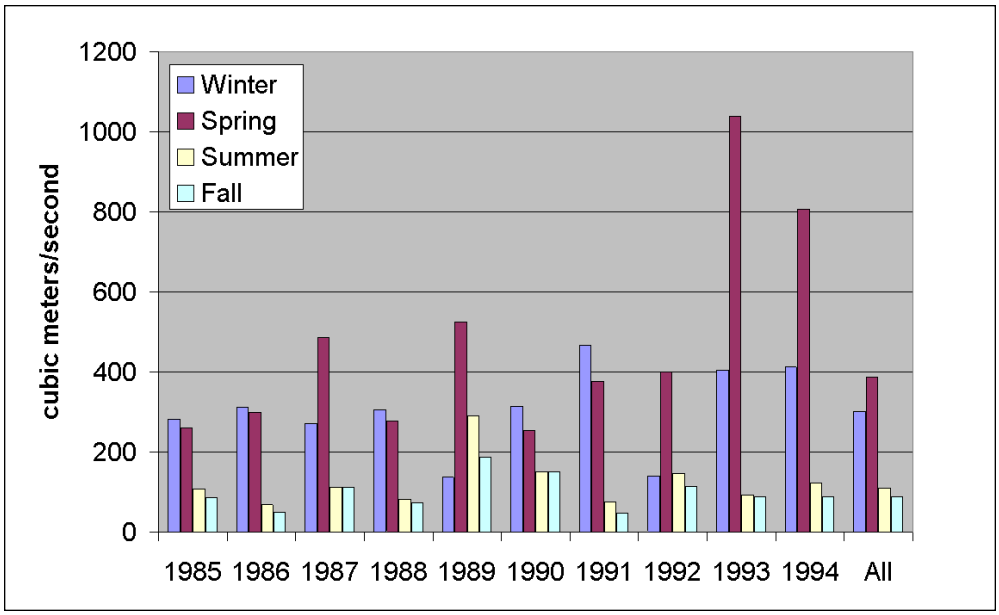

Figure 4-3. Potomac River Seasonal Median Flows 1985-1994.

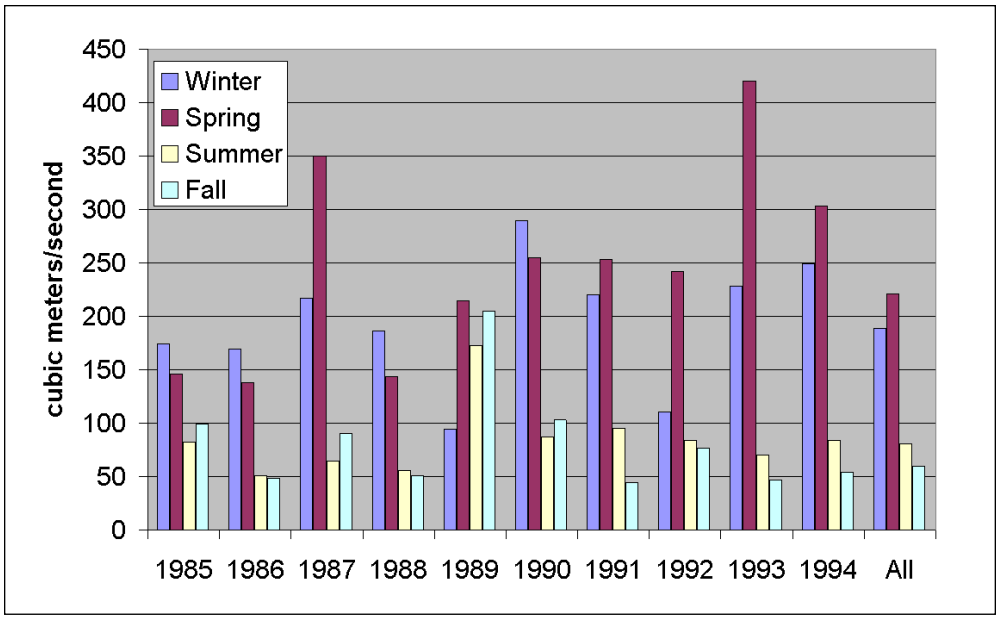

Figure 4-4. James River Seasonal Median Flows 1985-1994.

The remaining western-shore tributaries (Figures 4-5 to 4-7) exhibited individual variation but followed the general pattern of high flows in spring 1993 and 1994. Dry summer years varied but 1986 was consistently among the lowest flow in all three tributaries.

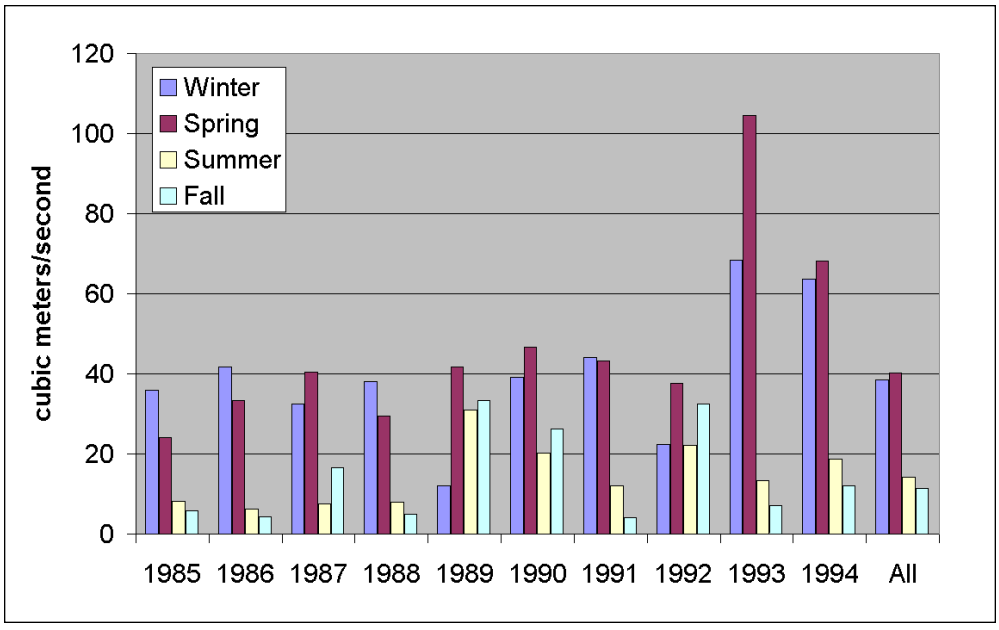

Figure 4-5. Rappahannock River Seasonal Median Flows 1985-1994.

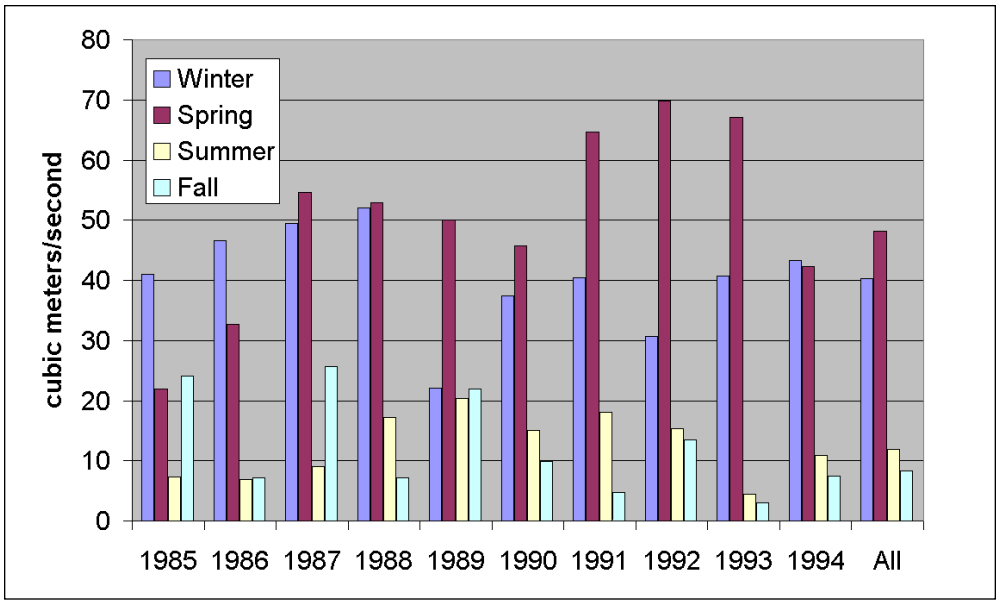

Figure 4-6. York River Seasonal Median Flows 1985-1994.

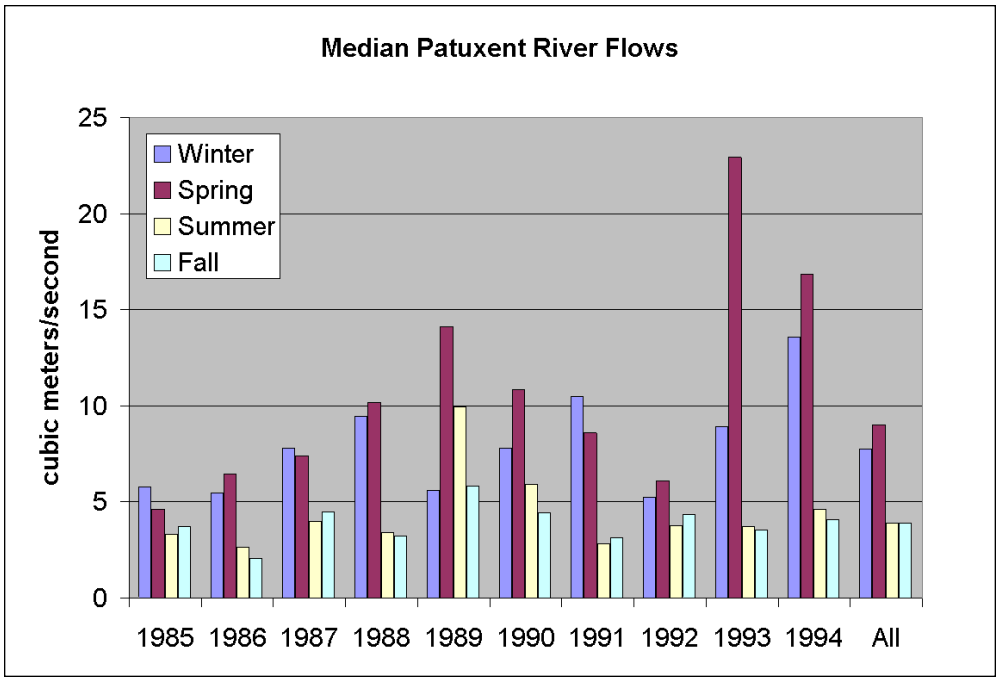

Figure 4-7. Patuxent River Seasonal Median Flows 1985-1994.

Loads

Loads to the system include distributed or nonpoint-source loads, point-source loads, atmospheric loads, bank loads, and wetlands loads. Nonpoint-source loads enter the system at tributary fall lines and as runoff below the fall lines. Point-source loads are from industries and municipal wastewater treatment plants. Atmospheric loads are from the atmosphere directly to the water surface. Atmospheric loads to the watershed are incorporated in the distributed loads. Bank loads originate with shoreline erosion. Wetland loads are materials created in and exported from wetlands.

Nonpoint-Source Loads

Nonpoint-source loads are from Phase IV of the EPA Chesapeake Bay Watershed Model (WSM). The WSM is a modified version of the HSPF (Hydrologic Simulation Program FORTRAN) model (Bicknell et al. 1996). Documentation of the latest version of the WSM may be found on the Chesapeake Bay Program web site http://www.chesapeakebay.net/modsc.htm. Loads were provided in December 2000. Some refinements to solids loads were performed in February 2002 after which loads were finalized.

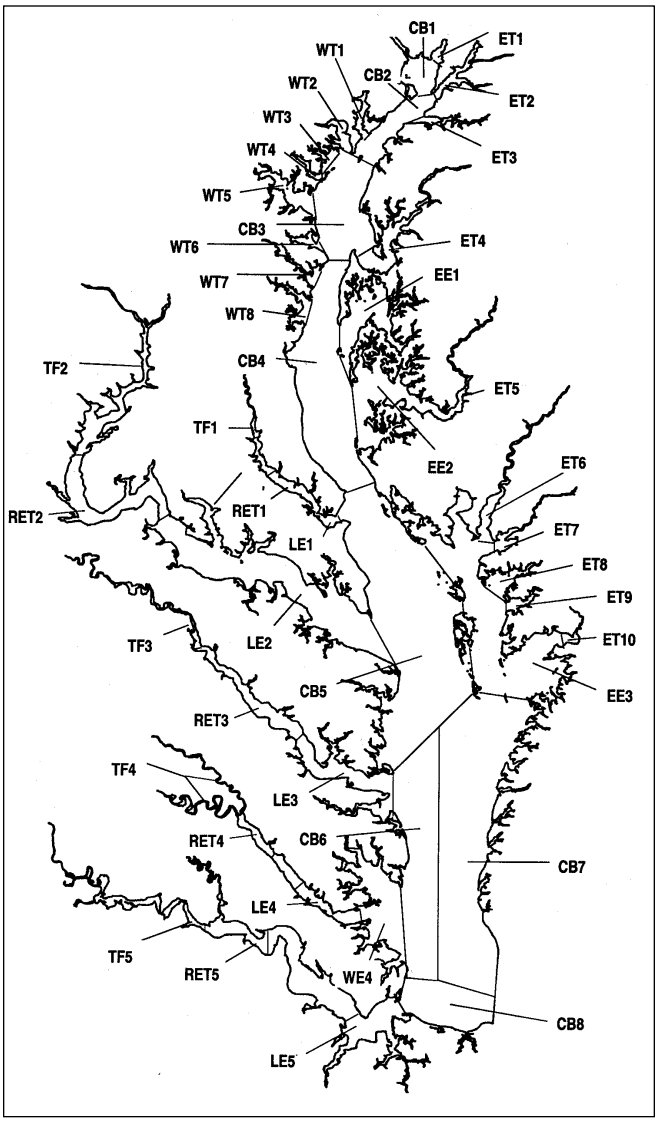

Figure 4-8. Chesapeake Bay Program Segments.

Loads were provided on a daily basis, routed to surface cells on the model grid. Routing was based on local watershed characteristics and on drainage area contributing to the cell. For reporting, loads are summed here by Chesapeake Bay Program Segments (CBPS, Figure 4-8). System-wide summaries are for 1990, a year central to the simulation period and with typical flows. Individual segments are selected for time-series presentation.

Nonpoint-Source Nitrogen Loads

Largest nitrogen loads, by far, come into segment CB1 which includes the input from the Susquehanna River (Figure 4-9). Lesser loads enter at the Potomac (TF2) and James (TF5) fall lines. Magnitude of loads corresponds to relative flows in these tributaries. In the Susquehanna and Potomac, 70% of the nitrogen load is in the form of

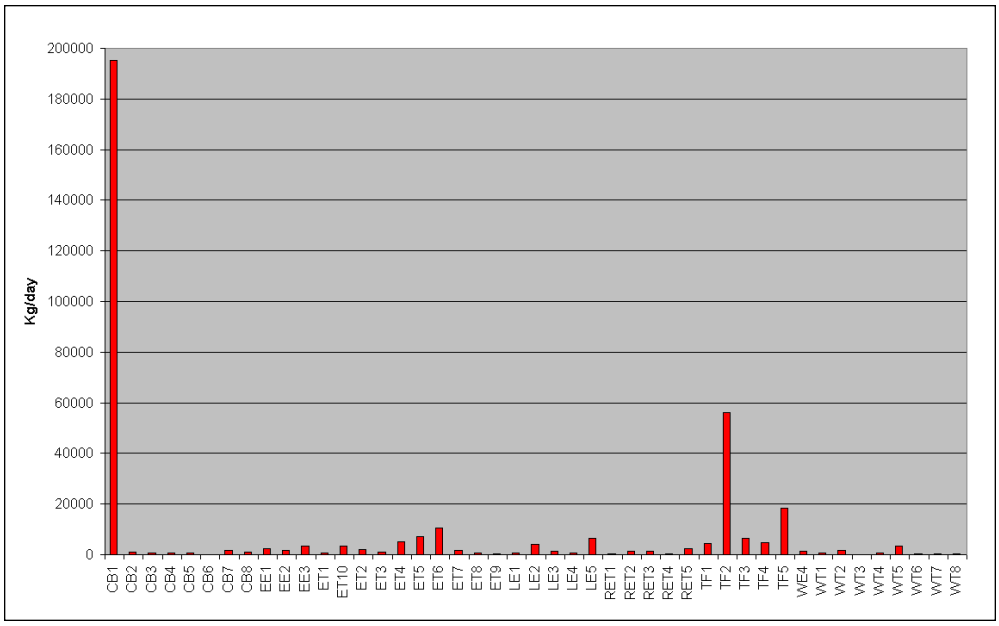

Figure 4-9. Nonpoint-Source Total Nitrogen by CBPS, 1990.

nitrate while in the James 43% is nitrate. Segment ET6, on the lower Eastern Shore, receives the greatest load not associated with a fall line, of which 80% is nitrate.

Time series of major loads (Figures 4-10 to 4-13) demonstrate little correspondence to flows. Correspondence may be obscured by the comparison of annual mean loads with seasonal median flows. Above all, inspection indicates no trend in nitrogen loading.

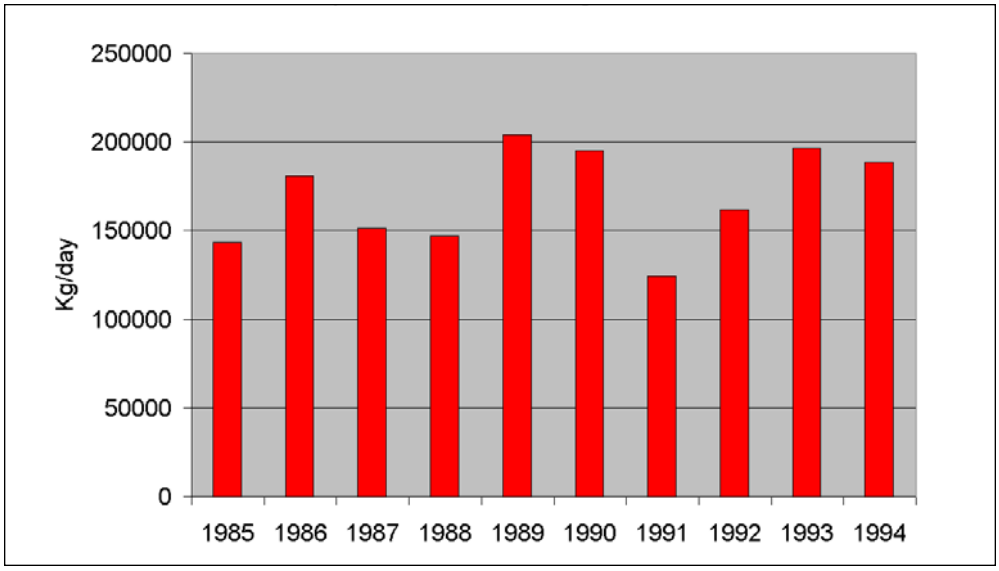

Figure 4-10. Annual Nonpoint-Source Nitrogen Loads in CB1, the Susquehanna Fall Line

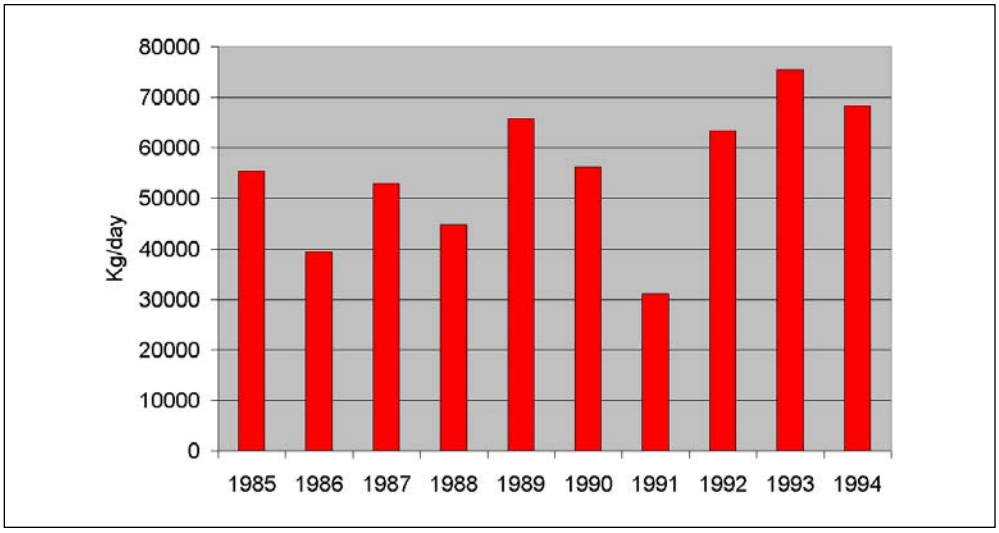

Figure 4-11. Annual Nonpoint-Source Nitrogen Loads in TF2, the Potomac Fall Line.

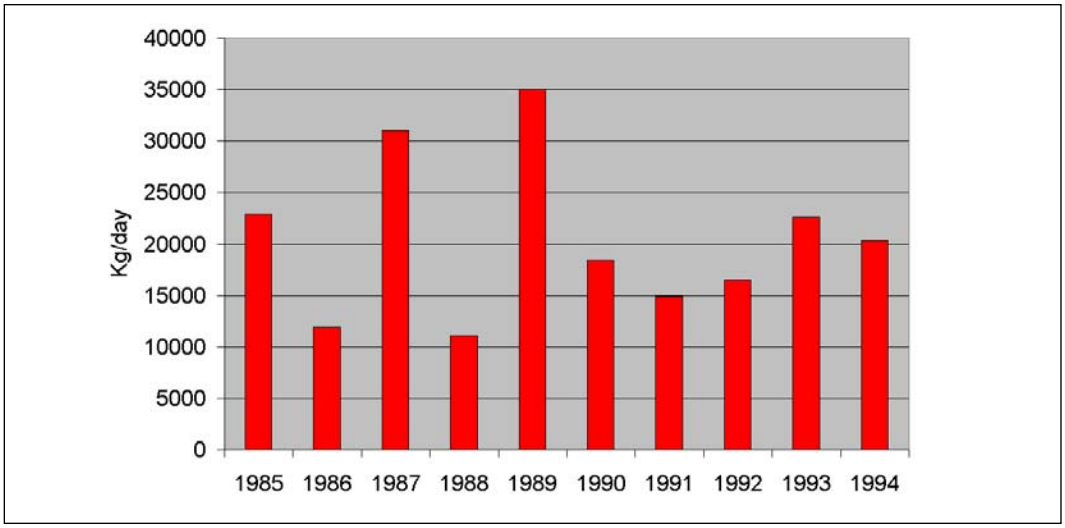

Figure 4-12. Annual Nonpoint-Source Nitrogen Loads in TF5, the James Fall Line.

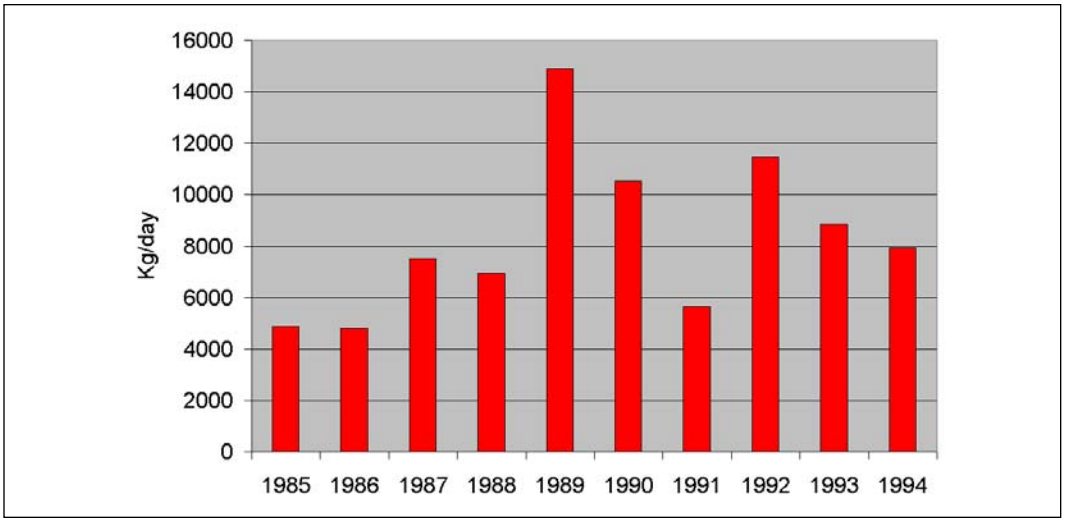

Figure 4-13. Annual Nonpoint-Source Nitrogen Loads in ET6, the Lower Eastern Shore.

Nonpoint-Source Phosphorus Loads

As with nitrogen, the greatest phosphorus loads enter at the Susquehanna, Potomac, and James fall lines (Figure 4-14). Less than 20% of the load in the Susquehanna and Potomac is as dissolved phosphate. In the James, roughly 30% is dissolved phosphate. Loads are not proportional to flows in these tributaries. In 1990, phosphorus load in the Potomac was 70% of the load in the Susquehanna although Potomac flow was 25% of the Susquehanna. Phosphorus load from the James amounted to half the load from the Susquehanna although flow was less than 25% of the Susquehanna. Reasons for the disparity between flow and load are not apparent. No doubt watershed characteristics and above-fall-line point-source loadings play a role. A speculation is that a portion of the Susquehanna particulate phosphorus load is retained in the Conowingo reservoir, just upstream of the fall line. Away from the three major tributaries, the largest nonpoint-source phosphorus load is in segment LE5, the lower James River.

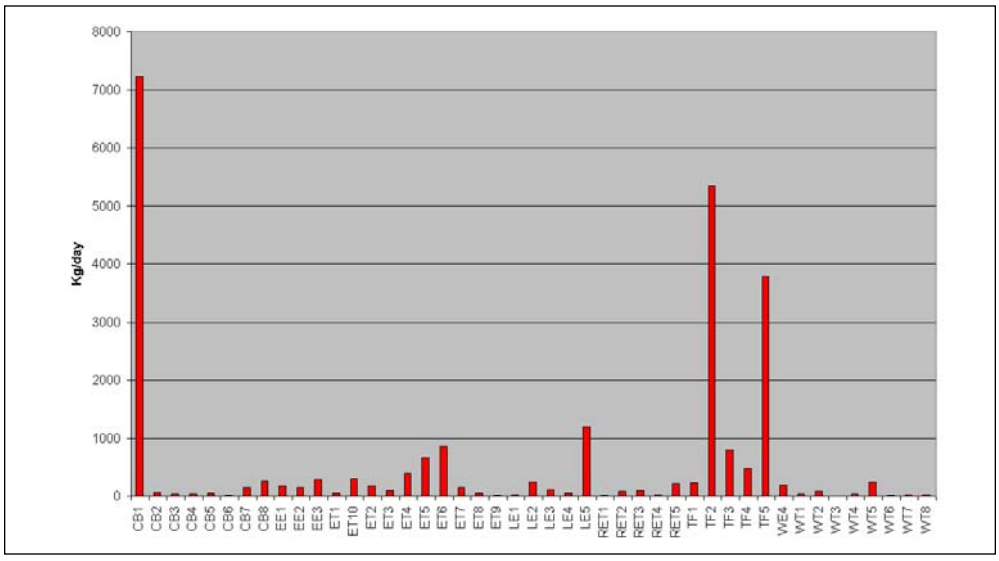

Figure 4-14. Nonpoint-Source Total Phosphorus by CBPS, 1990.

Inspection of time series in the major load segments indicates no trend in the Susquehanna (Figure 4-15), the Potomac (Figure 4-16), and the lower James (Figure 4-18). At the James fall line (Figure 4-17, loads from 1985 to 1989 oscillate between highest and lowest in the ten-year record. From 1990 to 1994, the loads settle into relatively constant, moderate values.

Results indicated no consistent difference between estimates (Figures 4-19 to 4-21) and none could be validated as true.

Nonpoint-Source Total Organic Carbon Loads

Organic carbon is not a state variable in the WSM. A variety of approaches to obtaining nonpoint-source carbon load were investigated. These included use of a constant concentration, determination of concentration via MVUE (minimum variance unbiased estimator) regression of concentration versus flow, and determination of load as a ratio to WSM organic nitrogen load. Results indicated no consistent

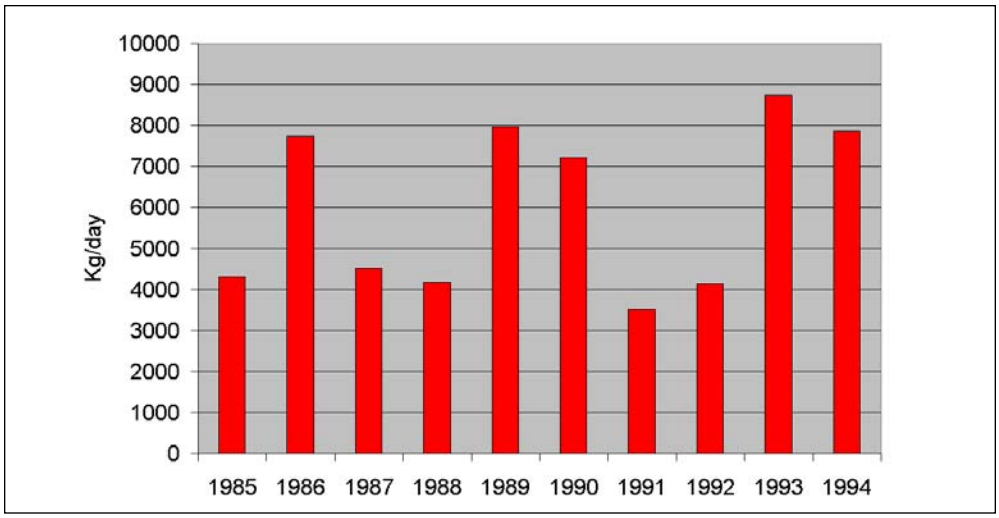

Figure 4-15. Annual Nonpoint-Source Phosphorus Loads in CB1, the Susquehanna Fall Line.

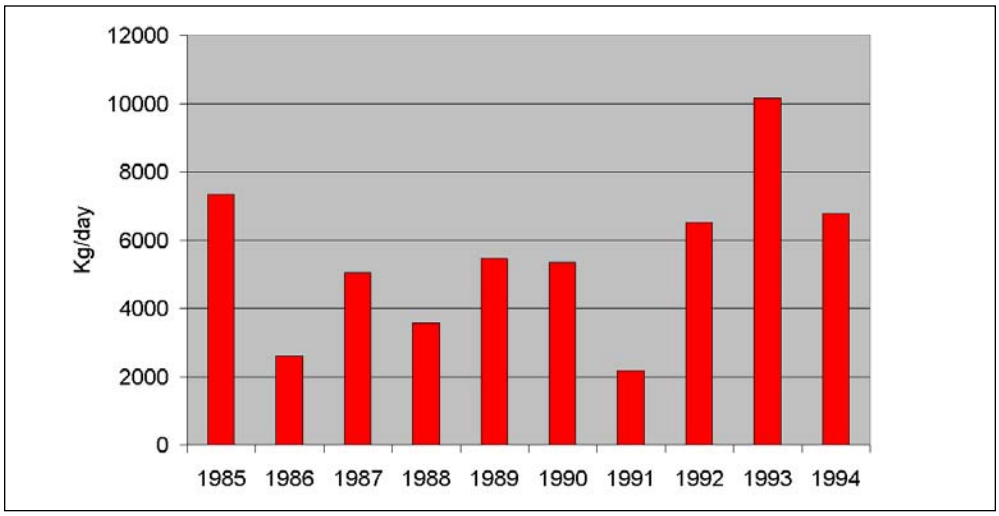

Figure 4-16. Annual Nonpoint-Source Phosphorus Loads in TF2, the Potomac Fall Line.

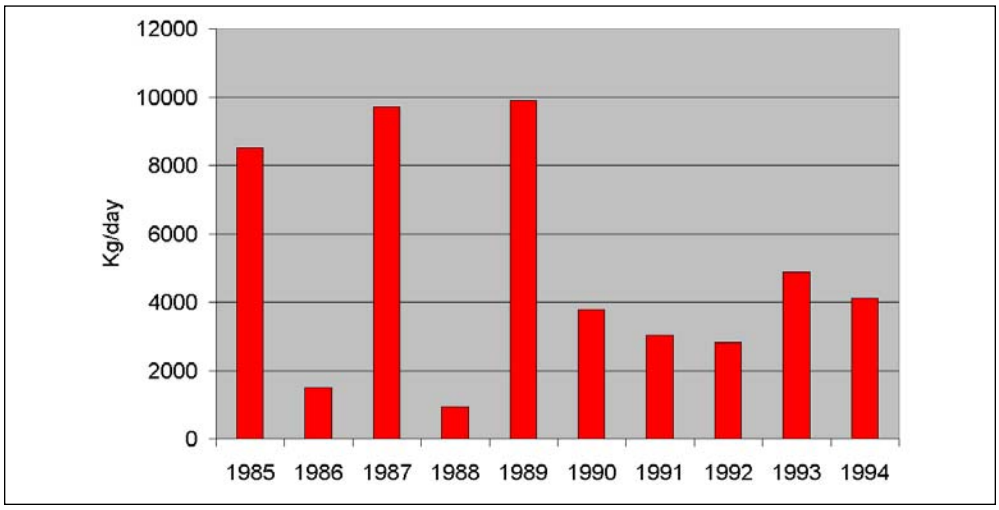

Figure 4-17. Annual Nonpoint-Source Phosphorus Loads in TF5, the James Fall Line.

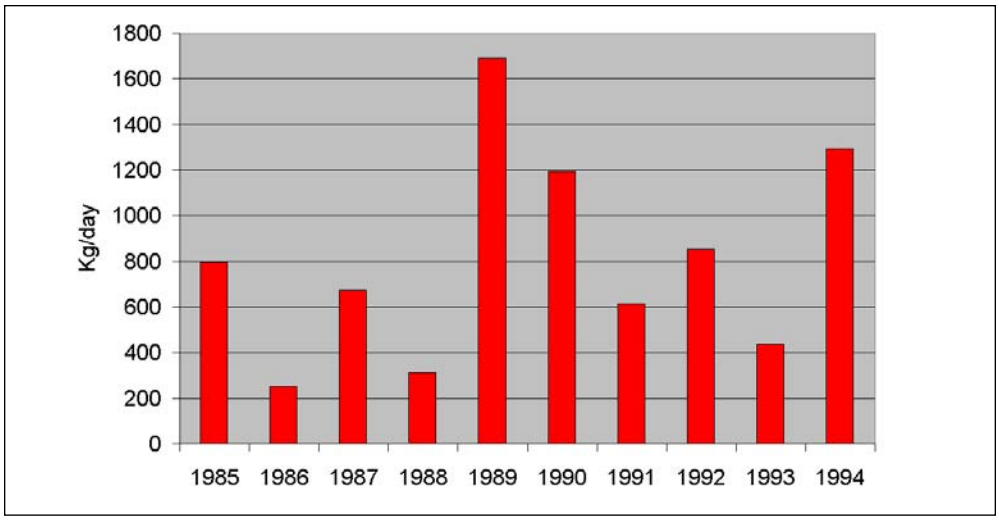

Figure 4-18. Annual Nonpoint-Source Phosphorus Loads in LE5, the Lower James River.

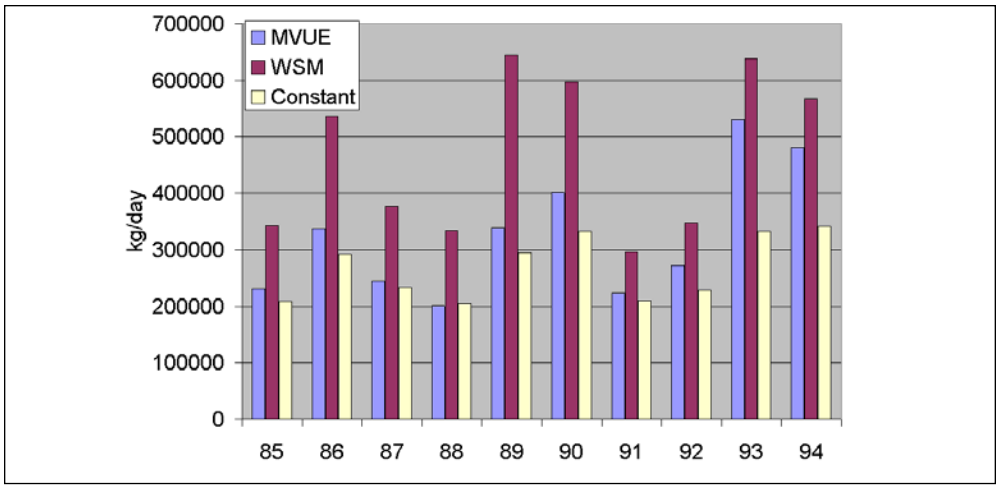

Figure 4-19. Susquehanna Total Organic Carbon Loads by Regression (MVUE), by Ratio to Watershed Model (WSM) and by Constant Concentration (Constant).

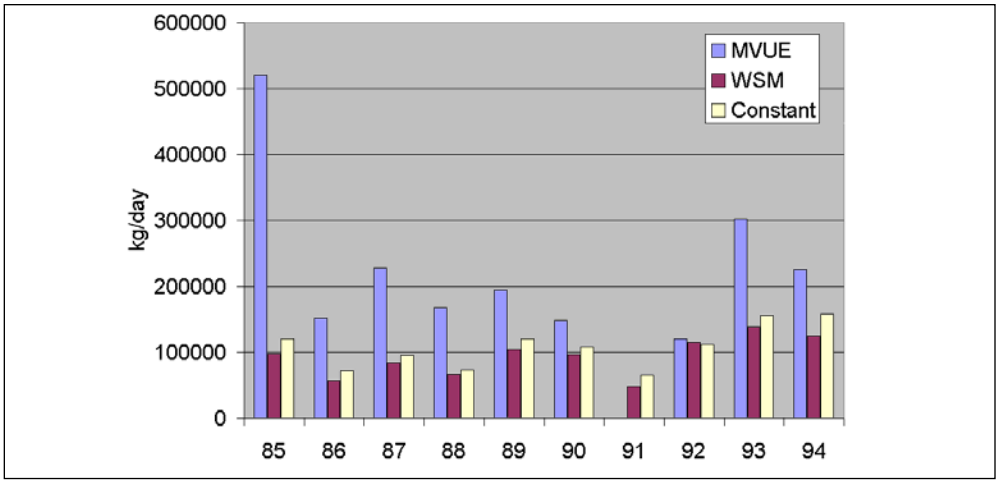

Figure 4-20. Potomac Total Organic Carbon Loads by Regression (MVUE), by Ratio to Watershed Model (WSM) and by Constant Concentration (Constant).

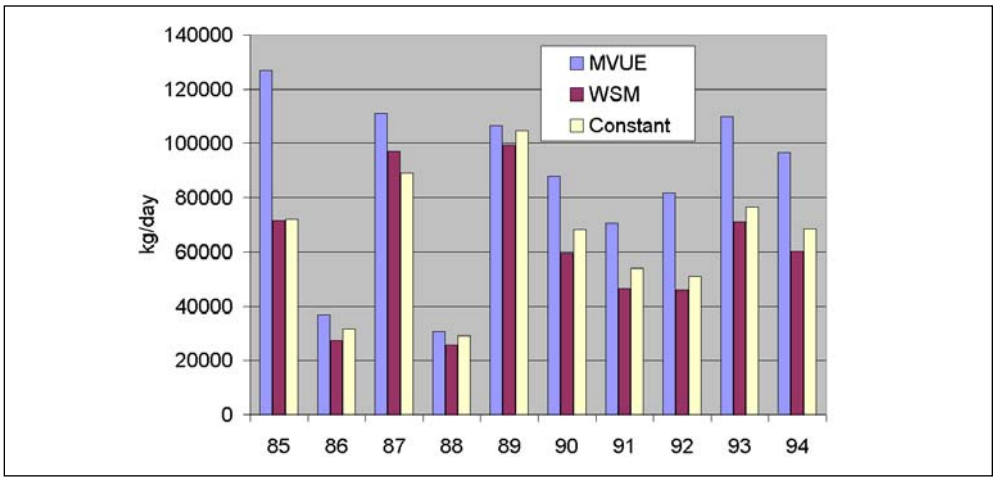

Figure 4-21. James Total Organic Carbon Loads by Regression (MVUE), by Ratio to Watershed Model (WSM) and by Constant Concentration (Constant).

difference between the estimates (Figures 4-19 to 4-21and none could be validated as true. Ratio to the WSM was selected since this method allowed for computation of carbon load reductions in response to watershed management. Carbon-to-nitrogen ratios were obtained from fall-line observations posted by the USGS Chesapeake Bay River Input Monitoring Program http://va.water.usgs.gov/chesbay/RIMP/). Observations were available for Maryland tributaries only. From these, a carbon-to-nitrogen ratio of 12 was specified system-wide except for the Potomac and Choptank. Ratios of 8 and 17.5 were specified for these fall lines, respectively. The distribution of nonpoint-source carbon loads across the system follows the patterns of nitrogen and phosphorus; largest loads are at the Susquehanna, Potomac, and James fall lines (Figure 4-22).

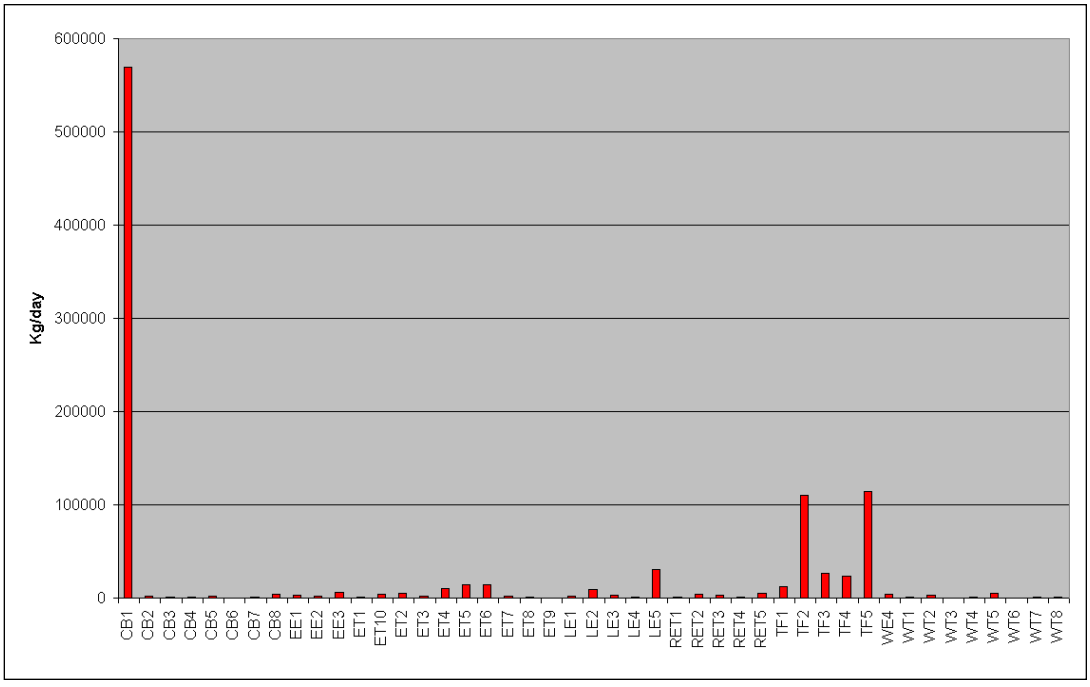

Figure 4-22. Nonpoint-Source Total Organic Carbon by CBPS, 1990.

Nonpoint-Source Total Suspended Solids

In 1990, the largest solids load was from the Potomac, followed by the Susquehanna and James (Figure 4-23). These loads show no relationship to relative flows in the three tributaries. For suspended solids, the Conowingo reservoir acts as a settling basin to remove solids from the Susquehanna before entering the bay (Donoghue et al. 1989; Schubel 1968). Although solids can be scoured from the Conowingo at high flows, the predominant effect of the reservoir is to diminish Susquehanna solids loads relative to the other major tributaries. Away from the fall lines, largest solids loads are received by segment LE5, the lower James River.

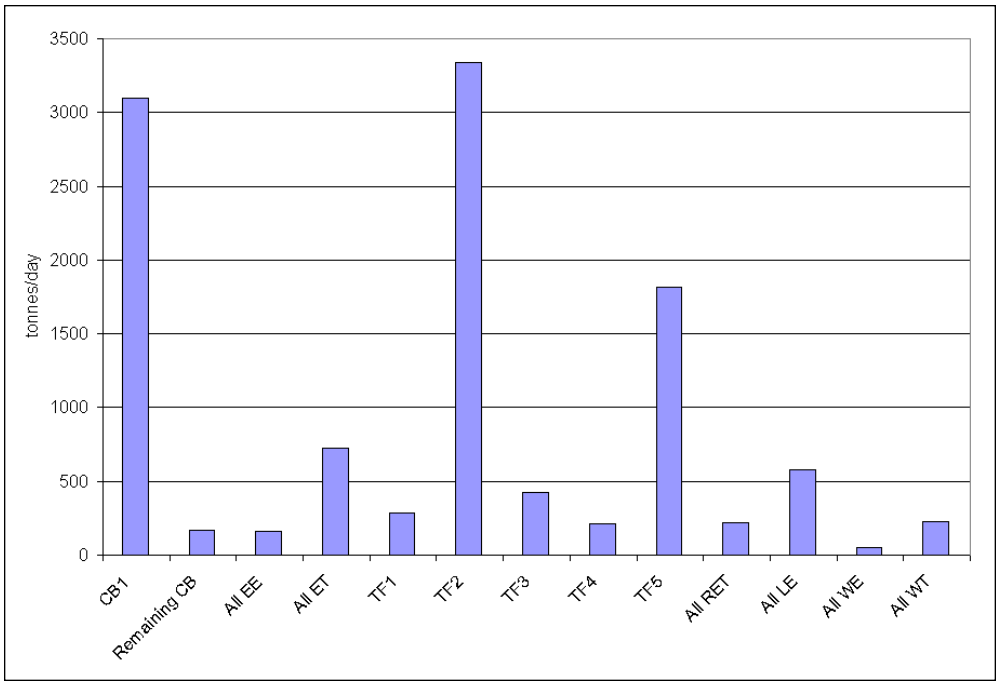

Figure 4-23. Nonpoint-Source Total Suspended Solids by CBPS, 1990.

On an annualized basis (Figures 4-24 to 4-27), solids loads show little correlation to flows although these correlations must exist. The averaging methods remove obvious dependencies. In the Potomac and James, largest annual loads occur in 1985. The loads are dominated by a November 1985 flood event that is obscured by the median statistic. Perhaps the major conclusion drawn from the time series is that solids loads in the major sources bear little correlation with each other.

Point-Source Loads

Point-source loads were provided by the EPA Chesapeake Bay Program Office in December 2000. These were based on reports provided by local regulatory agencies. Loads from individual sources were summed into loads to model surface cells and were provided on a monthly basis. Despite the provision of monthly values, loads from Virginia were most often specified on an annual basis while loads from Maryland varied monthly. In the Potomac River, loads on the Virginia side were

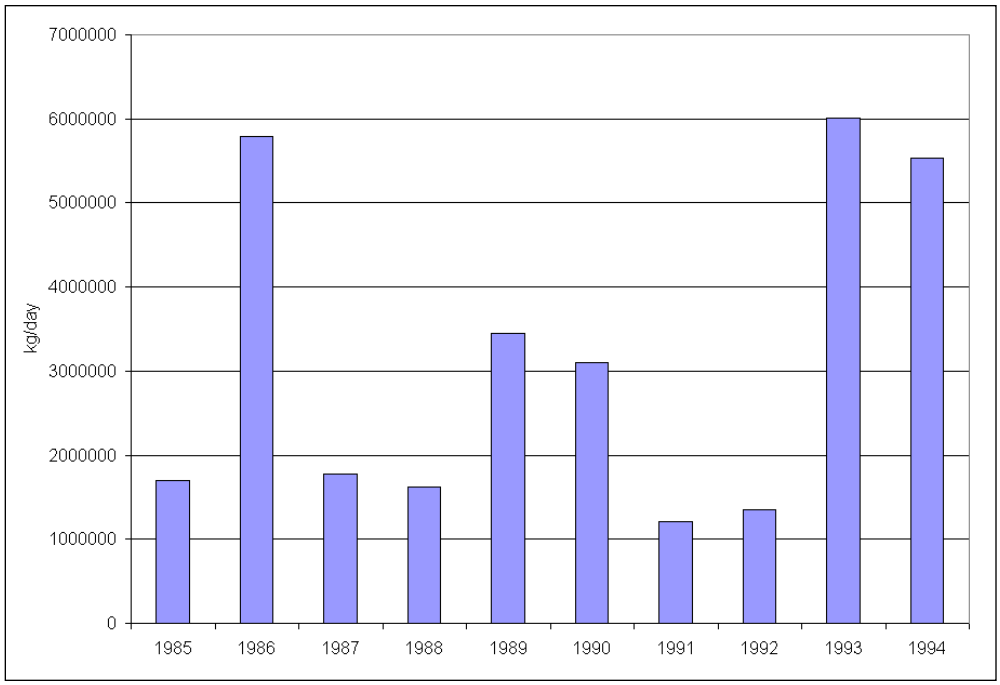

Figure 4-24. Annual Nonpoint-Source Suspended Solids Loads in CB1, the Susquehanna Fall Line.

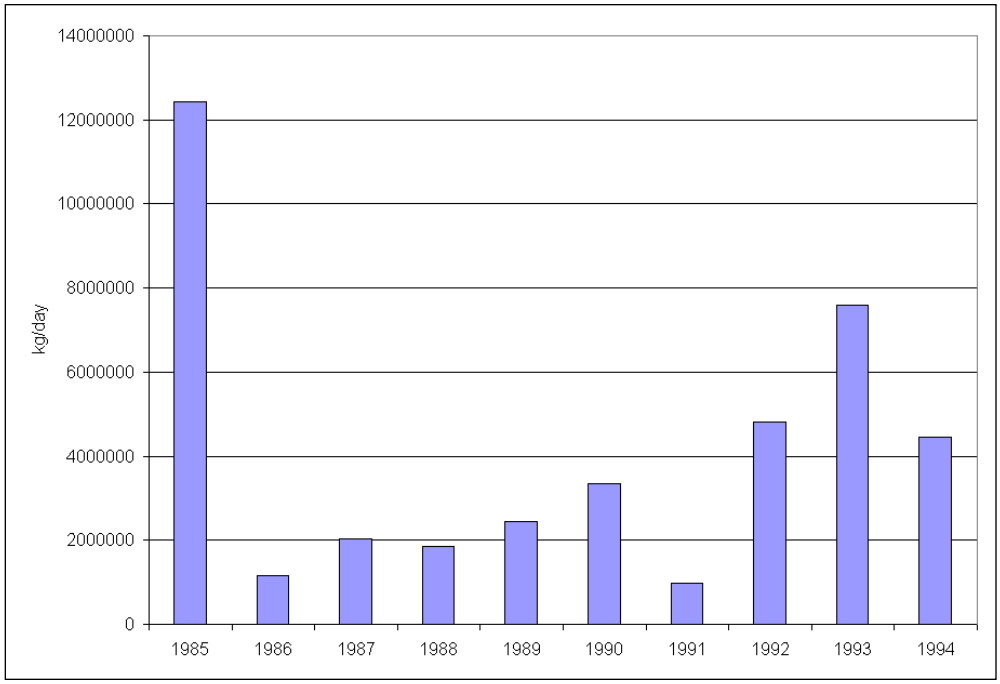

Figure 4-25. Annual Nonpoint-Source Suspended Solids Loads in TF2, the Potomac Fall Line.

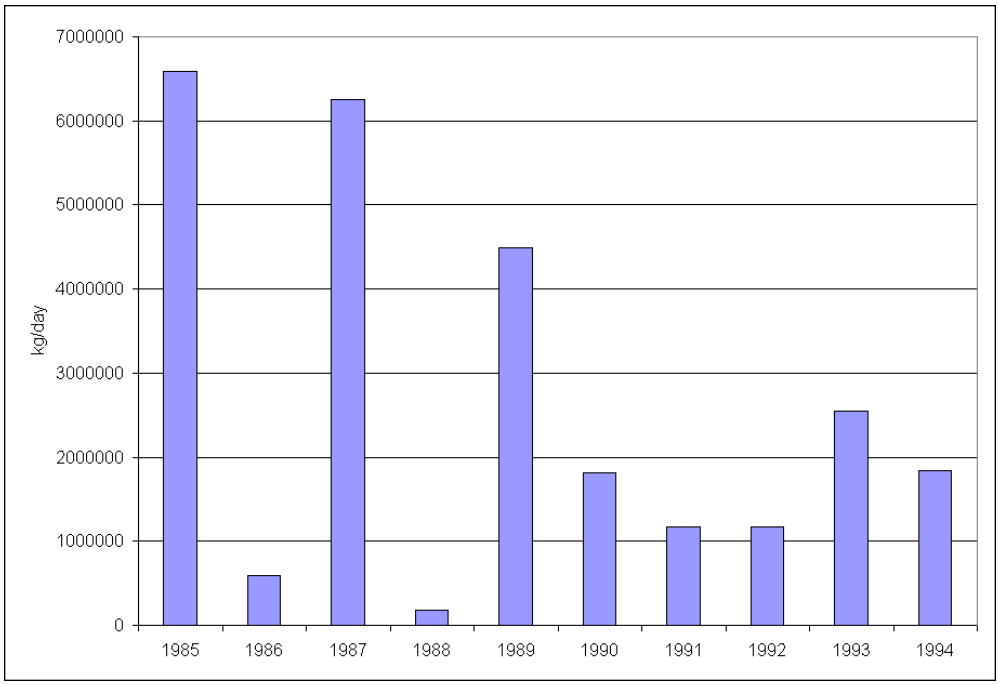

Figure 4-26. Annual Nonpoint-Source Suspended Solids Loads in TF5, the James Fall Line.

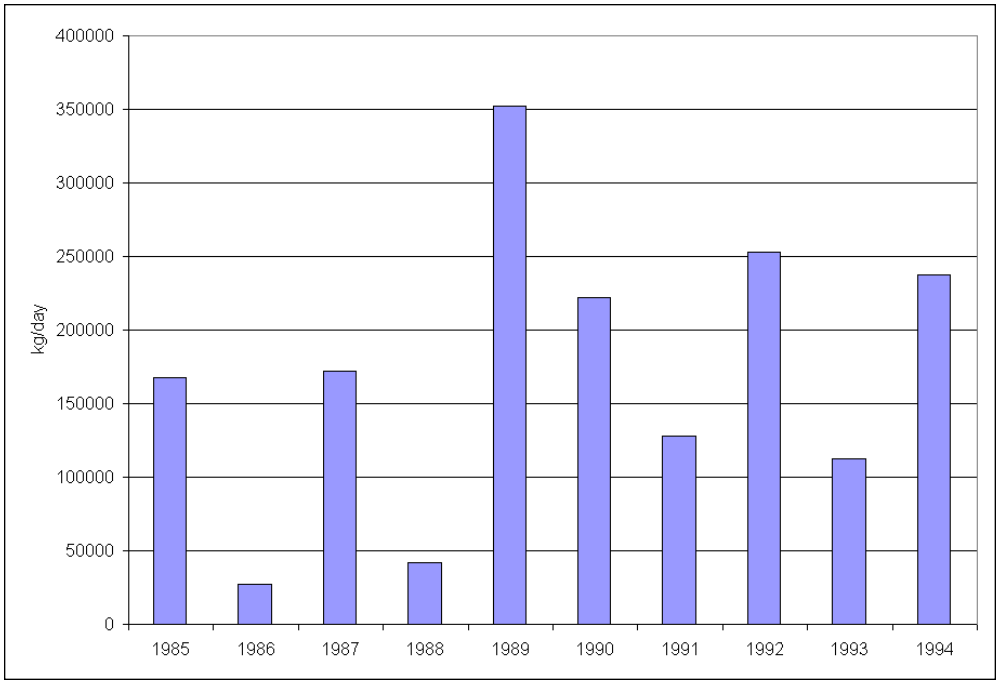

Figure 4-27. Annual Nonpoint-Source Suspended Solids Loads in LE5, the Lower James River.

annual loads while loads on the Maryland side were monthly loads. Examination of the Maryland loads indicates considerable variance (Figure 4-28) which is lacking in the specification of Virginia loads.

For reporting, loads are summed here by Chesapeake Bay Program Segments (CBPS, Figure 4-8). System-wide summaries are for 1990, a year central to the simulation period. Individual segments are selected for time-series presentation.

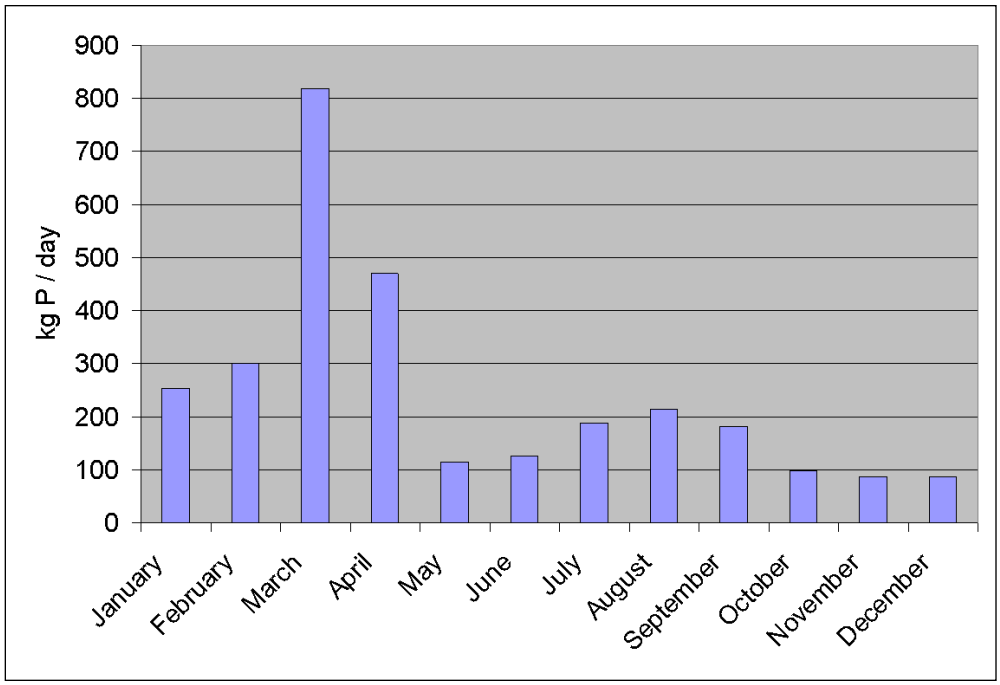

Figure 4-28. Monthly (1994) Point-Source Phosphorus Loads to Model Cell 2846 on the Maryland Shore of the Potomac River.

Point-Source Nitrogen Loads

Point-source loads are concentrated in urban areas (Figure 4-29). Major nitrogen loads originate in Northern Virginia/District of Columbia (TF2), Richmond Virginia (TF5), Baltimore Maryland (WT5, WT4), and Hampton Roads Virginia (LE5). Of these, only loads to the Patapsco (WT5, Figure 4-32) show a monotonic decreasing trend. Loads to the upper Potomac (TF2, Figure 4-30), and upper James (TF5, Figure 4-31) suggest a decrease after 1990. Point-source nitrogen loads to the Back River (WT4, Figure 4-33) and the lower James (LE5, Figure 4-34) show no trend.

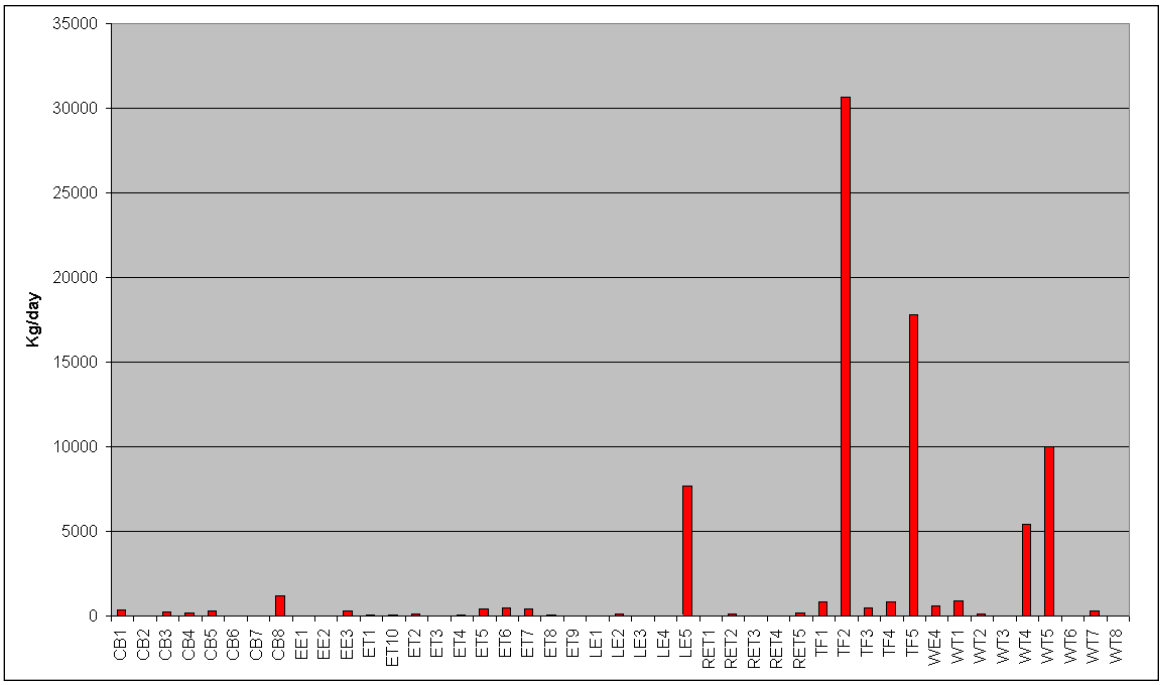

Figure 4-29. Point-Source Nitrogen Loads by CBPS, 1990.

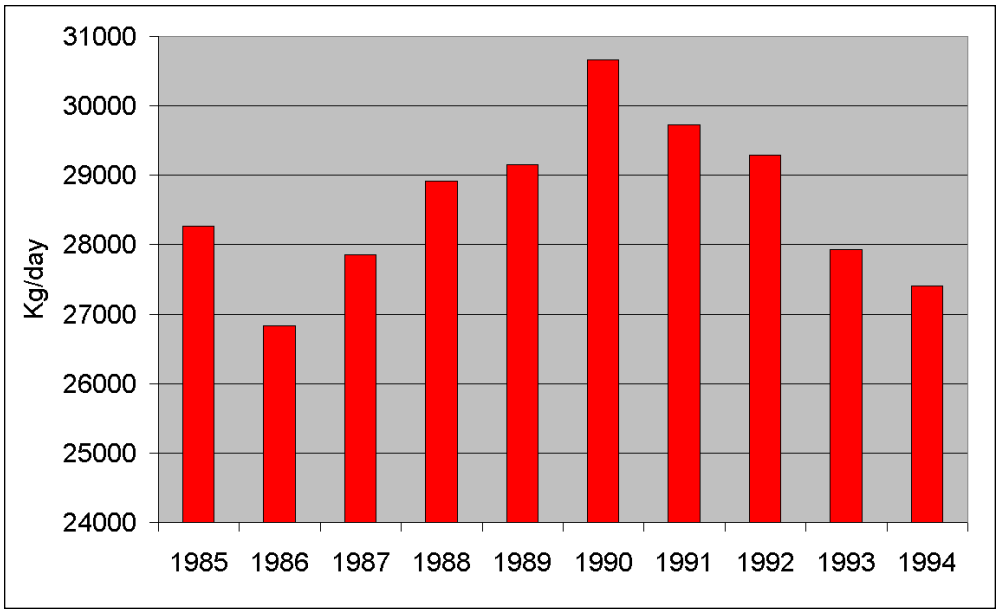

Figure 4-30. Annual Point-Source Nitrogen Loads in TF2, Northern Virginia/District of Columbia

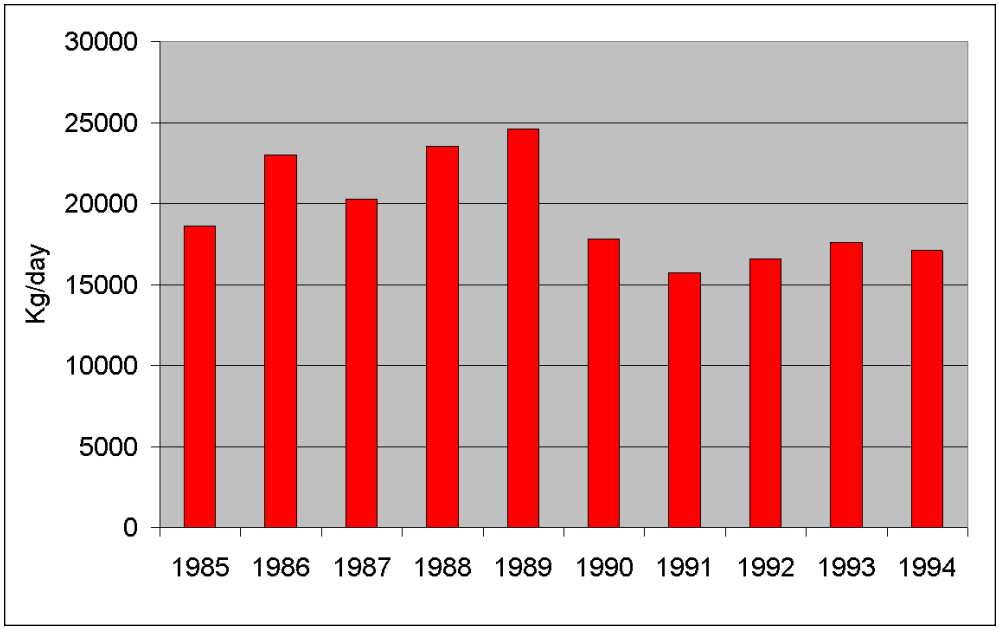

Figure 4-31. Annual Point-Source Nitrogen Loads in TF5, Richmond Virginia Vicinity.

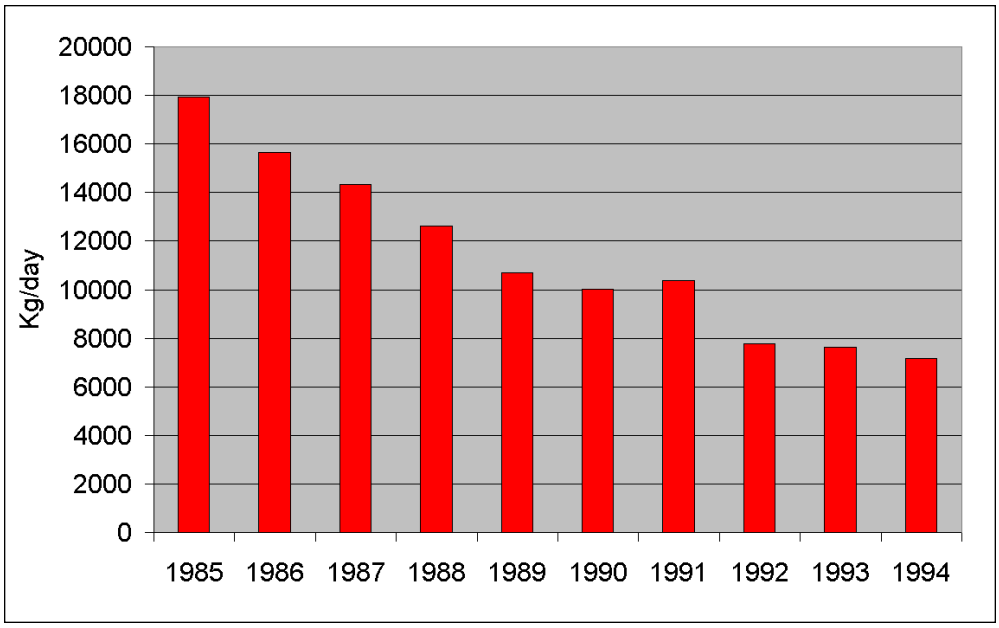

Figure 4-32. Annual Point-Source Nitrogen Loads in WT5, Patapsco River, Baltimore Maryland.

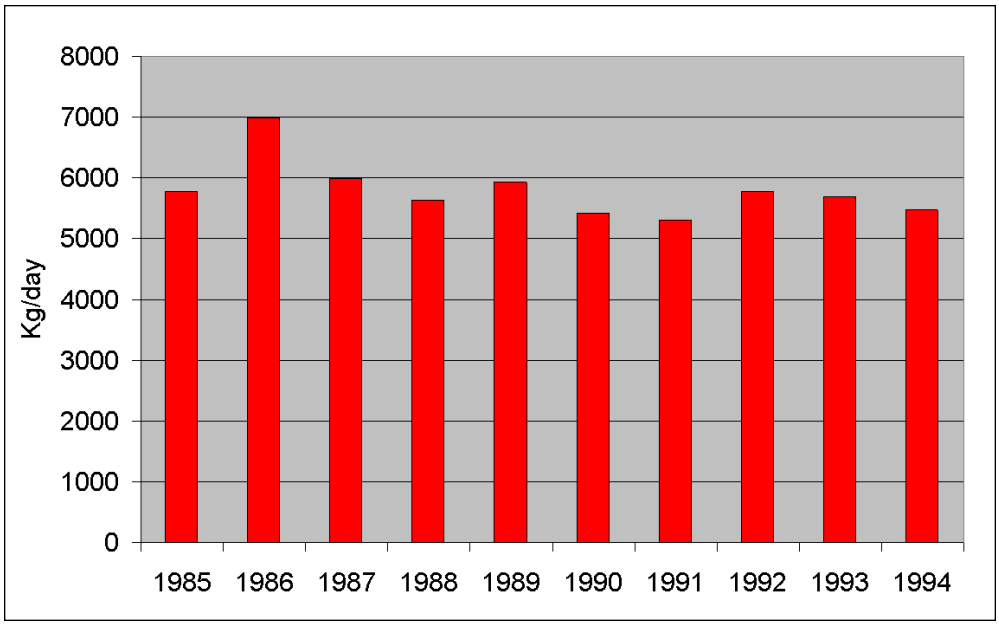

Figure 4-33. Annual Point-Source Nitrogen Loads in WT4, Back River, Baltimore Maryland.

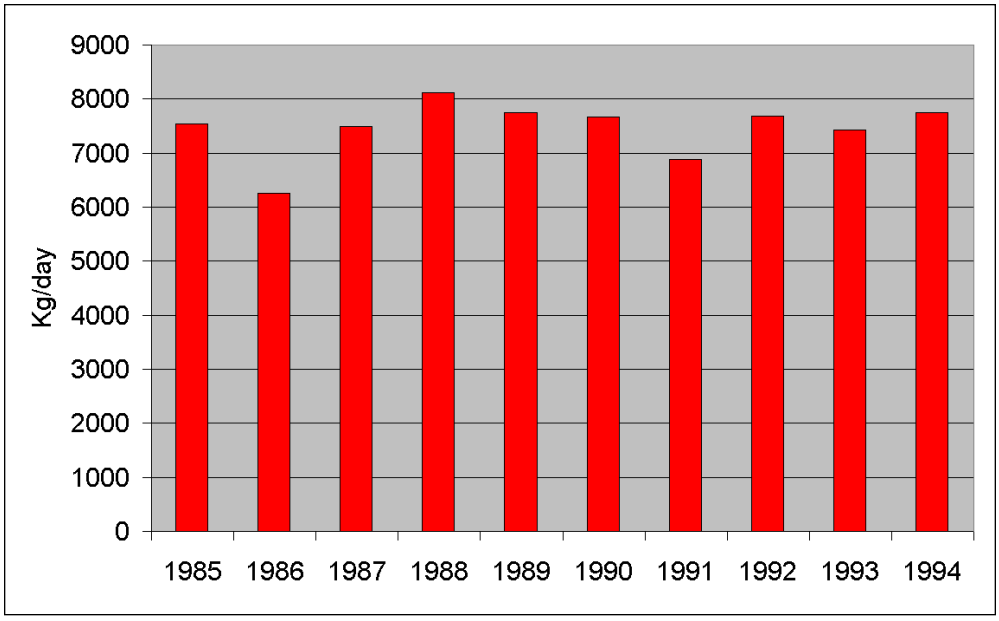

Figure 4-34. Annual Point-Source Nitrogen Loads in LE5, Hampton Roads Virginia.

Point-Source Phosphorus Loads

Point-source phosphorus loads are concentrated in the same urban areas as nitrogen although the relationship by size differs (Figure 4-35). In 1990, largest loads were from Hampton Roads and Richmond Virginia. Northern Virginia/ District of Columbia contributed the least phosphorus load of the major urban centers. The same area showed the least reduction of phosphorus loads over the simulation period (Figure 4-36), possibly a consequence of load reductions prior to 1985. In the remaining urban areas, point-source phosphorus loads were halved from 1985 to 1994 (Figures 4-37 to 4-40)

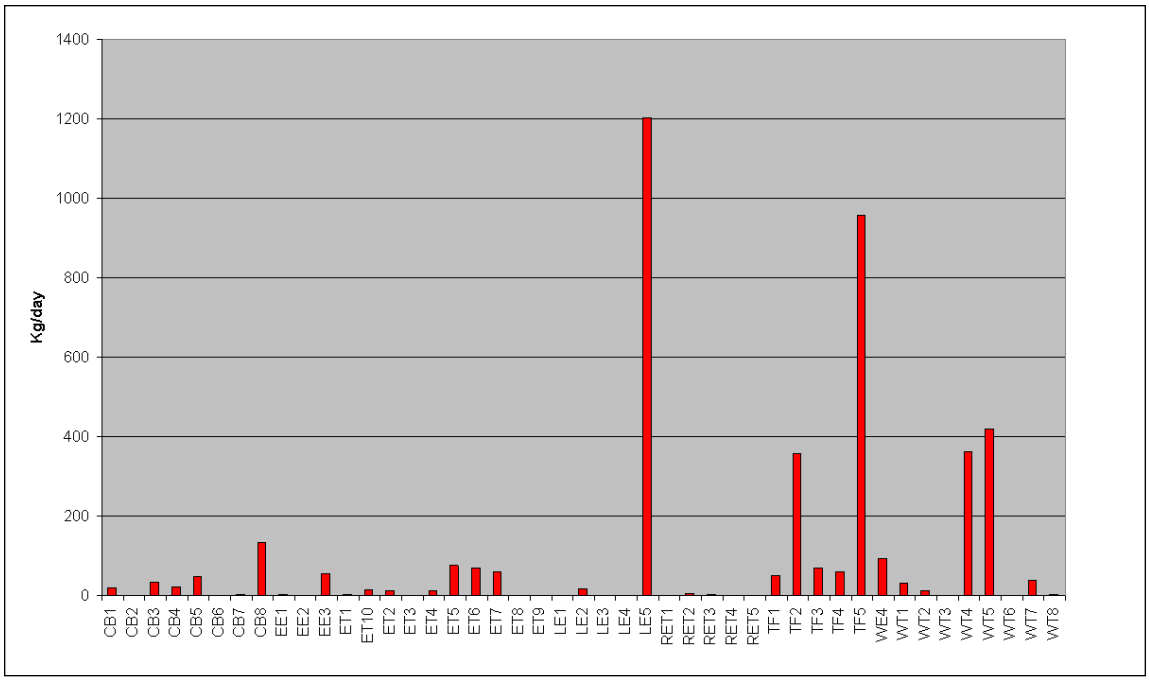

Figure 4-35. Point-Source Phosphorus Loads by CBPS, 1990.

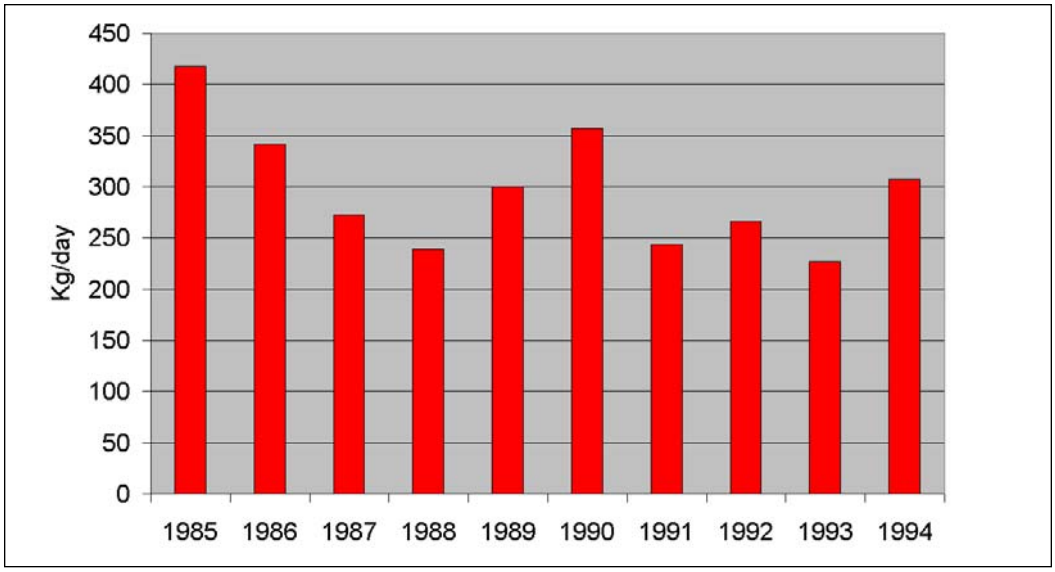

Figure 4-36. Annual Point-Source Phosphorus Loads in TF2, Northern Virginia/ District of Columbia.

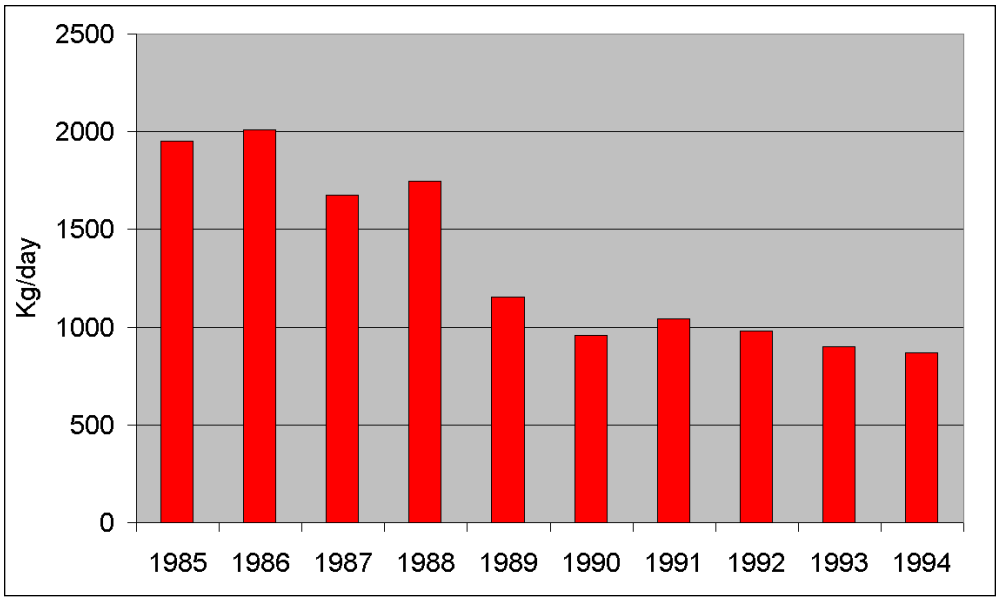

Figure 4-37. Annual Point-Source Phosphorus Loads in TF5, Richmond Virginia Vicinity.

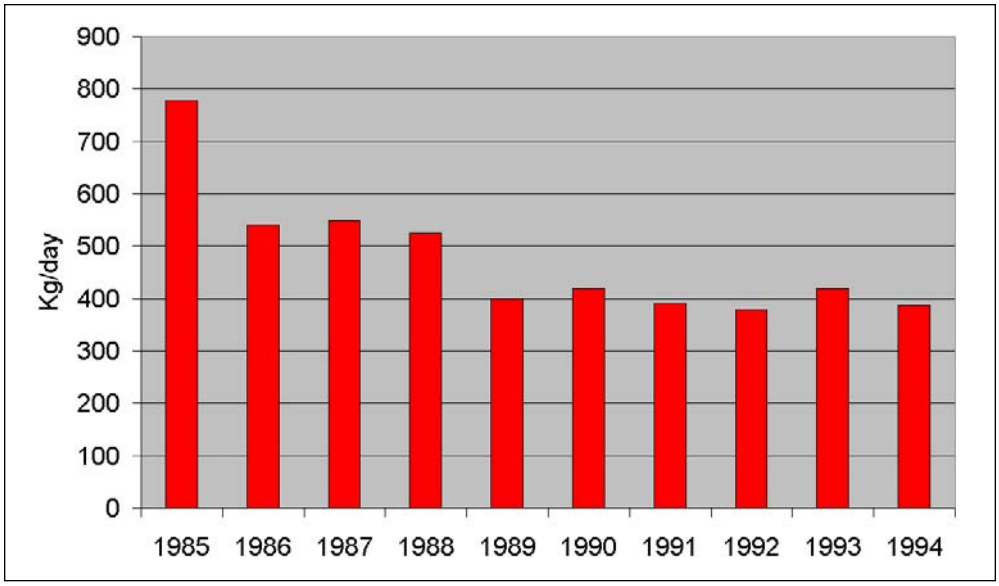

Figure 4-38. Annual Point-Source Phosphorus Loads in WT5, Patapsco River, Baltimore Maryland.

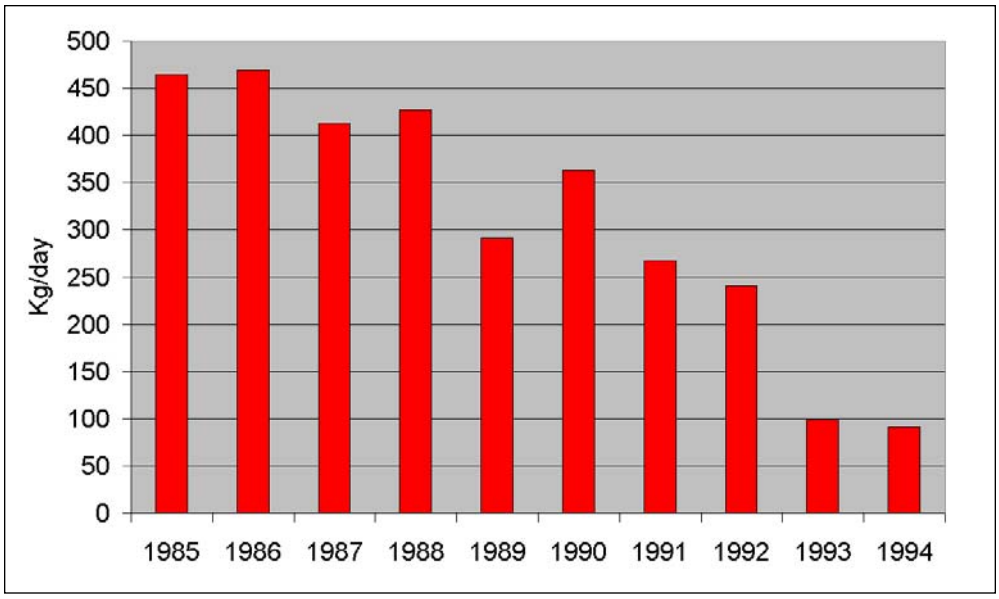

Figure 4-39. Annual Point-Source Phosphorus Loads in WT4, Back River, Baltimore Maryland.

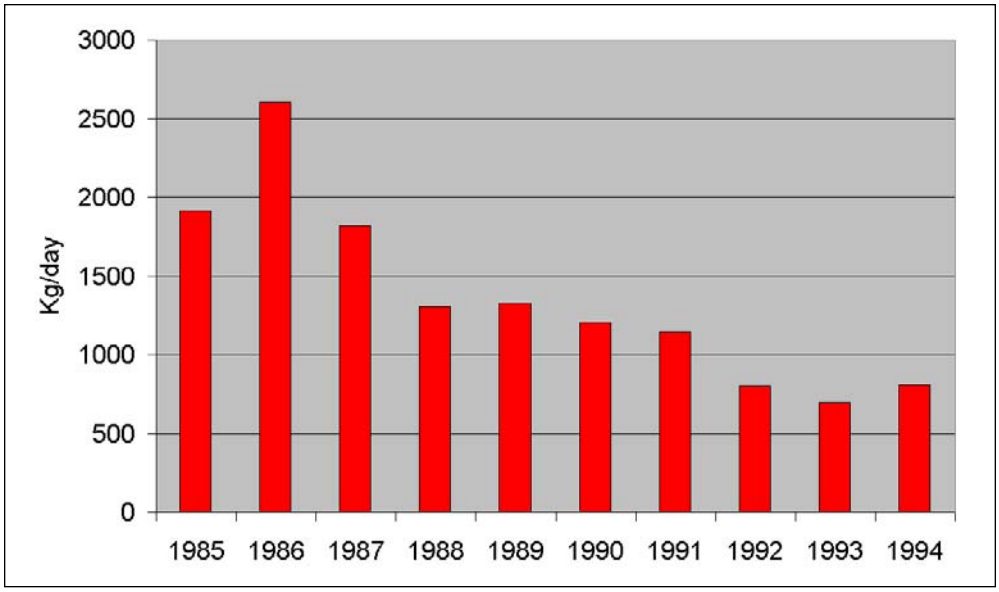

Figure 4-40. Annual Point-Source Phosphorus Loads in LE5, Hampton Roads Virginia.

Point-Source Total Organic Carbon

Organic carbon is not commonly monitored or reported in point-source loads. As part of the Tributary Refinements phase of this study, effluent from selected point sources in Virginia was analyzed for parameters included in the model. Total organic carbon in effluent showed enormous variation (Figure 4-41). When carbon concentration was normalized by total nitrogen concentration, the variance diminished but was still substantial (Figure 4-42). Based on these analyses, a

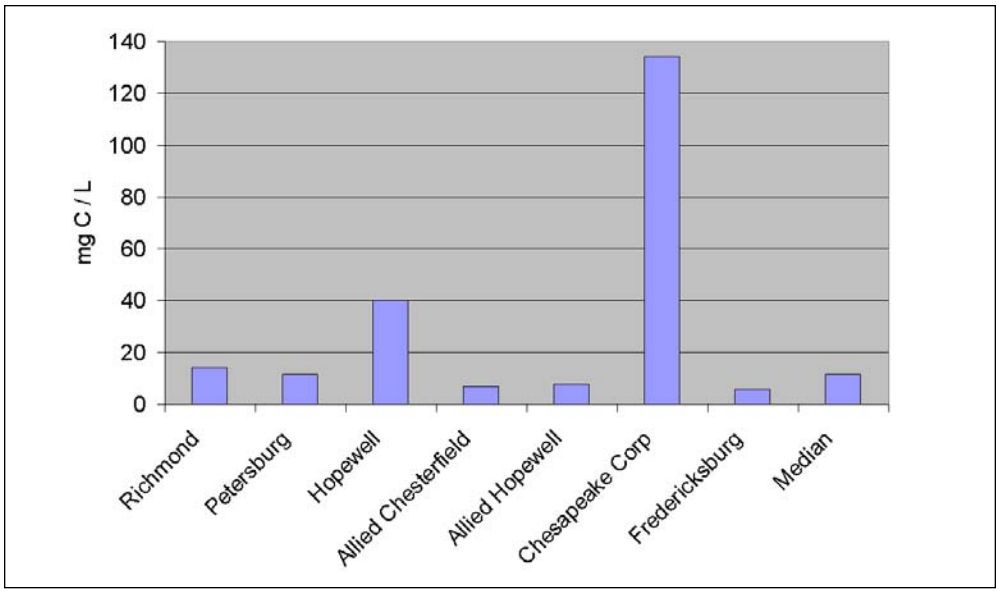

Figure 4-41. Mean Total Organic Carbon Concentration in Virginia Point-Source Effluent 1994-1995.

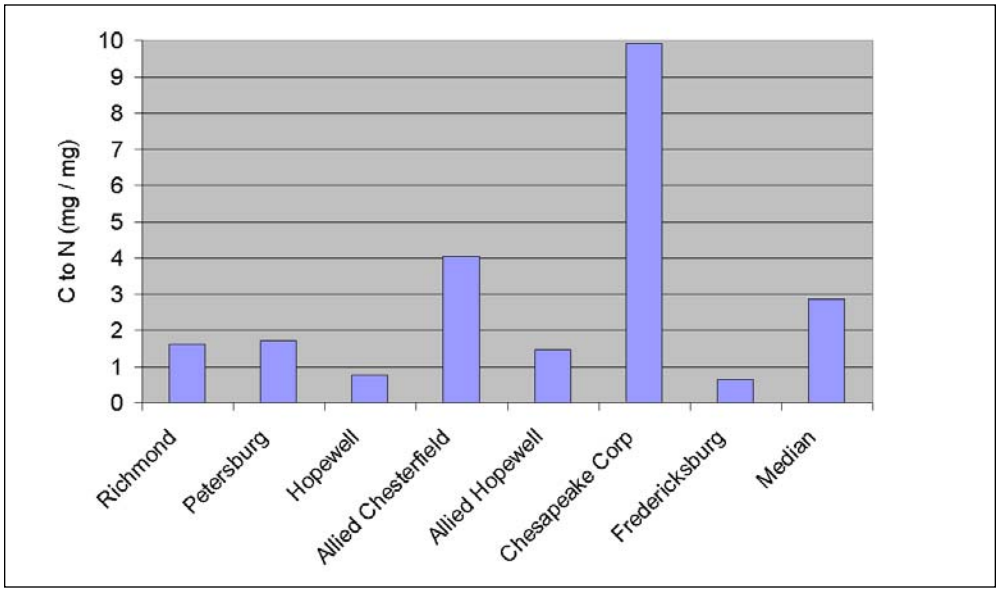

Figure 4-42. Carbon to Nitrogen Ratio in Virginia Point-Source Effluent 1994-1995.

carbon-to-nitrogen ratio of 2:1 was utilized for point sources system-wide except for the Chesapeake Corporation, located in the upper York River. Here, a ratio of 10:1 was employed. Since carbon loads were obtained by simple ratio to nitrogen loads, the distribution of carbon loads (Figure 4-43) reflects the nitrogen load on which it is based.

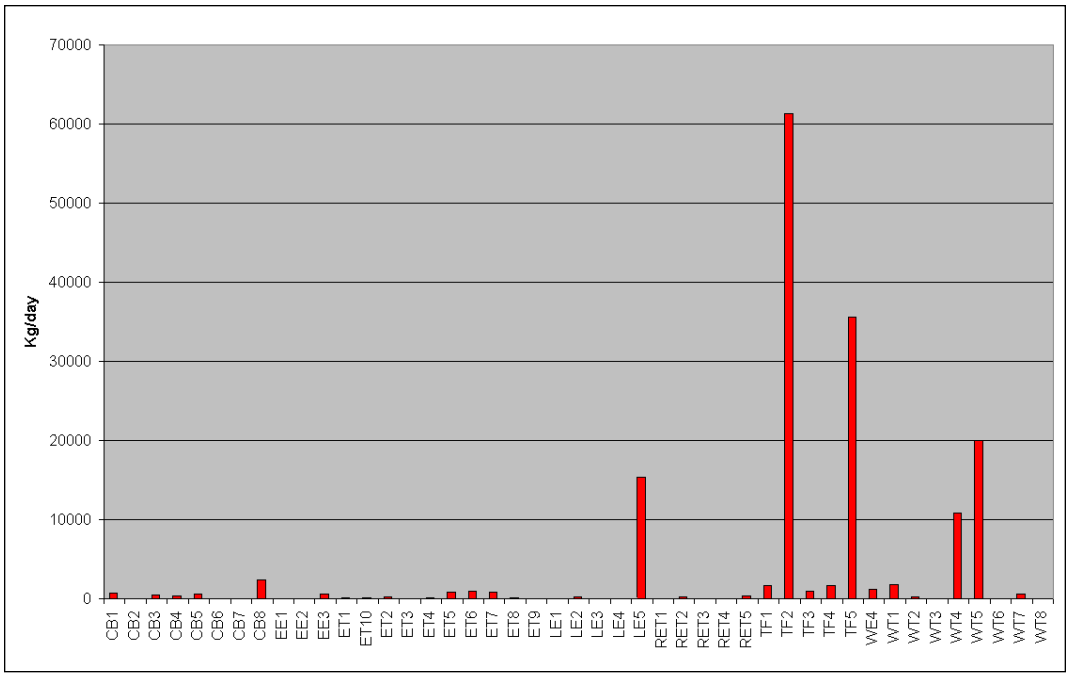

Figure 4-43. Point-Source Organic Carbon Loads by CBPS, 1990.

Atmospheric Loads

Atmospheric loads are deposited directly on the water surface. These originate in precipitation (wetfall) and as particle deposition (dryfall). Daily atmospheric loads for each surface cell were computed by the EPA Chesapeake Bay Program Office and provided in January 2000.

Wet deposition of ammonium and nitrate was derived from National Atmospheric Deposition Program observations. Data from 15 stations in the watershed, collected from 1984–1992, was employed to relate concentration to precipitation, month, and location. For each rainfall event in the calibration period, atmospheric loads were computed as the product of calculated concentration and precipitation volume.

Dry deposition of nitrate was derived from wet deposition using ratios calculated by the Regional Acid Deposition Model (Chang et al. 1987). The atmospheric load of organic nitrogen to water surfaces was determined as the product of concentration and rainfall volume. Deposition of organic and inorganic phosphorus was specified on a uniform, constant, areal basis derived from published values.

For reporting, loads are summed here by Chesapeake Bay Program Segments (CBPS, Figure 4-8). System-wide summaries are for 1990, a year central to the simulation period.

Although areal atmospheric nitrogen loads vary on a spatial basis, total loading to each CBPS is primarily a function of surface area; the largest segments receive the greatest loads (Figure 4-44). These include segments in the central bay, the

eastern embayments, and the lower portions of major western tributaries. Variability, on an annual basis, is roughly 40% of the mean load and exhibits no obvious trend (Figure 4-45). The spatial distribution of atmospheric phosphorus loads (Figure 4-46) is identical to the distribution of nitrogen loads and is temporally constant.

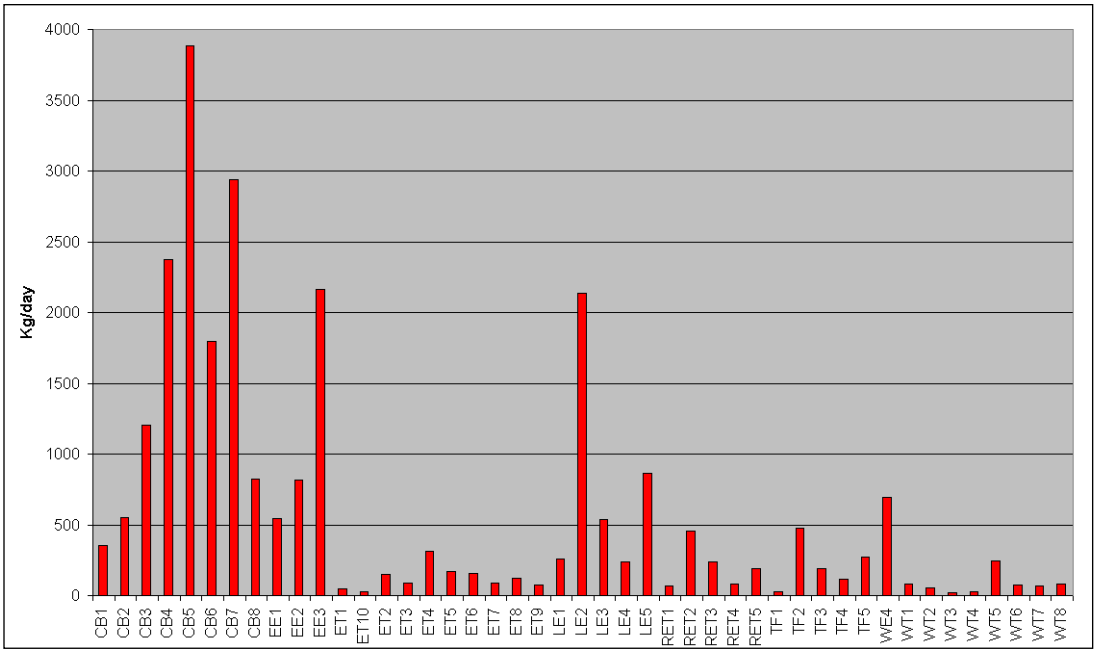

Figure 4-44. Atmospheric Nitrogen Loads by CBPS, 1990.

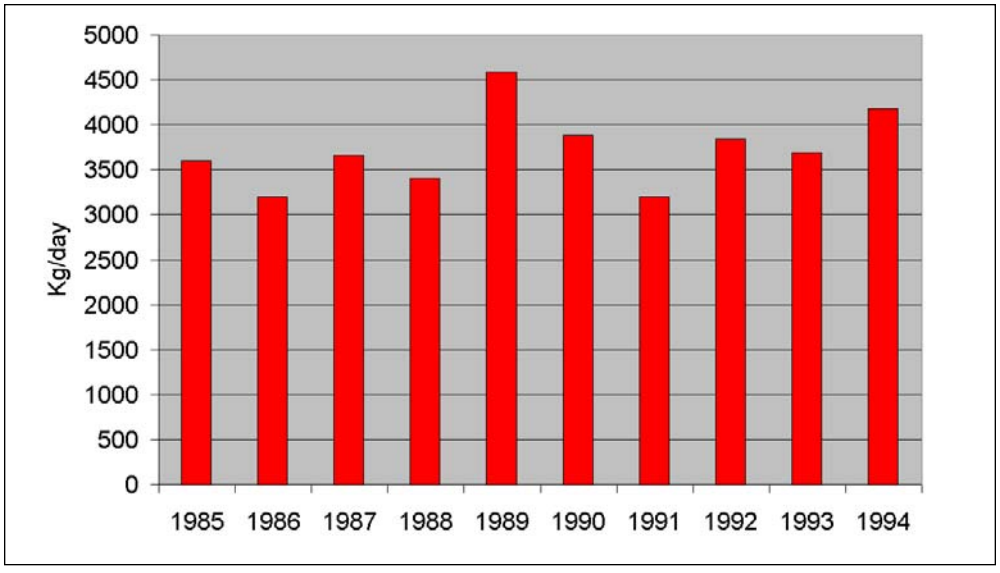

Figure 4-45. Annual Atmospheric Nitrogen Loads in CB5, Central Chesapeake Bay.

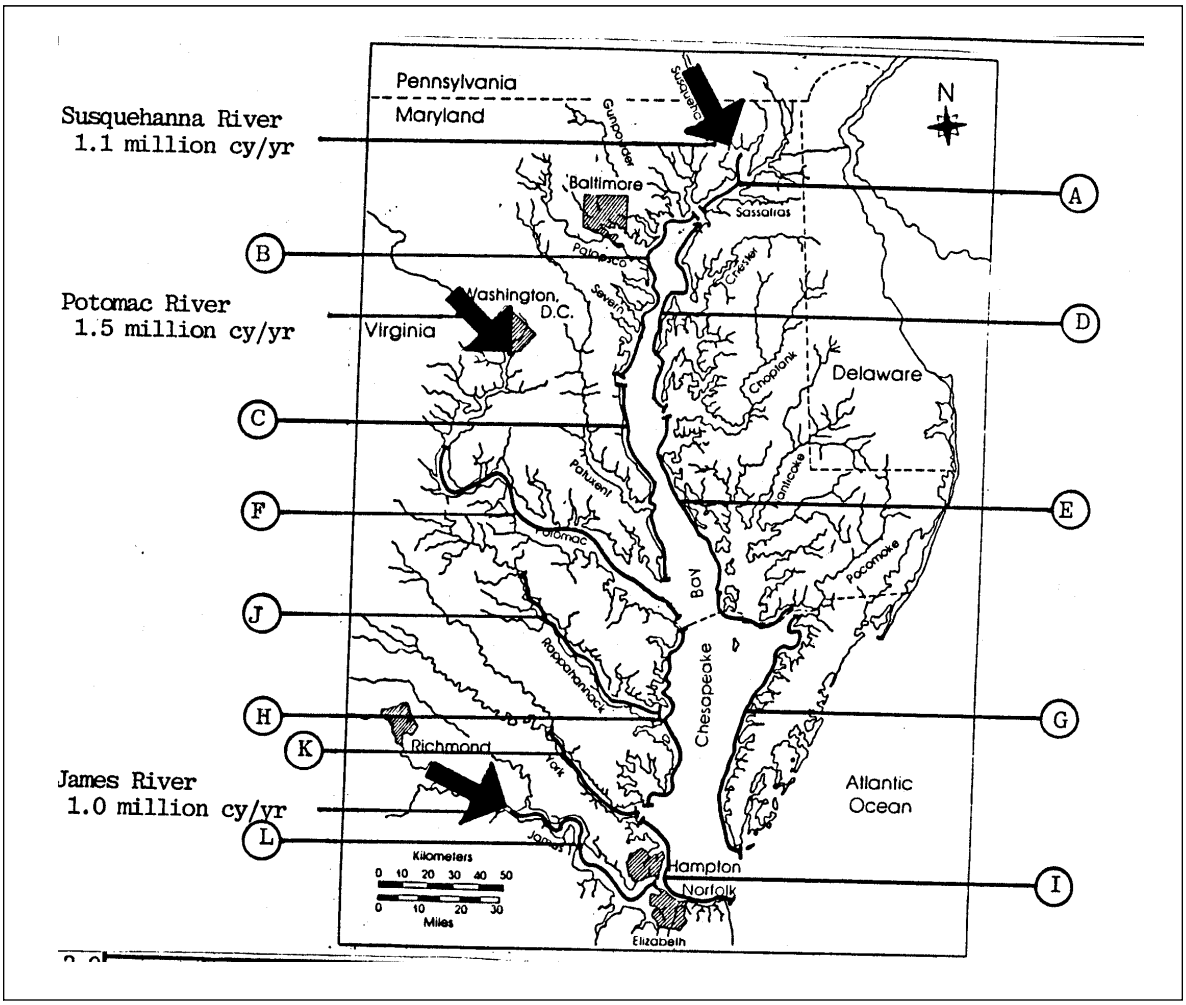

Figure 4-47. Annual Shoreline Erosion in Chesapeake Bay System (US Army Engineer District, Baltimore 1990).

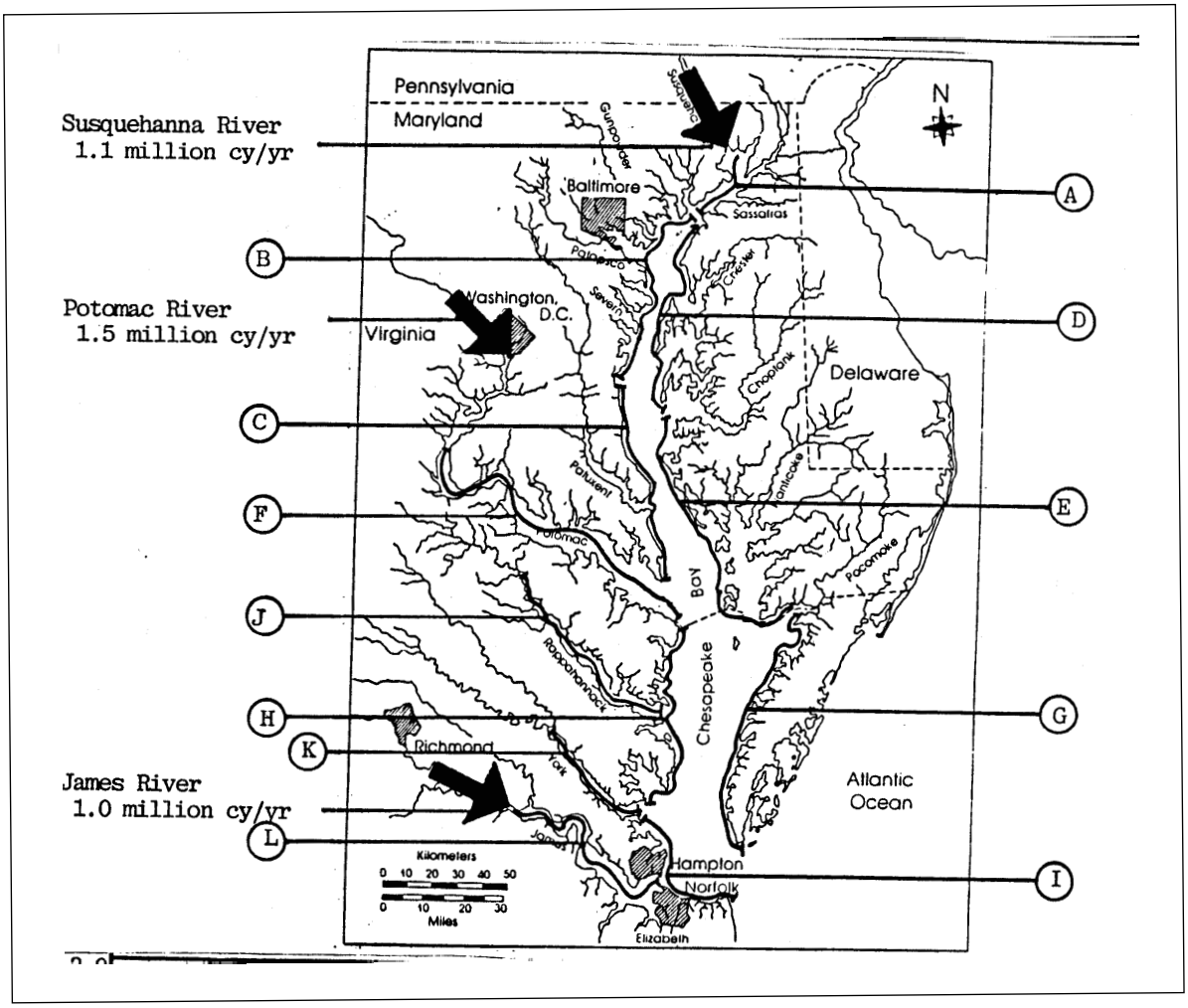

Figure 4-47. Annual Shoreline Erosion in Chesapeake Bay System (US Army Engineer District, Baltimore 1990).

(Table 4-1), we decided to consider bank loading as a spatially and temporally uniform process. Loads to each surface cell were computed:

$$\text{BankLoad} = L \bullet E \bullet Fsc \bullet \text{BankAdj} \bullet C \qquad (4\text{-}1)$$

in which:
Bank Load = load to surface cell (kg d^{-1})
L = length of cell adjacent to shoreline (m)
E = erosion rate (kg solids m^{-1} shoreline d^{-1})
Fsc = fraction silt and clay in total volume eroded ($0 \leq Fsc \leq 1$)
BankAdj = calibration factor used to adjust bank loads (1)
C = nutrient or carbon concentration associated with solids (kg kg^{-1})

Only cells adjacent to the shore received loads. In portions of tributaries which were one cell wide, the shoreline length was twice the cell length. Otherwise, the shoreline length was the cell length. We specified erosion rate based on a mean value and used parameter BankAdj to tune the solids concentration in the model. Alternately, we could have specified erosion rate based on observations, but not

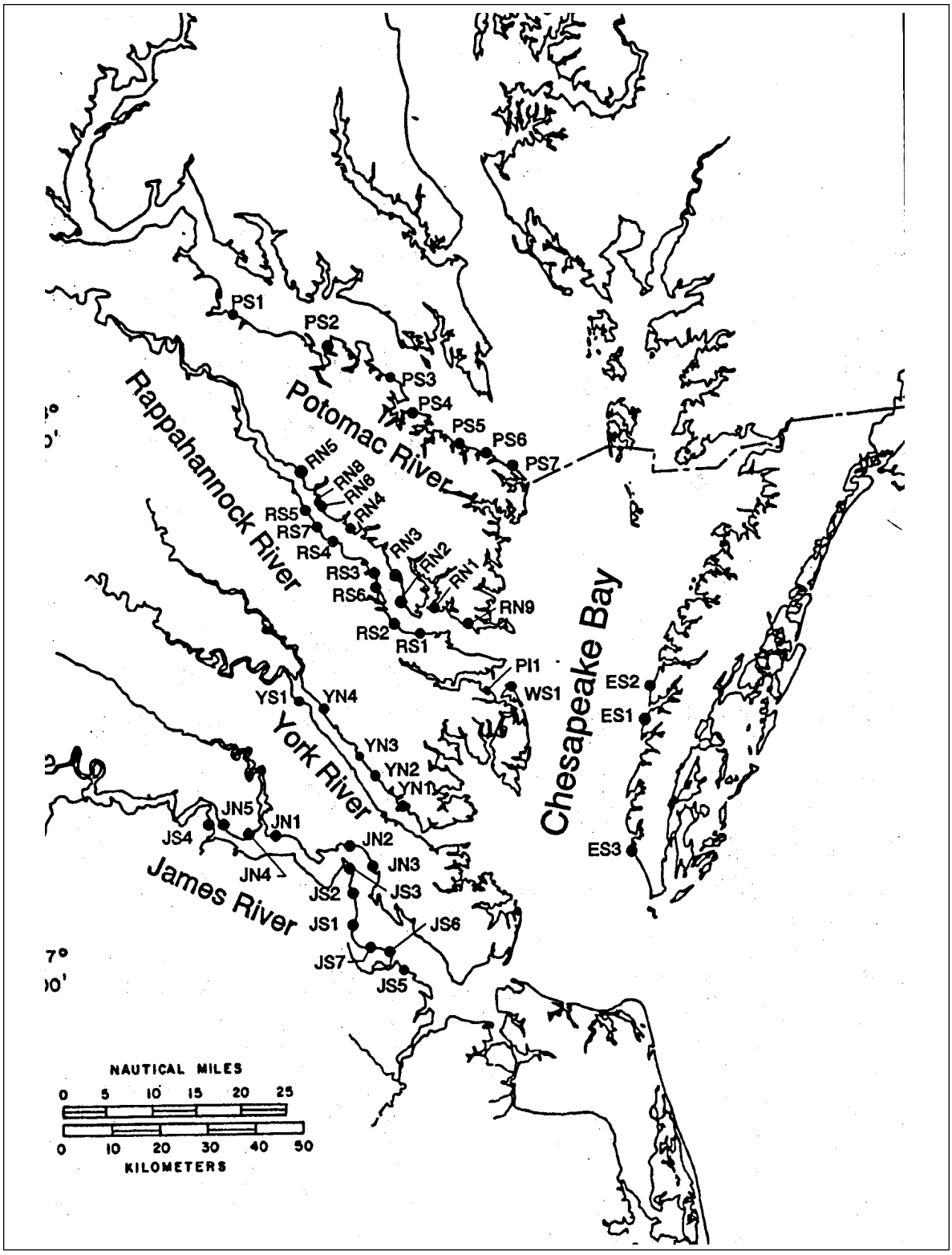

Figure 4-48. Sample Sites for Bank Load Composition (from Ibison et al. 1992).

Table 4-1
Composition of Bank Solids Loads

	Load, (kg m^{-1} d^{-1})	Gravel, (%)	Sand, (%)	Silt, (%)	Clay, (%)	Total Phosphorus, (mg/g)	Inorganic Phosphorus, (mg/g)	Total Nitrogen, (mg/g)	Particulate Carbon, (mg/g)
Mean	11.4	20.3	17.0	60.9	1.8	0.20	0.028	0.37	4.35
Median	8.6	16.3	16.3	63.1	0.1	0.07	0.003	0.20	1.22
Standard Deviation	8.8	16.0	14.1	26.0	5.6	0.44	0.154	0.60	8.43
Maximum	34.0	71.9	60.3	98.7	41.1	5.31	2.243	6.44	70.90
Minimum	0.8	0.7	0.1	1.6	0.0	0.00	0.000	0.00	0.03
N	43	255	255	255	255	255	255	255	255
Model	5.7			68		0.68		0.33	4.1

necessarily the mean, in which case parameter BankAdj would be unnecessary. Concentration is equal to unity when loading of solids is considered.

We found an erosion rate of 5.7 kg m^{-1} d^{-1} (0.7 ton ft^{-1} yr^{-1}) produced reasonable solids computations in the model. Our rate is two-thirds the median or one-half the mean of rates reported by Ibison et al. 1992 (Table 4-1). The reported rates are primarily for eroding banks. Our lesser rate, employed system-wide, may reflect the lower shorelines along the eastern shore and elsewhere, relative to selected eroding banks. The fraction of silt and clay and the carbon and nitrogen composition of the solids, as employed in the model, followed closely the observed means. Model phosphorus composition was considerably higher than the observed mean. The higher concentration was specified to represent an affinity of phosphorus for silt and clay particles rather than sand and gravel.

Summary of Model Loads

The spatial distribution of bank loads (Figures 4-49–4-52) depends directly on the length of the model shoreline in each CBPS. Segments receiving the greatest loads include the lower estuarine Potomac (LE2), Tangier Sound (EE3), and the tidal fresh portions of the major western tributaries (TF2–TF5).

One characteristic of bank nutrient loads is they are phosphorus-enriched relative to organic matter. The ratio of observed median nitrogen to phosphorus in bank loads is roughly 3:1 (Table 4-1) while the characteristic ratio in phytoplankton is 7:1 (Redfield et al. 1966). The modeled affinity of phosphorus for silt and clay produces a nitrogen-to-phosphorus ratio in modeled loads of 0.5:1 (Figures 4-49, 4-50).

Sensitivity to Bank Loads

Sensitivity to bank nutrient loads was examined during the model calibration process. In SENS65, nitrogen and phosphorus content of solids were as employed in the final calibration (Table 4-1). In SENS66, these were multiplied three-fold.

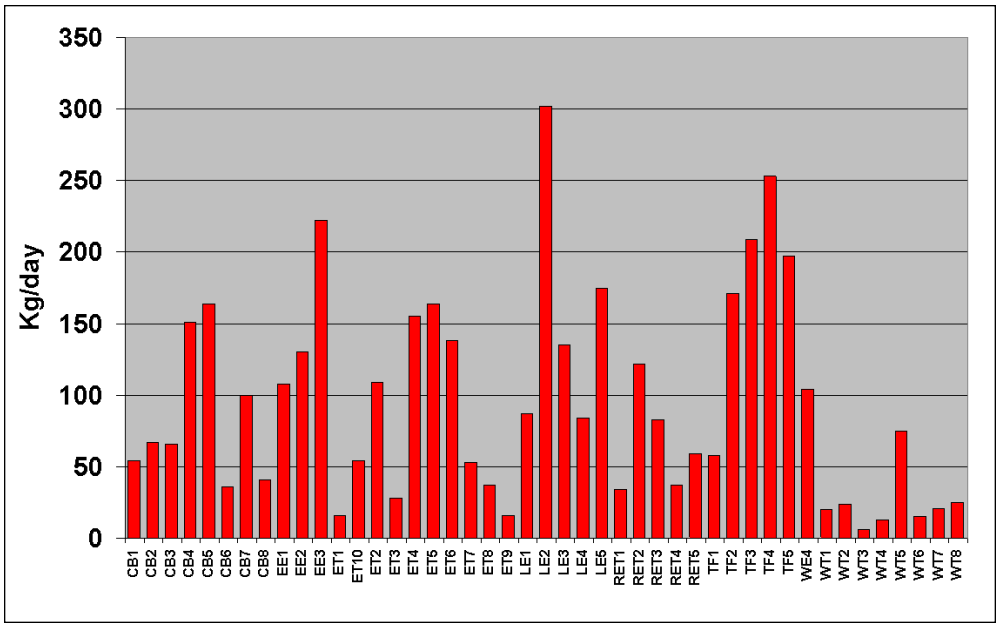

Figure 4-49. Total Nitrogen Bank Loads by CBPS

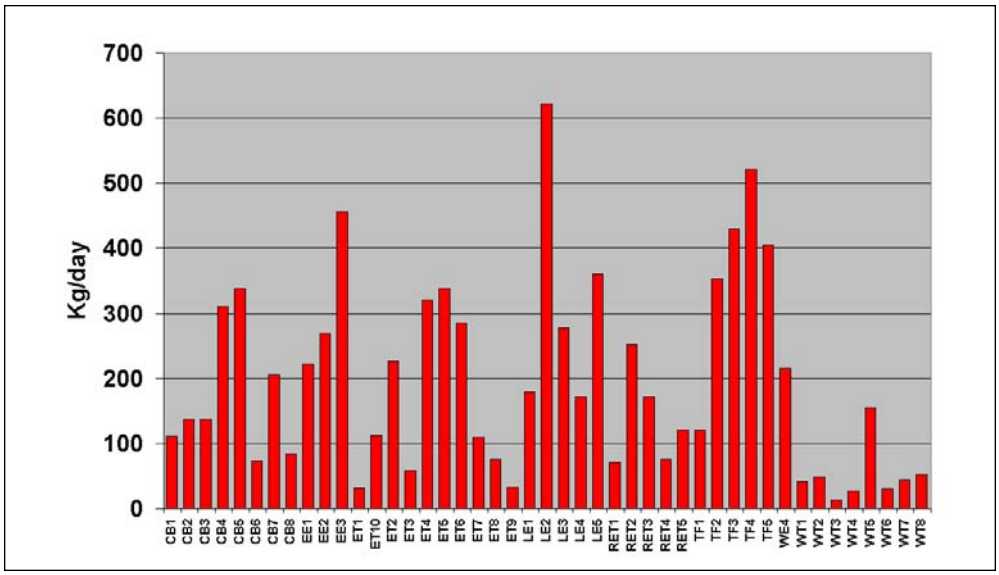

Figure 4-50. Total Phosphorus Bank Loads by CBPS

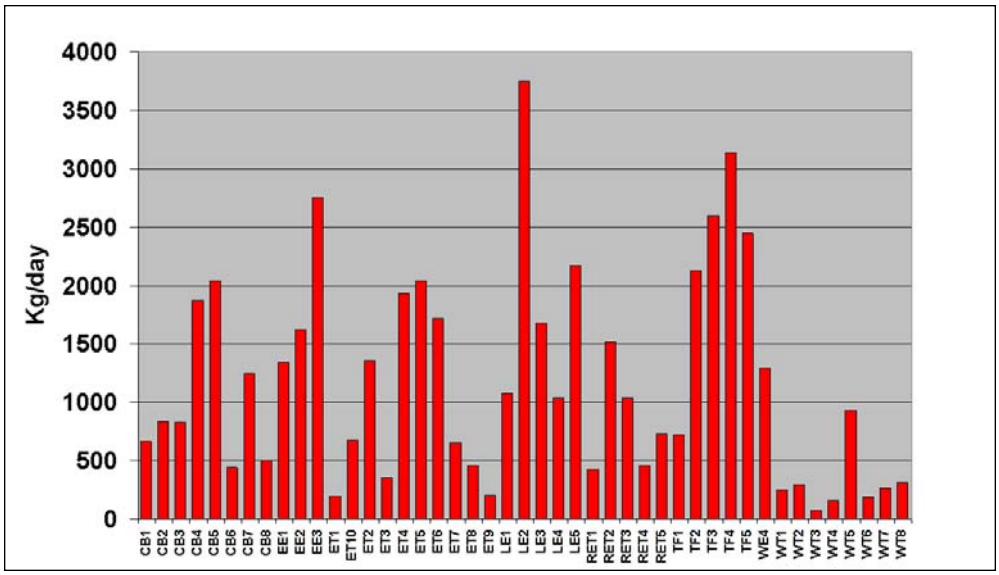

Figure 4-51. Total Organic Carbon Bank Loads by CBPS.

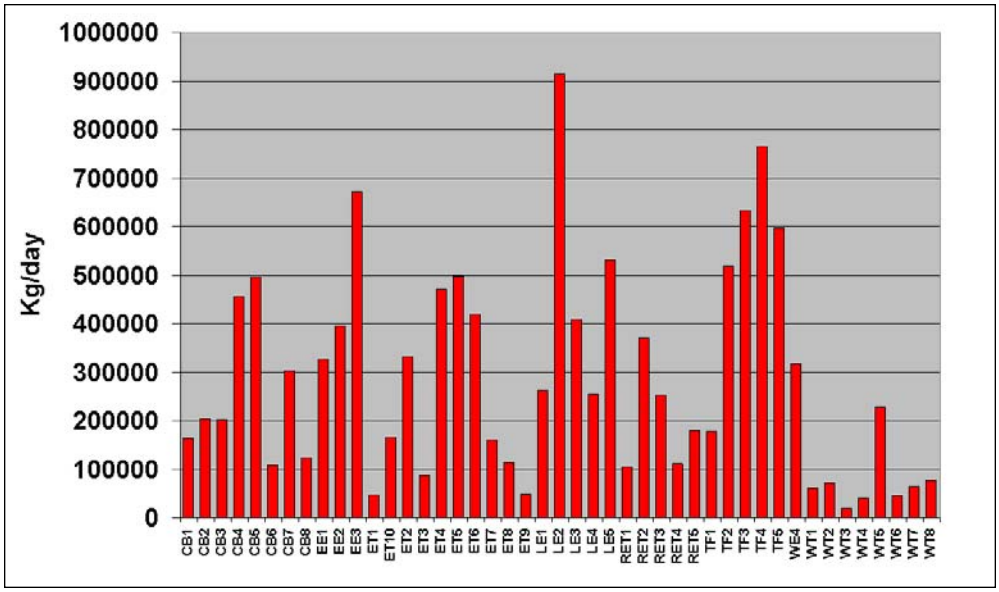

Figure 4-52. Suspended Solids Bank Loads by CBPS

Due to subsequent changes in parameters and inputs, these runs do not represent the model in its calibrated state but do provide useful insights.

The effect of a three-fold increase in bank nitrogen loads on the bay is nearly invisible (Figure 4-53) while a three-fold increase in bank phosphorus loads results in substantial increases in bay total phosphorus (Figure 4-54). As with the bay, tributary sensitivity is largely to phosphorus loads rather than nitrogen. Sensitivity is not uniform across tributaries. Response of the Potomac (Figure 4-55) and James (Figure 4-56) is limited. The Patuxent (Figure 4-57) and York (Figure 4-58) exhibit moderate responses in their upper reaches while the Rappahannock (Figure 4-59) shows high sensitivity throughout.

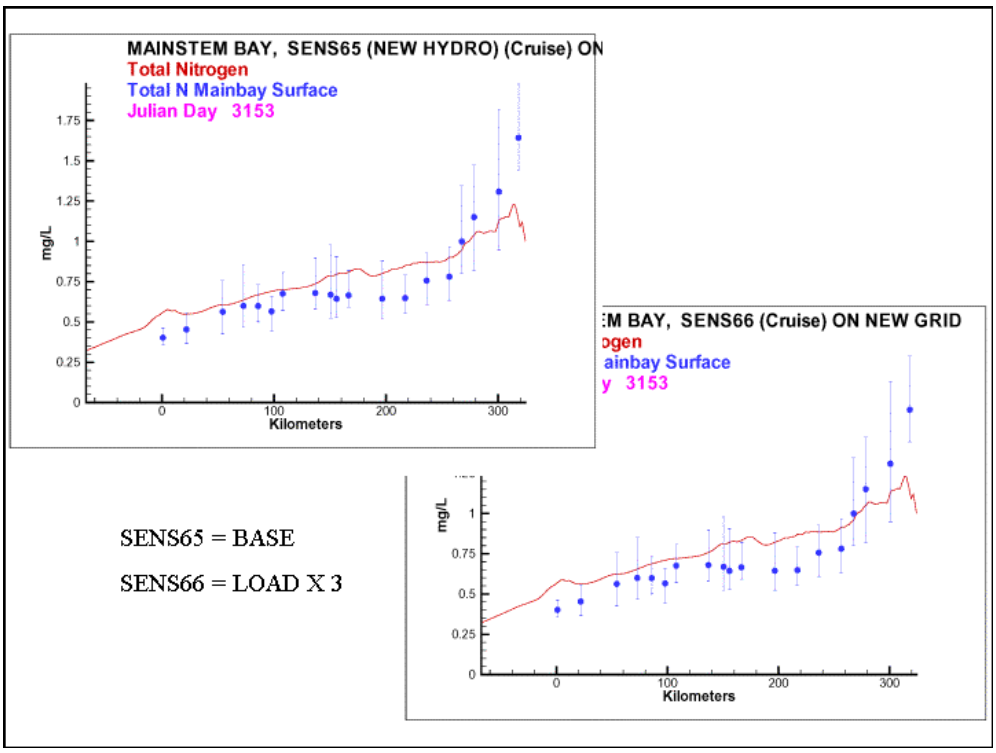

Figure 4-53. Sensitivity of Chesapeake Bay to Nitrogen Bank Loads (Summer 1993).

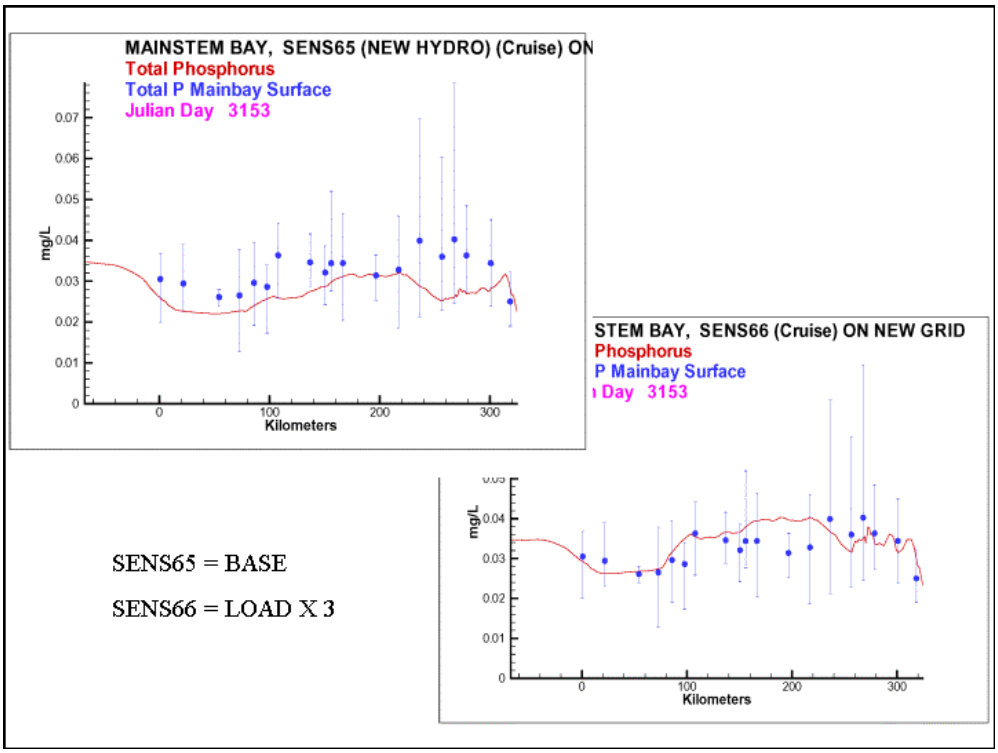

Figure 4-54. Sensitivity of Chesapeake Bay to Phosphorus Bank Loads (Summer 1993).

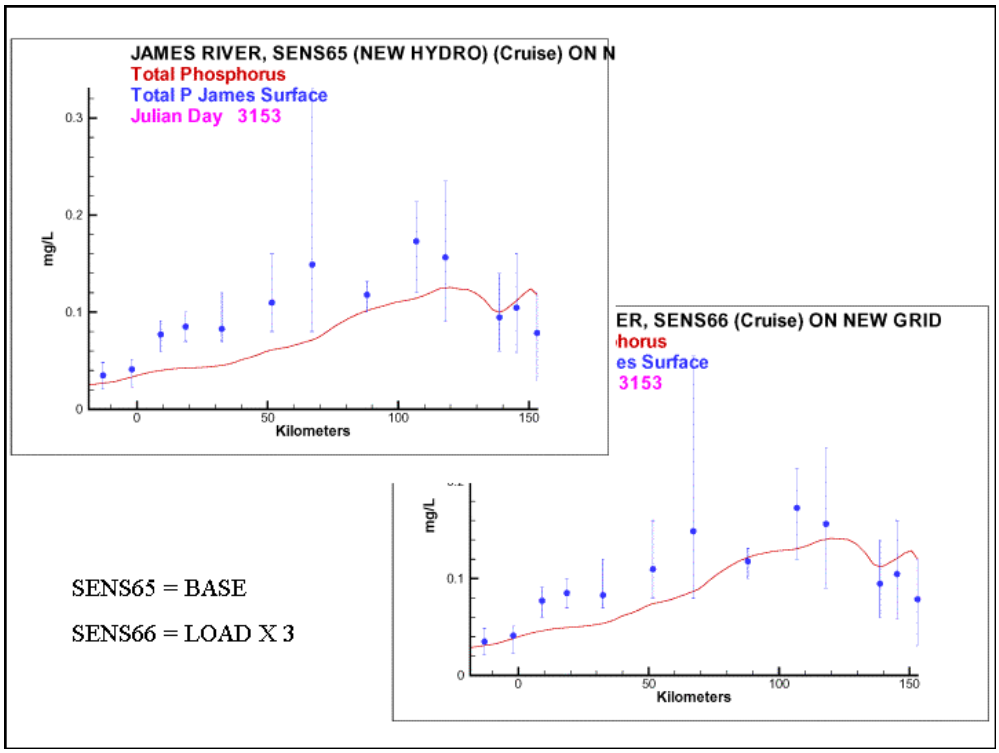

Figure 4-55. Sensitivity of James River Bank Loads (Summer 1993).

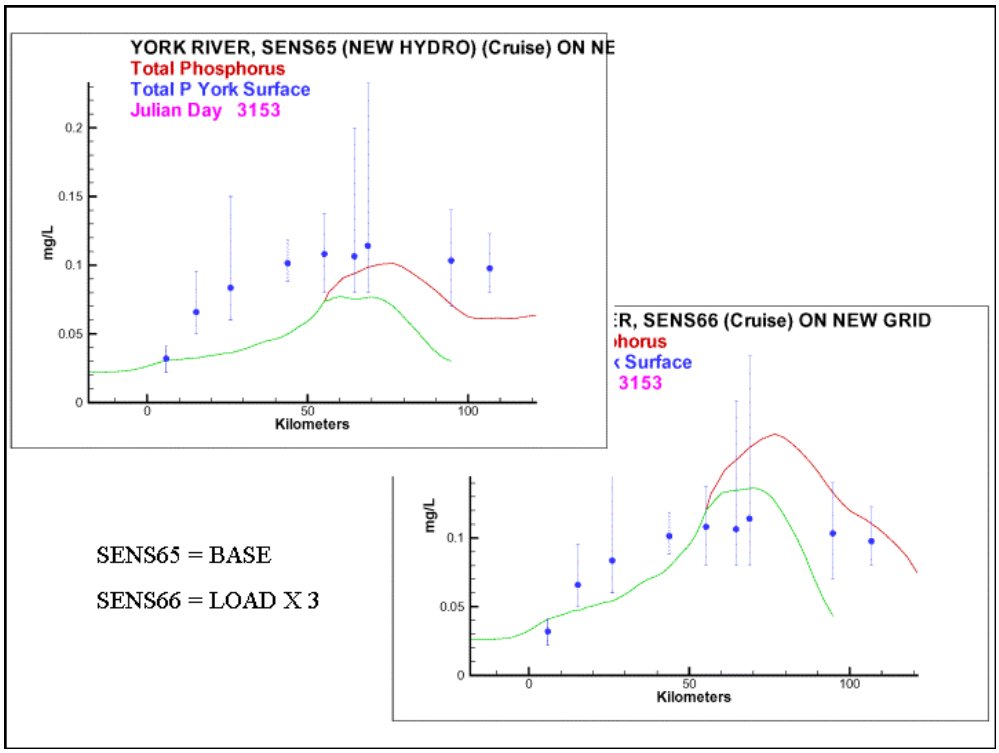

Figure 4-56. Sensitivity of York River to Phosphorus Bank Loads (Summer 1993).

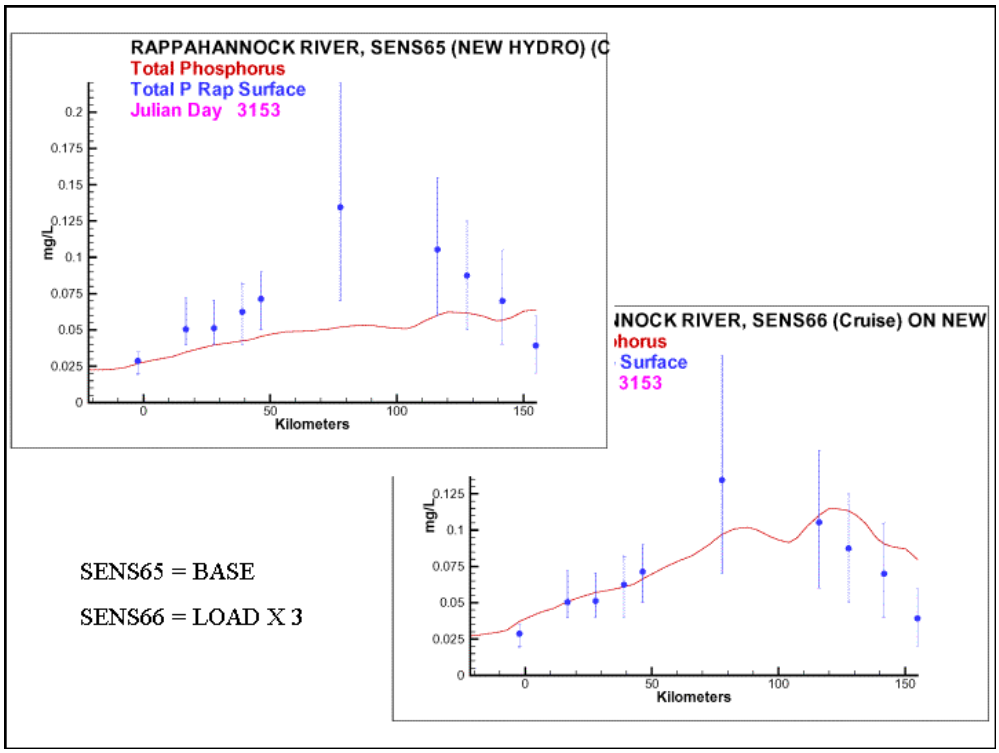

Figure 4-57. Sensitivity of Rappahannock River to Phosphorus Bank Loads (Summer 1993).

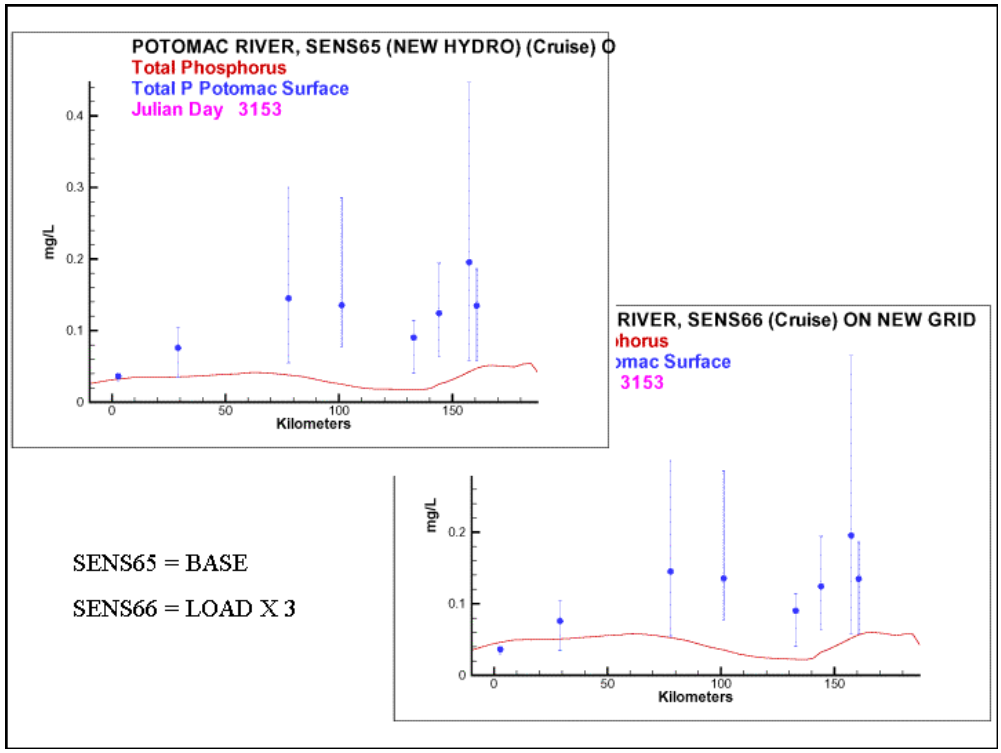

Figure 4-58. Sensitivity of Potomac River to Phosphorus Bank Loads (Summer 1993).

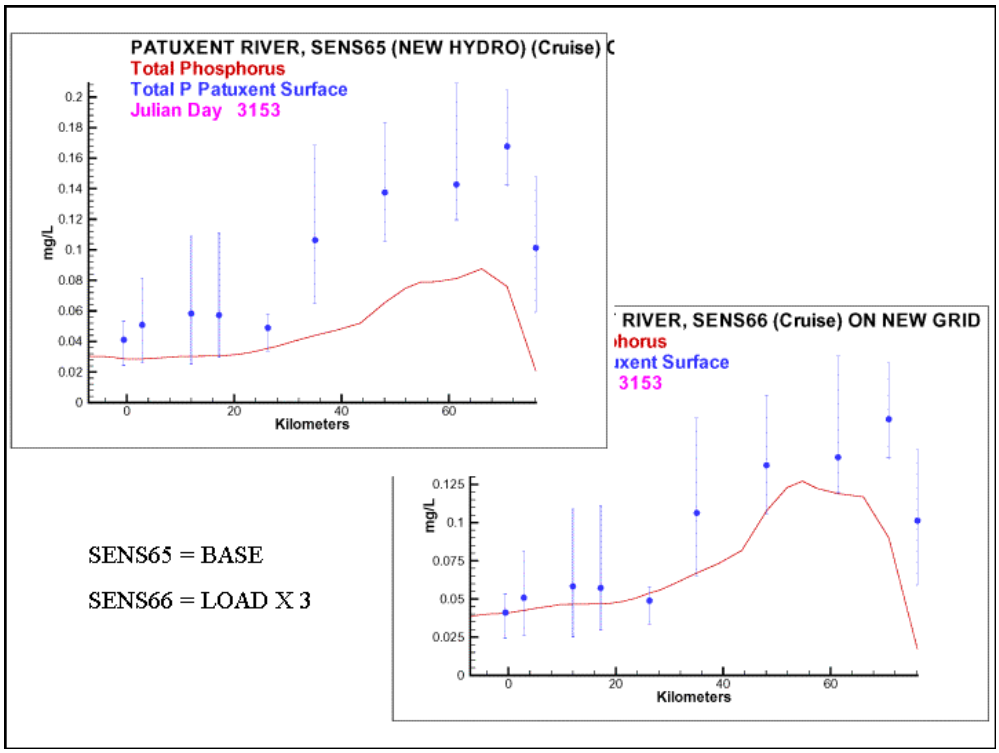

Figure 4-59. Sensitivity of Patuxent River to Phosphorus Bank Loads (Summer 1993).

Wetlands Loads

Wetlands loads are the sources (or sinks) of oxygen and oxygen-demanding material associated with wetlands that fringe the shore of the bay and tributaries. These loads are invoked primarily as an aid in calibration of tributary dissolved oxygen.

Quantifying the influence of wetlands on estuarine water quality has been an interest of scientists and engineers for decades. New methodologies have provided improved estimates but precise specification of wetlands effects remains impossible. The best that can be done is to bracket or "range" possible effects and then select values for use in the model from the range of potential values.

Neubauer et al. (2000) measured annual net macrophyte production of 1.4–2 g C m^{-2} d^{-1} in a tidal freshwater Pamunkey River marsh. Although episodic flooding or scouring of marshes may produce large loads, over long periods no more carbon can be exported from a marsh than is produced. Consequently, the Neubauer et al. study provides an upper range for marsh carbon export. Actual carbon export should be much less than annual net production due to burial; carbon import may be necessary to balance combined effects of burial and respiration (Neubauer et al. 2001). In the model, a uniform carbon export of 0.3 g C m^{-2} d^{-1} was employed.

Neubauer at al. (2000) calculated belowground marsh respiration of 516–723 g C m^{-2} yr^{-1}—equivalent to 3.8–5.3 g oxygen equivalents m^{-2} d^{-1}. Sediment oxygen consumption should be less than total respiration due to gas evolution, burial of sulfide, and other processes. A summary of sediment oxygen demand in the system

water column (DiToro 2001) indicates consumption of oxygen in sediments rarely exceeds 3 g O_2 m^{-2} d^{-1} while measures in salt marshes (Cai et al. 1999) indicate sediment oxygen flux of 1–1.3 g O_2 m^{-2} d^{-1}. In the model, a uniform oxygen demand of 2 g O_2 m^{-2} d^{-1} was employed.

Summary of Wetland Loads

Wetlands areas adjacent to model surface cells were derived via GIS analysis and provided by the EPA Chesapeake Bay Program in November 2001. Loads to each cell were computed as the product of adjacent wetlands area and areal carbon export or oxygen consumption.

Wetlands are distributed throughout the bay system. Basins with the greatest wetlands area (Figure 4-60) include the lower Eastern Shore, the lower James River, the York River, the upper Rappahannock River, and the upper Patuxent River. Segments receiving the largest carbon loads (Figure 4-61) and subject to the greatest oxygen consumption include the mid-portion of the bay (CB5),

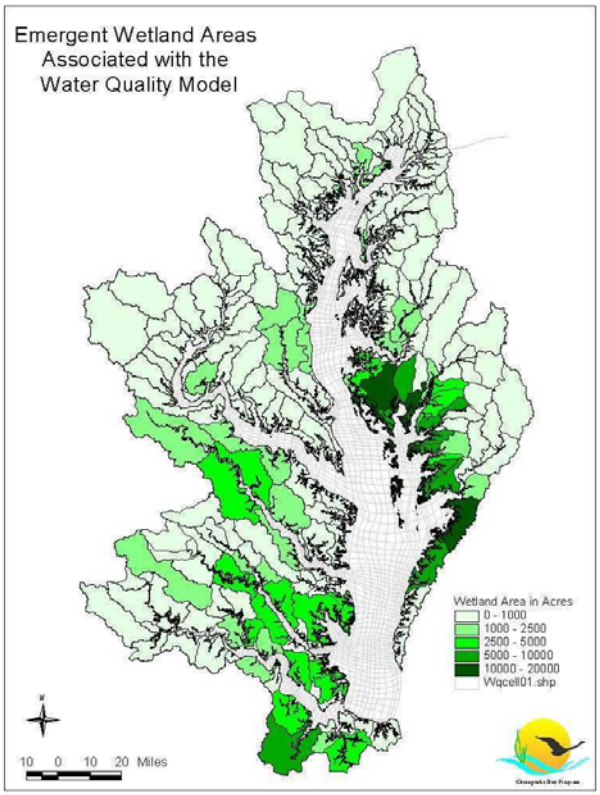

Figure 4-60. Emergent Wetlands in Chesapeake Bay System

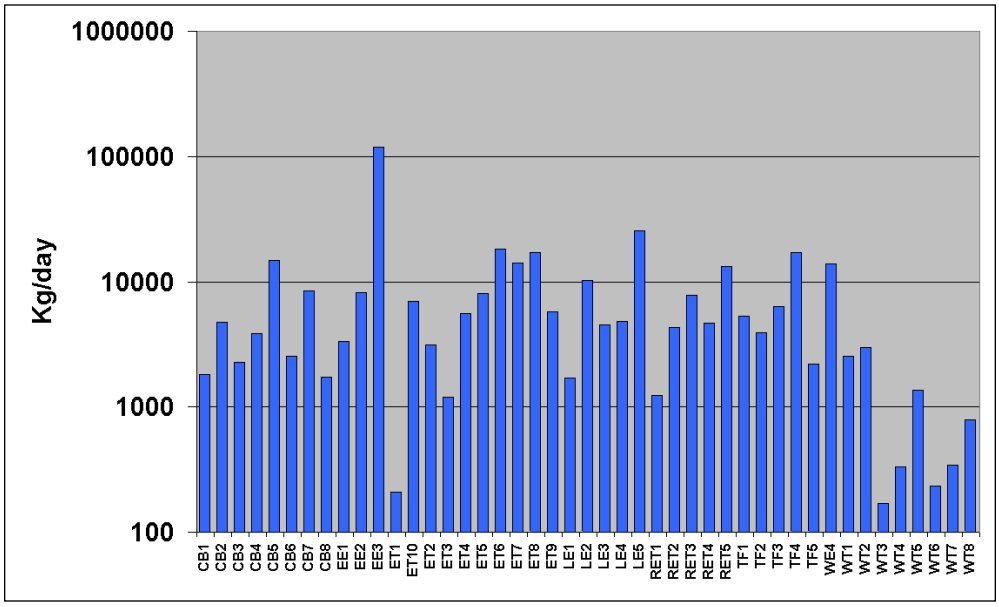

Figure 4-61. Wetland Carbon Loads by CBPS

Tangier Sound (EE3), several Eastern Shore tributaries (ET6, ET7, ET8), the middle and lower James River (RET5, LE5), the tidal fresh York River (TF4), and the York River mouth (WE4).

Sensitivity to Wetland Loads

Our ability to judge the impact of wetland loads on total organic carbon was clouded by large variance in the observations and by discontinuities apparently due to procedural changes. Our judgement was that moderate carbon loads, 1 g C m^{-2} d^{-1}, produced model results that were high relative to observations (Figure 4-62). The sensitivity of computed dissolved oxygen, the parameter of prime interest, to wetland carbon loads was negligible (Figure 4-63). Consequently, we assigned a small wetland carbon load (0.3 g C m^{-2} d^{-1}) which had little impact on computations. Our focus shifted to direct oxygen consumption in wetlands.

The response of the water column to wetland oxygen uptake depends on the ratio of wetland area to water surface area. CBPS with large surface areas show little response to wetlands along their perimeters (Figures 4-64, 4-65). Narrow reaches adjoining extensive wetlands show the greatest sensitivity. These include tidal fresh portions of the York (Figure 4-66), Rappahannock (Figure 4-67), and Patuxent (Figure 4-68) Rivers.

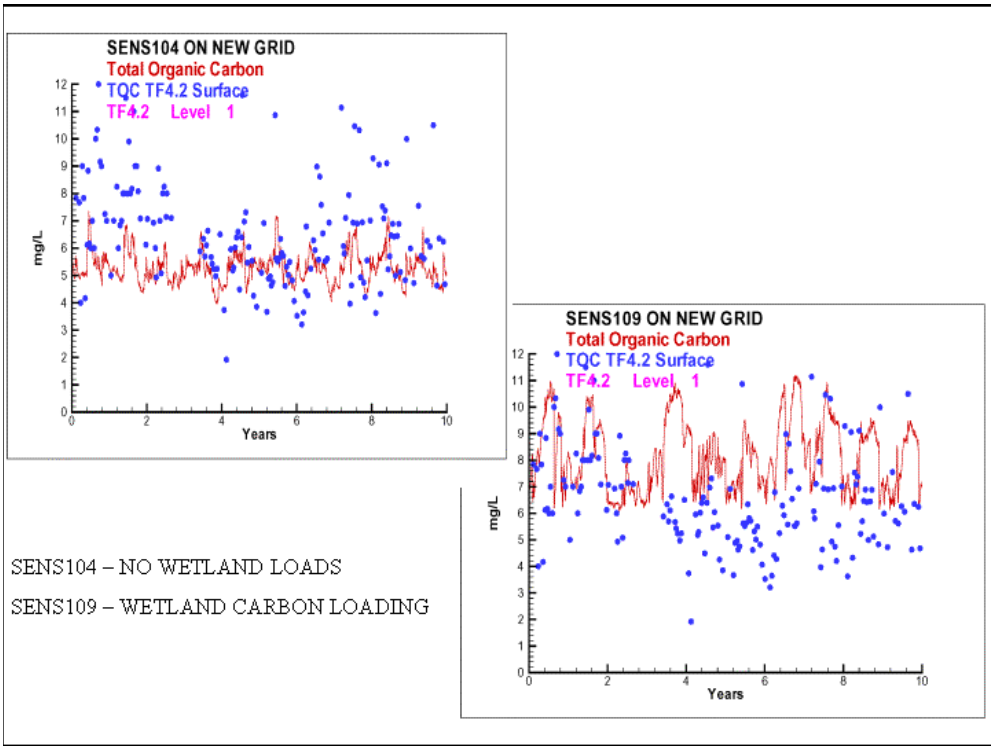

Figure 4-62. Sensitivity of Tidal Fresh York River to Wetland Carbon Loading (1 g m^{-2} d^{-1}).

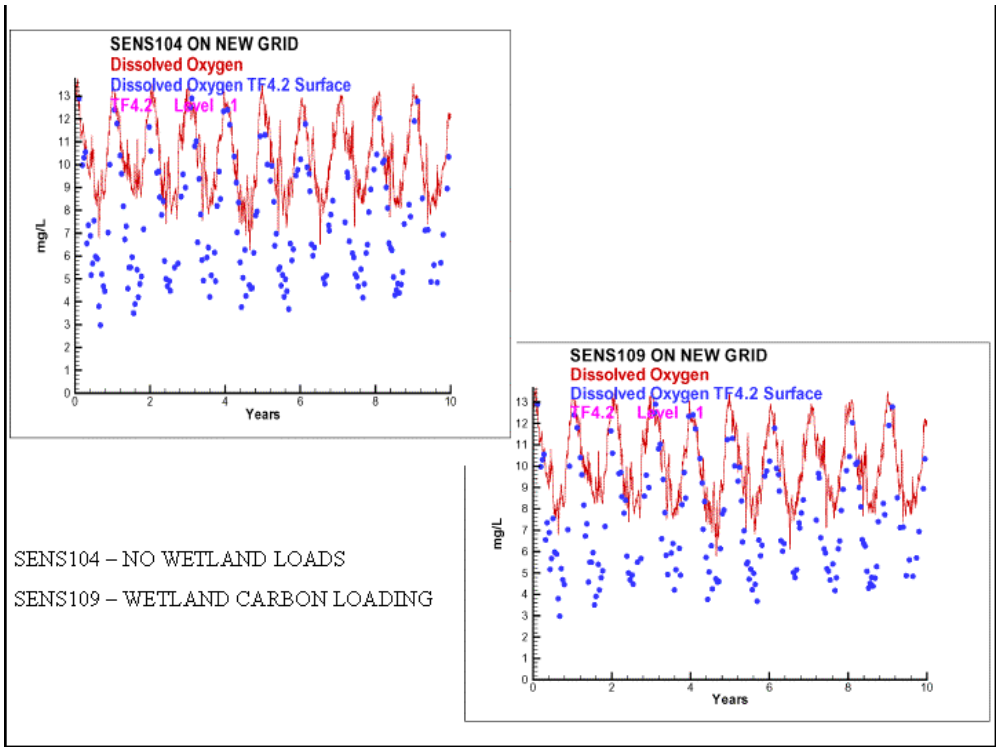

Figure 4-63. Sensitivity of Dissolved Oxygen in Tidal Fresh York River to Wetland Carbon Loading (1 g m^{-2} d^{-1}).

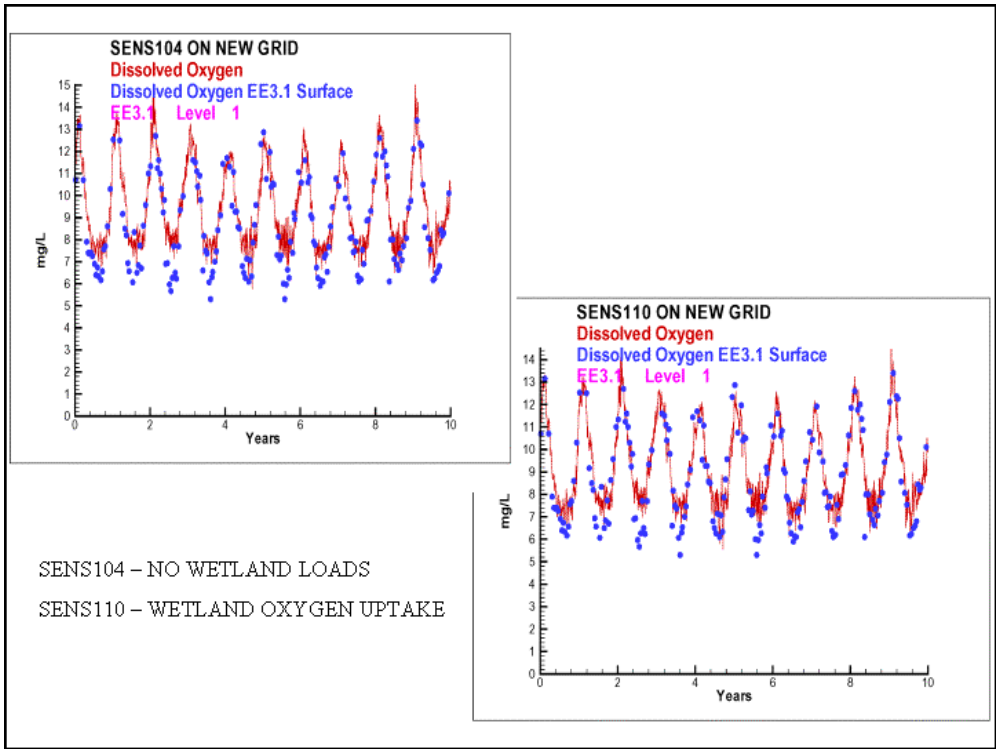

Figure 4-64. Sensitivity of Tangier Sound to Wetland Dissolved Oxygen Uptake (2 g m^{-2} d^{-1}).

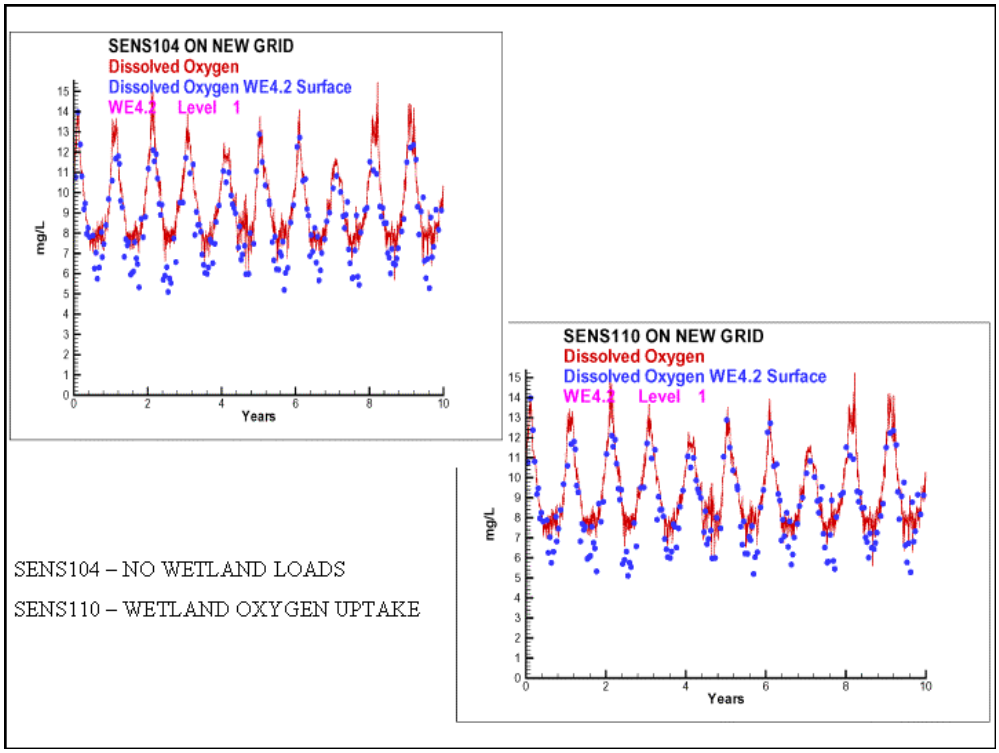

Figure 4-65. Sensitivity of York River Mouth to Wetland Dissolved Oxygen Uptake (2 g m^{-2} d^{-1}).

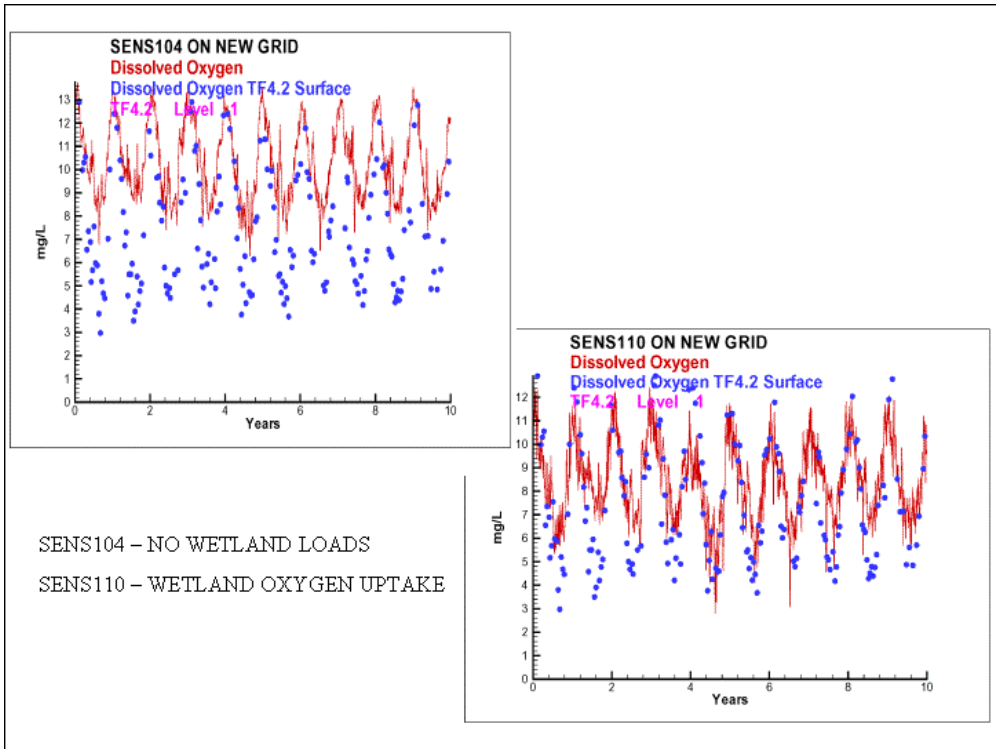

Figure 4-66. Sensitivity of Tidal Fresh York River to Wetland Dissolved Oxygen Uptake (2 g m^{-2} d^{-1}).

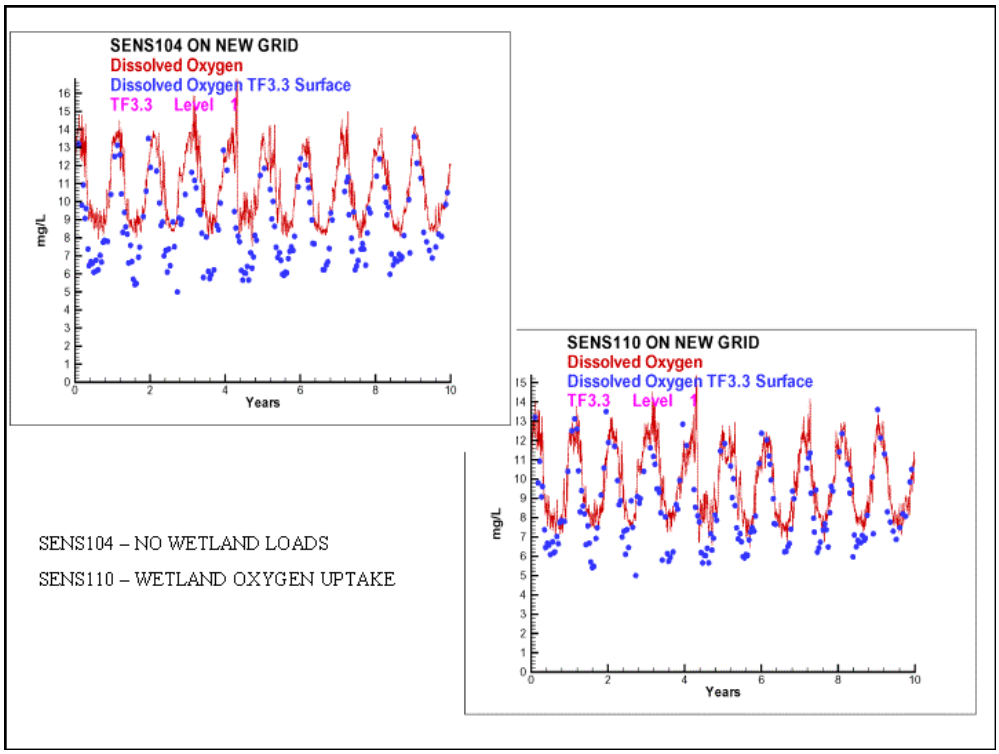

Figure 4-67. Sensitivity of Tidal Fresh Rappahannock River to Wetland Dissolved Oxygen Uptake (2 g m^{-2} d^{-1}).

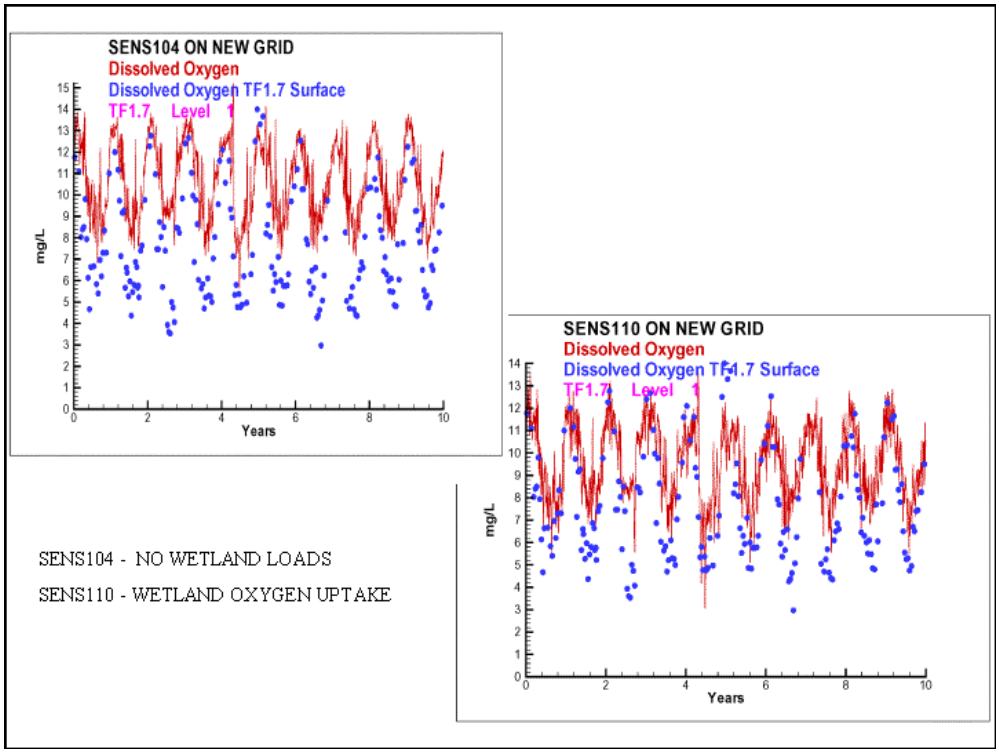

Figure 4-68. Sensitivity of Tidal Fresh Patuxent River to Wetland Dissolved Oxygen Uptake (2 g m^{-2} d^{-1}).

Summary of All Loads

Loads from all sources were compared by CBPS for 1990, a year central to the simulation period. Runoff in this year was moderate in the Susquehanna and James (Figures 4-1, 4-3) and low in the Potomac (Figure 4-2).

Nonpoint sources dominated the nitrogen loads (Figure 4-69, Table 4-2) except in a few segments adjacent to major urban areas including Richmond (TF5), Hampton Roads (LE5), Washington (TF2), and Baltimore (WT4, WT5). In these regions, point sources contributed a significant fraction of nitrogen loads. Atmospheric nitrogen loads were significant only in the large, open segments of the mainstem bay (CB3–CB7, EE3) and in the lower Potomac (LE2). Bank loads were negligibly small throughout.

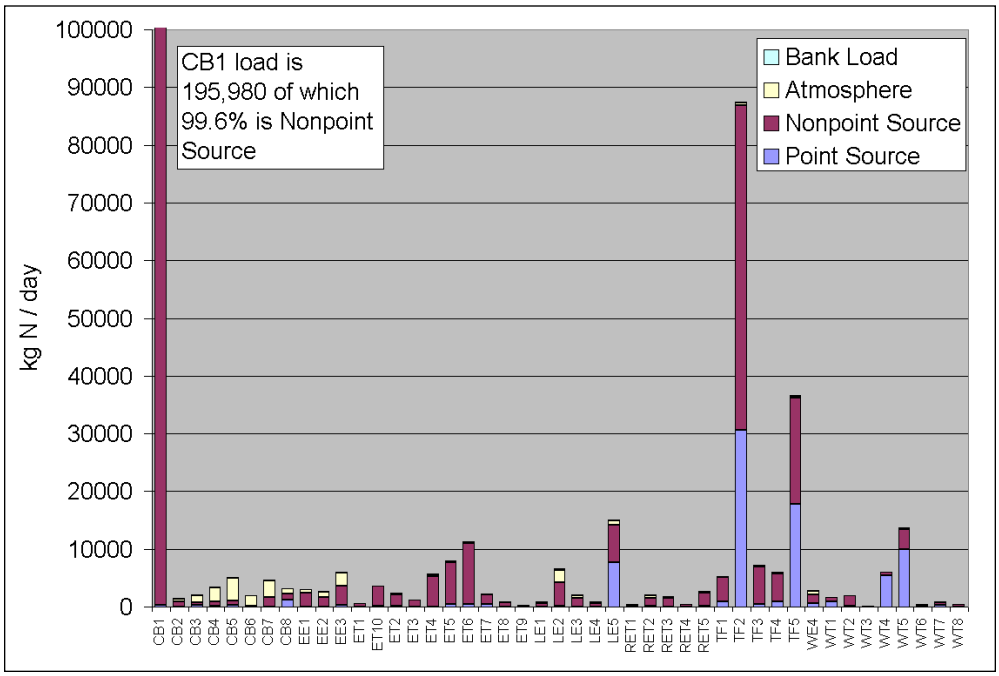

Figure 4-69. Summary of Nitrogen Loads for the Year 1990.

Table 4-2
System-wide Load Summary, 1990

	Point Source, (kg/day)	Nonpoint Source, (kg/day)	Atmosphere, (kg/day)	Bank Load, (kg/day)	Wetlands, (kg/day)
Nitrogen	80321	359506	26184	4218	
Phosphorus	4245	24600	1927	8695	
Carbon	160647	1014435		52424	1355742
Solids		11298430		12786991	

Nonpoint sources usually comprised the largest fraction of phosphorus loads (Figure 4-70, Table 4-2) but were not so predominant as for nitrogen. As with nitrogen, point-source loads were significant in urban areas and atmospheric loads contributed substantially to large open-water segments. A major contrast with nitrogen was in bank loading which equaled or exceed nonpoint-source phosphorus loads in segments distant from major inflows. These included the eastern embayments (EE1–EE3) and the river-estuarine transition segments of western tributaries (RET1–RET5).

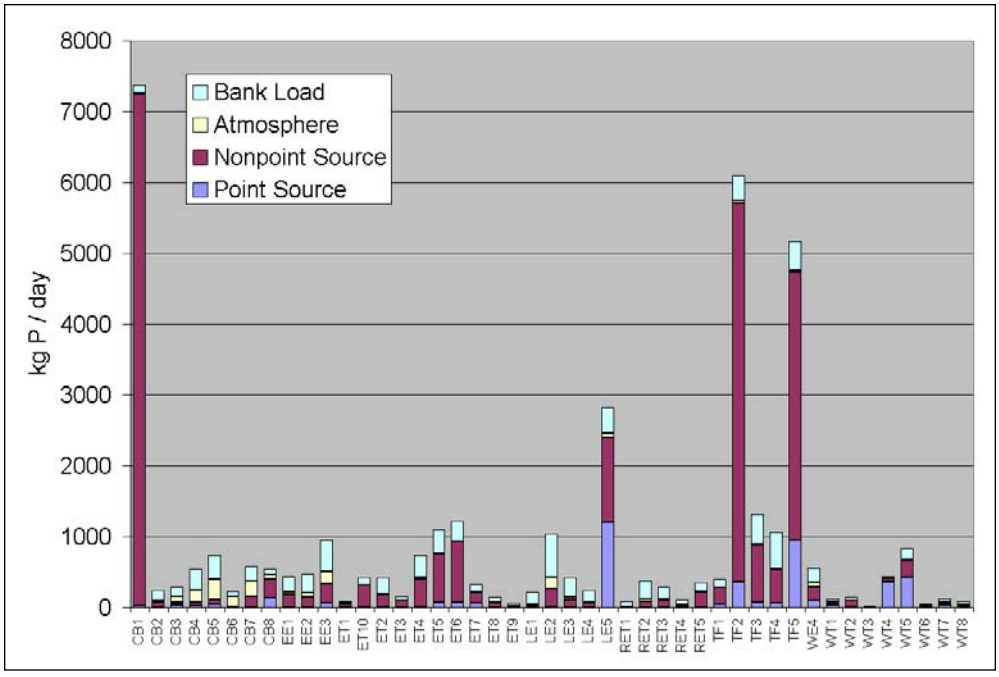

Figure 4-70. Summary of Phosphorus Loads for the Year 1990.

Nonpoint sources dominate the carbon loads (Figure 4-71, Table 4-2) in segments adjoining the inflows of the Susquehanna (CB1), Potomac (TF2), and James (TF5). Point sources contribute a significant fraction in segments adjacent to major urban areas including Richmond (TF5), Hampton Roads (LE5), Washington (TF2), and Baltimore (WT4, WT5). Otherwise, wetlands are the major source of carbon loads to the system. An assessment of loads provides an incomplete picture of the carbon budget, however. A complete assessment requires inclusion of carbon contributed by primary production as well as loads.

Nonpoint sources dominate the solids loads (Figure 4-72) in segments adjoining the inflows of the Susquehanna (CB1), Potomac (TF2), and James (TF5). Otherwise, bank loads are the dominant source. For 1990, bank loads contribute more solids, system-wide, than nonpoint sources (Table 4-2). Of course, the relative contribution of bank loads depends on annual hydrology. In high-flow years, nonpoint sources may dominate. Still, the summary indicates that control of bank erosion should be included in any solids management plan.

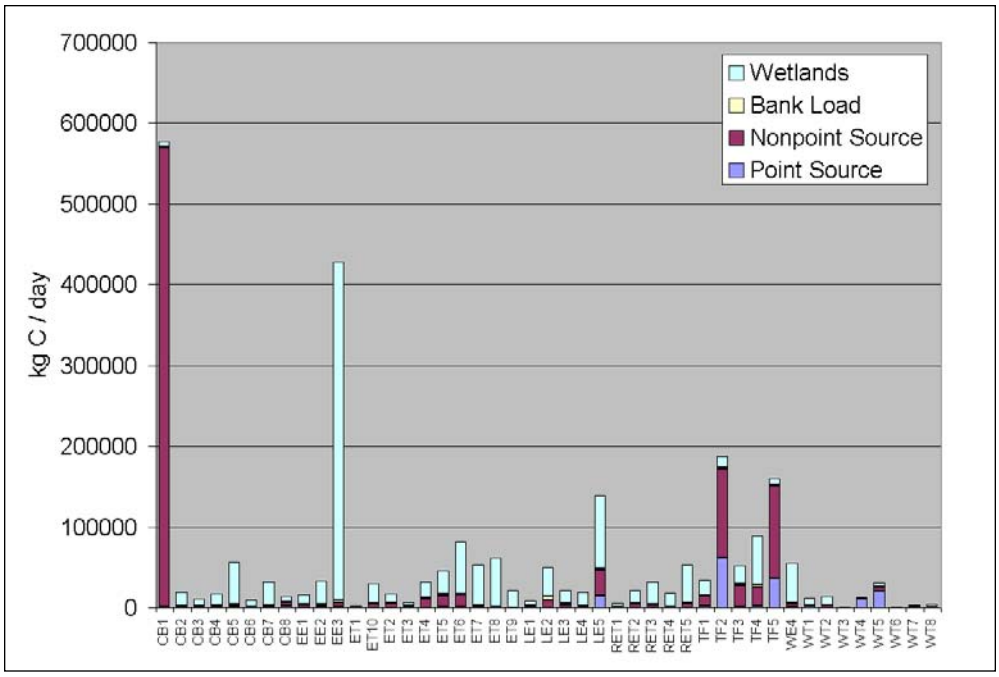

Figure 4-71. Summary of Carbon Loads for the Year 1990.

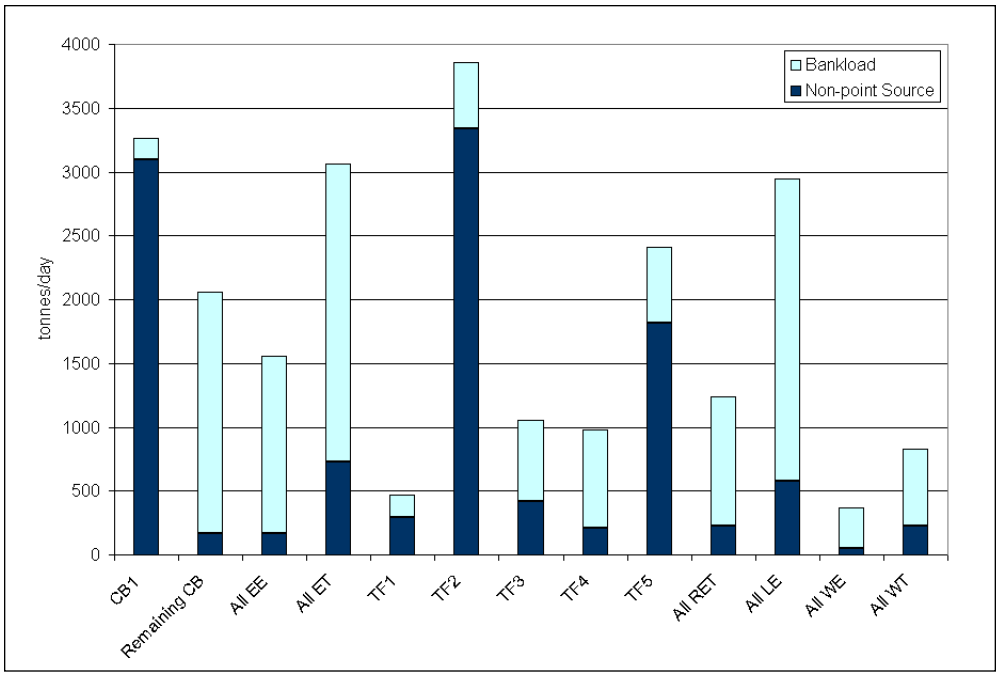

Figure 4-72. Summary of Solids Loads for the Year 1990.

References

Bicknell, B., Imhoff, J., Kittle, J., Donigian, A., Johanson, R., and Barnwell, T. (1996). "Hydrologic simulation program—FORTRAN user's manual for release 11," United States Environmental Protection Agency Environmental Research Laboratory, Athens GA.

Cai, W., Pomeroy, L., Moran, M., and Wang, Y. (1999). "Oxygen and carbon dioxide mass balance for the estuarine-intertidal marsh complex of five rivers in the southeastern U.S.," *Limnology and Oceanography*, 44(3), 639-649.

Chang, J., Brost, R., Isaksen, I., Madronich, S., Middleton, P., Stockwell, W., and Walcek, C. (1987). "A three-dimensional Eulerian acid deposition model— physical concepts and formulation," *Journal of Geophysical Research*, 92, 14681-14700.

DiToro, D. (2001). *Sediment Flux Modeling*. Wiley-Interscience, New York, NY.

Donoghue, J., Bricker, O., and Olsen, C. (1989). "Particle-bourne radionuclides as tracers for sediment in the Susquehanna River and Chesapeake Bay," *Estuarine, Coastal and Shelf Science*, 29, 341-360.

Ibison, N., Frye, C., Frye, J., Hill, C., and Burger, N. (1992). "Eroding bank nutrient verification study for the lower Chesapeake Bay," Department of Conservation and Recreation, Division of Soil and Water Conservation, Gloucester Point VA.

Neubauer, S., Anderson, I., Constantine, J., and Kuehl, S. (2001). "Sediment deposition and accretion in a mid-Atlantic (U.S.A.) tidal freshwater marsh," *Estuarine, Coastal, and Shelf Science*, 56, 000-000.

Neubauer, S.,Miller, W., and Anderson, I. (2000). "Carbon cycling in a tidal freshwater marsh ecosystem: a carbon gas flux study," *Marine Ecology Progress Series*, 199, 13-30.

Redfield, A., Ketchum, B., and Richards, F. 1966. "The influence of organisms on the composition of sea-water," in *The Sea Vol. II*, Interscience Publishers, New York, NY, pp 26-48.

Schubel, J. (1968). "Turbidity maximum of the northern Chesapeake Bay," *Science*, 161, 1013-1015.

US Army Corps of Engineers Baltimore District. (1990). "Chesapeake Bay shoreline erosion study feasibility report," Baltimore MD.

5 Linking in the Loads

Introduction

Major loads were mapped to model cells by the sponsor before they were provided to the model team. The linkage process between loads and model consisted of converting quantities in the loads into appropriate model state variables. The present chapter describes development of conversion guidelines and lists parameter values employed in the conversions.

Nonpoint-Source Loads

Linking of watershed model loads focused on the nitrogen and phosphorus state variables (Table 5-1). The watershed model loads distinguished particulate inorganic phosphorus from organic phosphorus. Discussion with the watershed model team indicated particulate inorganic phosphorus was utilized as a way of modeling scour from the bottom during high-flow intervals. No effort was made to truly distinguish particulate inorganic from organic phosphorus forms. The Tributary Refinements phase of water quality model application (Cerco et al. 2002) distinguished particulate organic and particulate inorganic phosphorus forms. This distinction was not carried forward into the present model. Consequently, the watershed model particulate inorganic and organic phosphorus forms were combined before mapping into water quality model variables. Since particulate phosphorus in the water quality model consists of both organic and inorganic forms, we have dropped the specification “organic” when referring to water quality model particulate phosphorus.

The watershed model produced loads of total suspended solids. The corresponding water quality model variable was fixed (inorganic) solids. Linkage with the watershed model required removal of the volatile (organic) solids from the total solids load. Volatile solids were still input to the water quality model but in the form of particulate organic carbon.

Table 5-1
Variables in Loads and Water-Quality Model

Load Variable	Maps to	Model Variable
Ammonium	--->	Ammonium
Nitrate	--->	Nitrate
Organic Nitrogen	--->	Dissolved Organic Nitrogen, Labile Particulate Organic Nitrogen, Refractory Particulate Organic Nitrogen
Dissolved Phosphate	--->	Phosphate
Organic Phosphorus plus Particulate Inorganic Phosphorus	--->	Dissolved Organic Phosphorus, Labile Particulate Phosphorus, Refractory Particulate Phosphorus
Total Organic Carbon	--->	Dissolved Organic Carbon, Labile Particulate Organic Carbon, Refractory Particulate Organic Carbon
Total Suspended Solids	--->	Fixed Solids

Nonpoint-source total organic carbon loads were derived by ratio to watershed model organic nitrogen loads. The total carbon loads also required mapping into water quality model state variables.

Guidelines for splitting total organic forms contained in the loads into dissolved and particulate forms for the water quality model were based on observations collected in the Chesapeake Bay River Input Monitoring Program. Data were obtained from the program web site: http://va.water.usgs.gov/chesbay/RIMP/. Inspection of the data base indicated collection of relevant observations at Virginia fall lines commenced in 1996. Relevant observations from earlier years were available for Maryland fall lines but detection levels and reporting increments were poor. Circa 1996, improvements were made to analytical methods and reporting. Consequently, analysis of Maryland observations was restricted to data collected from 1996 onwards. In all cases, reports of “less than” were converted to the detection level e.g. <.01 became 0.01. At the time our analysis was conducted, observations were available through 1999.

Nitrogen and Phosphorus

For the Virginia fall lines, suspended (particulate) nitrogen and phosphorus forms were reported directly. Dissolved organic nitrogen was determined as dissolved nitrogen less ammonium less nitrate+nitrite. Dissolved organic phosphorus was determined as dissolved phosphorus less dissolved inorganic phosphorus.

For the Maryland fall lines, dissolved organic nitrogen was determined as total Kjeldahl nitrogen (filtered) less ammonium. Particulate organic nitrogen was determined as total Kjeldahl nitrogen (whole) less total Kjeldahl nitrogen (filtered). Dissolved organic phosphorus was determined as dissolved phosphorus less dissolved inorganic phosphorus. Particulate phosphorus was determined as total phosphorus less dissolved phosphorus.

Inspection indicated dissolved organic nitrogen and phosphorus concentrations were independent of flow (Figures 5-1–5-6). Concentrations were similar at all fall lines except the Susquehanna which exhibited lower dissolved organic

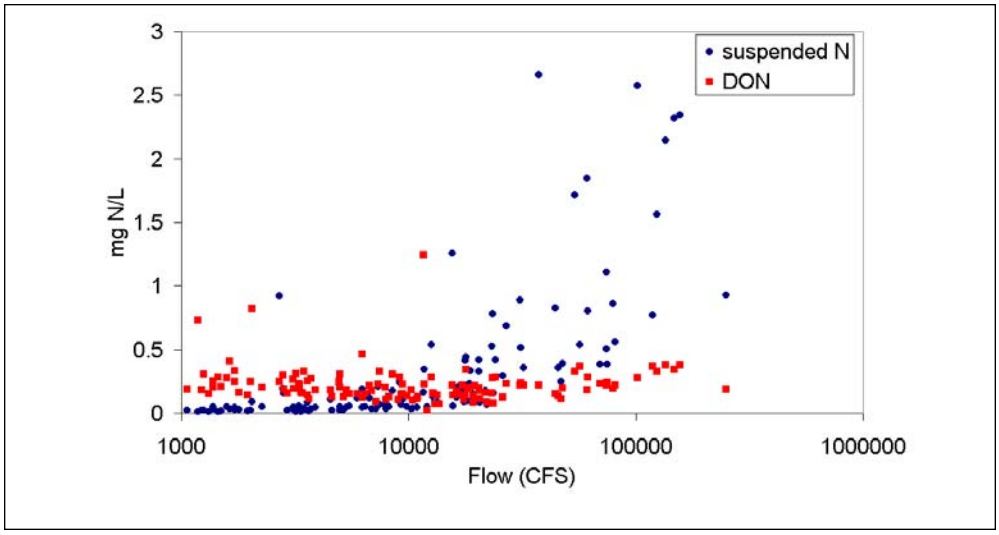

Figure 5-1. Observed particulate and dissolved organic nitrogen at the James River.

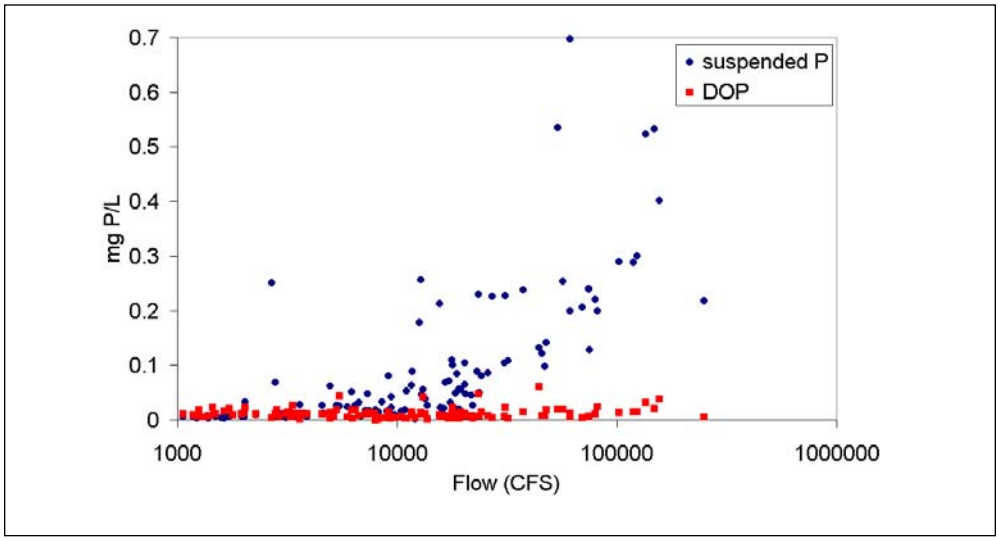

Figure 5-2. Observed particulate and dissolved organic phosphorus at the James River fall line.

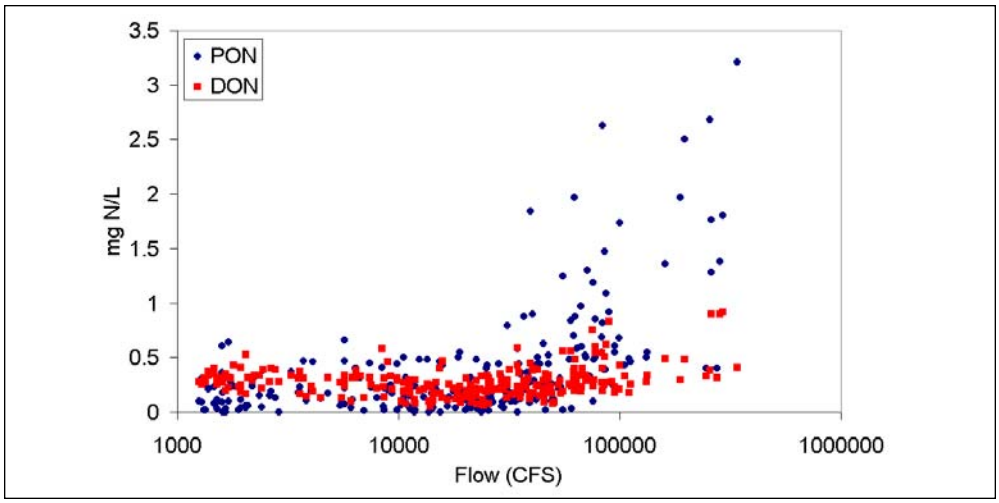

Figure 5-3. Observed particulate and dissolved organic nitrogen at the Potomac River fall line.

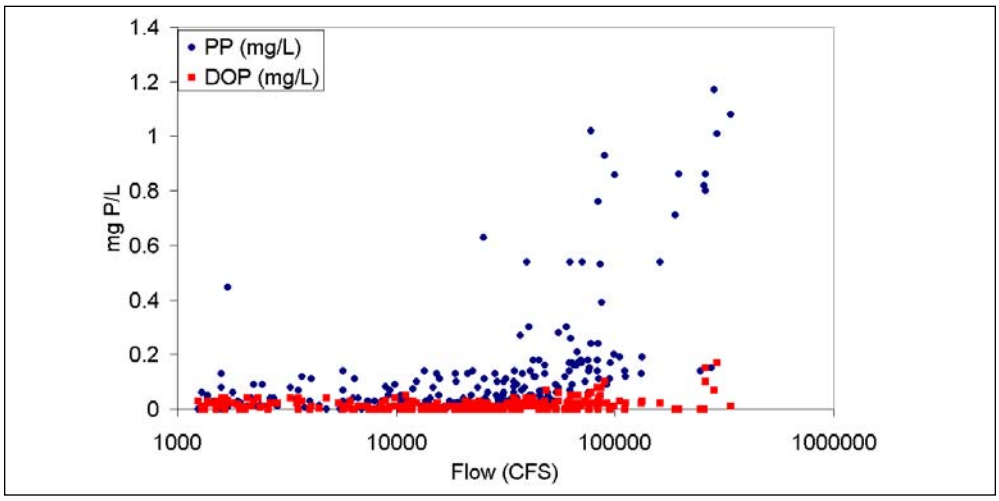

Figure 5-4. Observed particulate and dissolved organic phosphorus at the Potomac River fall line.

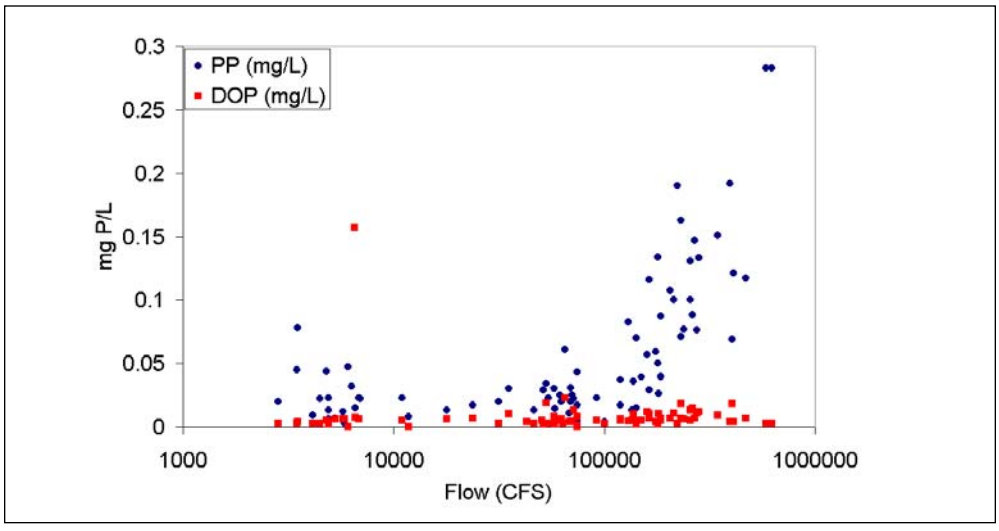

Figure 5-5. Observed particulate and dissolved organic nitrogen at the Susquehanna River fall line.

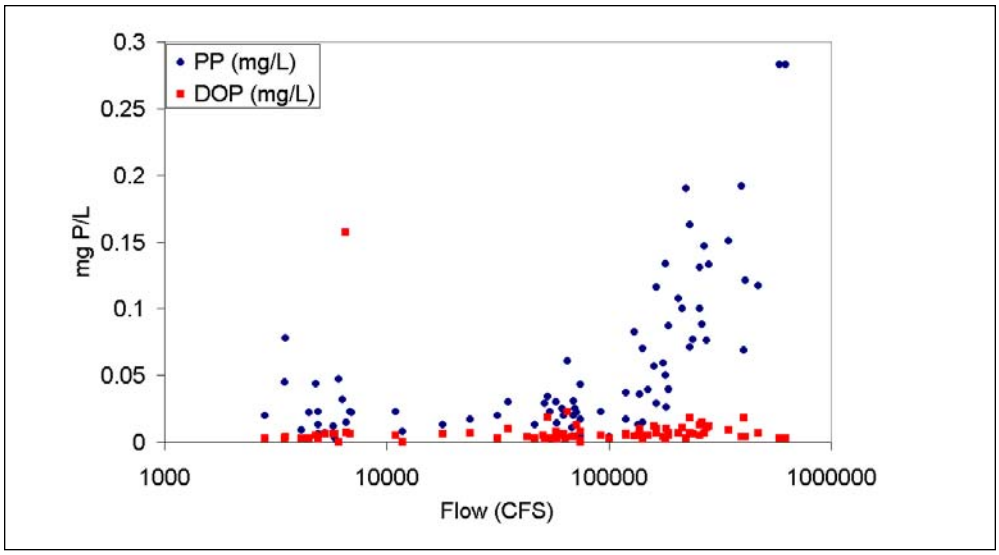

Figure 5-6. Observed particulate and dissolved organic phosphorus at the Susquehanna River fall line.

concentrations than elsewhere (Table 5-2). Particulate forms increased as a function of flow. Frequently a break was apparent in particulate nutrient concentrations that suggested initiation of bottom scour of particulates. These insights led to specification of constant dissolved organic concentrations in distributed sources. An algorithm (Figure 5-7) was developed to convert loads into dissolved and particulate fractions.

Particulate Inorganic Phosphorus. An analysis was conducted to distinguish organic and inorganic particulate phosphorus fractions. While the water quality model does not presently incorporate these distinctions, results are reported for future reference.

The EPA Chesapeake Bay Program Office conducted a special monitoring program in 1994 to measure particulate inorganic phosphorus (PIP) at the fall lines and in stream. We paired fall-line PIP observations with particulate phosphorus observations, collected on the same day, in the USGS data base. A total of 54 pairs were produced, half of which were in the Potomac River. The median ratio of PIP to particulate phosphorus was 0.50. That is, half of the particulate phosphorus load at the fall lines was in inorganic form. No effect of flow on composition of particulate phosphorus was evident but this finding was limited to the range of flows sampled. Sampling was concentrated in summer and at low to moderate flows.

Total Organic Carbon

Total organic carbon observations were available only at the Maryland fall lines. These showed a tendency for organic carbon concentration to increase with flow (Figures 5-8, 5-9). No data were available to partition total organic carbon into particulate and dissolved fractions. Both load and fractions were obtained by ratio to particulate and dissolved organic nitrogen using ratios presented in the chapter entitled “Hydrology and Loads.”

Table 5-2
Dissolved Organic Nutrients and Volatile Solids at Major Fall Lines

	James	York	Rappa-hannock	Potomac	Patuxent	Susque-hanna
Organic N, mg/L						
Median	0.20	0.27	0.21	0.26	0.29	0.16
Mean	0.22	0.29	0.26	0.28	0.30	0.18
Std. Dev.	0.14	0.11	0.29	0.11	0.11	0.11
Range	0.02 - 1.25	0 - 0.84	0 - 2.25	0 - 0.92	0.01 - 0.62	0 - 0.93
Number of Observations	127	279	87	241	79	83
Model	0.25	0.25	0.25	0.25	0.25	0.16
Organic P, mg/L						
Median	0.009	0.010	0.008	0.010	0	0.005
Mean	0.010	0.011	0.012	0.015	0.003	0.008
Std. Dev	0.010	0.012	0.020	0.016	0.018	0.017
Range	0 - 0.06	0 - 0.13	0 - 0.17	0 - 0.17	0 - 0.12	0 - 0.16
Number of Observations	127	279	87	241	79	83
Model	0.0085	0.0085	0.0085	0.0085	0.0085	0.005
Volatile Solids, fraction						
Median	0.19	0.38	0.17			
Mean	0.40	0.47	0.40			
	0.35	0.31	0.36			
Range	0.09 - 1	0.08 - 1	0.09 - 1			
Number of Observations	124	268	83			
Model	0.12	0.12	0.12	0.12	0.12	0.12

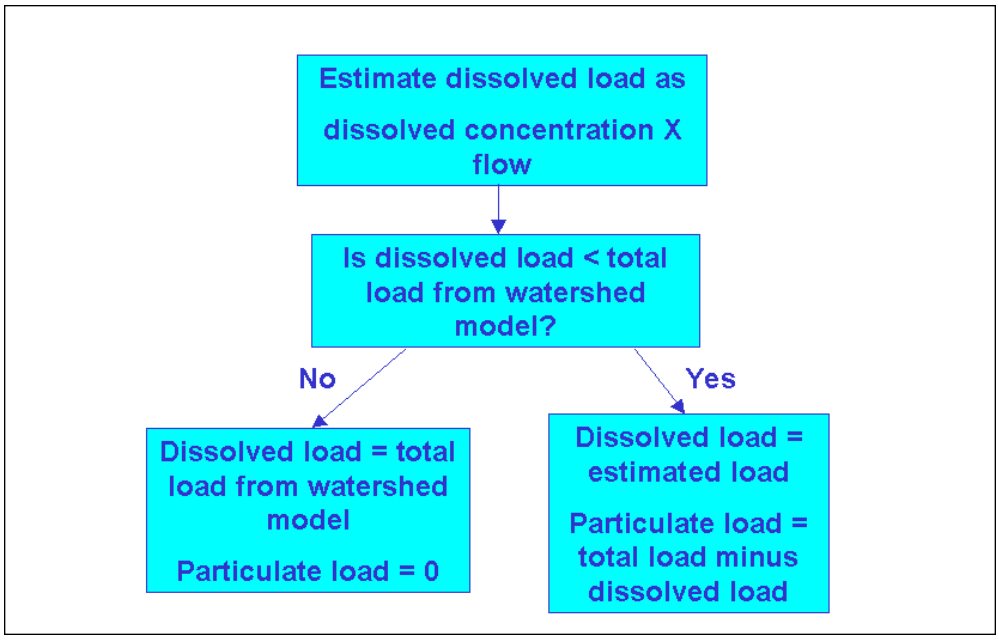

Figure 5-7. Determination of dissolved organic and particulate loads from watershed model total organic loads.

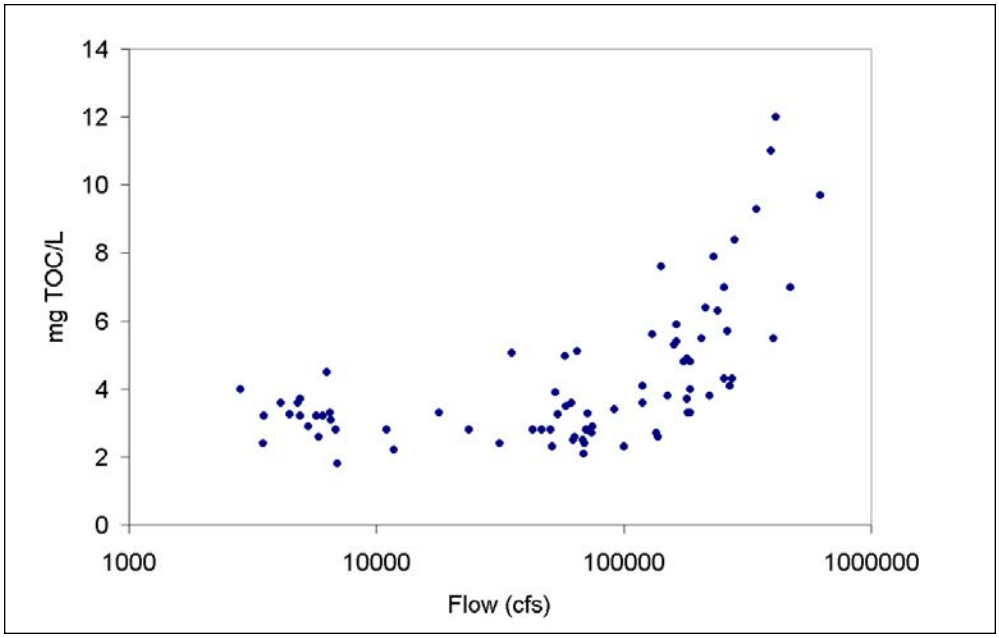

Figure 5-8. Observed total organic carbon versus flow at Potomac fall line.

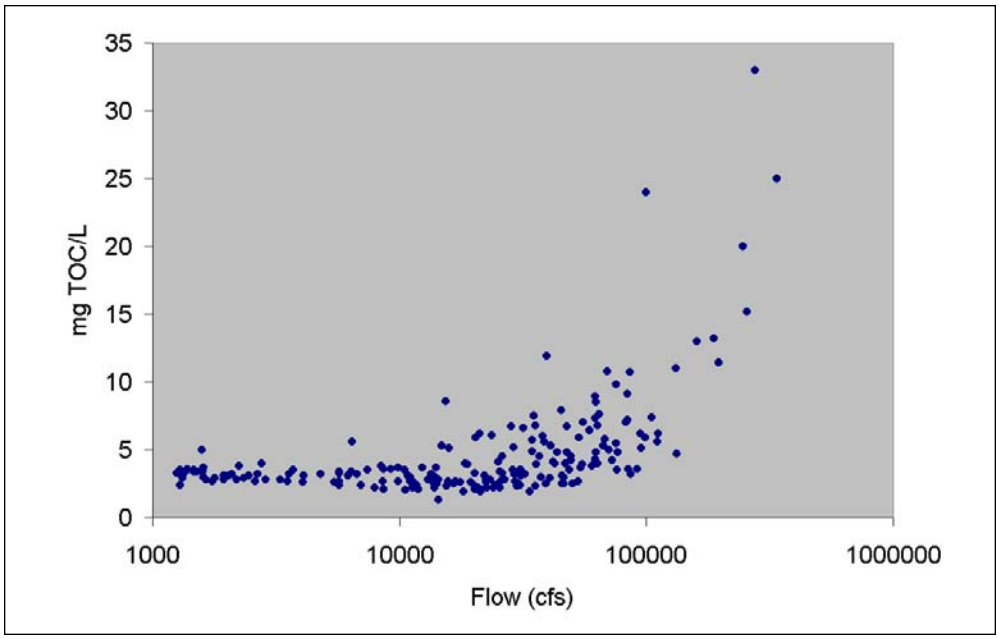

Figure 5-9. Observed total organic carbon versus flow at Susquehanna fall line.

Fixed Solids

Observations of total, fixed, and volatile solids were available at the Virginia fall lines. These observations indicated the solids fractionation was dependent on flow (Figure 5-10). At low flows, solids were almost entirely volatile (organic). The fraction volatile solids decreased to a constant value as flow increased. Also, the river with the lowest flow, the York, had the greatest median fraction volatile solids (Table 5-2). Since the greatest solids loads enter during storm events in major tributaries, we assigned our fraction volatile solids to reflect high flows. The watershed model total solids loads were reduced by 12% to provide fixed solids loads for the water quality model.

Labile and Refractory Particulates

Particulate matter in nonpoint-source loads must be split into labile and refractory portions to correspond to water quality model variables. The definition of labile organic matter derives from the sediment diagenesis model. In the sediment model, labile organic matter has a decay coefficient of 0.035 d^{-1} @ 20 ºC. At that rate, almost 90% of labile organic matter decays away in sixty days. Little guidance exists for partitioning particulate loads into labile and refractory fractions. A set of preliminary experiments conducted during the first portion of this study (Cerco and Cole 1994) indicated the labile fraction of particles at the fall line varied from 0.2 (carbon and phosphorus) to 0.6 (nitrogen). Experiments with the early model indicated these fractions adversely affected model calibration. Sediment diagenesis of labile particles deposited near the fall lines produced unrealistically large nutrient fluxes into the water column. As a result, the labile fraction of particles in nonpoint sources was set to zero. This fractionation was carried over into the present model.

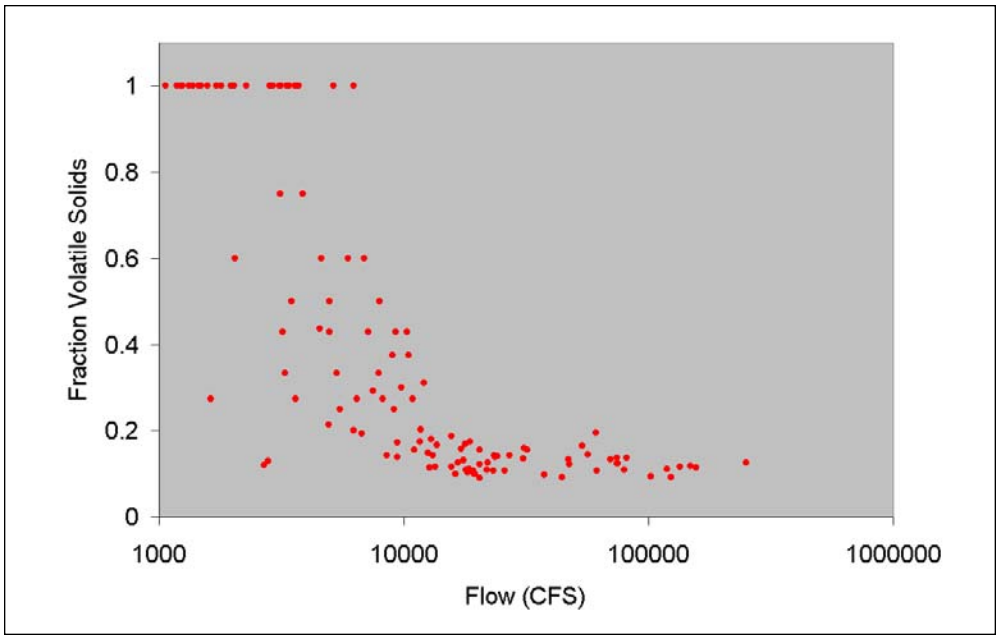

Figure 5-10. Observed fraction volatile solids at James River fall line.

Point-Source Loads

Linking point-source loads to the water quality model involves the same tasks as the nonpoint-source loads. Loads of total organic nutrients and carbon must be split into dissolved, labile particulate, and refractory particulate forms.

As part of the Tributary Refinements portion of the model study, seven point-source discharges in Virginia were sampled on two occasions in 1994. Effluent was analyzed specifically to provide quantities necessary to map reported effluent quantities into model state variables. The particulate fraction assigned to model loads closely reflected the median value determined from the 1994 observations (Table 5-3).

Little guidance was available to split particulates into labile and refractory fractions. A set of preliminary experiments conducted during the first portion of this study (Cerco and Cole 1994) indicated the labile fraction of particles from point sources was low for phosphorus (0.02) and moderate for nitrogen (0.5) and carbon (0.7). The values for carbon and nitrogen appeared unreasonable. Effluent from point sources is treated and is not expected to be highly reactive. Consequently, labile fractions assigned in the model were 0.15 for carbon, 0.15 for nitrogen, and 0.07 for phosphorus.

Other Loads

Bank loads were assumed to consist entirely of refractory particulate matter. Wetlands carbon loads were split equally into dissolved organic, labile particulate, and refractory particulate organic carbon. The organic fraction of atmospheric loads was split equally into dissolved, labile particulate, and refractory particulate forms.

Table 5-3
Particulate Fraction of Organic Matter at Point Sources

Facility	NPDES	PON/TON	PP/TOP	POC/TOC
Richmond	63177	0.53	0.59	0.23
Petersburg	25437	0.68	0.37	0.14
Hopewell	66630	0.05	0.45	0.12
Allied Chesterfield	5312	0.35	0.79	0.37
Allied Hopewell	5219	0.75	0.76	0.36
Chesapeake Corp	3115	0.64	0.60	0.20
Fredericksburg	25127	0.22	0.78	0.17
Median		0.53	0.60	0.20
Model		0.5	0.6	0.2

References

Cerco, C, Johnson, B., Wang, H. (2002). “Tributary refinements to the Chesapeake Bay model,” ERDC TR-02-4, US Army Engineer Research and Development Center, Vicksburg MS.

Cerco, C., and Cole, T. (1994). “Three-dimensional eutrophication model of Chesapeake Bay,” Technical Report EL-94-4, US Army Engineer Waterways Experiment Station, Vicksburg MS.

Water Quality Model Formulation 6

Introduction

CE-QUAL-ICM was designed to be a flexible, widely-applicable eutrophication model. Initial application was to Chesapeake Bay (Cerco and Cole 1994). Subsequent additional applications included the Delaware Inland Bays (Cerco et al. 1994), Newark Bay (Cerco and Bunch 1997), and the San Juan Estuary (Bunch et al. 2000). Each model application employed a different combination of model features and required addition of system-specific capabilities. This chapter describes general features and site-specific developments of the model as presently applied to the water column of Chesapeake Bay.

Conservation of Mass Equation

The foundation of CE-QUAL-ICM is the solution to the three-dimensional mass-conservation equation for a control volume. Control volumes correspond to cells on the model grid. CE-QUAL-ICM solves, for each volume and for each state variable, the equation:

$$\frac{\delta V_j \bullet C_j}{\delta t} = \sum_{k=1}^{n} Q_k \bullet C_k + \sum_{k=1}^{n} A_k \bullet D_k \bullet \frac{\delta C}{\delta x_k} + \Sigma S_j \qquad (6\text{-}1)$$

in which:
V_j = volume of j^{th} control volume (m^3)
C_j = concentration in j^{th} control volume (g m^{-3})
t, x = temporal and spatial coordinates
n = number of flow faces attached to j^{th} control volume
Q_k = volumetric flow across flow face k of j^{th} control volume (m^3 s^{-1})
C_k = concentration in flow across face k (g m^{-3})
A_k = area of flow face k (m^2)
D_k = diffusion coefficient at flow face k (m^2 s^{-1})
S_j = external loads and kinetic sources and sinks in j^{th} control volume (g s^{-1})

Solution of Equation 6-1 on a digital computer requires discretization of the continuous derivatives and specification of parameter values. The equation is solved using the QUICKEST algorithm (Leonard 1979) in the horizontal plane and a Crank-Nicolson scheme in the vertical direction. Discrete time steps, determined by computational stability requirements, are 15 minutes.

State Variables

At present, the CE-QUAL-ICM model incorporates 24 state variables in the water column including physical variables, multiple algal groups, two zooplankton groups, and multiple forms of carbon, nitrogen, phosphorus and silica (Table 6-1).

Table 6-1
Water Quality Model State Variables

Temperature	Salinity
Fixed Solids	Freshwater Cyanobacteria
Spring Diatoms	Other (Green) Algae
Microzooplankton	Mesozooplankton
Dissolved Organic Carbon	Labile Particulate Organic Carbon
Refractory Particulate Organic Carbon	Ammonium+Urea
Nitrate+Nitrite	Dissolved Organic Nitrogen
Labile Particulate Organic Nitrogen	Refractory Particulate Organic Nitrogen
Total Phosphate	Dissolved Organic Phosphorus
Labile Particulate Organic Phosphorus	Refractory Particulate Organic Phosphorus
Chemical Oxygen Demand	Dissolved Oxygen
Dissolved Silica	Particulate Biogenic Silica

Algae

Algae are grouped into three model classes: cyanobacteria, spring diatoms, and other green algae. The grouping is based upon the distinctive characteristics of each class and upon the significant role the characteristics play in the ecosystem. Cyanobacteria, commonly called blue-green algae, are characterized by their abundance (as picoplankton) in saline water and by their bloom-forming characteristics in fresh water. Cyanobacteria are unique in that some species fix atmospheric nitrogen although nitrogen fixers are not predominant in the Chesapeake Bay system. The Cyanobacteria distinguished in the model are the bloom-forming species found in the tidal, freshwater Potomac River. They are characterized as having negligible settling velocity and are subject to low predation pressure. The picoplankton are combined with the other green algae group since insufficient data

exists to consider them separately. Spring diatoms are large phytoplankton that produce an annual bloom in the saline portions of the bay and tributaries. Settling of spring diatom blooms to the sediments may be a significant source of carbon for sediment oxygen demand. Diatoms are distinguished by their requirement of silica as a nutrient to form cell walls. Algae that do not fall into the preceding two groups are lumped into the heading of green algae. The other green algae represent the mixture that characterizes saline waters during summer and autumn and fresh waters year round. Non-bloom forming diatoms comprise a portion of this mixture.

Zooplankton

Two zooplankton groups are considered: microzooplankton and mesozooplankton. The microzooplankton can be important predators on phytoplankton and they are one of the prey groups for mesozooplankton. Mesozooplankton consume phytoplankton and detritus as well as microzooplankton. The mesozooplankton are an important prey resource for carnivorous finfish such as Bay Anchovy. Zooplankton were included in the model as a first step towards computing the effect of eutrophication management on top-level predators.

Organic Carbon

Three organic carbon state variables are considered: dissolved, labile particulate, and refractory particulate. Labile and refractory distinctions are based upon the time scale of decomposition. Labile organic carbon decomposes on a time scale of days to weeks while refractory organic carbon requires more time. Labile organic carbon decomposes rapidly in the water column or the sediments. Refractory organic carbon decomposes slowly, primarily in the sediments, and may contribute to sediment oxygen demand years after deposition.

Nitrogen

Nitrogen is first divided into available and unavailable fractions. Available refers to employment in algal nutrition. Two available forms are considered: reduced and oxidized nitrogen. Reduced nitrogen includes ammonium and urea. Nitrate and nitrite comprise the oxidized nitrogen pool. Both reduced and oxidized nitrogen are utilized to fulfill algal nutrient requirements. The primary reason for distinguishing the two is that ammonium is oxidized by nitrifying bacteria into nitrite and, subsequently, nitrate. This oxidation can be a significant sink of oxygen in the water column and sediments.

Unavailable nitrogen state variables are dissolved organic nitrogen, labile particulate organic nitrogen, and refractory particulate organic nitrogen. The dissolved organic nitrogen state variable excludes urea which is directly available as an algal nutrient.

Phosphorus

As with nitrogen, phosphorus is first divided into available and unavailable fractions. Only a single available form, dissolved phosphate, is considered. The model framework allows for exchange of phosphate between dissolved and

particulate (sorbed to solids) forms but this option is not implemented in the present application. Three forms of unavailable phosphorus are considered: dissolved organic phosphorus, labile particulate organic phosphorus, and refractory particulate organic phosphorus.

Silica

Silica is divided into two state variables: dissolved silica and particulate biogenic silica. Dissolved silica is available to diatoms while particulate biogenic silica cannot be utilized. In the model, particulate biogenic silica is produced through diatom mortality. Particulate biogenic silica undergoes dissolution to available silica or else settles to the bottom sediments.

Chemical Oxygen Demand

Chemical oxygen demand is the concentration of reduced substances that are oxidized by abiotic processes. The primary component of chemical oxygen demand is sulfide released from sediments. Oxidation of sulfide to sulfate may remove substantial quantities of dissolved oxygen from the water column.

Dissolved Oxygen

Dissolved oxygen is required for the existence of higher life forms. Oxygen availability determines the distribution of organisms and the flows of energy and nutrients in an ecosystem. Dissolved oxygen is a central component of the water-quality model.

Salinity

Salinity is a conservative tracer that provides verification of the transport component of the model and facilitates examination of conservation of mass. Salinity also influences the dissolved oxygen saturation concentration and may be used in the determination of kinetics constants that differ in saline and fresh water.

Temperature

Temperature is a primary determinant of the rate of biochemical reactions. Reaction rates increase as a function of temperature although extreme temperatures may result in the mortality of organisms and a decrease in kinetics rates.

Fixed Solids

Fixed solids are the mineral fraction of total suspended solids. Solids are considered primarily for their role in light attenuation.

The remainder of this chapter is devoted to detailing the kinetics sources and sinks and to reporting parameter values. For notational simplicity, the transport terms are dropped in the reporting of kinetics formulations.

Algae

Equations governing the three algal groups are largely the same. Differences among groups are expressed through the magnitudes of parameters in the equations. Generic equations are presented below except when group-specific relationships are required.

Algal sources and sinks in the conservation equation include production, metabolism, predation, and settling. These are expressed:

$$\frac{\delta}{\delta t} B = \left(G - BM - Wa \bullet \frac{\delta}{\delta z} \right) B - PR \qquad (6\text{-}2)$$

in which:
B = algal biomass, expressed as carbon (g C m^{-3})
G = growth (d^{-1})
BM = basal metabolism (d^{-1})
Wa = algal settling velocity (m d^{-1})
PR = predation (g C m^{-3} d^{-1})
z = vertical coordinate

Production

Production by phytoplankton is determined by the intensity of light, by the availability of nutrients, and by the ambient temperature.

Light

The influence of light on phytoplankton production is represented by a chlorophyll-specific production equation (Jassby and Platt 1976):

$$P^B = P^B m \frac{I}{\sqrt{I^2 + Ik^2}} \qquad (6\text{-}3)$$

in which:
P^B = photosynthetic rate (g C g^{-1} Chl d^{-1})
$P^B m$ = maximum photosynthetic rate (g C g^{-1} Chl d^{-1})
I = irradiance (E m^{-2} d^{-1})

Parameter Ik is defined as the irradiance at which the initial slope of the production vs. irradiance relationship (Figure 6-1) intersects the value of $P^B m$

$$Ik = \frac{P^B m}{\alpha} \qquad (6\text{-}4)$$

in which:
α = initial slope of production vs. irradiance relationship (g C g^{-1} Chl (E m^{-2})$^{-1}$)

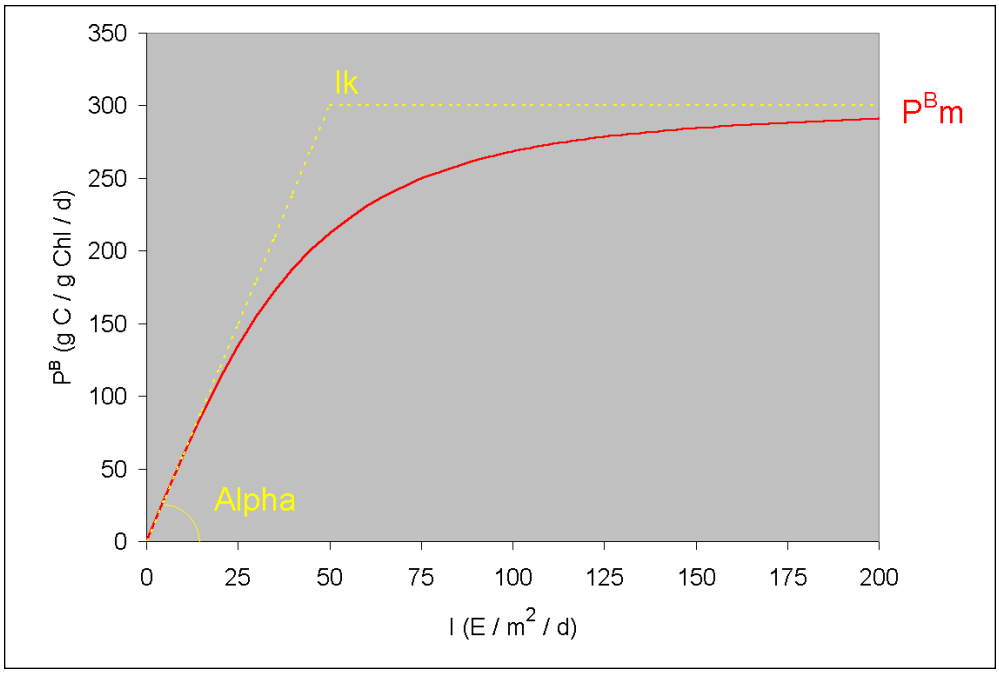

Figure 6-1. Production versus irradiance curve.

Chlorophyll-specific production rate is readily converted to carbon specific growth rate, for use in Equation 6-2, through division by the carbon-to- chlorophyll ratio:

$$G = \frac{P^B}{CChl} \tag{6-5}$$

in which:
CChl = carbon-to-chlorophyll ratio (g C g^{-1} chlorophyll a)

Specification of the carbon-to-chlorophyll ratio is detailed in a subsequent chapter entitled “Primary Production.”

Nutrients

Carbon, nitrogen, and phosphorus are the primary nutrients required for algal growth. Diatoms require silica, as well. Inorganic carbon is usually available in excess and is not considered in the model. The effects of the remaining nutrients on growth are described by the formulation commonly referred to as “Monod kinetics” (Figure 6-2; Monod 1949):

$$f(N) = \frac{D}{KHd + D} \tag{6-6}$$

in which:
f(N) = nutrient limitation on algal production ($0 \leq f(N) \leq 1$)
D = concentration of dissolved nutrient (g m^{-3})
KHd = half-saturation constant for nutrient uptake (g m^{-3})

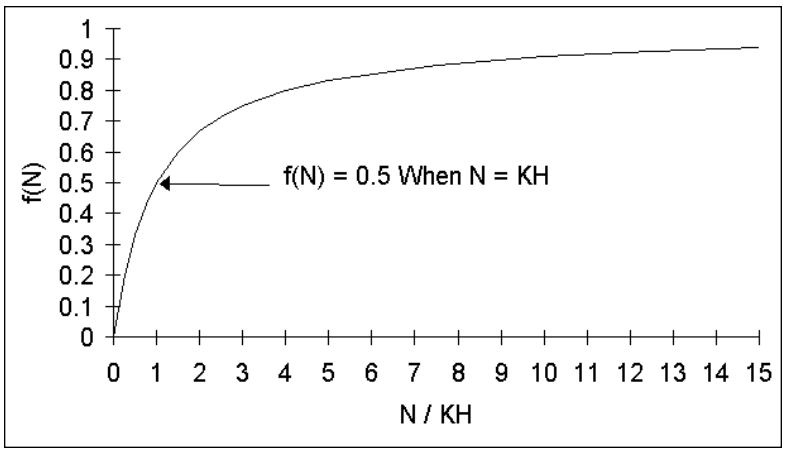

Figure 6-2. Monod formulation for nutrient-limited growth.

Temperature

Algal production increases as a function of temperature until an optimum temperature or temperature range is reached. Above the optimum, production declines until a temperature lethal to the organisms is attained. Numerous functional representations of temperature effects are available. Inspection of growth versus temperature data indicates a function similar to a Gaussian probability curve (Figure 6-3) provides a good fit to observations:

$$f(T) = e^{-KTg1 \bullet (T - Topt)^2} \text{ when } T \leq Topt$$

$$= e^{-KTg2 \bullet (Topt - T)^2} \text{ when } T > Topt \qquad (6\text{-}7)$$

in which:
T = temperature (°C)
Topt = optimal temperature for algal growth (°C)
KTg1 = effect of temperature below Topt on growth ($°C^{-2}$)
KTg2 = effect of temperature above Topt on growth ($°C^{-2}$)

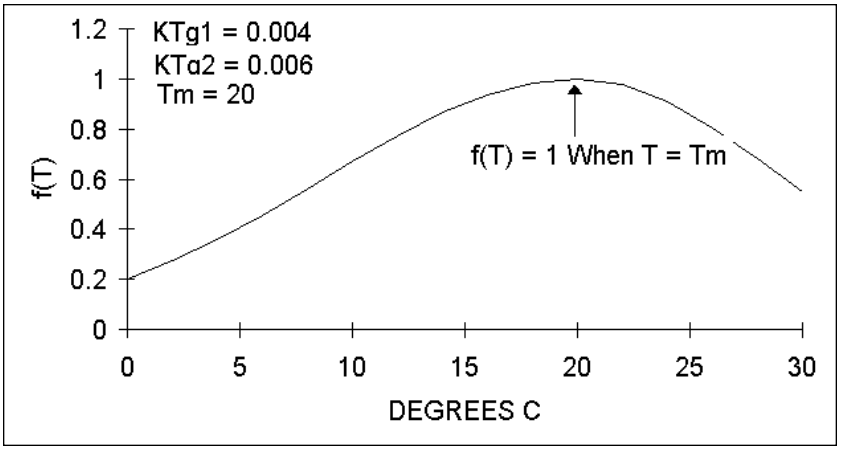

Figure 6-3. Relation of algal production to temperature.

Constructing the Photosynthesis vs. Irradiance Curve

A production versus irradiance relationship is constructed for each model cell at each time step. First, the maximum photosynthetic rate under ambient temperature and nutrient concentrations is determined:

$$P^B m(N,T) = P^B m \bullet f(T) \bullet \frac{D}{KHd + D} \qquad (6\text{-}8)$$

in which:
$P^B m(N,T)$ = maximum photosynthetic rate under ambient temperature and nutrient concentrations (g C g^{-1} Chl d^{-1})

The single most limiting nutrient is employed in determining the nutrient limitation.

Next, parameter Ik is derived from Equation 6-4. Finally, the production vs. irradiance relationship is constructed using $P^B m(N,T)$ and Ik. The resulting production versus irradiance curve exhibits three regions (Figure 6-4). For I >> Ik, the value of the term $I / (I^2 + Ik^2)^{½}$ approaches unity and temperature and nutrients are the primary factors that influence production. For I << Ik, production is determined solely by irradiance I. In the region where the initial slope of the production versus irradiance curve intercepts the line indicating production at optimal illumination, I = Ik, production is determined by the combined effects of temperature, nutrients, and light.

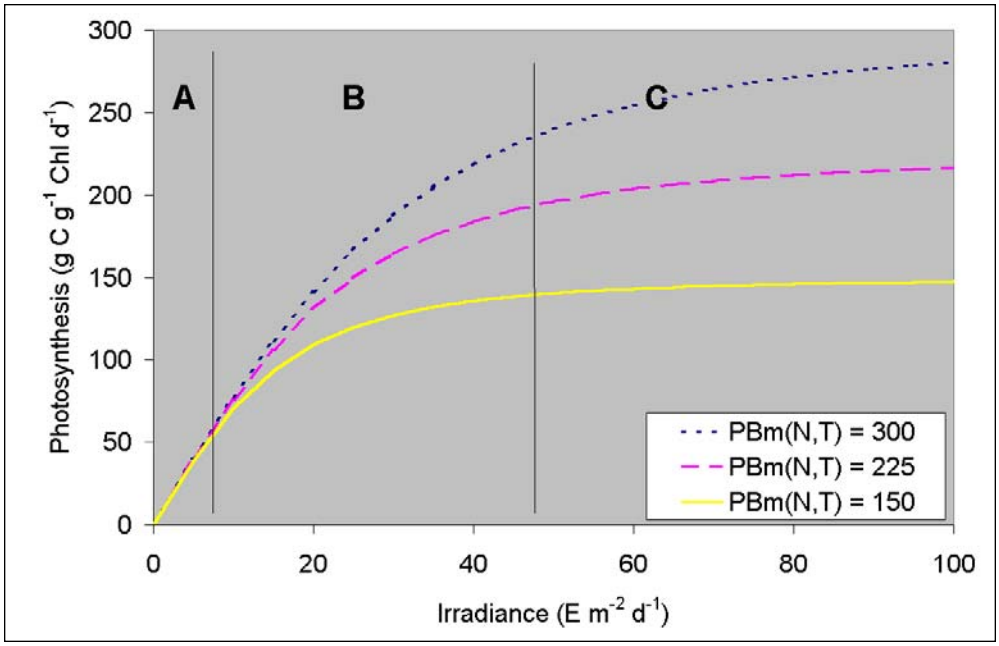

Figure 6-4. Effects of light and nutrients on production versus irradiance curve, determined for α = 8 g C g^{-1} Chl $(E\ m^{-2})^{-1}$.

Irradiance

Irradiance at the water surface is evaluated at each model time step. Instantaneous irradiance is computed by fitting a sin function to daily total irradiance:

$$Io = \frac{\Pi}{2 \bullet FD} \bullet IT \bullet \sin\left(\frac{\Pi \bullet DSSR}{FD}\right) \quad (6\text{-}9)$$

in which:
Io = irradiance at water surface (E m^{-2} d^{-1})
IT = daily total irradiance (E m^{-2})
FD = fractional daylength ($0 \leq FD \leq 1$)
DSSR = time since sunrise (d)

Io is evaluated only during the interval:

$$\frac{1 - FD}{2} \leq DSM \leq \frac{1 + FD}{2} \quad (6\text{-}10)$$

in which:
DSM = time since midnight (d)

Outside the specified interval, Io is set to zero.

Irradiance declines exponentially with depth below the surface. The diffuse attenuation coefficient, Kd, is computed as a function of color and concentrations of organic and mineral solids.

Respiration

Two forms of respiration are considered in the model: photo-respiration and basal metabolism. Photo-respiration represents the energy expended by carbon fixation and is a fixed fraction of production. In the event of no production (e.g. at night), photo-respiration is zero. Basal metabolism is a continuous energy expenditure to maintain basic life processes. In the model, metabolism is considered to be an exponentially increasing function of temperature (Figure 6-5). Total respiration is represented:

$$R = Presp \bullet G + BM \bullet e^{KTb \bullet (T - Tr)} \quad (6\text{-}11)$$

in which:
Presp = photo-respiration ($0 \leq Presp \leq 1$)
BM = metabolic rate at reference temperature Tr (d^{-1})
KTb = effect of temperature on metabolism ($^oC^{-1}$)
Tr = reference temperature for metabolism (^oC)

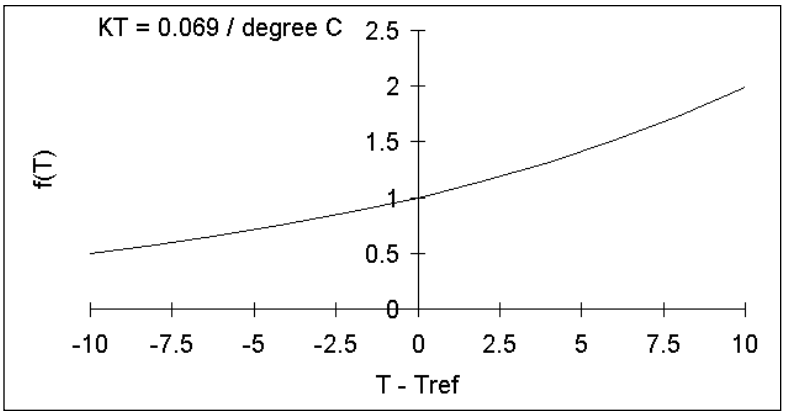

Figure 6-5. Exponential temperature relationship employed for metabolism and other processes.

Predation

The predation term includes the activity of zooplankton, filter-feeding benthos, and other pelagic filter feeders including planktivorous fish. Formulation and results of the zooplankton computation appear elsewhere in this report. Details of the benthos computations may be found in HydroQual (2000) and at http://www.chesapeakebay.net/model.htm. Predation by other planktivores is modeled by assuming predators clear a specific volume of water per unit biomass:

$$PR = F \bullet B \bullet M \tag{6-12}$$

F = filtration rate (m^3 g^{-1} predator C d^{-1})
M = planktivore biomass (g C m^{-3})

Detailed specification of the spatial and temporal distribution of the predator population is impossible. One approach is to assume predator biomass is proportional to algal biomass, M = γ B, in which case Equation 6-12 can be rewritten:

$$PR = \gamma \bullet F \bullet B^2 \tag{6-13}$$

Since neither γ nor F are known precisely, the logical approach is to combine their product into a single unknown determined during the model calibration procedure. Effect of temperature on predation is represented with the same formulation as the effect of temperature on respiration. The final representation of predation, including zooplankton, is:

$$PR = \frac{B}{KHsz + B} \bullet RMsz \bullet SZ + \frac{B}{KHlz + B} \bullet RMlz \bullet LZ + Phtl \bullet B^2 \tag{6-14}$$

RMsz = microzooplankton maximum ration (g algal C g^{-1} zoo C d^{-1})
SZ = microzooplankton biomass (g C m^{-3})
KHsz = half saturation concentration for carbon uptake by microzooplankton (g C m^{-3})

RMlz = mesozooplankton maximum ration (g algal C g^{-1} zoo C d^{-1})
LZ = mesozooplankton biomass (g C m^{-3})
KHlz = half saturation concentration for carbon uptake by mesozooplankton (g C m^{-3})
Phtl = rate of predation by other planktivores (m^3 g^{-1} C d^{-1})

Predation by filter-feeding benthos is represented as a loss term only in model cells that intersect the bottom.

Accounting for Algal Phosphorus

The amount of phosphorus incorporated in algal biomass is quantified through a stoichiometric ratio. Thus, total phosphorus in the model is expressed:

$$TotP = PO_4 + Apc \cdot B + DOP + LPOP + RPOP \qquad (6\text{-}15)$$

TotP = total phosphorus (g P m^{-3})
PO_4 = dissolved phosphate (g P m^{-3})
Apc = algal phosphorus-to-carbon ratio (g P g^{-1} C)
DOP = dissolved organic phosphorus (g P m^{-3})
LPP = labile particulate organic phosphorus (g P m^{-3})
RPP = refractory particulate organic phosphorus (g P m^{-3})

Algae take up dissolved phosphate during production and release dissolved phosphate and organic phosphorus through respiration. The fate of phosphorus released by respiration is determined by empirical distribution coefficients. The fate of algal phosphorus recycled by predation is determined by a second set of distribution parameters.

Accounting for Algal Nitrogen

Model nitrogen state variables include ammonium+urea, nitrate+nitrite, dissolved organic nitrogen, labile particulate organic nitrogen, and refractory particulate organic nitrogen. The amount of nitrogen incorporated in algal biomass is quantified through a stoichiometric ratio. Thus, total nitrogen in the model is expressed:

$$TotN = NH_4\text{-}Urea + NO_{23} + Anc \cdot B + DON + LPON + RPON \qquad (6\text{-}16)$$

TotN = total nitrogen (g N m^{-3})
NH_4-Urea = ammonium+urea (g N m^{-3})
NO_{23} = nitrate+nitrite (g N m^{-3})
Anc = algal nitrogen-to-carbon ratio (g N g^{-1} C)
DON = dissolved organic nitrogen (g N m^{-3})
LPON = labile particulate organic nitrogen (g N m^{-3})
RPON = refractory particulate organic nitrogen (g N m^{-3})

As with phosphorus, the fate of algal nitrogen released by metabolism and predation is represented by distribution coefficients.

Algal Nitrogen Preference

Algae take up ammonium+urea and nitrate+nitrite during production and release ammonium+urea and organic nitrogen through respiration. Nitrate+nitrite is internally reduced to ammonium before synthesis into biomass occurs (Parsons et al. 1984). Trace concentrations of ammonium+urea inhibit nitrate reduction so that, in the presence of multiple nitrogenous nutrients, ammonium+urea is utilized first. The "preference" of algae for ammonium+urea is expressed by an empirical function (Thomann and Fitzpatrick 1982):

$$PN = NH_4 - Urea \bullet \frac{NO_{23}}{(KHn + NH_4 - Urea) \bullet (KHn + NO_{23})} + NH_4 - Urea \bullet \frac{KHn}{(NH_4 - Urea + NO_{23}) \bullet (KHn + NO_{23})} \quad (6\text{-}17)$$

in which
PN = algal preference for ammonium uptake ($0 \leq Pn \leq 1$)
KHn = half saturation concentration for algal nitrogen uptake (g N m^{-3})

The function has two limiting values (Figure 6-6). When nitrate+nitrite is absent, the preference for ammonium+urea is unity. When ammonium+urea is absent, the preference is zero. In the presence of ammonium+urea and nitrate+nitrite, the preference depends on the abundance of both forms relative to the half-saturation constant for nitrogen uptake. When both ammonium+urea and nitrate+nitrite are abundant, the preference for ammonium+urea approaches unity. When ammonium+urea is scarce but nitrate+nitrite is abundant, the preference decreases in magnitude and a significant fraction of algal nitrogen requirement comes from nitrate+nitrite.

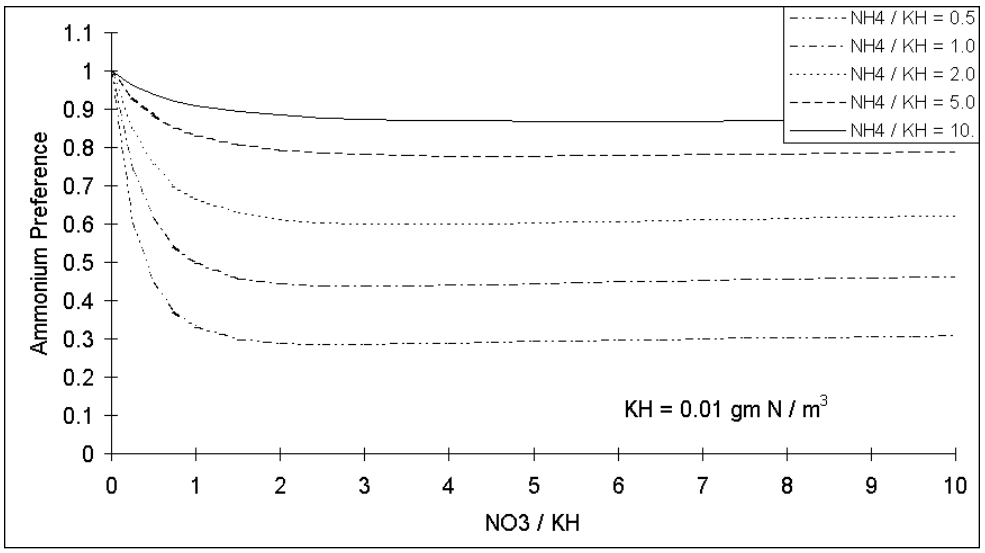

Figure 6-6. Algal ammonium preference.

Effect of Algae on Dissolved Oxygen

Algae produce oxygen during photosynthesis and consume oxygen through respiration. The quantity produced depends on the form of nitrogen utilized for growth. More oxygen is produced, per unit of carbon fixed, when nitrate is the algal nitrogen source than when ammonium is the source. Equations describing algal uptake of carbon and nitrogen and production of dissolved oxygen (Morel 1983) are:

$$106\ CO_2 + 16\ NH_4^+ + H_2PO_4^- + 106\ H_2O \text{ --> } \text{protoplasm} + 106\ O_2 + 15\ H^+ \quad (6\text{-}18)$$

$$106\ CO_2 + 16\ NO_3^- + H_2PO_4^- + 122\ H_2O + 17\ H^+ \text{ --> } \text{protoplasm} + 138\ O_2 \quad (6\text{-}19)$$

When ammonium is the nitrogen source, one mole oxygen is produced per mole carbon dioxide fixed. When nitrate is the nitrogen source, 1.3 moles oxygen are produced per mole carbon dioxide fixed.

The equation that describes the effect of algae on dissolved oxygen in the model is:

$$\frac{\delta}{\delta t} DO = \left[(1.3 - 0.3 \bullet PN) \bullet P - (1 - FCD) \bullet BM\right] \bullet AOCR \bullet B \quad (6\text{-}20)$$

in which:
FCD = fraction of algal metabolism recycled as dissolved organic carbon
($0 \leq FCD \leq 1$)
AOCR = dissolved oxygen-to-carbon ratio in respiration (2.67 g O_2 g^{-1} C)

The magnitude of AOCR is derived from a simple representation of the respiration process:

$$CH_2O + O_2 = CO_2 + H_2O \quad (6\text{-}21)$$

The quantity (1.3 - 0.3 • PN) is the photosynthesis ratio and expresses the molar quantity of oxygen produced per mole carbon fixed. The photosynthesis ratio approaches unity as the algal preference for ammonium approaches unity.

Accounting for Algal Silica

The amount of silica incorporated in algal biomass is quantified through a stoichiometric ratio. Thus, total silica in the model is expressed:

$$TotSi = Dsil + Asc \bullet B + PBS \quad (6\text{-}22)$$

TotSi = total silica (g Si m^{-3})
Dsil = dissolved silica (g Si m^{-3})
Asc = algal silica-to-carbon ratio (g Si g^{-1} C)
PBS = particulate biogenic silica (g Si m^{-3})

As with the other nutrients, the fate of algal silica released by metabolism and predation is represented by distribution coefficients.

Salinity Toxicity

The Cyanobacteria represented in the model are freshwater organisms that cease production when salinity exceeds 1 to 2 ppt (Sellner et al. 1988). The effect of salinity on Cyanobacteria was represented by a mortality term in the form of a rectangular hyperbola:

$$STOX1 = STF1 \bullet \frac{S}{KHst1 + S} \qquad (6\text{-}23)$$

in which
STOX1 = mortality induced by salinity on Cyanobacteria (d^{-1})
STF1 = maximum salinity mortality on Cyanobacteria (d^{-1})
S = salinity (ppt)
KHst1 = salinity at which mortality is half maximum value (ppt)

The spring diatom bloom is limited to saline water. The limiting mechanism is not defined but appears to be related to salinity. The upstream limit of the spring bloom was defined in the model by introducing a mortality term at low salinity:

$$STOX2 = STF2 \bullet \frac{KHst2}{KHst2 + S} \qquad (6\text{-}24)$$

in which
STOX2 = mortality induced by freshwater on spring diatoms (d^{-1})
STF2 = maximum freshwater mortality on spring diatoms (d^{-1})
S = salinity (ppt)
KHst2 = salinity at which mortality is half maximum value (ppt)

The salinity-related mortality (Figure 6-7) is added to the basal metabolism.

Representation of Blue-Green Algal Mats

Microcystis commonly form algal mats. Exact representation of algal mats is beyond the present capacity of the model. Mat formation was approximated by restricting Cyanobacteria growth to the surface model layer.

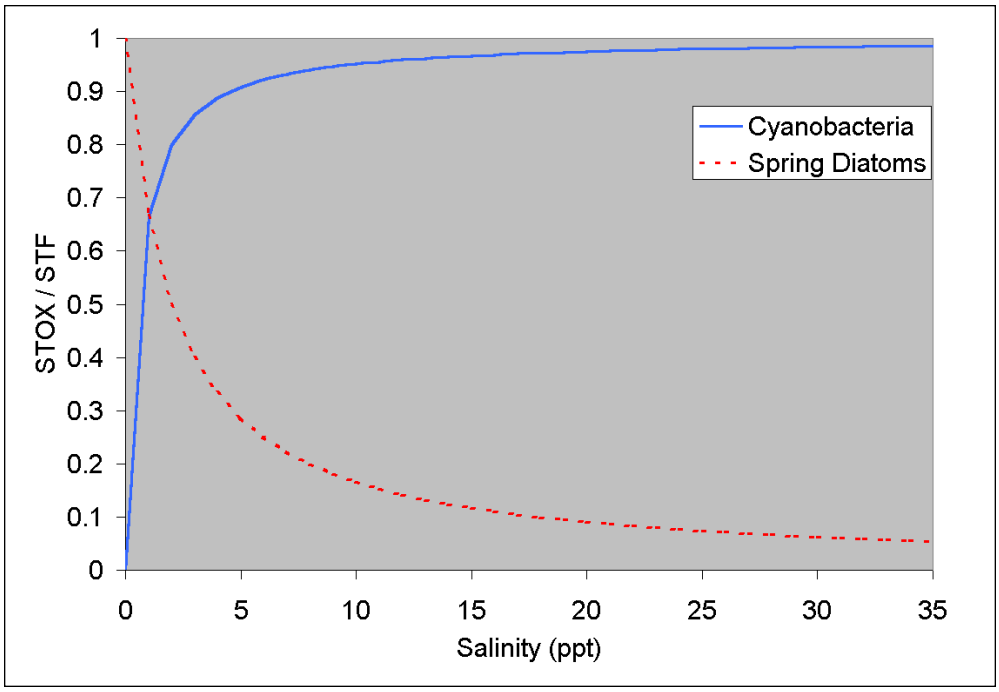

Figure 6-7. Salinity toxicity relationship.

Organic Carbon

Organic carbon undergoes innumerable transformations in the water column. The model carbon cycle (Figure 6-8) consists of the following elements:

- Phytoplankton production and excretion
- Zooplankton production and excretion
- Predation on phytoplankton
- Dissolution of particulate carbon
- Heterotrophic respiration
- Denitrification
- Settling

Algal production is the primary carbon source although carbon also enters the system through external loading. Predation on algae by zooplankton and other organisms releases particulate and dissolved organic carbon to the water column. A fraction of the particulate organic carbon undergoes first-order dissolution to dissolved organic carbon. Dissolved organic carbon produced by excretion, by predation, and by dissolution is respired at a first-order rate to inorganic carbon. Particulate organic carbon which does not undergo dissolution settles to the bottom sediments.

Zooplankton kinetics are detailed in a separate chapter. Kinetics of the organic carbon state variables are described below.

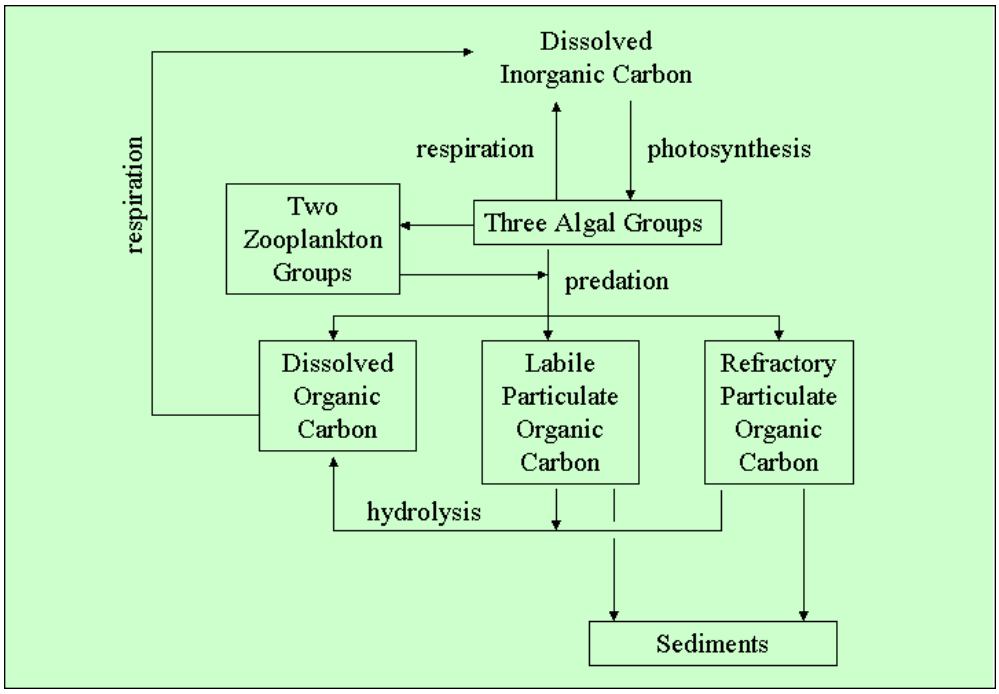

Figure 6-8. Model carbon cycle.

Dissolution and Respiration

Organic carbon dissolution and respiration are represented as first-order processes in which the reaction rate is proportional to concentration of the reactant. An exponential function (Figure 6-5) relates dissolution and respiration to temperature.

In the model, a Monod-like function diminishes respiration as dissolved oxygen approaches zero. As oxygen is depleted from natural systems, oxidation of organic matter is effected by the reduction of alternate oxidants. The sequence in which alternate oxidants are employed is determined by the thermodynamics of oxidation-reduction reactions. The first substance reduced in the absence of oxygen is nitrate. A representation of the denitrification reaction can be obtained by balancing standard half-cell redox reactions (Stumm and Morgan 1981):

$$4\ NO_3^- + 4\ H^+ + 5\ CH_2O \text{ --> } 2\ N_2 + 7\ H_2O + 5\ CO_2 \qquad (6\text{-}25)$$

Equation 6-25 describes the stoichiometry of the denitrification reaction. The kinetics of the reaction, represented in the model, are first-order. The dissolved organic carbon respiration rate, Kdoc, is modified so that significant decay via denitrification occurs only when nitrate is freely available and dissolved oxygen is depleted (Figure 6-9). A parameter is included so that the anoxic respiration rate is slower than oxic respiration:

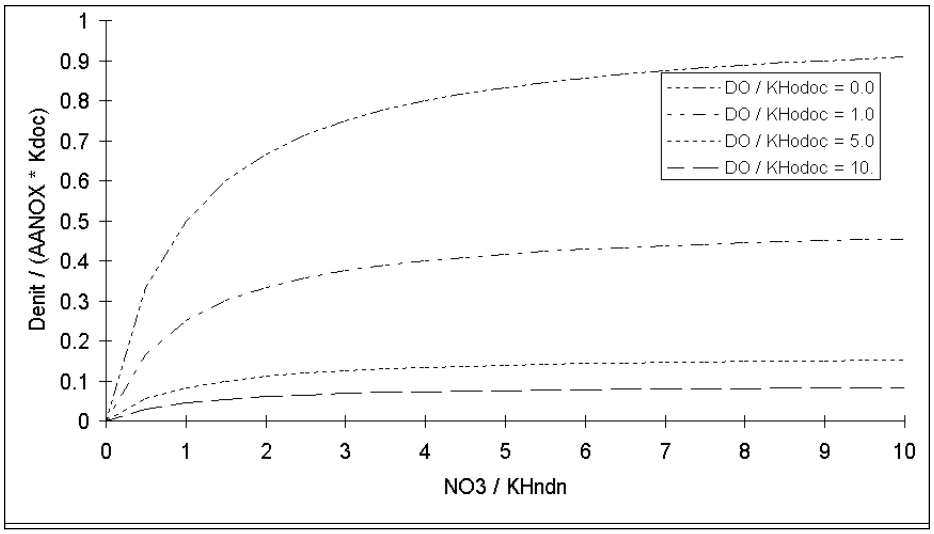

Figure 6-9. Effect of dissolved oxygen and nitrate on denitrification.

$$\text{Denit} = \frac{\text{KHodoc}}{\text{KHodoc} + \text{DO}} \bullet \frac{\text{NO}_3}{\text{KHndn} + \text{NO}_3} \bullet \text{AANOX} \bullet \text{Kdoc} \qquad (6\text{-}26)$$

in which:
Denit = denitrification rate of dissolved organic carbon (d^{-1})
Kdoc = first-order dissolved organic carbon respiration rate (d^{-1})
AANOX = ratio of denitrification to oxic carbon respiration rate
($0 \leq \text{AANOX} \leq 1$)
KHodoc = half-saturation concentration of dissolved oxygen required for oxic respiration (g O_2 m^{-3})
KHndn = half-saturation concentration of nitrate required for denitrification (g N m^{-3})

Dissolved Organic Carbon

The complete representation of dissolved organic carbon sources and sinks in the model ecosystem is:

$$\frac{\partial}{\partial t}\text{DOC} = \text{FCD} \bullet \text{R} \bullet \text{B} + \text{FCDP} \bullet \text{PR} + \text{Klpoc} \bullet \text{LPOC} + \text{Krpoc} \bullet \text{RPOC} - \frac{\text{DO}}{\text{KHodoc} + \text{DO}} \bullet \text{Kdoc} \bullet \text{DOC} - \text{DENIT} \bullet \text{DOC} \qquad (6\text{-}27)$$

in which:
DOC = dissolved organic carbon (g m^{-3})
LPOC = labile particulate organic carbon (g m^{-3})
RPOC = refractory particulate organic carbon (g m^{-3})
FCD = fraction of algal respiration released as DOC ($0 < FCD < 1$)
FCDP = fraction of predation on algae released as DOC ($0 < FCDP < 1$)
Klpoc = dissolution rate of LPOC (d^{-1})
Krpoc = dissolution rate of RPOC (d^{-1})
Kdoc = respiration rate of DOC (d^{-1})

Labile Particulate Organic Carbon

The complete representation of labile particulate organic carbon sources and sinks in the model ecosystem is:

$$\frac{\delta}{\delta t} LPOC = FCL \bullet R \bullet B + FCLP \bullet PR - Klpoc \bullet LPOC - Wl \bullet \frac{\delta}{\delta z} LPOC \quad (6\text{-}28)$$

in which:
FCL = fraction of algal respiration released as LPOC ($0 < FCL < 1$)
FCLP = fraction of predation on algae released as LPOC ($0 < FCLP < 1$)
Wl = settling velocity of labile particles (m d^{-1})

Refractory Particulate Organic Carbon

The complete representation of refractory particulate organic carbon sources and sinks in the model ecosystem is:

$$\frac{\delta}{\delta t} RPOC = FCR \bullet R \bullet B + FCRP \bullet PR - Krpoc \bullet RPOC - Wr \bullet \frac{\delta}{\delta z} RPOC \quad (6\text{-}29)$$

in which:
FCR = fraction of algal respiration released as RPOC ($0 < FCR < 1$)
FCRP = fraction of predation on algae released as RPOC ($0 < FCRP < 1$)
Wr = settling velocity of refractory particles (m d^{-1})

Phosphorus

The model phosphorus cycle (Figure 6-10) includes the following processes:

- Algal uptake and excretion
- Zooplankton excretion
- Predation
- Hydrolysis of particulate organic phosphorus
- Mineralization of dissolved organic phosphorus
- Settling and resuspension

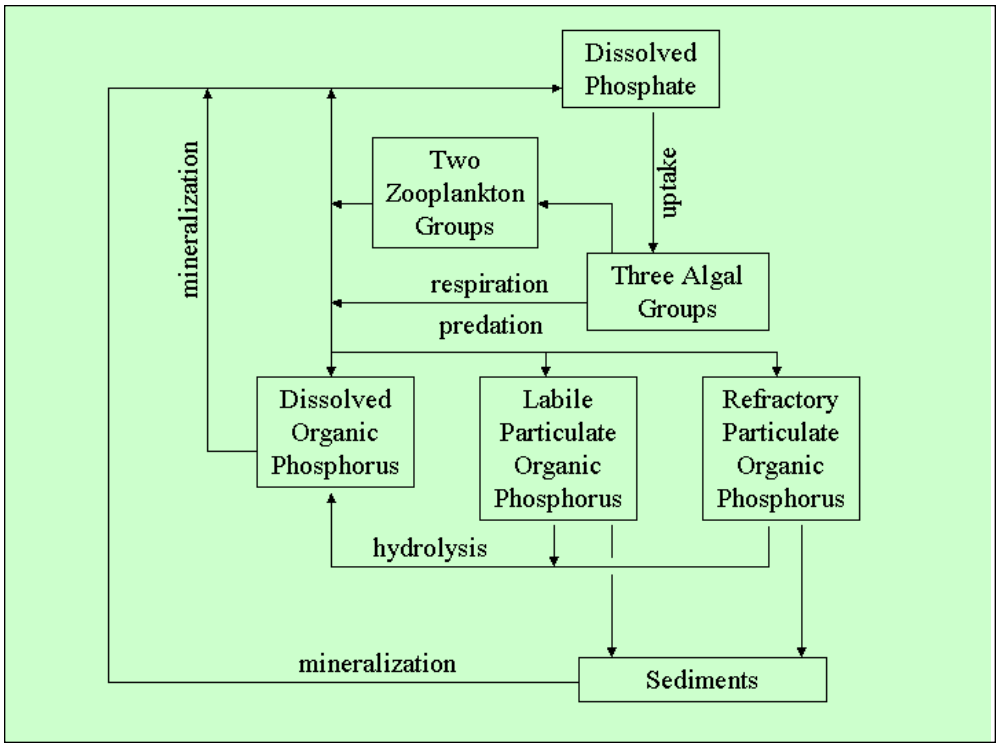

Figure 6-10. Model phosphorus cycle.

External loads provide the ultimate source of phosphorus to the system. Dissolved phosphate is incorporated by algae during growth and released as phosphate and organic phosphorus through respiration and predation. Dissolved organic phosphorus is mineralized to phosphate. A portion of the particulate organic phosphorus hydrolyzes to dissolved organic phosphorus. The balance settles to the sediments. Within the sediments, particulate phosphorus is mineralized and recycled to the water column as dissolved phosphate.

Hydrolysis and Mineralization

Within the model, hydrolysis is defined as the process by which particulate organic substances are converted to dissolved organic form. Mineralization is defined as the process by which dissolved organic substances are converted to dissolved inorganic form. Conversion of particulate organic phosphorus to phosphate proceeds through the sequence of hydrolysis and mineralization. Direct mineralization of particulate organic phosphorus does not occur.

Mineralization of organic phosphorus is mediated by the release of nucleotidase and phosphatase enzymes by bacteria (Ammerman and Azam 1985; Chrost and Overbeck 1987) and algae (Matavulj and Flint 1987; Chrost and Overbeck 1987; Boni et al. 1989). Since the algae themselves release the enzyme and since bacterial abundance is related to algal biomass, the rate of organic phosphorus mineralization is related, in the model, to algal biomass. A most remarkable property of the enzyme process is that alkaline phosphatase activity is inversely proportional to ambient phosphate concentration (Chrost and Overbeck 1987; Boni

et al. 1989). Put in different terms, when phosphate is scarce, algae stimulate production of an enzyme that mineralizes organic phosphorus to phosphate. This phenomenon is simulated by relating mineralization to the algal phosphorus nutrient limitation. Mineralization is highest when algae are strongly phosphorus limited and is least when no limitation occurs.

The expression for mineralization rate is:

$$Kdop = Kdp + \frac{KHp}{KHp + PO_4} \bullet Kdpalg \bullet B \qquad (6\text{-}30)$$

in which:
Kdop = mineralization rate of dissolved organic phosphorus (d^{-1})
Kdp = minimum mineralization rate (d^{-1})
KHp = half-saturation concentration for algal phosphorus uptake (g P m^{-3})
PO_4 = dissolved phosphate (g P m^{-3})
Kdpalg = constant that relates mineralization to algal biomass (m^3 g^{-1} C d^{-1})

Potential effects of algal biomass and nutrient limitation on the mineralization rate are shown in Figure 6-11. When nutrient concentration greatly exceeds the half-saturation concentration for algal uptake, the rate roughly equals the minimum. Algal biomass has little influence. As nutrient becomes scarce relative to the half-saturation concentration, the rate increases. The magnitude of the increase depends on algal biomass. Factor of two to three increases are feasible.

Exponential functions (Figure 6-4) relate mineralization and hydrolysis rates to temperature.

Precipitation and Bacterial Uptake

Functions to represent precipitation and uptake by sulfide-oxidizing bacteria were added during the model calibration procedure. These functions are described in a subsequent chapter.

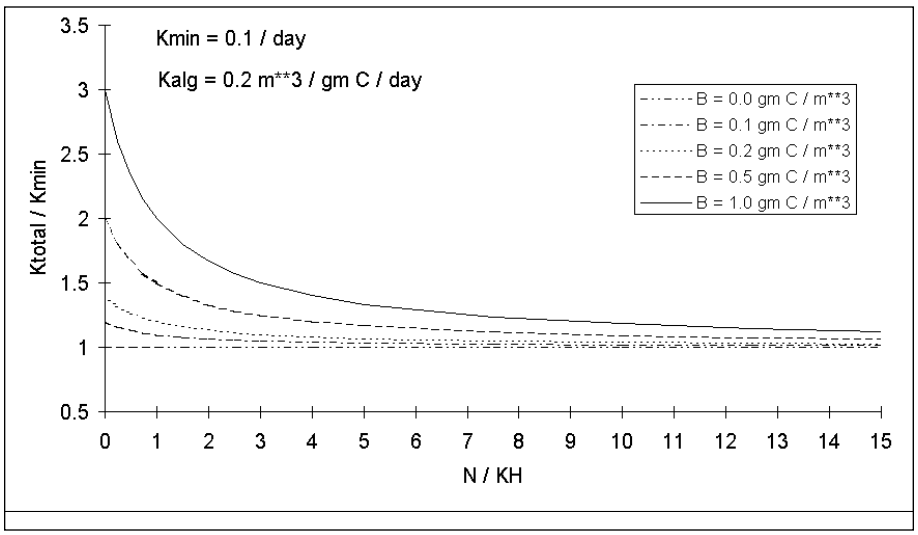

Figure 6-11. Effect of algal biomass and nutrient concentration on phosphorus mineralization.

Dissolved Phosphate

The mass-balance equation for dissolved phosphate is:

$$\frac{\delta}{\delta t} PO_4 = Kdop \bullet DOP - APC \bullet G \bullet B + APC \bullet \left[FPI \bullet BM \bullet B + FPIP \bullet PR\right] \quad (6\text{-}31)$$

in which:
FPI = fraction of algal metabolism released as dissolved phosphate ($0 \leq FPI \leq 1$)
FPIP = fraction of predation released as dissolved phosphate ($0 \leq FPIP \leq 1$)

Dissolved Organic Phosphorus

The mass balance equation for dissolved organic phosphorus is:

$$\frac{\delta}{\delta t} DOP = APC \bullet (BM \bullet B \bullet FPD + PR \bullet FPDP) + Klpop \bullet LPOP + Krpop \bullet RPOP - Kdop \bullet DOP \quad (6\text{-}32)$$

in which:
DOP = dissolved organic phosphorus (g P m^{-3})
LPOP = labile particulate organic phosphorus (g P m^{-3})
RPOP = refractory particulate organic phosphorus (g P m^{-3})
FPD = fraction of algal metabolism released as DOP ($0 < FPD < 1$)
FPDP = fraction of predation on algae released as DOP ($0 < FPDP < 1$)
Klpop = hydrolysis rate of LPOP (d^{-1})
Krpop = hydrolysis rate of RPOP (d^{-1})
Kdop = mineralization rate of DOP (d^{-1})

Labile Particulate Organic Phosphorus

The mass balance equation for labile particulate organic phosphorus is:

$$\frac{\delta}{\delta t} LPOP = APC \bullet (BM \bullet B \bullet FPL + PR \bullet FPLP) - Klpop \bullet LPOP - Wl \bullet \frac{\delta}{\delta z} LPOP \quad (6\text{-}33)$$

in which:
FPL = fraction of algal metabolism released as LPOP ($0 < FPL < 1$)
FPLP = fraction of predation on algae released as LPOP ($0 < FPLP < 1$)

Refractory Particulate Organic Phosphorus

The mass balance equation for refractory particulate organic phosphorus is:

$$\frac{\delta}{\delta t} RPOP = APC \bullet (BM \bullet B \bullet FPR + PR \bullet FPRP) - Krpop \bullet RPOP - Wr \bullet \frac{\delta}{\delta z} RPOP \quad (6\text{-}34)$$

in which:
FPR = fraction of algal metabolism released as RPOP (0 < FPR < 1)
FPRP = fraction of predation on algae released as RPOP (0 < FPRP < 1)

Nitrogen

The model nitrogen cycle (Figure 6-12) includes the following processes:

- Algal production and metabolism
- Predation
- Hydrolysis of particulate organic nitrogen
- Mineralization of dissolved organic nitrogen
- Settling
- Nitrification
- Denitrification

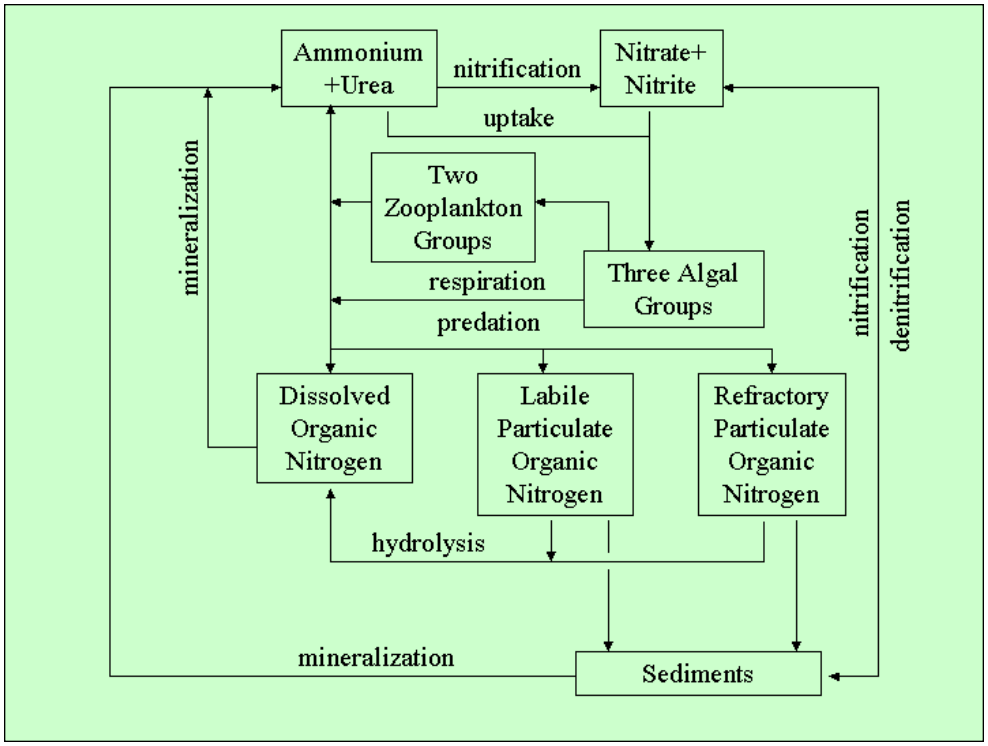

Figure 6-12. Model nitrogen cycle.

External loads provide the ultimate source of nitrogen to the system. Available nitrogen is incorporated by algae during growth and released as ammonium+urea and organic nitrogen through respiration and predation. A portion of the particulate organic nitrogen hydrolyzes to dissolved organic nitrogen. The balance settles to the sediments. Dissolved organic nitrogen is mineralized to ammonium+urea. In an oxygenated water column, a fraction of the ammonium+urea is subsequently oxidized to nitrate+nitrite through the nitrification process. In anoxic water, nitrate+nitrite is lost to nitrogen gas through denitrification. Particulate nitrogen that settles to the sediments is mineralized and recycled to the water column, primarily as ammonium+urea. Nitrate+nitrite moves in both directions across the sediment-water interface, depending on relative concentrations in the water column and sediment interstices.

Nitrification

Nitrification is a process mediated by specialized groups of autotrophic bacteria that obtain energy through the oxidation of ammonium to nitrite and oxidation of nitrite to nitrate. A simplified expression for complete nitrification (Tchobanoglous and Schroeder 1987) is:

$$NH_4^+ + 2\ O_2 \text{ - - > } NO_3^- + H_2O + 2\ H^+ \qquad (6\text{-}35)$$

The simplified stoichiometry indicates that two moles of oxygen are required to nitrify one mole of ammonium into nitrate. The simplified equation is not strictly true, however. Cell synthesis by nitrifying bacteria is accomplished by the fixation of carbon dioxide so that less than two moles of oxygen are consumed per mole ammonium utilized (Wezernak and Gannon 1968).

The kinetics of complete nitrification are modeled as a function of available ammonium, dissolved oxygen, and temperature:

$$NT = \frac{DO}{KHont + DO} \bullet \frac{NH_4 - Urea}{KHnnt + NH_4 - Urea} \bullet f(T) \bullet NTm \qquad (6\text{-}36)$$

in which:
NT = nitrification rate (g N m^{-3} d^{-1})
KHont = half-saturation constant of dissolved oxygen required for nitrification (g O_2 m^{-3})
KHnnt = half-saturation constant of NH_4 required for nitrification (g N m^{-3})
NTm = maximum nitrification rate at optimal temperature (g N m^{-3} d^{-1})

The kinetics formulation (Figure 6-13) incorporates the products of two Monod-like functions. The first function diminishes nitrification at low dissolved oxygen concentration. The second function expresses the influence of ammonium concentration on nitrification. When ammonium concentration is low, relative to KHnnt, nitrification is proportional to ammonium concentration. For NH4 = KHnnt, the reaction is approximately first-order. (The first-order decay constant NTm/KHnnt.) When ammonium concentration is large, relative to KHnnt, nitrification approaches a maximum rate. This formulation is based on a concept proposed by Tuffey et al. (1974). Nitrifying bacteria adhere to benthic or suspended sediments. When ammonium is scarce, vacant surfaces suitable for nitrifying bacteria exist. As ammonium

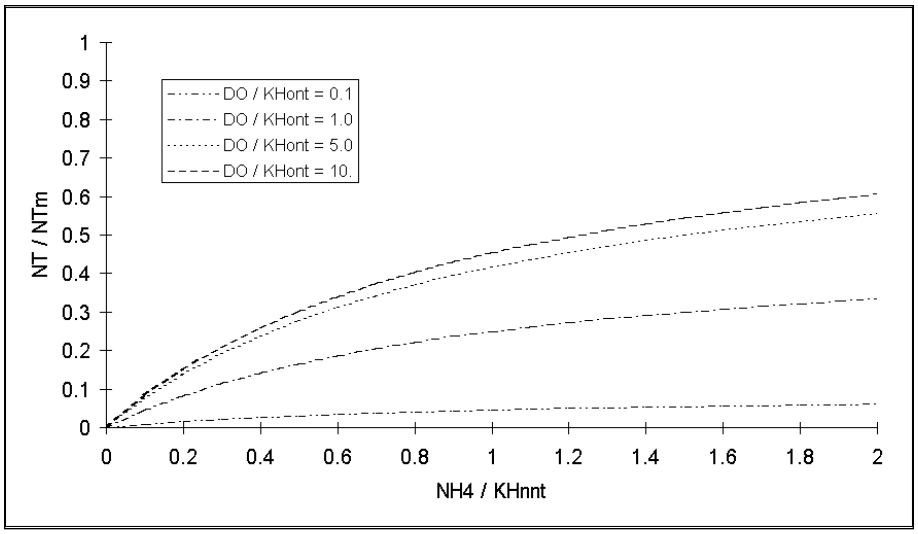

Figure 6-13. Effect of dissolved oxygen and ammonium concentration on nitrification rate.

concentration increases, bacterial biomass increases, vacant surfaces are occupied, and the rate of nitrification increases. The bacterial population attains maximum density when all surfaces suitable for bacteria are occupied. At this point, nitrification proceeds at a maximum rate independent of additional increase in ammonium concentration.

The optimal temperature for nitrification may be less than peak temperatures that occur in coastal waters. To allow for a decrease in nitrification at superoptimal temperature, the effect of temperature on nitrification is modeled in the Gaussian form of Equation 6-7.

Effect of Denitrification on Nitrate

The effect of denitrification on dissolved organic carbon has been described. Denitrification removes nitrate from the system in stoichiometric proportion to carbon removal:

$$\frac{\delta}{\delta t} NO_3 = -ANDC \bullet Denit \bullet DOC \qquad (6\text{-}37)$$

in which:

ANDC = mass nitrate-nitrogen reduced per mass dissolved organic carbon oxidized (0.933 g N g^{-1} C)

Nitrogen Mass Balance Equations

The mass-balance equation for nitrogen state variables are written by summing all previously-described sources and sinks:

Ammonium+Urea

$$\frac{\delta}{\delta t} NH_4\text{-Urea} = ANC \bullet [(BM \bullet FNI - PN \bullet P) \bullet B + PR \bullet FNIP] + Kdon \bullet DON - NT \quad (6\text{-}38)$$

in which:
FNI = fraction of algal metabolism released as NH4 ($0 \leq FNI \leq 1$)
PN = algal ammonium preference ($0 \leq PN \leq 1$)
FNIP = fraction of predation released as NH4 ($0 \leq FNIP \leq 1$)

Nitrate+Nitrite

$$\frac{\delta}{\delta t} NO_{23} = -ANC \bullet (1 - PN) \bullet P \bullet B + NT - ANDC \bullet Denit \bullet DOC \quad (6\text{-}39)$$

Dissolved Organic Nitrogen

$$\frac{\delta}{\delta t} DON = ANC \bullet (BM \bullet B \bullet FND + PR \bullet FNDP) + Klpon \bullet LPON + Krpon \bullet RPON - Kdon \bullet DON \quad (6\text{-}40)$$

in which:
DON = dissolved organic nitrogen (g N m^{-3})
LPON = labile particulate organic nitrogen (g N m^{-3})
RPON = refractory particulate organic nitrogen (g N m^{-3})
FND = fraction of algal metabolism released as DON ($0 < FND < 1$)
FNDP = fraction of predation on algae released as DON ($0 < FNDP < 1$)
Klpon = hydrolysis rate of LPON (d^{-1})
Krpon = hydrolysis rate of RPON (d^{-1})
Kdon = mineralization rate of DON (d^{-1})

Labile Particulate Organic Nitrogen

$$\frac{\delta}{\delta t} LPON = ANC \bullet (BM \bullet B \bullet FNL + PR \bullet FNLP) - Klpon \bullet LPON - Wl \bullet \frac{\delta}{\delta z} LPON \quad (6\text{-}41)$$

in which:
FNL = fraction of algal metabolism released as LPON ($0 < FNL < 1$)
FNLP = fraction of predation on algae released as LPON ($0 < FNLP < 1$)

Refractory Particulate Organic Nitrogen

$$\frac{\delta}{\delta t} RPON = ANC \bullet (BM \bullet B \bullet FPR + PR \bullet FPRN) - Krpon \bullet RPON - Wr \bullet \frac{\delta}{\delta z} RPON \quad (6\text{-}42)$$

in which:
FNR = fraction of algal metabolism released as RPON ($0 < FNR < 1$)
FNRP = fraction of predation on algae released as RPON ($0 < FNRP < 1$)

Silica

The model incorporates two siliceous state variables, dissolved silica and particulate biogenic silica. The silica cycle (Figure 6-14) is a simple one in which diatoms take up disolved silica and recycle dissolved and particulate biogenic silica through the actions of metabolism and predation. Particulate silica dissolves in the water column or settles to the bottom. A portion of the settled particulate biogenic dissolves within the sediments and returns to the water column as dissolved silica. Sources and sinks represented are:

- Diatom production and metabolism
- Predation
- Dissolution of particulate to dissolved silica
- Settling

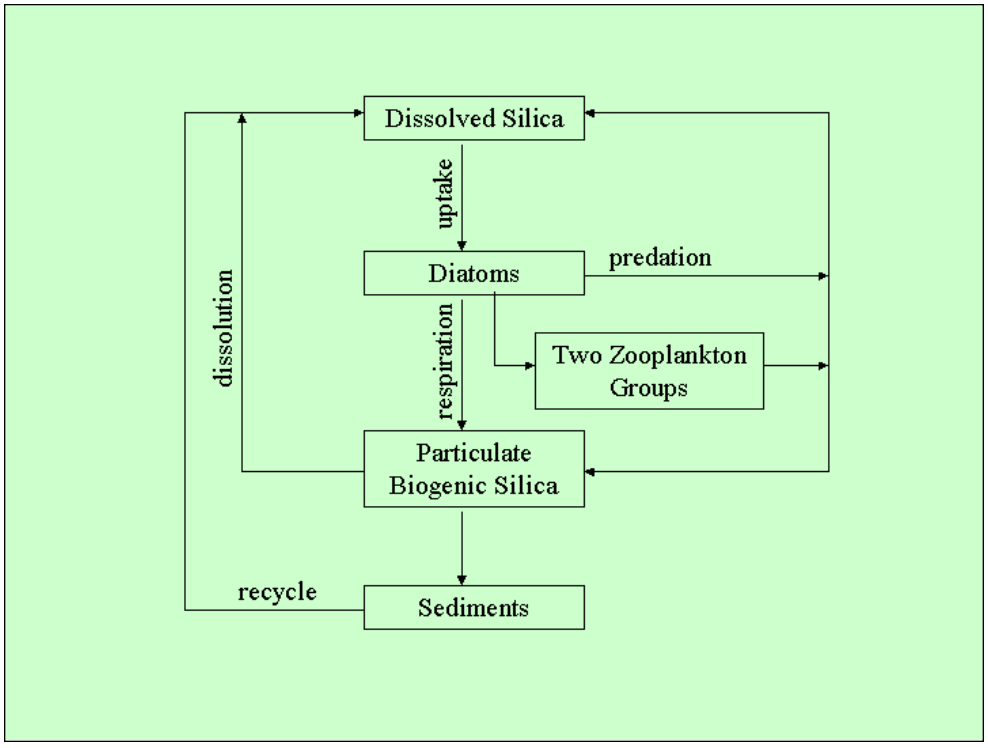

Figure 6-14. Model silica cycle.

Dissolved Silica

The kinetics equation for dissolved silica is:

$$\frac{\delta}{\delta t}\,\mathrm{Dsil} = (\mathrm{FSAP} \bullet \mathrm{PR} - \mathrm{P}) \bullet \mathrm{ASC} \bullet \mathrm{B} + \mathrm{Ksua} \bullet \mathrm{PBS} \qquad (6\text{-}43)$$

in which:
Dsil = dissolved silica (g Si m^{-3})
PBS = particulate biogenic silica concentration (g Si m^{-3})
FSAP = fraction of diatom silica made available by predation ($0 \leq \mathrm{FSAP} \leq 1$)
ASC = algal silica-to-carbon ratio (g Si g^{-1} C)
Ksua = particulate silica dissolution rate (d^{-1})

Particulate Biogenic Silica

The kinetics equation for particulate biogenic silica is:

$$\frac{\delta}{\delta t}\,\mathrm{PBS} = \left(\mathrm{BM} + (1 - \mathrm{FSAP}) \bullet \mathrm{PR}\right) \bullet \mathrm{ASC} \bullet \mathrm{B} - \mathrm{Wpbs}\,\frac{\delta}{\delta z}\,\mathrm{PBS} - \mathrm{Ksua} \bullet \mathrm{PBS} \qquad (6\text{-}44)$$

in which:
Wpbs = biogenic silica settling rate (m d^{-1})

An exponential function (Figure 6-4) describes the effect of temperature on silica dissolution.

Chemical Oxygen Demand

Chemical oxygen demand is the concentration of reduced substances that are oxidized through abiotic reactions. The source of chemical oxygen demand in saline water is sulfide released from sediments. A cycle occurs in which sulfate is reduced to sulfide in the sediments and reoxidized to sulfate in the water column. In freshwater, methane is released to the water column by the sediment model. Both sulfide and methane are quantified in units of oxygen demand and are treated with the same kinetics formulation:

$$\frac{\delta}{\delta\ t}\,\mathrm{COD} = -\frac{\mathrm{DO}}{\mathrm{KHocod} + \mathrm{DO}} \bullet \mathrm{Kcod} \bullet \mathrm{COD} \qquad (6\text{-}45)$$

in which:
COD = chemical oxygen demand concentration (g oxygen-equivalents m^{-3})
KHocod = half-saturation concentration of dissolved oxygen required for exertion of chemical oxygen demand (g O_2 m^{-3})
Kcod = oxidation rate of chemical oxygen demand (d^{-1})

An exponential function (Figure 6-5) describes the effect of temperature on exertion of chemical oxygen demand.

Dissolved Oxygen

Sources and sinks of dissolved oxygen in the water column (Figure 6-15) include:

- Algal photosynthesis
- Atmospheric reaeration
- Algal respiration
- Heterotrophic respiration
- Nitrification
- Chemical oxygen demand

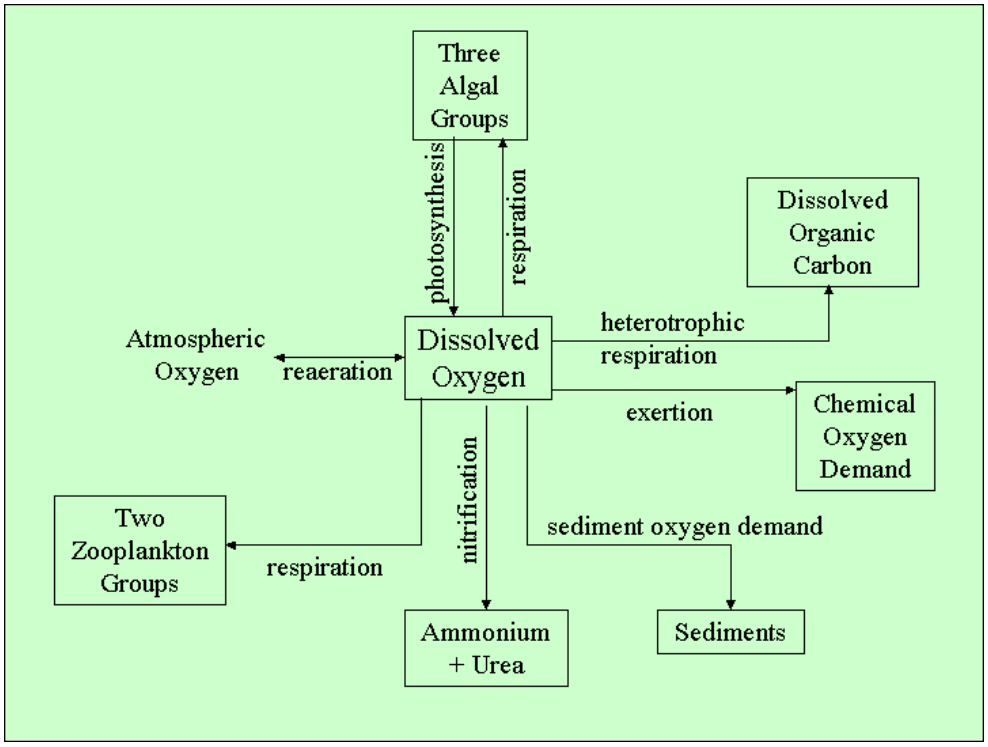

Figure 6-15. Oxygen sources and sinks.

Reaeration

The rate of reaeration is proportional to the dissolved oxygen deficit in model segments that form the air-water interface:

$$\frac{\delta}{\delta t} DO = \frac{Kr}{\Delta z} \bullet (DOs - DO) \qquad (6\text{-}46)$$

in which:
DO = dissolved oxygen concentration (g O_2 m^{-3})
Kr = reaeration coefficient (m d^{-1})
DOs = dissolved oxygen saturation concentration (g O_2 m^{-3})
Δz = model layer thickness (m)

In freeflowing streams, the reaeration coefficient depends largely on turbulence generated by bottom shear stress (O'Connor and Dobbins 1958). In lakes and coastal waters, however, wind effects may dominate the reaeration process (O'Connor 1983). For Chesapeake Bay, a relationship for wind-driven gas exchange (Hartman and Hammond 1985) was employed:

$$Kr = Arear \bullet R\nu \bullet Wms^{1.5} \qquad (6\text{-}47)$$

in which:
Arear = empirical constant (0.1)
Rν = ratio of kinematic viscosity of pure water at 20 °C to kinematic viscosity of water at specified temperature and salinity
Wms = wind speed measured at 10 m above water surface (m s^{-1})

Hartman and Hammond (1985) indicate Arear takes the value 0.157. In the present model, Arear is treated as a variable to allow for effects of wind sheltering, for differences in height of local wind observations, and for other factors.

An empirical function (Figure 6-16) that fits tabulated values of Rν is:

$$R\nu = 0.54 + 0.0233 \bullet T - 0.0020 \bullet S \qquad (6\text{-}48)$$

in which:
S = salinity (ppt)
T = temperature (°C)

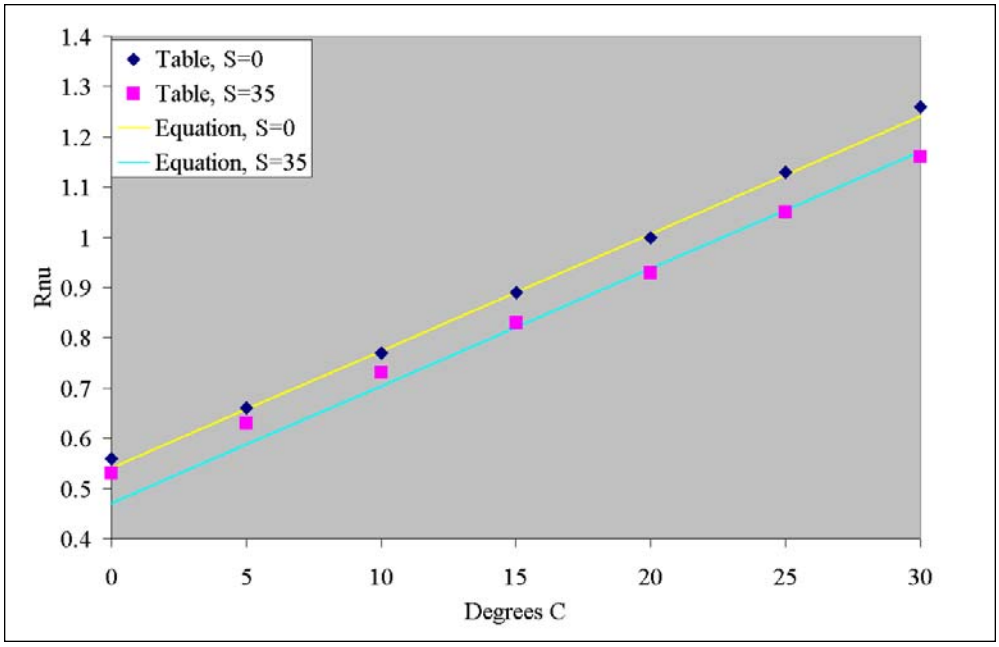

Figure 6-16. Computed and tabulated values of Rν.

Saturation dissolved oxygen concentration diminishes as temperature and salinity increase. An empirical formula that describes these effects (Genet et al. 1974) is:

$$DOs = 14.5532 - 0.38217 \bullet T + 0.0054258 \bullet T^2 - CL \bullet (1.665 \times 10^{-4} - 5.866 \times 10^{-6} \bullet T + 9.796 \times 10^{-8} \bullet T^2) \quad (6\text{-}49)$$

in which:
CL = chloride concentration (= salinity/1.80655)

Mass Balance Equation for Dissolved Oxygen

$$\frac{\delta}{\delta t} DO = AOCR \bullet \left[(1.3 - 0.3 \bullet PN) \bullet P - (1 - FCD) \bullet BM\right] \bullet B - AONT \bullet NT - \frac{DO}{KHodoc + DO} \bullet AOCR \bullet Kdoc \bullet DOC - \frac{DO}{KHocod + DO} \bullet Kcod \bullet COD + \frac{Kr}{H} \bullet (DOs - DO) \quad (6\text{-}50)$$

in which:
AOCR = oxygen-to-carbon mass ratio in production and respiration (= 2.67 g O_2 g^{-1} C)
AONT = oxygen consumed per mass ammonium nitrified (= 4.33 g O_2 g^{-1} N)

Temperature

Computation of temperature employs a conservation of internal energy equation that is analogous to the conservation of mass equation. For practical purposes, the internal energy equation can be written as a conservation of temperature equation. The only source or sink of temperature considered is exchange with the atmosphere. Atmospheric exchange is considered proportional to the temperature difference between the water surface and a theoretical equilibrium temperature (Edinger et al. 1974):

$$\frac{\delta}{\delta t} T = \frac{KT}{\rho \bullet Cp \bullet H} \bullet (Te - T) \quad (6\text{-}51)$$

in which:
T = water temperature (°C)
Te = equilibrium temperature (°C)
KT = Heat exchange coefficient (watt m^{-2} $°C^{-1}$)
Cp = specific heat of water (4200 watt s kg^{-1} $°C^{-1}$)
ρ = density of water (1000 kg m^{-3})

Inorganic (Fixed) Solids

The only kinetics transformation of fixed solids is settling:

$$\frac{\delta}{\delta t} ISS = - Wiss \bullet \frac{\delta}{\delta z} ISS \qquad (6\text{-}52)$$

in which:
ISS = fixed solids concentration (g m^{-3})
Wiss = solids settling velocity (m d^{-1})

Salinity

Salinity is modeled by the conservation of mass equation with no internal sources or sinks

Parameter Values

Model parameter evaluation is a recursive process. Parameters are selected from a range of feasible values, tested in the model, and adjusted until satisfactory agreement between predicted and observed variables is obtained. Ideally, the range of feasible values is determined by observation or experiment. For some parameters, however, no observations are available. Then, the feasible range is determined by parameter values employed in similar models or by the judgement of the modeler. A review of parameter values was included in documentation of the first application of this model (Cerco and Cole 1994). Parameters from the initial study were refined, where necessary, for the Virginia Tributary Refinements (Cerco et al. 2002) and refined again for the present model. A complete set of parameter values is provided in Table 6-2. Subsequent chapters describe derivation of parameters that were not in the original study.

Table 6-2
Parameters in Kinetics Equations

Symbol	Definition	Value	Units
AANOX	ratio of anoxic to oxic respiration	0.5	$0 \leq AANOX \leq 1$
ANC	nitrogen-to-carbon ratio of algae	0.135 (spring), 0.175 (other)	g N g^{-1} C
AOCR	dissolved oxygen-to-carbon ratio in respiration	2.67	g O_2 g^{-1} C
AONT	mass dissolved oxygen consumed per mass ammonium nitrified	4.33	g O_2 g^{-1} N
APC	algal phosphorus-to-carbon ratio	0.0175 (green), 0.0125 (other)	g P g^{-1} C
Areaer	empirical constant in reaeration equation	0.078	
ASC	algal silica-to-carbon ratio	0.0 (cyan), 0.4 (spring), 0.3 (green)	g Si g^{-1} C
BM	basal metabolic rate of algae at reference temperature Tr	0.03 (cyan), 0.01 (spring), 0.02 (green)	d^{-1}
FCD	fraction of dissolved organic carbon produced by algal metabolism	0.0	$0 \leq FCD \leq 1$
FCDP	fraction of dissolved organic carbon produced by predation	0.15	$0 \leq FCDP \leq 1$
FCL	fraction of labile particulate carbon produced by algal metabolism	0.0	$0 \leq FCL \leq 1$
FCLP	fraction of labile particulate carbon produced by predation	0.65	$0 \leq FCLP \leq 1$
FCR	fraction of refractory particulate carbon produced by algal metabolism	0.0	$0 \leq FCR \leq 1$
FCRP	fraction of refractory particulate carbon produced by predation	0.2	$0 \leq FCRP \leq 1$
FNI	fraction of inorganic nitrogen produced by algal metabolism	0.55	$0 \leq FNI \leq 1$
FNIP	fraction of inorganic nitrogen produced by predation	0.4	$0 \leq FNIP \leq 1$
FND	fraction of dissolved organic nitrogen produced by algal metabolism	0.2	$0 \leq FND \leq 1$

continued

Table 6-2 *(continued)*
Parameters in Kinetics Equations

Symbol	Definition	Value	Units
FNDP	fraction of dissolved organic nitrogen produced by predation	0.2	$0 \leq FNDP \leq 1$
FNL	fraction of labile particulate nitrogen produced by algal metabolism	0.2	$0 \leq FNL \leq 1$
FNLP	fraction of labile particulate nitrogen produced by predation	0.25	$0 \leq FNLP \leq 1$
FNR	fraction of refractory particulate nitrogen produced by algal metabolism	0.05	$0 \leq FNR \leq 1$
FNRP	fraction of refractory particulate nitrogen produced by predation	0.15	$0 \leq FNRP \leq 1$
FPD	fraction of dissolved organic phosphorus produced by algal metabolism	0.25	$0 \leq FPD \leq 1$
FPDP	fraction of dissolved organic phosphorus produced by predation	0.4	$0 \leq FPDP \leq 1$
FPI	fraction of dissolved inorganic phosphorus produced by algal metabolism	0.5	$0 \leq FPI \leq 1$
FPIP	fraction of dissolved inorganic phosphorus produced by predation	0.75	$0 \leq FPIP \leq 1$
FPL	fraction of labile particulate phosphorus produced by algal metabolism	0.0	$0 \leq FPL \leq 1$
FPLP	fraction of labile particulate phosphorus produced by predation	0.07	$0 \leq FPLP \leq 1$
FPR	fraction of refractory particulate phosphorus produced by algal metabolism	0.0	$0 \leq FPR \leq 1$
FPRP	fraction of refractory particulate phosphorus produced by predation	0.03	$0 \leq FPRP \leq 1$
FSAP	fraction of dissolved silica produced by predation	0.5	$0 \leq FSAP \leq 1$
Kcod	oxidation rate of chemical oxygen demand	20	d^{-1}
Kdoc	dissolved organic carbon respiration rate	0.011 to 0.075	d^{-1}
Kdon	dissolved organic nitrogen mineralization rate	0.025	d^{-1}
Kdp	minimum mineralization rate of dissolved organic phosphorus	0.15	d^{-1}
Kdpalg	constant that relates mineralization rate to algal biomass	0.4	$m^3\ g^{-1}\ C\ d^{-1}$
KHn	half-saturation concentration for nitrogen uptake by algae	0.02 (cyan), 0.025 (other)	$g\ N\ m^{-3}$

(continued)

Table 6-2 *(continued)*
Parameters in Kinetics Equations

Symbol	Definition	Value	Units
KHndn	half-saturation concentration of nitrate required for denitrification	0.1	g N m^{-3}
KHnnt	half-saturation concentration of NH_4 required for nitrification	1.0	g N m^{-3}
KHocod	half-saturation concentration of dissolved oxygen required for exertion of COD	0.5	g O_2 m^{-3}
KHodoc	half-saturation concentration of dissolved oxygen required for oxic respiration	0.5	g O_2 m^{-3}
KHont	half-saturation concentration of dissolved oxygen required for nitrification	1.0	g O_2 m^{-3}
KHp	half-saturation concentration for phosphorus uptake by algae	0.0025	g P m^{-3}
KHs	half-saturation concentration for silica uptake by algae	0.0 (cyan), 0.03 (spring), 0.01 (green)	g Si m^{-3}
KHst	salinity at which algal mortality is half maximum value	0.5 (cyan), 2.0 (spring)	ppt
Klpoc	labile particulate organic carbon dissolution rate	0.02 to 0.15	d^{-1}
Klpon	labile particulate organic nitrogen hydrolysis rate	0.12	d^{-1}
Klpop	labile particulate organic phosphorus hydrolysis rate	0.24	d^{-1}
Krpoc	refractory particulate organic carbon dissolution rate	0.005 to 0.01	d^{-1}
Krpon	refractory particulate organic nitrogen hydrolysis rate	0.005	d^{-1}
Krpop	refractory particulate organic phosphorus hydrolysis rate	0.01	d^{-1}
Ksua	biogenic silica dissolution rate	0.1	d^{-1}
KTb	effect of temperature on basal metabolism of algae	0.032	$^oC^{-1}$
KTcod	effect of temperature on exertion of chemical oxygen demand	0.041	d^{-1}
KTg1	effect of temperature below Tm on growth of algae	0.005 (cyan), 0.0018 (spring), 0.0035 (green)	$^oC^{-2}$

continued

Table 6-2 *(continued)*
Parameters in Kinetics Equations

Symbol	Definition	Value	Units
KTg2	effect of temperature above Tm on growth of algae	0.004 (cyan), 0.006 (spring), 0.0 (green)	$^{o}C^{-2}$
KThdr	effect of temperature on hydrolysis rates	0.032	$^{o}C^{-1}$
KTmnl	effect of temperature on mineralization rates	0.032	$^{o}C^{-1}$
KTnt1	effect of temperature below Tmnt on nitrification	0.003	$^{o}C^{-2}$
KTnt2	effect of temperature above Tmnt on nitrification	0.003	$^{o}C^{-2}$
KTsua	effect of temperature on biogenic silica dissolution	0.092	$^{o}C^{-1}$
NTm	maximum nitrification rate at optimal temperature	0.1 to 0.5	g N m^{-3} d^{-1}
Phtl	predation rate on algae	0.0 (cyan), 0.1 to 0.2 (spring), 0.5 to 2 (green)	m^3 g^{-1} C d^{-1}
Pm^B	maximum photosynthetic rate	100 (cyan), 300 (spring), 350 (green)	g C g^{-1} Chl d^{-1}
Presp	photo-respiration fraction	0.25	$0 \leq Presp \leq 1$
STF	salinity toxicity factor	0.3 (cyan), 0.1 (spring)	d^{-1}
Topt	optimal temperature for growth of algae	29 (cyan), 16 (spring), 25 (green)	^{o}C
Tmnt	optimal temperature for nitrification	30	^{o}C
Tr	reference temperature for metabolism	20	^{o}C
Trhdr	reference temperature for hydrolysis	20	^{o}C
Trmnl	reference temperature for mineralization	20	^{o}C
Trsua	reference temperature for biogenic silica dissolution	20	^{o}C
Wa	algal settling rate	0.0 (cyan), 0.1 (other)	m d^{-1}

continued

Table 6-2 *(continued)*
Parameters in Kinetics Equations

Symbol	Definition	Value	Units
Wl	settling velocity of labile particles	0.1	m d^{-1}
Wr	settling velocity of refractory particles	0.1	m d^{-1}
Wiss	settling velocity of fixed solids	1 to 4	m d^{-1}
Wpbs	settling velocity of biogenic silica	0.1	m d^{-1}
α	initial slope of production vs. irradiance relationship	3.15 (cyan), 8.0 (other)	g C g^{-1} Chl (E m^{-2})$^{-1}$

References

Ammerman, J., and Azam, F. (1985). "Bacterial 5'-nucleodase in aquatic ecosystems: a novel mechanism of phosphorus regeneration," Science, 227, 1338-1340.

Boni, L., Carpene, E., Wynne, D., and Reti, M. (1989). "Alkaline phosphatase activity in Protogonyaulax Tamarensis," Journal of plankton research, 11, 879-885.

Bunch, B., Cerco, C., Dortch, M., Johnson, B., and Kim, K. (2000). "Hydrodynamic and water quality model study of San Juan Bay and Estuary," ERDC TR-00-1, U.S. Army Engineer Research and Development Center, Vicksburg MS.

Cerco, C., and Cole, T. (1994). "Three-dimensional eutrophication model of Chesapeake Bay," Technical Report EL-94-4, US Army Engineer Waterways Experiment Station, Vicksburg, MS.

Cerco, C., Bunch, B., Cialone, M., and Wang, H. (1994). "Hydrodynamic and eutrophication model study of Indian River and Rehoboth Bay, Delaware," Technical Report EL-94-5, US Army Engineer Waterways Experiment Station, Vicksburg, MS.

Cerco, C., and Bunch, B. (1997). "Passaic River tunnel diversion model study, Report 5, water quality modeling," Technical Report HL-96-2, US Army Engineer Waterways Experiment Station, Vicksburg, MS.

Cerco, C., Johnson, B., and Wang, H. (2002). "Tributary refinements to the Chesapeake Bay model," ERDC TR-02-4, US Army Engineer Research and Development Center, Vicksburg, MS.

Chrost, R., and Overbeck, J. (1987). "Kinetics of alkaline phosphatase activity and phosphorus availability for phytoplankton and bacterioplankton in Lake Plubsee (north German eutrophic lake)," Microbial Ecology, 13, 229-248.

Edinger, J., Brady, D., and Geyer, J. (1974). "Heat exchange and transport in the environment," Report 14, Department of Geography and Environmental Engineering, Johns Hopkins University, Baltimore, MD.

Genet, L., Smith, D., and Sonnen, M. (1974). "Computer program documentation for the Dynamic Estuary Model," US Environmental Protection Agency, Systems Development Branch, Washington, DC.

Hartman, B., and Hammond, D. (1985). "Gas exchange in San Francisco Bay," *Hydrobiologia* 129, 59-68.

HydroQual (2000). “Development of a suspension feeding and deposit feeding benthos model for Chesapeake Bay,” Project USCE0410, prepared for US Army Engineer Research and Development Center, Vicksburg MS.

Jassby, A., and Platt, T. (1976). “Mathematical formulation of the relationship between photosynthesis and light for phytoplankton,” *Limnology and Oceanography* 21, 540-547.

Leonard, B. (1979). “A stable and accurate convection modelling procedure based on quadratic upstream interpolation,” Computer Methods in Applied Mechanics and Engineering, 19, 59-98.

Matavulj, M., and Flint, K. (1987). “A model for acid and alkaline phosphatase activity in a small pond,” Microbial Ecology, 13, 141-158.

Monod, J. (1949). “The growth of bacterial cultures,” *Annual Review of Microbiology* 3, 371-394.

Morel, F. (1983). Principles of Aquatic Chemistry, John Wiley and Sons, New York, NY, 150.

O’Connor, D., and Dobbins, W. (1958). “Mechanisms of reaeration in natural streams,” Transactions of the American Society of Civil Engineers, 123, 641-666.

O’Connor, D. (1983). “Wind effects on gas-liquid transfer coefficients,” Journal of the Environmental Engineering Division, 190, 731-752.

Parsons, T., Takahashi, M., and Hargrave, B. (1984). *Biological oceanographic processes*. 3rd ed., Pergamon Press, Oxford.

Sellner, K., Lacoutre, R., and Parrish, C. (1988). “Effects of increasing salinity on a Cyanobacteria bloom in the Potomac River Estuary,” Journal of Plankton Research, 10, 49-61.

Stumm, W., and Morgan, J. (1981). *Aquatic chemistry.* 2nd ed., Wiley- Interscience, New York.

Thomann, R., and Fitzpatrick, J. (1982). “Calibration and verification of a mathematical model of the eutrophication of the Potomac Estuary,” HydroQual Inc., Mahwah, NJ.

Tchobanoglous, G., and Schroeder, E. (1987). Water quality, Addison Wesley, Reading, MA.

Tuffey, T., Hunter, J., and Matulewich, V. (1974). “Zones of nitrification”, Water Resources Bulletin, 10, 555-564.

Wezernak, C., and Gannon, J. (1968). “Evaluation of nitrification in streams,” Journal of the Sanitary Engineering Division, 94(SA5), 883-895.

Introduction to Calibration 7

The Monitoring Data Base

The water quality model was applied to a ten-year time period, 1985-1994. The monitoring data base maintained by the Chesapeake Bay Program (Chesapeake Bay Program 1989, 1993) was the principal source of data for model calibration. A summary of the monitoring program, as it operated from 1985 to 1994, is provided below. Details of the data base and information on the current program may be found at the Chesapeake Bay Program web site http://www.chesapeakebay.net/data/index.htm.

Observations were collected at 49 stations in the bay and 89 stations in major embayments and tributaries (Figure 7-1). Sampling was conducted once or twice per month with more frequent sampling from March through October. Samples were collected during daylight hours with no attempt to coincide with tide stage or flow. Sampling periods were designated as "cruises." Under ideal circumstances, cruises were completed in two to three days. Inclement weather or equipment failures occasionally produced cruises as long as two weeks.

At each station, salinity, temperature, and dissolved oxygen were measured in situ at one- or two-meter intervals. Samples were collected one meter below the surface and one meter above the bottom for laboratory analyses. At stations showing significant salinity stratification, additional samples were collected above and below the pycnocline. Analyses relevant to this study are listed in Table 7-1. The listed parameters are either analyzed directly or derived from direct analyses.

The major portion of the data base was obtained from the sponsor, in SAS transport format, in June 1996. Observations from 1991 through 1995 were updated in a second transmission from the sponsor in June 1998. We discovered that observations in the Potomac River and Maryland eastern shore were not complete. These were provided by Maryland Department of Environment in March 1999. Additional observations were obtained from multiple sources. Descriptions are provided as these observations are cited.

Figure 7-1. Chesapeake Bay Program monitoring stations.

Table 7-1
Direct or Derived Laboratory Analyses

Grouping	Parameter	Code
Phosphorus	Total Phosphorus	TP
	Total Dissolved Phosphorus	TDP
	Particulate Phosphorus	PHOSP
	Orthophosphate	PO4F
	Dissolved Inorganic Phosphorus	DIP
	Dissolve Organic Phosphorus	DOP
Nitrogen	Total Nitrogen	TN
	Total Dissolved Nitrogen	TDN
	Particulate Organic Nitrogen	PON
	Total Kjeldahl Nitrogen, Whole/Filtered	TKNW, TKNF
	Nitrate + Nitrite	NO23
	Ammonium	NH4F
	Dissolved Inorganic Nitrogen	DIN
	Dissolved Organic Nitrogen	DON
	Total Organic Nitrogen	TON
Carbon	Total Organic Carbon	TOC
	Dissolved Organic Carbon	DOC
	Particulate Organic Carbon	POC
Other	Silica, filtered	SI
	Total Suspended Solids	TSS
	Chlorophyll >a=	CHLA

Comparison with the Model

Time Series

Time series comparisons of computations and observations were produced at 42 locations (Figure 7-2). These were selected to provide coverage throughout the system. At least one station was selected within each of the Chesapeake Bay Program Segments (CBPS) represented on the grid (Figure 7-3). This segmentation scheme was based on salinity and circulation patterns. Within the model code, daily-average concentrations were derived from computations at discrete time steps (15 minutes). These were compared to individual observations, at surface and bottom, for parameters listed in Table 7-2.

We wished to provide comparisons for the model cell corresponding to location and depth at which samples were collected. For the surface sample, locating the cell was straightforward. For the bottom sample, finding the corresponding model cell was more difficult. The depth of the model grid usually represented the average depth beneath the area covered by the surface cell. Consequently, grid depth was less than the maximum prototype depth within the surface cell area. The monitoring program usually sampled at the maximum local depth, often within a channel or deep hole. Depth of the bottom sample sometimes exceeded the maximum depth of the model grid. In the event the sample depth exceeded the grid depth, the vertical samples were interpolated into one-meter depth increments and the model was matched to the corresponding interpolated data. For the few cases in which grid depth exceeded the sample depth, the bottom sample was compared to the bottom cell. No extrapolation was employed.

Time series comparisons of selected stations and parameters are provided in the text of this report. Complete results are provided on CD-ROM that accompanies printed copies of the report and are archived at the Chesapeake Bay Program Office.

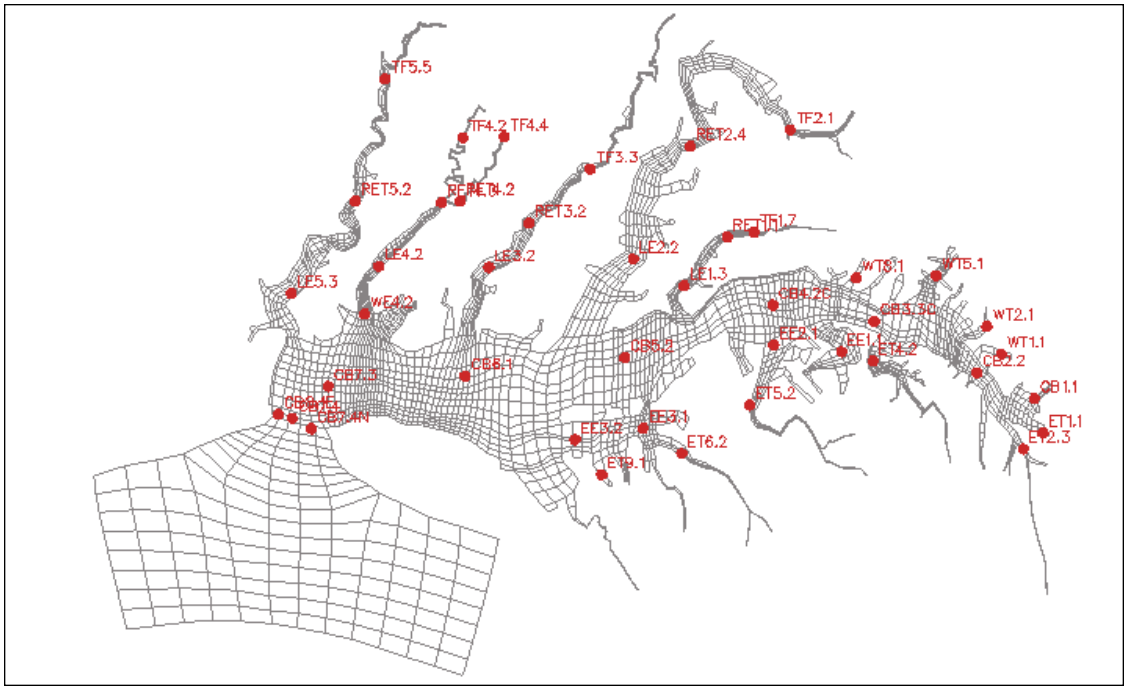

Figure 7-2. Locations for time series comparisons.

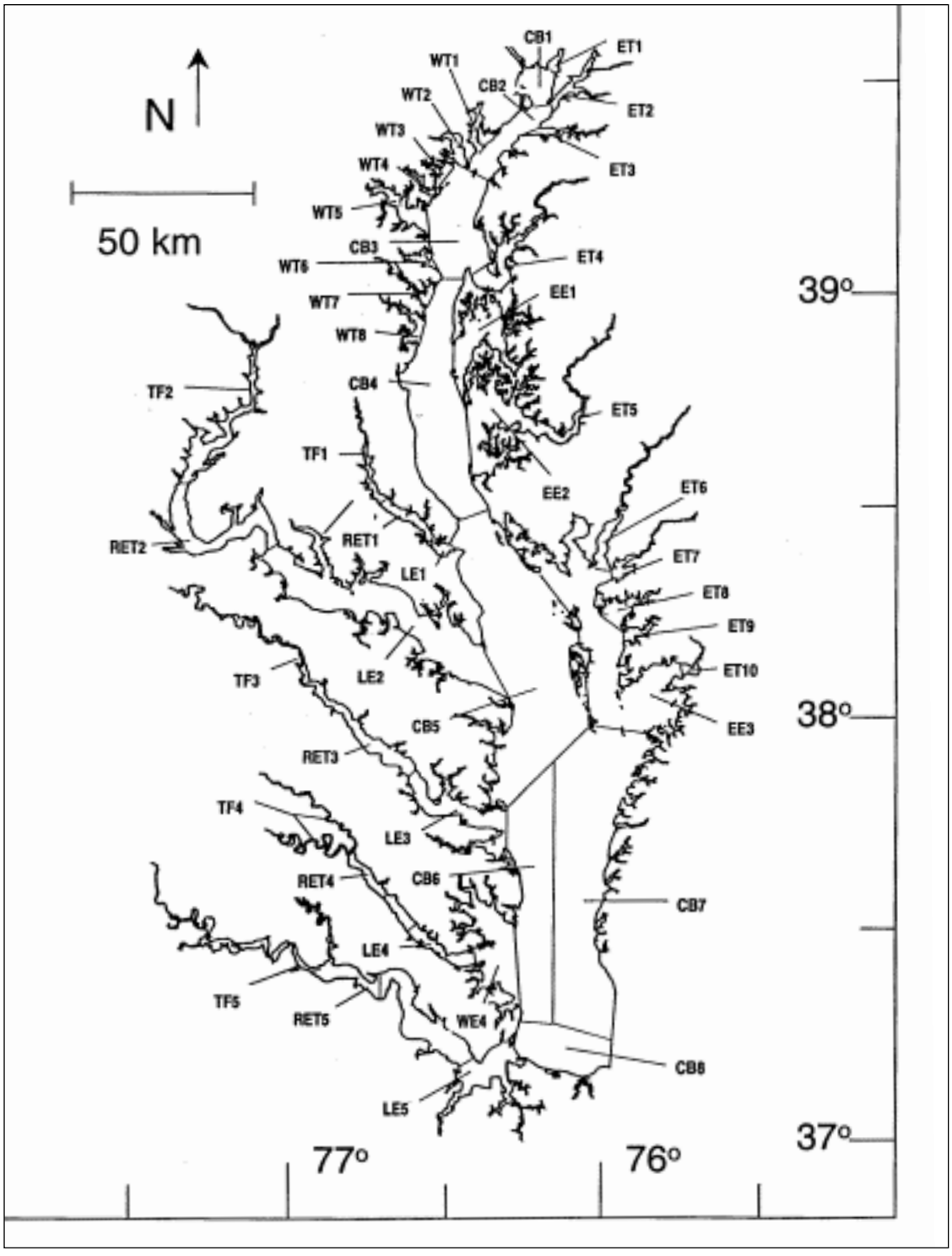

Figure 7-3. Chesapeake Bay Program Segments.

Table 7-2
Constituents in Model-Data Comparisons

Constituent	Time-Series	Longitudinal	Vertical
Chlorophyll >a=	X	X	
Dissolved Inorganic Nitrogen	X		
Dissolved Inorganic Phosphorus	X	X	
Dissolved Organic Nitrogen	X		
Dissolved Organic Phosphorus	X		
Dissolved Oxygen	X	X	X
Light Attenuation	X	X	
Ammonium	X	X	
Nitrate+Nitrite	X	X	
Particulate Organic Carbon	X	X	
Particulate Organic Nitrogen	X		
Particulate Phosphorus	X		
Salinity	X	X	X
Total Nitrogen	X	X	
Total Organic Carbon	X	X	
Total Phosphorus	X	X	
Total Suspended Solids	X	X	
Temperature	X		X
Dissolved Silica	X	X	

Longitudinal Comparisons

The spatial distributions of observed and computed properties were compared in a series of plots along the axes of the bay and major tributaries (Figures 7-4, 7-5). The calibration period encompassed nearly 200 cruises. Reducing this number of surveys into a manageable volume of comparisons required selection and aggregation. Three years were selected for comparisons: 1985, 1990, and 1993. The year 1985 was a low-flow year although the western tributaries were impacted by an enormous flood event in November. Flows in 1990 were characterized as average while major spring runoff occurred in 1993.

Model results and observations were averaged into four seasons:

- Winter—December through February
- Spring—March through May
- Summer—June through August
- Fall—September through November

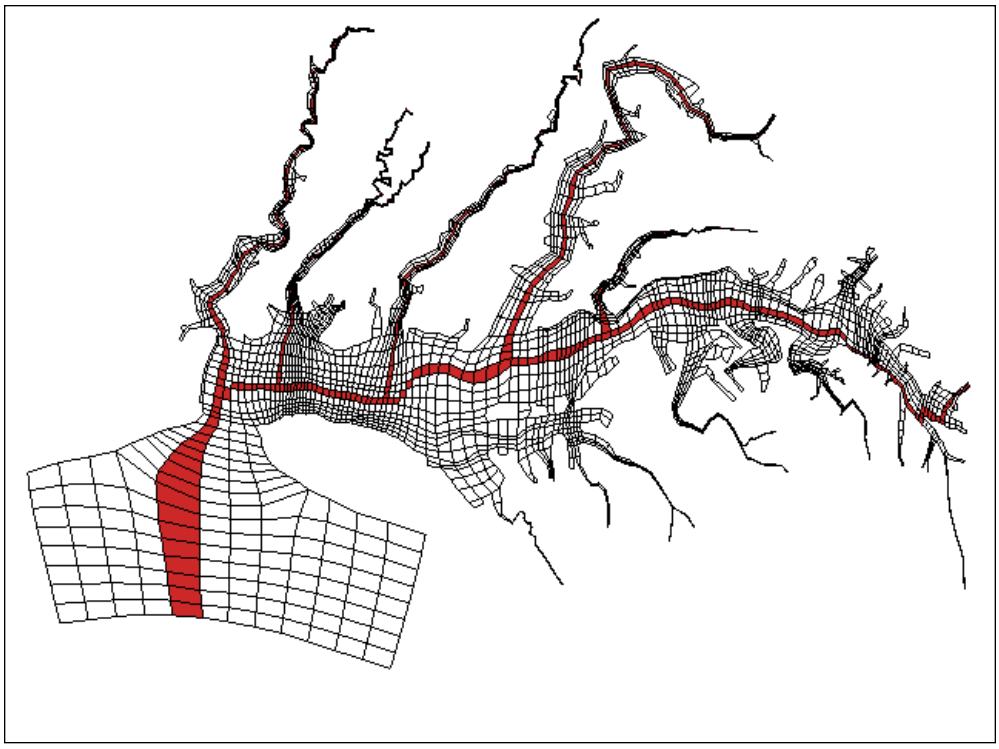

Figure 7-4. Longitudinal transects in the bay and major tributaries.

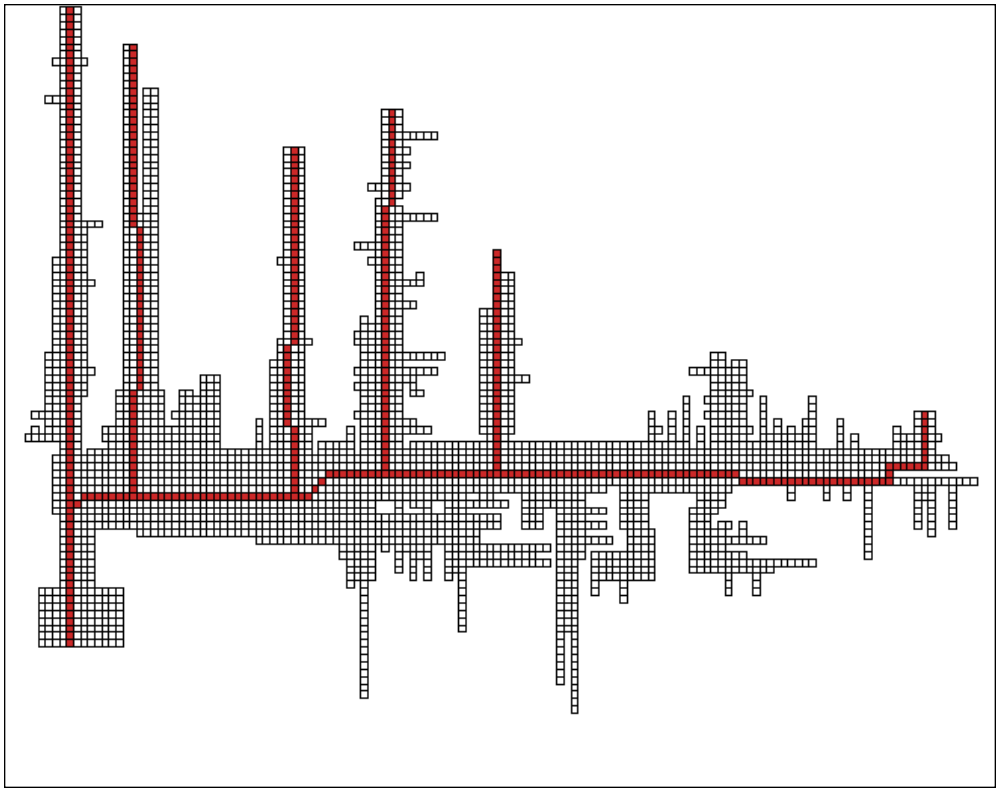

Figure 7-5. Longitudinal transects in the bay and major tributaries on transformed grid.

Conventional arithmetic means were calculated for the observations. Model results were subjected to a process denoted as “cruise averaging.” Within each season, model results were considered only during intervals coinciding with sample cruises. Cruise averaging diminished discrepancies between model and observations attributed to consideration of model results for periods when no data was collected. Daily averages of model results were computed within the model code. Cruise averaging was completed in a postprocessor. The postprocessor also extracted the maximum and minimum computed daily averages.

The mean and range of the observations, at surface and bottom, were compared to the cruise average and range of daily-average model results. A parameter list is presented in Table 7-2. The longitudinal axes largely followed the maximum depths represented on the model grid. Only stations located exactly on the transect (Figures 7-6 to 7-11) were considered for comparison with the model. In the event the depth of the bottom sample and grid depth did not coincide, observations were treated as described for the time series.

Longitudinal comparisons of selected stations and parameters are provided in the text of this report. Complete results are provided on CD-ROM that accompanies printed copies of the report and are archived at the Chesapeake Bay Program Office.

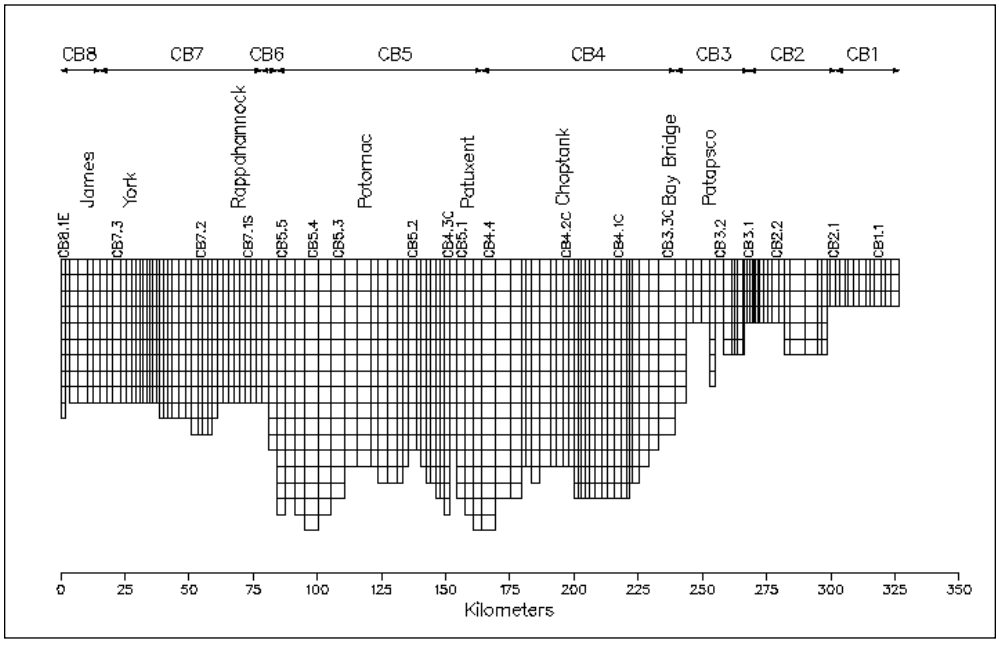

Figure 7-6. Elevation view of Chesapeake Bay transect showing kilometers from mouth, sample stations, grid bathymetry, and Chesapeake Bay Program Segments.

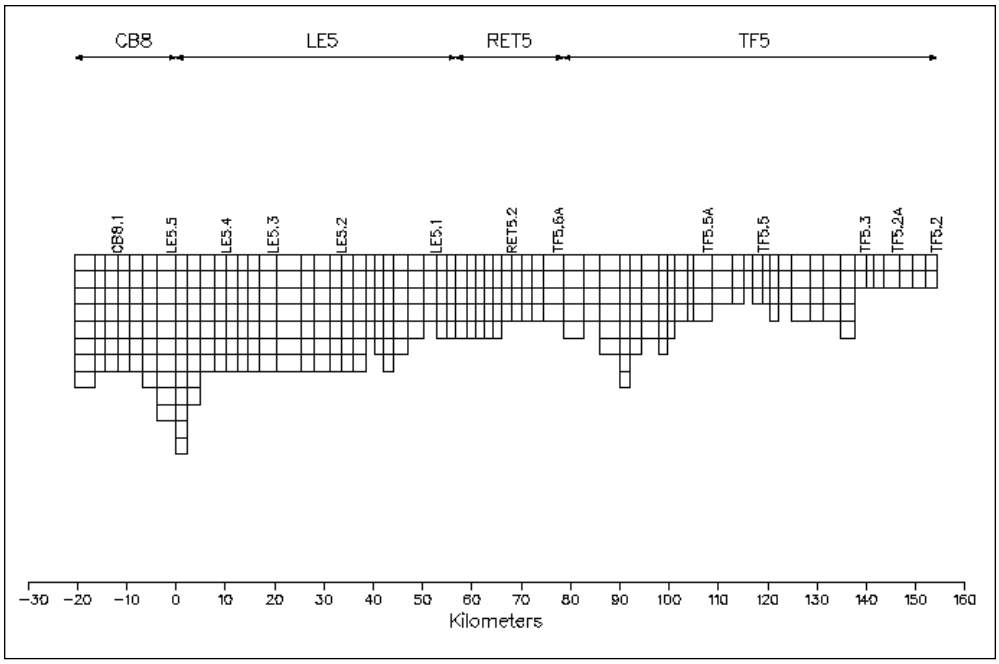

Figure 7-7. Elevation view of James River transect showing kilometers from mouth, sample stations, grid bathymetry, and Chesapeake Bay Program Segments.

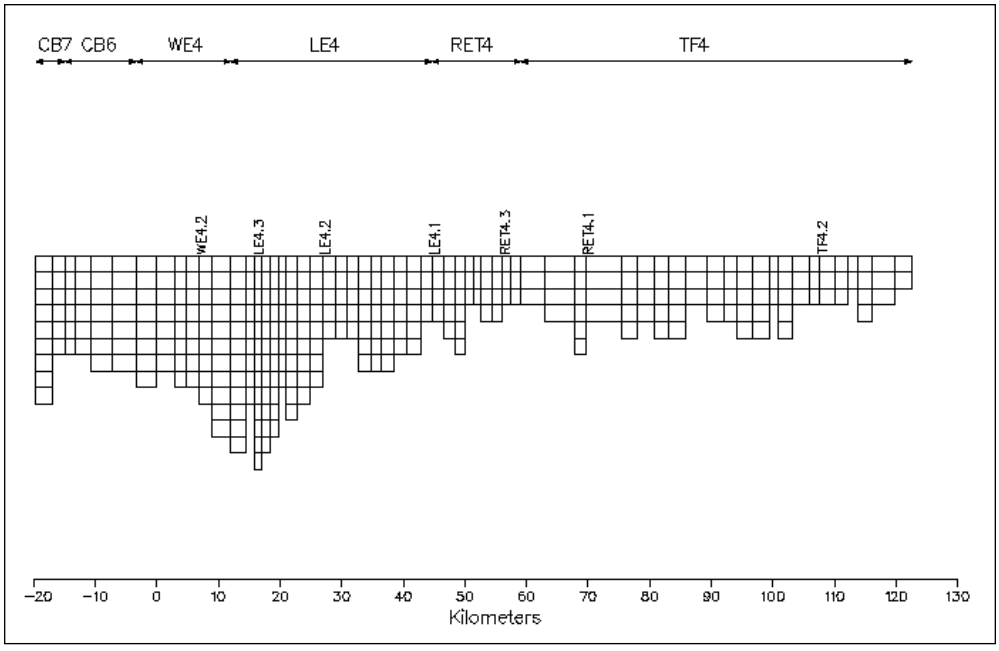

Figure 7-8. Elevation view of York River transect showing kilometers from mouth, sample stations, grid bathymetry, and Chesapeake Bay Program Segments.

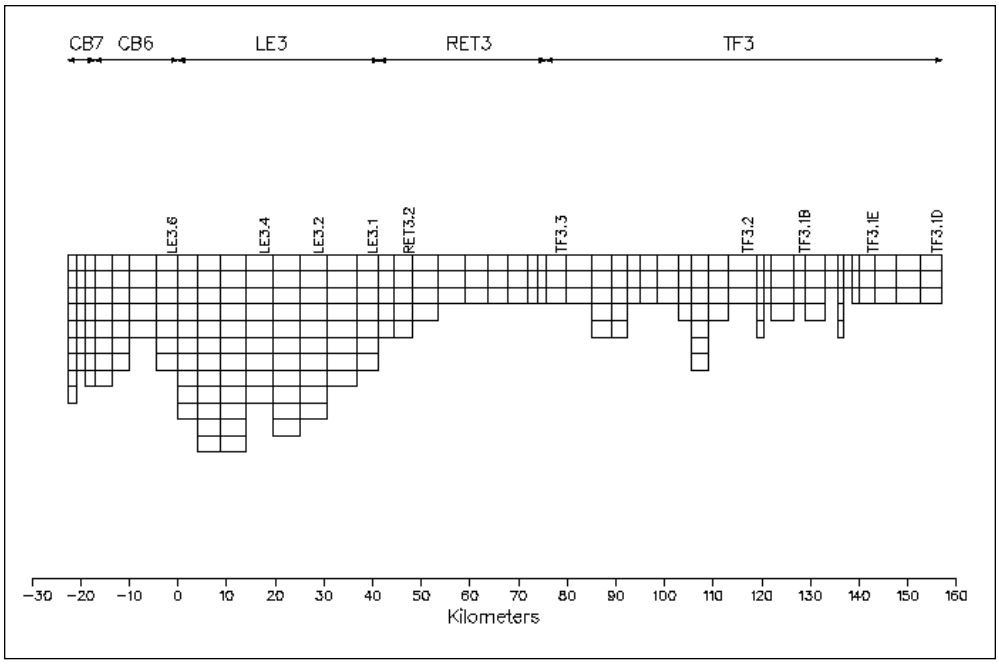

Figure 7-9. Elevation view of Rappahannock River transect showing kilometers from mouth, sample stations, grid bathymetry, and Chesapeake Bay Program.

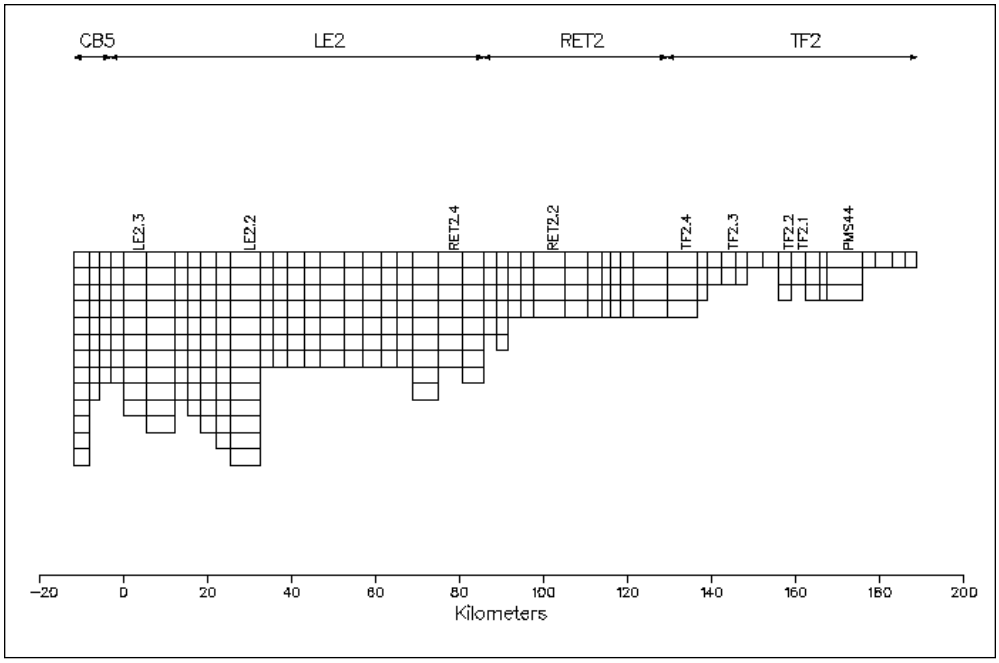

Figure 7-10. Elevation view of Potomac River transect showing kilometers from mouth, sample stations, grid bathymetry, and Chesapeake Bay Program Segments.

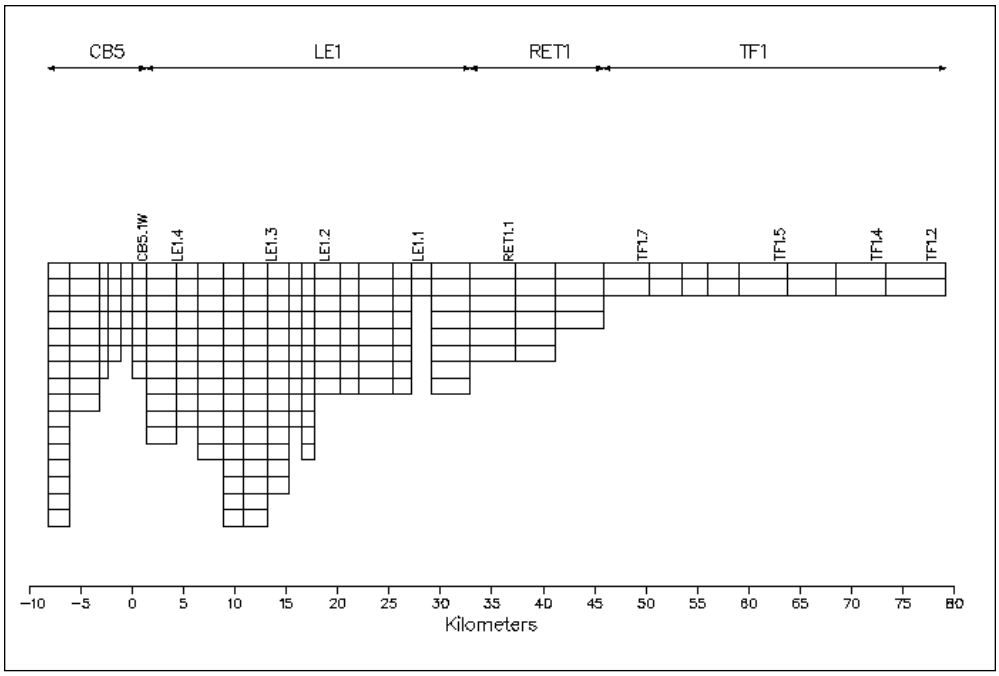

Figure 7-11. Elevation view of Patuxent River transect showing kilometers from mouth, sample stations, grid bathymetry, and Chesapeake Bay Program Segments.

Vertical Comparisons

The vertical distributions of observed and computed properties were compared at selected stations in the bay and major tributaries. As with the longitudinal comparisons, selection and aggregation were required to produce a manageable volume of information. Comparisons were completed for three years and were subjected to seasonal averaging as previously described. Parameters were limited to the three for which detailed vertical observations were available: temperature, salinity, and dissolved oxygen.

Examination of the seasonally-averaged vertical data frequently showed a break or jump near the bottom. The break was an artifact of the sampling program. Due to varying topography and sampling methods, the bottom was not always found at the same depth. Consequently, averages computed near the bottom sometimes contained fewer samples than averages closer to the surface.

Vertical comparisons of selected stations and parameters are provided in the text of this report. Complete results are provided on CD-ROM that accompanies printed copies of the report and are archived at the Chesapeake Bay Program Office.

References

Chesapeake Bay Program. (1989). “Chesapeake Bay Basin Monitoring Program Atlas,” CBP/TRS 34/89, US Environmental Protection Agency, Chesapeake Bay Liaison Office, Annapolis MD.

Chesapeake Bay Program. (1993). “Guide to Using Chesapeake Bay Program Water Quality Monitoring Data,” CBP/TRS 78/92, Annapolis MD.

The Zooplankton Model 8

Introduction

Many of the earliest eutrophication models (e.g. DiToro et al. 1971; DiToro and Matystik 1980) included one or more zooplankton groups as state variables. Later efforts omitted zooplankton (e.g. Thomann and Fitzpatrick 1982). At present, eutrophication models sans zooplankton are widely accepted (e.g. Cerco and Cole 1993). The reasons for dropping zooplankton are unclear. Lack of observations and difficulty in calibration are two possibilities.

The present chapter details the formulation of zooplankton kinetics in the Chesapeake Bay Environmental Model Package. Zooplankton were incorporated into the model during the tributary refinements phase (Cerco, Johnson, and Wang 2002; Cerco and Meyers 2000). The primary reason was to advance the model into the realm of living resources. Although zooplankton have no commercial value, they are a prime food source for commercially-valuable finfish. Addition of zooplankton to the model framework was a first step towards modeling the effects of eutrophication management on top-level predators. A secondary goal of modeling zooplankton was to improve model accuracy in the computation of algal biomass and other parameters.

Model Conceptualization

A conceptual food web for the bay exhibits seven components (Figure 8-1). At the base of the food web are the phytoplankton. The phytoplankton are preyed upon by zooplankton and by herbivorous finfish (in Chesapeake Bay, menhaden). Dissolved organic carbon (DOC) secreted by plankton and produced from detritus is consumed by heterotrophic bacteria which, along with phytoplankton, form a food source for the microzooplankton. Microzooplankton are one of the prey groups for the mesozooplankton which also consume phytoplankton and detritus. The mesozooplankton are a primary food source for carnivorous finfish (in Chesapeake Bay, anchovy).

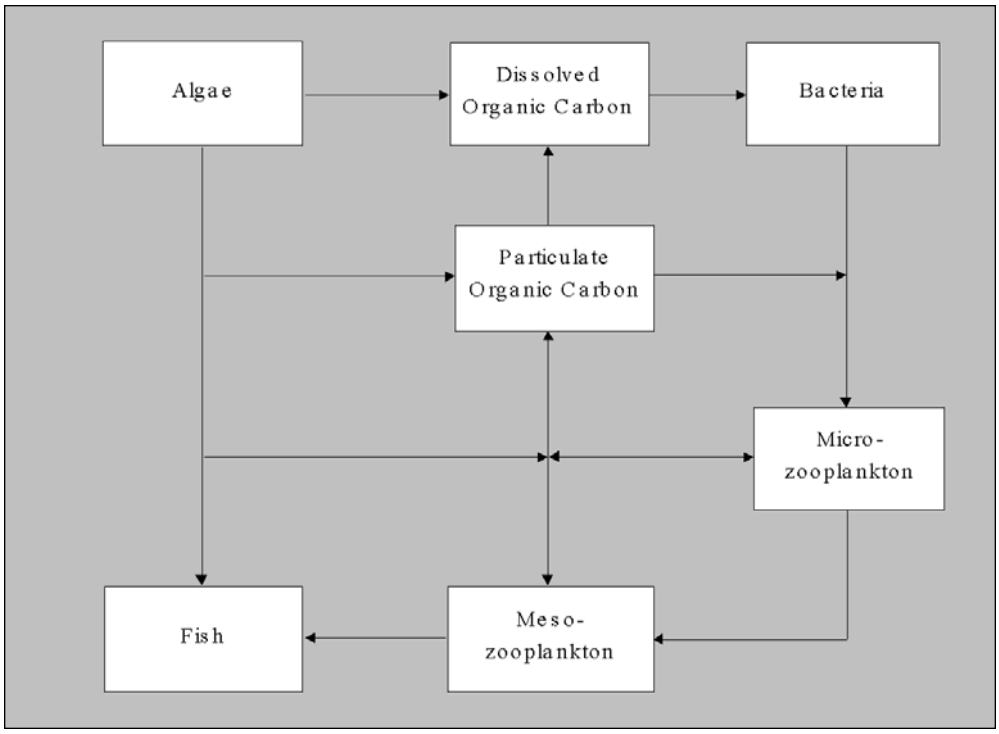

Figure 8-1. The conceptual carbon cycle.

The art in modeling is to determine which of the food web components are to be modeled and to describe the carbon and nutrient transfers between the groups. As the primary producers, the phytoplankton must be modeled. The mesozooplankton are the primary food source for the bay anchovies. Modeling the prey biomass and mass flows into the finfish are among the primary goals of the introduction of living resources into the model suite, so mesozooplankton must be modeled. The microzooplankton have no commercial value nor are they a primary food source for the finfish. They are an important prey for the mesozooplankton, however. More importantly, they can be significant predators on the phytoplankton. Omission of the microzooplankton requires a hybrid predation term on the phytoplankton in which predation by mesozooplankton is computed but predation by microzoo-plankton is specified. In view of the problems associated with a formulation of this sort it is easier to include microzooplankton in the model than it is to omit them. Heterotrophic bacteria are crucial components of the ecosystem. Their role in water-column respiration and in nutrient recycling is conventionally represented as first-order organic matter decay processes. These representations are adequate and, in view of the complication of modeling both bacterial biomass and activity, can be left unchanged. Any problem with omitting bacteria lies not with inadequate repre-sentation of bacterial processes but with omission of a microzooplankton food source. For the present, the omission is circumvented by allowing microzoo-plankton to graze directly on DOC. The predation on mesozooplankton by finfish is handled as a predation term which closes the mesozooplankton equation.

Model Carbon Cycle

Once the conceptual model has been formulated, the new state variables can be added to the previously-established (Cerco and Cole 1994) model carbon cycle. The resulting cycle (Figure 8-2) includes: three algal groups (spring diatoms, green algae, and freshwater bloom-forming cyanobacteria); two zooplankton groups (mesozooplankton and microzooplankton); two detritus groups (labile and refractory particulate organic carbon); and dissolved organic carbon. In the absence of finfish biomass, mass is conserved by routing consumed mesozooplankton back to the detrital and dissolved organic carbon pools.

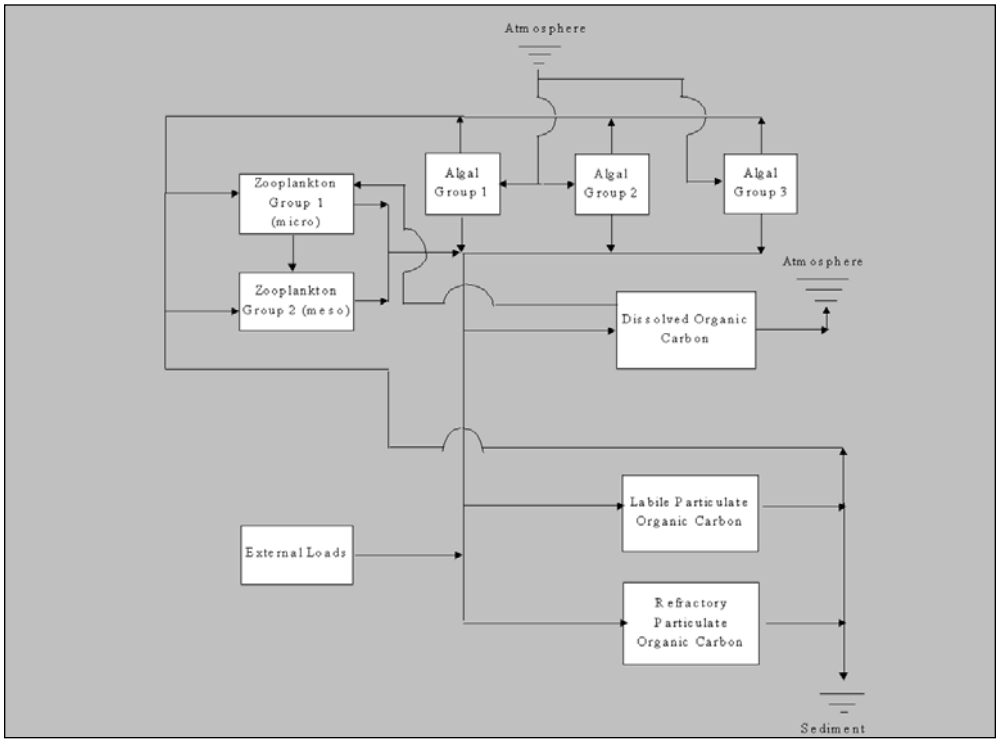

Figure 8-2. The model carbon cycle.

Additional Cycles

The eutrophication model also simulates cycling of nitrogen, phosphorus, silica, and dissolved oxygen. The flows of nitrogen and phosphorus through the system largely resemble the flow of carbon. Diagrams for all these cycles can be derived from inspection of the revised carbon cycle (Figure 8-2) and from diagrams provided by elsewhere in this report.

Zooplankton Kinetics

The Algal Production Equation

Effects of zooplankton on phytoplankton are computed in the predation term of the algal production equation:

$$\frac{\delta\ Bx}{\delta\ t} = \left[Gx - BMx - WSx \bullet \frac{\delta}{\delta\ z} \right] \bullet Bx - PRx \qquad (8\text{-}1)$$

in which:
Bx = biomass of algal group x (g C m^{-3})
Gx = growth rate of algal group x (d^{-1})
BMx = basal metabolic rate of algal group x (d^{-1})
WSx = settling rate of algal group x (m d^{-1})
PRx = predation on algal group x (g C m^{-3} d^{-1})
z, t = vertical (m) and temporal (d) coordinates

Zooplankton Production Equation

Each zooplankton group is represented by an identical production equation. The two groups are distinguished largely by parameter evaluation.

$$\frac{\delta\ Z}{\delta\ t} = \left[Gz - BMz - Mz \right] \bullet Z - PRz \qquad (8\text{-}2)$$

in which:
Z = zooplankton biomass (g C m^{-3})
Gz = growth rate of zooplankton group z (d^{-1})
BMz = basal metabolic rate of zooplankton group z (d^{-1})
Mz = mortality (d^{-1})
PRz = predation on zooplankton group z (g C m^{-3} d^{-1})

Growth Rate

Grazing is represented by a maximum ration formulation equivalent to the familiar Monod formulation used to represent algal nutrient uptake. Grazing is not equivalent to growth, however. Not all prey grazed is assimilated. Grazing also requires effort which results in respiration above the basic metabolic rate. The representation of growth rate which incorporates grazing, assimilation, and respiratory loss is:

$$Gz = \frac{PAz}{KHCz + PAz} \bullet RMAXz \bullet Ez \bullet (1 - RFz) \bullet f(T) \qquad (8\text{-}3)$$

in which:
PAz = prey available to zooplankton group z (g C m^{-3})
KHCz = prey density at which grazing is halved (g C m^{-3})
RMAXz = maximum ration of zooplankton group z
(g prey C g^{-1} zooplankton C d^{-1})
Ez = assimilation efficiency of zooplankton group z ($0 \leq E \leq 1$)
RFz = fraction of assimilated prey lost to respiration ($0 \leq RF \leq 1$)
f(T) = effect of temperature on grazing

Available Prey

The computation of available prey incorporates two principles:

1) A constant, between zero and unity, determines the utilization of a prey group by a predator,

2) A threshold density exists below which prey is not utilized.

The available portion of an algal group, for example, is determined:

$$BAxz = Max\ (Bx - CTz,\ 0) \tag{8-4}$$

in which:
BAxz = The portion of algal group x available to zooplankton group z (g C m^{-3})
CTz = The threshold concentration below which prey will not be utilized by zooplankton group z (g C m^{-3})

Prey Available to Microzooplankton. Microzooplankton are conceived to graze on dissolved organic carbon (a surrogate for bacteria), three algal groups, and organic detritus. The total prey available to microzooplankton is:

$$PAsz = UDsz \bullet DOCAsz + \Sigma\ UBxsz \bullet BAxsz + ULsz \bullet LPOCAsz + URsz \bullet RPOCAsz \tag{8-5}$$

in which:
PA = prey available to microzooplankton (g C m^{-3})
UDsz = utilization of dissolved organic carbon by microzooplankton
UBxsz = utilization of algal group x by microzooplankton
ULsz = utilization of labile particulate organic carbon by microzooplankton
URsz = utilization of refractory particulate organic carbon by microzooplankton
DOCAsz = dissolved organic carbon available to microzooplankton (g C m^{-3})
BAxsz = algal group x available to microzooplankton (g C m^{-3})
LPOCAsz = labile particulate organic carbon available to microzooplankton (g C m^{-3})
RPOCAsz = refractory particulate organic carbon available to microzooplankton (g C m^{-3})

Prey Available to Mesozooplankton. Mesozooplankton are conceived to graze on three algal groups, microzooplankton, and organic detritus. The total prey available to mesozooplankton is:

$$PAlz = \Sigma\ UBxlz \bullet BAxlz + USZlz \bullet SZA + ULlz \bullet LPOCAlz + URlz \bullet RPOCAlz \tag{8-6}$$

in which:
SZ = microzooplankton biomass (g C m^{-3})

Definitions and notation for remaining terms largely follow those for microzooplankton.

Utilization of Each Prey Group. The fraction of the total ration removed from each prey group is determined by the fraction of each utilizable prey group relative to total utilizable prey.

Basal Metabolism

Basal metabolism of both zooplankton groups is represented as an exponentially increasing function of temperature:

$$BMz = BMREFz \bullet e^{KTBz \bullet (T - Trz)} \quad (8\text{-}7)$$

in which:
BMREFz = metabolic rate of zooplankton group z at temperature Trz (d^{-1})
T = temperature (^oC)
KTBz = effect of temperature on metabolism of zooplankton group z ($^oC^{-1}$)

Mortality

Both zooplankton groups are subject to mortality at low dissolved oxygen concentrations. The mortality term is zero until dissolved oxygen falls below a threshold (Figure 8-3). Thereafter, mortality increases as dissolved oxygen decreases:

$$Mz = MZEROz \bullet \left[1 - \frac{DOREF}{DOCRITz}\right] \quad (8\text{-}8)$$

in which:
Mz = mortality of zooplankton group z (d^{-1})
MZEROz = mortality at zero dissolved oxygen concentration (d^{-1})
DOCRITz = threshold below which dissolved-oxygen-induced mortality occurs (g DO m^{-3})
DOREF = dissolved oxygen concentration when DO < DOCRIT, otherwise zero (g DO m^{-3})

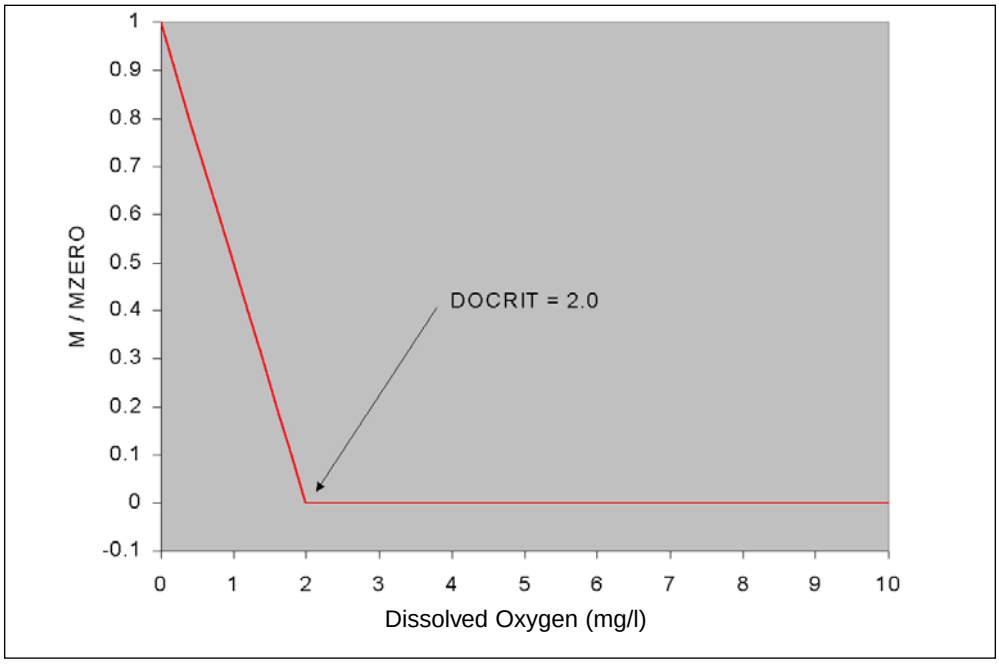

Figure 8-3. Dissolved oxygen mortality function.

Predation on Zooplankton

Mesozooplankton graze on microzooplankton. In addition, grazing on mesozooplankton by organisms not represented in the model (jellyfish, finfish) is considered. Representation of predation by organisms that are not modeled is a classic problem. Our approach results in a quadratic formulation that closes the mesozooplankton system.

Assume the predators clear a specific volume of water per unit biomass. Then predation on zooplankton is the product of the clearance rate, prey abundance, and predator abundance:

$$PRlz = F \bullet LZ \bullet HTL \tag{8-9}$$

in which:
F = clearance rate ($m^3\ g^{-1}$ predator C d^{-1})
LZ = mesozooplankton biomass (g C m^{-3})
HTL = predator biomass (g C m^{-3})

In the absence of detailed data regarding the temporal and spatial predator distribution, a reasonable assumption is that predator biomass is proportional to prey biomass, HTL = α • LZ. In that case, Equation 8-9 can be re-written:

$$PRz = \alpha \bullet F \bullet LZ^2 \tag{8-10}$$

Since neither α nor F are known precisely, the logical approach is to combine their product into a single unknown, PHTlz, determined during the model calibration procedure. In addition to closure, the quadratic predation term adds desirable stability to the potential oscillatory system represented by algae and zooplankton alone.

Interfacing with the Eutrophication Model

The basic principles of the zooplankton model have been outlined above. Since this chapter is the first documentation of the zooplankton model, additional detail of the interfacing of the zooplankton component with the remaining model state variables is presented here.

Effect of Zooplankton on Carbon

The rate of total carbon uptake by zooplankton is the product of the maximum ration and biomass, modified by any existing food limitation:

$$Rz = \frac{PAz}{KHCz + PAz} \bullet RMAXz \bullet f(T) \tag{8-11}$$

in which:
Rz = ration of zooplankton group z (g prey C g^{-1} zooplankton C d^{-1})

The rate at which carbon is recycled to the environment is determined by the fraction of the ration not assimilated, by the mortality, and by predation from higher trophic levels. The recycling of all zooplankton consumed by predators

enforces mass conservation on the system. Mass conservation implies that zooplankton carbon permanently removed from the system due to harvest of predators is negligibly small. The carbon recycle rate is:

$$CRRATEz = \left[(1 - Ez) \bullet Rz + Mz\right] \bullet Z + PRz \qquad (8\text{-}12)$$

in which:
CRRATEz = rate of carbon recycling by zooplankton group z (g C m^{-3} d^{-1})

Once the total carbon uptake and recycle are defined, the uptake and release of each carbonaceous state variable can be obtained. The uptake is determined by the ratio of utilization of a single component to total available carbon. The distribution of released carbon is determined by a set of empirical coefficients. The effect of microzooplankton on dissolved organic carbon, for example, is:

$$\frac{\delta\ DOC}{\delta\ t} = -\frac{UDsz \bullet DOCAsz}{PAsz} \bullet Rsz \bullet SZ + CRRATEsz \bullet FDOCsz \qquad (8\text{-}13)$$

in which:
FDOCsz = fraction of carbon recycled to the dissolved organic pool by microzooplankton ($0 \leq FDOC \leq 1$)

Effect of Zooplankton on Algae

Algae are a fraction of the total carbon uptake. No carbon is recycled to the algal pool, however. The effect of mesozooplankton on algal group 2, for example, is:

$$\frac{\delta\ B2}{\delta\ t} = -\frac{UB2lz \bullet B2Alz}{PAlz} \bullet Rlz \bullet LZ \qquad (8\text{-}14)$$

Effect of Zooplankton on Dissolved Oxygen

Zooplankton consume dissolved oxygen through the respiratory cost of assimilating food and through basal metabolism:

$$\frac{\delta\ DO}{\delta\ t} = -\left[Ez \bullet RFz \bullet Rz + BMz\right] \bullet AOCR \bullet Z \qquad (8\text{-}15)$$

in which:
Aocr = ratio of oxygen consumed to carbon metabolized (2.67 g DO g^{-1} C)

Effect of Zooplankton on Nitrogen

The computation of zooplankton effects on nutrients must account for differing composition of zooplankton and prey. An additional complication is that the model considers organic nitrogen and phosphorus to exist independently from organic carbon. In reality, these exist as organic matter composed of carbon, nitrogen, and phosphorus, among other elements. We consider that particulate organic nitrogen and phosphorus are consumed in proportion to detrital carbon.

First, evaluate the nitrogen-to-carbon ratio in the total prey consumed. For mesozooplankton, this is:

$$ANCPlz = \left[\Sigma ANCx \bullet UBxlz \bullet BxAlz + ANCsz \bullet USZlz \bullet SZAlz\right] / PAlz + \left[\frac{ULlz \bullet LPON \bullet LPOCAlz}{LPOC} + \frac{URlz \bullet RPON \bullet RPOCAlz}{RPOC}\right] / PAlz \quad (8\text{-}16)$$

in which:
ANCPlz = nitrogen-to-carbon ratio in prey of mesozooplankton (g N g^{-1} C)
ANCx = nitrogen-to-carbon ratio in algal group x (g N g^{-1} C)
ANCsz = nitrogen-to-carbon ratio in microzooplankton group x (g N g^{-1} C)

Additional terms follow previous definitions and notation.

All nitrogen consumed is recycled except for the amount assimilated. Additional nitrogen is recycled through respiration, mortality, and predation on zooplankton. For mesozooplankton, for example, the nitrogen recycle rate is:

$$NRRATElz = \left[ANCPlz - ANClz \bullet Elz \bullet (1 - RFlz)\right] \bullet Rlz \bullet LZ + \left[BMlz + Mlz\right] \bullet ANClz \bullet LZ + PRlz \bullet ANClz \quad (8\text{-}17)$$

in which:
NRRATElz = nitrogen recycled by mesozooplankton (g N m^{-3} d^{-1})
ANClz = nitrogen-to-carbon ratio of mesozooplankton (g N g^{-1} C)

Zooplankton do not take up dissolved organic nitrogen or ammonium. Recycle of these constituents is determined by the total recycle rate and empirical distribution coefficients. Ammonium recycle by mesozooplankton, for example, is:

$$\frac{\delta\ NH_4}{\delta\ t} = NRRATElz \bullet FNH_4lz \quad (8\text{-}18)$$

in which:
FNH_4lz = fraction of nitrogen recycled to the ammonium pool by mesozooplankton ($0 \le FNH_4lz \le 1$)

For particulate organic nitrogen, the recycle rate is the difference between detritus consumed and recycled. The effect of mesozooplankton on labile particulate organic nitrogen, for example, is:

$$\frac{\delta\ LPON}{\delta\ t} = -\frac{ULlz \bullet LPOCAlz}{PAlz} \bullet \frac{LPON}{LPOC} \bullet Rlz \bullet LZ + NRRATElz \bullet FLPONlz \quad (8\text{-}19)$$

Effect of Zooplankton on Phosphorus

The effect of zooplankton on phosphorus is analogous to the effects described for nitrogen.

Effect of Zooplankton on Silica

Zooplankton consume silica solely through the uptake of phytoplankton. All silica consumed is recycled. Computation of the effect of zooplankton on silica requires summation of silica consumed and allocation to the two external silica pools. The effect of microzooplankton on dissolved silica, for example, is:

$$\frac{\delta\ SA}{\delta\ t} = \frac{\Sigma ASCx \bullet UBxsz \bullet BxAsz}{PAsz} \bullet Rsz \bullet SZ \bullet FRSAsz \qquad (8\text{-}20)$$

in which:
ASCx = silica to carbon ratio of algal group x (g Si g^{-1} C)
FRSAsz = fraction of silica recycled to dissolved pool by microzooplankton
($0 \leq FRSAsz \leq 1$)

Parameter Evaluation

Parameters in the zooplankton model (Tables 8-1, 8-2) were adapted from published values, when available, and adjusted to provide improved model results. Published values were not available for a number of empirical parameters which were evaluated largely through a recursive calibration procedure. The evaluation procedure for significant parameters is detailed below.

Composition

The classic Redfield ratios for zooplankton (Redfield et al. 1963) indicate the following ratios: nitrogen-to-carbon = 0.19 g N g^{-1} C; phosphorus to carbon = 0.025 g P g^{-1} C. A summary by Parsons et al. (1984) indicates median values of 0.22 g N g^{-1} C and 0.017 g P g^{-1} C for nitrogen-to-carbon and phosphorus-to-carbon. Model composition for both zooplankton groups closely reflects these values.

Microzooplankton Ration

The microzooplankton community in the mainstem bay consists largely of rotifers and tintinnids as well as juvenile forms of mesozooplankton and other organisms (Brownlee and Jacobs 1987). A survey of specific grazing rates (Table 8-3) indicates maximum rates in excess of 2 d^{-1} are observed.

The effect of temperature on grazing (Figure 8-4) was described with a function of the form:

$$f(t) = e^{-KTg1 \bullet (T - Topt)^2} \text{ when } T \leq Topt$$

$$= e^{-KTg2 \bullet (T - Topt)^2} \text{ when } T \geq Topt \qquad (8\text{-}21)$$

in which:
T = temperature (°C)
Topt = optimal temperature for grazing (°C)
KTg1 = effect of temperature below optimal on grazing ($°C^{-2}$)
KTg2 = effect of temperature above optimal on grazing ($°C^{-2}$)

Table 8-1
Parameters in Microzooplankton Model

Parameter	Description	Value	Units
ANCsz	nitrogen to carbon ratio	0.2	g N g^{-1} C
AOCRsz	ratio of oxygen consumed to carbon metabolized	2.67	g DO g^{-1} C
APCsz	phosphorus to carbon ratio	0.02	g P g^{-1} C
BMREFsz	basal metabolism at reference temperature	0.254	d^{-1}
CTsz	carbon threshold for grazing	0.01	g C m^{-3}
DOCRITsz	concentration below which dissolved oxygen mortality occurs	2.0	g DO m^{-3}
Esz	assimilation efficiency	0.3	$0 \leq E \leq 1$
FDOCsz	fraction of carbon recycled to dissolved organic pool	0.25	$0 \leq FDOC \leq 1$
FDONsz	fraction of nitrogen recycled to dissolved organic pool	0.20	$0 \leq FDON \leq 1$
FDOPsz	fraction of phosphorus recycled to dissolved organic pool	0.40	$0 \leq FDOP \leq 1$
FLPOCsz	fraction of carbon recycled to labile particulate organic pool	0.50	$0 \leq FLPOC \leq 1$
FLPONsz	fraction of nitrogen recycled to labile particulate organic pool	0.25	$0 \leq FLPON \leq 1$
FLPOPsz	fraction of phosphorus recycled to labile particulate organic pool	0.07	$0 \leq FLPOP \leq 1$
FNH4sz	fraction of nitrogen recycled to dissolved inorganic pool	0.40	$0 \leq FNH4 \leq 1$
FPO4sz	fraction of phosphorus recycled to dissolved inorganic pool	0.50	$0 \leq FPO4 \leq 1$
FRPOCsz	fraction of carbon recycled to refractory particulate organic pool	0.25	$0 \leq FRPOC \leq 1$
FRPONsz	fraction of nitrogen recycled to refractory particulate organic pool	0.15	$0 \leq FRPON \leq 1$
FRPOPsz	fraction of phosphorus recycled to refractory particulate organic pool	0.03	$0 \leq FRPOP \leq 1$
FRSAsz	fraction of silica recycled to dissolved pool	0.55	$0 \leq FRSA \leq 1$
KHCsz	prey density at which grazing is halved	0.05	g C m^{-3}
KTBGsz	effect of temperature on basal metabolism	0.069	$^{o}C^{-1}$
KTGsz1	effect of sub-optimal temperature on grazing	0.0035	$^{o}C^{-2}$

continued

Table 8-1 *(continued)*
Parameters in Microzooplankton Model

Parameter	Description	Value	Units
KTGsz2	effect of super-optimal temperature on grazing	0.025	$^{o}C^{-2}$
MZEROsz	mortality at zero dissolved oxygen concentration	4.0	d^{-1}
RMAXsz	maximum ration	2.25	g prey C g^{-1} zooplankton C d^{-1}
RFsz	fraction of assimilated prey lost to respiration	0.5	$0 \leq RF \leq 1$
TMsz	optimal temperature for grazing	25	^{o}C
TRsz	reference temperature for basal metabolism	20	^{o}C
UB1sz	utilization of algal group 1	0.0	$0 \leq UB1sz \leq 1$
UB2sz	utilization of algal group 2	1.0	$0 \leq UB2sz \leq 1$
UB3sz	utilization of algal group 1	1.0	$0 \leq UB3sz \leq 1$
UDsz	utilization of dissolved organic carbon	0.1	$0 \leq UDsz \leq 1$
ULsz	utilization of labile particulate organic carbon	0.1	$0 \leq ULsz \leq 1$
URsz	utilization of refractory particulate organic carbon	0.1	$0 \leq URsz \leq 1$

Table 8-2
Parameters in Mesozooplankton Model

Parameter	Description	Value	Units
ANClz	nitrogen to carbon ratio	0.2	g N g^{-1} C
AOCRlz	ratio of oxygen consumed to carbon metabolized	2.67	g DO g^{-1} C
APClz	phosphorus to carbon ratio	0.02	g P g^{-1} C
BMREFlz	basal metabolism at reference temperature	0.186	d^{-1}
CTlz	carbon threshold for grazing	0.05	g C m^{-3}
DOCRITlz	concentration below which dissolved oxygen mortality occurs	2.0	g DO m^{-3}
Elz	assimilation efficiency	0.30	$0 \leq E \leq 1$
FDOClz	fraction of carbon recycled to dissolved organic pool	0.25	$0 \leq FDOC \leq 1$
FDONlz	fraction of nitrogen recycled to dissolved organic pool	0.20	$0 \leq FDON \leq 1$
FDOPlz	fraction of phosphorus recycled to dissolved organic pool	0.40	$0 \leq FDOP \leq 1$
FLPOClz	fraction of carbon recycled to labile particulate organic pool	0.50	$0 \leq FLPOC \leq 1$
FLPONlz	fraction of nitrogen recycled to labile particulate organic pool	0.25	$0 \leq FLPON \leq 1$
FLPOPlz	fraction of phosphorus recycled to labile particulate organic pool	0.07	$0 \leq FLPOP \leq 1$
FNH4lz	fraction of nitrogen recycled to dissolved inorganic pool	0.40	$0 \leq FNH4 \leq 1$
FPO4lz	fraction of phosphorus recycled to dissolved inorganic pool	0.50	$0 \leq FPO4 \leq 1$
FRPOClz	fraction of carbon recycled to refractory particulate organic pool	0.25	$0 \leq FRPOC \leq 1$
FRPONlz	fraction of nitrogen recycled to refractory particulate organic pool	0.15	$0 \leq FRPON \leq 1$
FRPOPlz	fraction of phosphorus recycled to refractory particulate organic pool	0.03	$0 \leq FRPOP \leq 1$
FRSAlz	fraction of silica recycled to dissolved pool	0.55	$0 \leq FRSA \leq 1$
KHClz	prey density at which grazing is halved	0.175	g C m^{-3}
KTBGlz	effect of temperature on basal metabolism	0.069	$^{o}C^{-1}$
KTGlz1	effect of sub-optimal temperature on grazing	0.008	$^{o}C^{-2}$

continued

Table 8-2 *(continued)*
Parameters in Mesozooplankton Model

KTglz2	effect of super-optimal temperature on grazing	0.03	$^{o}C^{-2}$
KTPRlz	effect of temperature on predation by higher trophic levels	0.069	$^{o}C^{-1}$
MZEROlz	mortality at zero dissolved oxygen concentration	4.0	d^{-1}
PHTlz	predation by higher trophic levels	2.0	$m^3\ g^{-1}\ C\ d^{-1}$
RMAXlz	maximum ration	1.75	g prey C g^{-1} zooplankton C d^{-1}
RFlz	fraction of assimilated prey lost to respiration	0.07	$0 \leq RF \leq 1$
TMlz	optimal temperature for grazing	25	^{o}C
TPRlz	reference temperature for predation by higher trophic levels	20	^{o}C
TRlz	reference temperature for basal metabolism	20	^{o}C
UB1sz	utilization of algal group 1	0.0	$0 \leq UB1sz \leq 1$
UB2sz	utilization of algal group 2	1.0	$0 \leq UB2sz \leq 1$
UB3sz	utilization of algal group 1	1.0	$0 \leq UB3sz \leq 1$
ULsz	utilization of labile particulate organic carbon	0.1	$0 \leq ULsz \leq 1$
URsz	utilization of refractory particulate organic carbon	0.1	$0 \leq URsz \leq 1$
USZlz	utilization of microzooplankton	1.0	$0 \leq USZlz \leq 1$

Table 8-3
Microzooplankton Specific Ingestion

Temperature (^{o}C)	Ingestion (1/d)	Organism	Source
5.5	0.79	A. hudsonica nauplii	White and Roman, 1992b
9.5	0.37	rotifer	White and Roman, 1992b
18.5	0.54	ciliate	Dagg, 1995
20.5	2.8	A. tonsa nauplii	White and Roman, 1992b
20.5	0.32	ciliate	Dagg, 1995
30.1	1.08	ciliate	Dagg, 1995
30.3	0.84	ciliate	Dagg, 1995
30.4	2.11	ciliate	Dagg, 1995
30.4	1.38	ciliate	Dagg, 1995

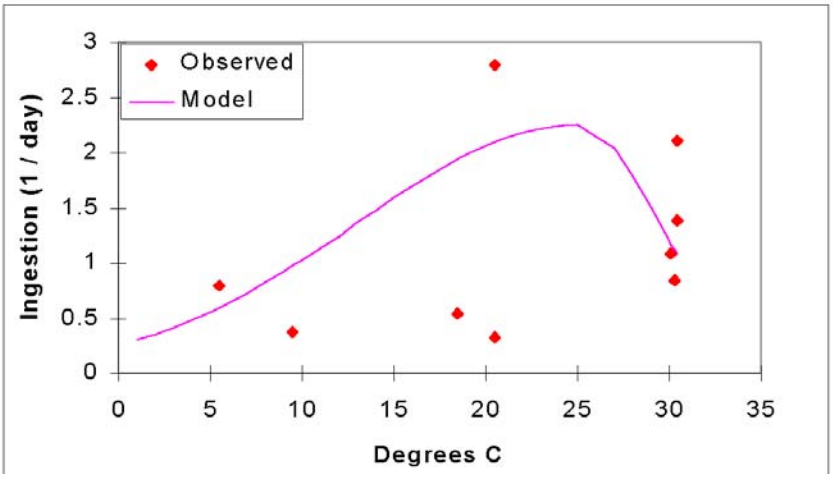

Figure 8-4. Effect of temperature on microzooplankton grazing.

Mesozooplankton Grazing

The mesozooplankton community of the mainstem bay consists largely of three species of copepods: *Acartia tonsa*, *Eurytemora affinis*, and *Acartia hudsonica* (Brownlee and Jacobs 1987, White and Roman 1992b). Of these, an abundance of data exists for *Acartia tonsa*. Consequently, parameterization of the mesozooplankton component was based largely on this species.

Observations collected by White and Roman (1992a) provide an excellent basis for evaluation of several model parameters. The observations are based on the body weight of an adult copepod female. Ingestion, growth, and respiration were converted to carbon specific rates (Table 8-4) using a mass 2.6 µg C individual^{-1} derived from White and Roman (1992b).

Table 8-4
Ingestion, Growth, and Respiration for an Adult Female Acartia Tonsa (after White and Roman 1992a)

Temp (°C)	Growth (µg C/ female/ d)	Phyto Ingest (µg C/ female/d)	MicroZ Ingest (µg C/ female/d)	Respiration (µg C/ female/d)	Growth (1/d)	Phyto Ingest (1/d)	Respiration (1/d)
16.8	1.16	0.69		0.7	0.45	0.27	0.27
23.5	0.67	2.26		0.98	0.26	0.87	0.38
26.9	2.07	3.35		0.9	0.80	1.29	0.35
27.6	0.68	6.86		0.93	0.26	2.64	0.36
17.1	0.64	0.28	1.15	0.72	0.25	0.11	0.28
18.7	1.58	0.99		0.8	0.61	0.38	0.31
19.3	1.89	0.01		0.81	0.73	0.00	0.31
20	1.91	9.2		0.82	0.73	3.54	0.32
27.2	1.06	4.71		1.12	0.41	1.81	0.43
29.4	1.21	2.4	0.36	1.2	0.47	0.92	0.46
26	2.01	4.69		0.98	0.77	1.80	0.38
24.2	2.3	5.82		0.89	0.88	2.24	0.34
15.8	0.71	0.68		0.64	0.27	0.26	0.25

The observations indicate maximum specific ingestion rates of 2 to 3 d^{-1}. Early experiments with the model indicated the computed phytoplankton population was not sustainable with ingestion greatly in excess of 2 d^{-1}. Consequently a value of 1.75 d^{-1} was selected. The observations are for *Acartia tonsa* which predominates from May through October (White and Roman 1992b). To account for grazing by the cold-water species, a piecewise temperature function was devised that provided grazing in winter and spring in excess of observations for *Acartia* (Figure 8-5).

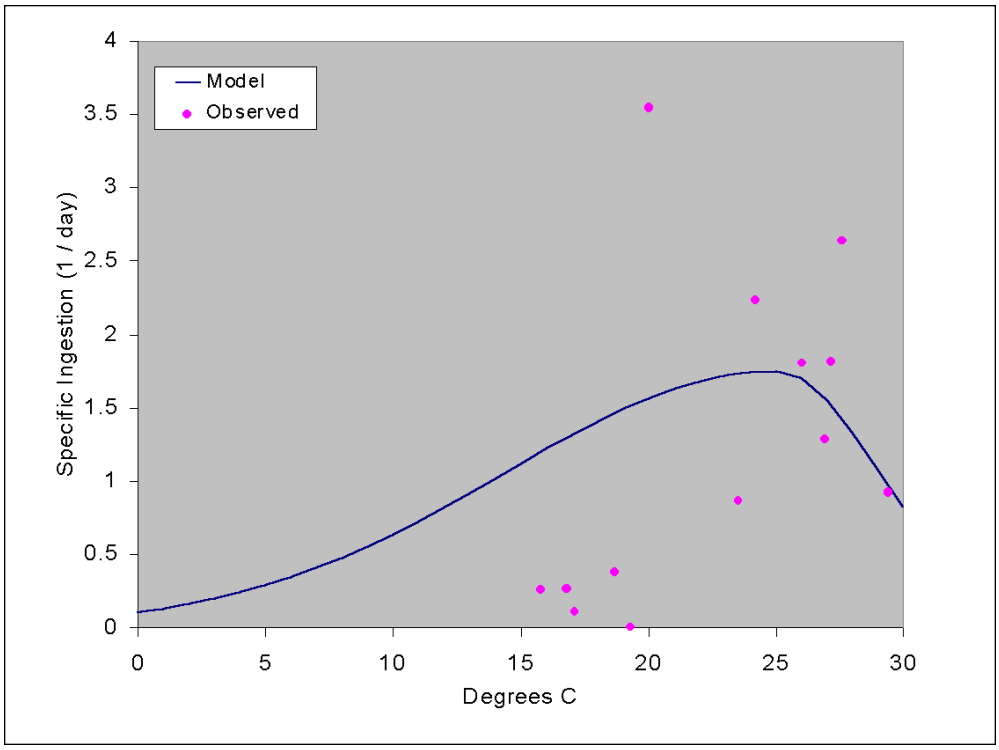

Figure 8-5. Effect of temperature on mesozooplankton grazing.

Basal Metabolism

Ikeda (1985) presented a relationship for routine metabolism:

$$Y = a \bullet c \bullet M^{b} \bullet d^{T} \qquad (8\text{-}22)$$

in which:
Y = oxygen consumption (µL O_2 $individual^{-1}$ $hour^{-1}$)
M = body mass (mg C $individual^{-1}$)
T = temperature (°C)
a, b, c, d = empirical constants

Ikeda linearized his equation through logarithmic transformation and evaluated parameters via linear regression.

Ikeda's relationship is, no doubt, convenient for employment in terms of conventionally-measured quantities. The equation is a dimensional nightmare, however. Several pages of conversion factors eventually yield the more tractable relationship:

$$BM = \frac{0.072 \bullet e^{0.06 \bullet (T - 20)}}{M^{0.165}} \qquad (8\text{-}23)$$

in which:
BM = carbon specific metabolic rate (d^{-1})
M = body mass (mg C $individual^{-1}$)

An interesting insight is that Ikeda's original relationship indicates respiration per individual increases with body mass while the converted relationship indicates specific respiration decreases as a function of body mass (Figure 8-6).

Using body masses of 0.0012 mg DW and 0.008 mg DW for a rotifer and adult *Acartia* (White and Roman 1992b) and the conversion 0.4 mg C mg^{-1} DW yields the basal metabolic rates employed in the model (Tables 8-1, 8-2). The multiplier 0.06 in Equation 8-23 was increased to 0.069 in the model to provide a rounded, classic Q10 of 2.

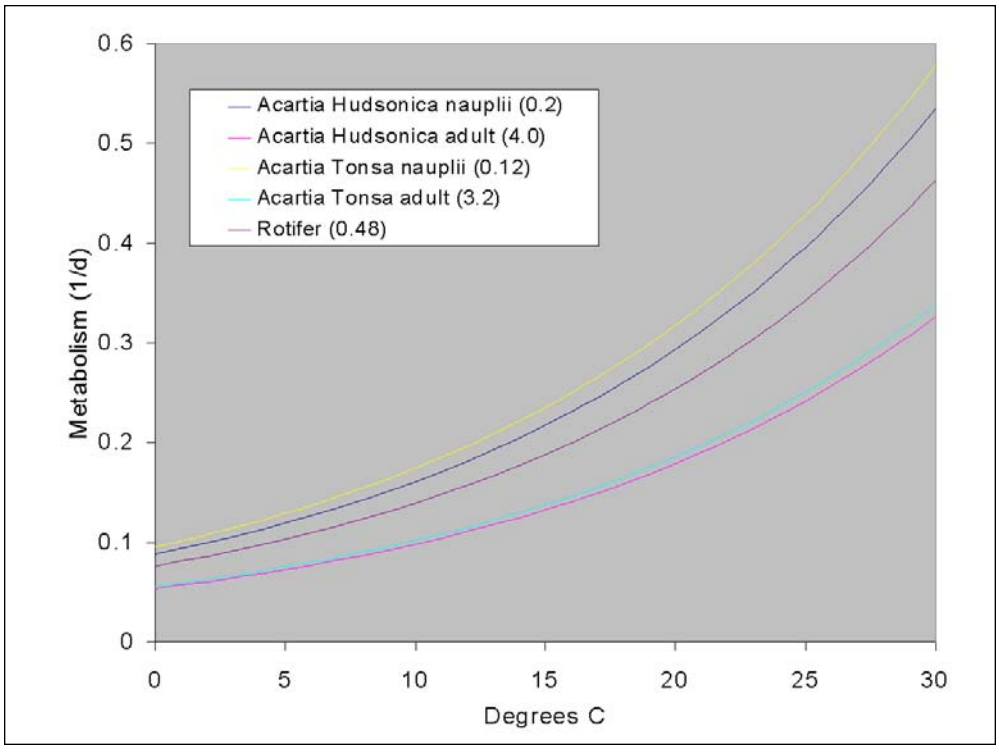

Figure 8-6. Effect of body size (µg C) and temperature on specific, basal metabolism. Size from White and Roman (1992b).

Respiration Fraction and Efficiency

Data presented by White and Roman (1992a) indicates respiration accounts for 40 to 50% of total microzooplankton and phytoplankton consumed by *Acartia*. This includes both basal metabolism and the respiratory cost of feeding. Basal metabolism by Ikeda's formula (0.185 d^{-1}) is roughly half the specific respiration derived from White and Roman's data (Table 8-4). These proportions indicate the respiratory fraction is the remaining half of specific respiration or 20 to 25% of prey consumed. We found a lower fraction, 7% of prey consumed, provided reasonable results when employed in the mesozooplankton computations. A higher value, 50% of prey consumed, was employed for microzooplankton to reflect the effect of body size on respiration.

The same observations indicate growth and respiration account for 87 to 95% of total ingestion. Roughly 10% of total ingestion is unaccounted for, indicating efficiency is roughly 90%. Modeled efficiencies are only one third of that value, however. While the observed efficiency seems high (White and Roman assume 80%), the model values are unrealistically low. Reduced efficiencies were initially assigned to the model based on need. Efficiencies of 80 to 90% produced wide oscillations in computed populations and resulted in collapse of the phytoplankton population. Lower efficiencies resulted in damped oscillations and more stable communities.

Later insights indicated why lower efficiencies are appropriate. In the model, adult zooplankton instantaneously reproduce adult zooplankton. In reality, reproduction is in the form of eggs. Eggs hatch into juvenile forms that eventually mature into adults. The true growth process installs temporal lags in the system and reduces efficiency as eggs and juveniles are lost to predation and other processes. While the temporal lags are difficult to introduce into the present model, the losses that occur to eggs and juveniles are simulated though employment of relatively low efficiencies.

Additional Parameters

Selection of the dissolved oxygen threshold for mortality was guided by the observation that concentrations below 1 gm DO m^{-3} result in reduced survival of copepod adults and inhibited hatching of *Acartia tonsa* eggs (Roman et al. 1993).

Sellner et al. (1993) noted neither rotifers nor copepods grazed heavily on *Microcystis*. Consequently, utilization of Group 1 algae, which represent cyanobacteria in the tidal fresh Potomac River, was set to zero. White and Roman's (1992a) observations indicate consumption of microzooplankton by mesozooplankton is comparable to consumption of phytoplankton. Consequently utilization of microzooplankton was set to unity.

Selection of half-saturation and threshold concentrations for mesozooplankton was guided by interpretation of numerous studies (Table 8-5). Smaller concentrations were employed for microzooplankton to reflect their smaller body size.

Table 8-5
Mesozooplankton Threshold and Half Saturation Concentrations

mg C / L	Comment	Source
0.01	for growth	Kiorboe and Nielson (1994)
0.7	egg production	Durbin et al. (1983)
0.05	clearance rates decrease	Paffenhofer and Stearns (1988)
0.175	A. nauplii growth	Berggreen et al. (1988)
0.2	ingestion	Kiorboe et al. (1985)

Observations

Zooplankton biomass was monitored at 27 stations throughout the mainstem and tributaries (Figure 8-7). Mesozooplankton were sampled monthly, using a 202 µm net towed obliquely from bottom to surface, and quantified as dry weight. For comparison with the model, mesozooplankton biomass was converted from dry weight to carbon using the ratio 0.4 gm C gm^{-1} DW. Microzooplankton were sampled monthly, in the Maryland portion of the bay only, using a 44 µm net. Five samples from above the pycnocline were combined into "surface mixed layer" composites. Five samples from below the pycnocline were combined into "bottom mixed layer" composites. The investigators computed total biomass, as carbon, from species counts using standard biomass for individuals of each species. The data base, extending from mid-1984 through 1994, was provided by the Chesapeake Bay Program Office (Maryland) and by investigators at Old Dominion University (Virginia).

Model Results

Harmonic Analysis of Observations

The zooplankton observations exhibit an enormous amount of variability that confounds visual interpretation and model-data comparisons. To provide insight, basic harmonic analysis was applied to the observations. First, observations were grouped into four units:

Unit 1—Mainstem Bay (Segments CB2-CB7, EE3)

Unit 2—Tidal Fresh (Segments CB1, TF1-TF5)

Unit 3—Transition Zone (Segments RET1-RET5)

Unit 4— Lower Estuary (Segments LE1-LE5)

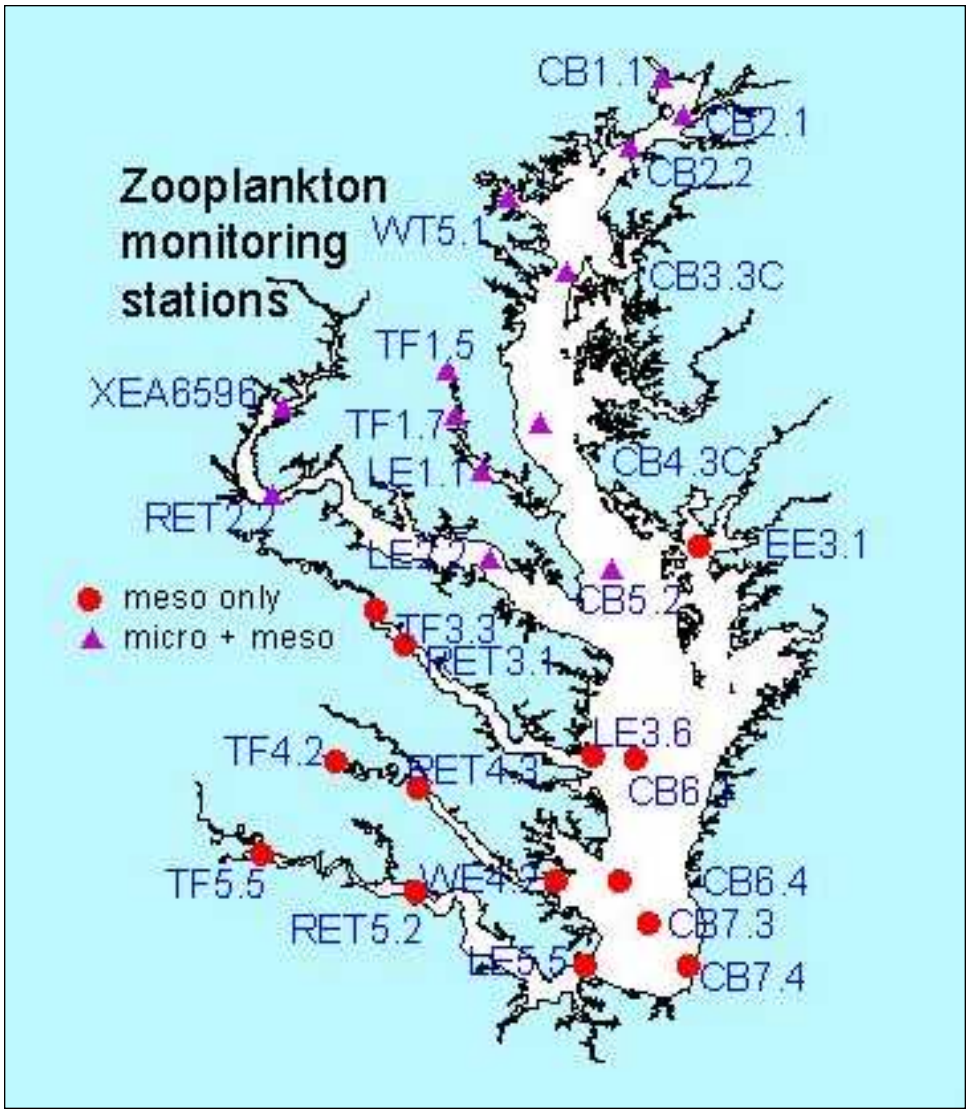

Figure 8-7. Zooplankton sampling stations.

For each unit, a relationship was proposed that included annual, semi-annual, and seasonal cycles:

$$\log_{10}(Z) = A_1 + A_2 \bullet \sin\left(\frac{2\pi \bullet d}{365} + \theta\right) \tag{8-24}$$

$$+ A_3 \bullet \sin\left(\frac{2\pi \bullet d}{182.5} + \varphi\right) + A_4 \bullet \sin\left(\frac{2\pi \bullet d}{91.25} + \psi\right)$$

in which:
Z = zooplankton (g C m^{-3})
A_1 = mean of log-transformed concentration
A_2, A_3, A_4 = amplitude of annual, semi-annual, and seasonal components
θ, ϕ, ψ = phase lags
d = julian day

Linear regression was used to evaluate the amplitudes and phase lags.

The proposed relationship accounted for 25% to 30% of the mesozooplankton log-variance in the mainstem bay and in the lower estuaries. Only 10% to 15% of the variance could be explained in the tidal fresh and transition regions. The analysis indicated that seasonal patterns exist in the estuarine areas but seasonality accounts for only a small portion of the total variance. In the remaining regions, virtually no seasonal pattern exists in the aggregate data. A reconstruction of the annual time series, obtained by substituting the regression coefficients into Equation 8-24, indicates a bi-modal pattern. Maximum biomass occurs in spring while a secondary maximum occurs in summer (Figure 8-8). These peaks indicate the spring bloom of *Eurytemora* and *A. hudsonica* and the summer population of *A. tonsa*.

The harmonic analysis of microzooplankton strongly contrasted with mesozooplankton. The proposed relationship accounted for 25% of the log-variance in the tidal fresh and transition regions but less than 10% of the log-variance in the estuarine areas. Within the tidal fresh and transition regions, the reconstructed time series shows a single annual peak that corresponds to the annual temperature cycle (Figure 8-9). In the lower estuaries and mainstem bay, the microzooplankton time series has no structure and is essentially "white noise."

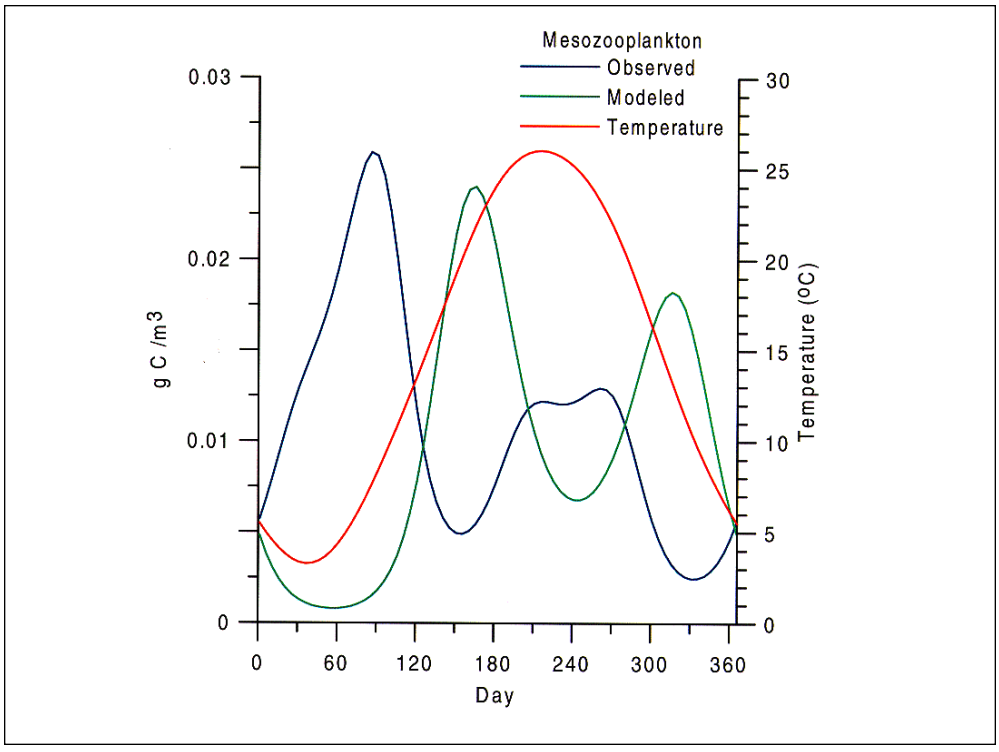

Figure 8-8. Annual time series of observed mesozooplankton, computed mesozooplankton, and temperature. Observations from CB2–CB7 and EE3. Computations from surface at station CB5.2.

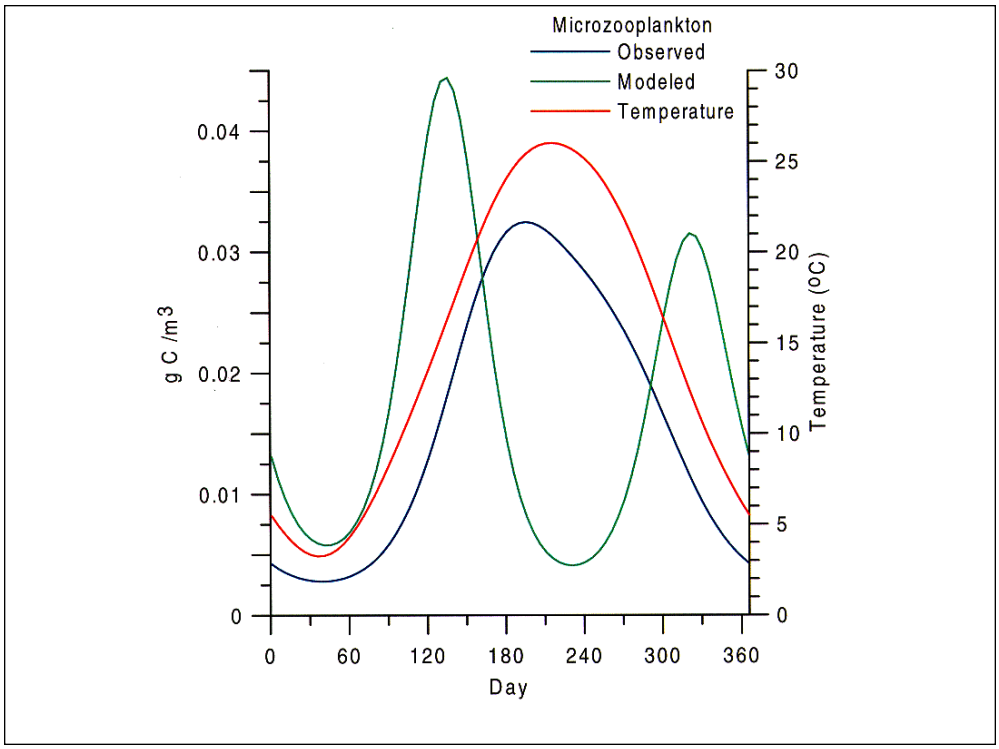

Figure 8-9. Annual time series of observed microzooplankton, computed microzooplankton, and temperature. Observations from TF1–TF2 and RET1—RET2. Computations from station TF1.7.

Model Time Series

Model results were compared to observed time series at all stations for which data were available. Comparisons were consistent with sampling procedure. Mesozooplankton were sampled in oblique vertical casts that provided a vertically-integrated sample. Modeled mesozooplankton was vertically averaged for comparison with the observations. Microzooplankton observations were composite samples representing “above pycnocline” and “below pycnocline” concentrations. Model results from individual cells were combined into above- and below-pycnocline values. The observed pycnocline depth varies spatially and temporally and is not always distinct. For comparison with the observations, the model pycnocline was assumed to occur at a consistent depth of 6.7 m (upper four model layers). In the event the total depth was less than 6.7 m, the entire model water column was combined into the above pycnocline value. A sampling of results is presented here. Complete comparisons are provided in the CD-ROM that accompanies this report.

The time series of observed and modeled zooplankton are difficult to interpret, primarily due to the large variance inherent in the observations. Some basic observations are possible, however. The model does not capture the abundance of microzooplankton in the tidal fresh regions. Peak concentrations in excess of 0.1 gm m^{-3} commonly occur in tidal fresh waters while the model peaks are

roughly less than half the observed (Figure 8-10). Within the lower estuaries, microzooplankton are less abundant and both model and observations show similar peak abundance, roughly 0.05 gm m^{-3} (Figure 8-11). Within the mainstem of the bay, observed peak microzooplankton abundance is roughly twice as high above pycnocline than below pycnocline. The model demonstrates lesser difference above and below pycnocline and is closer to the observed below-pycnocline values (Figures 8-12, 8-13).

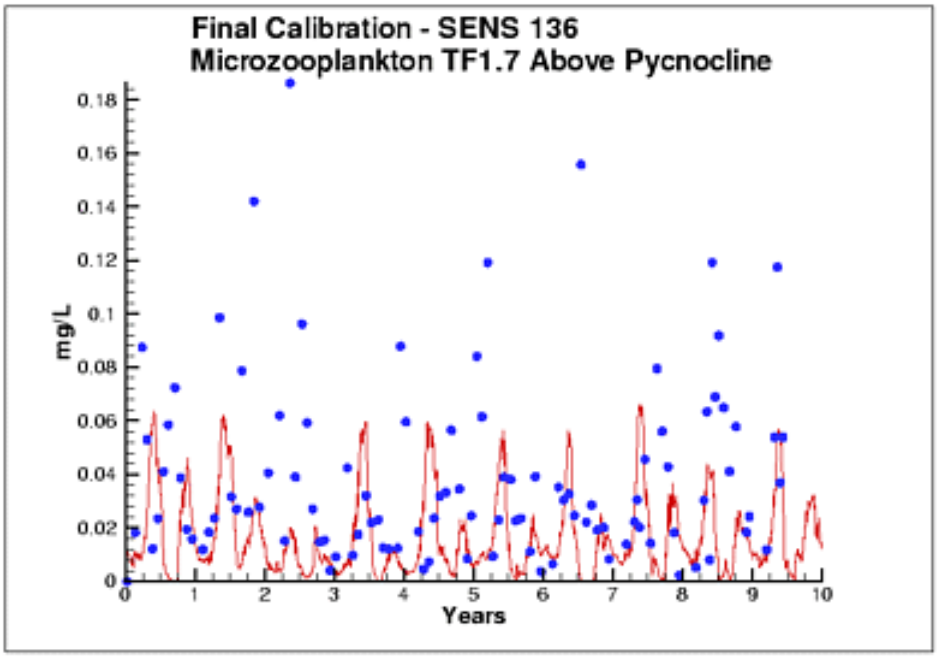

Figure 8-10. Time series of computed and observed microzooplankton at Station TF1.7 in the tidal fresh Patuxent River.

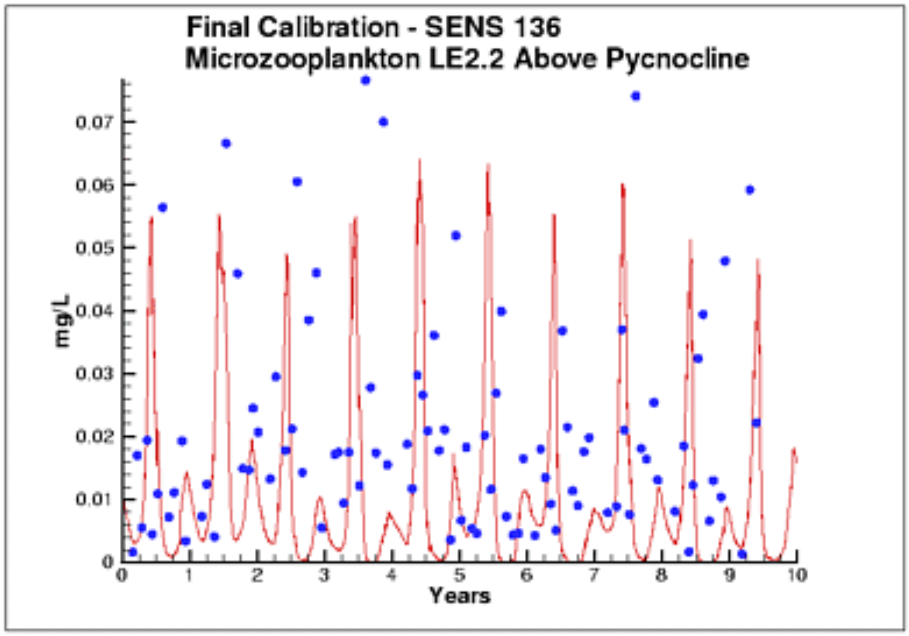

Figure 8-11. Time series of computed and observed microzooplankton at Station LE2.2 in the lower Potomac estuary.

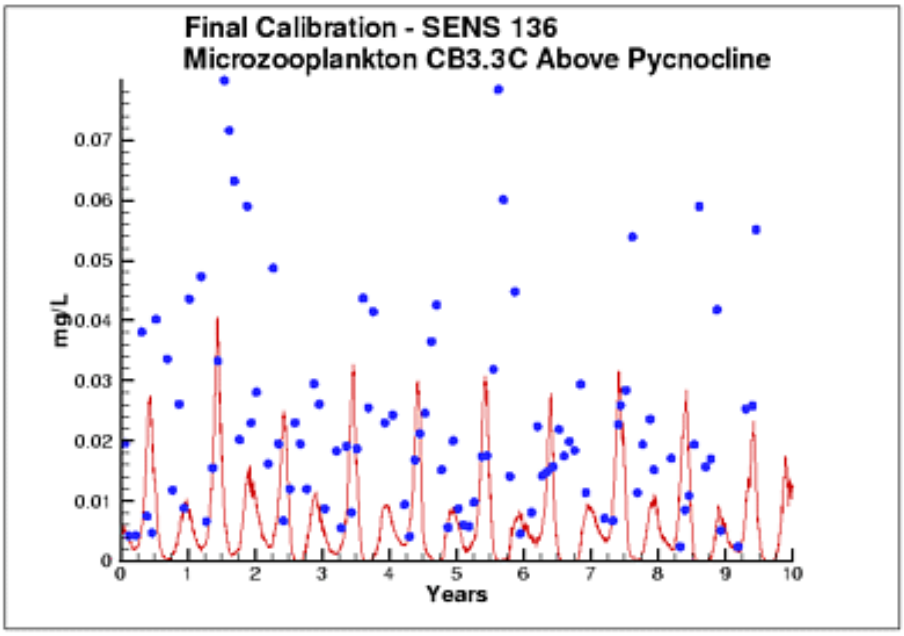

Figure 8-12. Time series of computed and observed microzooplankton, above pycnocline, at Station CB3.3C in the mainstem Chesapeake Bay.

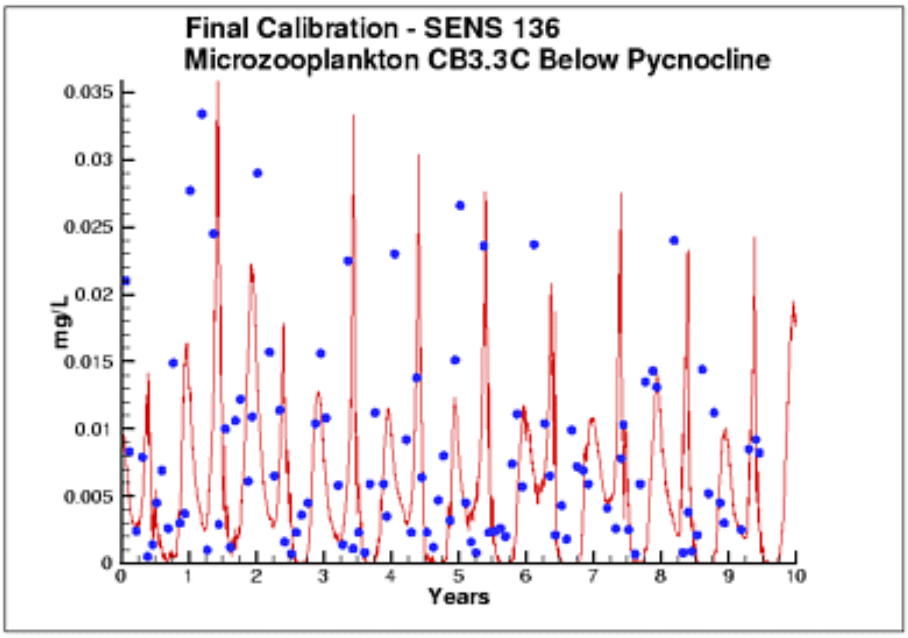

Figure 8-13. Time series of computed and observed microzooplankton, below pycnocline, at Station CB3.3C in the mainstem Chesapeake Bay.

Inspection indicates enormous differences in mesozooplankton between the tidal fresh Patuxent and other estuaries (Figures 8-14, 8-15). If the observations are correct, the Patuxent is a unique system that requires unique treatment. For the majority of tidal fresh and transition waters, computed mesozooplankton peaks, roughly 0.06 gm m^{-3}, are nearly double observed peaks (Figures 8-15, 8-16). Within the lower estuaries, observed and computed maximum values are comparable at roughly 0.05 gm m^{-3} (Figure 8-17). Agreement between computed and observed mesozooplankton continues for the mainstem bay (Figure 8-18).

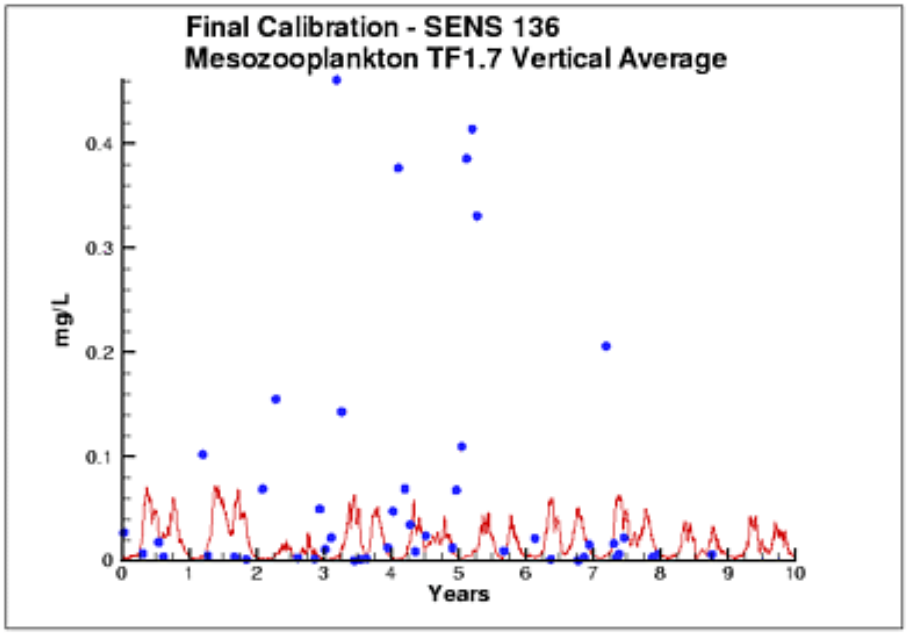

Figure 8-14. Time series of computed and observed mesozooplankton at Station TF1.7 in the tidal fresh Patuxent River.

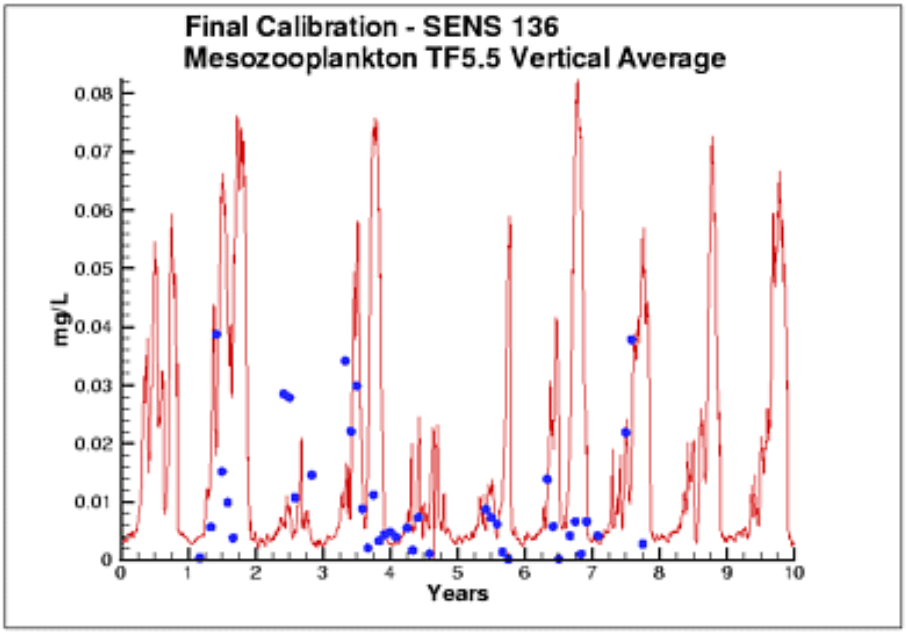

Figure 8-15. Time series of computed and observed mesozooplankton at Station TF5.5 in the tidal fresh James River.

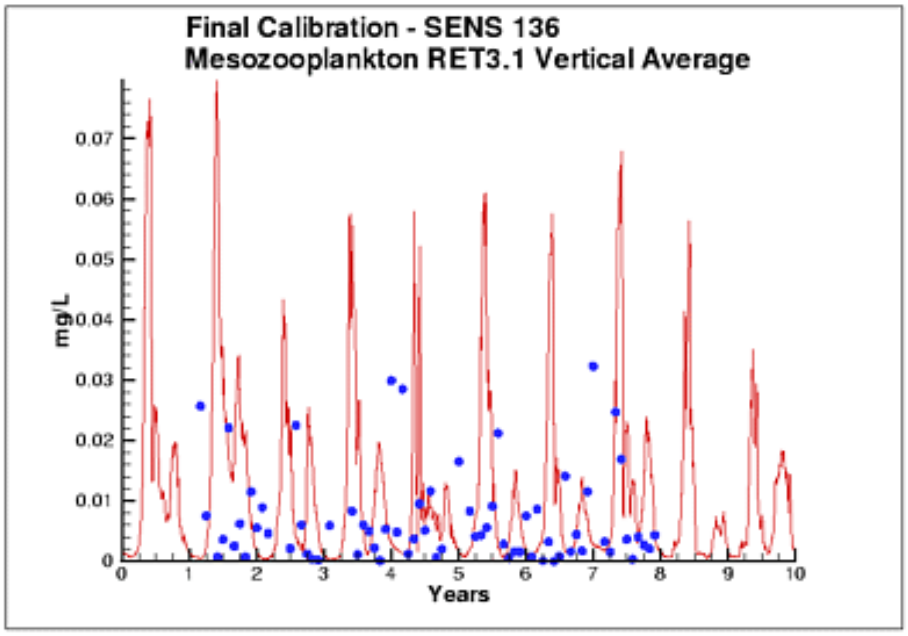

Figure 8-16. Time series of computed and observed mesozooplankton at Station RET3.1 in the Rappahannock River transition from fresh to salt water.

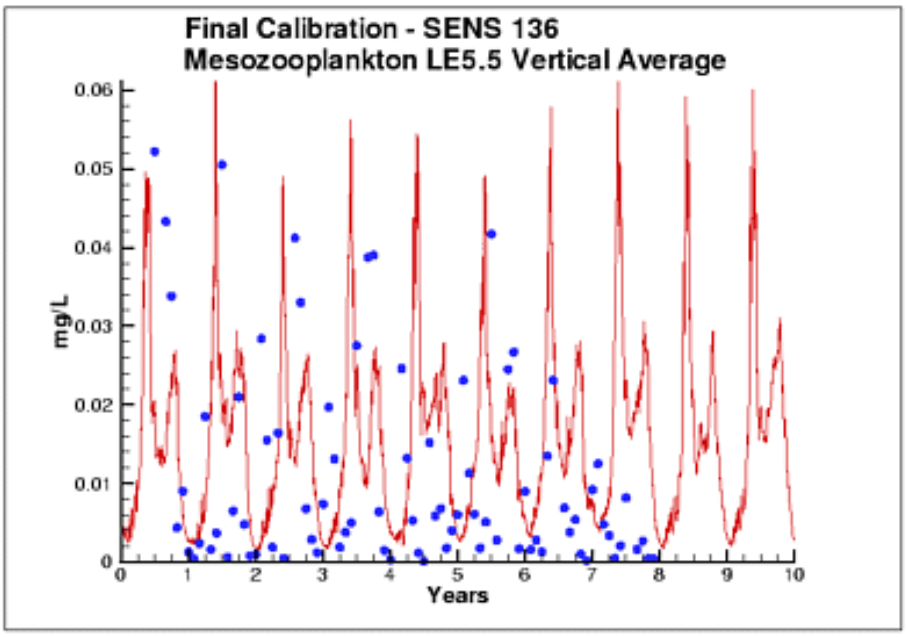

Figure 8-17. Time series of computed and observed mesozooplankton at Station RET3.1 in the Rappahannock River transition from fresh to salt water.

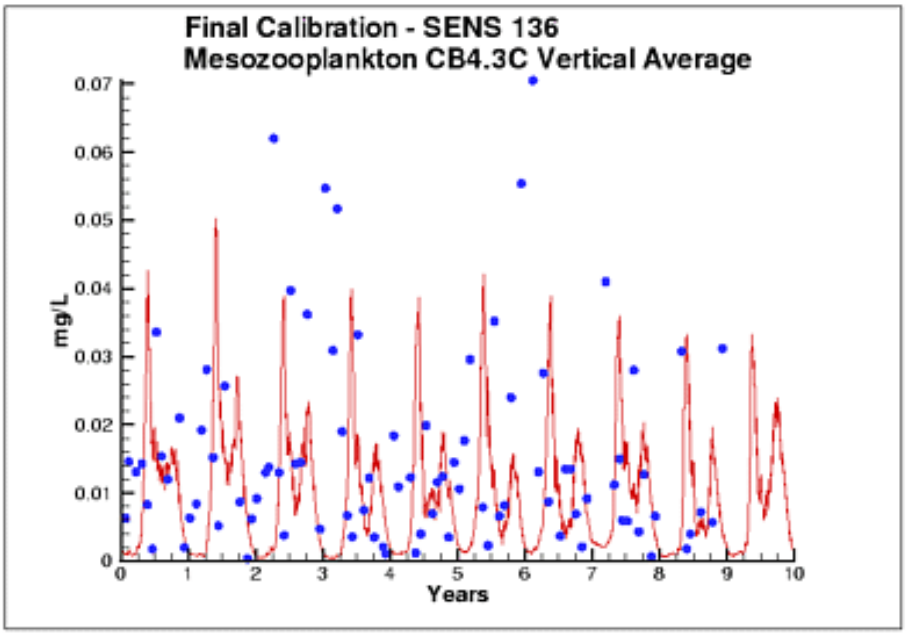

Figure 8-18. Time series of computed and observed mesozooplankton at Station CB4.3C in the mainstem Chesapeake Bay.

Effect of Dissolved Oxygen

The model includes a mortality factor to account for the impact of anoxia on zooplankton (Equation 8-8). The vertical tows used to sample mesozooplankton do not allow distinction of surface and bottom populations in regions where anoxia occurs. The model computes substantial differences between surface and bottom populations in the presence of anoxia. At a mid-bay station, computed surface and bottom populations of mesozooplankton are nearly identical from January thorough April (Figure 8-19). In April the populations diverge and mesozooplankton at the bottom are nearly extinct from June through August. In September, the bottom population recovers and is equivalent to the surface by November. The mesozooplankton time series at bottom is consistent with the time series of computed dissolved oxygen (Figure 8-20). The divergence between surface and bottom populations begins when computed bottom dissolved oxygen plunges towards zero. Mesozooplankton at the bottom remain at low levels until the autumn turnover period and gradually recover to surface levels throughout the autumn.

Harmonic Analysis of Model

The time series of computed zooplankton was subjected to the same harmonic analysis and reconstruction as the observations. Variance in the computed time series was much less than in the observations and the time series relationship accounted for much more variance in the computed time series (R^2 = 0.58 to 0.83) than in the observed time series.

The computed time series of both microzooplankton and mesozooplankton exhibit semi-annual cycles with two peaks per year (Figures 8-8, 8-9). For

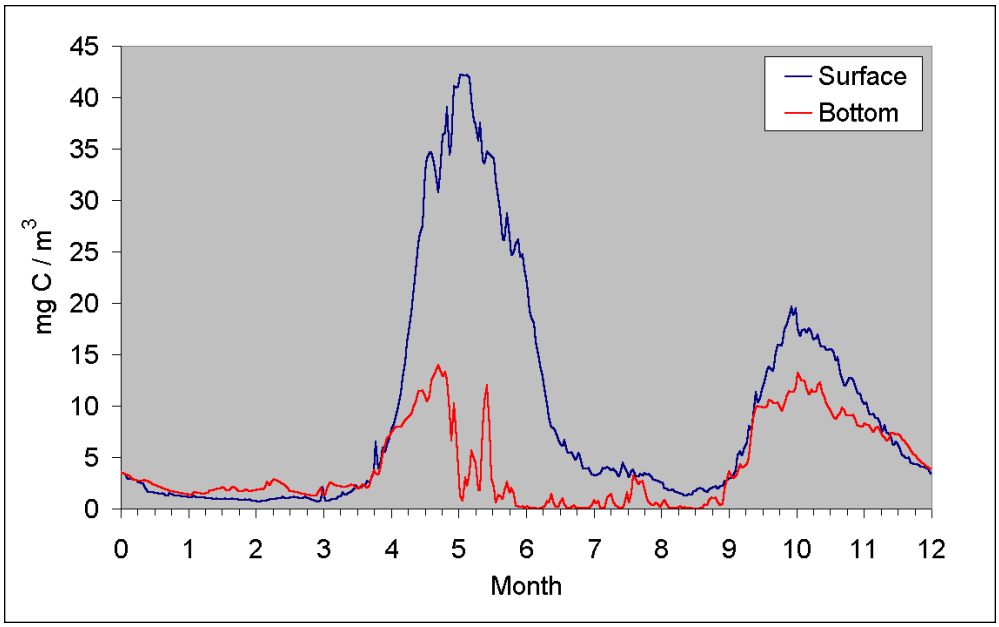

Figure 8-19. Time series of computed mesozooplankton, surface and bottom, at Station CB5.2 in the mainstem Chesapeake Bay for 1993.

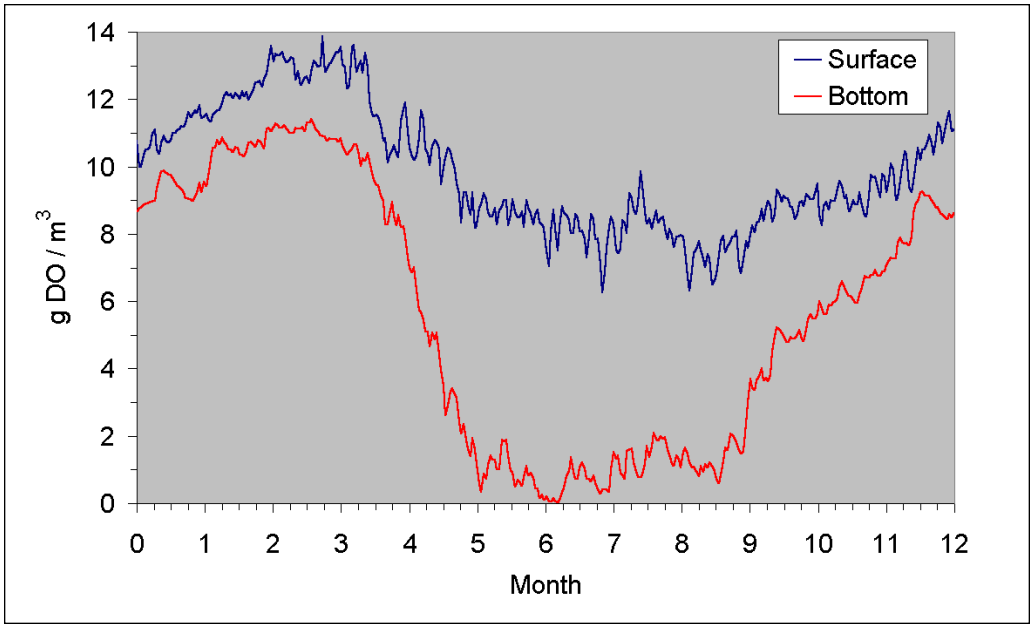

Figure 8-20. Time series of computed dissolved oxygen, surface and bottom, at Station CB5.2 in the mainstem Chesapeake Bay for 1993.

microzooplankton, the semi-annual cycle conflicts with the observed annual cycle in tidal fresh water. For mesozooplankton, the semi-annual cycle is consistent with observations but computed peaks lag observed by 90 days.

Analysis of model results from the Virginia Tributary Refinements phase (Cerco and Meyers 2000) indicated the mid-year dip in microzooplankton was due to grazing by mesozooplankton. The dip in mesozooplankton was attributed to anoxia in the mainstem bay. An alternate explanation for the dips in both populations may lie with the temperature dependence of the grazing and respiration functions. Grazing in both populations peaks at roughly 25ºC (Figures 8-4, 8-5) while metabolism increases indefinitely as a function of temperature (Equation 8-7). Consequently, at high mid-summer temperatures, an excess of metabolism over grazing may cause a decline in computed zooplankton.

Cumulative Distributions

Little or no correspondence exists between individual observations and model computations. In view of the large, random variance in the observations, lack of one-to-one correspondence is expected. An alternate, more informative view can be obtained by comparing the cumulative distributions of observed and computed zooplankton. The computed distributions are based on model computations corresponding to sample locations and days. The computed distributions do not represent the population of computations.

The lower portions of the distributions of computed and observed microzooplankton agree well within the tidal fresh and transition regions (Figure 8-21). The median observed value exceeds the model by 50% while the upper range of the observed distribution greatly exceeds the model. Excess of observed over computed peaks was noted in the time series as well (Figure 8-10). Within the lower estuaries

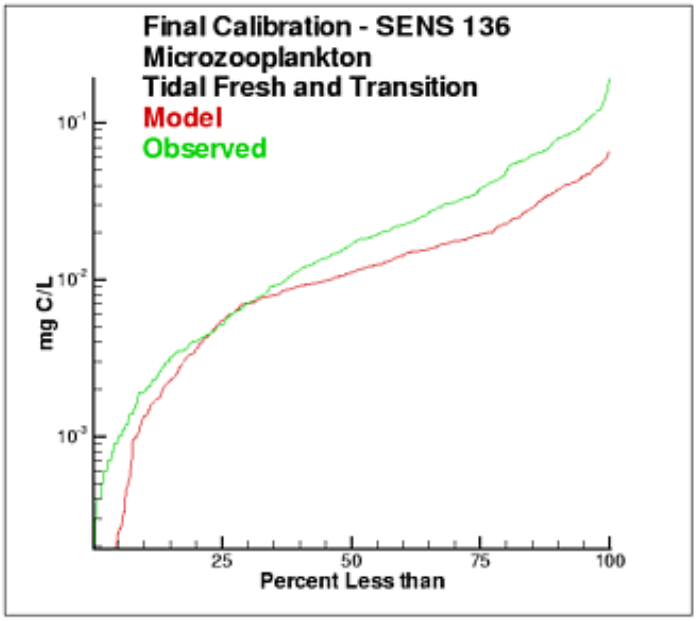

Figure 8-21. Cumulative distribution of computed and observed microzooplankton in tidal fresh and transition regions (CB1, TF1, TF2, RET2).

and mainstem bay, the observed microzooplankton exceed computed by 50% to 100% throughout most of the distributions (Figures 8-22, 8-23).

At any percentile of the distributions, computed mesozooplankton exceed observed by 50% to 100% in the tidal fresh (Figure 8-24), transition (Figure 8-25), and lower estuary (Figure 8-26) regions. Agreement between computed and observed mesozooplankton is excellent throughout the distribution in the mainstem bay (Figure 8-27).

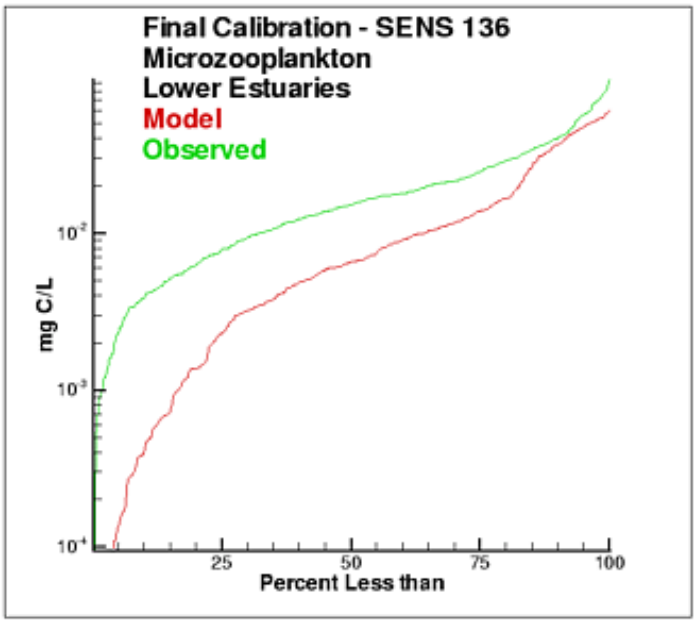

Figure 8-22. Cumulative distribution of computed and observed microzooplankton in lower estuaries (LE1, LE2).

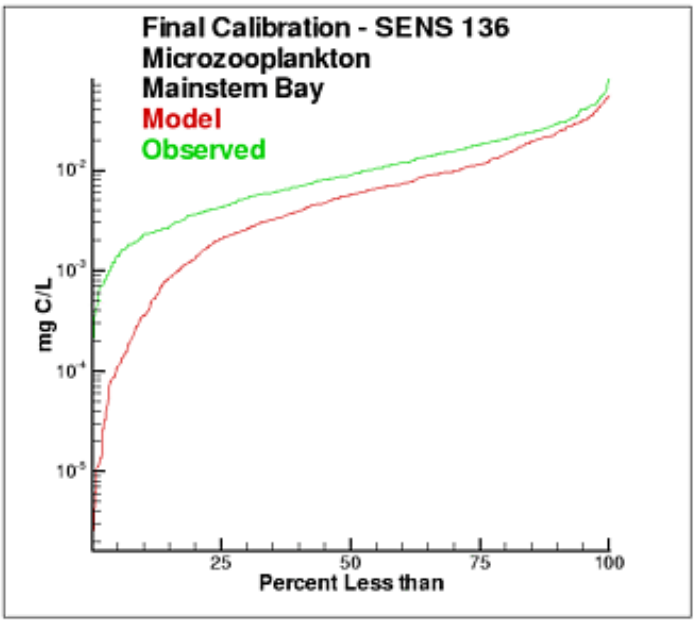

Figure 8-23. Cumulative distribution of computed and observed microzooplankton in the mainstem bay (CB2-CB5).

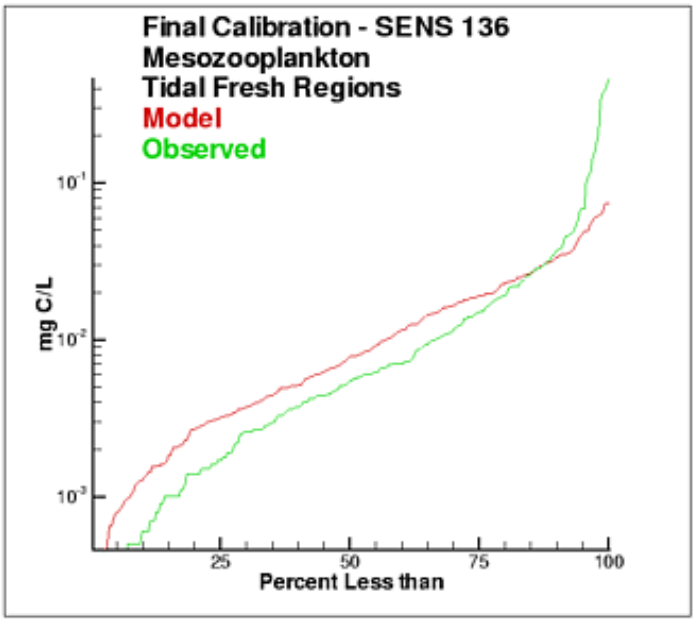

Figure 8-24. Cumulative distribution of computed and observed mesozooplankton in tidal fresh regions (CB1, TF1-TF5).

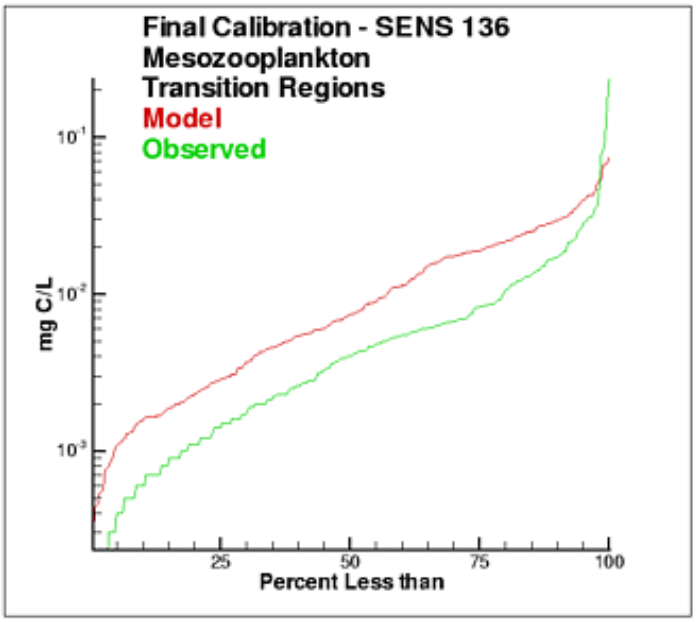

Figure 8-25. Cumulative distribution of computed and observed mesozooplankton in transition regions (RET1-RET5).

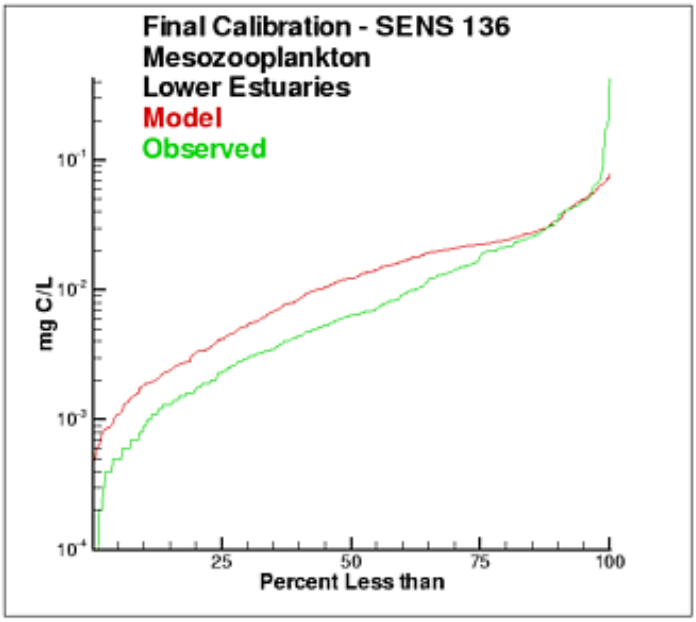

Figure 8-26. Cumulative distribution of computed and observed mesozooplankton in lower estuaries (LE1-LE5).

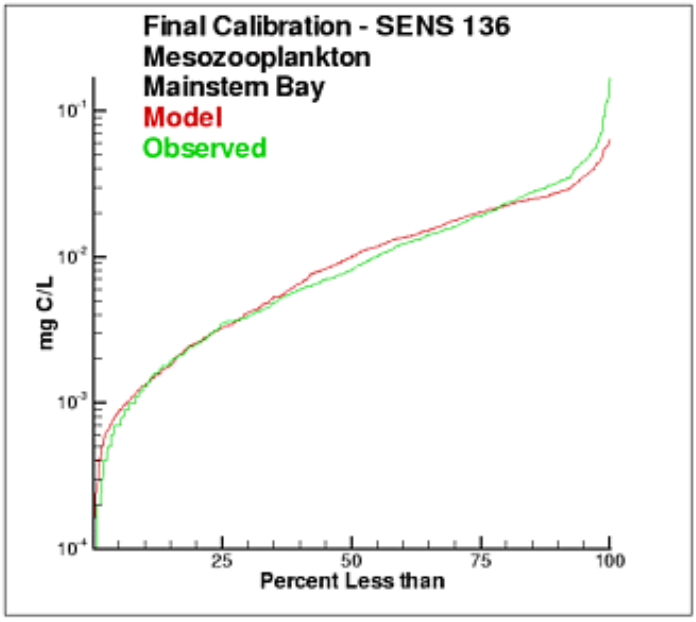

Figure 8-27. Cumulative distribution of computed and observed mesozooplankton in the mainstem bay (CB2-CB7).

Recommendations for Improvement

The present model represents zooplankton biomass within 50% to 100% of observed values, as determined by comparisons of cumulative distributions. Discrepancies between observations and model certainly indicate shortcomings in the model. A large portion of the discrepancies, however, must be attributed to observational methodology and to the variance inherent in the populations. A high degree of accuracy is unlikely to be obtained but more realism and, potentially, more accuracy can be added to the model. Suggestions for improvement range from parameter re-evaluation through complete model reformulation.

A basic improvement in the model is to distinguish, through parameter values, freshwater and estuarine zooplankton populations. Differentiation between individual tributaries may also be appropriate. Differentiation of freshwater and saltwater populations is readily justified and this approach will likely prove successful.

The effects of temperature on grazing and respiration should be reviewed and the cause of the mid-year population dips re-established. If the dips are due to the temperature functions, re-evaluation of the parameters that describe temperature effects on grazing is called for.

Another potential improvement is to add a second mesozooplankton group. One group would represent the winter-spring population; the second group would represent the summer population. No doubt, these two populations exist and can be differentiated. The second group can be readily included and adds realism to the model. The potential quantitative improvement in model computations cannot be foreseen.

The final improvement is the most difficult. Add age structure to the mesozooplankton model. As previously noted, adults in the present model instantaneously reproduce adults. In the most realistic model, adults would produce eggs. Eggs would hatch into larvae, mature into juveniles and, later, into adults. A model of this sort offers the highest probability of success in representing the time series of observed mesozooplankton. A multi-stage population model requires tremendous resources in programming, calibration, and execution. The additional effort is likely not worthwhile in the present multi-purpose model. The improvement is highly recommended if the present model is employed in an application that focuses largely on zooplankton.

References

Berggreen, U., Hansen, B. and Kiorboe, T. (1988). "Food size spectra, ingestion and growth of the copepod *Acartia tonsa* during development: implications for determination of copepod production," *Marine Biology*, 99, 341-352.

Brownlee, D., and Jacobs, F. (1987). "Mesozooplankton and microzooplankton in the Chesapeake Bay," *Contaminant Problems and Management of Living Chesapeake Bay Resources*, Majumdar, S., Hall, L., and Austin, H., eds. The Pennsylvania Academy of Science, Philadelphia.

Cerco, C., Johnson, B., and Wang, H. (2002). "Tributary refinements to the Chesapeake Bay model," ERDC TR-02-4, U.S. Army Engineer Research and Development Center, Vicksburg, MS.

Cerco, C., and Meyers, M. (2000). "Tributary refinements to the Chesapeake Bay Model," *Journal of Environmental Engineering*, 126(2), 164-174.

Cerco, C., and Cole, T. (1994). "Three-dimensional eutrophication model of Chesapeake Bay," Technical Report EL-94-4, U.S. Army Engineer Waterways Experiment Station, Vicksburg, MS.

Cerco, C., and Cole, T. (1993). "Three-dimensional eutrophication model of Chesapeake Bay," *Journal of Environmental Engineering*, 119(6), 1006- 10025.

Dagg, M. (1995). "Ingestion of phytoplankton by the micro- and mesozooplankton communities in a productive subtropical estuary," *Journal of Plankton Research*, 17(4), 845-857.

DiToro, D., and Matystik, W. (1980). "Mathematical models of water quality in large lakes part 1: Lake Huron and Saginaw Bay," EPA-600/3-80-056, Environmental Research Laboratory, Office of Research and Development, US Environmental protection Agency, Duluth MN.

DiToro, D., O'Connor, S., and Thomann, R. (1971). "A dynamic model of the phytoplankton population in the Sacramento-San Joaquin Delta," *Nonequilibrium systems in water chemistry*, American Chemical Society, Washington, DC, 131-180.

Durbin, E., Durbin, Ann G., Smayda, Thomas J., and Verity, Peter G. (1983). "Food limitation of production by adult *Acartia tonsa* in Naragansett Bay, Rhode Island," Limnology and Oceanography, 28(6), 1199-1213.

Ikeda, T. (1985). "Metabolic rates of epipelagic marine zooplankton as a function of body mass and temperature," *Marine Biology* 85, 1-11.

Kiorboe, T., and Neilson, T. (1994). "Regulation of zooplankton biomass and production in a temperate, coastal ecosystem. 1. Copepods," *Limnology and Oceanography*, 39(3), 493-507.

Paffenhofer, G., and Stearns, D. (1988). "Why is *Acartia tonsa* (Copepoda: Calanoida) restricted to nearshore environments?," *Marine Ecology Progress Series*, 42, 33-38.

Parsons, T., Takahashi, M., and Hargrave, B. (1984). *Biological Oceanographic Processes*, *3rd ed.*, Pergamon Press, Oxford.

Redfield, A., Ketchum, B., and Richards, F. (1966). "The influence of organisms on the composition of sea-water." *The Sea Volume II*. Interscience Publishers, New York, 26-48.

Roman, M., Gauzens, A., Rhinehart, W., and White, J. (1993). "Effects of low oxygen waters on Chesapeake Bay zooplankton," *Limnology and Oceanography* 38(8), 1603-1614.

Sellner, K., Brownlee, D., Bundy, M., Brownlee, S., and Braun, K. (1993). "Zooplankton grazing in a Potomac River cyanobacteria bloom," *Estuaries* 16(4), 859-872. White, J., and Roman M. (1992a). "Egg production by the calanoid copepod *Acartia tonsa* in the mesohaline Chesapeake Bay: the importance of food resources and temperature," *Marine Ecology Progress Series* 86, 239-249.

Thomann, R., and Fitzpatrick, J. (1982). "Calibration and verification of a mathematical model of the eutrophication of the Potomac Estuary," HydroQual Inc., Mahwah, NJ.

White, J., and Roman M. (1992b). "Seasonal study of grazing by metazoan zooplankton in the mesohaline Chesapeake Bay," *Marine Ecology Progress Series* 86, 251-261.

Analysis of Predation and Respiration on Primary Production

9

The N-P-Z Model

Start by considering a system consisting of a single nutrient form, one phytoplankton group, and one zooplankton group. This system is commonly referred to as an N-P-Z (nutrient, phytoplankton, zooplankton) model. The system is well-mixed, has a volume V, and is flushed at flow rate Q. For analytical purposes, examine the system at steady state. Employing the formulations for growth, respiration, and predation employed in the Chesapeake Bay Environmental Model Package yields the following equations:

$$\left[\frac{N}{Khb+N} \bullet G - Rb\right] \bullet B - P \bullet \left[\frac{B}{Khz+B}\right] \bullet Z - Phtb \bullet B^2 - \frac{Q}{V} \bullet B = 0 \quad (9\text{-}1)$$

$$\left[\frac{B}{Khz+B} \bullet P - Rz\right] \bullet Z - Phtz \bullet Z^2 - \frac{Q}{V} \bullet Z = 0 \quad (9\text{-}2)$$

$$- Anb \bullet \left[\frac{N}{Khb+N} \bullet G - Rb\right] \bullet B + Anb \bullet Rz \bullet Z + Anb \bullet Phtb \bullet B^2 + Anb \bullet Phtz \bullet Z^2 + \frac{Q}{V} \bullet [No - N] = 0 \quad (9\text{-}3)$$

in which:
N = nutrient concentration (g N m^{-3})
No = influent nutrient concentration (g N m^{-3})
B = algal biomass (g C m^{-3})
Z = zooplankton biomass (g C m^{-3})
G = algal growth rate (d^{-1})
P = zooplankton specific feeding rate (d^{-1})
Rb = algal respiration rate (d^{-1})
Rz = zooplankton respiration rate (d^{-1})
Khb = half-saturation constant for algal nutrient uptake (g N m^{-3})
Khz = half-saturation constant for algal uptake by zooplankton (g C m^{-3})
Phtb = constant representing predation on algae by higher trophic levels (m^3 g^{-1} C d^{-1})
Phtz = constant representing predation on zooplankton by higher trophic levels (m^3 g^{-1} C d^{-1})
Anb = nutrient fraction contained in algal and zooplankton biomass (g N g^{-1} C)
Q = volumetric flow through system (m^3 d^{-1})
V = system volume (m^3)

Gross primary production in the N-P-Z system is computed:

$$GPP = \frac{N}{Khb + N} \bullet G \bullet B \qquad (9\text{-}4)$$

in which:
GPP = gross primary production (g C m^{-3} d^{-1})

No exact analytical solution for the complete set of equations exists. Moreover the number of terms and constants confound examination of numerical solutions. We will proceed by examining successive sets of reduced equations. Analytical solution of these is often simplified by substitution of a mass-conservation equation for one of the three original equations. At steady state, the mass of nutrient flowing into the system must equal the mass flowing out:

$$Q \bullet No = Q \bullet (N + Anb \bullet B + Anb \bullet Z) \qquad (9\text{-}5)$$

Basic Parameter Set

The purpose of this analysis is to examine the effects of respiration and predation terms on system composition and production. The analysis employs the basic parameter set listed in Table 9-1. These parameters are characteristic of model parameters for a summer algal population grazed on by mesozooplankton. Nitrogen is the nutrient of interest. System residence time is ten days.

Table 9-1
Basic Parameter Set

Parameter	Value
No	1 g m^{-3}
G	2 d^{-1}
Rb	0.1 d^{-1}
Rz	0.5 d^{-1}
Khb	0.05 g m^{-3}
Khz	0.1 g m^{-3}
Anb	0.1 g g^{-1}
Q/V	0.1 d

Phytoplankton with Respiration Only

The simplest system contains phytoplankton and a nutrient with no predators or predation term. For this system, Equation 9-1 becomes:

$$\left[\frac{N}{Khb + N} \bullet G - Rb\right] \bullet B - \frac{Q}{V} \bullet B = 0 \tag{9-6}$$

Employing the mass-conservation equation, solutions are readily obtained:

$$B = \frac{No - N}{Anb} \tag{9-7}$$

$$N = \frac{Khb \bullet \left[Rb - \frac{Q}{V}\right]}{\left[G - Rb - \frac{Q}{V}\right]} \tag{9-8}$$

Since respiration is the independent variable, it is worthwhile to examine net production as well as gross:

$$NPP = \left[\frac{N}{Khb + N} \bullet G - Rb\right] \bullet B \tag{9-9}$$

in which:
NPP = net primary production (g C m^{-3} d^{-1})

Sensitivity to respiration is examined over the range 0.01 $d^{-1} \leq Rb \leq 1.8$ d^{-1} (larger values result in negative nutrient concentrations indicating no feasible steady state solution). As expected, algal biomass declines as respiration increases (Figure 9- 1). Nutrient concentration increases as algal biomass decreases.

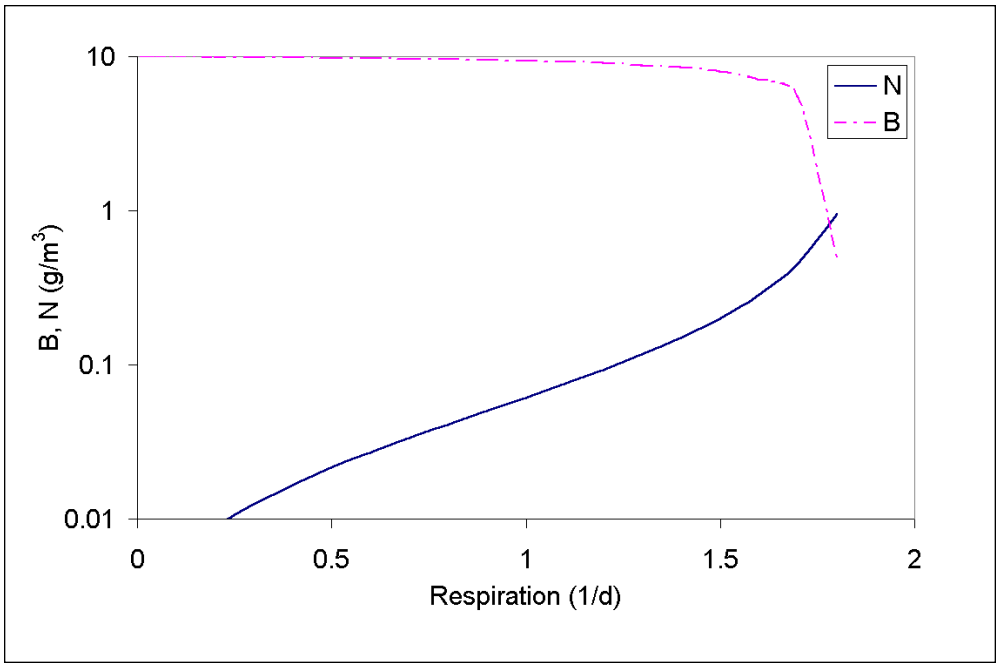

Figure 9-1. Algal biomass and nutrient concentration for a system with algal respiration only.

Gross production increases as a function of respiration over much of the range, then declines precipitously as respiration attains roughly 75% of the maximum growth rate (Figure 9-2). Net production also exhibits a curvilinear relationship to respiration with a peak at roughly 50% of the maximum growth rate. The potential increase in production along with respiration is counter-intuitive. Since biomass declines as respiration increases, a simultaneous decline in production is expected. The key is to realize that production is the product of biomass and the nutrient-

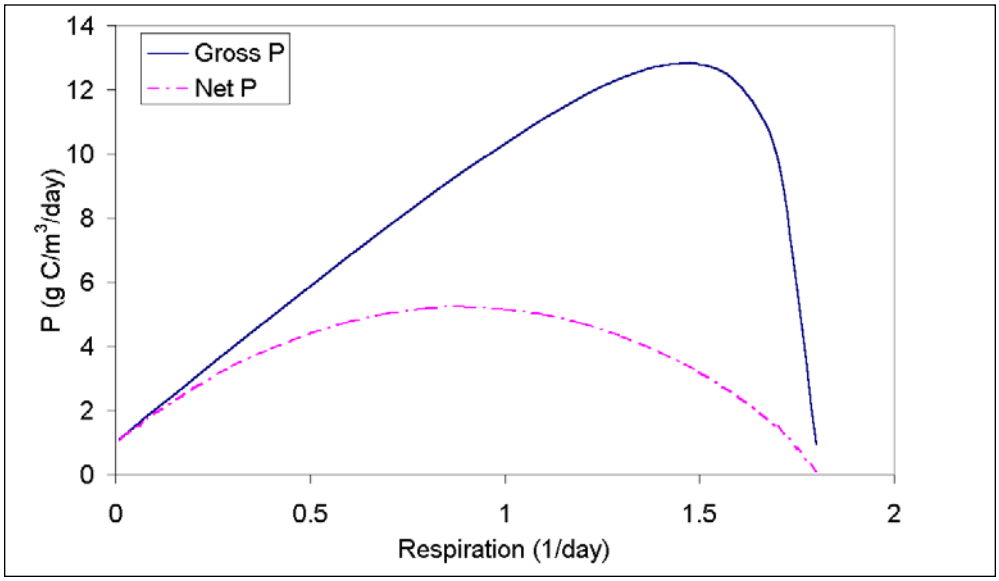

Figure 9-2. Gross and net primary production for a system with algal respiration only.

limited growth rate. As respiration increases over much of its range, nutrients are released from algal biomass, the nutrient limitation to growth is relaxed, and the product of growth and biomass increases.

Phytoplankton with Zooplankton

The system which includes zooplankton but no higher-order predation terms is examined next. The equation set includes Equation 9-2 (with Phtz = 0), Equation 9-3 (with Phtb = 0), and Equation 9-5. Algal biomass can be obtained directly from Equation 9-2:

$$B = \frac{Khz \bullet \left[Rz + \frac{Q}{V} \right]}{\left[P - Rz - \frac{Q}{V} \right]} \tag{9-10}$$

Zooplankton biomass is readily expressed from the mass-conservation relationship:

$$Z = \frac{No - N - Anb \bullet B}{Anb} \tag{9-11}$$

Nutrient concentration is expressed by a quadratic relationship:

$$a \bullet N^2 + b \bullet N + c = 0 \tag{9-12}$$

in which:

$$a = Rz + \frac{Q}{V} \tag{9-13}$$

$$b = Anb \bullet B \bullet [G - Rb] + Rz \bullet [-No + Anb \bullet B + Khb] + \frac{Q}{V} \bullet [-No + Khb] \tag{9-14}$$

$$c = Khb \bullet \left[-Anb \bullet Rb \bullet B - Rz \bullet No + Rz \bullet Anb \bullet B - \frac{Q}{V} \bullet No \right] \tag{9-15}$$

The solution for N is obtained via the classic quadratic formula. Since the relationship is quadratic, two values of N result for any parameter set. One value is consistently negative for the basic parameter set (Table 9-1) and is not considered. Negative values of B and/or Z can result, as well, from specification of predation rate, P. Sensitivity results are shown for the range 0.7 d^{-1} < P < 2 d^{-1} that results in feasible concentrations for all parameters.

Algal biomass decreases rapidly and approaches zero asymtotically as predation rate is increased from the minimum feasible value (Figure 9-3). Surprisingly, zooplankton biomass also diminishes as predation rate is increased. The steady state solution indicates maximum biomass occurs at low predation rates in which zooplankton slowly feed on a large algal standing stock.

Primary production responds in direct proportion to algal biomass (Figure 9-4). Maximum production occurs a minimum predation rate. The steady-state solution for the basic parameter set indicates little or no nutrient limitation and the small increase in nutrient concentration at higher predation rates has little effect on

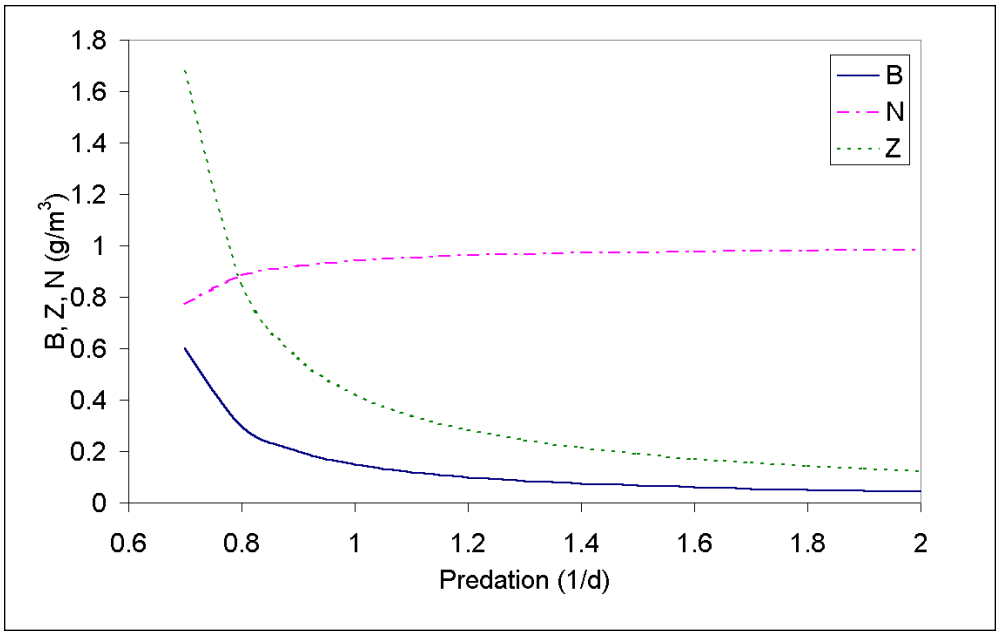

Figure 9-3. Algal biomass, zooplankton biomass, and nutrient concentration for a system with algae, zooplankton, and a nutrient.

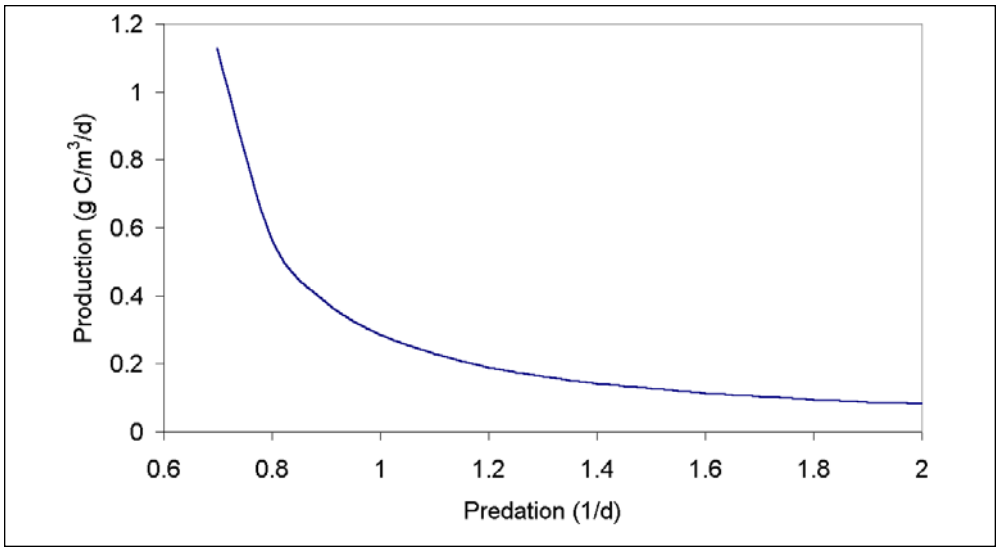

Figure 9-4. Gross primary production for a system with algae, zooplankton, and a nutrient.

growth. Consequently production, the product of nutrient-limited growth and biomass, responds primarily to changes in biomass.

Phytoplankton with Quadratic Predation

Predation by higher trophic levels (other than zooplankton) on phytoplankton is represented by a quadratic term in the algal mass-balance equation. The quadratic formulation is derived by assuming the biomass of predators is linearly proportional to the biomass of prey. The proportionality constant and the specific feeding rate are lumped into the parameter Phtb.

The effect of the quadratic predation term is examined by solving a simplified algal mass-balance equation:

$$\left[\frac{N}{Khb + N} \bullet G - Rb\right] \bullet B - Phtb \bullet B^2 - \frac{Q}{V} \bullet B = 0 \qquad (9\text{-}16)$$

and the mass-conservation equation.

The solution for algal biomass is quadratic with the following coefficients:

$$a = Anb \bullet Phtb \qquad (9\text{-}17)$$

$$b = Anb \bullet \left[-G + R\right] - Phtb \bullet \left[Khb + No\right] + Anb \bullet \frac{Q}{V} \qquad (9\text{-}18)$$

$$c = No \bullet G - \left[Khb + No\right] \bullet \left[Rb + \frac{Q}{V}\right] \qquad (9\text{-}19)$$

For the basic parameter set, one solution for B results in consistently negative nutrient concentrations. The second solution indicates an algal concentration that declines as predation rate increases (Figure 9-5). Mass conservation dictates nutrient concentration must increase as biomass decreases.

Despite the decrease in algal biomass, primary production increases as predation is raised from minimum levels (Figure 9-6). The increase occurs because the nutrient limit to production is relaxed as predation liberates nutrients from algal biomass. Consequently, the product of nutrient-limited growth rate and algal biomass increases despite the decrease in biomass. The increasing trend in production continues until nutrients are no longer limiting. That is, until N/(Khb + N) approaches unity. At that point, production declines in proportion to biomass.

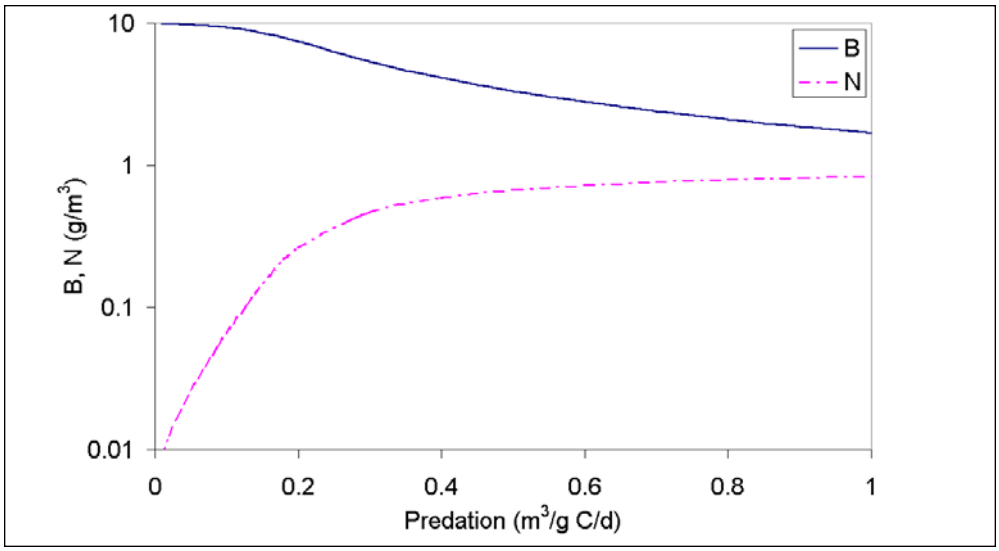

Figure 9-5. Algal biomass and nutrient concentration for a system with quadratic predation and no zooplankton.

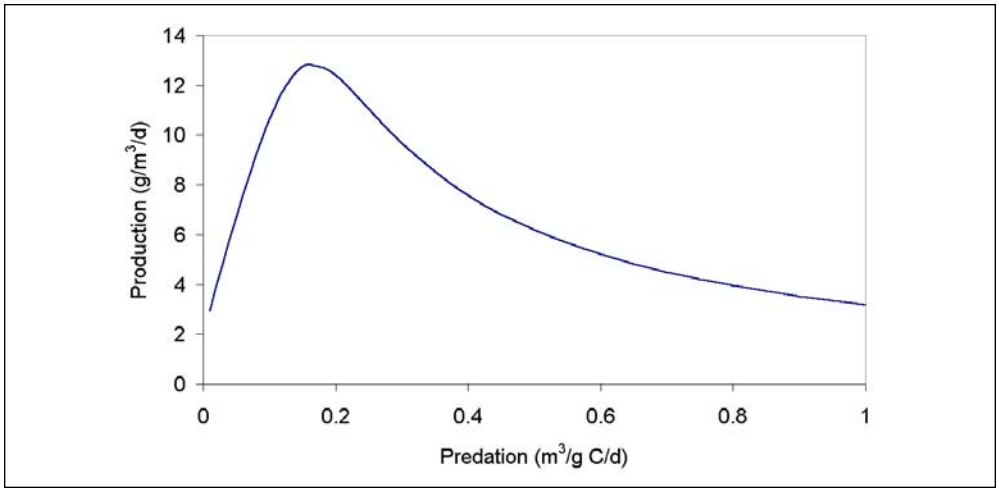

Figure 9-6. Gross primary production for a system with quadratic predation and no zooplankton.

Process-Based Primary Production Modeling in Chesapeake Bay 10

Introduction

Primary production models may be placed in two categories. We call the first category "observation based." Observation-based models employ observations of a photoadaptive variable, chlorophyll, and perhaps other quantities, to quantify depth-integrated production at the time and location of the observations. This class of models has been extensively reviewed by Behrenfield and Falkowski (1997).

We call the second category "process based." Process-based models quantify production as a function of computed algal biomass and computed processes that may include growth (as affected by temperature, nutrients, and light), respiration, predation, and transport. Parameters in process-based models are commonly assigned so that computations match one or more observed quantities. The assignment process is commonly denoted "calibration."

We have noticed that process-based models frequently encounter difficulty in simultaneously matching observed biomass and production. Most commonly, process-based models provide reasonable representations of biomass but fall short in computing production. Less commonly, the models adequately compute production but misrepresent biomass and/or growth-limiting nutrient concentration.

Doney et al. (1996) modeled phytoplankton, zooplankton, and nutrients in a subtropical region near Bermuda. They noted the model showed "skill in capturing the major features of the annual chlorophyll field." Computed primary production was almost always less than observed, however. Model performance was weakest "during late summer, when the model cannot supply enough nutrients to support the high production observed."

McGillicuddy et al. (1995) showed computed and observed vertical profiles of primary production in the North Atlantic. In ten of thirteen cases, primary production was under-computed at the surface, where light is abundant and nutrients are scarce. In deeper waters, where light is attenuated and nutrients are more abundant, model-data comparisons were much improved.

Fasham et al. (1990) applied a model that included phytoplankton, zooplankton, bacteria and nutrients to ocean Station "S" near Bermuda. They calibrated their

model to match observed primary production. During the summer, computed nitrate concentrations were much less than observed. Their simulations "greatly overestimated the phytoplankton biomass in the summer and autumn."

Moll (1998) simulated chlorophyll, phosphate, and primary production in the North Sea. Observed primary production was well-matched by the model. At several stations, the computed phosphate agreed with observed while at other stations computed exceeded observed by several hundred percent. At all stations, the computed concentration exceeded the specified half-saturation concentration by two to three times. Consequently, the effect of nutrient limitation on computed production was minimal.

Based on the cited studies, process-based models have the following characteristics. Observed production can be matched when light rather than nutrients appears to limit production (the North Atlantic at depths greater than 20 to 30 m, the North Sea as modeled). In regions where nutrients appear to be more limiting than light (North Atlantic surface waters, the sub-tropical Atlantic), observed production cannot be computed without compromising computations of algal biomass and nutrients (Ocean Station "S").

The objective of the present study is to create a process-based model of Chesapeake Bay that simultaneously matches observations of phytoplankton biomass, limiting nutrient concentration, light attenuation, and primary production.

Chesapeake Bay

Chesapeake Bay is an extensive estuarine system located on the east coast of the United States of America (Figure 10-1). The mainstem of the bay extends 300 km from the Susquehanna River, at the head, to the Atlantic Ocean, at the mouth. Mean depth of the mainstem bay is 8 m although a deep trench with depths to 50 m runs up the center. The Susquehanna provides the majority of freshwater flow (64 %) and nutrient loading (Malone et al. 1988, Boynton et al. 1995.) Virtually all remaining runoff and loads originate in several major western tributaries. The bay and major tributaries are classic examples of partially-mixed estuaries by Pritchard's (1967) classification.

The physics, chemistry, and biology of the bay have been extensively studied for decades. Significant studies relative to primary production include nutrient (Boynton et al. 1995) and carbon budgets (Kemp et al. 1997), examinations of nutrient limitations (Fisher et al. 1999, Malone et al. 1996, Fisher et al. 1992), and measures of primary production (Harding et al. 2002, Smith and Kemp 1995, Harding et al. 1986).

These studies describe a system in which maximum phytoplankton biomass and maximum production are out of phase. Peak biomass occurs during the spring bloom while peak production occurs concurrent with the summer temperature maximum (Malone et al. 1988, Smith and Kemp 1995, Malone et al. 1996, Harding et al. 2002). During the spring bloom, phosphorus and silica tend to be the limiting nutrients while nitrogen is the primary limiting nutrient in summer (Fisher et al. 1992, Malone et al. 1996, Fisher et al. 1999). Peak nitrogen loads delivered during spring runoff are coupled to summer production through a nutrient trapping mechanism. Nitrogen present is spring runoff is taken up during the phytoplankton bloom, deposited in bottom sediments, and recycled to the water column by temperature-induced diagenesis (Malone et al. 1988).

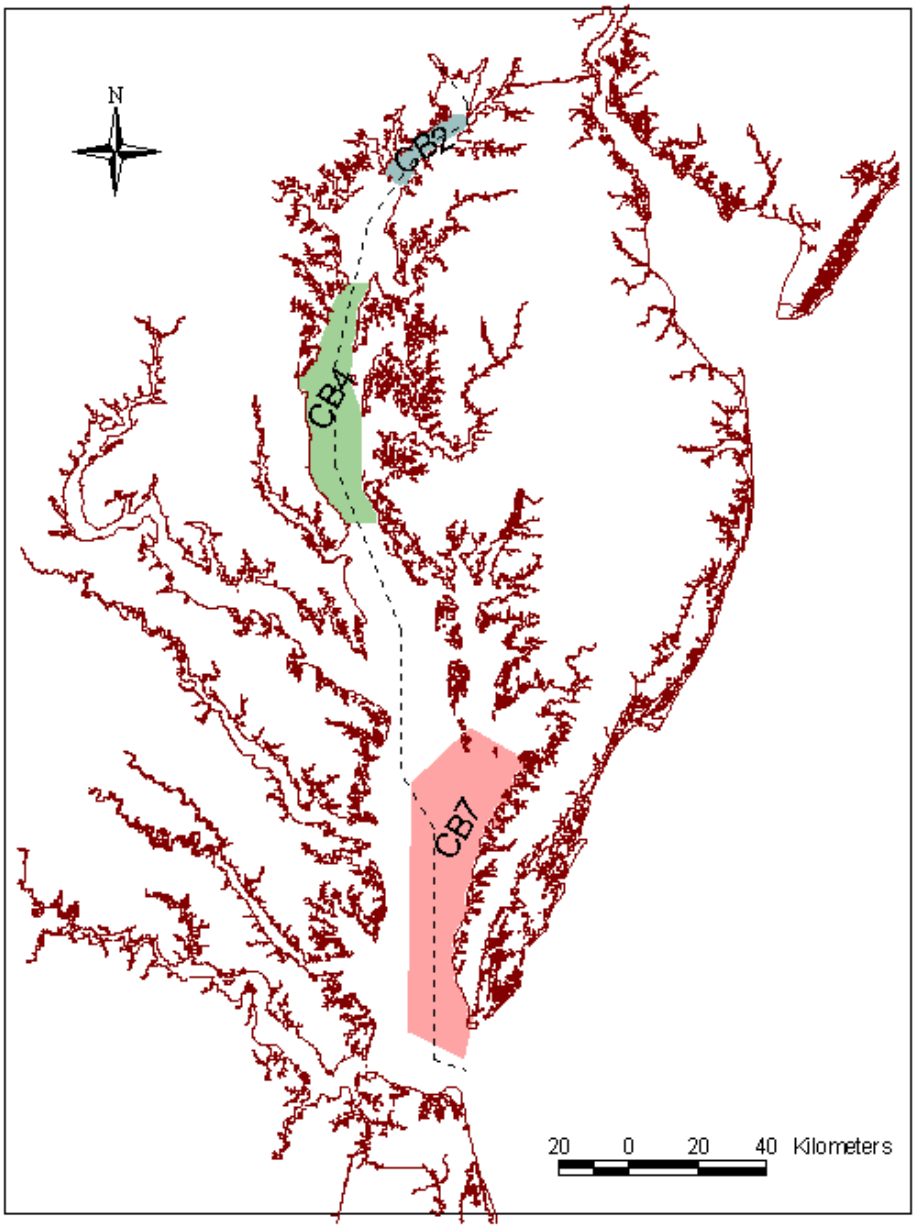

Figure 10-1. Chesapeake Bay showing longitudinal axis and segments CB2, CB4, CB7.

The Chesapeake Bay Environmental Model Package (CBEMP)

The CBEMP is a system of interactive models including a three-dimensional hydrodynamic model (Johnson et al. 1993, Wang and Johnson 2000), a eutrophication model (Cerco and Cole 1993, Cerco and Meyers 2000), and a sediment diagenesis model (DiToro 2001). The CBEMP was developed primarily to assist management of eutrophication within Chesapeake Bay and tributaries. Since management involves attaining water quality standards, emphasis in the model was placed on representing observed properties of the system including nutrients, chlorophyll, dissolved oxygen, and light attenuation.

By our classification, the CBEMP is a process-based model. Primary production calculations in initial versions of the CBEMP were consistent with characteristics of other process-based models (Cerco 2000). That is, computed production matched or exceeded observed in the turbidity maximum region of the bay where nutrients are abundant but light is limited. In the middle and lower portions of the bay, where light attenuation is diminished but nutrients are sparse relative to the turbidity maximum, computed production fell short of observed.

Management efforts in the Bay now require investigation of the effects of filter-feeders, especially oysters and menhaden, in reducing eutrophication (Gilmore et al. 2000) so that the amount of production available to these organisms must be represented. At the same time, water quality standards are becoming more stringent such that accurate computations of chlorophyll and nutrient concentrations cannot be ignored. Consequently, the CBEMP must now represent both properties of the system and production rates. The present chapter details formulation and parameterization of a model which meets these requirements.

Data Bases

Carbon Fixation

Phytoplankton photosynthetic rates were monitored 12 to 18 times per year at six stations in the upper portion of the mainstem bay (Figure 10-2). Methodology was a ^{14}C technique outlined by Strickland and Parsons (1972). Replicate surface-layer composite samples were incubated within six hours of collection. Incubation was conducted for an hour or more at in-situ temperature and constant, saturating, light intensity (> 250 $\mu E\ m^{-2}\ s^{-1}$). Carbon fixation rates were reported as $\mu g\ C\ L^{-1}\ h^{-1}$.

The data base for the period 1985–1994 was obtained from the US Environmental Protection Agency Chesapeake Bay Program monitoring data base http://www.chesapeakebay.net/data/index.htm. For consistency with other measures of production and model units, reported rates were converted to $g\ C\ m^{-3}\ d^{-1}$. This process involved units conversion only. Carbon fixation reported here as $g\ C\ m^{-3}\ d^{-1}$ represents a short-term, nearly-instantaneous rate and should not be confused with daily carbon fixed.

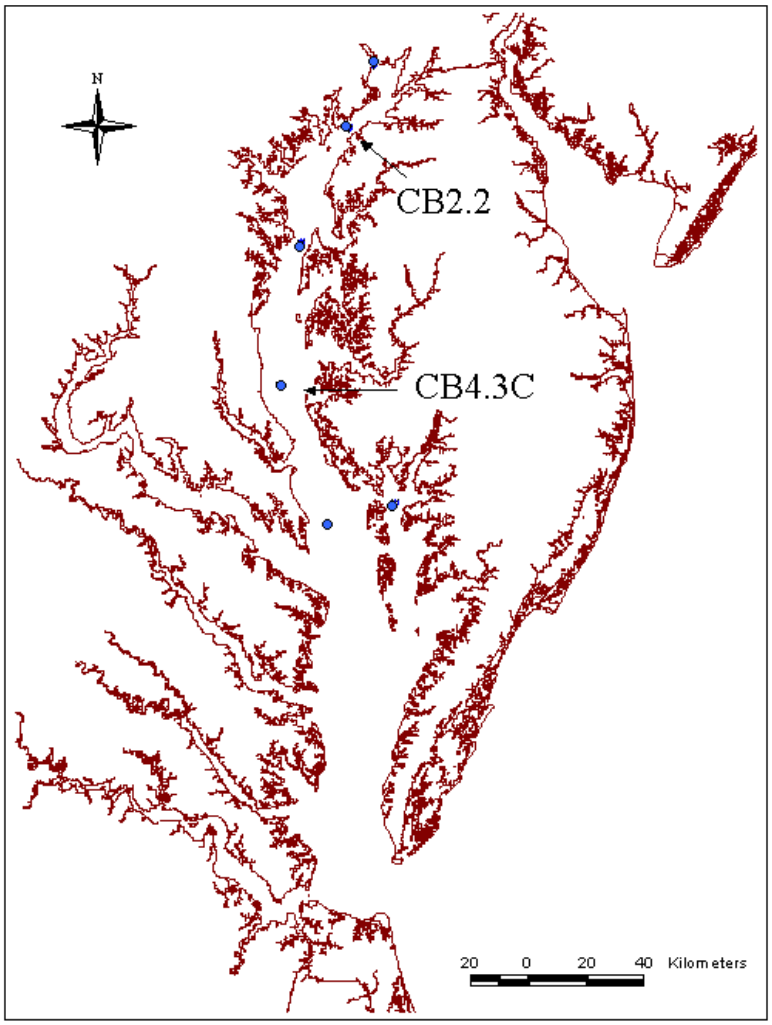

Figure 10-2. Location of sampling stations for carbon fixation, algal biomass, and carbon-to-chlorophyll ratio.

Net Primary Production

Net production was measured via a ^{14}C method conducted on deck at in- situ temperatures (Harding et al. 2002). Neutral density screening was used on a series of replicate bottles to simulate in-situ light intensity from the surface to 1% light level. Incubations were conducted over a 24-hour period. More than 160 observations, conducted throughout the mainstem bay (Figure 10-3), were provided for the period 1987–1994. Integral daily primary production was reported as mg C m^{-2}.

Gross Primary Production

Gross production was measured by an oxygen evolution method (Smith and Kemp 1995). Planktonic oxygen production was measured on deck, at in-situ temperature and five irradiance levels, over a period of four to five hours. Production of oxygen at each light level was normalized to chlorophyll. From these measures, a photosynthesis versus irradiance (P vs. I) curve was created. The P vs. I curve was employed to integrate production over the depth of the euphotic zone

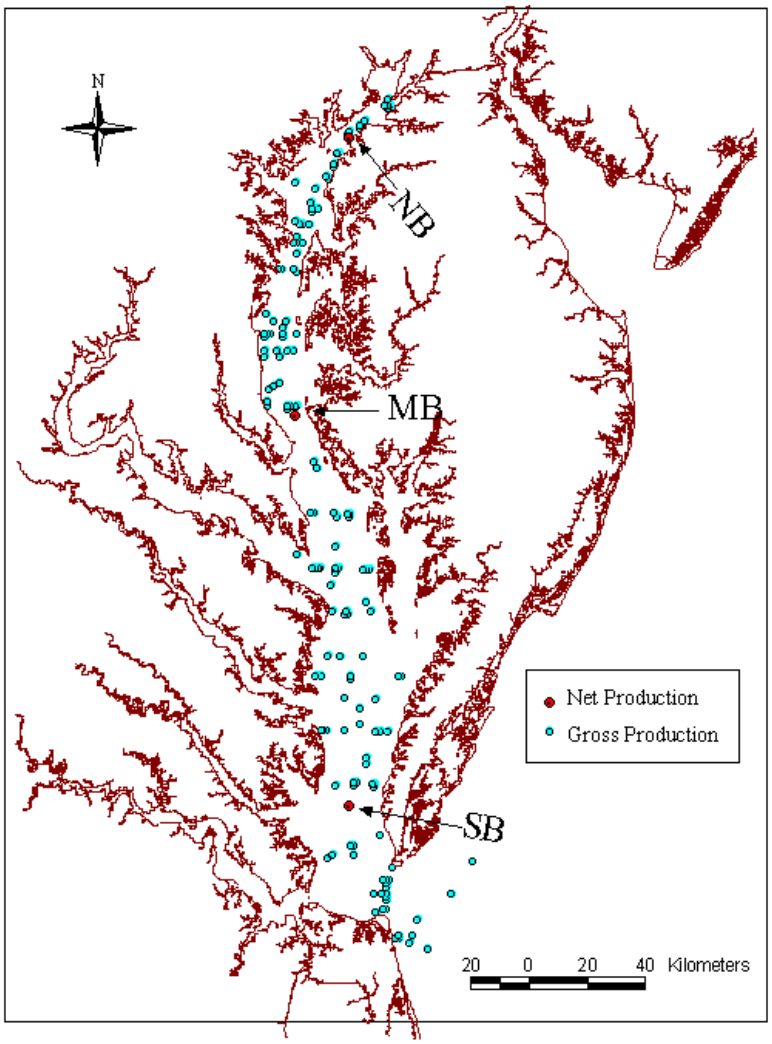

Figure 10-3. Location of gross and net primary production stations.

based on vertical attenuation of light and chlorophyll distribution. Daytime net production was estimated as the product of depth-integrated production (g O_2 m^{-2} h^{-1}) and number of daylight hours when incident light exceeded 100 µE m^{-2} s^{-1}.

Respiration rates were measured as decreases in oxygen concentration in bottles incubated for four to five hours in the dark at in-situ temperatures. Volumetric rates were multiplied by depth to obtain vertically integrated respiration rates. The summed absolute values of net daytime production and daytime respiration resulted in estimates of daily gross production.

Roughly 60 measures, collected in the interval 1989–1992, were collected at three stations (Figure 10-3). Daily gross production was reported as g O_2 m^{-2}. For consistency with other measures and with model units, gross production was converted to carbon equivalents using the relationship:

$$\frac{g\ O_2}{m^2} \bullet \frac{mol\ O_2}{32\ g\ O_2} \bullet \frac{mol\ C}{1.4\ mol\ O_2} \bullet \frac{12\ g\ C}{mol\ C} = \frac{g\ C}{m^2} \qquad (10\text{-}1)$$

The photosynthetic quotient was based on empirical comparisons of production measured by ^{14}C methods and by oxygen evolution (Harding et al. 2002).

Measures of light-saturated assimilation ratio, reported as $\mu g\ O_2\ \mu g^{-1}\ Chl\ h^{-1}$, were produced in the course of the production measures. For consistency with other measures and with model units, the assimilation ratio was converted to carbon equivalents using the relationship:

$$\frac{\mu g\ O_2}{\mu g\ Chl\ h} \bullet \frac{mol\ O_2}{32\ g\ O_2} \bullet \frac{mol\ C}{1.4\ mol\ O_2} \bullet \frac{12\ g\ C}{mol\ C} \bullet \frac{24\ h}{d} = \frac{g\ C}{g\ Chl\ d} \qquad (10\text{-}2)$$

Algal Biomass

Phytoplankton species counts and chlorophyll analyses were conducted at monthly intervals on composite samples collected at six locations in the upper bay (Figure 10-2). Depending on the depth of the water column, the composites represented "above pycnocline," "below pycnocline," or "water column." Observations were provided by the principal investigator (Richard Lacouture, Smithsonian Environmental Research Center). Prior to the data transfers, algal counts were converted to carbon using published values of biomass per individual. Division of carbonaceous biomass by chlorophyll concentration provided estimates of phytoplankton carbon-to-chlorophyll ratio.

Chlorophyll, Nutrients, and Associated Observations

The Chesapeake Bay Program conducted 12 to 18 sample cruises per year at 50 stations throughout the mainstem bay. Chlorophyll, nutrient concentrations, and other observations for calibrating the model were obtained from an on-line data base, http://www.chesapeakebay.net/data/index.htm. Methods and metadata are available at the same site.

Model Formulation

The eutrophication portion of the CBEMP considers three algal groups and two zooplankton groups. These groups interact with simulated cycles of carbon, nitrogen, phosphorus, and silica. Mass-balance equations for 24 state variables are solved on a three-dimensional computational grid of over 12,000 cells. Details provided here focus on recent developments required to simulate primary production. Additional descriptions of model formulation and applications may be found elsewhere (Cerco and Cole 1993, Cerco and Meyers 2000).

Conservation of Mass Equation

The foundation of CE-QUAL-ICM is the solution to the three- dimensional mass-conservation equation for a control volume. Control volumes correspond to cells on the model grid. CE-QUAL-ICM solves, for each volume and for each state variable, the equation:

$$\frac{\delta\ V_j \bullet C_j}{\delta\ t} = \sum_{k=1}^{n} Q_k \bullet C_k + \sum_{k=1}^{n} A_k \bullet D_k \bullet \frac{\delta\ C}{\delta\ Xk} + \Sigma\ S_j \qquad (10\text{-}3)$$

in which:
V_j = volume of j^{th} control volume (m^3)
C_j = concentration in j^{th} control volume (g m^{-3})
t, x = temporal and spatial coordinates
n = number of flow faces attached to j^{th} control volume
Q_k = volumetric flow across flow face k of j^{th} control volume (m^3 s^{-1})
C_k = concentration in flow across face k (g m^{-3})
A_k = area of flow face k (m^2)
D_k = diffusion coefficient at flow face k (m^2 s^{-1})
S_j = external loads and kinetic sources and sinks in j^{th} control volume (g s^{-1})

Solution to the mass-conservation equation is via the finite-difference method. For notational simplicity, the transport terms are dropped in the succeeding reporting of kinetics formulations.

Phytoplankton Kinetics

The model simulates three algal groups. The blue-green algal group represents the *Microcystis* that are found only in the tidal freshwater portion of the Potomac River, one of the western tributaries. The spring algal group comprises the diatoms that dominate saline waters from January to May. The summer algal group represents the assemblage of flagellates, diatoms and other phytoplankton that dominate the system from May to December. Each algal group is represented by identical formulations. Differences between groups are determined by parameter specifications.

Algal sources and sinks in the conservation equation include production, respiration, predation, and settling. These are expressed:

$$\frac{\delta}{\delta t} B = \left(G - R - Wa \frac{\delta}{\delta z} \right) B - PR \qquad (10\text{-}4)$$

in which:
B = algal biomass, expressed as carbon (g C m^{-3})
G = growth (d^{-1})
R = respiration (d^{-1})
Wa = algal settling velocity (m d^{-1})
PR = predation (g C m^{-3} d^{-1})

Production

Production by phytoplankton is determined by the intensity of light, by the availability of nutrients, and by the ambient temperature.

Light

The influence of light on phytoplankton production is represented by a chlorophyll-specific production equation (Jassby and Platt 1976):

$$P^B = P^B m \frac{I}{\sqrt{I^2 + Ik^2}} \qquad (10\text{-}5)$$

in which:
P^B = production (g C g^{-1} Chl d^{-1})
P^Bm = maximum photosynthetic rate (g C g^{-1} Chl d^{-1})
I = irradiance (E m^{-2} d^{-1})

Parameter Ik is defined as the irradiance at which the initial slope of the production vs. irradiance relationship (Figure 10-4) intersects the value of P^Bm:

$$Ik = \frac{P^B m}{\alpha} \tag{10-6}$$

in which:
α = initial slope of production vs. irradiance relationship (g C g^{-1} Chl (E m^{-2})$^{-1}$)

Chlorophyll-specific production rate is readily converted to carbon-specific growth rate, for use in Equation 10-4, through division by the carbon-to-chlorophyll ratio:

$$G = \frac{P^B}{CChl} \tag{10-7}$$

in which:
CChl = carbon-to-chlorophyll ratio (g C g^{-1} chlorophyll a)

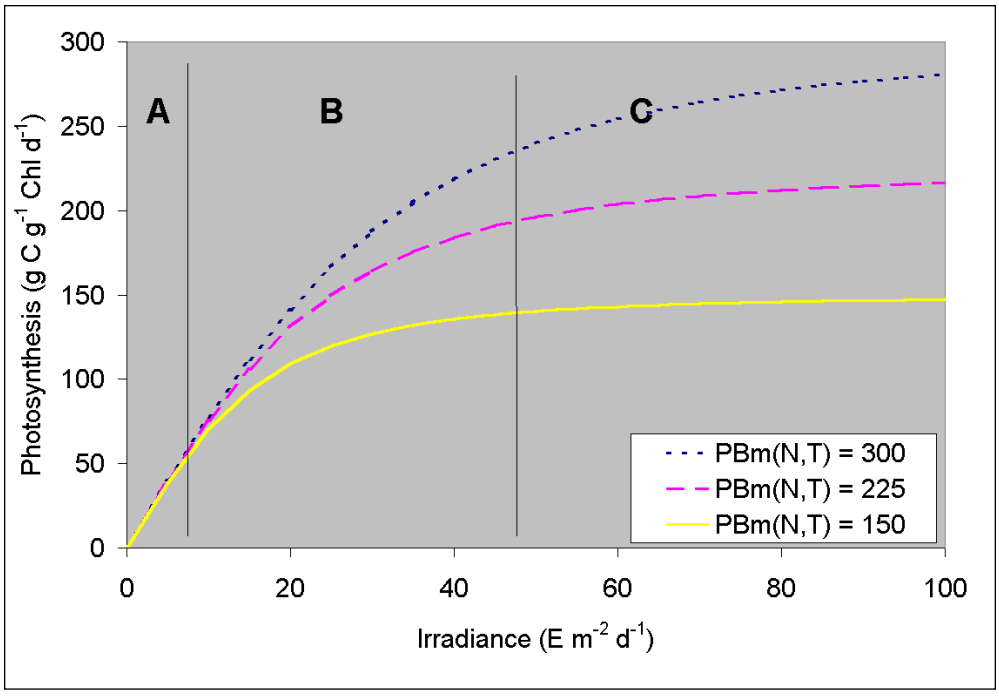

Figure 10-4. Production versus irradiance relationship showing regions of light limitation, nutrient limitation, and mixed limitations.

Nutrients

Carbon, nitrogen, and phosphorus are the primary nutrients required for algal growth. Diatoms require silica, as well. Inorganic carbon is usually available in excess and is not considered in the model. The effects of the remaining nutrients on growth are described by the formulation commonly referred to as "Monod kinetics" (Monod 1949):

$$f(N) = \frac{D}{KHd + D} \tag{10-8}$$

in which:
f(N) = nutrient limitation on algal production ($0 \leq f(N) \leq 1$)
D = concentration of dissolved nutrient (g m^{-3})
KHd = half-saturation constant for nutrient uptake (g m^{-3})

Temperature

Algal production increases as a function of temperature until an optimum temperature or temperature range is reached. Above the optimum, production declines until a temperature lethal to the organisms is attained. Numerous functional representations of temperature effects are available. Inspection of growth versus temperature curves indicates a function similar to a Gaussian probability curve provides a good fit to observations:

$$f(T) = e^{-KTg1 \bullet (T - Topt)^2} \text{ when } T \leq Topt$$
$$= e^{-KTg2 \bullet (Topt - T)^2} \text{ when } T > Topt \tag{10-9}$$

in which:
T = temperature (°C)
Topt = optimal temperature for algal growth (°C)
KTg1 = effect of temperature below Topt on growth ($°C^{-2}$)
KTg2 = effect of temperature above Topt on growth ($°C^{-2}$)

Constructing the Photosynthesis vs. Irradiance Curve

A production versus irradiance relationship is constructed for each model cell at each time step. First, maximum photosynthetic rate under ambient temperature and nutrient concentrations is determined:

$$P^B m(N,T) = P^B m \bullet f(T) \bullet \frac{D}{KHd + D} \tag{10-10}$$

in which:
$P^B m(N,T)$ = Maximum photosynthetic rate at ambient temperature and nutrient concentrations (g C g^{-1} Chl d^{-1})

The single most limiting nutrient is employed in determining the nutrient limitation.

Next, parameter Ik is derived from Equation 10-6. Finally, the production vs. irradiance relationship is constructed using $P^B m(N,T)$ and Ik. The resulting production versus irradiance curve exhibits three regions (Figure 10-4). For I >> Ik, the value of the term $I / (I^2 + Ik^2)^{½}$ approaches unity and temperature and nutrients are the primary factors that influence production. For I << Ik, production is determined solely by and irradiance I. In the region where the initial slope of the production versus irradiance curve intercepts the line indicating production at optimal illumination, I Ik, production is determined by the combined effects of temperature, nutrients, and light.

Respiration

Two forms of respiration are considered in the model: photo-respiration and basal metabolism. Photo-respiration represents the release or leakage of carbon fixed during the photosynthetic process (Goldsworthy 1970) and is represented as a fixed fraction of production. Basal metabolism is the continuous energy expenditure to maintain basic life processes. In the model, metabolism is considered to be an exponentially increasing function of temperature. Total respiration is represented:

$$R = Presp \bullet G + BMr \bullet e^{KTb \bullet (T - Tr)} \qquad (10\text{-}11)$$

in which:
Presp = photo-respiration ($0 \leq Presp \leq 1$)
BMr = metabolic rate at reference temperature Tr (d^{-1})
KTb = effect of temperature on metabolism ($^oC^{-1}$)
Tr = reference temperature for metabolism (^oC)

Predation

The predation term includes the activity of zooplankton, filter-feeding benthos, and other pelagic filter feeders including planktivorous fish. Formulation and results of the zooplankton and benthos computations may be found in Cerco and Meyers (2000). Predation by other planktivores is modeled by assuming predators clear a specific volume of water per unit biomass:

$$PR = F \bullet B \bullet M \qquad (10\text{-}12)$$

in which:
F = filtration rate ($m^3\ g^{-1}$ predator C day^{-1})
M = planktivore biomass (g C m^{-3})

Detailed specification of the spatial and temporal distribution of the predator population is impossible. One approach is to assume predator biomass is proportional to algal biomass, $M = \gamma B$, in which case Equation 10-12 can be rewritten:

$$PR = \gamma \bullet F \bullet B^2 \qquad (10\text{-}13)$$

Since neither γ nor F are known precisely, the logical approach is to combine their product into a single unknown determined during the model calibration procedure. Effect of temperature on predation is represented with the same formulation as the effect of temperature on respiration. The final representation of predation, including zooplankton, is:

$$PR = \frac{B}{KHsz + B} \bullet RMsz \bullet SZ + \frac{B}{KHlz + B} \bullet RMlz \bullet LZ + Phtl \bullet B^2 \quad (10\text{-}14)$$

in which:
RMsz = microzooplankton maximum ration (g algal C g^{-1} zoo C d^{-1})
SZ = microzooplankton biomass (g C m^{-3})
KHsz = half saturation concentration for carbon uptake by microzooplankton (g C m^{-3})
RMlz = mesozooplankton maximum ration (g algal C g^{-1} zoo C d^{-1})
LZ = mesozooplankton biomass (g C m^{-3})
KHlz = half saturation concentration for carbon uptake by mesozooplankton (g C m^{-3})
Phtl = rate of predation by other planktivores (m^3 g^{-1} C d^{-1})

Predation by filter-feeding benthos is represented as a loss term only in model cells that intersect the bottom.

The Model Nitrogen Cycle

Nitrogen is first divided into available and unavailable fractions. Available refers to employment in algal nutrition. Two available forms are considered: reduced and oxidized nitrogen. Reduced nitrogen includes ammonium and urea. Nitrate and nitrite comprise the oxidized nitrogen pool. Both reduced and oxidized nitrogen are utilized to fulfill algal nutrient requirements. The primary reason for distinguishing the two is that ammonium is oxidized by nitrifying bacteria into nitrite and, subsequently, nitrate. This oxidation can be a significant sink of oxygen in the water column and sediments.

In the presence of multiple nitrogenous nutrients, ammonium and urea are utilized first (McCarthy et al. 1977). In the model, the preference for reduced nitrogen is expressed by an empirical function (Thomann and Fitzpatrick 1982) with two limiting values (Figure 10-5). When oxidized nitrogen is absent, the preference for reduced nitrogen is unity. When reduced nitrogen is absent, the preference is zero. In the presence of reduced and oxidized nitrogen, the preference depends on the abundance of both forms relative to the half-saturation constant for nitrogen uptake. When both forms are abundant, the preference for reduced nitrogen approaches unity. When reduced nitrogen is scarce but oxidized nitrogen is abundant, the preference decreases in magnitude and a significant fraction of algal nitrogen requirement comes from oxidized nitrogen.

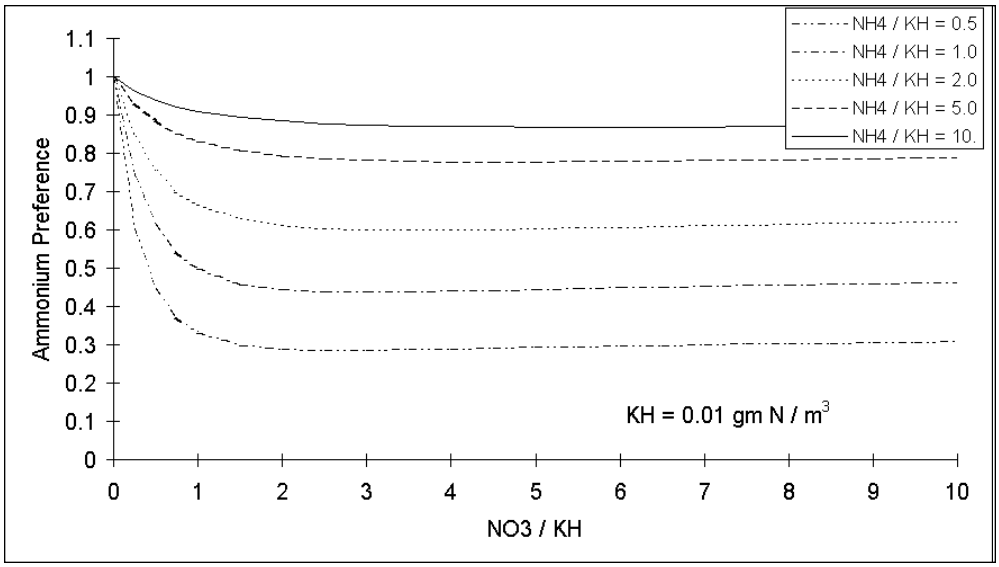

Figure 10-5. Nitrogen preference function.

Irradiance

Irradiance at the water surface is evaluated at each model time step by fitting a sin function to daily total irradiance. Irradiance declines exponentially with depth below the surface. The diffuse attenuation coefficient, Kd, is computed as a function of color and concentrations of organic and mineral solids (Cerco and Meyers 2000).

Primary Production Equations

Computed production, for comparison with the observations, was derived from the model by three relationships.

Carbon Fixation

Carbon fixation measures were conducted at ambient temperature and nutrient concentrations and saturating light intensity. The appropriate relationship for comparison with the observations is:

$$Cfix = \left(\frac{P^B m}{CChl} \bullet f(N) \bullet f(T) \bullet (1 - Presp) - BMr(T) \right) \bullet B \qquad (10\text{-}15)$$

in which:
Cfix = carbon fixed (g C m^{-3} d^{-1})

Algal biomass, nutrient limitation, temperature effects, and carbon-to-chlorophyll ratio are all based on model computations at the sample location.

Gross Primary Production

The relationship for depth-integrated daily gross primary production is:

$$GPP = \int_0^D \int_0^{Z_{1\%}} \frac{P^B m}{CChl} \bullet \frac{I(t)}{\sqrt{I(t)^2 + Ik^2}} \bullet f(N) \bullet f(T) \bullet B \bullet dz \bullet dt \qquad (10\text{-}16)$$

in which:
GPP = daily gross primary production (g C m^{-2})
D = daylength (1 day)
$Z_{1\%}$ = depth at which irradiance is 1% of surface irradiance (m)
I(t) = time-varying irradiance (E m^{-2} d^{-1})

Algal biomass, nutrient limitation, temperature effects, irradiance, and carbon-to-chlorophyll ratio are all based on model computations at the sample location and at 1.5 m depth increments.

Net Primary Production

The relationship for depth-integrated daily net primary production is:

$$NPP = \int_0^D \int_0^{Z_{1\%}} \left(\left(\frac{P^B m}{CChl} \bullet \frac{I(t)}{\sqrt{I(t)^2 + Ik^2}} \bullet f(N) \bullet f(T) \right) \bullet (1 - Presp) - BMr(T) \right) \bullet B \bullet dz \bullet dt \qquad (10\text{-}17)$$

in which:
NPP = daily net primary production (g C m^{-2})

Algal biomass, nutrient limitation, temperature effects, irradiance, and carbon-to-chlorophyll ratio are all based on model computations at the sample location and at 1.5 m depth increments.

Parameter Evaluation

Parameters are reported here for the spring and summer algal groups which inhabit the mainstem of Chesapeake Bay. Model parameters are based on published values reported in a variety of units. For comparison with the model, reported parameters are converted to model units of meter, gram, and day.

Algal Production Parameters

Maximum photosynthetic rates and their temperature dependence were based on observations collected by Harding et al. (1986) and by Smith and Kemp (1995). The observed rates were subject to in-situ nutrient limitations. Since the maximum photosynthetic rates employed by the model are for nutrient-unlimited situations, parameter values (Table 10-1) were specified at the upper range of reported rates (Figure 10-6) based on the assumption that lower observations represented nutrient-limited conditions.

Table 10-1
Phytoplankton Parameters

Symbol	Definition	Units	Spring Group	Summer Group
Wa	settling velocity	$m\ d^{-1}$	0.1	0.1
PBm	maximum photosynthetic rate	$g\ C\ g^{-1}\ Chl\ d^{-1}$	300	350
α	initial slope of production vs. irradiance relationship	$g\ C\ g^{-1}\ Chl\ (E\ m^{-2})^{-1}$	8	8
Khn	half-saturation concentration for nitrogen uptake	$g\ N\ m^{-3}$	0.025	0.025
Khp	half-saturation concentration for phosphorus uptake	$g\ P\ m^{-3}$	0.0025	0.0025
Khs	half-saturation concentration for silica uptake	$g\ S\ m^{-3}$	0.03	
Topt	optimal temperature for algal growth	^{o}C	16	25
KTg1	effect of temperature below Topt on growth	$^{o}C^{-2}$	0.0018	0.0035
KTg2	effect of temperature above Topt on growth	$^{o}C^{-2}$	0.006	0
Presp	photo-respiration		0.25	0.25
BMr	metabolic rate at reference temperature	d^{-1}	0.01	0.02
Tr	reference temperature for metabolism	^{o}C	20	20
KTb	effect of temperature on metabolism	$^{o}C^{-1}$	0.0322	0.0322
Phtl	rate of predation by other planktivores	$m^{3}\ g^{-1}\ C\ d^{-1}$	0.1 to 0.2	0.5 to 2

continued

Table 10-1 *(continued)*
Phytoplankton Parameters

a	minimum carbon-to-chlorophyll ratio	g C g^{-1} Chl	30	30
b	incremental carbon-to-chlorophyll ratio	g C g^{-1} Chl	150	90
c	effect of light attenuation on carbon-to-chlorophyll ratio	m	1.18	1.19

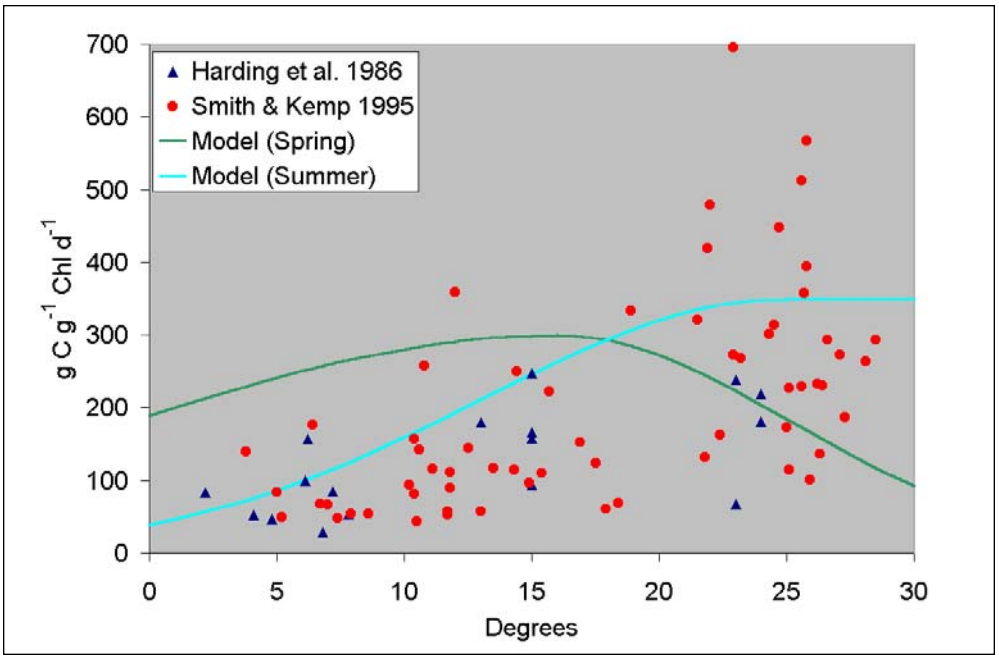

Figure 10-6. Observed and modeled photosynthetic rates.

.

Respiration

Laws and Chalup (1990) report values of 0.03 d^{-1} for basal metabolism and 0.28 for photo-respiration. Other investigators have found that from 15% to 35% of carbon fixed is lost to metabolism (Groeger and Kimmel 1989; Kiddon et al. 1995). Model values (Table 10-1) were based on these reports.

Predation

Parameters for the zooplankton model have been reported elsewhere in this report. The parameter that determines predation by other planktivores (Table 10-1) was determined empirically to fit model results to observed algal biomass and production. Substantially lower rates were used for the spring algal group than for the summer algal group. The differential predation rates were based on the life cycle of Atlantic menhaden (Durbin and Durbin 1975; Rippetoe 1993; Luo et al.

2001), a species represented by the predation term. Menhaden enter the bay in spring and initially feed almost entirely on zooplankton. As they mature, gill rakers develop to filter phytoplankton. Menhaden leave the bay in late fall and spawn in coastal ocean waters. Consequently, predation pressure exerted by menhaden on phytoplankton occurs primary in summer and early autumn, concurrent with dominance by the modeled summer algal group.

Algal Composition

Carbon-to-Chlorophyll Ratio. Carbon-to-chlorophyll ratios obtained from the enumerations and chlorophyll analyses varied over an enormous range. The extreme values were well outside the ratios reported for algal cultures which range from 20:1 to 333:1 (Cloern et al. 1995). More then 70% of the enumerations indicated carbon-to-chlorophyll ratios less than 75:1 and the most common values were between 25:1 and 50:1 (Figure 10-7).

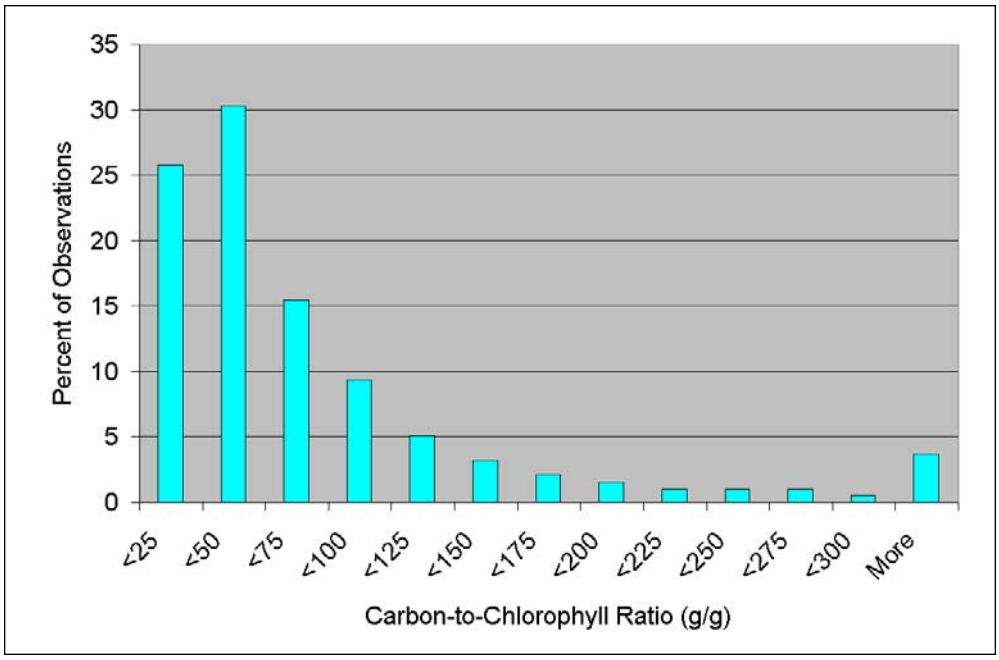

Figure 10-7. Histogram of observed carbon-to-chlorophyll ratios.

We noted two characteristics of the data set. First, carbon-to-chlorophyll ratio was related to disk visibility (Figure 10-8) and, therefore, inversely related to light attenuation. For example, at Station CB2.2, in the turbidity maximum, median carbon-to-chlorophyll ratio was 33 while median disk visibility was 0.7 m. At Station CB5.2, roughly 140 km below the turbidity maximum, median carbon-to-chlorophyll ratio was 89 while median disk visibility was 1.8 m. Summary of reports of algae grown in culture indicates carbon-to-chlorophyll ratio is proportional to irradiance (Cloern et al. 1995). This proportionality was apparent in our data set as an increase in carbon-to-chlorophyll ratio as a function of depth of light penetration into the water column.

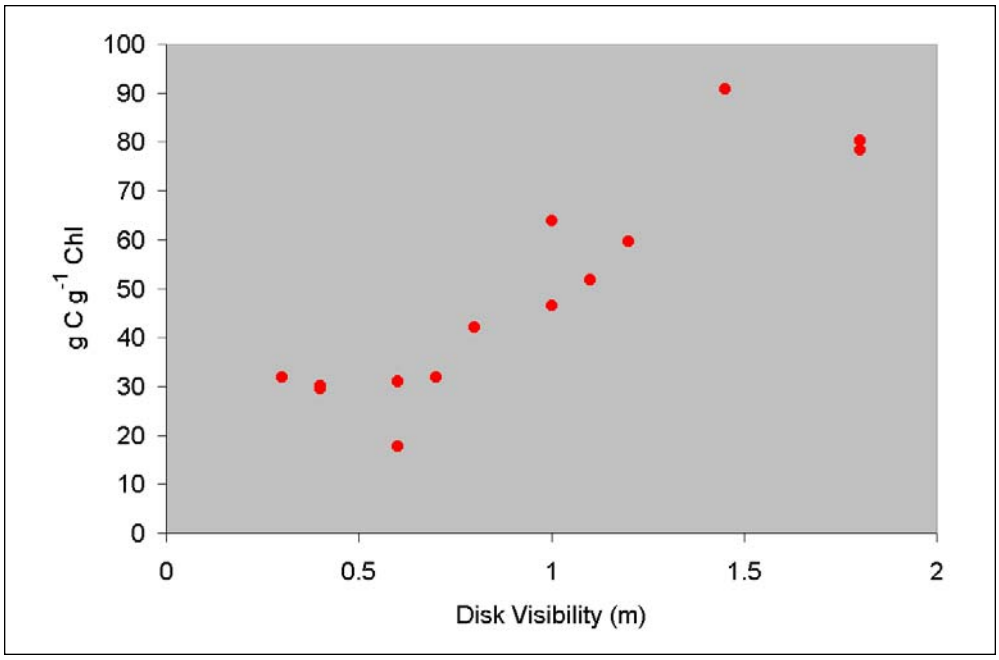

Figure 10-8. Algal carbon-to-chlorophyll ratio versus disk visibility. Data points represent median values at 14 stations in the bay and adjacent tributaries.

A second characteristic, apparent at stations that experience a spring algal bloom, was a higher carbon-to-chlorophyll ratio during the bloom months (February–May) versus other months (Figure 10-9). The difference was too large to assign to differences in disk visibility in spring versus other months. We attributed the distinction in carbon-to-chlorophyll ratio between bloom months and other months as a taxonomic property of bloom species versus other species (Chan 1980).

We desired to represent carbon-to-chlorophyll ratio with a function that was consistent with available observations and with quantities computed in the model. We proceeded as follows. The carbon-to-chlorophyll ratios were paired with disk visibility measures collected on the same day. These were obtained from the Chesapeake Bay Program monitoring data base. This produced a set of 2462 paired observations. Disk visibility was converted to light attenuation via the relationship:

$$Ke = \frac{1.4}{DV} \qquad (10\text{-}18)$$

in which:
Ke = diffuse light attenuation (m^{-1})
DV = disk visibility (m)

Regression was used to evaluate parameters (Table 10-1) in a proposed relationship:

$$CChl = a + b \bullet e^{-c \bullet Ke} \qquad (10\text{-}19)$$

in which:
a = minimum carbon-to-chlorophyll ratio (g C g^{-1} Chl)
b = incremental carbon-to-chlorophyll ratio at zero light attenuation (g C g^{-1} Chl)
c = effect of light attenuation on carbon-to-chlorophyll ratio (m)

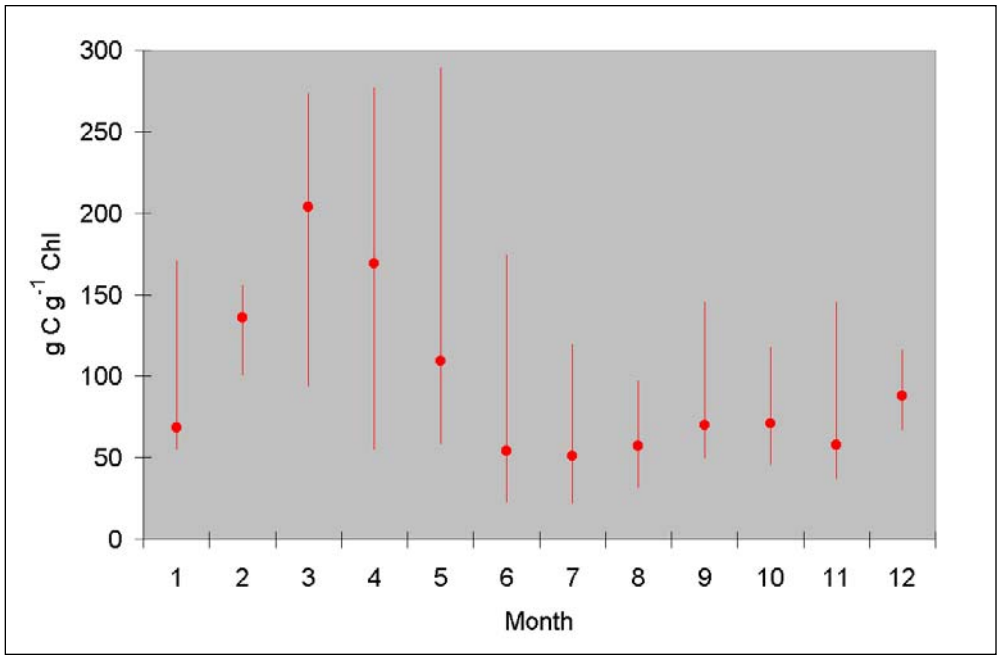

Figure 10-9. Carbon-to-chlorophyll ratio at station CB5.2 in the mainstem bay. Data points are monthly median, 10th and 90th percentiles.

Observations characteristic of the spring bloom (February–May at mainstem and lower estuary stations) were treated separately from the rest resulting in distinct relationships for the model spring and summer algal groups (Table 10-1).

Nutrients. Algal nitrogen-to-carbon and phosphorus-to-carbon ratios were initially set to Redfield composition (Redfield et al. 1966). Adjustments were made to improve model fit to observed chlorophyll, nutrients, and production (Table 10-1). Nitrogen composition remains close to Redfield composition while the phosphorus stoichiometry of the spring group reflects the limiting nature of this nutrient during the spring bloom. The silica fraction of the spring group (Table 10-1) was specified within the range of reported values (D'Elia et al. 1983; Parsons et al. 1984). Silica fraction of the summer group (Table 10-1) was specified at a low value since diatoms comprise only a fraction of the summer species.

Nutrient Uptake. Reported half-saturation concentrations for algal nutrient uptake in Chesapeake Bay are 0.001 to 0.008 g N m^{-3} for ammonium (Wheeler et al. 1982) and 0.003 to 0.053 g P m^{-3} for phosphate (Taft et al. 1975). Both studies comprised a limited number of observations conducted over a short term. The half-saturation concentrations reported by Wheeler et al. (1982) are much less than the range of values commonly reported for neritic phytoplankton. Means of values summarized by Eppley et al. (1969) are in the range 0.028 to 0.052 g N m^{-3}, depending on substrate composition and plankton division. Model half-saturation constants, 0.025 g N m^{-3} and 0.0025 g P m^{-3}, correspond with the lower end of reported ranges (Eppley et al. 1969; Taft et al. 1975).

The model half-saturation concentration for silica uptake by spring diatoms, 0.03 g Si m^{-3}, is well within reported values, 0.02 to 0.082 g Si m^{-3}, for oceanic diatoms (Davis et al. 1978; Parsons et al. 1984). A lower half saturation concentration was

specified for the summer group to emphasize nitrogen limitation during this season (Fisher et al. 1999).

Algal Settling Rates. Reported algal settling rates typically range from 0.1 to 5 m d^{-1} (Bienfang et al.1982; Riebesell 1989; Waite et al. 1992). In part, this variation is a function of physical factors related to algal size, shape, and density (Hutchinson 1967). The variability also reflects regulation of algal buoyancy as a function of nutritional status (Bienfang et al. 1982; Richardson and Cullen 1995) and light (Waite et al. 1992). The algal settling rate employed in the model represents the net effect of all factors that result in downward transport of phytoplankton. The settling rate employed, 0.1 m d^{-1}, was derived through tuning of observed chlorophyll and nutrient concentrations and is at the lower end of reported rates.

Results

The CBEMP was applied to the ten-year period 1985-1994. The model was run continuously throughout the simulated period. Boundary conditions and loads were updated on a daily or monthly basis. Integration time step was fifteen minutes. Output from the model was produced at one-day increments.

Spatial Distribution of Production

Carbon Fixation. Computed and observed primary production parameters were compared along an axis (Figure 10-1) extending from the mouth of the bay (km 0) to the Susquehanna River (km 325). Observed carbon fixation shows a minimum at km 275, in the turbidity maximum region of the bay, and a maximum immediately downstream of the turbidity maximum (Figure 10-10). Nutrients in the upper bay are abundant, and the measures were conducted under uniform, saturating light intensity. Consequently, the fixation minimum in the turbidity maximum suggests a minimum in algal biomass rather than a minimum in biomass-specific production. The model faithfully reproduces the observed spatial trend as well as the range of the observations. The model indicates a factor-of-two difference between maximum long-term mean fixation in the upper bay (km 240) and minimum fixation in the lower bay (km 60).

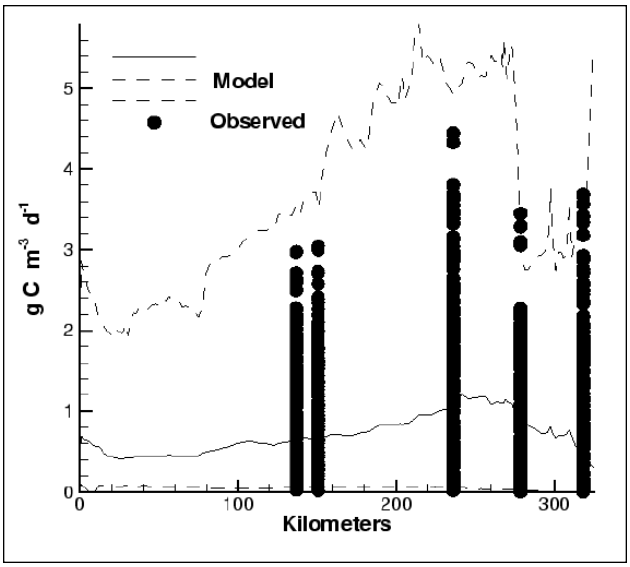

Figure 10-10. Observed and modeled carbon fixation (mean and range) along bay axis. Model and observations represent a ten-year interval | 1985-1994.

Gross Production. Observed gross production exhibits a minimum in the turbidity maximum (Figure 10-11). Observations in the mid- and lower bay exhibit the same range of values although the mean in mid-bay is higher than in the lower

bay. The model reproduces the observed spatial trend although the model mean and range exceed observed in the turbidity maximum station. A factor-of- two separates the long-term mean maximum production at km 230 from production upstream in the turbidity maximum.

Net Production. At first glance, the observed net production exhibits a peculiar spatial distribution (Figure 10-12). The apparent spatial distribution is affected by non-uniform temporal distribution of the sampling. At some transects, samples represent up to 9 months of the calendar year while at other locations, samples represent as few two months. Modeled mean and range provide good agreement with the frequently-sampled transects. The spatial distribution of computed long-term mean net production matches the pattern of gross production. The maximum occurs around km 230 and is double production further upstream in the turbidity maximum.

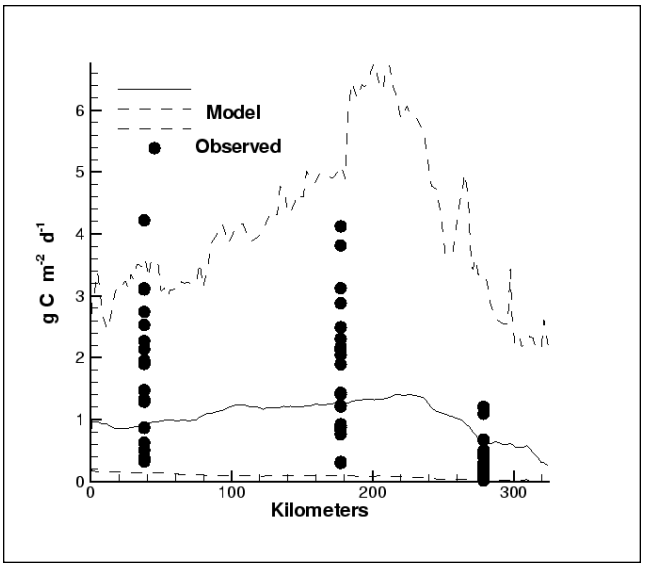

Figure 10-11. Observed and modeled gross primary production (mean and range) along bay axis. Observations from 1989-1992 are compared to model results from 1985-1994.

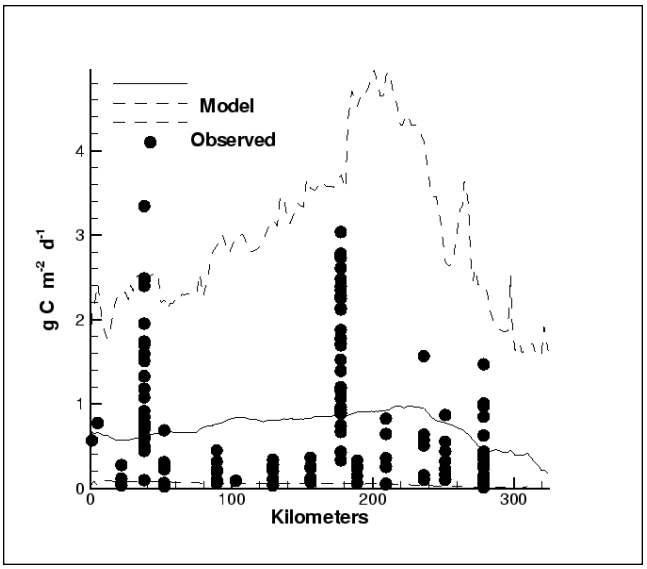

Figure 10-12. Observed and modeled net primary production (mean and range) along bay axis. Observations from 1987-1992 are compared to model results from 1985-1994.

Temporal Distribution of Production

The temporal distribution of production parameters was examined at three locations—one in the upper bay, one in the mid-bay, and one in the lower bay. For carbon fixation, computations were drawn from single model cells corresponding to the locations of stations CB2.2 (upper bay) and CB4.3C (mid-bay). For gross production, computations were drawn from single model cells corresponding to the locations of stations NB (upper bay), MB (mid-bay), and SB (lower bay). For net production, daily spatial averages over regions CB2 (upper bay), CB4 (mid-bay), and CB7 (lower bay) were compared to all observations within these regions.

Carbon Fixation. Inspection of the observed and computed carbon fixation (Figures 10-13, 10-14) indicates a distinct seasonal pattern in which minimum fixation, near zero, takes place in winter and maximum fixation takes place in

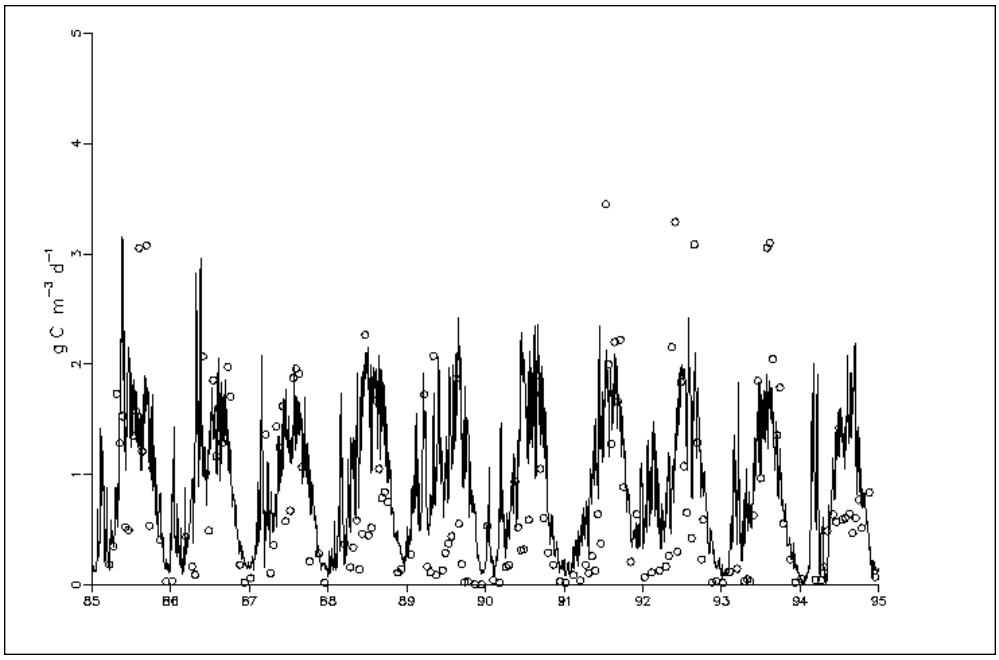

Figure 10-13. Observed and computed carbon fixation at Station CB2.2 (upper bay).

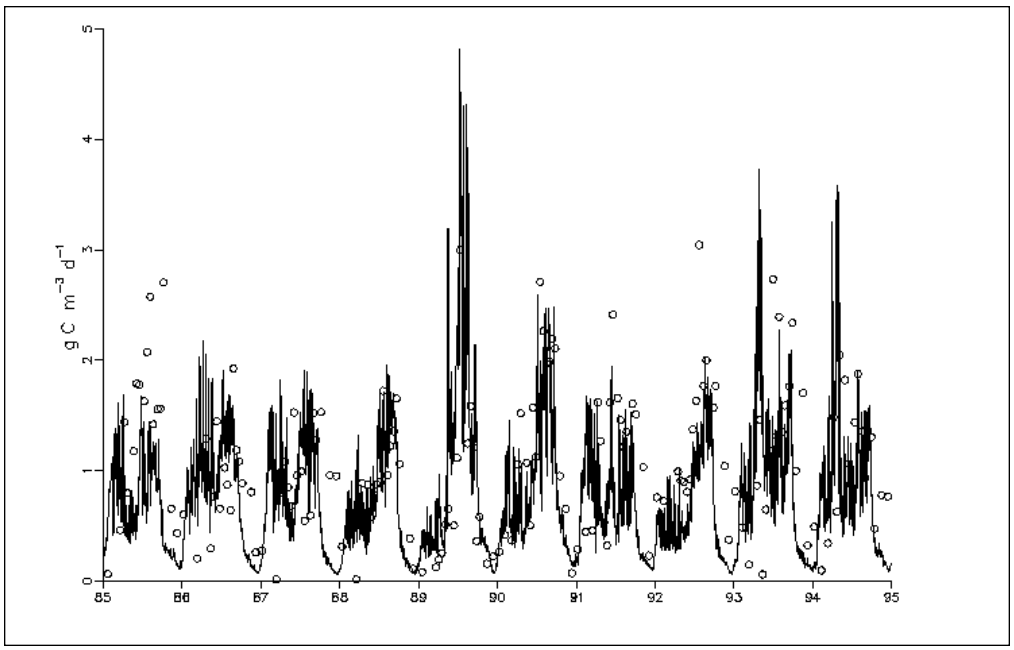

Figure 10-14. Observed and computed carbon fixation at Station CB4.3C (mid-bay).

mid-summer. Neither observations or model show trends or inter-annual variability. Neither is there a clear distinction between the two stations.

Gross Production. Seasonal trends are difficult to discern in the observed gross production observations (Figures 10-15 to 10-17). In the mid- and lower bay, lowest observations were collected in winter but intervals of nearly-zero gross production were observed in spring and autumn in the upper bay. Observations in the mid- and lower bay suggest production was diminished in 1992 relative to the two preceding years. Modeled production exhibits a regular seasonal pattern and, as with carbon fixation, shows not consistent inter-annual differences. Computations agree well with observations in the upper and mid-bay. In the lower bay, the computations show best agreement with the lower observations collected in 1992.

Net Production. Net production observations exhibit characteristics similar to the gross production observations. Seasonal patterns and inter-annual differences are difficult to discern (Figures 10-18 to 10-20). The difficulty is at least partially attributable to the uneven temporal distribution of the sampling. The observations suggest net production in the mid- and lower bay was lower in 1987 and 1988 than in subsequent years. Computed net production exhibits a distinct seasonal pattern. Computations indicate peak production in mid-bay in 1989 and 1990 but inter-annual variations are not strong.

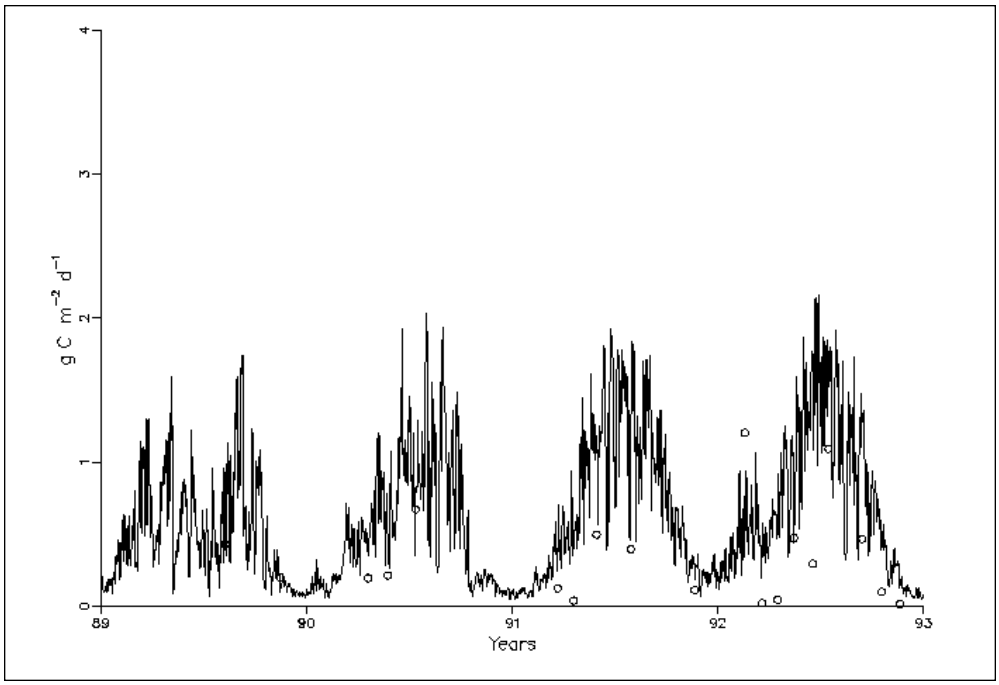

Figure 10-15. Observed and computed gross primary production at station NB (upper bay).

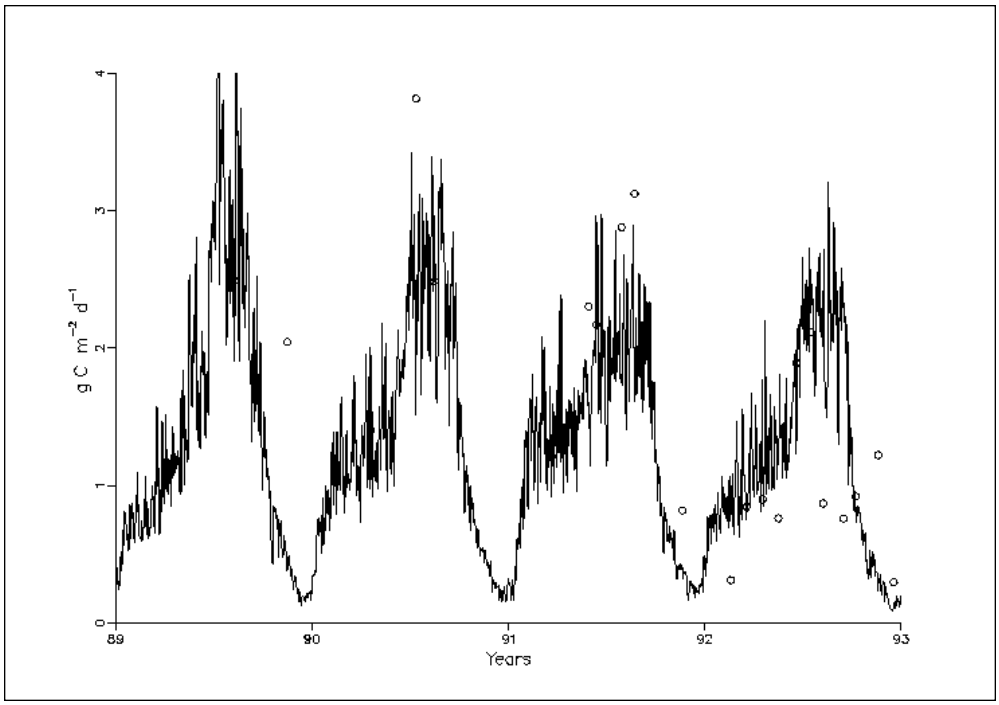

Figure 10-16. Observed and computed gross primary production at station MB (mid-bay).

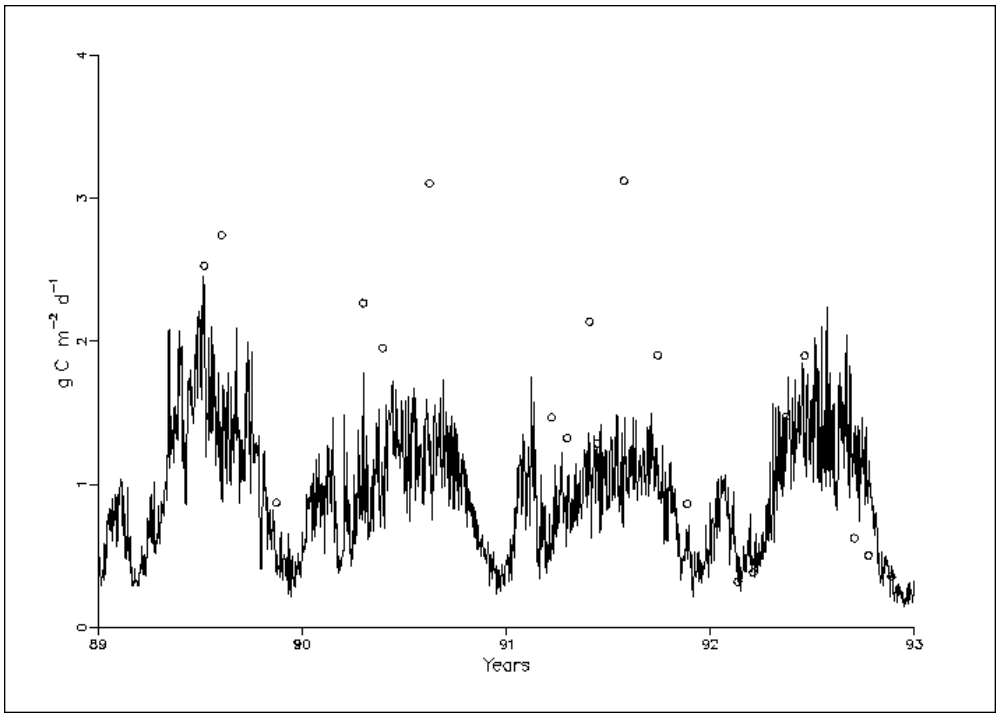

Figure 10-17. Observed and computed gross primary production at station SB (lower bay).

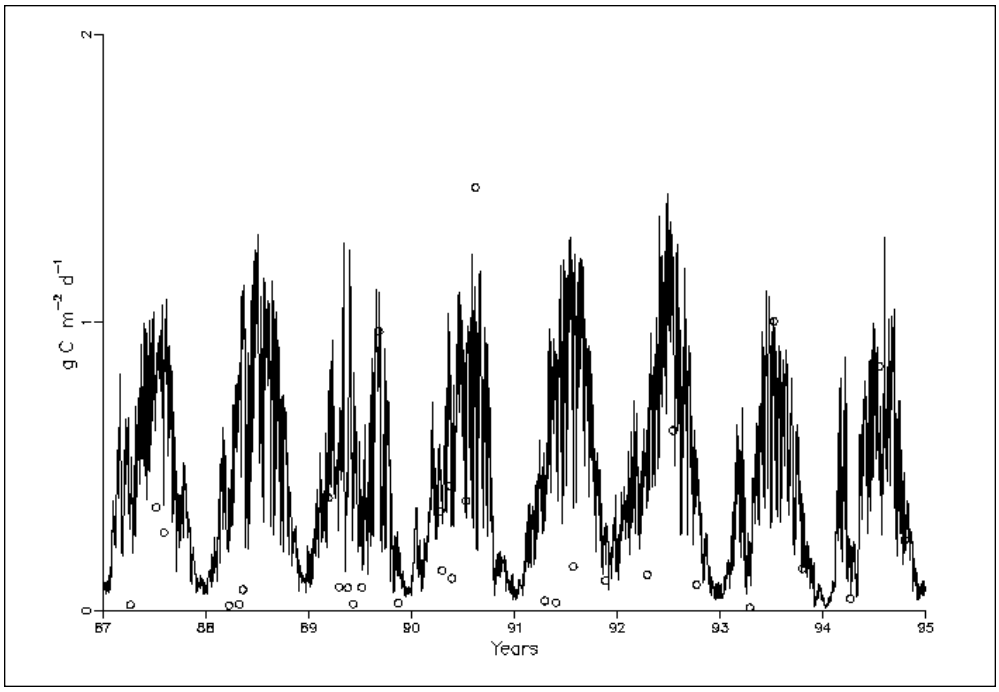

Figure 10-18. Observed and computed net primary production in segment CB2 (upper bay).

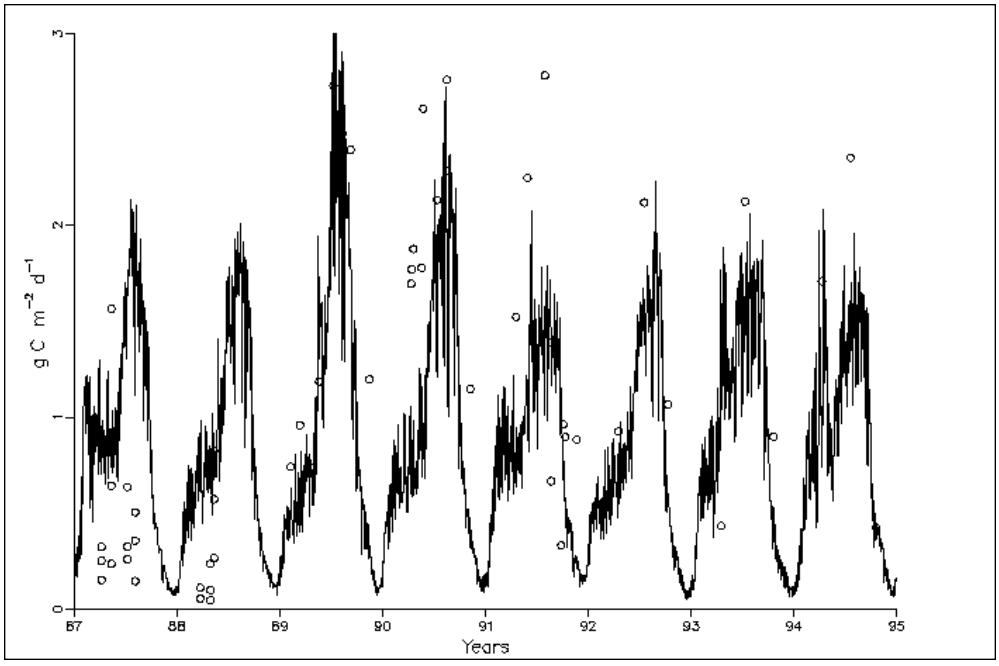

Figure 10-19. Observed and computed net primary production in segment CB4 (mid-bay).

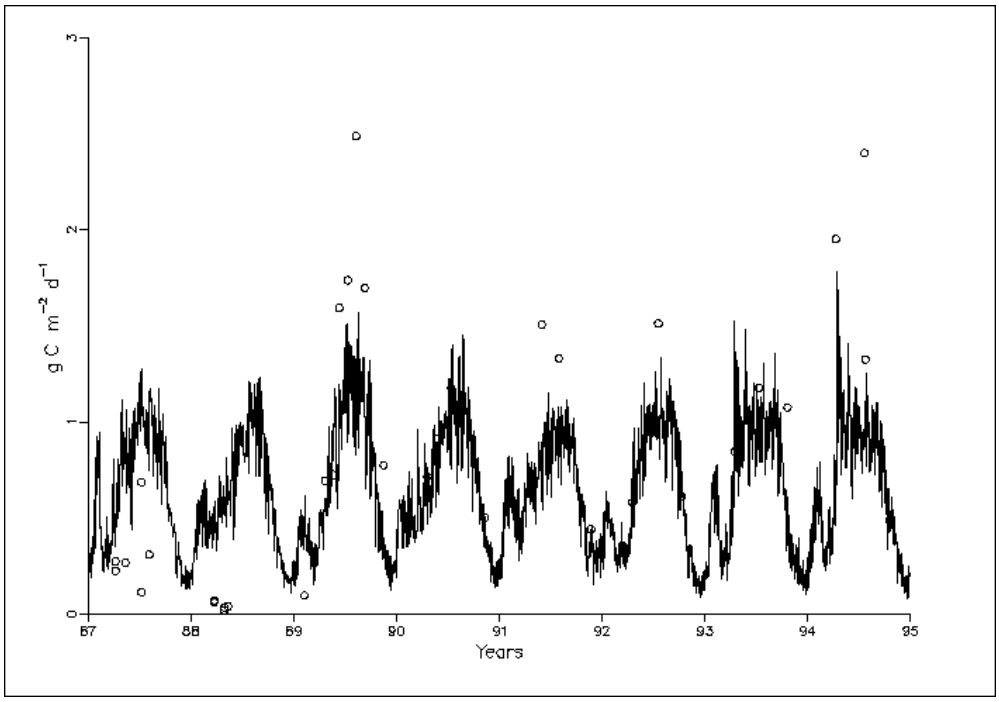

Figure 10-20. Observed and computed net primary production in segment CB7 (lower bay).

Seasonal Summaries

The sporadic nature of the observations makes confounds interpretation of temporal characteristics. To clarify temporal behavior of the model and observations, seasonal summaries are provided for primary production and other key parameters. Model results, as seasonal averages, are compared to observations from three regions of the bay. The seasons are designated winter (December–February), spring (March–May), summer (June–August), and Fall (September–November). The northernmost region, designated CB2, is within the estuarine turbidity maximum. In this region, nutrients are abundant and light is considered to be the primary limit to algal production (Fisher et al. 1999). Both nutrient concentrations and light attenuation diminish with distance down the bay axis. In the segment designated CB4, limits to production are mixed. Limiting factors exhibit a seasonal progression from light (winter), to phosphorus (spring), to nitrogen (summer) (Fisher et al. 1999). In the lower bay segment CB7, nitrogen is the primary limit to algal production (Fisher et al. 1999).

Primary Production. Observations of carbon fixation (Figure 10-21) indicate a summer maximum, consistent with numerous studies (Malone et al. 1988, Smith and Kemp 1995, Malone et al. 1996, Harding et al. 2002). The model shows the same seasonal trends in carbon fixation as the observations. The model also shows a spatial trend that corresponds to the trend in nutrient availability. Highest fixation is in the upper bay, close to the Susquehanna River nutrient source. Lowest fixation is at the station most distant from the Susquehanna. On a seasonal basis, differences in mean carbon fixed range from +227% (model greater than observed) to -52% (model less than observed). Median difference is +15%.

Observed net production demonstrates a significant summer maximum and substantial differences between the turbidity maximum and stations further downstream (Figure 10-22). Computations are consistent with the observed trends. Computed net production peaks in summer at all locations and is highest in mid-bay. In the turbidity maximum, production is diminished due to light limitation while nutrient limitation limits net production in the lower bay. The magnitude of the light limitation may be under-computed since mean net production exceeds observed by 31% in the turbidity maximum. System-wide differences between seasonal mean computed and observed net production range from 316% to –49%. Median difference is –3%.

Observed trends and model behavior for gross production largely correspond to net production. Observations indicate a significant summer maximum and substantial differences between the turbidity maximum and stations further downstream (Figure 10-23). Computed gross production peaks in summer at all locations and is highest in mid-bay. System-wide differences between seasonal mean computed and observed gross production range from 221% to –50%. Median difference is 3%.

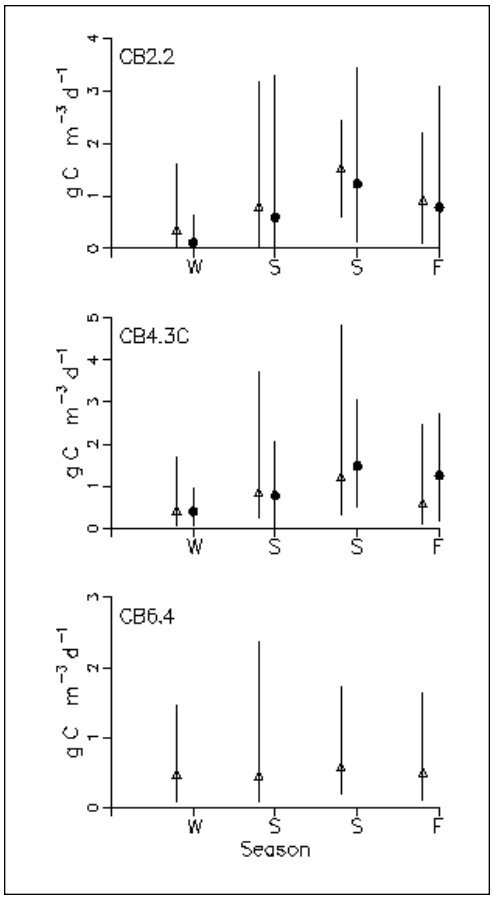

Figure 10-21. Observed (circles) and computed (triangles) seasonal (mean and range) carbon fixation in the upper, mid-, and lower bay.

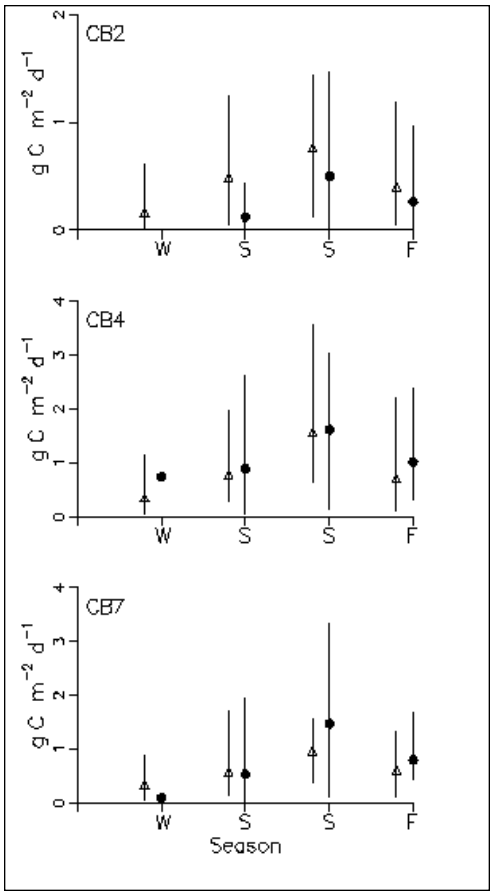

Figure 10-22. Observed (circles) and computed (triangles) seasonal (mean and range) net primary production in the upper, mid-, and lower bay.

Algal Biomass. Observations in the upper bay indicate the spring bloom barely intrudes into the turbidity maximum while in mid-bay, mean algal carbon in spring is double the biomass during other seasons (Figure 10-24). The model shows little seasonal variability in mean algal biomass in the turbidity maximum but a substantial spring bloom elsewhere. Observations also indicate biomass is lower in the turbidity maximum than in mid-bay, a trend which is replicated in the model. System-wide differences between seasonal mean computed and observed algal biomass range from 15% to -48%. Median difference is -27%.

The spring bloom is not as evident in the observed surface chlorophyll concentrations as in the carbonaceous biomass (Figure 10-25). Consistent with the biomass observations, observed chlorophyll within the turbidity maximum is lower than further downstream. Computed chlorophyll concentrations are greatest in the mid-bay and a spring bloom is evident in the mid and lower bay. System-wide differences between seasonal mean computed and observed surface chlorophyll range from 58% to -27%. Median difference is 15%.

Limiting Factors. Observed light attenuation shows a strong spatial trend but no seasonal behavior (Figure 10-26). Attenuation in the turbidity maximum exceeds attenuation downstream by a factor of three or more. The model replicates the

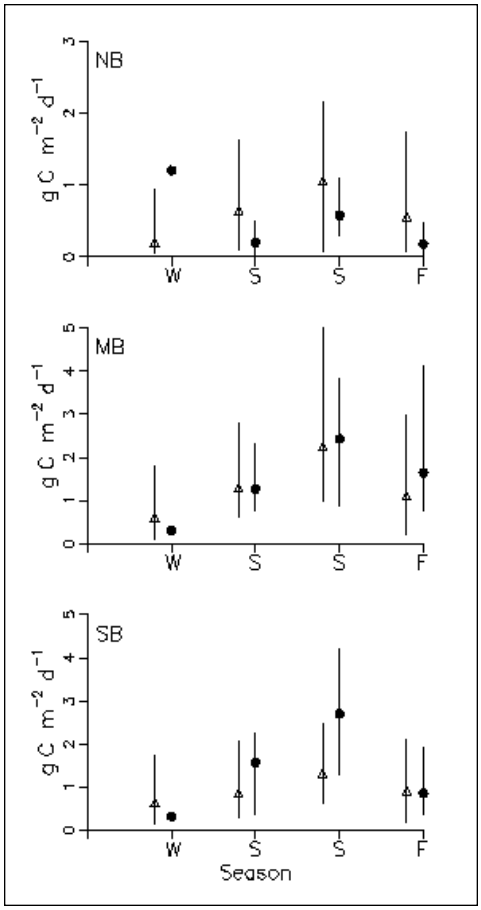

Figure 10-23. Observed (circles) and computed (triangles) seasonal (mean and range) gross primary production in the upper, mid-, and lower bay.

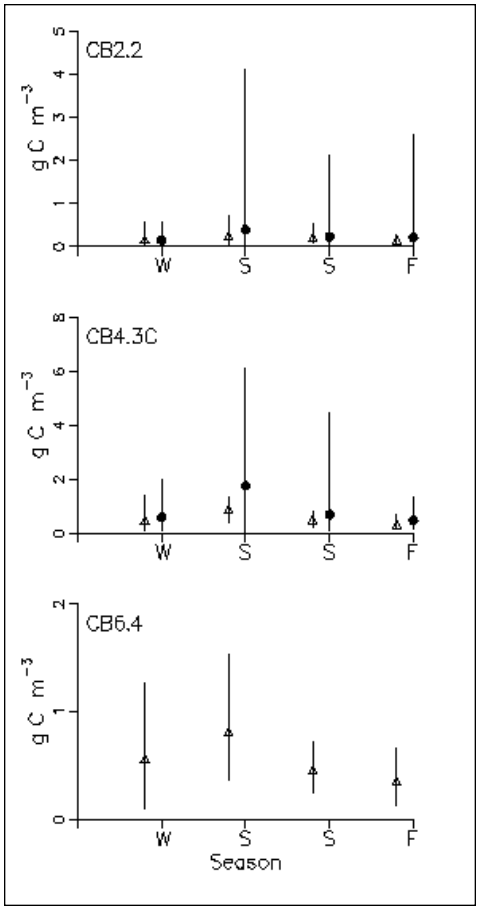

Figure 10-24. Observed (circles) and computed (triangles) seasonal (mean and range) algal biomass in the upper, mid-, and lower bay.

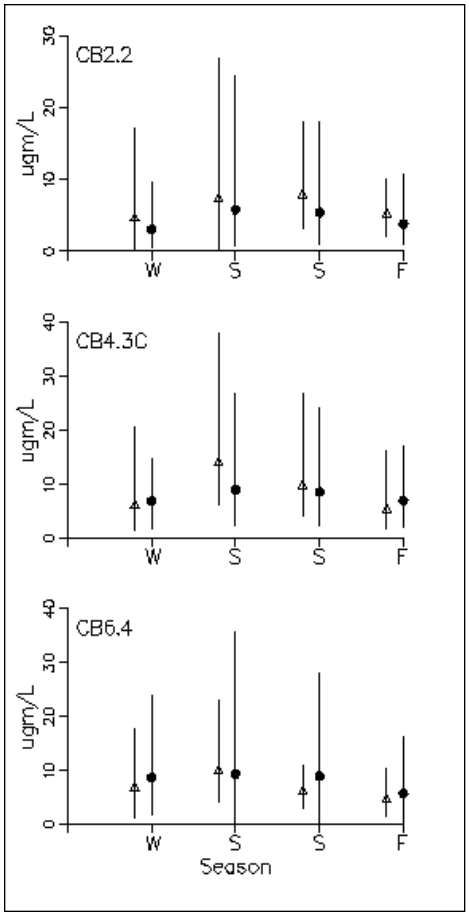

Figure 10-25. Observed (circles) and computed (triangles) seasonal (mean and range) surface chlorophyll in the upper, mid-, and lower bay.

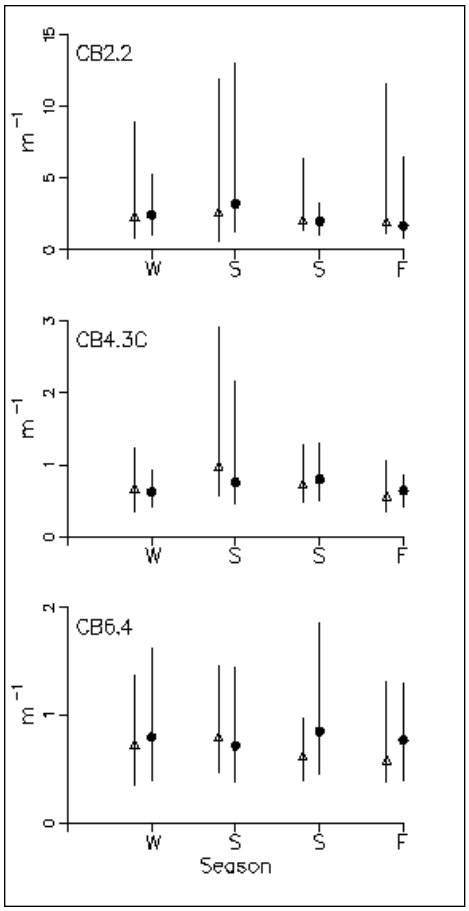

Figure 10-26. Observed (circles) and computed (triangles) seasonal (mean and range) light attenuation in the upper, mid-, and lower bay.

observed pattern and magnitude. Differences of 31% to –27% exist between observed and computed seasonal means. Median difference is –6%.

Nutrient limitations within the bay exhibit a pattern which is dependent on location, season, and runoff (Fisher et al. 1999, Malone et al. 1996, Fisher et al. 1992). During the spring bloom, phosphorus and, perhaps, silica play a role while nitrogen is commonly considered to be the most limiting nutrient in the mainstem bay during summer. We emphasize nitrogen here since summer is the period of peak production (Harding et al 2002), and since summer production has been linked to nitrogen loading (Malone et al. 1988).

The Chesapeake Bay Program provided an enormous data base of ammonium, nitrate, and nitrite observations concurrent with the model application. A less comprehensive data base of urea observations was also available (Lomas et al. 2002) but few observations coincided with the model application period. For comparison with the model, we pooled ammonium, nitrate and nitrite observations from the application period with mean observed surface urea concentrations (0.0056 to 0.0076 gm m^{-3}), averaged within spatial regions of the bay, from later years. The sum is referred to here as “available nitrogen.”

Observed available nitrogen (Figure 10-27) shows a strong trend down bay away from the primary source at the Susquehanna River. Temporally, minimum concentrations occur in summer, coincident with minimum runoff and maximum algal uptake. Computed available nitrogen conforms with observed spatial and temporal behavior. System-wide differences between seasonal mean computed and observed surface nitrogen range from 155% to –53%. Median difference is 13%. The greatest relative differences occur in the lower bay and reflect the difficulty in assigning boundary conditions at the mouth of the bay.

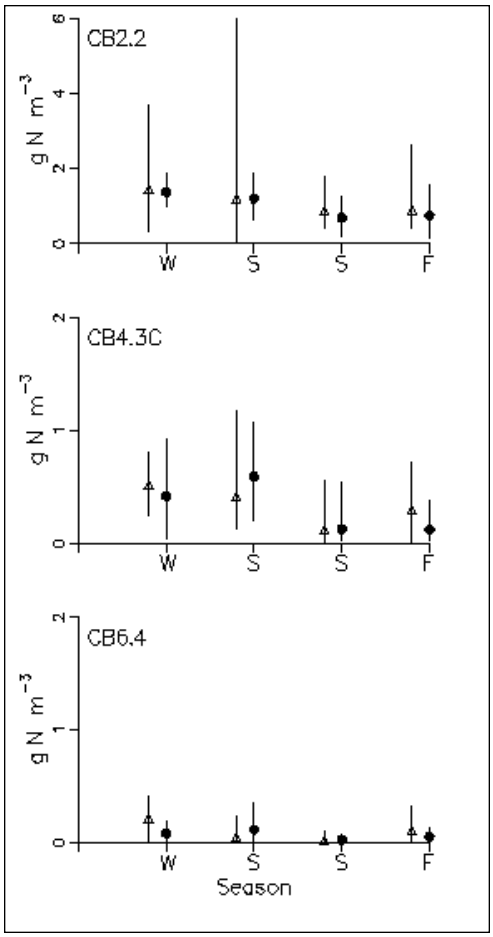

Figure 10-27. Observed (circles) and computed (triangles) seasonal (mean and range) available nitrogen in the upper, mid-, and lower bay.

Discussion

Specific Growth Rate

Three primary features distinguish the present model from earlier versions and from models employed in similar applications. The first is the determination of specific growth rate as the quotient of photosynthetic rate and carbon-to-chlorophyll ratio (Equation 10-7). In the first version of the Chesapeake Bay model (Cerco and Cole 1993) and in several investigative models (McGillicuddy et al. 1995; Fasham et al. 1990; Moll 1998; Doney et al. 1996), specific growth rate was specified directly.

Instantaneous, carbon-specific growth rates that result from the model relationship are high relative to commonly accepted values. Employing the maximum photosynthetic rate for the summer group, 350 g C g^{-1} Chl d^{-1} (14.6 µg C µg^{-1} Chl hr^{-1}), and a typical carbon-to-chlorophyll ratio of 50 yields an instantaneous specific growth rate of 7 d^{-1}. By contrast, the classic work of Eppley (1972) indicates maximum specific growth rate is roughly 2 d^{-1} at 20 ^{o}C. Alternate investigations of primary production (McGillicuddy et al. 1995; Fasham et al. 1990; Moll 1998; Doney et al. 1996) employ growth rates of 0.66 to 2.9 d^{-1}.

Care must be employed in the definition and comparison of growth rates. The instantaneous growth rate is not the daily average growth rate. The daily average growth rate can be obtained:

$$\overline{G} = \frac{1}{24} \bullet \int_0^{24} \frac{P^B m}{CChl} \bullet \frac{I(t)}{\sqrt{I(t)^2 + Ik^2}} \bullet dt \qquad (10\text{-}10)$$

in which
Gbar = daily average growth rate (d^{-1})
I(t) = instantaneous irradiance (E m^{-2} hr^{-1})

Employing a total daily irradiance of 60 E m^{-2}, a 12-hour daylight period, and a sinusoidal time series of irradiance yields a daily average specific growth rate of 3 d^{-1} for the summer group. This rate is still not realized within the water column, however. At a depth of 1 m (mid-point of model surface layer), with Ke = 1 m^{-1}, daily average specific growth rate is reduced to 2.24 d^{-1}. This growth rate is within conventional ranges and is subject to further reduction as a function of nutrient limitation and sub-optimal temperature. This analysis indicates that conventional growth rates result in-situ when maximum photosynthetic rate is influenced by light attenuation and averaged over a day.

Models that initially specify maximum specific growth rate $2d^{-1}$ and attenuate this rate due to the influence of daylength and other factors likely employ daily average growth that is much less than actual in-situ growth. We examined the effect of our growth rate formulation on computed production. Maximum instantaneous specific growth rate was forced to 2 d^{-1} by fixing carbon-to-chlorophyll ratio at 50 g C g^{-1} Chl and adjusting maximum photosynthetic rate to give a quotient 2 d^{-1} at optimal temperature. Baywide annual production was reduced by 15% when lower, conventional growth rates were imposed.

Urea

A second distinctive feature of the present model is the use of urea ($CO(NH_2)_2$) as an algal nutrient. The role of urea as a nitrogenous nutrient in Chesapeake Bay has been recognized for over 25 years. McCarthy et al. (1977) found that urea comprised an average of 20% of algal nitrogen uptake. More recent work (Lomas and Glibert 1999) indicates, at times, urea comprises as much as 40% of algal nitrogen uptake in the bay.

Despite the importance of urea as a nutrient, this compound is omitted from popular management models (Cerco and Cole 1993) as well as primary production models (McGillicuddy et al. 1995; Fasham et al. 1990; Moll 1998; Doney et al. 1996). One reason for the omission may be the complication of adding an additional state variable to the models. The approach taken here of combining ammonium and urea into a single state variable is a reasonable compromise. Both are reduced nitrogen forms and share common origins including zooplankton excretion (Miller and Glibert 1998) and benthic sediment regeneration (Lomas et al 2002). Ammonium and urea are both “preferred” over nitrate as algal nutrients (McCarthy et al. 1977).

Urea observations within the bay did not permit a one-to-one calibration of the model to contemporaneous observations. Our approach to incorporating urea was to adjust model parameters such that model computations of reduced nitrogen agreed with contemporaneous ammonium observations plus regional, temporal average urea concentrations observed in later years.

To test the effect of incorporating urea in the model, we ran the model with urea removed from the reduced nitrogen pool. The amount removed, 0.0082 g N m^{-3}, was determined as the long-term mean concentration in bay surface waters. Baywide annual production was reduced by less than 2% when urea was removed. This

result was surprising in view of the cited importance of urea in algal nutrition. We attribute this result largely to the nature of the sensitivity run. Urea concentrations vary with season, location, hydrology, and other factors (Lomas et al. 2002). Removal of a constant amount does not represent the true role of urea at various times and locations. Available observations did not allow a more detailed sensitivity analysis, however.

We believe urea is important as a nutrient and that the substance should not be ignored in eutrophication modeling. Our present knowledge base, however, does not allow a detailed representation of urea. Extension of the application period of the present model into a more data-rich period may allow more detailed modeling. Additional monitoring of concentrations and loads is also required before urea can be represented at a level of realism concurrent with other model state variables.

Predation by Higher Trophic Levels

A third distinctive feature of the model is the use of a quadratic term (Equation 10-14) to represent predation by higher trophic levels not included in the model. Doney et al. (1996) incorporated a similar quadratic term that represented aggregation. A key difference between their formulation and the present model is that nutrients incorporated in aggregated algae sink from the photic zone. The quadratic predation term recycles algal nutrients at the location where predation occurs.

Computed primary production is sensitive to the specification of the predation term, Phtl (Figure 10-28). Maximum production occurs at Phtl 0.3 although algal biomass declines monotonically from lower to high values of Phtl. Consequently,

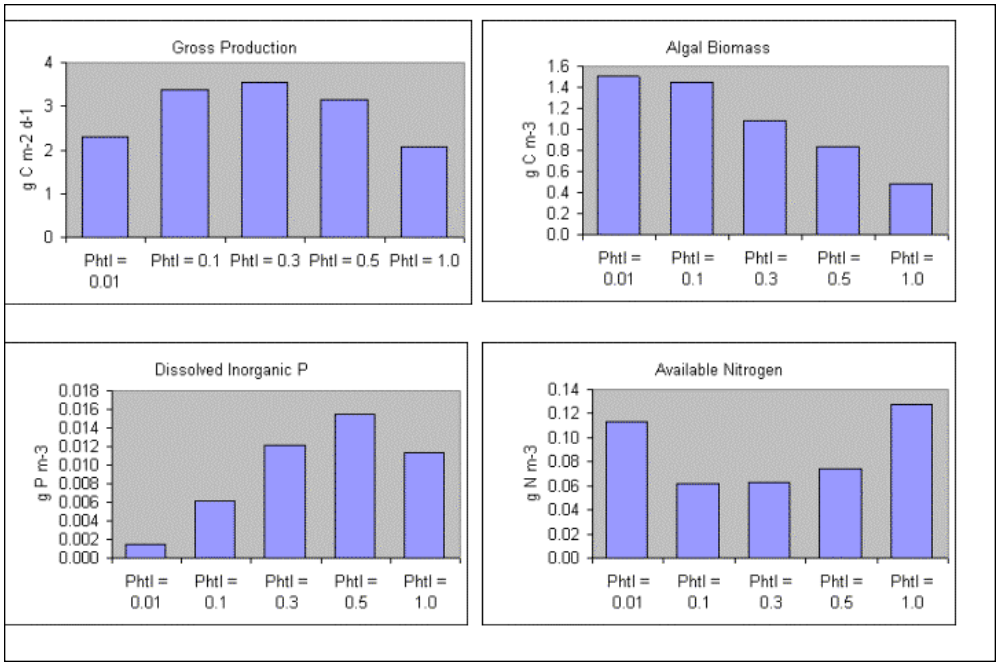

Figure 10-28. Sensitivity of primary production to quadratic predation term. Panels indicate summer average gross production, surface algal biomass, surface dissolved inorganic phosphorus, and surface available nitrogen at the mid-bay (MB) location.

maximum production occurs at moderate algal biomass rather than at low or high extremes. This behavior is explained by examining concentrations of dissolved inorganic phosphorus and available nitrogen. At the lowest predation rate examined, algal biomass was maximized but dissolved inorganic phosphorus was largely depleted. Due to the stringent nutrient limitation, growth was minimal. Production, which is the product of biomass and growth (Equation 10-16), was low. As predation increased, biomass decreased but the nutrient limitation was relaxed as phosphorus bound up in algal biomass was released, through predation, to the water column. At moderate predation levels, the limiting nutrient in mid-bay tended towards nitrogen rather than phosphorus. Although biomass was diminished, relaxation of the stringent nutrient limitation allow higher growth. Production was maximized. As predation approached the maximum rate examined, nutrient limitations to growth were eliminated but algal biomass was diminished so that the production was less than at lower predation rates.

Predation by non-specific higher trophic levels is the dominant predation term in the model, consuming 60% to 75% of annual net production (Table 10-2). As originally conceived, the higher-trophic-level predation term was intended to simulate activity by menhaden. Attribution of this level of predation to menhaden seems unreasonable. A bioenergetics model (Luo et al. 2001) that estimated the carrying capacity of Chesapeake Bay for menhaden assumed menhaden consume 10% of production. A second argument against menhaden is that our predation term immediately recycles algal biomass as nutrients. The assumption that predator biomass is minimal and that turnover is rapid is implicit in our formulation.

Our model provides good representation of the distribution of mesozooplankton biomass (Figure 10-29). Observations collected near our mid-bay station indicated predation by mesozooplankton consumed 12% to 103% of net production in four samples from March to October (White and Roman 1992). Our model average over

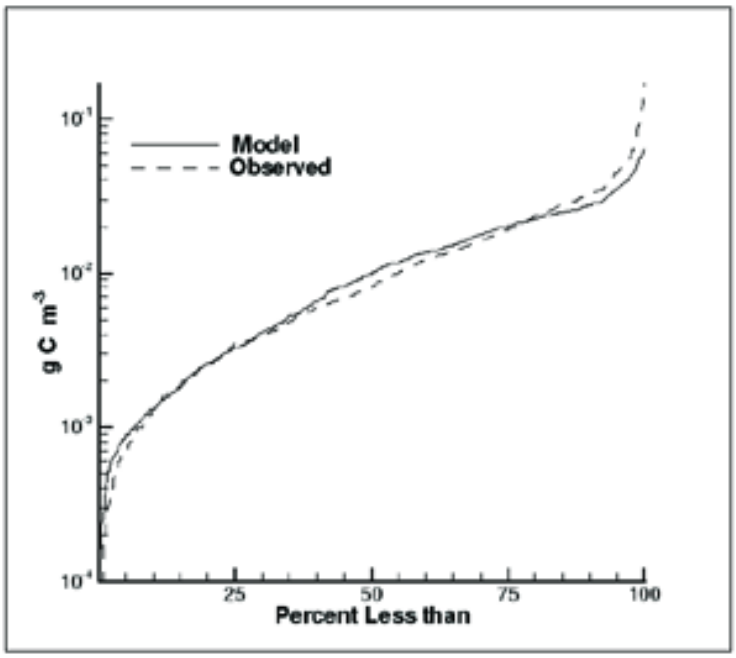

Figure 10-29. Cumulative distribution of observed and modeled mesozooplankton biomass

the same months indicates mesozooplankton consume 19% of net production. Interestingly, both the observations and our model indicate consumption can exceed net production, suggesting an import of phytoplankton to the mid-bay station. While the observations do not permit an exact determination of model performance versus actual mesozooplankton grazing, comparison to available measures of biomass and grazing indicates performance is reasonable, at least.

Measures of microzooplankton grazing using the dilution technique (Gallegos 1989) indicate microzoplankton potentially consume 45% to 105% of production in the Rhode River, a Chesapeake Bay tributary. The same methodology applied to Chesapeake Bay (McManus and Ederington-Cantrell 1992) indicated microzooplankton grazing rates averaged 57% of phytoplankton growth rates. Our annual estimates of microzooplankton consumption, 6% to 16% of net production, are low by comparison to the measures. The computed distribution of microzooplankton biomass (Figure 10-30) is also low relative to observations. At the median, computed microzooplankton biomass is about half observed. Improvements to our microzooplankton model to double the biomass might raise computed consumption to 12 to 32% of net production.

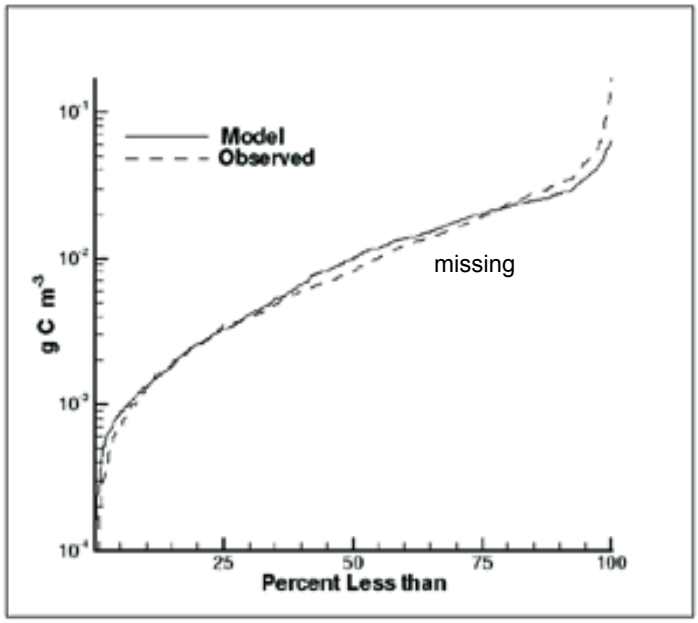

Figure 10-30. Cumulative distribution of observed and modeled microzooplankton biomass

Doubling the computed microzooplankton consumption still leaves a substantial fraction of non-specific predation. We attribute the remaining predation to heterotrophs not quantified in the microzooplankton observations. Microzooplankton sampling in the bay was conducted with a 44 µm net. Collection of microzooplankton with nets is no longer recommended since soft-bodied zooplankton may be destroyed by plankton mesh (Harris et al. 2000). Heterotrophic flagellates of size less than 44 µm will pass through the net entirely. In future applications, we may wish to re-parameterize the microzooplankton algorithm to increase computed biomass and compare results with improved microzooplankton observations presently being collected.

Annual Integrated Production and Nutrient Loads

The nature of the model facilitates computation of annual integrated production. The model computes daily production for each of the 1215 cells that represent the surface of the bay. These are readily combined into bay-wide daily areal-average production and into areal-average annual production. Our computations indicate the ten-year mean bay-wide areal-average daily gross production is 1.02 g C m^{-2} d^{-1}. Corresponding net production is 0.70 g C m^{-2} d^{-1}.

Areal-average production in any year shows no relationship to nutrient loading from the Susquehanna River, the major source to the mainstem bay (Figure 10-31). An obvious explanation is the limitation of the calendar in defining years. A late-November storm will influence annual loads but can have limited influence on production in the same year. However, attempts by us to relate production to nutrient loads in shorter, more significant periods (i.e. spring months) produced no apparent relationship.

Absence of tight coupling between loads and production is partially attributable to residence time of nutrients in bottom sediments. Numerical experiments with the model (Cerco 1995) indicate two years are required for sediment nutrient release to largely adjust to load reductions. Some "memory" of loads persists for ten years or more. Parameters in the sediment model (DiToro 2001) are based on decomposition experiments (Westrich and Berner 1984) that showed 65% of organic matter remained after two years incubation. As a consequence of sediment residence and recycling, production in any year is a function of contemporary loading as well as loading in previous years.

A second factor in damping response of production to loads is nutrient exchange with the continental shelf. Transport across the mouth of the bay results in net

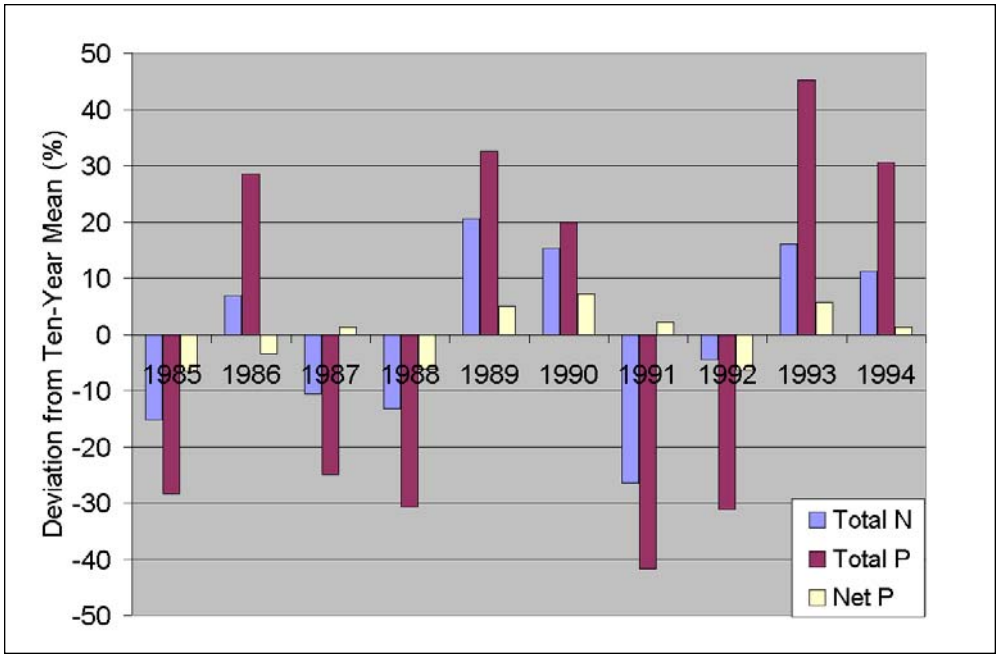

Figure 10-31. Annual nutrient loads from the Susquehanna River and bay-wide annual net production relative to ten-year mean.

export of nitrogen and net import of phosphorus (Boynton et al. 1995). The net fluxes represent differences in nutrients transported in both directions across the bay mouth as a result of tides, meteorological forcing, and other factors. Mass-balance modeling at the mouth of the bay (Cerco 1995) indicates the unidirectional transport of new nitrogen into the bay, imported from the shelf reservoir, is equivalent to 38% of system loads from other sources. New phosphorus is by far the dominant source, equivalent to 81% of system loads from other sources. Analyses that relate production solely to loads from upland sources omit a large fraction of the total loads to the system.

Our computations of annual integrated production over the ten-year simulation period range from 0.66 to 0.95 g C m^{-2} d^{-1} net and 0.95 to 1.07 g C m^{-2} d^{-1} gross. Our computations represent 50% to 85% of net production and 60% to 100% of gross production estimated from the same data base by alternate means (Harding et al. 2001). One immediate explanation for the discrepancy lies in the averaging periods. Our model represents 1985-1994 while the entire data base extends from 1982 to 1998. We attribute the differences, however, not to the averaging period but to the averaging methods.

The observations were collected at discrete locations and times. Arbitrary interpolations are required to average the discrete observations into system-wide annual averages. The model uses a different technique in which production system-wide is continuously computed as a function of nutrient concentrations, light attenuation, temperature, and other factors. Inevitably, the employment of the model to compute production in locations and time for which observations are missing will result in different estimates than using interpolation or other methods to fill in gaps in the data base.

In Conclusion

Computation of concentrations and processes within the CBEMP is a demanding task that requires accurate computations and linkages between models as well as an extensive data base. Daily nutrient and solids loads are generated and distributed along the bay perimeter by the CBP Watershed Model, a modified version of HSPF (Donigian et al. 1991). Nutrients and solids are transported throughout the bay from their input locations based on computations from the hydrodynamic model (Johnson et al. 1993, Wang and Johnson, 2000). As they are transported, nutrients are cycled within the water column and between the water column and sediments (DiToro 2001). We believe we have constructed a model that accurately represents primary production rates (Table 10-3) while maintaining reasonable agreement with observed properties including algal biomass, chlorophyll, and light and nutrient limitation. Discrepancies between observed and computed properties are attributable to inevitable limitations in our ability to quantify loads, boundary conditions, and forcing functions within multiple models rather than to shortcomings in model formulation.

Table 10-3
Statistical Summary of Modeled and Observed Production

	Carbon Fixation, g C m^{-3} d^{-1}		Gross Production, g C m^{-2} d^{-1}		Net production, g C m^{-2} d^{-1}	
	Observed	**Model**	**Observed**	**Model**	**Observed**	**Model**
Mean	1.08	0.91	1.30	1.19	0.72	0.87
Median	0.93	0.79	0.91	1.01	0.41	0.82
Minimum	0.00	0.00	0.02	0.10	0.01	0
maximum	4.44	4.6	4.22	3.26	3.34	2.72
Standard Deviation	0.84	0.64	1.09	0.73	0.77	0.50
# Observed	876		64		166	

References

Behrenfield, M., and Falkowski, P. (1977). "A consumer's guide to phytoplankton primary production models," *Limnology and Oceanography*, 42(7), 1479-1491.

Bienfang, P., Harrison, P., and Quarmby, L. (1982). "Sinking rate response to depletion of nitrate, phosphate, and silicate in four marine diatoms," *Marine Biology*, 67, 295-302.

Boynton, W., Garber, J., Summers, R., and Kemp, W. (1995). "Inputs, transformations, and transport of nitrogen and phosphorus in Chesapeake Bay and selected tributaries," *Estuaries*, 18, 285-314.

Cerco, C., and Cole, T. (1993). "Three-dimensional eutrophication model of Chesapeake Bay," *Journal of Environmental Engineering*, 119(6), 1006-10025.

Cerco, C. (1995). "Response of Chesapeake Bay to nutrient load reductions," *Journal of Environmental Engineering*, 121(8), 549-557.

Cerco, C. (2000). "Phytoplankton kinetics in the Chesapeake Bay Eutrophication Model," *Journal of Water Quality and Ecosystem Modeling*, 1, 5-49.

Cerco, C., and Meyers, M. (2000). "Tributary refinements to the Chesapeake Bay Model," *Journal of Environmental Engineering*, 126(2), 164-174.

Chan, A. (1980). "Comparative physiological study of marine diatoms and dinoflagellates in relation to irradiance and cell size. 2. Relationship between photosynthesis, growth, and carbon/chlorophyll ratio. *Journal of Phycology*, 16, 428-432.

Cloern, J., Grenz, C., and Vidergar-Lucas, L. (1995). "An empirical model of the phytoplankton chlorophyll:carbon ratio—the conversion factor between productivity and growth rate," *Limnology and Oceanography*, 40(7), 1313-1321.

Davis, C., Breitner, N., and Harrison, P. (1978). "Continuous culture of marine diatoms under silicon limitation. 3. a model of Si-limited diatom growth," *Limnology and Oceanography*, 23, 41-52.

D'Elia, C., Nelson, D., and Boynton, W. 1983. "Chesapeake Bay Nutrient and Plankton Dynamics: III. The Annual Cycle of Silicon," *Geochimica et Cosmochimica Acta*, 47:1945-1955.

DiToro, D. (2001). *Sediment Flux Modeling*, John Wiley and Sons, New York.

Doney, S., Glover, D., and Najjar, R. (1996). "A new coupled, one-dimensional biological-physical model for the upper ocean: Applications to the JGOFS Bermuda Atlantic Time-series Study (BATS) site," *Deep Sea Research II*, 43(2- 3), 591-624.

Donigian, A., Bicknell, B., Patwardhan, A., Linker, L., Alegre, D., Chang, C., and Reynolds, R. (1991). "Watershed model application to calculate bay nutrient loadings," Chesapeake Bay Program Office, US Environmental Protection Agency, Annapolis MD.

Durbin, A., and Durgin, E. (1975). "Grazing rates of the Atlantic menhaden *Brevoortia tyrannus* as a function of particle size and concentration," *Marine Biology*, 33, 265-277.

Eppley, R., Rogers, J., and McCarthy, J. (1969). "Half-saturation constants for uptake of nitrate and ammonium by marine phytoplankton," *Limnology and Oceanography*, 14(6), 912-920.

Eppley, R. (1972). "Temperature and phytoplankton growth in the sea," *Fishery Bulletin*, 70(4), 1063-1085.

Fasham, M., Ducklow, H., and McKelvie, S. (1990). "A nitrogen-based model of plankton dynamics in the oceanic mixed layer," *Journal of Marine Research*, 48, 591-639.

Fisher, T., Gustafson, A., Sellner, K., Lacouture, R., Haas, L., Wetzel, R., Magnien, R., Everitt, D., Michaels, B., and Karrh, R. (1999). "Spatial and temporal variation of resource limitation in Chesapeake Bay," *Marine Biology*, 133, 763-778.

Fisher, T., Peele, E., Ammerman, J., and harding, L. (1992). "Nutrient limitation of phytoplankton in Chesapeake Bay," *Marine Ecology Progress Series*, 82, 51- 63.

Gallegos, C. (1989). "Microzooplankton grazing on phytoplankton in the Rhode River, maryland: nonlinear feeding kinetics," *Marine Ecology Progress Series*, 57, 23-33.

Gilmore, J., Glendening, P., Ridgeway, T., Williams, A., Browner, C., and Bullaway, M. (2000). "Chesapeake 2000," Chesapeake Bay Program, US Environmental Protection Agency, Annapolis MD.

Goldsworthy, A. (1970). "Photorespiration," *The Botanical Review*, 36(4), 321- 340.

Groeger, A., and Kimmel, B. (1989). "Relationship between photosynthetic and respiratory carbon metabolism in freshwater plankton," *Hydrobiologia*, 173, 107-117.

Harding, L., Mallonee, M., and Perry, E. (2002). "Toward a predictive understanding of primary productivity in a temperature, partially stratified estuary," *Estuarine, Coastal and Shelf Science*, in press.

Harding, L., Meeson, B., and Fisher, T. (1986). "Phytoplankton in two east coast estuaries: photosynthesis-light curves and patterns of carbon assimilation," *Estuarine, Coastal and Shelf Science*, 23, 773-806.

Harris, R., Wiebe, P., Lenz, J., Skjodal, H., and Huntley, M. (2000). "Sampling, preservation, enumeration and biomass of marine protozooplankton." *ICES zooplankton methodology manual*. Academic Press, San Diego, 193-221.

Hutchinson, G. (1967). *A treatise on limnology*, *Volume II*, John Wiley and Sons, New York, 245-305.

Jassby, A., and Platt, T. (1976). "Mathematical formulation of the relationship between photosynthesis and light for phytoplankton," *Limnology and Oceanography*, 21, 540-547.

Johnson, B., Kim, K., Heath, R., Hsieh, B., and Butler, L. (1993). "Validation of a three-dimensional hydrodynamic model of Chesapeake Bay," *Journal of Hydraulic Engineering*, 199(1), 2-20.

Kemp, W., Smith, E., DiPasquale, M., and Boynton, W. (1997). "Organic carbon balance and net ecosystem metabolism in Chesapeake Bay," *Marine Ecology Progress Series*, 150, 229-248.

Kiddon, J., Bender, M., and Marra, J. (1995). "Production and respiration in the 1989 North Atlantic spring bloom: an analysis of irradiance-dependent changes," *Deep-Sea Research*, 42(4), 553-576.

Laws, E., and Chalup, M. (1990). "A microalgal growth model," *Limnology and Oceanography*, 35(3), 597-608.

Lomas, M., and Glibert, P. (1999). "Temperature regulation of nitrate uptake: A novel hypothesis about nitrate uptake and reduction in cool-water diatoms," *Limnology and Oceanography*, 44(3), 556-572.

Lomas, M., Trice, T., Glibert, P., Bronk, D., and McCarthy, J. (2002) "Temporal and spatial dynamics of urea concentrations in Chesapeake Bay: Biological versus physical forcing," *Estuaries*, submitted.

Luo, J., Hartman, K., Brandt, S., Cerco, C., and Rippetoe, T. (2001). "A spatially-explicit approach for estimating carrying capacity: an application for the Atlantic menhaden (*Brevoortia tyrannus*) in Chesapeake Bay," *Estuaries*, 24(4), 545-556.

Malone, T., Crocker, L., Pike, S., and Wendler, B. (1988). "Influences of river flow on the dynamics of phytoplankton production in a partially stratified estuary," *Marine Ecology Progress Series*, 48, 235-249.

Malone, T., Conley, D., Fisher, T., Glibert, P., Harding, and Sellner, K. (1996). "Scales of nutrient-limited phytoplankton productivity in Chesapeake Bay," *Estuaries*, 19, 371-385.

McCarthy, J., Taylor, W., and Taft, J. (1977). "Nitrogenous nutrition of the plankton in the Chesapeake Bay. 1. Nutrient availability and phytoplankton preferences," *Limnology and Oceanography*, 22(6), 996-1011.

McGillicuddy, D., McCarthy, J., and Robinson, A. (1995). "Coupled physical and biological modeling of the spring bloom in the North Atlantic (I): model formulation and one dimensional bloom processes," *Deep Sea Research I*, 42(8), 1313-1357.

McManus, G., and Ederington-Cantrell, M. (1992). "Phytoplankton pigments and growth rates, and microzooplankton grazing in a large temperate estuary," *Marine Ecology Progress Series*, 87, 77-85.

Miller, C., and Glibert, P. (1998). "Nitrogen excretion by the calanoid copepod Acartia tonsa: results of mesocosm experiments," *Journal of Plankton Research*, 20(9), 1767-1780.

Moll, A. (1998). "Regional distribution of primary production in the North Sea simulated by a three-dimensional model," *Journal of Marine Systems*, 16, 151- 170.

Monod, J. (1949). "The growth of bacterial cultures," *Annual Review of Microbiology*, 3, 371-394.

Pritchard, D. (1967). "Observations of circulation in coastal plain estuaries." Estuaries. G. Lauff ed., American Association for the Advancement of Science, Washington D.C., 37-44.

Parsons, T., Takahashi, M., and Hargrave, B. (1984). *Biological Oceanographic Processes*, Pergamon Press, Oxford.

Redfield, A., Ketchum, B., and Richards, F. (1966). "The influence of organisms on the composition of sea-water." *The Sea Volume II*. Interscience Publishers, New York, 26-48.

Richardson, T., and Cullen, J. (1995). "Changes in buoyancy and chemical composition during growth of a coastal marine diatom: ecological and biogeochemical consequences," *Marine Ecology Progress Series*, 128, 77-90.

Riebesell, U. (1989). "Comparison of sinking and sedimentation rate measurements in a diatom winter/spring bloom," *Marine Ecology Progress Series*, 54, 109-119.

Rippetoe, T. (1993). "Production and energetics of Atlantic menhaden in Chesapeake Bay," M.S. Thesis, University of Maryland, College Park MD.

Smith, E., and Kemp, W. (1995). "Seasonal and regional variations in plankton community production and respiration for Chesapeake Bay," *Marine Ecology Progress Series*, 116, 217-231.

Strickland, J., and Parsons, T. (1972). "A practical handbook of seawater analysis," *Bulletin of the Fisheries Research Board of Canada*," 167, 310 pp.

Taft, J., Taylor, W., and McCarthy, J. (1975). "Uptake and release of phosphorus by phytoplankton in the Chesapeake Bay estuary, USA," *Marine Biology*, 33, 21- 32.

Thomann, R., and Fitzpatrick, J. (1982). "Calibration and verification of a mathematical model of the eutrophication of the Potomac Estuary," HydroQual Inc., Mahwah, NJ.

Waite, A., Thompson, P., and Harrison, P. (1992). "Does energy control the sinking rates of marine diatoms?." *Limnology and Oceanography*, 37(3), 468- 477.

Wang, H., and Johnson, B. (2000). "Validation and application of the second-generation, three-dimensional hydrodynamic model of Chesapeake Bay," *Journal of Water Quality and Ecosystem Modeling*, 1, 51-90.

Westrich, J., and Berner, R. (1984). "The role of sedimentary organic matter in bacterial sulfate reduction: The G model tested," *Limnology and Oceanography*, 29(2), 236-249.

Wheeler, P., Gilbert, P., and McCarthy, J. (1982). "Ammonium uptake and incorporation by Chesapeake Bay phytoplankton: short-term uptake kinetics," *Limnology and Oceanography*, 27, 1113-1128.

White, J., and Roman, M. (1992). "Seasonal study of grazing by metazoan zooplankton in the mesohaline Chesapeake Bay," *Marine Ecology Progress Series*, 86, 251-261.

Suspended Solids and Light Attenuation 11

Data Bases

Solids

Suspended solids observations in the monitoring data base included total suspended solids, fixed solids, volatile solids, and particulate organic carbon. (For practical purposes, fixed and volatile solids correspond to inorganic and organic solids.) Direct analyses of organic solids were limited to stations in the Virginia tributaries (Table 11-1, Figure 11-1). The preponderance of organic solids observations was in the form of particulate organic carbon. We converted particulate organic carbon to organic solids through the relationship:

$$VSS = 2.5 \bullet POC \qquad (11\text{-}1)$$

in which:
VSS = organic solids concentration (g m^{-3})
POC = particulate organic carbon concentration (g C m^{-3})

This commonly-employed relationship assumes organic matter is comprised of a simple carbohydrate CH_2O. The total mass of this compound is 2.5 times the carbonaceous mass. Organic solids were subtracted from total suspended solids to obtain inorganic solids concentration.

Examination of the system-wide solids distribution indicates that organic solids represent a small fraction of the total suspended solids (Figures 11-2 to 11-4). Only in regions characterized by two stations, CB4.2C and CB5.2, do organic solids comprise as much a half the total suspended solids. The observed solids composition has significant implications for management activities in the bay system. Attempts to reduce organic solids concentrations, and thereby light attenuation, through nutrient controls address only a small fraction of the total suspended solids in the water column. Analyses using the submerged aquatic vegetation model (Cerco and Moore 2001) indicate system-wide restoration of submerged aquatic vegetation through nutrient controls alone is impossible.

Table 11-1
Number of Solids Analyses in Surface Samples 1985-1994

Station	Total Suspended Solids	Total Volatile Solids	Fixed Solids	Particulate Organic Carbon
CB1.1	186	0	0	181
CB2.2	201	0	0	197
CB3.3C	293	0	0	227
CB4.2C	206	0	0	200
CB5.2	208	0	0	196
CB6.1	194	0	0	193
CB7.3	204	0	0	208
CB7.4	204	0	0	204
CB7.4N	176	0	0	186
CB8.1E	182	0	0	181
EE1.1	197	0	0	182
EE2.1	268	0	0	254
EE3.1	380	0	0	288
EE3.2	344	0	0	253
ET1.1	176	0	0	155
ET2.3	102	0	0	90
ET4.2	204	0	0	191
ET5.2	225	0	0	207
ET6.2	108	0	0	101
ET9.1	102	0	0	93
LE1.3	194	0	0	181
LE2.2	422	0	0	123
LE3.2	151	95	151	12
LE4.2	114	60	114	12
LE5.3	138	88	138	11
RET1.1	194	0	0	179
RET2.4	391	0	0	20
RET3.2	116	60	116	12
RET4.2	148	93	148	12
RET4.3	113	59	113	12
RET5.2	113	60	113	11
TF1.7	415	0	0	388
TF2.1	376	0	0	23
TF3.3	111	58	111	12
TF4.2	116	63	116	12
TF4.4	176	86	176	17
TF5.5	119	65	119	12
WE4.2	187	0	0	186
WT1.1	205	0	0	190
WT2.1	204	0	0	186
WT5.1	420	0	0	322
WT8.1	113	0	0	103

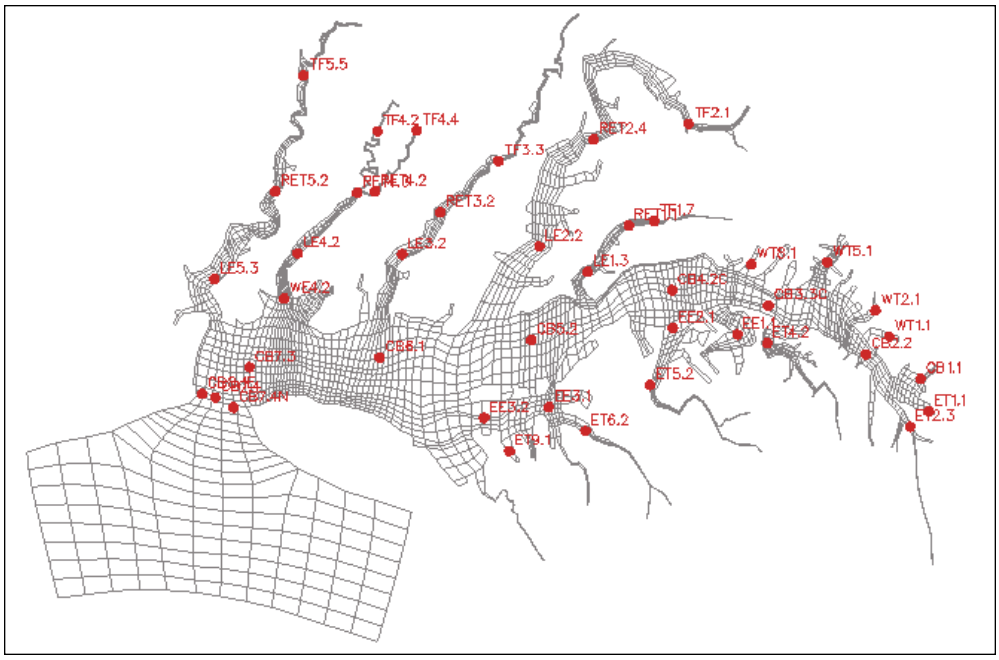

Figure 11-1. Monitoring stations used in analysis of suspended solids and light attenuation.

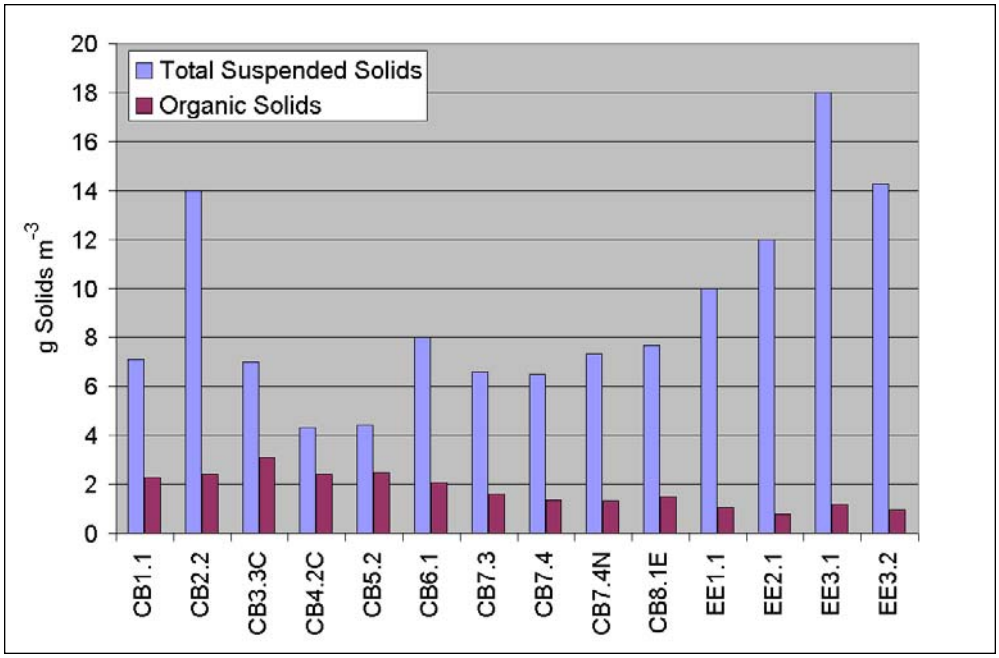

Figure 11-2. Median surface total suspended solids and organic solids concentrations at mainstem bay monitoring stations, 1985-1994.

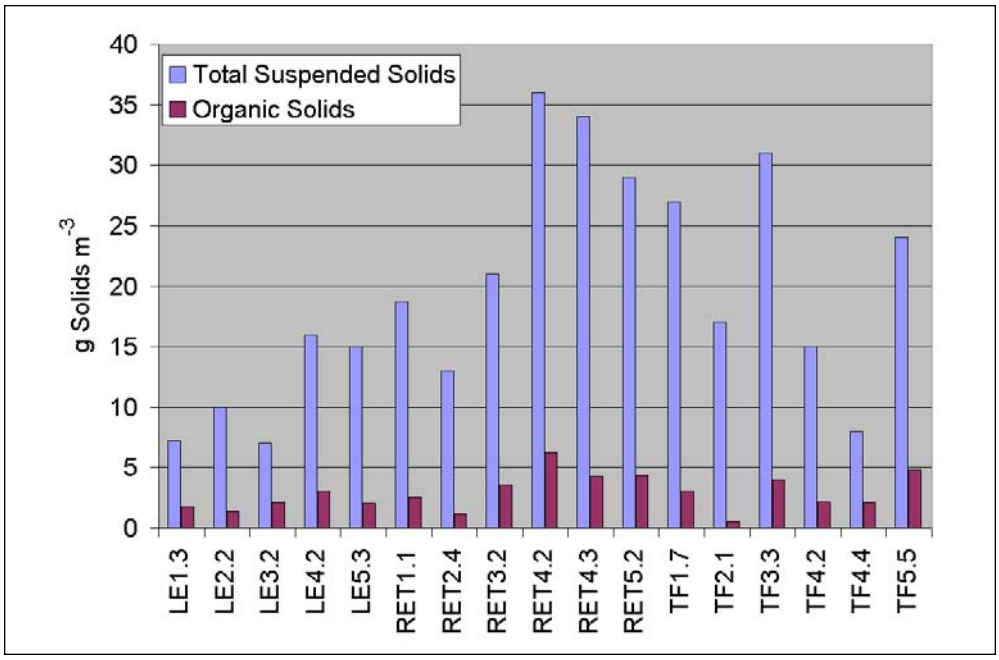

Figure 11-3. Median surface total suspended solids and organic solids concentrations at western tributary monitoring stations, 1985-1994.

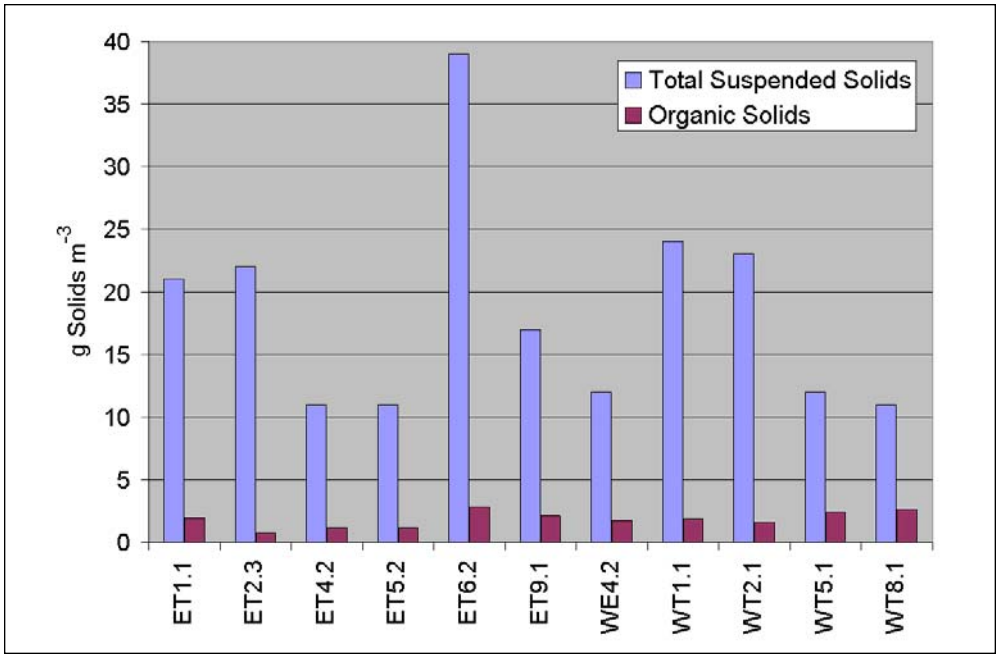

Figure 11-4. Median surface total suspended solids and organic solids concentrations are minor tributary monitoring stations, 1985-1994.

Light Attenuation

Two measurements of light attenuation were in the monitoring data base. The first was disk visibility or Secchi depth. The second was measurement of downwelling irradiance at multiple depths. Measures of disk visibility were almost universal from the inception of the monitoring program while measures of irradiance were phased in at various dates and locations. Analysis of light attenuation over the model simulation period therefore relied on disk visibility as the primary measure of light attenuation.

Attenuation can be obtained from disk visibility through the relationship:

$$Ke \bullet DV = \kappa \qquad (11\text{-}2)$$

in which:
Ke = coefficient of diffuse light attenuation (m^{-1})
DV = Secchi depth (m)
κ = empirical constant

The value of usually ranges between 1 and 2 although extremes from 0.5 to nearly 4 have been observed (Koenings and Edmundson 1991). The median value in clear water is 1.9. Higher values prevail in colored water while lower values are prevalent in turbid systems.

We obtained from Richard Lacouture, of the Academy of Natural Sciences, a data base consisting of simultaneous measures of disk visibility and downwelling irradiance. Measures were collected in the Maryland portion of the bay and in Maryland tributaries from 1985 to 1996. For each sampling, we computed light attenuation by fitting an exponential relationship to the irradiance observations:

$$I(z) = Io \bullet e^{-Ke \bullet z} \qquad (11\text{-}3)$$

in which:
I(z) = irradiance at depth z ($\mu E\ m^{-2}\ s^{-1}$)
Io = surface irradiance ($\mu E\ m^{-2}\ s^{-1}$)
z =depth (m)

Ke was determined by linear regression on log-transformed data. The value of R-squared for the individual regressions usually exceeded 0.9.

A set of paired observations of attenuation and disk visibility resulted after the determination of attenuation at each sampling. We again employed regression to obtain an estimate of parameter κ. We attempted to relate κ to location, solids concentration, and other variables but found no significant trends. Variance in the observations and the probabilistic nature of regression analysis prevented determination of an absolute, precise value for κ. We settled on the value κ = 1.3. Our value is slightly lower but comparable to a median of 1.44 (range 1.15 to 2.31) determined for turbid waters (Holmes 1970) and the value 1.43 determined for the Patuxent River (Keefe et al. 1976).

The Light Attenuation Model

We proposed a model that related light attenuation to attenuation from water, from inorganic suspended solids, from organic suspended solids, from dissolved organic matter, and from chlorophyll:

$$Ke = a_1 + a_2 \bullet ISS + a_3 \bullet VSS + a_4 \bullet DOC + a_5 \bullet Chl \qquad (11\text{-}4)$$

in which:
a_1 to a_5 = empirical constants
ISS = inorganic suspended solids concentration (g m^{-3})
VSS = organic suspended solids concentration (g m^{-3})
DOC = dissolved organic carbon (g C m^{-3})
Chl = chlorophyll (mg m^{-3})

We adopted dissolved organic carbon as a surrogate for the dissolved organic matter that provides color in water.

Parameters in the model were determined through linear regression. Regression was performed for each sample station to allow for regional variations in parameters. We found no significant relationship of attenuation to dissolved organic carbon. Various explanations for absence of a relationship may hold. The first is that dissolved organic carbon is a poor surrogate for colored organic matter. The second is that no significant spatial gradients of dissolved organic carbon exist. The third is that enormous variance is present in the analysis of dissolved organic carbon and masks any relationship to attenuation. Likely all of these explanations have validity.

We also found we could not distinguish attenuation from both chlorophyll and organic solids. The two variables were too closely correlated for their properties to be isolated by regression. We decided to drop chlorophyll from the model and retain organic solids. We reasoned we would like the model to distinguish potential differences in attenuation between inorganic and organic solids. Since our parameters were determined by regression, attenuation by chlorophyll was included as part of the total attenuation by organic solids.

The resulting attenuation relationship had the form:

$$Ke = a_1 + a_2 \bullet ISS + a_3 \bullet VSS \qquad (11\text{-}5)$$

in which:
a_1 = background attenuation (m^{-1})
a_2 = attenuation by inorganic suspended solids (m^2 g^{-1})
a_3 = attenuation by organic suspended solids (m^2 g^{-1})

The “background” attenuation term included attenuation from both water and dissolved organic matter.

Individual parameters were determined for each Chesapeake Bay Program Segment represented in the model domain (Figure 11-5). These were refined to provide reasonable consistency in the parameterization. In a few cases, background attenuation was adjusted to counter problems with the model solids computation. The result (Table 11-2) was a model in which background attenuation was highest

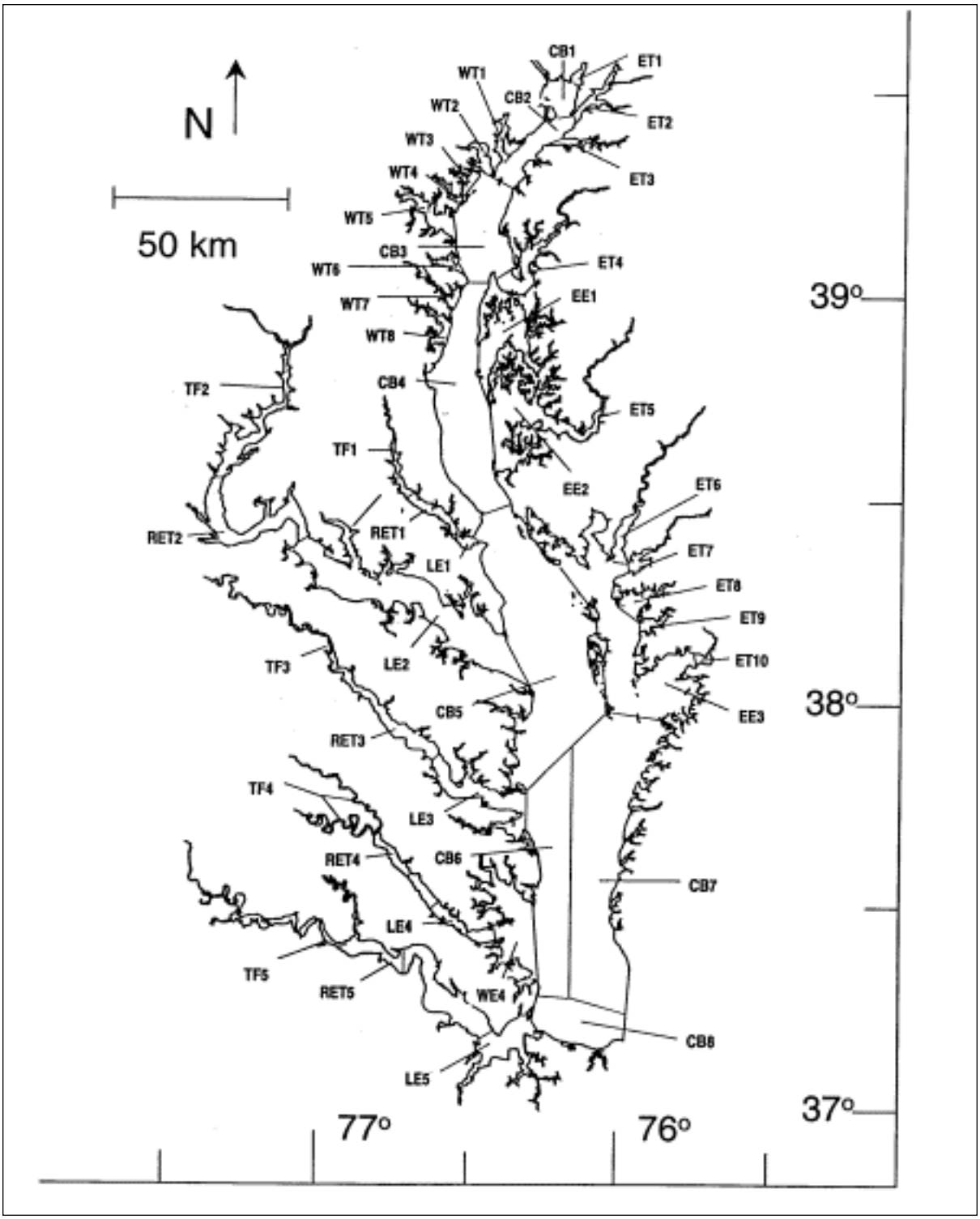

Figure 11-5. Chesapeake Bay Program Segments.

Table 11-2
Coefficients for Light Attenuation Model

Segment	a1, m^{-1}	a2, $m^2 g^{-1}$	a3, $m^2 g^{-1}$
CB1	0.7	0.117	0.117
CB2	0.47	0.117	0.117
CB3	0.3	0.117	0.117
CB4	0.2	0.083	0.083
CB5	0.2	0.083	0.083
CB6	0.2	0.083	0.083
CB7	0.2	0.083	0.083
CB8	0.2	0.083	0.083
EE1	0.2	0.083	0.083
EE2	0.2	0.083	0.083
EE3	0.2	0.083	0.083
ET1	0.47	0.117	0.117
ET2	0.47	0.117	0.117
ET3	0.47	0.117	0.117
ET4	0.3	0.117	0.117
ET5	0.2	0.083	0.083
ET6	0.2	0.083	0.083
ET7	0.2	0.083	0.083
ET8	0.2	0.083	0.083
ET9	0.2	0.083	0.083
ET10	0.2	0.083	0.083
LE1	0.3	0.083	0.083
LE2	0.3	0.083	0.083
LE3	0.3	0.083	0.083
LE4	0.3	0.083	0.083
LE5	0.3	0.083	0.083
RET1	0.47	0.083	0.083
RET2	0.47	0.083	0.083
RET3	0.47	0.083	0.083
RET4	0.47	0.083	0.083
RET5	0.47	0.083	0.083
TF1	0.05	0.083	0.083
TF2	0.47	0.083	0.083
TF3	0.47	0.083	0.083
TF4	0.47	0.083	0.083
TF5	0.47	0.083	0.083
WE4	0.2	0.083	0.083
WT1	0.47	0.117	0.117
WT2	0.3	0.117	0.117
WT3	0.3	0.117	0.117
WT4	0.3	0.117	0.117
WT5	0.2	0.117	0.117
WT6	0.3	0.117	0.117
WT7	0.2	0.083	0.083
WT8	0.2	0.083	0.083

near the freshwater sources and lowest near the ocean interface. This conceptualization was consistent with the observation that freshwater is more colored than seawater (Kirk 1994). During the refinement, the distinction of coefficients for inorganic and organic solids was dropped but solids near the fall lines were characterized as having higher attenuation than solids in regions distant from sources in upland watersheds.

Comparison with the SAV Technical Synthesis II

An additive light attenuation model similar to our own was created as part of the second technical synthesis on submerged aquatic vegetation and water quality (Chesapeake Bay Program 2000). The model incorporated background attenuation, attenuation from total suspended solids, and attenuation from chlorophyll. As with our model, parameters were initially obtained from regression and then refined to improve agreement with observations.

Regressions produced background attenuation in range 0.393 to 3.32 m^{-1}. The value 0.32 m^{-1} was recommended for use system-wide. This value is centrally located within the values 0.05 to 0.7 m^{-1} used in our model and is close to our predominant value of 0.2 m^{-1}.

Regressions indicated the coefficient that related total suspended solids contribution to light attenuation was in the range 0.013 to 0.101 m^2 g^{-1}. The coefficient recommended for use system-wide was 0.094 m^2 g^{-1}. This value is nearly identical to the average of the two values, 0.083 and 0.117 m^2 g^{-1}, used in our own model.

Fewer than half of the regressions conducted as part of the "Tech Syn II" resulted in significant relationships between chlorophyll and light attenuation. Several of the statistically significant relationships were negative, indicating a physically-impossible relationship. These results echoed our own difficulty in isolating the effect of chlorophyll via regression. The attenuation coefficient of chlorophyll is well-known, however (e.g. Pennock 1985). Consequently, the Tech Syn II investigators elected to include chlorophyll attenuation, 0.016 m^2 mg^{-1}, in their model. If we assume a carbon-to-chlorophyll ratio of 75 and utilize the ratio of 2.5 between solids and organic carbon, we find the chlorophyll attenuation used in Tech Syn II is equivalent to 0.085 m^2 g^{-1} organic solids, remarkably close to the prevailing value used in our own model.

We are relieved and reassured that the light attenuation relationships obtained in independent investigations are equivalent. Managers and other users of the two models, ours and Tech Syn II, should be confident that guidance obtained from the two models will be consistent.

Solids Settling Velocities

The principal suspended solids variable in the CBEMP was inorganic (fixed) suspended solids. Organic solids were derived from particulate carbon variables (phytoplankton, zooplankton, detritus) and added to inorganic solids for comparison to observed total suspended solids.

No internal sources or sinks of inorganic solids were considered in the model. Aside from loads, the distribution of inorganic solids in the water column was determined by two settling velocities. One represented settling through the water

column and the other represented net settling to the bed sediments. Within the water column, the transport equation for inorganic solids was identical to the equation for all other variables. A modification applied in cells that interfaced the bed sediments:

$$\frac{\delta C}{\delta t} = [\text{transport}] + \frac{W}{\Delta z} \bullet Cu - \frac{Wnet}{\Delta z} \bullet C \qquad (11\text{-}6)$$

in which:
C = solids concentration in cell adjoining bed sediments (g m^{-3})
Cu = solids concentration two cells above bed sediments (g m^{-3})
W = settling velocity in water column (m d^{-1})
Wnet = settling velocity from water to bed sediments (m d^{-1})
z = cell thickness (m)
t = time (d)

Net settling was always less than or equal to settling through the water column. The reduced magnitude of net settling represented the net effect of resuspension. The ratio of net settling to settling through the water column may be viewed as the fraction of material deposited on the bed that remains in the bed. The employment of net settling is a primary distinction between our own suspended solids model and a true sediment transport model. Our model included no resuspension mechanism. Once a particle was deposited on the bottom, it remained there.

Settling and net settling were evaluated through a recursive calibration process based on visual fitting of computed to observed solids. Settling velocities obtained in this fashion were highest near the fall lines of several western tributaries and in a few minor Eastern Shore tributaries (Table 11-3). The high settling velocities in the western tributaries diminished with distance from the head of tide, perhaps indicating sorting out of large particles carried over the fall line. Our estimates of loading from bank erosion were highly uncertain in the Eastern Shore embayments. The high settling velocities assigned in some tributaries there may reflect depositional environments or may be a compensation for overestimated bank loads. Settling velocities assigned in the mainstem bay (Table 11-3) also diminished away from the source in the Susquehanna River but were less than in several western tributaries. The velocities assigned suggested particles with high settling velocities settled out in Conowingo Reservoir before reaching the bay.

Net settling velocities were five to ten percent of settling in the water column. (Table 11-3).

Net settling was enhanced in the presence of submerged aquatic vegetation (Cerco and Moore 2001) to represent the damping effect of vegetation on waves and on resuspension.

Our model did not consider solids size classes. We found a modification to assigned settling velocities was required during major storm events. Storm events were defined as intervals in which inorganic solids concentration exceeded 100 g m^{-3}. During storm events, the inorganic solids settling rate was specified as 5 m d^{-1} and no resuspension was allowed. This assignment simulated rapid settling of large particles carried over the fall line during floods. If we did not assign rapid settling during storms, solids loads associated with storms remained in the water column perpetually.

Table 11-3
Inorganic Solids Settling Rates

Segment	Settling, m d^{-1}	Net Settling, m d^{-1}
CB1	1.25	0.1
CB2	1.25	0.1
CB3	1.25	0.05
CB4	1	0.05
CB5	1	0.05
CB6	1	0.05
CB7	1	0.05
CB8	1	0.05
EE1	1.5	0.15
EE2	1.5	0.15
EE3	1	0.025
ET1	1.5	0.15
ET2	1	0.025
ET3	1.5	0.15
ET4	2.5	0.25
ET5	2.5	0.25
ET6	1.5	0.15
ET7	2	0.2
ET8	2	0.2
ET9	2.5	0.25
ET10	2	0.2
LE1	1.75	0.175
LE2	1.5	0.15
LE3	2	0.2
LE4	2	0.2
LE5	1.5	0.1
RET1	2.5	0.25
RET2	1.5	0.15
RET3	2	0.1
RET4	2	0.2
RET5	2	0.1
TF1	2.5	0.25
TF2	1	0.05
TF3	3	0.3
TF4L	4	0.4
TF4R	3.5	0.35
TF5	3	0.3
WE4	1	0.1
WT1	1.5	0.15
WT2	1.5	0.15
WT3	1.5	0.15
WT4	1.5	0.15
WT5	2	0.2
WT6	1.5	0.15
WT7	1.5	0.15
WT8	1.5	0.15

Model Results

The time series, spatial plots, and summary plots of suspended solids and light attenuation produced during the model calibration comprise over 350 figures. Obviously, not all can be pulled into this chapter. We present a sampling here. A complete set of plots is provided on the CD-ROM that accompanies this report.

Time Series

Time series of computed and observed total suspended solids and light attenuation are presented for Station CB2.2 in the upper bay (Figures 11-6 to 11-8), Station CB5.2 at mid-bay (Figures 11-9 to 11-11), and Station CB7.3 in the lower bay (Figures 11-12 to 11-14). The high degree of short-term variability in both observations and model confounds interpretation of results although several properties are apparent. Certainly, the model represents the central tendency and extremes of the observations although one-to-one agreement between model and instantaneous observations is not always present. Higher computed values of solids concentrations and light attenuation occur in winter and spring, the periods of maximum runoff and solids loading from the watershed. In the upper bay, concentration and attenuation maxima are "flashy," exhibiting large excursions over short periods. In the mid-bay, the excursions are spread out in time and damped in amplitude while they are barely noticeable in the lower bay. The model exhibits a large impact from the wet years of 1993 and 1994 although this impact is not so pronounced in the observations. Observed suspended solids concentrations show a greater range at the bottom than at the surface, no doubt due to sediment resuspension. The model demonstrates higher sediment concentrations at the bottom that at the surface but the observed range is under-estimated. The specification of net settling less than settling through the water column results in higher computed concentrations at the bottom than at the surface. A true resuspension algorithm is required for the model to reproduce the full range of observed concentrations.

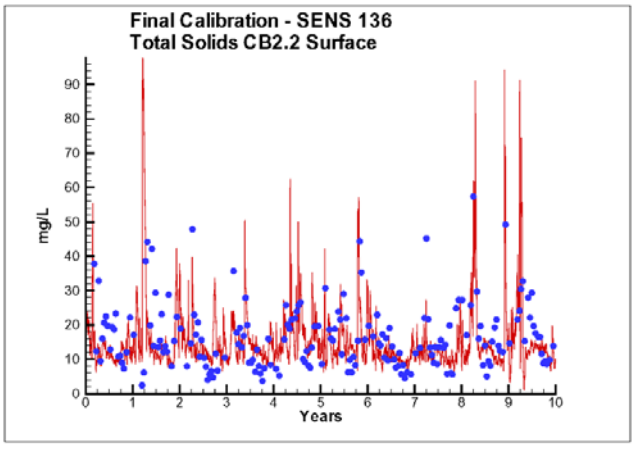

Figure 11-6. Computed and observed total suspended solids at Station CB2.2 (surface).

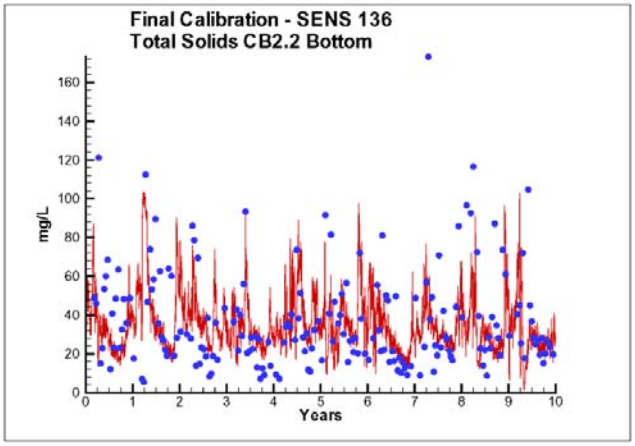

Figure 11-7. Computed and observed total suspended solids at Station CB2.2 (bottom).

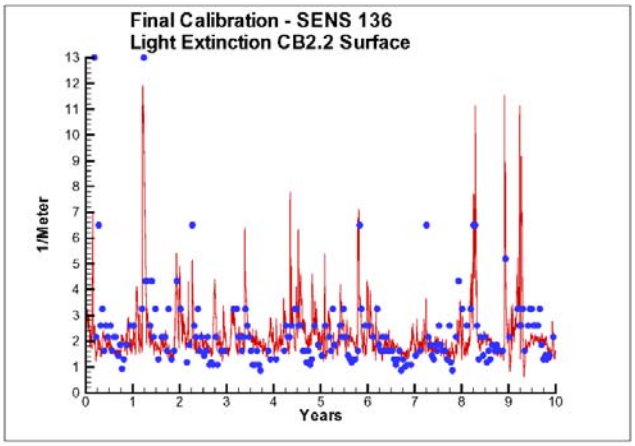

Figure 11-8. Computed and observed light attenuation at Station CB2.2.

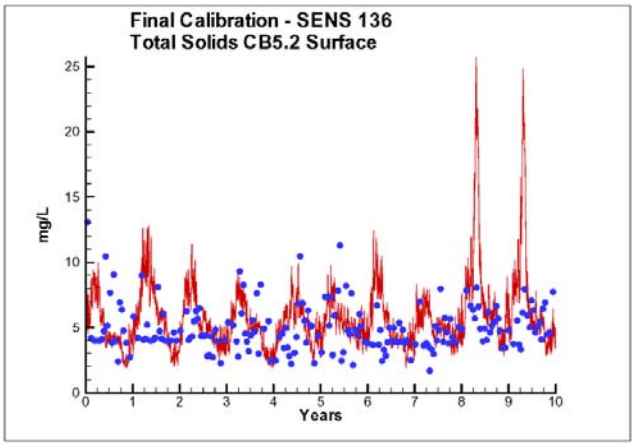

Figure 11-9. Computed and observed total suspended solids at Station CB5.2 (surface).

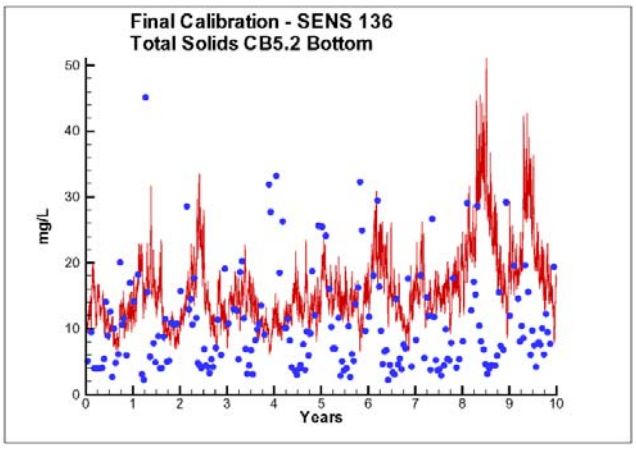

Figure 11-10. Computed and observed total suspended solids at Station CB5.2 (bottom).

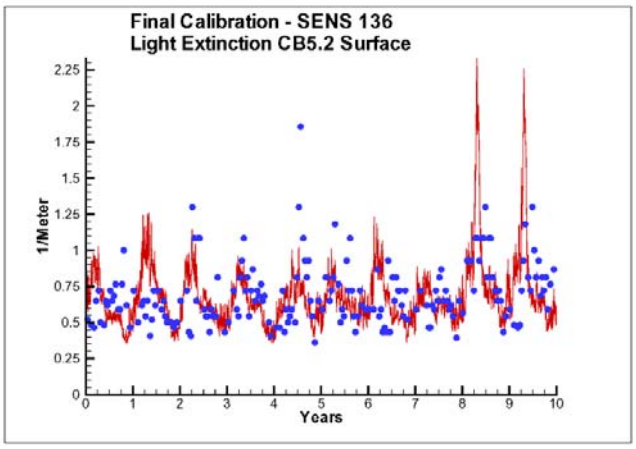

Figure 11-11. Computed and observed light attenuation at Station CB5.2.

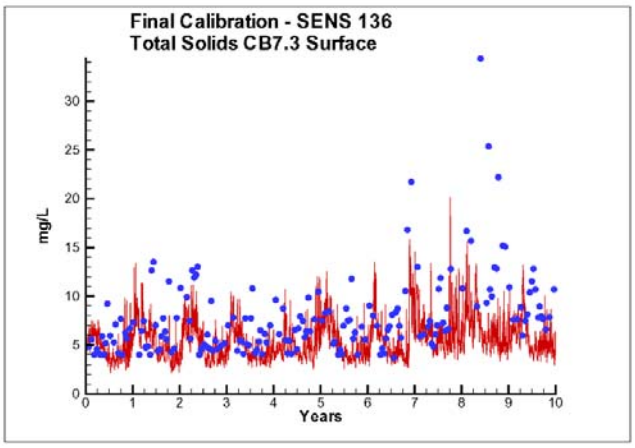

Figure 11-12. Computed and observed total suspended solids at Station CB7.3 (surface).

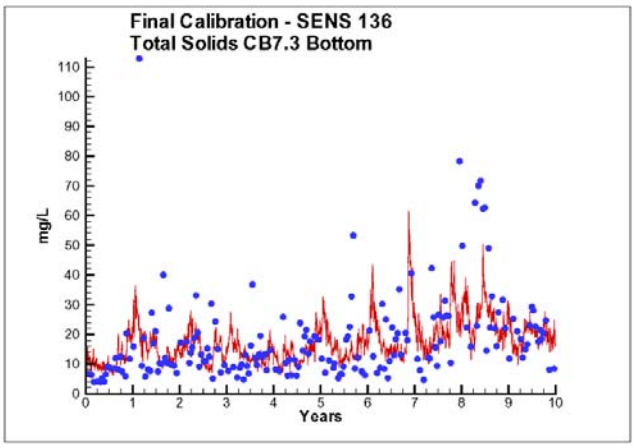

Figure 11-13. Computed and observed total suspended solids at Station CB7.3 (bottom).

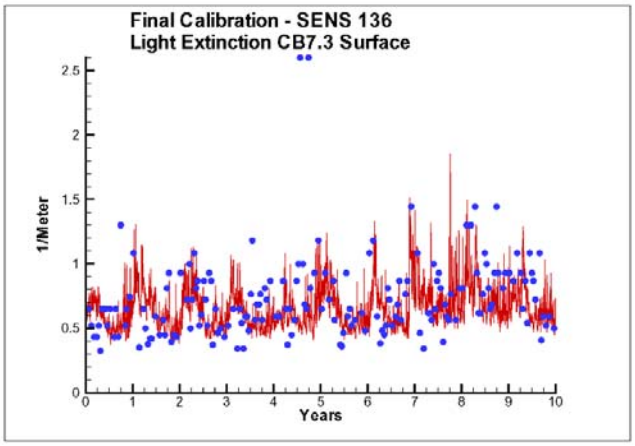

Figure 11-14. Computed and observed light attenuation at Station CB7.3.

Longitudinal Distributions

The spatial distribution of suspended solids and light attenuation were examined, on a seasonal basis, along the axes of the bay and major tributaries. Details of the averaging process and transect maps were presented in the chapter entitled "Introduction to the Calibration."

Chesapeake Bay. The most interesting feature of the observed solids distribution is the presence of two solids maxima in Chesapeake Bay (Figures 11-15 to 11-26). One maximum, at km 280 to 300, is the classic turbidity maximum noted by Schubel (1968) and others. The second maximum occurs roughly 70 km above the mouth of the bay. Hood et al. (1999) noted regions of high particle concentrations in the lower bay. They attributed these concentrations to a persistent eddy and to processes including convergence and downwelling. The concentrations noted by Hood et al. were downstream (km 25 on our axis) of the maximum observed here and primarily to the east of our transect. We cannot be certain if the high observed concentrations around km 70 are a result of the processes noted by Hood et al. or not. Our model preforms reasonably in reproducing the solids maximum at km 280 while the maximum at km 70 is not reproduced at all. Hood et al. used a particle-tracking algorithm to reproduce the maxima in the lower bay. Particle tracking is not implemented in our model nor is this envisioned as a reasonable improvement for future model versions.

The solids maximum in the lower bay is not accompanied by a corresponding peak in light attenuation. As part of our modeling scheme, we assigned more color to water in the upper bay and assigned higher attenuation properties to solids in the upper bay. The absence of an observed attenuation maximum associated with the observed solids maximum in the lower bay suggests our interpretation of color and attenuation is correct. The solids in the lower bay do not attenuate light to the same degree as solids in the upper bay. The bay exhibits one turbidity maximum associated with the solids maximum at km 280 to 300. Our model provides a reasonable representation of attenuation in the turbidity maximum.

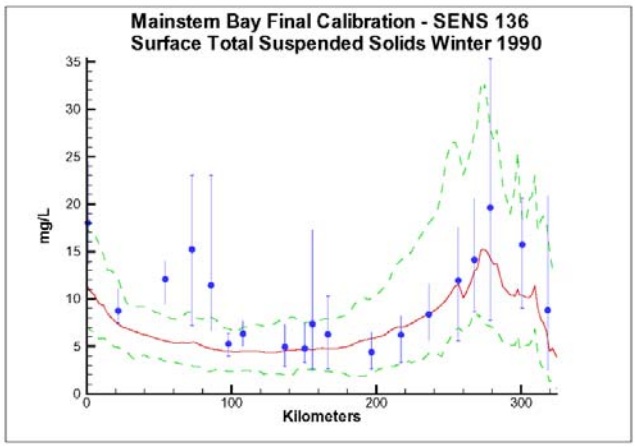

Figure 11-15. Computed (mean and range) and observed (mean and range) total suspended solids along Chesapeake Bay axis, winter 1990 (surface).

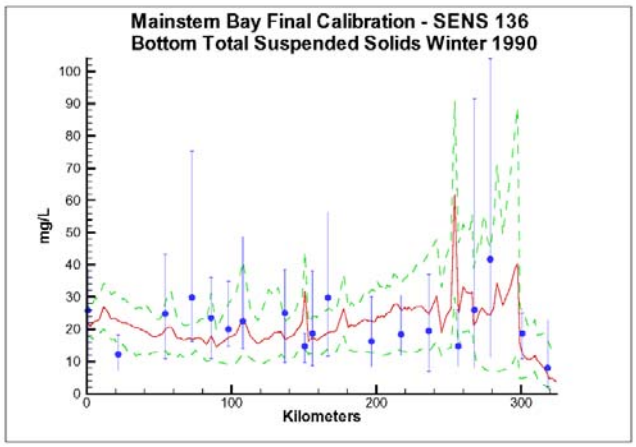

Figure 11-16. Computed (mean and range) and observed (mean and range) total suspended solids along Chesapeake Bay axis, winter 1990 (surface).

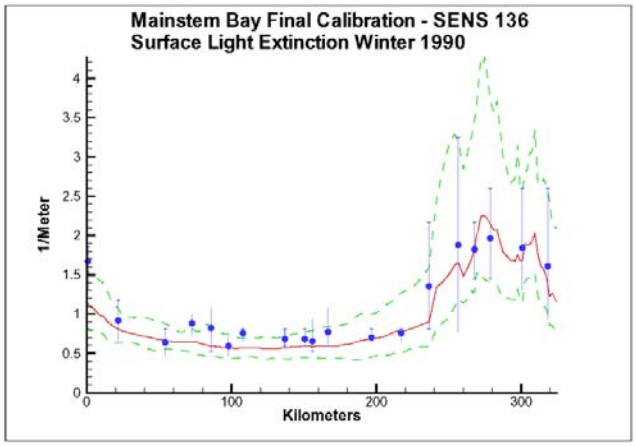

Figure 11-17. Computed (mean and range) and observed (mean and range) light attenuation along Chesapeake Bay axis, winter 1990.

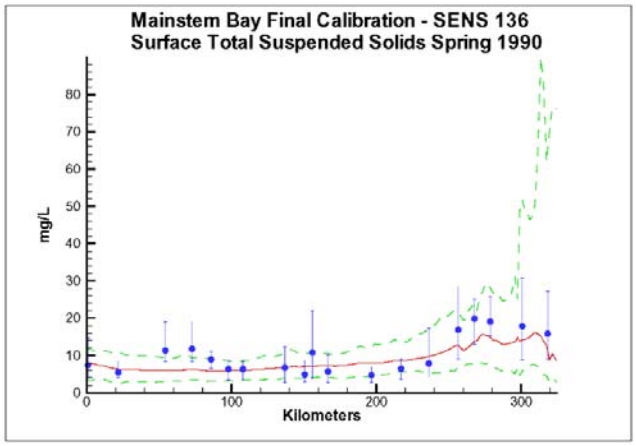

Figure 11-18. Computed (mean and range) and observed (mean and range) total suspended solids along Chesapeake Bay axis, spring 1990 (surface).

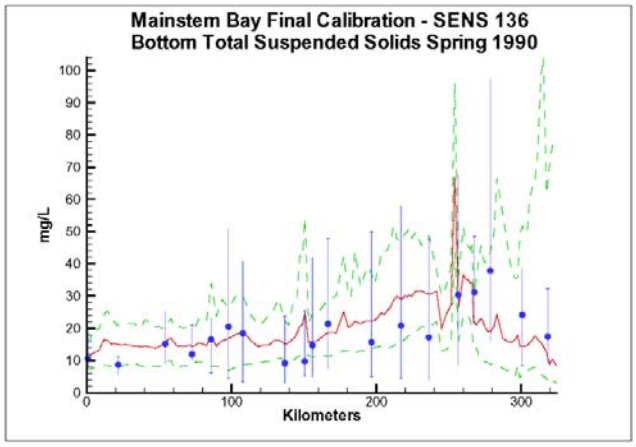

Figure 11-19. Computed (mean and range) and observed (mean and range) total suspended solids along Chesapeake Bay axis, spring 1990 (bottom).

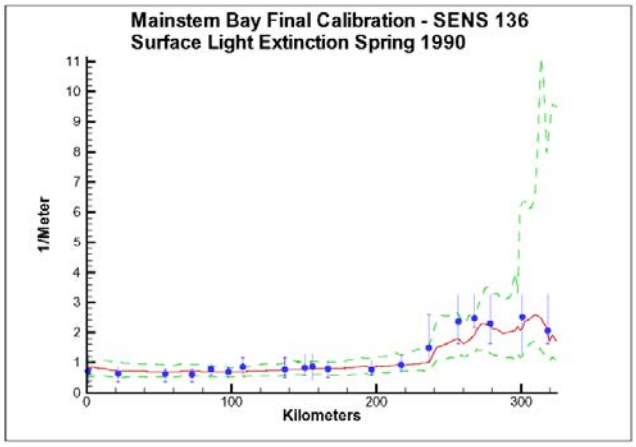

Figure 11-20. Computed (mean and range) and observed (mean and range) light attenuation along Chesapeake Bay axis, spring 1990.

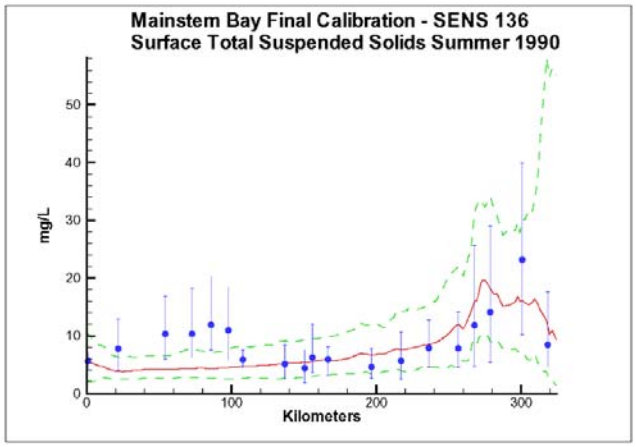

Figure 11-21. Computed (mean and range) and observed (mean and range) total suspended solids along Chesapeake Bay axis, summer 1990 (surface).

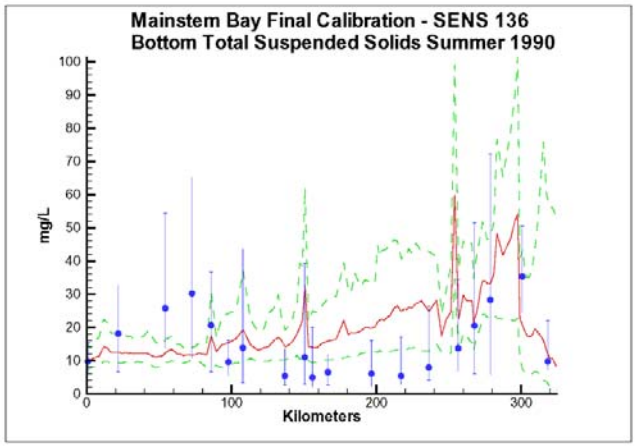

Figure 11-22. Computed (mean and range) and observed (mean and range) total suspended solids along Chesapeake Bay axis, summer 1990 (bottom).

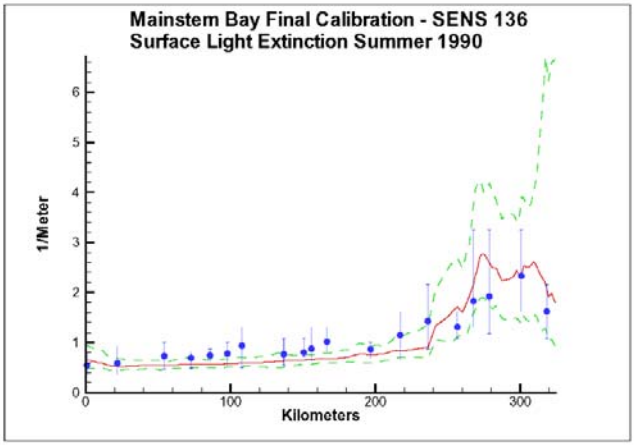

Figure 11-23. Computed (mean and range) and observed (mean and range) light attenuation along Chesapeake Bay axis, summer 1990.

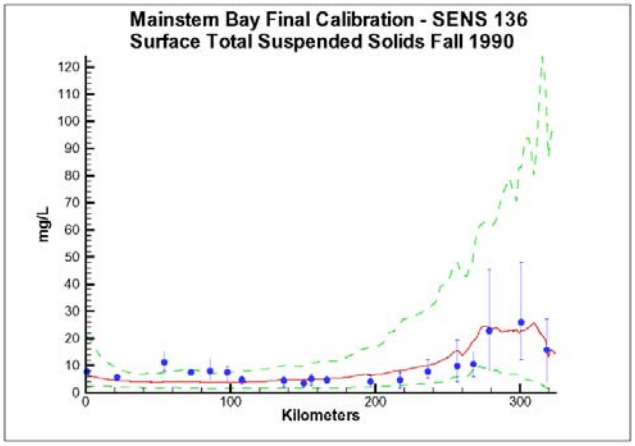

Figure 11-24. Computed (mean and range) and observed (mean and range) total suspended solids along Chesapeake Bay axis, fall 1990 (surface).

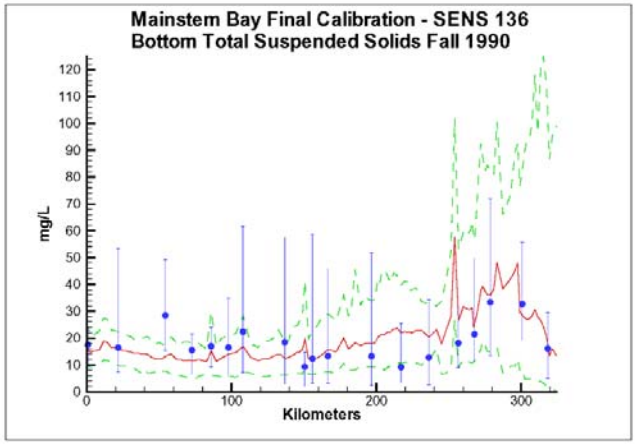

Figure 11-25. Computed (mean and range) and observed (mean and range) total suspended solids along Chesapeake Bay axis, fall 1990 (bottom).

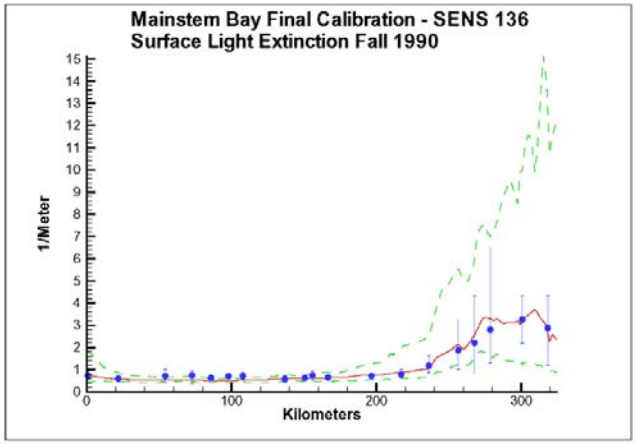

Figure 11-26. Computed (mean and range) and observed (mean and range) light attenuation along Chesapeake Bay axis, fall 1990.

Western Tributaries. A conspicuous feature of the solids and attenuation computations in the western tributaries (Figures 11-27 to 11-41) is enormous variance in computations near the fall lines. The variance corresponds to variance in loadings from the watershed. We employed "cruise averaging" so that model results are averaged only over sampling intervals. Still, in view of the variance in loads, ideal agreement between computed and observed means near the fall lines should not be expected. Improved comparisons should be expected downstream of the fall lines as the impact of loads is damped with distance from the source.

Both the location and magnitude of the turbidity maximum in the James River are well represented (Figures 11-27 to 11-29). Above the maximum, the computed surface solids and attenuation distributions are flat to the fall line. We found it difficult to replicate the observed increase in surface solids concentration between the fall line and the turbidity maximum. Computed solids concentration along the

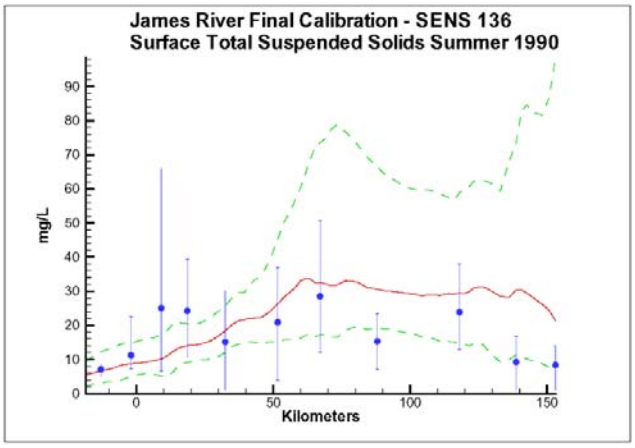

Figure 11-27. Computed (mean and range) and observed (mean and range) total suspended solids along James River axis, summer 1990 (surface).

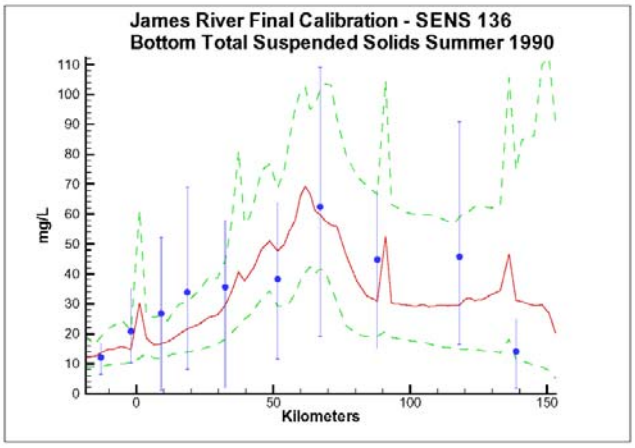

Figure 11-28. Computed (mean and range) and observed (mean and range) total suspended solids along James River axis, summer 1990 (bottom).

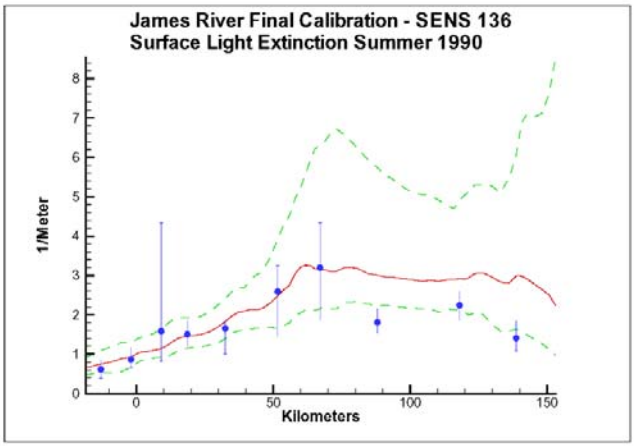

Figure 11-29. Computed (mean and range) and observed (mean and range) light attenuation along James River axis, summer 1990.

bottom provides a better approximation of the increase from the fall line to the turbidity maximum around km 70. Downstream of the turbidity maximum, the model provides good representation of the solids concentration and excellent representation of light attenuation.

The observed turbidity maximum in the York River occurs around km 70 (Figures 11-30 to 11-32). Computed solids concentration climbs from the intersection with the bay (km 0) to around km 40. From km 40 to the fall line, computed solids distribution is flat. Computed solids concentration in the turbidity maximum is underestimated. Computed light attenuation agrees well with observed through to km 70. Above km 70, observations are sparse but the model tends to overestimate light attenuation.

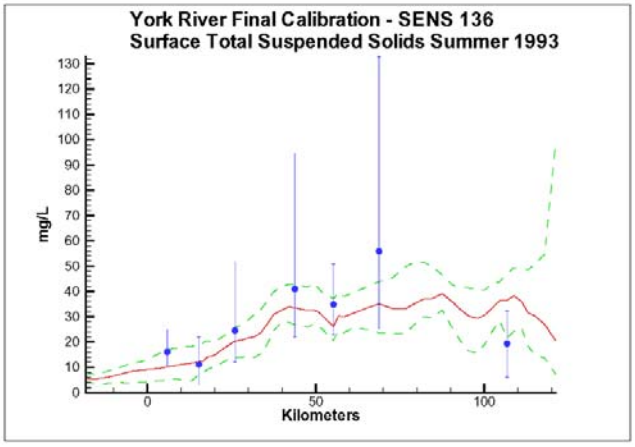

Figure 11-30. Computed (mean and range) and observed (mean and range) total suspended solids along York River axis, summer 1993 (surface).

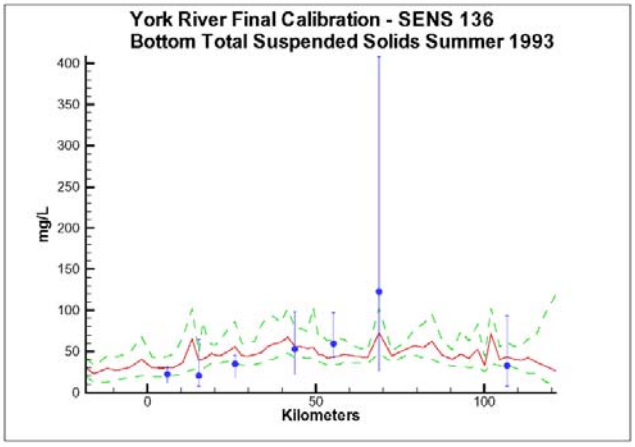

Figure 11-31. Computed (mean and range) and observed (mean and range) total suspended solids along York River axis, summer 1993 (bottom).

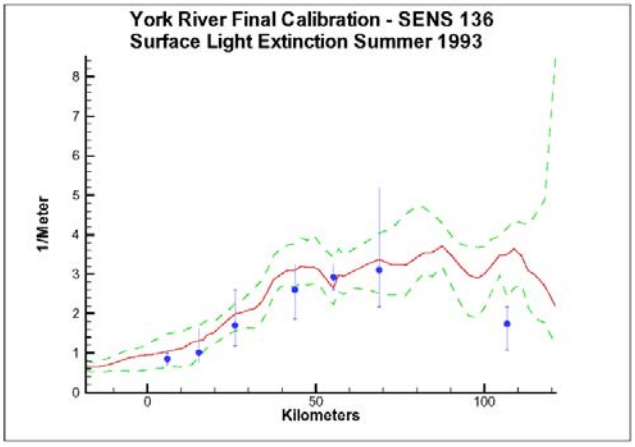

Figure 11-32. Computed (mean and range) and observed (mean and range) light attenuation along York River axis, summer 1993

Observations from 1990 indicate a turbidity maximum in the Rappahannock around km 80 (Figures 11-33 to 11-35). The model computes a maximum of the correct magnitude at km 70. Owing to the spatial distribution of observations, the location of the computed maximum cannot be disputed. In this year, the solids concentration in the bottom is well represented but solids are underestimated in the surface layer below km 70. In alternate years e.g. 1993 (see CD-ROM), computed solids are high in the bottom but match the surface observations well. Computed solids concentrations exhibit a consistent secondary peak around km 130. The observations are spaced too far apart to determine if the secondary peak is real or an artifact of the model. Computed light attenuation follows the solids distribution. Peak computed attenuation occurs in the turbidity maximum around km 70 and in the second maximum upstream around km 130. The model provides reasonable agreement with observed attenuation magnitude and distribution.

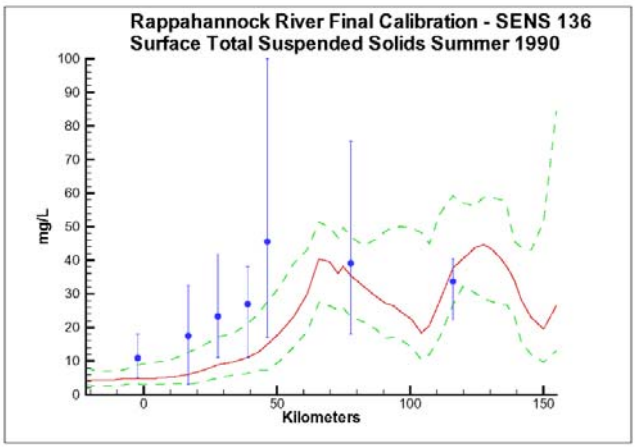

Figure 11-33. Computed (mean and range) and observed (mean and range) total suspended solids along Rapahannock River axis, summer 1990 (surface).

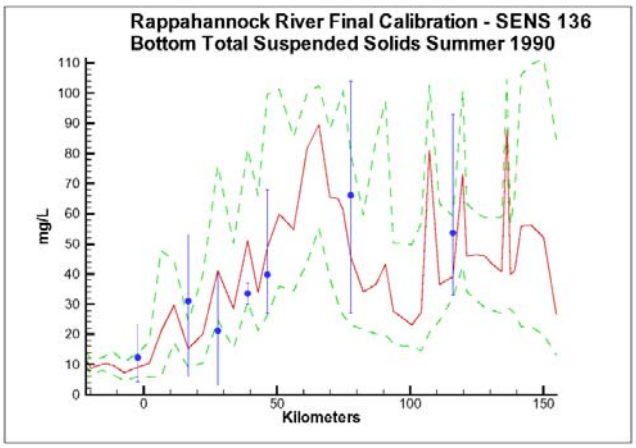

Figure 11-34. Computed (mean and range) and observed (mean and range) total suspended solids along Rappahannock River axis, summer 1990 (bottom).

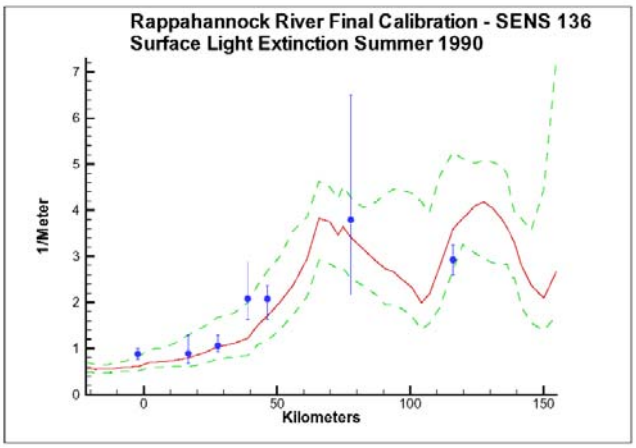

Figure 11-35. Computed (mean and range) and observed (mean and range) light attenuation along Rappahannock River axis, summer 1990.

The predominant characteristic of the Potomac River solids observations is an enormous concentration peak in the bottom waters around km 100 (Figures 11-36 to 11-38). The peak barely penetrates into the surface waters, however, so that pronounced peaks in surface solids and in light attenuation are not apparent at the location of the subsurface solids maximum. In 1985 and in other seasons (see CD-ROM), surface solids and attenuation are as likely to peak further upstream, around km 140, as they are to peak coincident with the bottom solids maximum. Interestingly, in 1985, the observed upstream limit of salt intrusion was around km 130 (Figure 11-39). The location of the salt intrusion suggests the solids peak around km 130 represents a classic turbidity maximum located at the convergence of upstream and downstream circulation. The subsurface peak at km 100 may result from an alternate process such as a concentration of solids in a deep hole or in a location of large shear stress. In summer, modeled solids and attenuation peak still further upstream and are associated with the freshwater algal bloom.

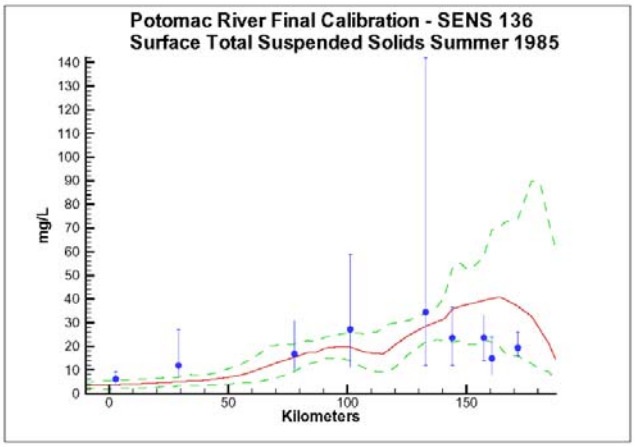

Figure 11-36. Computed (mean and range) and observed (mean and range) total suspended solids along Potomac River axis, summer 1985 (surface).

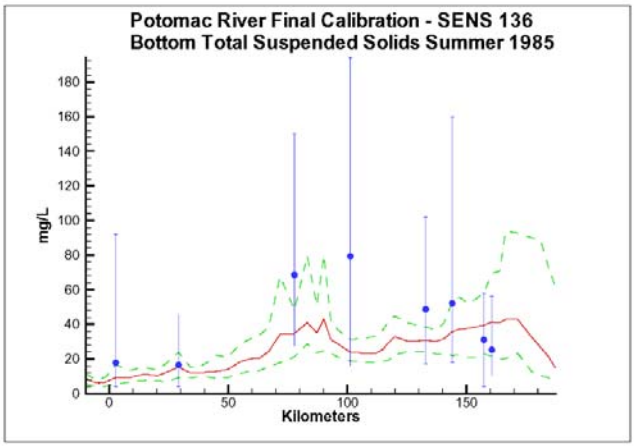

Figure 11-37. Computed (mean and range) and observed (mean and range) total suspended solids along Potomac River axis, summer 1985 (bottom).

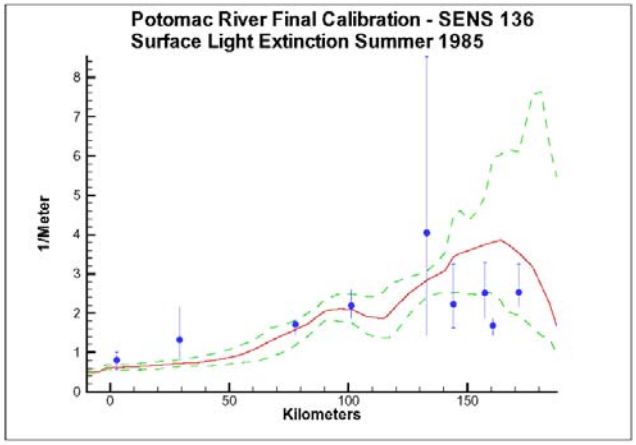

Figure 11-38. Computed (mean and range) and observed (mean and range) light attenuation along Potomac River axis, summer 1985.

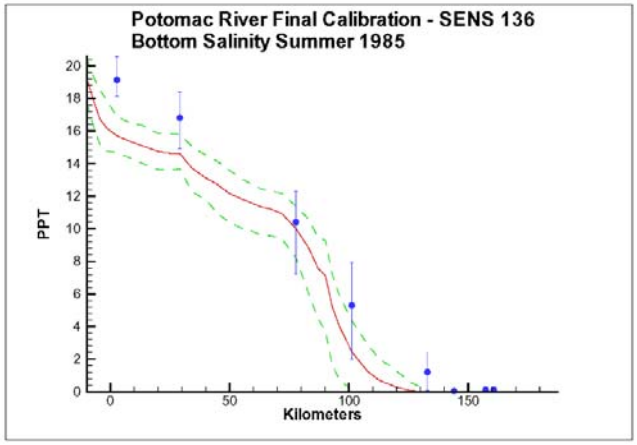

Figure 11-39. Computed (mean and range) and observed (mean and range) salinity along Potomac River axis, summer 1985 (bottom).

The turbidity maximum in the Patuxent occurs around km 60 (Figures 11-40 to 11-42). The model provides a reasonable representation of solids concentration from the mouth of the Patuxent up to km 60. Near the upstream limit of the model, computed solids tend to exceed observed during 1985. The computed concentrations at the upper end of the Patuxent exhibit enormous variance in this year and in others (see CD-ROM). Calculated concentrations reflect the loading and can be affected to only a minimum extent by assignment of parameters with the model. Except for one improbable observation, the model provides a reasonable representation of light attenuation in the Patuxent. As with solids, computed attenuation at the upper end of the river reflects enormous variance in the loads and can be affected only minimally through adjustment of the model.

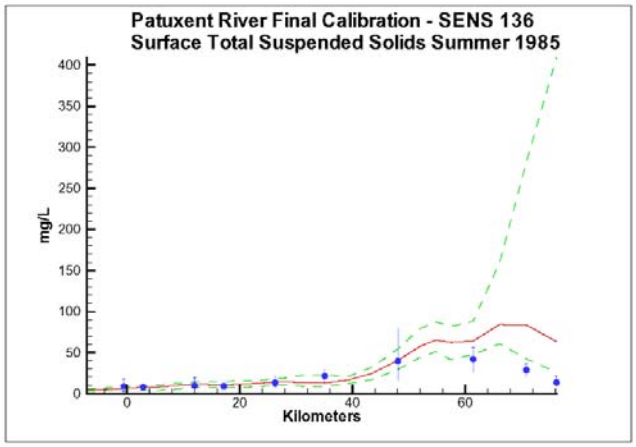

Figure 11-40. Computed (mean and range) and observed (mean and range) total suspended solids along Patuxent River axis, summer 1985 (surface).

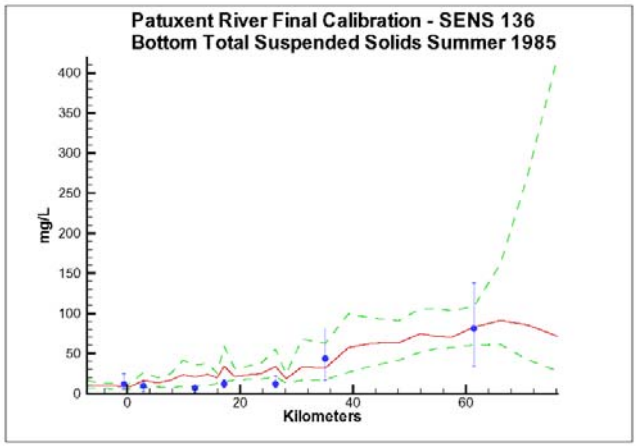

Figure 11-41. Computed (mean and range) and observed (mean and range) total suspended solids along Patuxent River axis, summer 1985 (bottom).

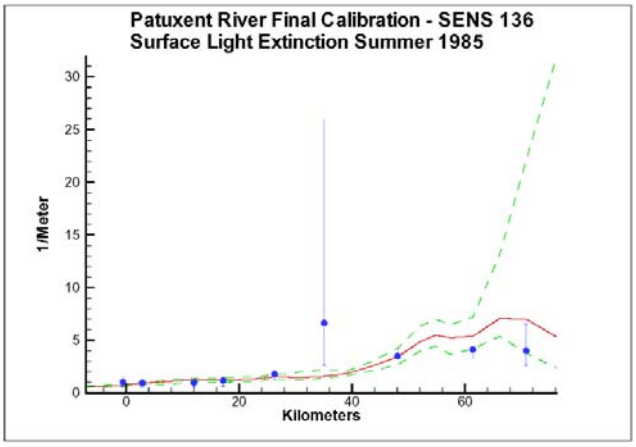

Figure 11-42. Computed (mean and range) and observed (mean and range) light attenuation along Patuxent River axis, summer 1985.

Distribution Plots

Observations and computations from our time series stations (Figure 11-1) were compared on cumulative distribution plots. Observations were paired with daily-average computations on sample days so that the plots compared distributions of observations and computations matched in location and time. Each station contributed ≈150 to 250 attenuation observations and double that quantity (surface plus bottom) of suspended solids observations. Observations from only our time series stations were considered and these were pooled into distributions for the bay, major tributaries, and minor tributaries. More extensive comparisons of selected parameters were prepared by the Chesapeake Bay Program Office, on a station-by-station basis, for use in TMDL analyses.

The upper percentiles of the observations (> ≈98%) are frequently dominated by a few extreme observations. These extremes are often improbable e.g. light attenuation of 25 m^{-1}. The use of automated data processing and plotting routines on enormous numbers of observations makes detection and elimination of bad data almost impossible. The viewer is cautioned against placing great emphasis on the extreme observations.

Since disk visibility was recorded at fixed intervals, the distribution of attenuation observations appears as a series of steps.

The distributions of computed and observed solids and attenuation for the bay (Figures 11-43 to 11-44) show remarkable agreement. The solids distributions agree at both extremes and are offset by roughly 1 gm m^{-3} at the median. Computed and observed attenuation are coincident through most of the distribution and depart only in the lower 10% to 15%. In this range, the model computes attenuation that exceeds the observations by ≈0.1 m^{-1}.

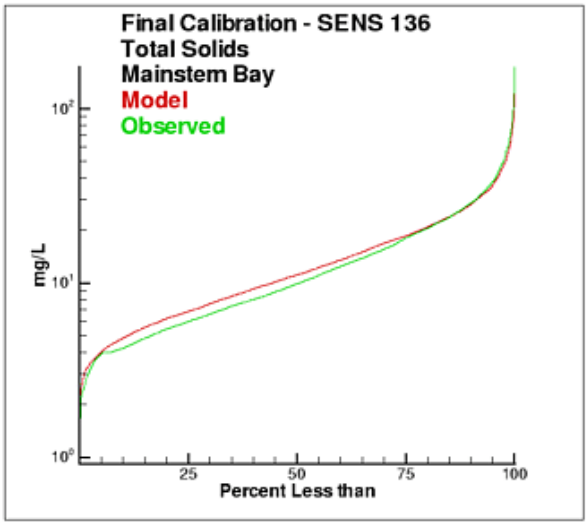

Figure 11-43. Cumulative distribution of computed and observed total suspended solids in Chesapeake Bay.

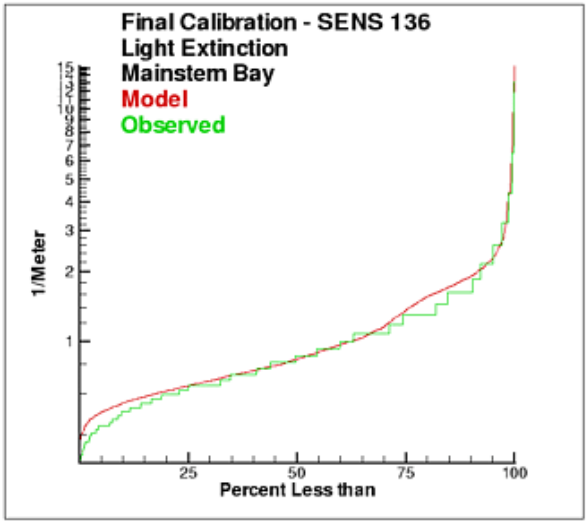

Figure 11-44. Cumulative distribution of computed and observed light attenuation in Chesapeake Bay.

Computed and observed solids in the James River show reasonable agreement though the lower half of the distribution but observed solids exceed computed in the upper half (Figure 11-45). Inspection of the time-series plots indicates inability of the model to match extreme solids concentrations in the bottom waters of the turbidity maximum contributes substantially to the mis-match. The attenuation distributions (Figure 11-46), which are based solely on surface solids, agree well.

The distributions of computed and observed solids and attenuation for the York River show good agreement (Figure 11-47) through the upper half of the distribution. In the lower half, computed solids exceed observed by less than 5 g m^{-3}. Computed and observed attenuation follow a similar pattern (Figure 11-48). Agreement is good in the upper half of the distribution but the model overestimates by $\approx$0.2 m^{-1} in the lower half.

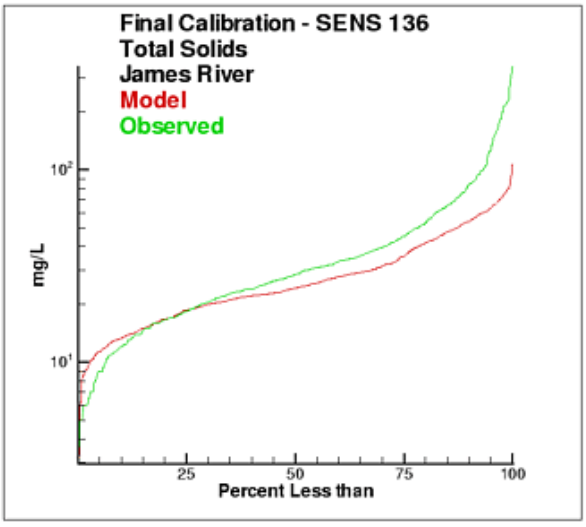

Figure 11-45. Cumulative distribution of computed and observed total suspended solids in James River.

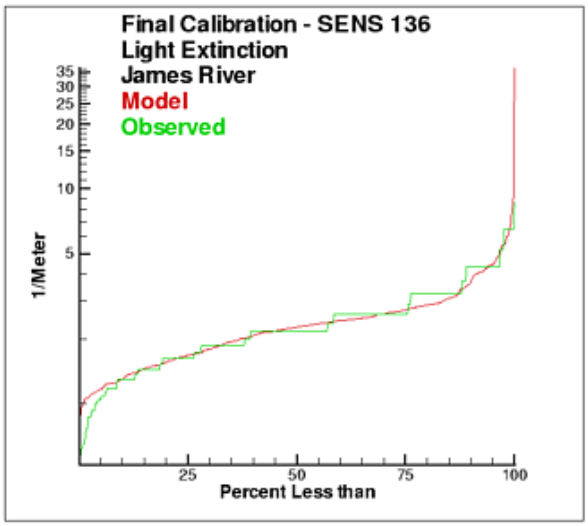

Figure 11-46. Cumulative distribution of computed and observed light attenuation in James River.

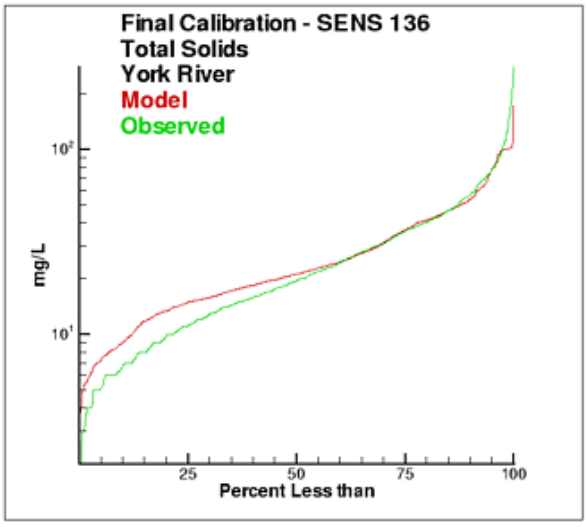

Figure 11-47. Cumulative distribution of computed and observed total suspended solids in York River.

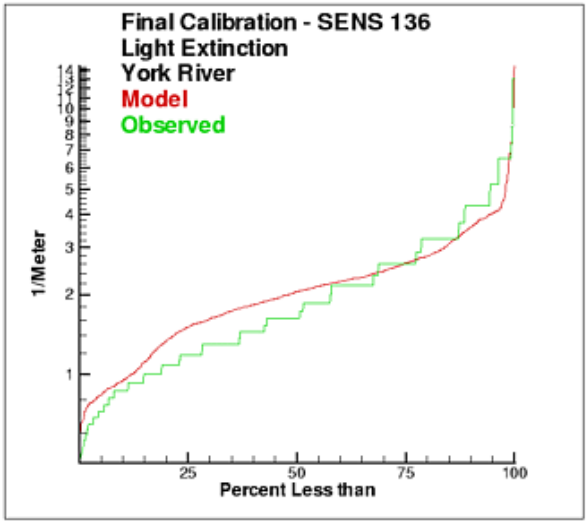

Figure 11-48. Cumulative distribution of computed and observed light attenuation in York River.

The computed and observed solids distributions in the Rappahannock demonstrate different shapes (Figure 11-49). The model demonstrates a bulge at the median that exceeds the observed median by ≈10 gm m^{-3}. Interpretation of the bulge is difficult but inspection of the time-series plots indicates computed solids in the bottom waters of the mid and lower estuary are biased on the high side. The attenuation distributions (Figure 11-50), which are based solely on surface solids, agree well. The greatest discrepancy between computed and observed attenuation is ≈0.2 m^{-1} in the lowest 5% of the observations. The upper 75% of the distributions are virtually coincident.

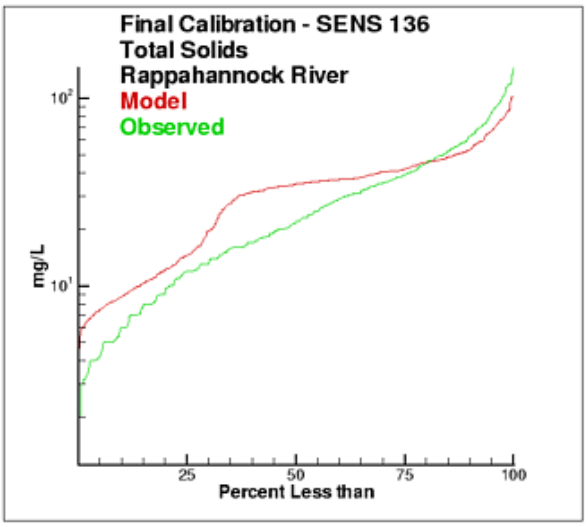

Figure 11-49. Cumulative distribution of computed and observed total suspended solids in Rappahannock River.

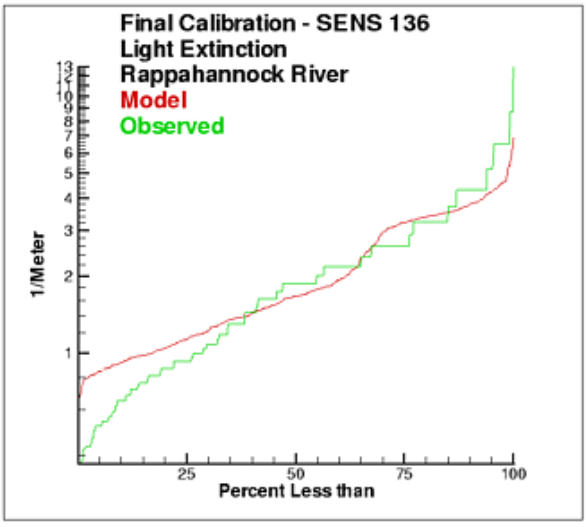

Figure 11-50. Cumulative distribution of computed and observed light attenuation in Rappahannock River.

Computed and observed solids in the Potomac River show reasonable agreement though the lower half of the distribution but computed solids exceed observed in the upper half (Figure 11-51). Inspection of the time series indicates at least a portion of the discrepancy is attributable to over-computation of solids concentrations at the bottom of Station RET2.2. Computed and observed attenuation show good agreement throughout the distributions (Figure 11-52).

The computed and observed solids distributions in the Patuxent demonstrate different shapes (Figure 11-53). The distributions agree well at the median and at the upper end but the model demonstrates bulges at the 25th and 75th percentiles. Interpretation of the bulges is difficult. Inspection of the time- series plots indicates several breaks in the observations. At Station TF1.7, the observations for the first two years are higher than observations in the succeeding years. At Station LE2.3, observations in years 5 and 6 exceed observations in earlier and succeeding years. While the observations are discontinuous, the model computes relatively constant values for ten years. The discontinuities in the observations may be the cause of the different shapes in the computed and observed solids distributions. The computed and observed attenuation distributions (Figure 11-54) agree well through most of the range but the minimum attenuation computed by the model exceeds observed by ≈0.5 m^{-1}.

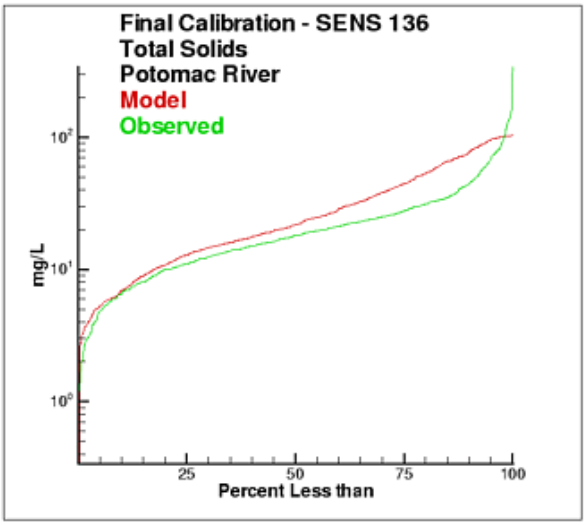

Figure 11-51. Cumulative distribution of computed and observed total suspended solids in Potomac River.

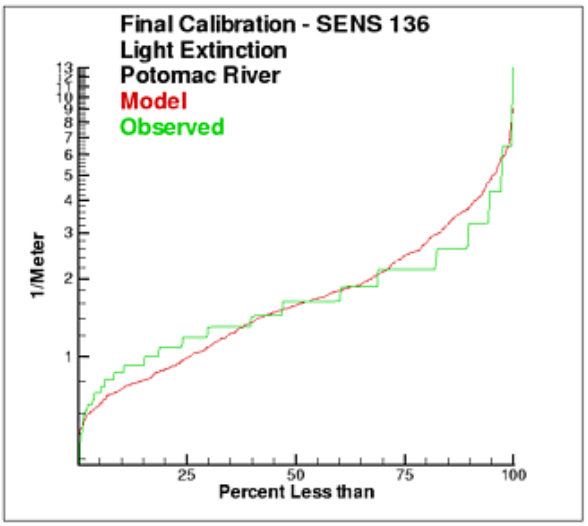

Figure 11-52. Cumulative distribution of computed and observed light attenuation in Potomac River.

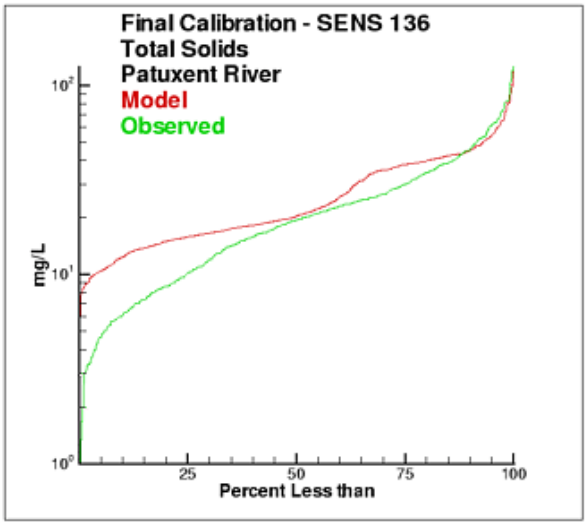

Figure 11-53. Cumulative distribution of computed and observed total suspended solids in Patuxent River.

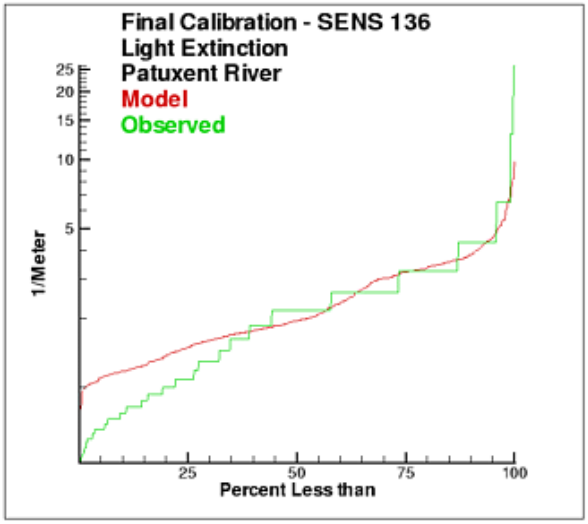

Figure 11-54. Cumulative distribution of computed and observed light attenuation in Patuxent River.

Computed and observed solids distributions in the Eastern Shore minor tributaries (Figure 11-55) agree well at the upper and lower extremes but at the median, the model underestimates solids concentrations by 3 to 5 g m^{-3}. Inspection of the time series indicates the model consistently underestimates solids at Stations EE2.1 and ET9.1. Comparisons at these stations may influence the distributions near the median. The distributions of computed and observed attenuation agree well throughout the range (Figure 11-56). At the median, the difference between computed and observed light attenuation is ≈0.1 m^{-1}

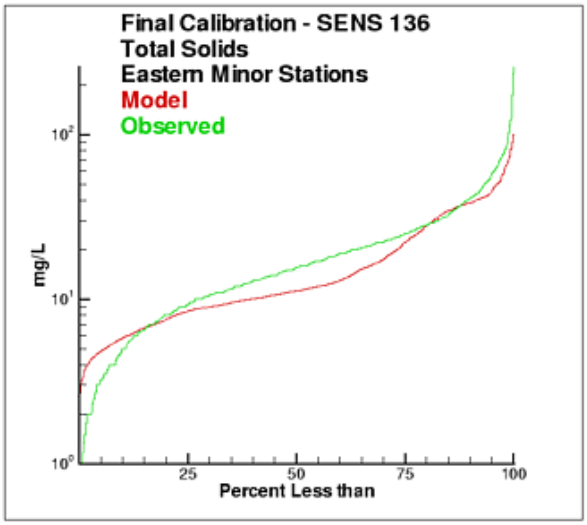

Figure 11-55. Cumulative distribution of computed and observed total suspended solids in Eastern Shore minor tributaries.

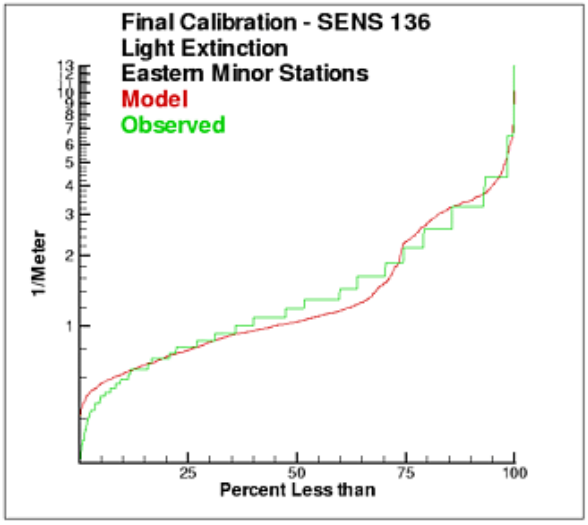

Figure 11-56. Cumulative distribution of computed and observed light attenuation in Eastern Shore minor tributaries.

Computed and observed solids in the Western Shore minor tributaries show reasonable agreement though the lower three-fourths of the distribution but computed solids exceed observed in the remainder (Figure 11-57). Inspection of the time series identifies WT2.1 as a station at which computed solids greatly exceed observed. Comparison of the attenuation distributions shows a tendency opposite to the solids (Figure 11-58). The computed and observed distributions show good agreement in the upper 25% but the observations exceed the computations for most of the distribution. Computations at stations WT5.1 and WT8.1 appear to have most influence on the computed distribution relative to observed.

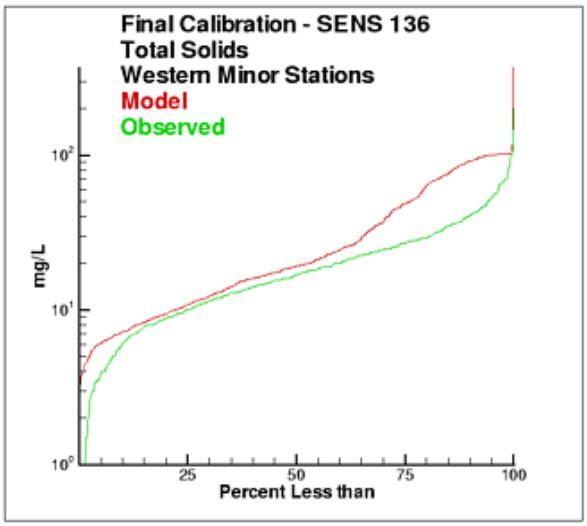

Figure 11-57. Cumulative distribution of computed and observed total suspended solids in Western Shore minor tributaries.

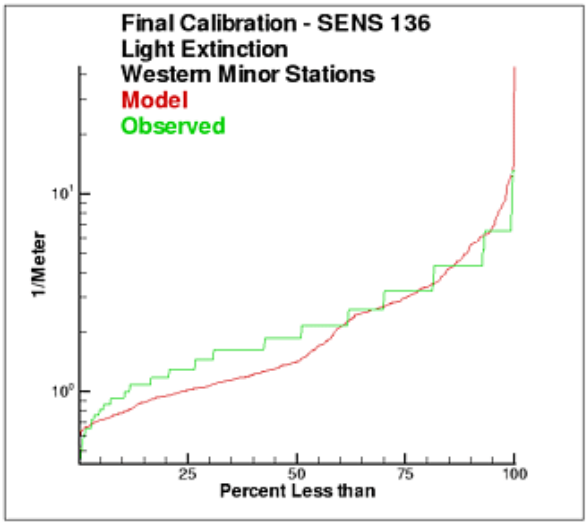

Figure 11-58. CCumulative distribution of computed and observed light attenuation in Western Shore minor tributaries.

References

Cerco, C., and Moore, K. (2001). "System-wide submerged aquatic vegetation model for Chesapeake Bay," *Estuaries*, 24(4), 522-534.

Chesapeake Bay Program, United States Environmental Protection Agency. (2000). "Submerged aquatic vegetation water quality and habitat-based requirements for restoration targets: A second technical synthesis," CBP/TRS 245/00, EPA 903-R-00-014, Annapolis MD.

Holmes, R. (1970). "The Secchi disk in turbid coastal waters," *Limnology and Oceanography*, 15, 688-694.

Hood, R., Wang, H., Purcell, J., Houde, E., and Harding, L. (1999). "Modeling particles and pelagic organisms in Chesapeake Bay: Convergent features control plankton distributions," *Journal of Geophysical Research*, 104(C1), 1223-1243.

Keefe, C., Flemer, D., and Hamilton, D. (1976). "Seston distribution in the Patuxent River Estuary," *Chesapeake Science*, 17, 56-59.

Kirk, J. (1994). *Light and photosynthesis in aquatic ecosystems*. 2nd edition., Cambridge University Press, Cambridge

Koenings, J., and Edmundson, J. (1991). "Secchi disk and photometer estimates of light regimes in Alaskan lakes: Effects of yellow color and turbidity," *Limnology and Oceanography*, 36(1), 91-105.

Pennock, J. (1985). "Chlorophyll distributions in the Delaware Estuary: Regulation by light limitation," *Estuarine, Coastal and Shelf Science*, 21, 711- 725.

Schubel, J. (1968). "Turbidity maximum of the northern Chesapeake Bay," *Science*, 161, 1013-1015.

Tributary Dissolved Oxygen 12

Introduction

Analysis and modeling of tributary dissolved oxygen has largely focused on persistent or intermittent anoxia that occurs in bottom waters near the mouths of four major western tributaries: the York, Rappahannock, Potomac, and Patuxent. The occurrence of surface dissolved oxygen concentrations substantially below saturation seems to have escaped notice of the scientific and management communities. In fact, the tributaries that exhibit bottom-water anoxia commonly exhibit surface dissolved oxygen less than 5 g m^{-3} in regions overlying the anoxic bottom waters (Figures 12-1 to 12-4). Surface dissolved oxygen in the York and Patuxent falls below 5 g m^{-3} in multiple locations along the river axes (Figures 12-1, 12-4).

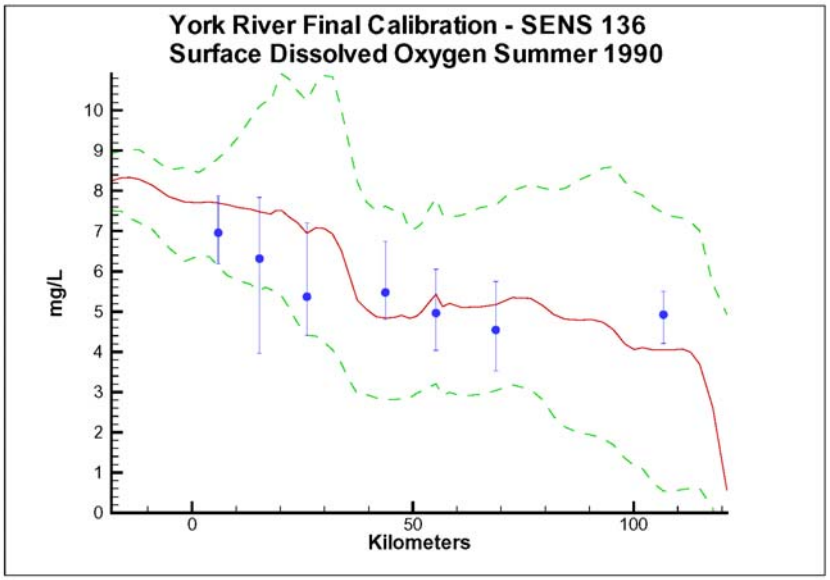

Figure 12-1. Computed and observed surface dissolved oxygen in the York River, summer 1990. Computed mean and range shown as lines, observed mean and range shown as solid circles and vertical bars.

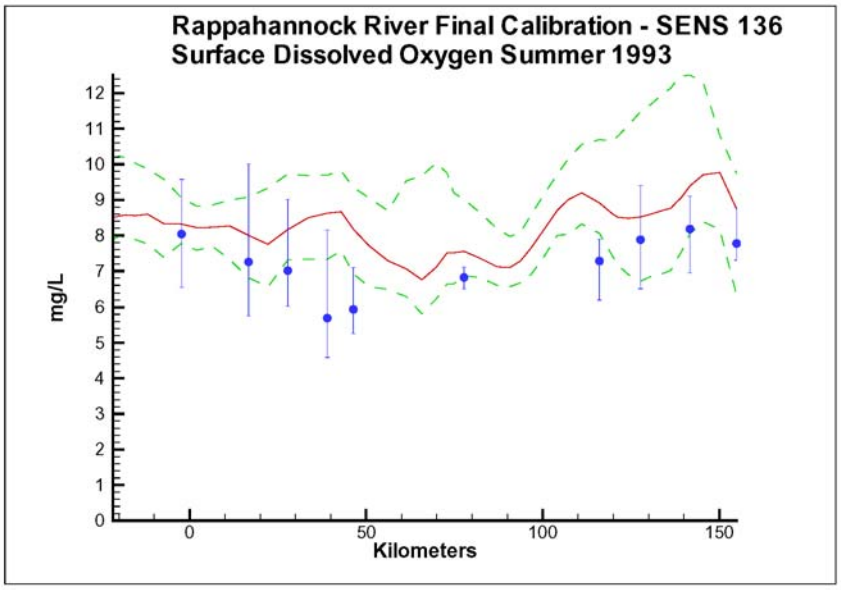

Figure 12-2. Computed and observed surface dissolved oxygen in the Rappahannock River, summer 1993. Computed mean and range shown as lines, observed mean and range shown as solid circles and vertical bars.

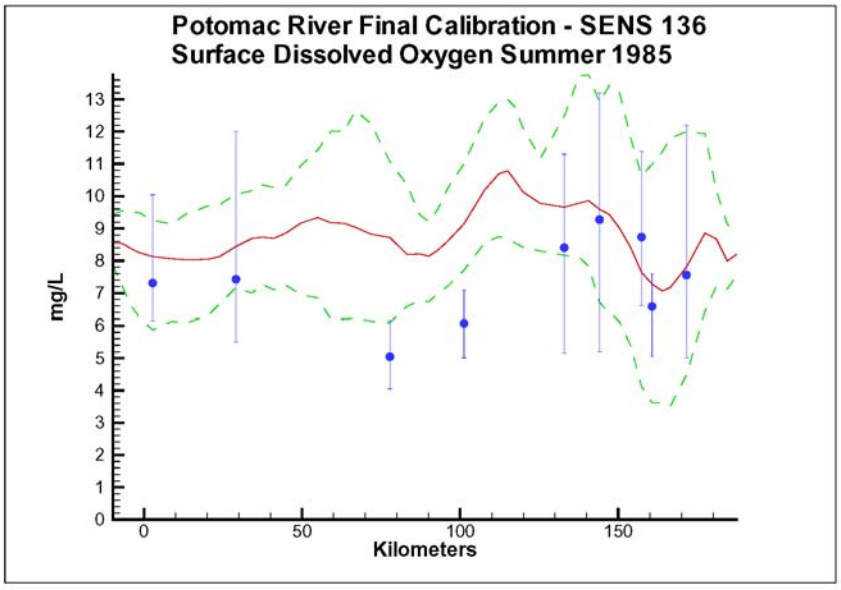

Figure 12-3. Computed and observed surface dissolved oxygen in the Potomac River, summer 1985. Computed mean and range shown as lines, observed mean and range shown as solid circles and vertical bars.

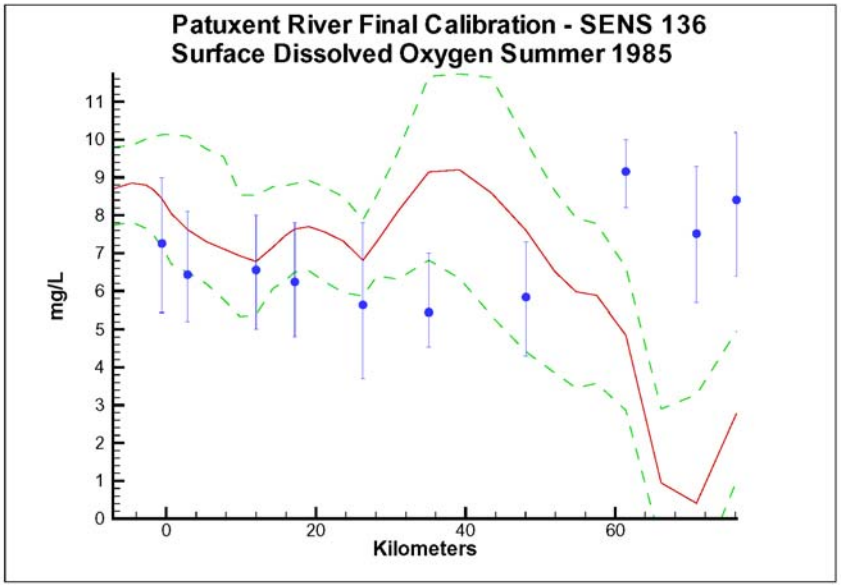

Figure 12-4. Computed and observed surface dissolved oxygen in the Patuxent River, summer 1985. Computed mean and range shown as lines, observed mean and range shown as solid circles and vertical bars.

A tendency present in the model since the earliest application is the over-prediction of surface dissolved oxygen in the tributaries, especially in the tidal freshwater portions (Figures 12-5, 12-6). This performance characteristic was overlooked when attention was focused on bottom waters. During the present study, sponsors noted the discrepancies between computed and observed surface dissolved oxygen concentrations and asked for improved model performance. An extensive number of calibration and sensitivity runs were performed while attempting to improve the model. The present chapter documents a portion of these runs. As with other sensitivity comparisons, the model runs are not always sequential and may incorporate multiple changes. Still, the comparisons provide insight into model sensitivities and illustrate plausible and implausible mechanisms for observed and computed properties.

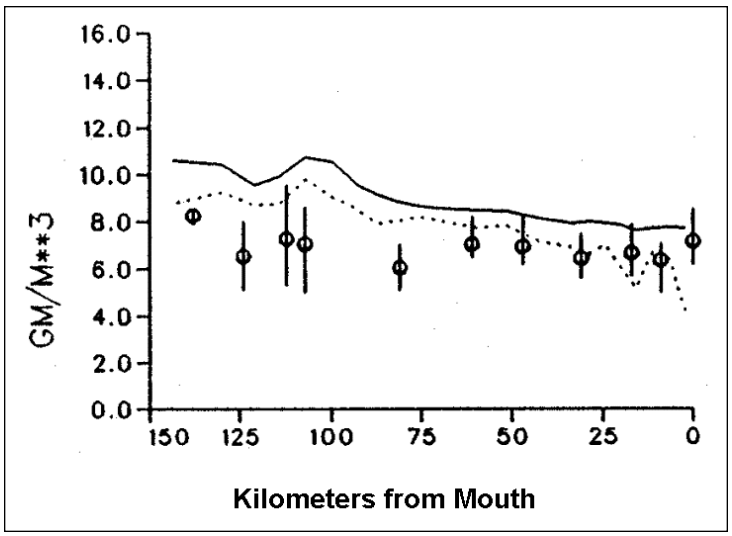

Figure 12-5. Computed and observed surface dissolved oxygen in the James River, summer 1986, from the original 4,000 cell model (Cerco and Cole 1993). Computed mean and minimum shown as lines, observed mean and range shown as circles and vertical bars.

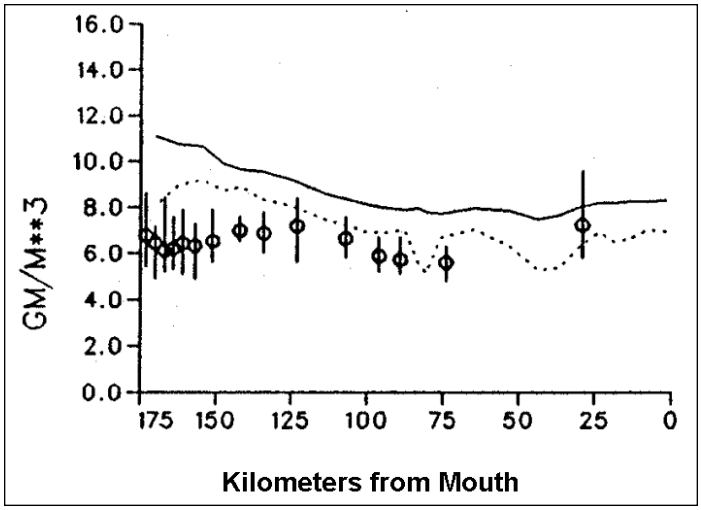

Figure 12-6. Computed and observed surface dissolved oxygen in the Potomac River, summer 1986, from the original 4,000 cell model (Cerco and Cole 1993). Computed mean and minimum shown as lines, observed mean and range shown as circles and vertical bars.

Dissolved Organic Carbon Mineralization Rate

The dissolved organic carbon mineralization (or respiration) rate is a key determinant of oxygen consumption in the water column. As a sensitivity test, we multiplied the respiration rate by an order of magnitude, from 0.01 d^{-1} to 0.1 d^{-1} at 20 ºC. Major reaches of the tributaries were insensitive to an order-of- magnitude increase in the first-order rate (Figures 12-7, 12-8). Only reaches in the immediate vicinity of a carbon source, e.g. the Potomac below the District of Columbia, showed significant response to an increase in respiration rate. Lack of general response indicated that oxygen consumption could not be increased without an increase in oxygen-demanding material. An increase in first-order rate alone would not suffice. In addition, the rate increase produced unacceptably low computations of total organic carbon (Figures 12-9, 12-10).

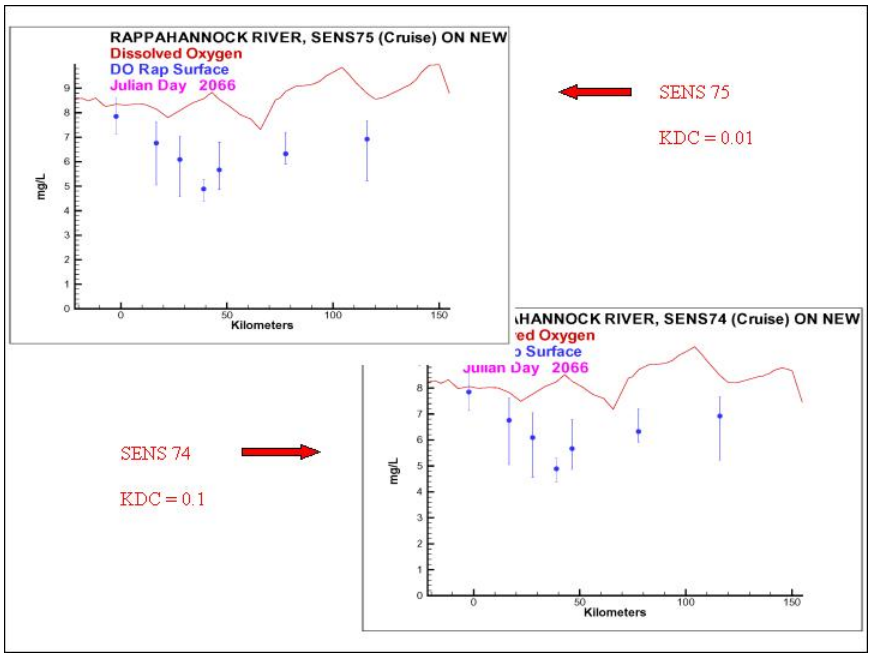

Figure 12-7. Sensitivity of Rappahannock River surface dissolved oxygen to dissolved organic carbon mineralization rate, summer 1990.

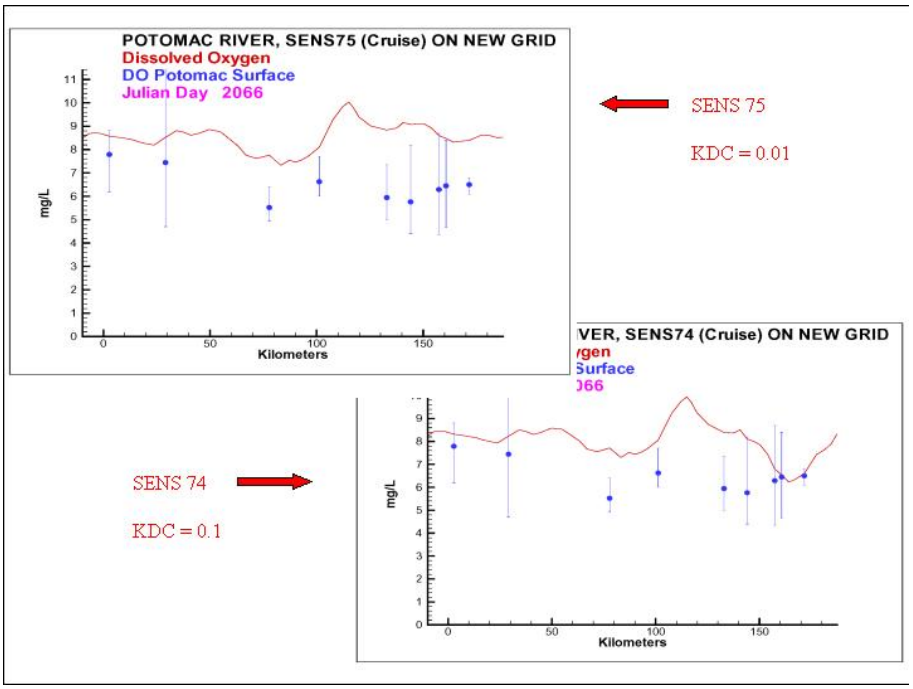

Figure 12-8. Sensitivity of Potomac River surface dissolved oxygen to dissolved organic carbon mineralization rate, summer 1990.

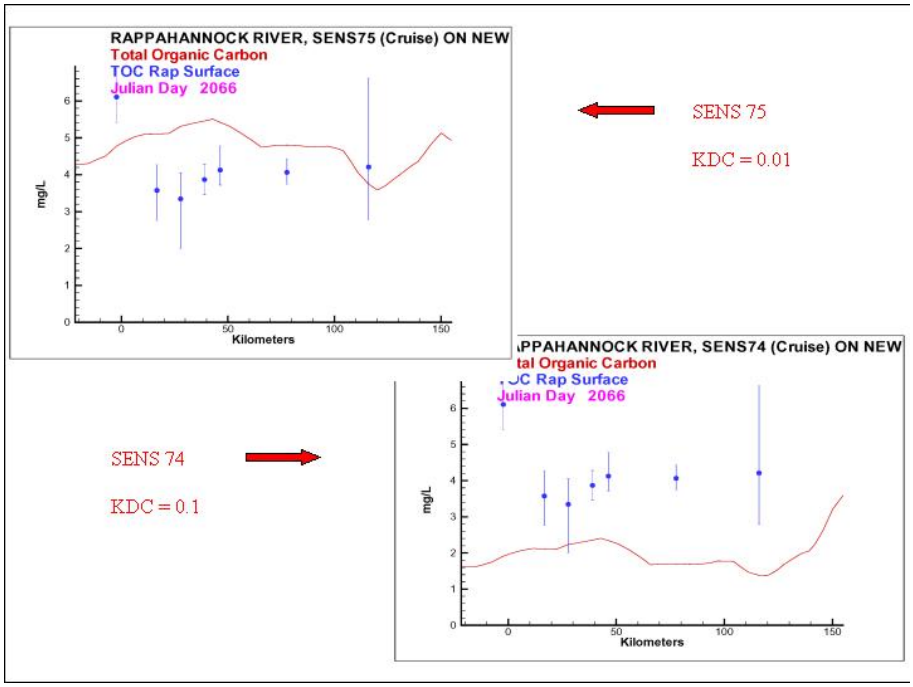

Figure 12-9. Sensitivity of Rappahannock River surface total organic carbon to dissolved organic carbon mineralization rate, summer 1990.

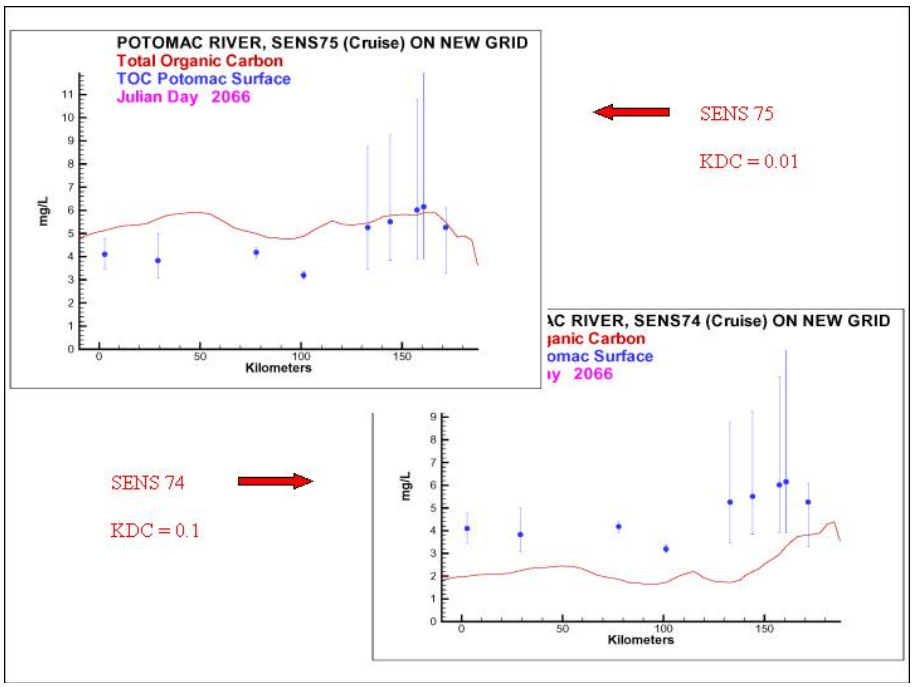

Figure 12-10. Sensitivity of Potomac River surface total organic carbon to dissolved organic carbon mineralization rate, summer 1990.

Our conclusion from this run was that computation of high surface dissolved oxygen could not be corrected with an increase in respiration rate. The run did suggest, however, that surface dissolved oxygen could be depressed locally by altering the respiration rate.

Wetland Dissolved Oxygen Uptake

The sensitivity of surface dissolved oxygen to wetland oxygen uptake was examined on a time-series basis in the chapter entitled "Hydrology and Loads." When wetlands impact is examined on a spatial scale, in the York River for example, we see that the effect is confined to the upper reaches of the estuary (Figure 12-11). Wetlands impact is greatest where the estuary is narrow and the ratio of wetlands area to water area is large. In the wide lower estuary, fringing wetlands can do little to affect dissolved oxygen in open water. In the York, for example, the low surface dissolved oxygen 20 km above the mouth cannot be due to wetland uptake.

Nonpoint-Source Carbon Loads

Carbon loads to the tributaries are not well-known. Organic carbon is not a state variable in the watershed model nor is it monitored at the Virginia tributary fall lines. In the Potomac and Patuxent, total organic carbon measures are collected but no information is available to partition the total into particulate and dissolved fractions. For our model, we obtained nonpoint-source organic carbon loads by ratio to organic nitrogen computed by the watershed model (see the chapter "Hydrology and Loads"). We multiplied carbon loads by a factor of ten to examine sensitivity in the face of uncertainty. While the order-of-magnitude load increase certainly

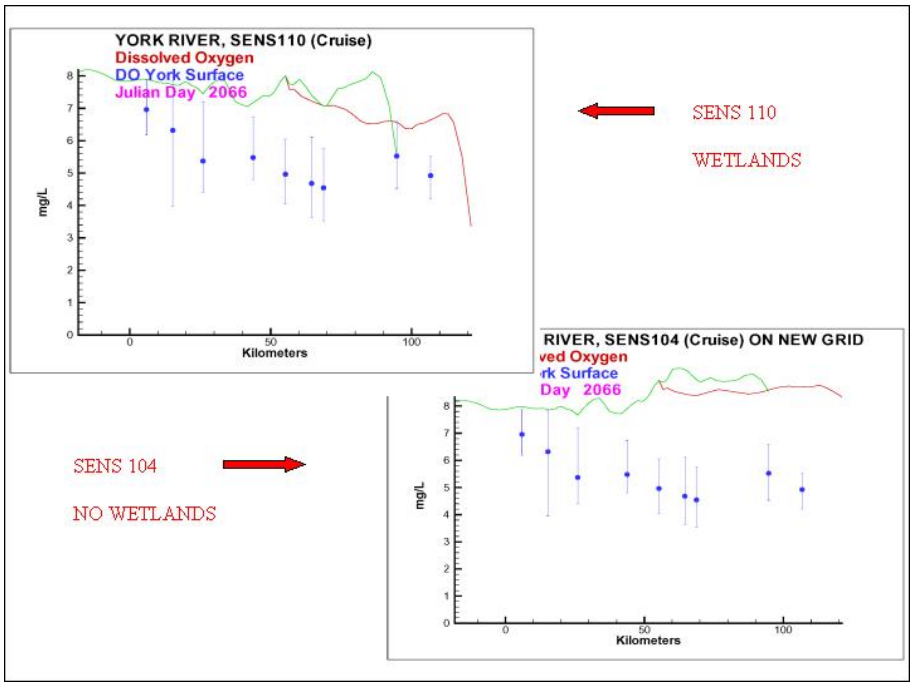

Figure 12-11. Sensitivity of York River surface dissolved oxygen to wetlands oxygen uptake, summer 1990.

improved computed surface dissolved oxygen, even this increase could not account for the low dissolved oxygen occurring at the surface of the lower Potomac and James Rivers (Figures 12-12, 12-13). Moreover, the computed organic carbon increased to unrealistic levels (Figures 12-14, 12-15). Our conclusion is that the modeler has freedom to adjust loads within reasonable levels but uncertainty in the loads can not account for the over-computation of surface dissolved oxygen.

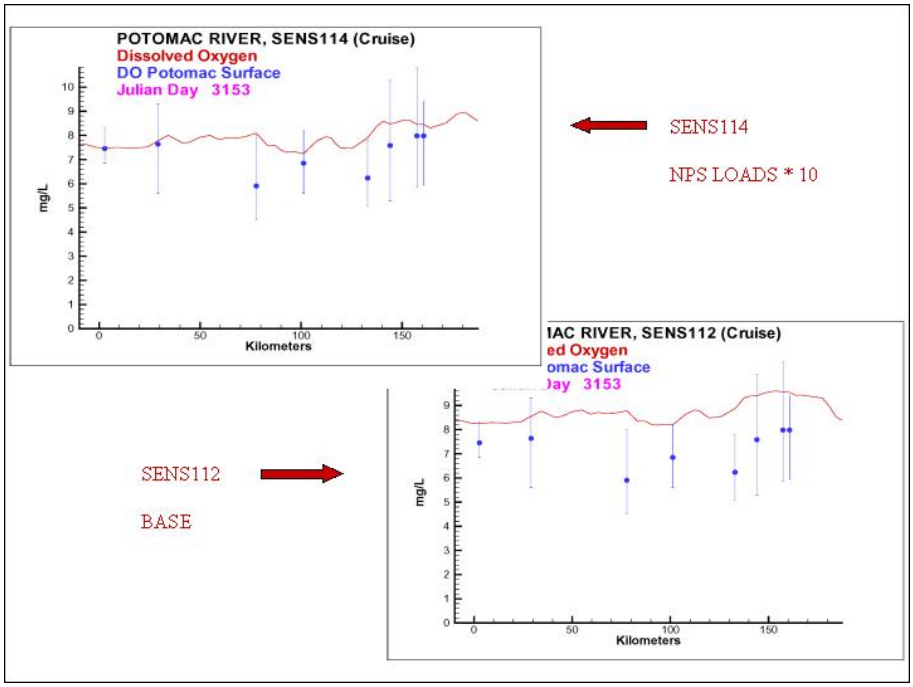

Figure 12-12. Sensitivity of Potomac River surface dissolved oxygen to nonpoint-source organic carbon load, summer 1990.

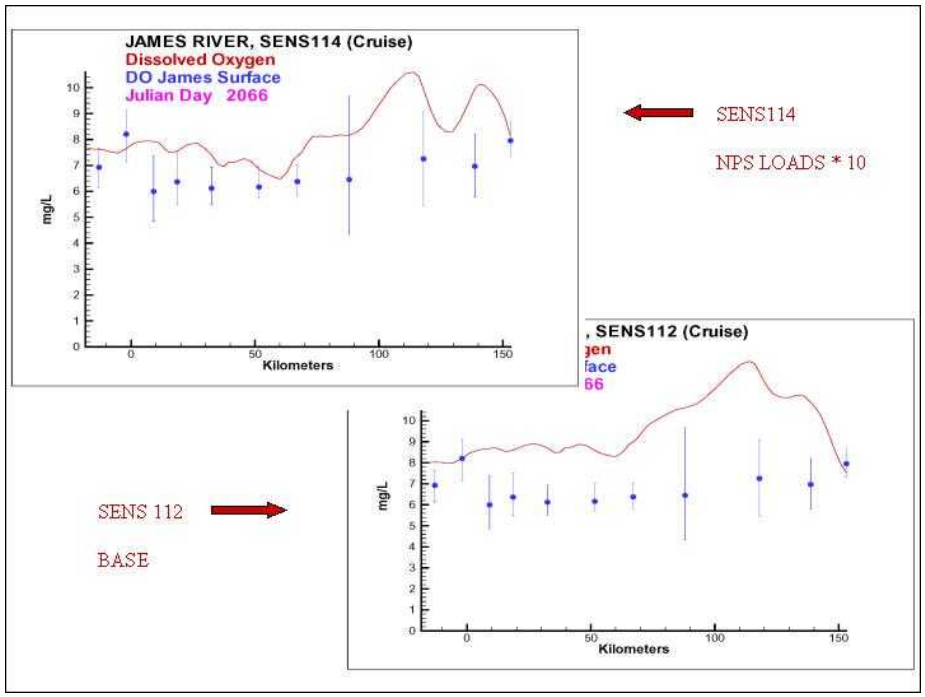

Figure 12-13. Sensitivity of James River surface dissolved oxygen to nonpoint-source organic carbon load, summer 1990.

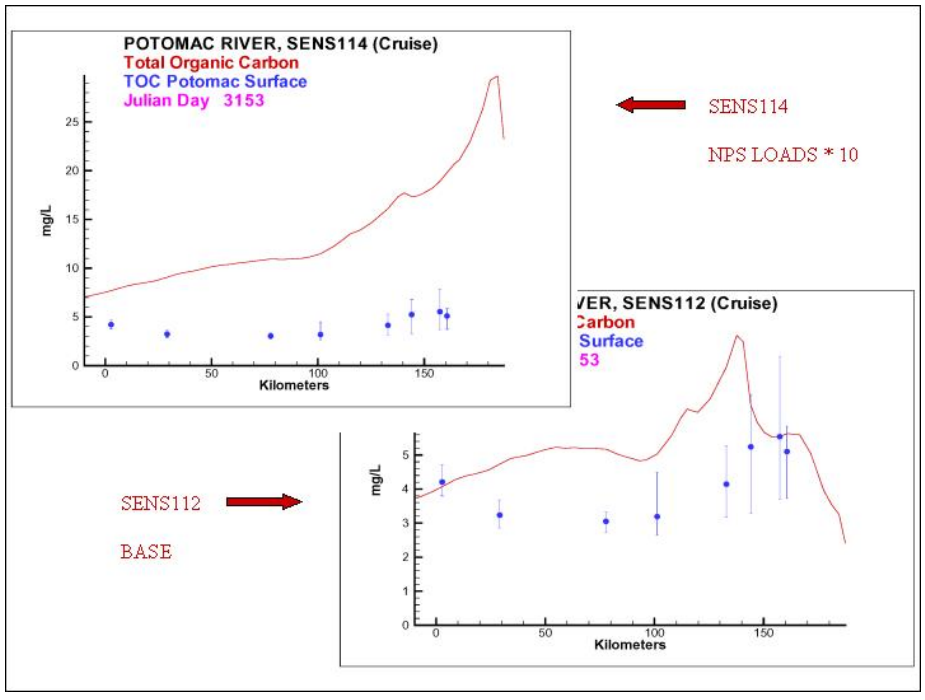

Figure 12-14. Sensitivity of Potomac River surface total organic carbon to nonpoint-source organic carbon load, summer 1990.

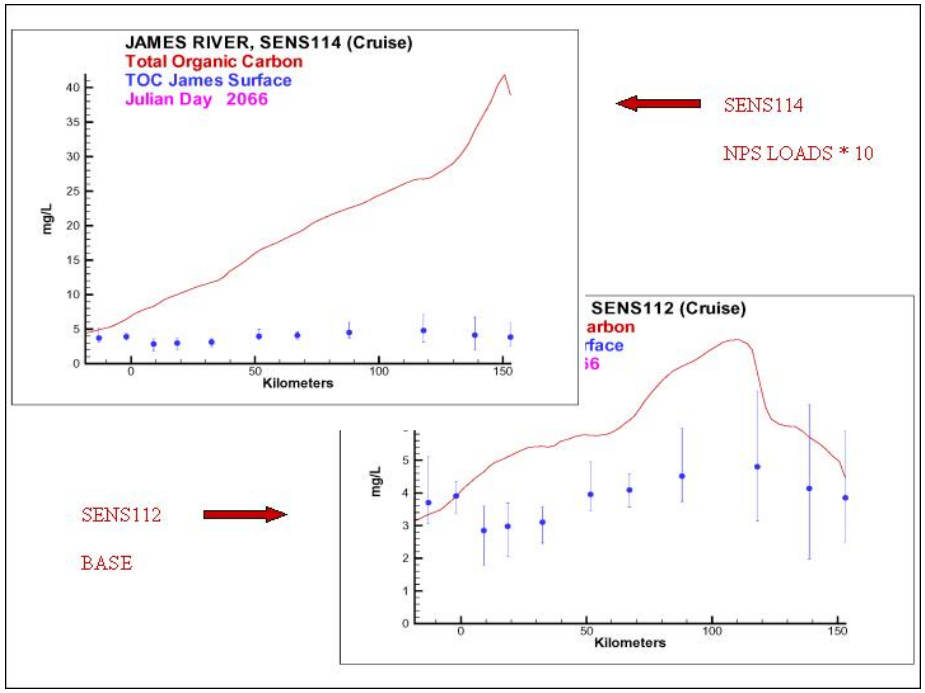

Figure 12-15. Sensitivity of James River surface total organic carbon to nonpoint-source organic carbon load, summer 1990.

Spatially-Varying Dissolved Organic Carbon Mineralization Rate

The initial sensitivity examination of dissolved organic carbon mineralization rate indicated this parameter could affect dissolved oxygen locally but not globally. In an attempt to improve surface dissolved oxygen computations in the tidal fresh portions of the tributaries, we imposed spatially-varying mineralization rates. The first-order rate was increased from a global value of 0.011 d^{-1} at 20 ^{o}C to 0.1 d^{-1} in tidal fresh water (TF segments); to 0.05 d^{-1} in the river-estuarine transition regions (RET segments); and to 0.025 d^{-1} in the lower estuaries (LE segments). All other portions of the system were left at their original value.

This test indicated computed surface dissolved oxygen could be lowered by 1 to 2 g m^{-3} in the upper portions of the James River (Figure 12-16) while improving total organic carbon computations (Figure 12-17). Similar dissolved oxygen improvements were obtained in the upper 50 km of the Potomac (Figure 12-18) although total organic carbon computations suffered (Figure 12-19).

This sensitivity run guided assignment of the dissolved organic carbon mineralization rate in the final calibration. We assigned a rate of 0.011 d^{-1} at 20 ^{o}C everywhere except in the tidal fresh portions of the James (0.075 d^{-1}), Rappahannock (0.05 d^{-1}) and Potomac (0.05 d^{-1}). We reasoned that the higher values were appropriate due to the input of organic matter from point sources, combined sewer overflows, and urban runoff near the heads of these three estuaries.

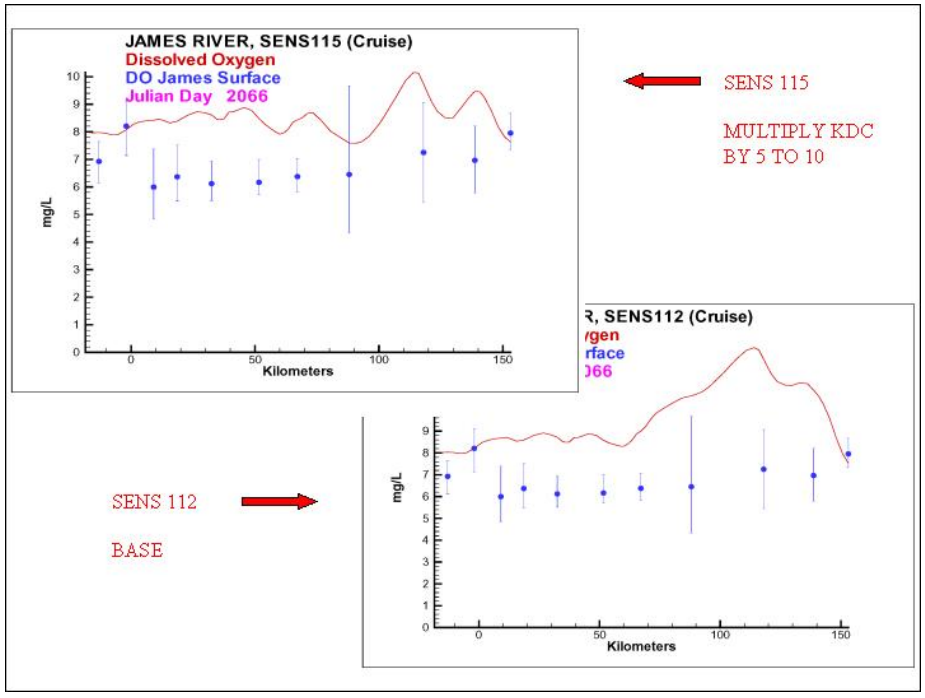

Figure 12-16. Sensitivity of James River surface dissolved oxygen to spatially-varying dissolved organic carbon mineralization rate, summer 1990.

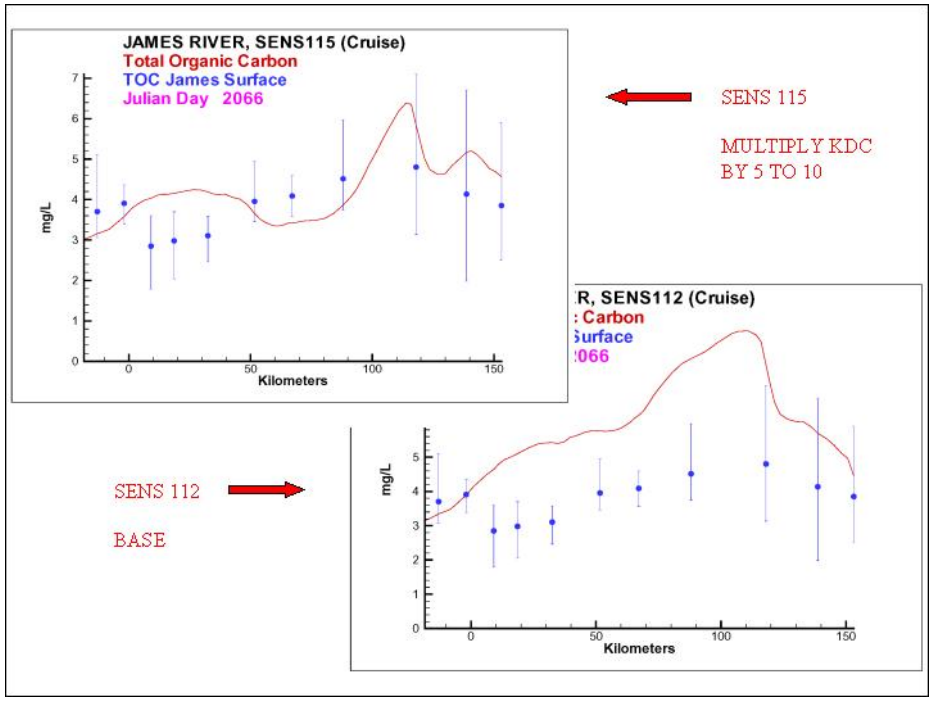

Figure 12-17. Sensitivity of James River surface total organic carbon to spatially-varying dissolved organic carbon mineralization rate, summer 1990.

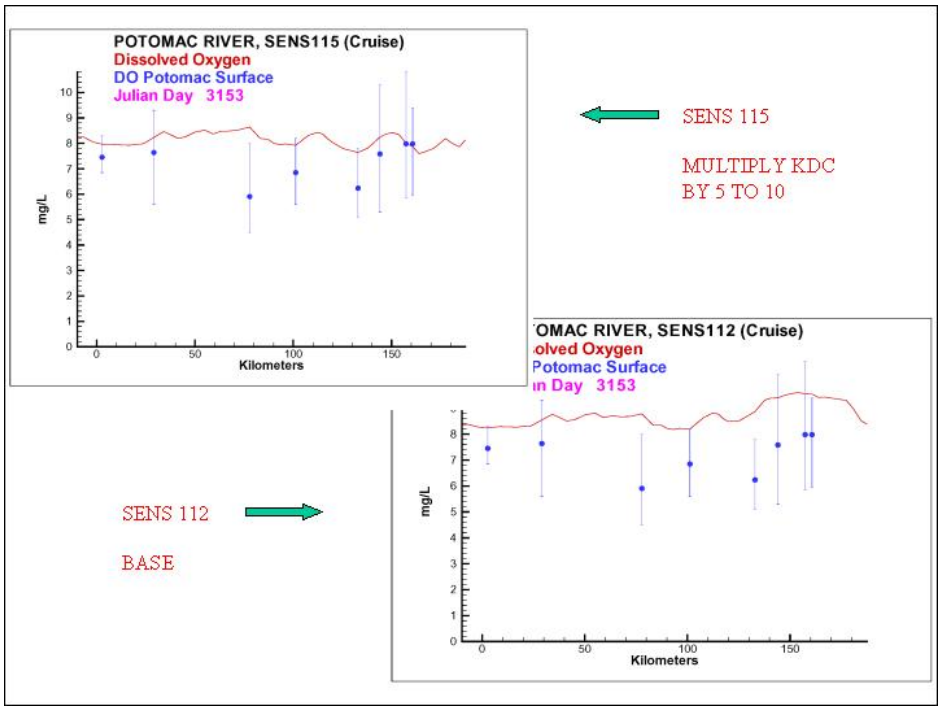

Figure 12-18 Sensitivity of Potomac River surface dissolved oxygen to spatially-varying dissolved organic carbon mineralization rate, summer 1990.

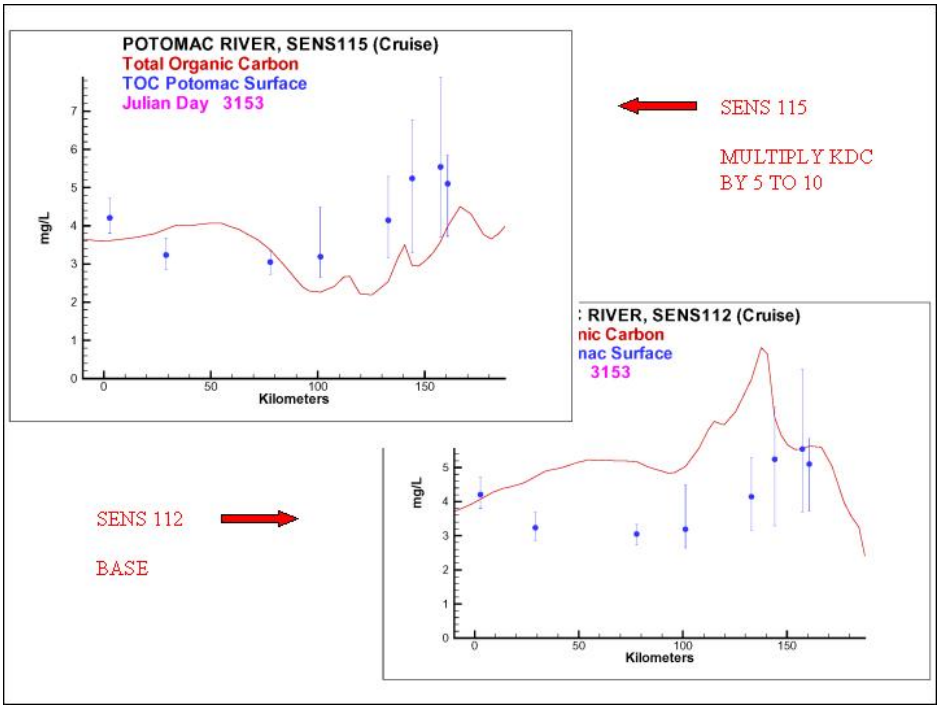

Figure 12-19. Sensitivity of Potomac River surface total organic carbon to spatially-varying dissolved organic carbon mineralization rate, summer 1990.

Reaeration Rate

The reaeration rate may be viewed as the speed with which the surface dissolved oxygen concentration achieves equilibrium with the atmosphere. Adjustment in the reaeration rate is useful as a tool to reduce computed surface dissolved oxygen only when dissolved oxygen is below equilibrium concentration. In that case, reduced reaeration will retard the return of surface dissolved oxygen to equilibrium. If computed surface dissolved oxygen exceeds equilibrium, then a reduction in reaeration rate will exacerbate any over-computation by retarding the escape of excess oxygen to the atmosphere. Since the sensitivity run with spatially-varying dissolved organic carbon mineralization rate indicated the possibility of pulling surface dissolved oxygen below saturation, we decide to combine that run with a reduction in reaeration rate.

For Chesapeake Bay, a relationship for wind-driven gas exchange (Hartman and Hammond 1985) was employed:

$$Kr = Arear \bullet Rv \bullet Wms^{1.5} \qquad (12\text{-}1)$$

in which:
Kr = reaeration coefficient (m d^{-1})
Arear = empirical constant (0.1)
Rv = ratio of kinematic viscosity of pure water at 20 ºC to kinematic viscosity of water at specified temperature and salinity
Wms = wind speed measured at 10 m above water surface (m s^{-1})

Hartman and Hammond (1985) indicate Arear takes the value 0.157. We halved that value for the sensitivity run. Results indicated halving reaeration could depress surface dissolved oxygen by up to 1 g m^{-3} in the upper Potomac, where dissolved oxygen was below saturation (Figure 12-20). At other locations in the Potomac, dissolved oxygen increased slightly. The results were similar in other estuaries. Halving reaeration decreased dissolved oxygen in the upper York, where dissolved oxygen was drawn down by wetlands (Figure 12-21). Elsewhere in the York, effects were unnoticeable or else dissolved oxygen increased slightly.

Upon assessing the results of these and other sensitivity runs, we opted to retain the value of Arear = 0.078. Use of this value is readily justified. Fetch in the estuaries is reduced by embankments and channel sinuosity. Consequently, reaeration is expected to be less than over open water.

Sensitivity to G3 Carbon

Organic matter deposited to the sediments is routed into three G fractions. The G3 fraction is inert and does not contribute to diagenetic processes including sediment oxygen demand. To examine the sensitivity of tributary surface dissolved oxygen to the specification of the inert fraction, we set the G3 fraction to zero. For phytoplankton carbon, the 5% of organic matter previously routed to G3 was instead routed to G2 (refractory) making a total of 35% refractory. For the refractory particulate organic carbon state variable, the 27% previously routed to G3 was routed to G2. As a result of these revisions, all deposited organic carbon contributed to sediment oxygen demand at a fast (labile) or slow (refractory) rate.

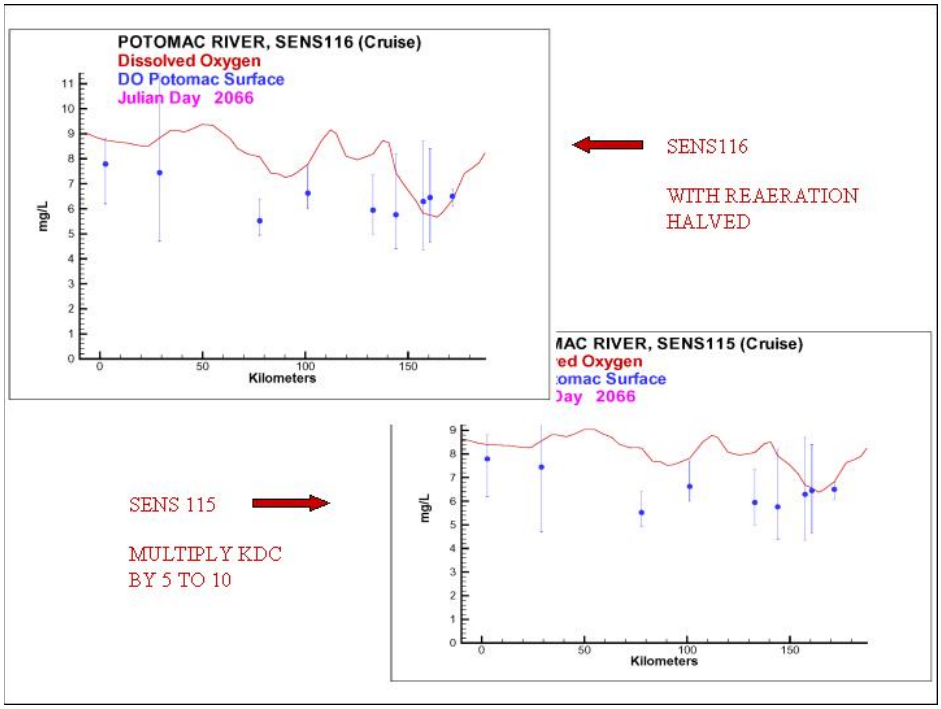

Figure 12-20. Sensitivity of Potomac River surface dissolved oxygen to reaeration rate, summer 1990.

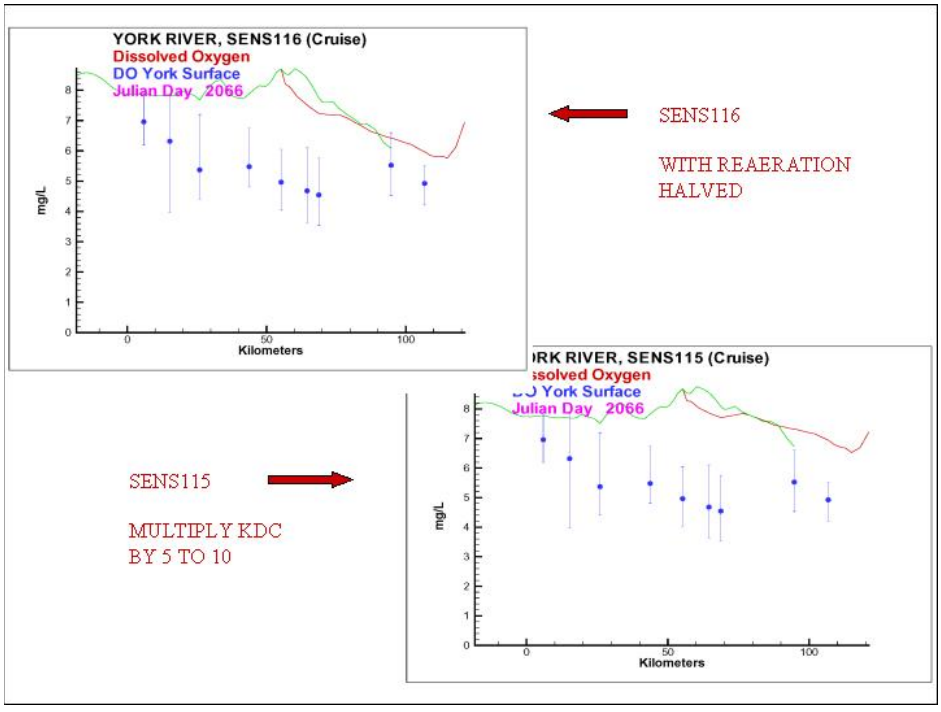

Figure 12-21. Sensitivity of York River surface dissolved oxygen to reaeration rate, summer 1990.

The effect of G3 specification on surface dissolved oxygen was barely discernable (Figure 12-22). At best 0.1 to 0.2 g DO m^{-3} additional could be consumed by eliminated the G3 fraction completely.

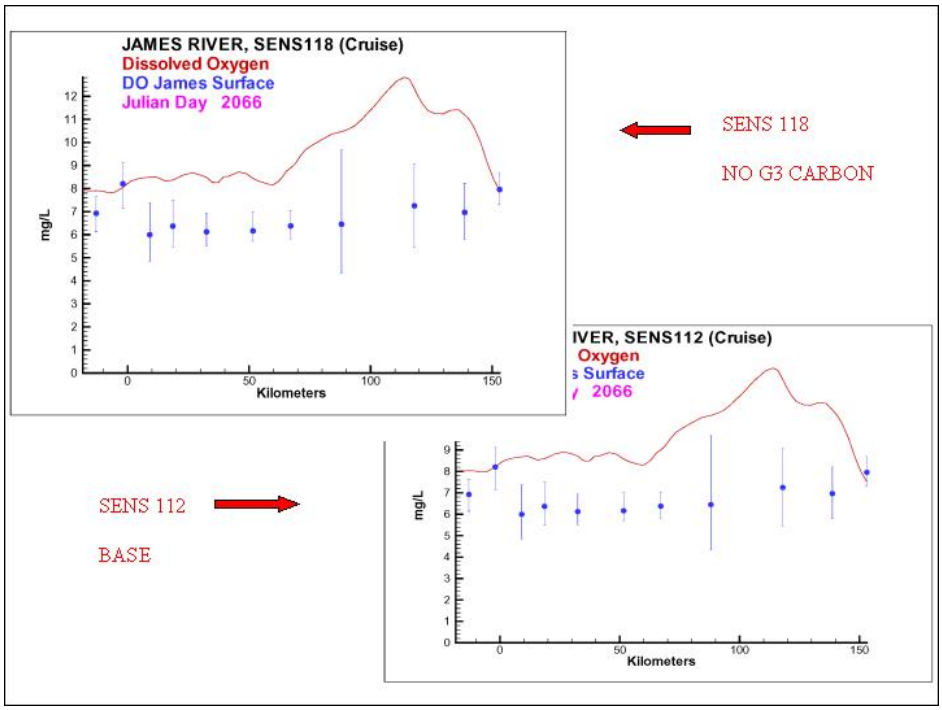

Figure 12-22. Sensitivity of James River surface dissolved oxygen to specification of G3 organic fraction, summer 1990.

Sensitivity to Algal Predation Rate

The source of excess dissolved oxygen in the tidal fresh portions of the tributaries is algal production. During the calibration process, we altered the predation rate on algae from BPR = 0.4 (SENS120) to BPR = 0.5 (SENS122) in the tidal fresh James River. The additional predation dropped computed chlorophyll at km 115 by ≈6 mg m^{-3} (Figure 12-23) and reduced computed dissolved oxygen at the same location by ≈1 g m^{-3} (Figure 12-24). Computed chlorophyll moved away from the observed mean while computed dissolved oxygen moved closer to the observed mean. In the lower estuary, we increased predation from BPR = 0.9 (SENS120) to BPR = 1.5 (SENS122). At km 50, computed chlorophyll dropped by 6 mg m^{-3} and computed surface dissolved oxygen dropped by ≈1 g m^{-3}. In this case, both computed chlorophyll and dissolved oxygen moved closer to observed means.

This run illustrated the sensitivity of surface dissolved oxygen to algal production. This run also illustrates the dilemma faced by the modeler when trying to obtain optimal calibration of multiple variables.

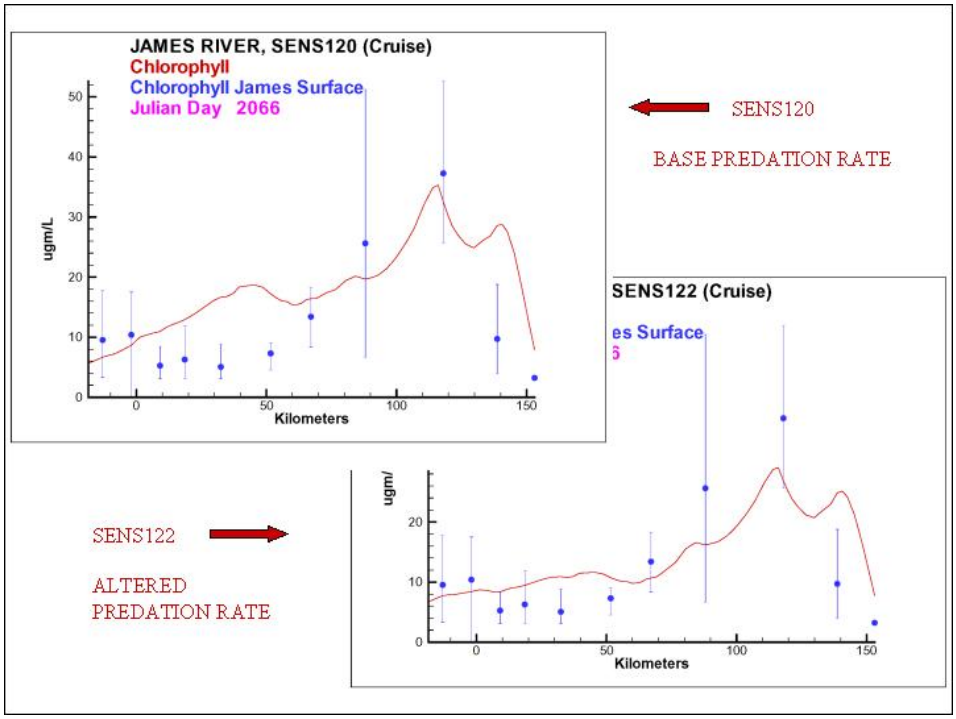

Figure 12-23. Sensitivity of James River chlorophyll to specification of base predation rate, summer 1990.

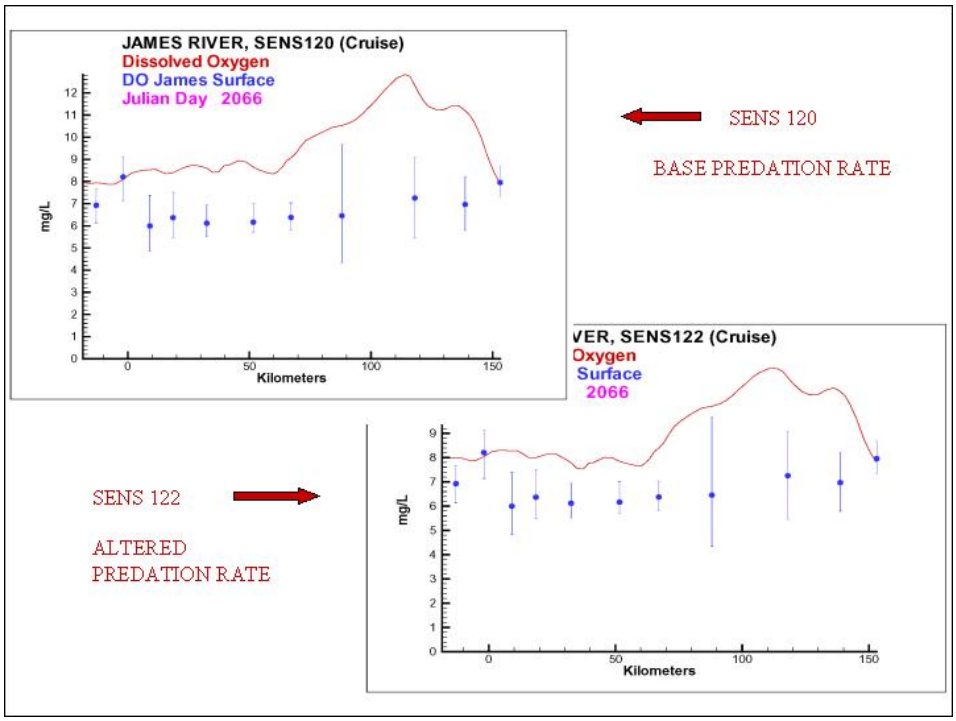

Figure 12-24. Sensitivity of James River surface dissolved oxygen to specification of base predation rate, summer 1990.

Sensitivity to Vertical Diffusion Coefficient

In the lower portions of the estuaries, the occurrence of depressed surface dissolved oxygen immediately over the location of bottom-water anoxia suggests the transfer of oxygen demand or of anoxic water from bottom to surface. The vertical diffusion coefficient is computed in the hydrodynamic model and is not a "tuning" parameter available to the water quality modeler. Still, we thought examining the effect of increased diffusion would be illustrative so we performed a run with vertical diffusion doubled. This doubling was performed in the water quality model code and did not feed back upon computed circulation.

The results of this run were mixed. In the lower James, bottom dissolved oxygen increased by 0.5 to 1 g m^{-3} (Figure 12-25) while surface dissolved oxygen decreased by a lesser amount (Figure 12-26). In both cases, the changes brought computed dissolved oxygen closer to observed. We previously noted (see chapter entitled "Coupling with the Hydrodynamic Model") our preference for greater vertical diffusion in the James. Still, bottom-water dissolved oxygen was undercomputed even with the higher diffusion.

In the York, bottom-water dissolved oxygen increased by up to 1 g m^{-3}, arguably an improvement (Figure 12-27), while surface dissolved oxygen barely moved (Figure 12-28). Geometry appears to play a role in this result. The deep channel in the York is narrow while the surface is wide. The volume of anoxic water mixed up from the bottom is insufficient to affect the surface dissolved oxygen concentration.

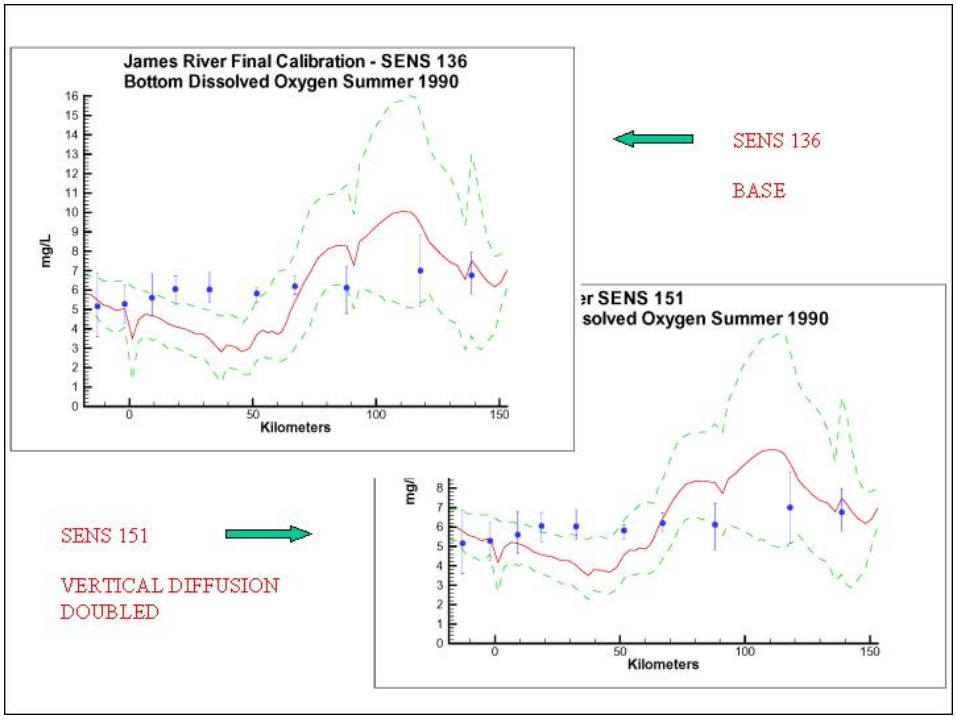

Figure 12-25. Sensitivity of James River bottom dissolved oxygen to vertical diffusion coefficient, summer 1990.

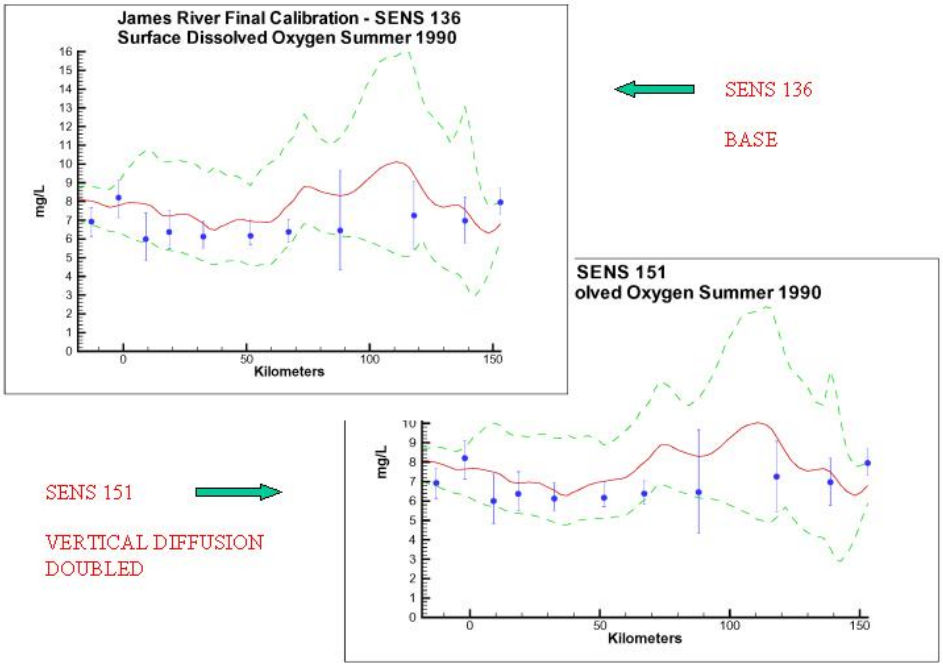

Figure 12-26. Sensitivity of James River surface dissolved oxygen to vertical diffusion coefficient, summer 1990.

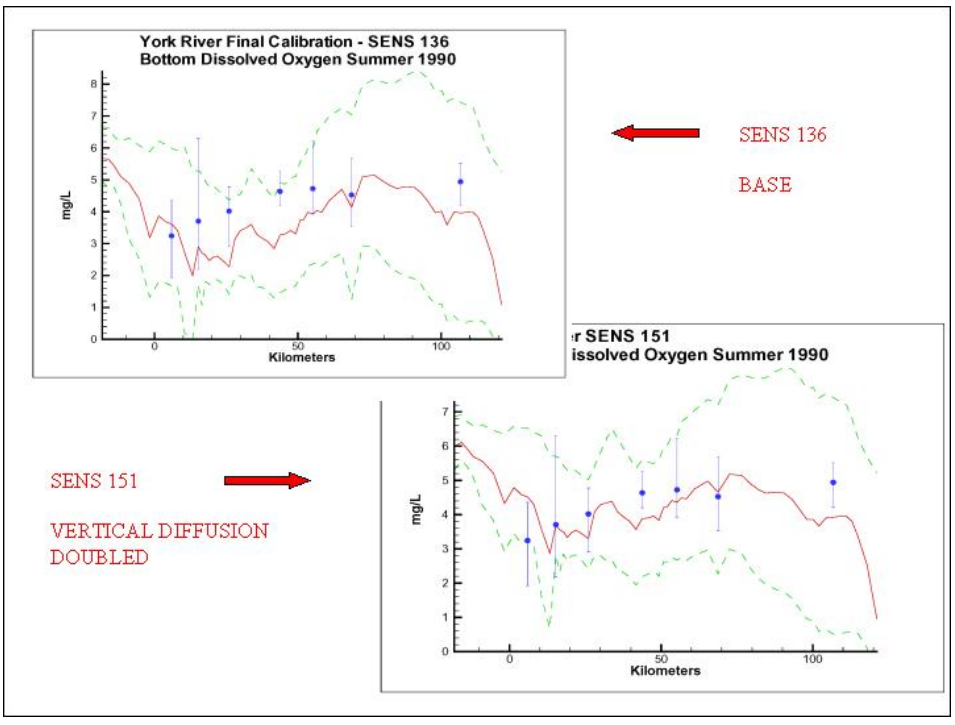

Figure 12-27. Sensitivity of York River bottom dissolved oxygen to vertical diffusion coefficient, summer 1990.

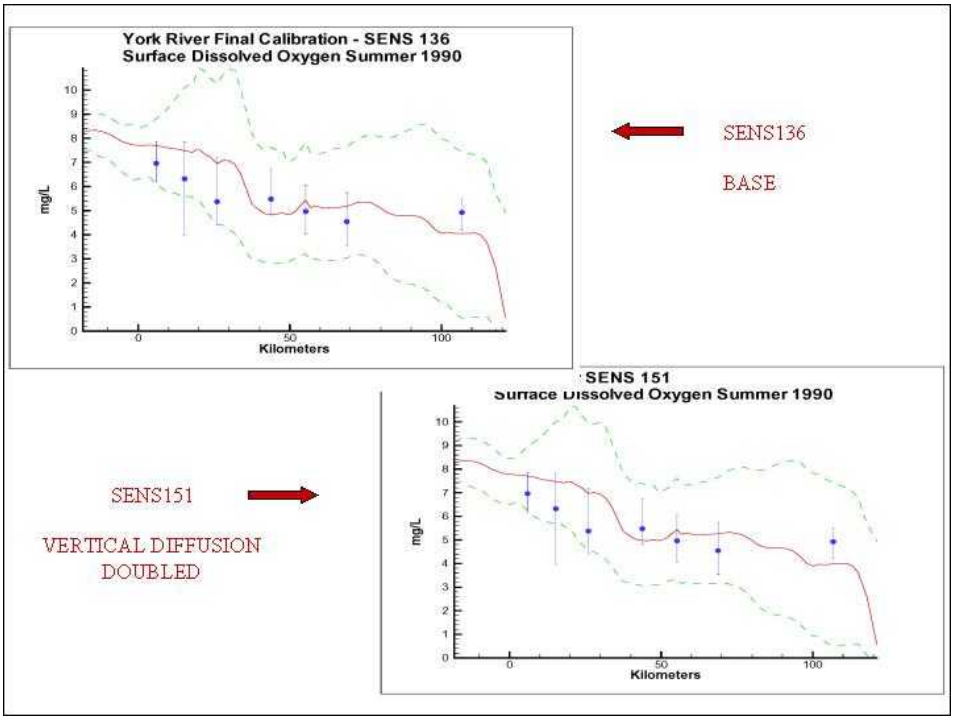

Figure 12-28. Sensitivity of York River surface dissolved oxygen to vertical diffusion coefficient, summer 1990.

In the Potomac, computed bottom-water dissolved oxygen increased by up to 1 g m^{-3} (Figure 12-29). At two stations, kms. 0 to 30, agreement with observed means diminished while at a third station (km 80) agreement improved. In the

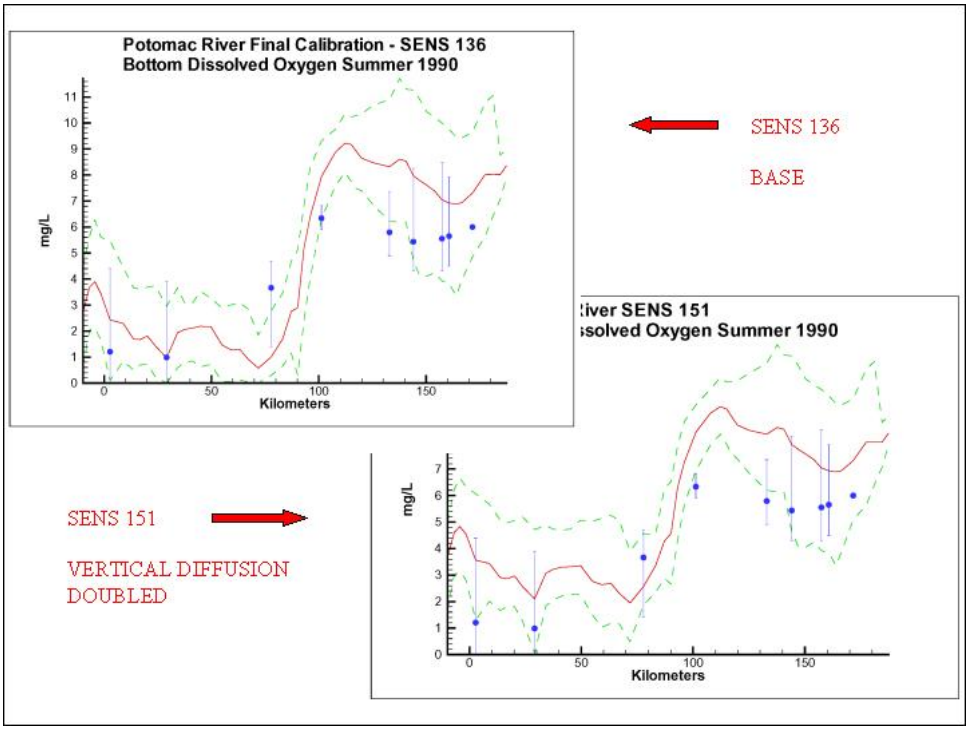

Figure 12-29. Sensitivity of Potomac River bottom dissolved oxygen to vertical diffusion coefficient, summer 1990.

surface waters, computed dissolved oxygen decreased by up to 1 g m^{-3} resulting in improved agreement with observed means from kms. 0 to 30 (Figure 12-30). At km 80, surface dissolved oxygen barely moved despite the increase in bottom dissolved oxygen. As with the York, we believe geometry influenced the results at this location. The volume of anoxic water at the bottom is insufficient to significantly affect the surface through mixing.

These runs indicate that exchange between the surface and bottom can influence surface dissolved oxygen but that no simple, universal "fix" such as changing vertical diffusion exists.

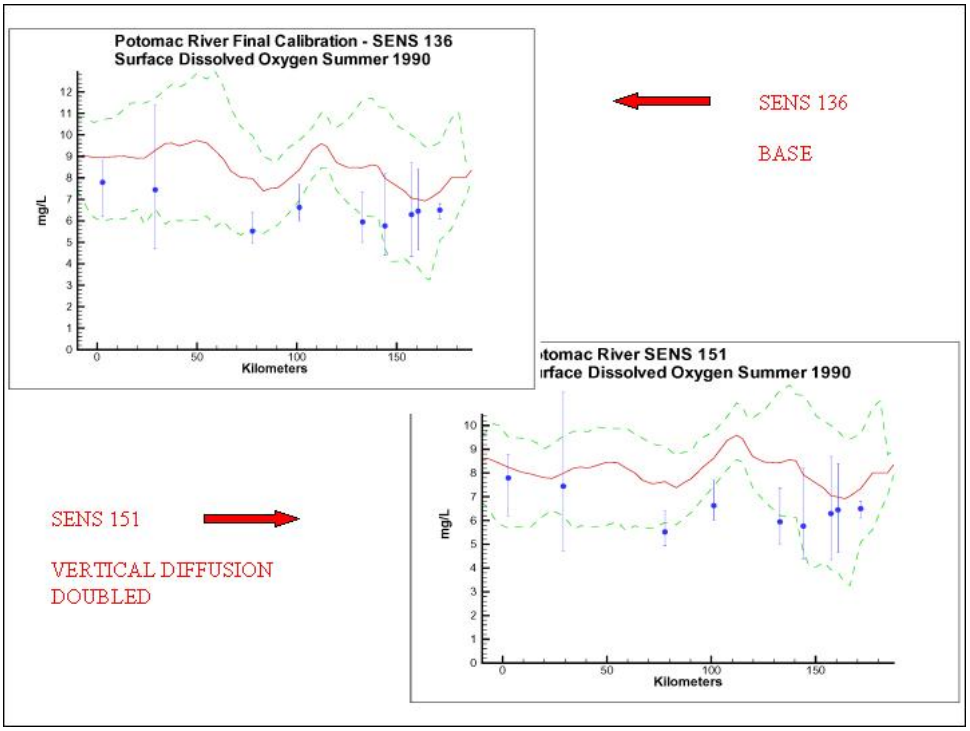

Figure 12-30. Sensitivity of Potomac River surface dissolved oxygen to vertical diffusion coefficient, summer 1990.

Discussion

Two phenomenon vex the computation of dissolved oxygen in the western tributaries. The first is the computation of excess dissolved oxygen in the tidal fresh portions of the James (Figures 12-31 to 12-36) and Potomac Rivers (Figures 12-49 to 12-54). The excess dissolved oxygen is the result of an excess of computed production over consumption. Computed production can be readily adjusted but a constraint exists to provide reasonable agreement with observed chlorophyll concentrations. We believe the problem lies more on the side of consumption. Riverine organic carbon loads to the Virginia tributaries are virtually unknown as are point-source carbon loads to all tributaries. In addition, the James and Potomac receive loads from combined-sewer overflows and urban runoff. Improved dissolved oxygen computations require improved information on loading. Ideally, measures of respiration or of biochemical oxygen demand in the water column should also be conducted.

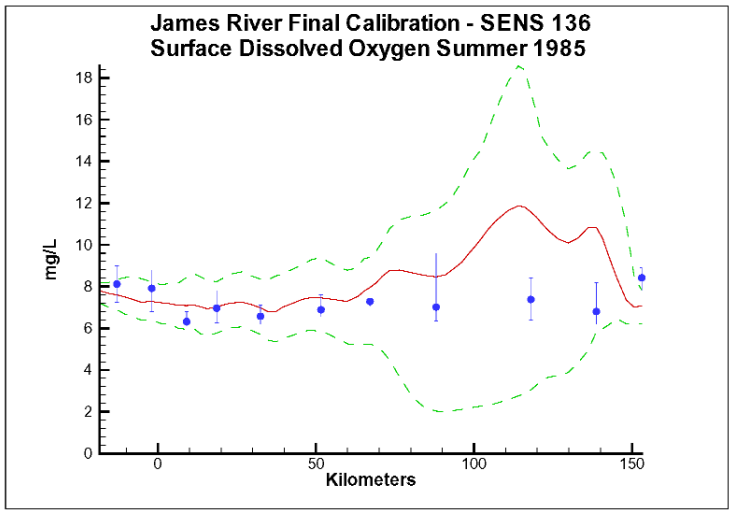

Figure 12-31. Computed and observed surface dissolved oxygen in the James River, summer 1985. Computed mean and range shown as lines, observed mean and range shown as solid circles and vertical bars.

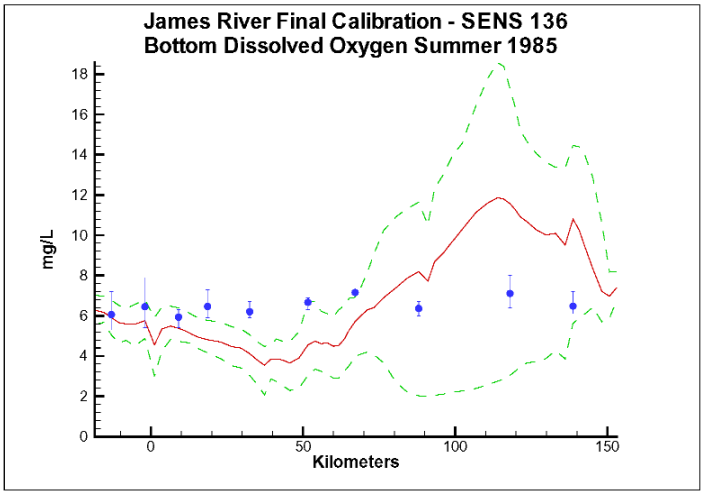

Figure 12-32. Computed and observed bottom dissolved oxygen in the James River, summer 1985. Computed mean and range shown as lines, observed mean and range shown as solid circles and vertical bars.

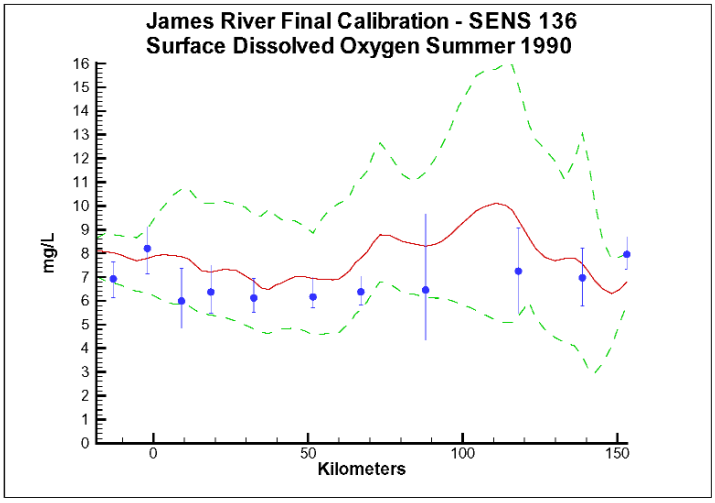

Figure 12-33. Computed and observed surface dissolved oxygen in the James River, summer 1990. Computed mean and range shown as lines, observed mean and range shown as solid circles and vertical bars.

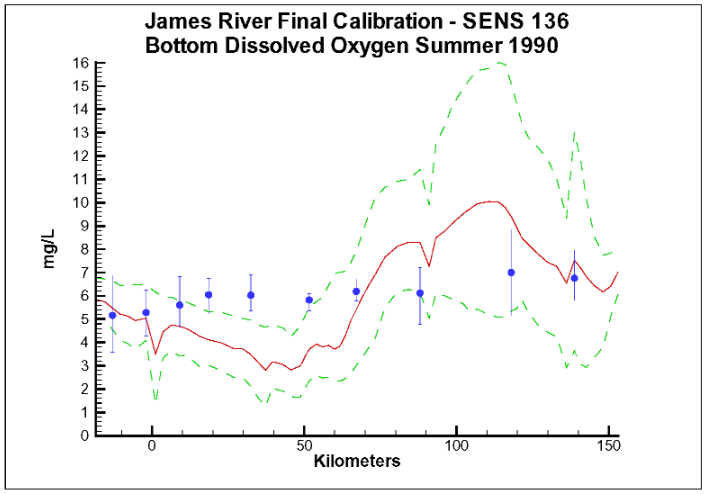

Figure 12-34. Computed and observed bottom dissolved oxygen in the James River, summer 1990. Computed mean and range shown as lines, observed mean and range shown as solid circles and vertical bars.

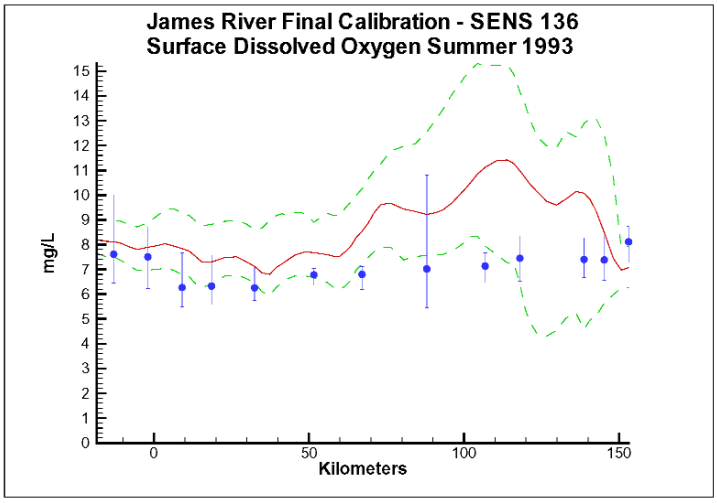

Figure 12-35. Computed and observed surface dissolved oxygen in the James River, summer 1993. Computed mean and range shown as lines, observed mean and range shown as solid circles and vertical bars.

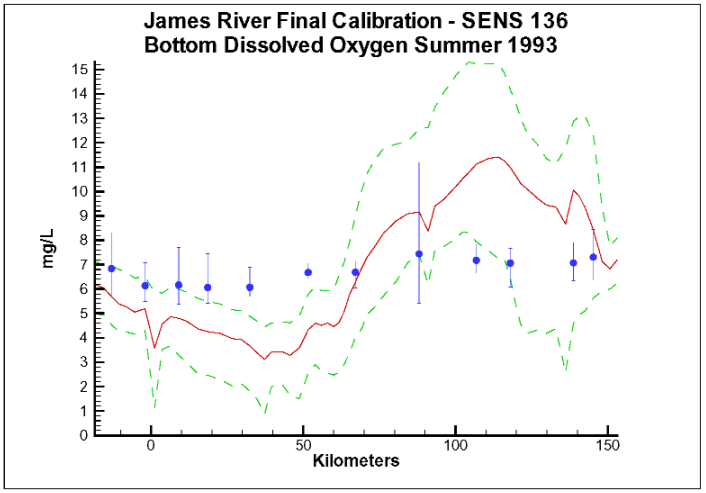

Figure 12-36. Computed and observed bottom dissolved oxygen in the James River, summer 1993. Computed mean and range shown as lines, observed mean and range shown as solid circles and vertical bars.

The second vexing process is the occurrence of depressed surface dissolved oxygen in the lower estuaries, notably the York circa km 25 (Figures 12-37 to 12-42), the Rappahannock at km 40 (Figures 12-43 to 12-48), and the Potomac circa kms 30 to 80 (Figures 12-49 to 12-54). Our best explanation of the phenomenon is transfer of oxygen demand and/or oxygen-depleted water from the bottom to the surface. The phenomena cannot be represented by simple adjustments vertical mixing, however. At several locations, the volume of anoxic bottom water is insufficient to significantly alter the surface concentration when mixed with surface water. Perhaps a larger volume of anoxic water intrudes from adjacent Chesapeake Bay. The phenomenon requires additional study and may be beyond modeling without process-based field observations.

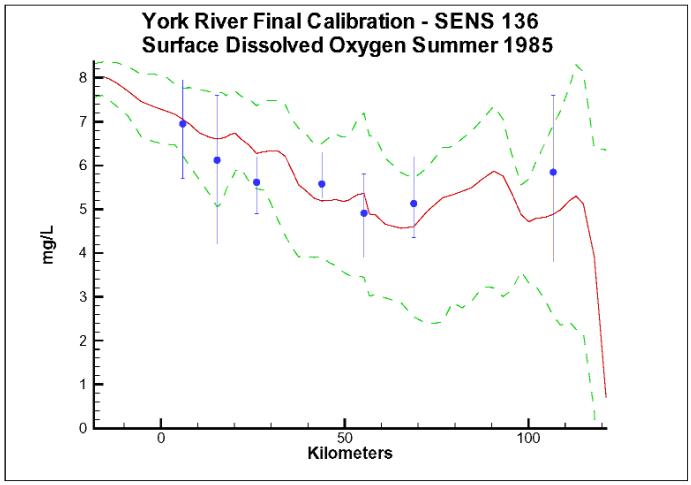

Figure 12-37. Computed and observed surface dissolved oxygen in the York River, summer 1985. Computed mean and range shown as lines, observed mean and range shown as solid circles and vertical bars.

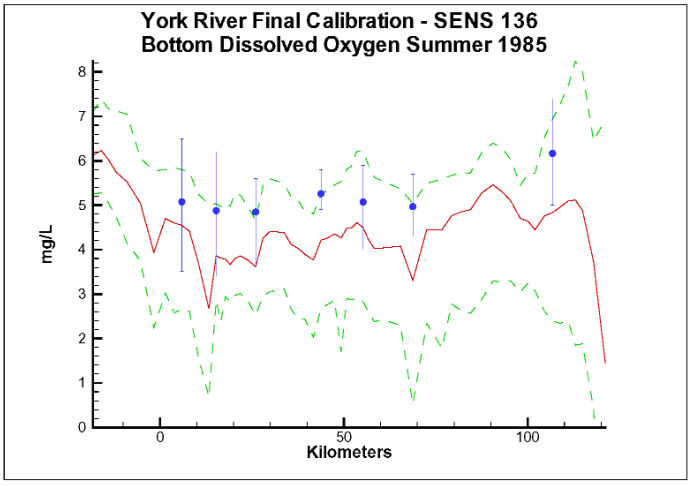

Figure 12-38. Computed and observed bottom dissolved oxygen in the York River, summer 1985. Computed mean and range shown as lines, observed mean and range shown as solid circles and vertical bars.

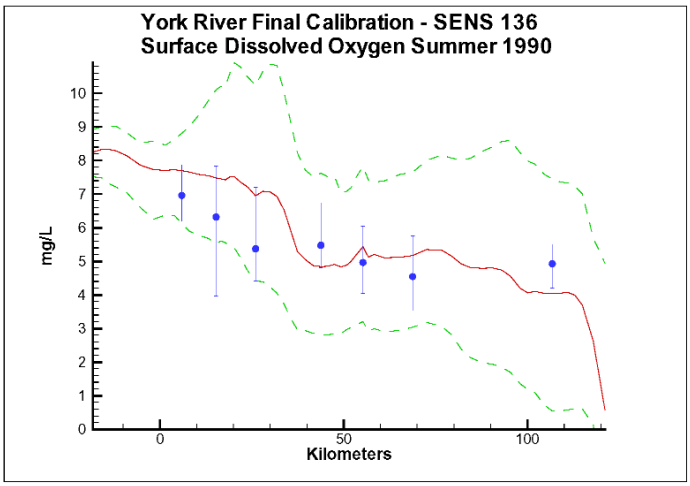

Figure 12-39. Computed and observed surface dissolved oxygen in the York River, summer 1990. Computed mean and range shown as lines, observed mean and range shown as solid circles and vertical bars.

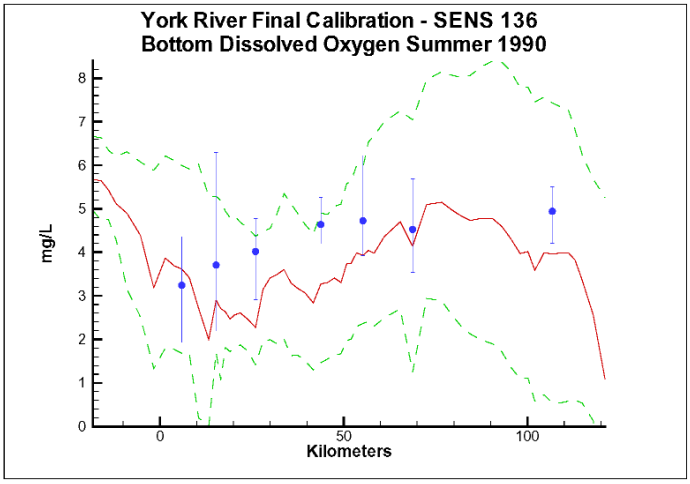

Figure 12-40. Computed and observed bottom dissolved oxygen in the York River, summer 1990. Computed mean and range shown as lines, observed mean and range shown as solid circles and vertical bars.

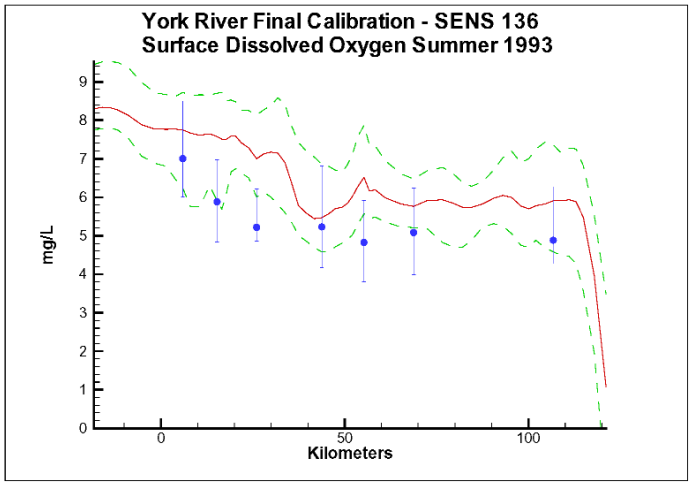

Figure 12-41. Computed and observed surface dissolved oxygen in the York River, summer 1993. Computed mean and range shown as lines, observed mean and range shown as solid circles and vertical bars.

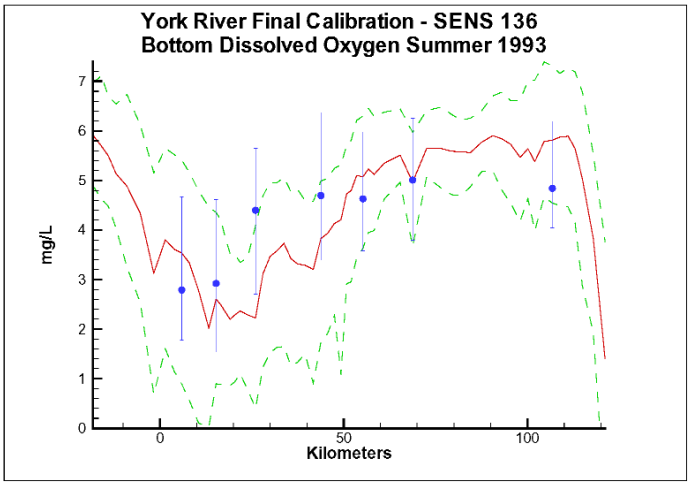

Figure 12-42. Computed and observed bottom dissolved oxygen in the York River, summer 1993. Computed mean and range shown as lines, observed mean and range shown as solid circles and vertical bars.

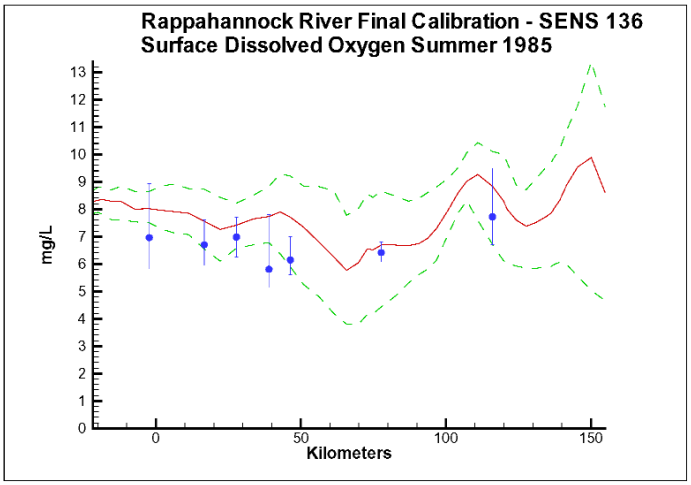

Figure 12-43. Computed and observed surface dissolved oxygen in the Rappahannock River, summer 1985. Computed mean and range shown as lines, observed mean and range shown as solid circles and vertical bars.

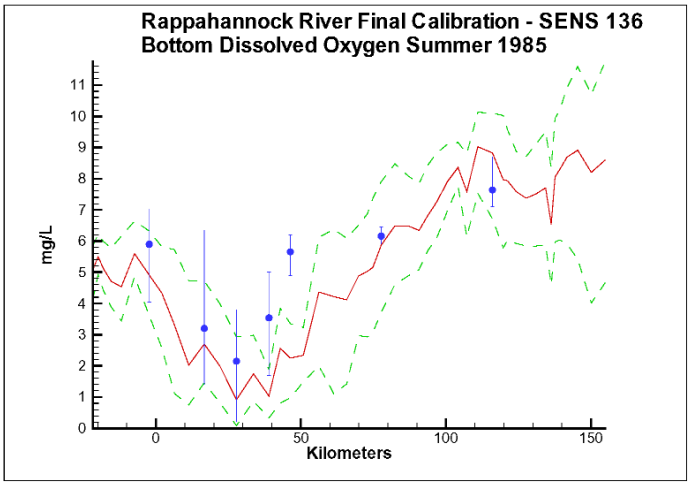

Figure 12-44. Computed and observed bottom dissolved oxygen in the Rappahannock River, summer 1985. Computed mean and range shown as lines, observed mean and range shown as solid circles and vertical bars.

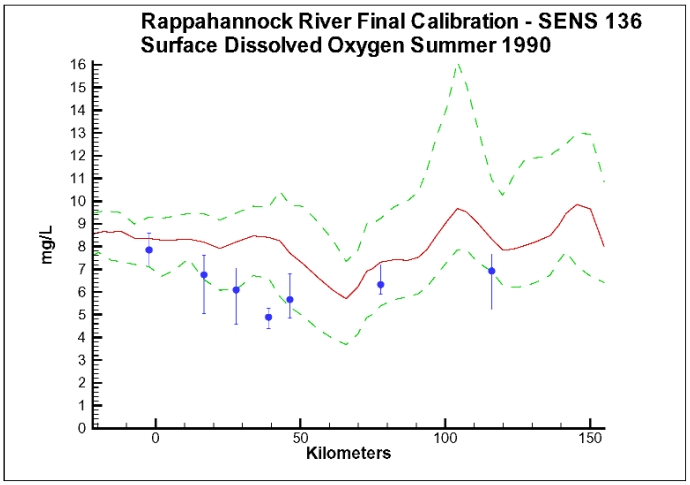

Figure 12-45. Computed and observed surface dissolved oxygen in the Rappahannock River, summer 1990. Computed mean and range shown as lines, observed mean and range shown as solid circles and vertical bars.

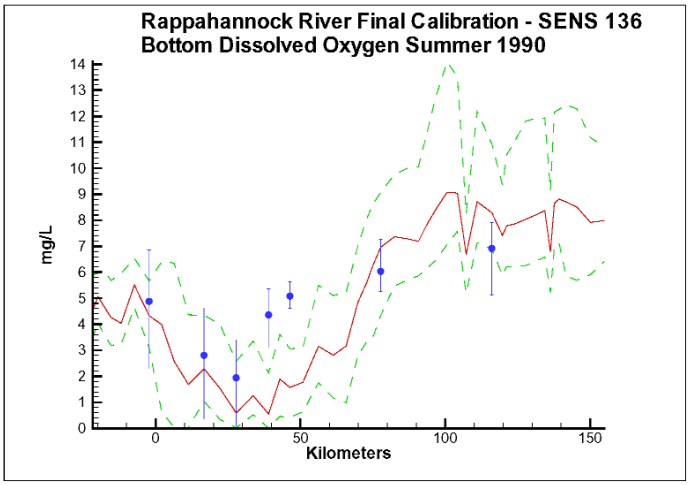

Figure 12-46. Computed and observed bottom dissolved oxygen in the Rappahannock River, summer 1990. Computed mean and range shown as lines, observed mean and range shown as solid circles and vertical bars.

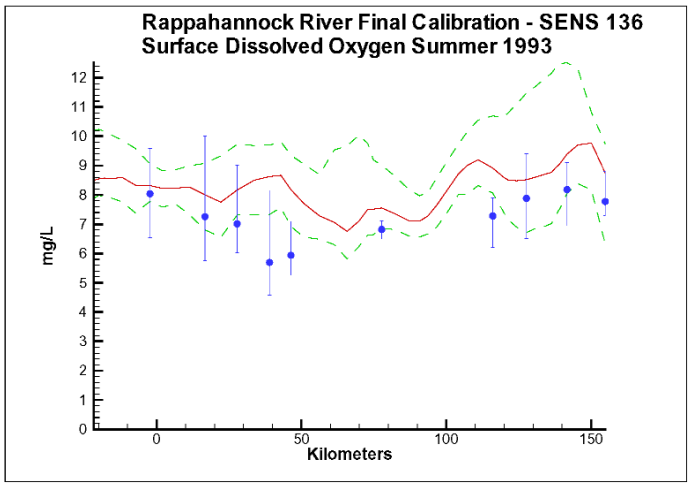

Figure 12-47. Computed and observed surface dissolved oxygen in the Rappahannock River, summer 1993. Computed mean and range shown as lines, observed mean and range shown as solid circles and vertical bars.

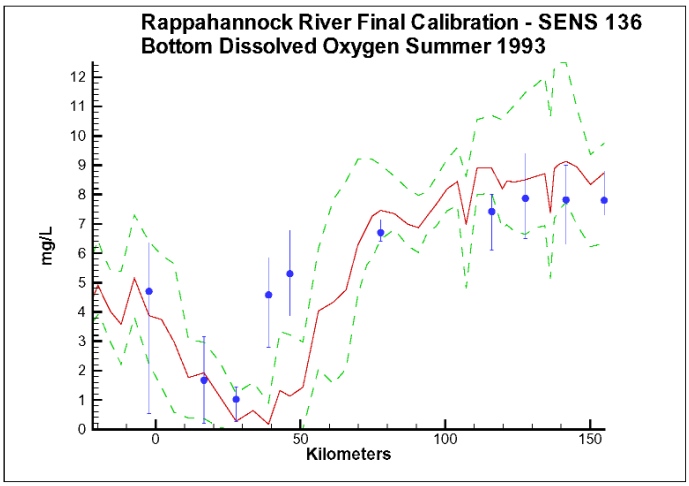

Figure 12-48. Computed and observed bottom dissolved oxygen in the Rappahannock River, summer 1993. Computed mean and range shown as lines, observed mean and range shown as solid circles and vertical bars.

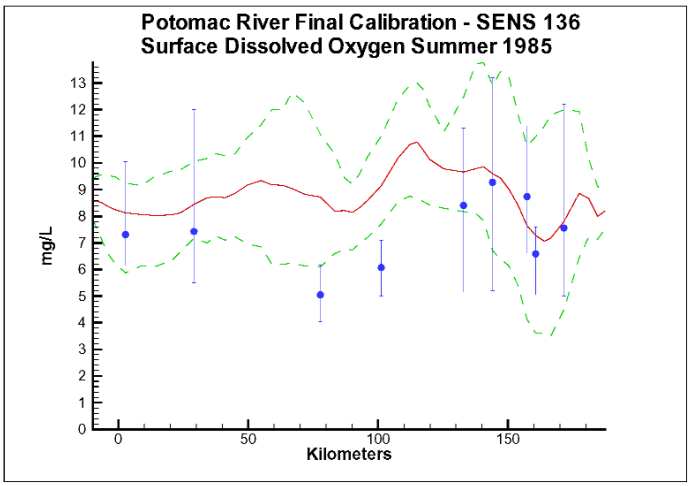

Figure 12-49. Computed and observed surface dissolved oxygen in the Rappahannock River, summer 1993. Computed mean and range shown as lines, observed mean and range shown as solid circles and vertical bars.

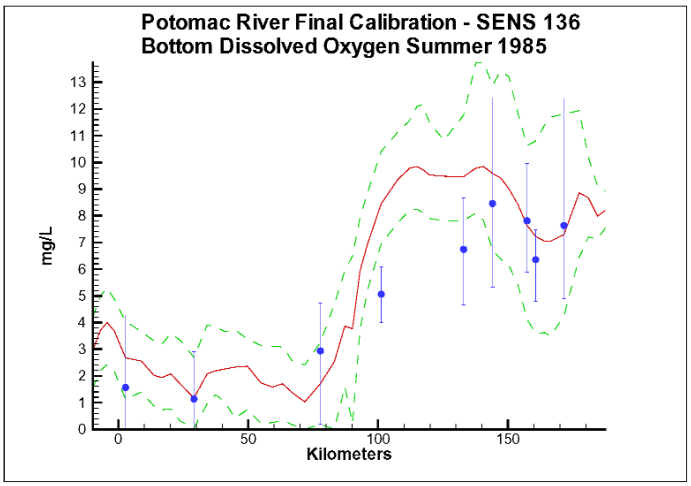

Figure 12-50. Computed and observed bottom dissolved oxygen in the Potomac River, summer 1985. Computed mean and range shown as lines, observed mean and range shown as solid circles and vertical bars.

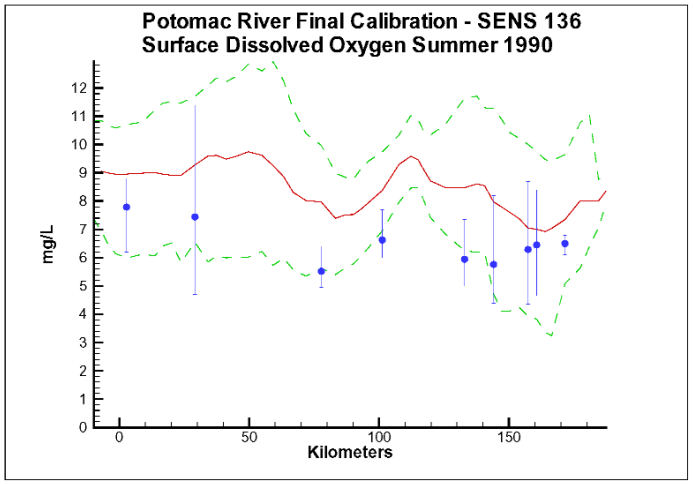

Figure 12-51. Computed and observed surface dissolved oxygen in the Potomac River, summer 1990. Computed mean and range shown as lines, observed mean and range shown as solid circles and vertical bars.

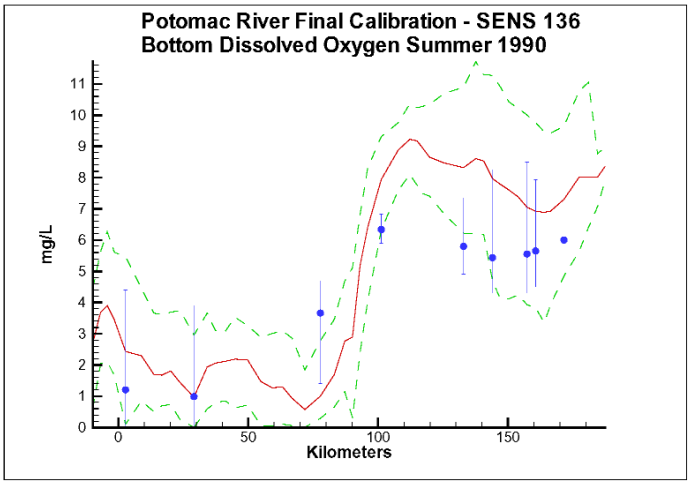

Figure 12-52. Computed and observed bottom dissolved oxygen in the Potomac River, summer 1990. Computed mean and range shown as lines, observed mean and range shown as solid circles and vertical bars.

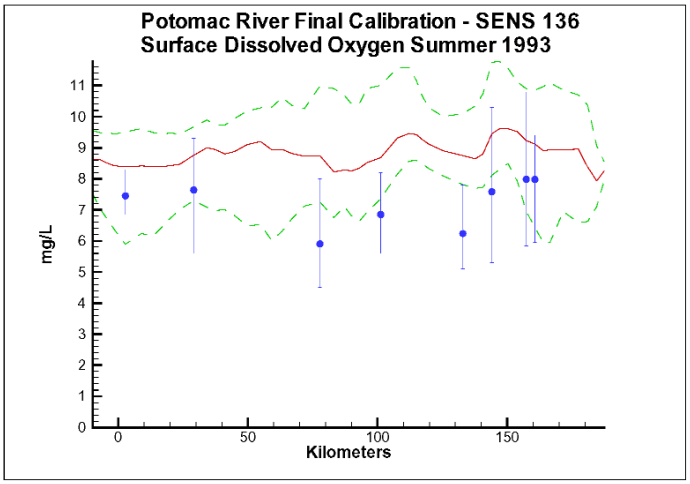

Figure 12-53. Computed and observed surface dissolved oxygen in the Potomac River, summer 1993. Computed mean and range shown as lines, observed mean and range shown as solid circles and vertical bars.

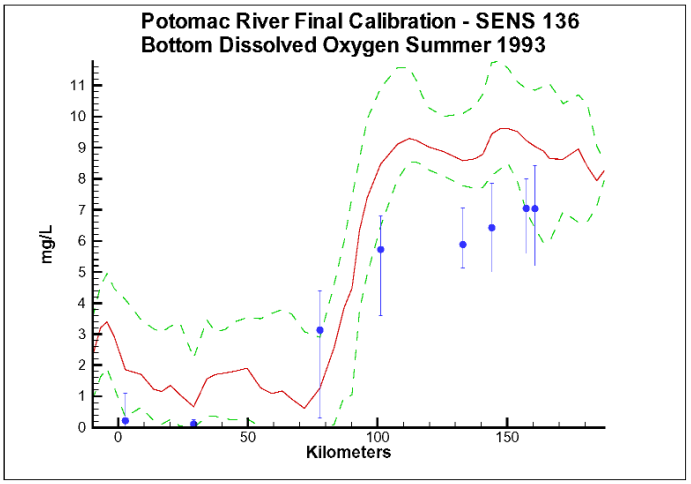

Figure 12-54. Computed and observed bottom dissolved oxygen in the Potomac River, summer 1993. Computed mean and range shown as lines, observed mean and range shown as solid circles and vertical bars.

Our model consistently under-computes dissolved oxygen in the bottom water of the lower James estuary (Figures 12-31 to 12-36). Here, an increase in vertical mixing is a fruitful approach to improving the computation. We did not adapt this approach since we were required to use a single formulation for vertical mixing system-wide. An alternative approach to improving dissolved oxygen in the James may be to increase longitudinal net circulation. Kuo and Neilson (1987) determined dissolved oxygen concentration in James River bottom water was maintained by strong circulation; residence time in the bottom water was too short for anoxia to develop. Increasing net circulation requires adjustments in the hydrodynamic model representations of viscosity and diffusivity. Whether simple adjustments in vertical mixing are made or whether more complex adjustments in circulation are attempted, refinement of the hydrodynamic model of the James is required before improvements in the water quality model can result.

We have said little about the dissolved oxygen computation in the Patuxent River (Figures 12-55 to 12-60). Despite two increments in resolution since the original model application (Cerco and Cole 1994), this tributary seems too coarsely gridded to provide more than a first-order representation of dissolved oxygen. Problems are especially apparent in the upper river. The channel there is tortuous, the limit of tidal intrusion is indefinite, and extensive wetlands influence water quality. Surface dissolved oxygen in the lower Patuxent is depressed, possibly for the same reasons as depression in the lower York, Rappahannock, and Potomac.

Each western tributary possesses unique properties and each alone could consume as much study as the entire Chesapeake Bay. We note that an individual model of the Patuxent is underway and a model of the Potomac is in the planning stages.

Gridding of each western tributary should be sufficient to provide detailed representation of the complex geometry. This requirement calls for roughly the same number of cells as in the present representation of Chesapeake Bay. The tributary cells will, of course, be much smaller than the current bay cells. Once a detailed grid is completed, careful model (and perhaps field) examination of circulation and mixing processes is required, with emphasis on the lower estuaries.

The York, Rappahannock, and Patuxent Rivers adjoin extensive tidal wetlands which appear to influence water quality. Nutrients, as well as dissolved oxygen, are, no doubt, exchanged between wetlands and channel. To represent the wetlands physically, addition of wetting-and-drying to the hydrodynamic model is required. A wetland biogeochemical module should be added to the water quality model. And, as with so many processes, field investigations may also be necessary.

Measures of loads of carbonaceous oxygen-demanding material to the tributaries are nearly unknown. Large-scale eutrophication modeling presupposes that algal production is the predominant source of oxygen demand. System-wide, this premise is certainly true but in confined portions of the tributaries, in the presence of inputs from multiple sources, external loads of oxygen-demanding material cannot be ignored. Monitoring of inputs and, perhaps, addition of organic carbon to the watershed model are recommended.

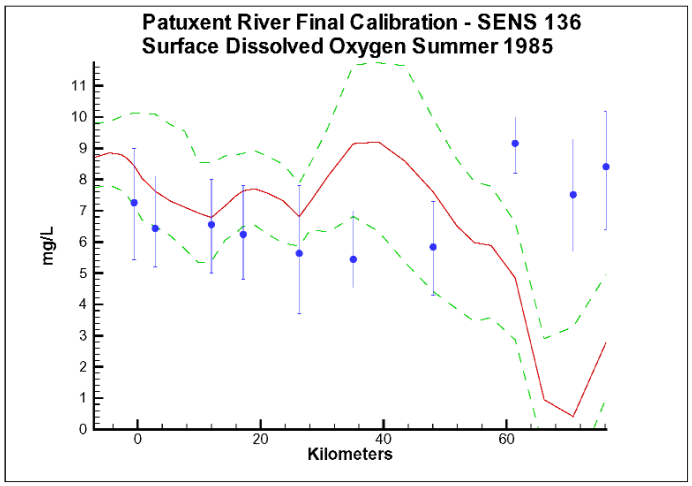

Figure 12-55. Computed and observed surface dissolved oxygen in the Patuxent River, summer 1985. Computed mean and range shown as lines, observed mean and range shown as solid circles and vertical bars.

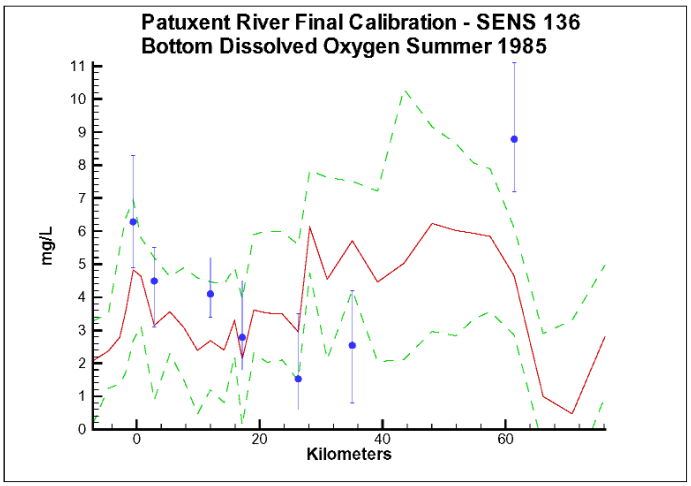

Figure 12-56. Computed and observed bottom dissolved oxygen in the Patuxent River, summer 1985. Computed mean and range shown as lines, observed mean and range shown as solid circles and vertical bars.

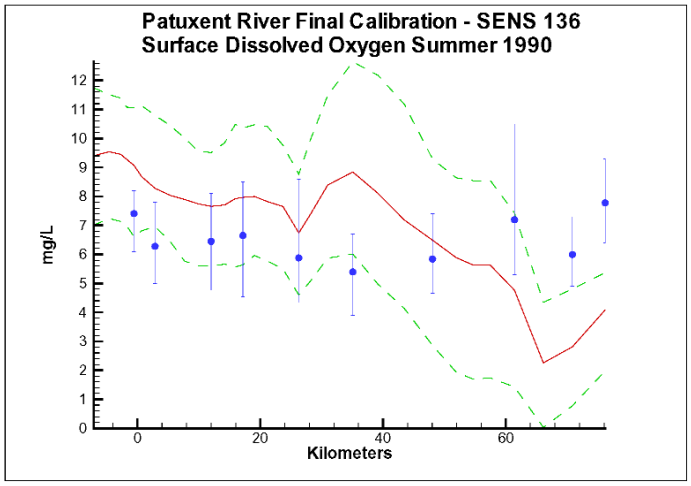

Figure 12-57. Computed and observed surface dissolved oxygen in the Patuxent River, summer 1990. Computed mean and range shown as lines, observed mean and range shown as solid circles and vertical bars.

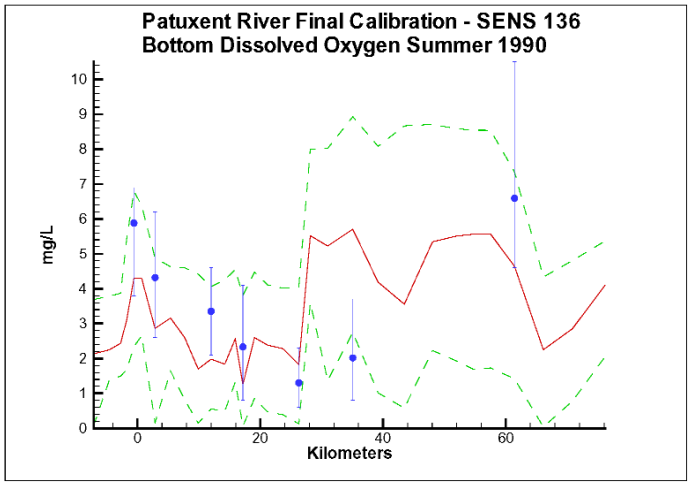

Figure 12-58. Computed and observed bottom dissolved oxygen in the Patuxent River, summer 1990. Computed mean and range shown as lines, observed mean and range shown as solid circles and vertical bars.

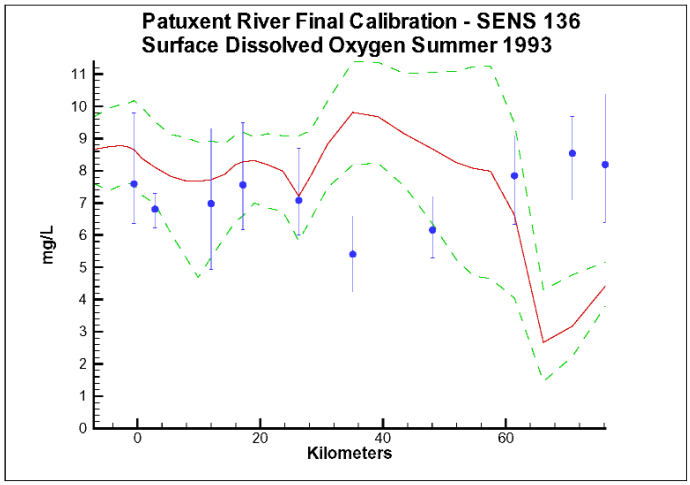

Figure 12-59. Computed and observed surface dissolved oxygen in the Patuxent River, summer 1993. Computed mean and range shown as lines, observed mean and range shown as solid circles and vertical bars.

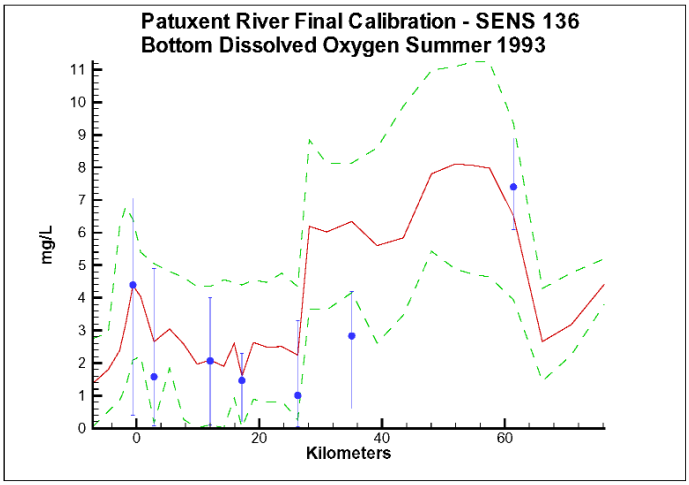

Figure 12-60. Computed and observed bottom dissolved oxygen in the Patuxent River, summer 1993. Computed mean and range shown as lines, observed mean and range shown as solid circles and vertical bars.

References

Cerco, C., and Cole, T. (1994). "Three-dimensional eutrophication model of Chesapeake Bay," Technical Report EL-94-4, US Army Engineer Waterways Experiment Station, Vicksburg, MS.

Hartman, B., and Hammond, D. (1985). "Gas exchange in San Francisco Bay," *Hydrobiologia* 129, 59-68.

Kuo, A., and Neilson, B. (1987). "Hypoxia and salinity in Virginia estuaries," *Estuaries*, 10(4), 277-283.

Modeling Processes at the Sediment-Water Interface 13

Introduction

The Sediment Diagenesis Model

The need for a predictive benthic sediment model was revealed in a steady-state model study (HydroQual 1987) that preceded Corps' modeling activity. The study indicated sediments were the dominant sources of phosphorus and ammonium during the summer period of minimum dissolved oxygen. Simultaneously, basic scientific investigations were illustrating the importance of sediment-water exchange processes in Chesapeake Bay and other estuarine systems (Boynton and Kemp 1985; Seitzinger, Nixon, and Pilson 1984; Fisher, Carlson, and Barber 1982).

For management purposes, a model was required with two fundamental capabilities:

- Predict effects of management actions on sediment-water exchange processes, and
- Predict time scale for alterations in sediment-water exchange processes.

A sediment model to meet these requirements was created for the initial three-dimensional coupled hydrodynamic-eutrophication model (Cerco and Cole 1993).

The model (Figure 13-1, Table 13-1) is driven by net settling of organic matter from the water column to the sediments. In the sediments, the model simulates the diagenesis (decay) of the organic matter. Diagenesis produces oxygen demand and inorganic nutrients. Oxygen demand, as sulfide (in saltwater) or methane (in freshwater), takes three paths out of the sediments: export to the water column as chemical oxygen demand, oxidation at the sediment-water interface as sediment oxygen demand, or burial to deep, inactive sediments. Inorganic nutrients produced by diagenesis take two paths out of the sediments: release to the water column, or burial to deep, inactive sediments.

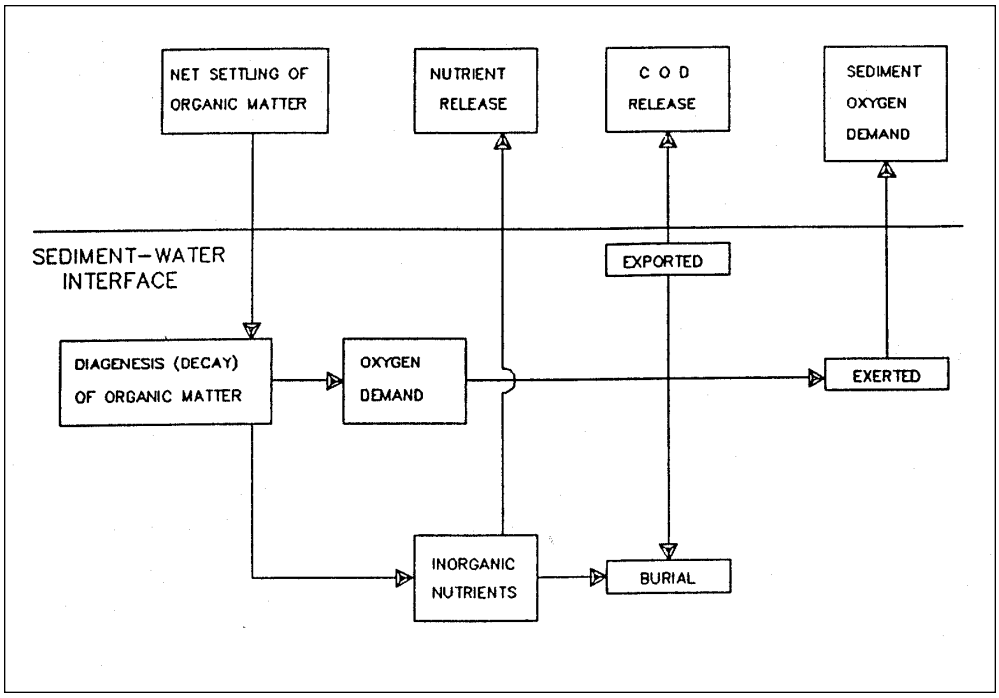

Figure 13-1. Sediment model schematic

Table 13-1
Sediment Model State Variables and Fluxes

State Variable	Sediment-Water Flux
Temperature	
Particulate Organic Carbon	Sediment Oxygen Demand
Sulfide/Methane	Release of Chemical Oxygen Demand
Particulate Organic Nitrogen	
Ammonium	Ammonium Flux
Nitrate	Nitrate Flux
Particulate Organic Phosphorus	
Phosphate	Phosphate Flux
Particulate Biogenic Silica	
Available Silica	Silica Flux

Additional details of the sediment model, required to understand the coupling of the sediment submodel to the model of the water column, are provided in this chapter. Complete model documentation was provided by DiToro and Fitzpatrick (1993). More accessible documentation may presently be found in DiToro (2001).

The Benthos Model

The ultimate aim of eutrophication modeling is to preserve precious living resources. Usually, the modeling process involves the simulation of living-resource parameters such as dissolved oxygen. For the "Virginia Tributary Refinements" phase of the model activities (Cerco et al. 2002), a decision was made to initiate direct interactive simulation of three living resource groups: zooplankton, benthos, and SAV.

Benthos were included in the model because they are an important food source for crabs, finfish, and other economically and ecologically significant biota. In addition, benthos can exert a substantial influence on water quality through their filtering of overlying water (Cohen et al. 1984; Newell 1988). Benthos within the model were divided into two groups: deposit feeders and filter feeders (Figure 13-2). The deposit-feeding group represents benthos which live within bottom sediments and feed on deposited material. The filter-feeding group represents benthos which live at the sediment surface and feed by filtering overlying water.

The primary reference for the benthos model is HydroQual (2000). This report is available on-line at http://www.chesapeakebay.net/modsc.htm. Less comprehensive documentation may be found in Cerco and Meyers (2000) and in Meyers at al. (2000).

Benthic Algae

In shallow coastal systems, benthic algae can markedly reduce the release of nutrients from sediments by assimilating some or all of the nutrients as they diffuse across the surface. At times, the algae can induce substantial flux of nutrients from the overlying water into the sediments.

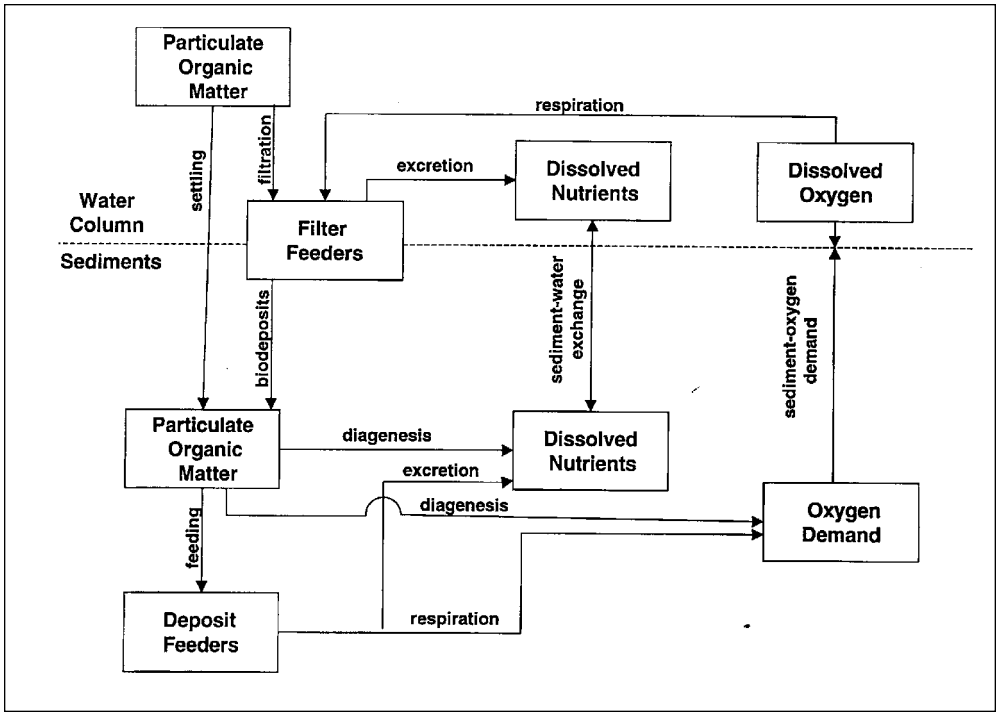

Figure 13-2. Benthos model schematic.

The benthic algal module in the Chesapeake Bay model was originally developed for the Delaware Inland Bays (Cerco and Seitzinger 1997). Benthic algae are considered to occupy a thin layer between the water column and benthic sediments (Figure 13-3). Biomass within the layer is determined by the balance between production, respiration, and losses to predation. Nutrients from diagenetic sediment production and from the overlying water are both available to the benthic algae. Formulation of the benthic algal module is detailed in Cerco and Seitzinger (1997). Several parameter changes were implemented since the original model development. A complete parameter suite is presented here.

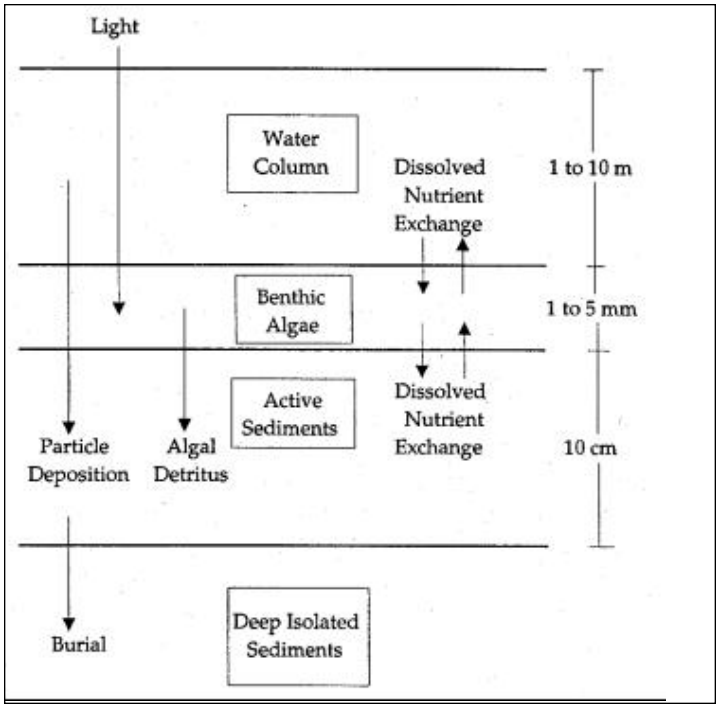

Figure 13-3. Benthic algal model schematic

Submerged Aquatic Vegetation (SAV)

SAV provides habitat for numerous living resources of economic importance and partly supports the estuarine food chain as well. Major portions of the SAV beds in Chesapeake Bay disappeared between 1970 and 1975 (Orth and Moore 1984). Restoration of the beds is a priority goal in management of the system.

An SAV submodel (Figure 13-4), which interacted with the main model of the water column and with the sediment diagenesis submodel, was created for the "Virginia Tributary Refinements" phase of the model activities (Cerco et al. 2002). Three state variables were modeled: shoots (above-ground biomass), roots (below-ground biomass), and epiphytes (attached growth). Three dominant SAV communities were identified in the bay based largely on salinity regimes (Moore et al. 2000). Within each community, a target species was selected: *Vallisneria americana*, *Ruppia maritima*, or *Zostera marina*. Each community was modeled using the same relationships but with parameter values selected for the target species. The primary reference for the SAV submodel is Cerco and Moore (2001).

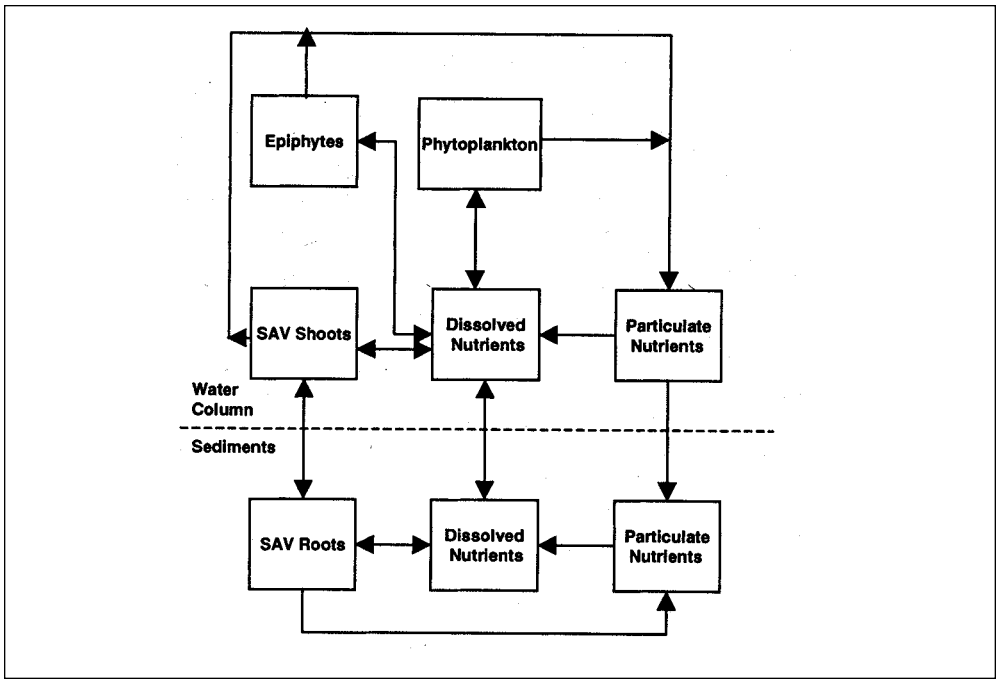

Figure 13-4. Submerged aquatic vegetation model schematic

Coupling With the Sediment Diagenesis Model

Benthic sediments are represented as two layers with a total depth of 10 cm (Figure 13-5). The upper layer, in contact with the water column, may be oxic or anoxic depending on dissolved oxygen concentration in the water. The lower layer is permanently anoxic. The thickness of the upper layer is determined by the penetration of oxygen into the sediments. At its maximum thickness, the oxic layer depth is only a small fraction of the total.

The sediment model consists of three basic processes. The first is deposition of particulate organic matter from the water column to the sediments. Due to the negligible thickness of the upper layer, deposition proceeds from the water column directly to the lower, anoxic layer. Within the lower layer, organic matter is subject to the second basic process, diagenesis (or decay). The third basic process is flux of substances produced by diagenesis to the upper sediment layer, to the water column, and to deep, inactive sediments. The flux portion of the model is the most complex. Computation of flux requires consideration of reactions in both sediment layers, of partitioning between particulate and dissolved fractions in both layers, of sedimentation from the upper to lower layer and from the lower layer to deep inactive sediments, of particle mixing between layers, of diffusion between layers, and of mass transfer between the upper layer and the water column.

The water quality and sediment models interact on a time scale equal to the integration time step of the water quality model. After each integration, predicted particle deposition, temperature, nutrient and dissolved oxygen concentrations are passed from the water quality model to the sediment model. The sediment model computes sediment-water fluxes of dissolved nutrients and oxygen based on predicted diagenesis and concentrations in the sediments and water. The computed

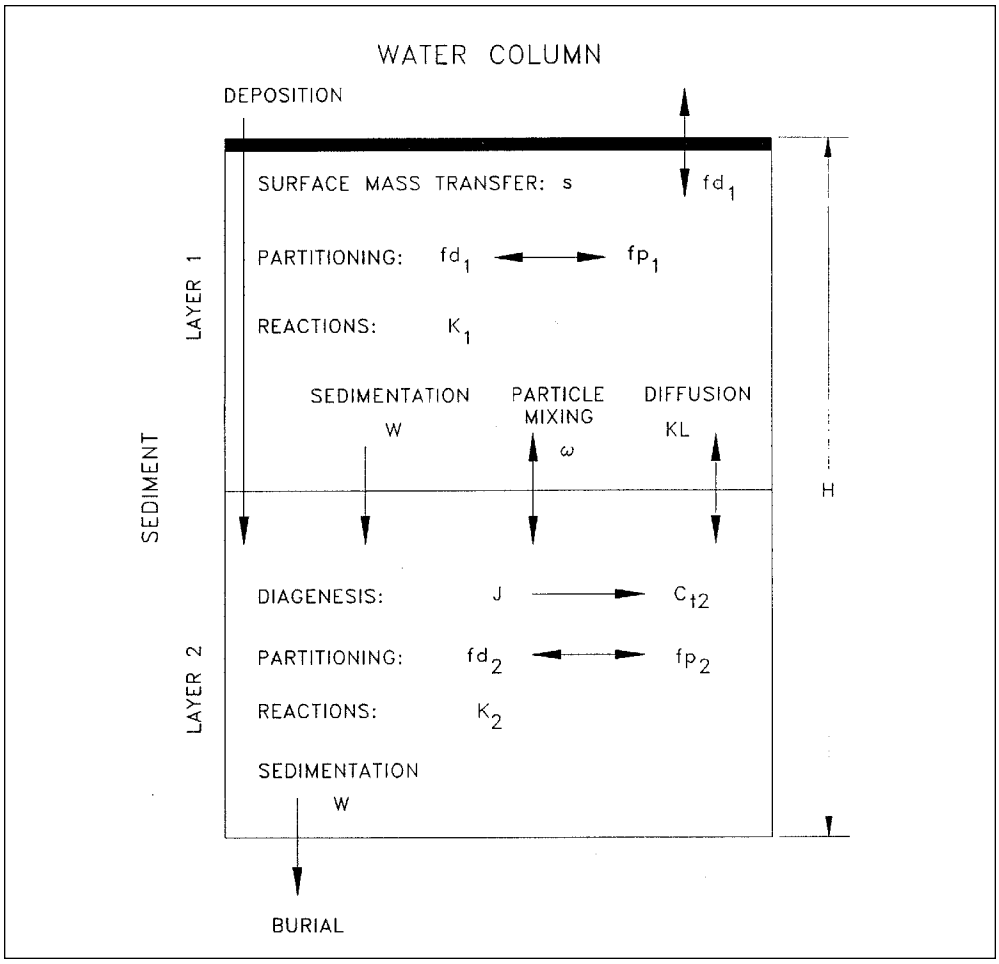

Figure 13-5. Sediment model elevation.

sediment-water fluxes are incorporated by the water quality model into appropriate mass balances and kinetic reactions.

Deposition

Deposition is one process which couples the model of the water column with the model of the sediments. Consequently, deposition is represented in both the sediment and water-column models. In the water column, deposition is represented with a modification of the mass-balance equation applied only to cells that interface the sediments:

$$\frac{\delta C}{\delta t} = [\text{transport}] + [\text{kinetics}] + \frac{WS}{\Delta z} \bullet C_{up} - \frac{W_{net}}{\Delta z} \bullet C \qquad (13\text{-}1)$$

in which:
C concentration of particulate constituent in cell above sediments (g m^{-3})
WS = settling velocity in water column (m d^{-1})
Cup = constituent concentration two cells above sediments (g m^{-3})
Wnet = net settling to sediments (m d^{-1})
Δz = cell thickness (m)

Net settling to the sediments may be less than or equal to settling in the water column. Sediment resuspension is implied when settling to the sediments is less than settling through the water column.

Diagenesis

Organic matter in the sediments is divided into three G classes or fractions, in accordance with principles established by Westrich and Berner (1984). Division into G classes accounts for differential decay rates of organic matter fractions. The G1, labile, fraction has a half life of 20 days. The G2, refractory, fraction has a half life of one year. The G3, inert, fraction undergoes no significant decay before burial into deep, inactive sediments. Each G class has its own mass-conservation equation:

$$H \bullet \frac{\delta Gi}{\delta t} = W_{net} \bullet f_i \bullet C - W \bullet Gi - H \bullet K_i \bullet Gi \bullet \theta_i^{(T-20)} \qquad (13\text{-}2)$$

in which:
H = total thickness of sediment layer (m)
Gi = concentration organic matter in G class i (g m^{-3})
f_i = fraction of deposited organic matter assigned to G class i
W = burial rate (m d^{-1})
K_i = decay rate of G class i (d^{-1})
θ_i = constant that expresses effect of temperature on decay of G class i

Since the G3 class is inert, $K_3 = 0$.

Sediment-Water Flux

The exchange of dissolved substances between the sediments and water column is driven by the concentration difference between the surface sediment layer and the overlying water. Flux may be in either direction across the sediment-water interface, depending on concentration gradient. Sediment-water flux is computed within the diagenesis model as the product of concentration difference and an internally-computed mass-transfer coefficient. In the water column, sediment-water exchange of dissolved substances is represented with a modification of the mass-balance equation applied only to cells that interface with bottom sediments:

$$\frac{\delta C}{\delta t} = [\text{transport}] + [\text{kinetics}] + \frac{\text{BENFLX}}{\Delta z} \qquad (13\text{-}3)$$

in which:
BENFLX = sediment-water flux of dissolved substance (g m^{-2} d^{-1})

By convention, positive fluxes are from sediment to water. Negative fluxes, including sediment oxygen demand, are from water to sediments.

Parameter Specification

Coupling with the sediment model requires specification of net settling rates, of the G splits of organic matter, and of burial rates.

Net Settling Rates

Net settling was specified identical to particle settling velocities in the water column. These rates were 1 m d^{-1} for particulate organic matter and 0.1 m d^{-1} for the spring and summer algal groups. Net settling of zero was specified for the blue-green algae, reflecting their buoyant properties. Net settling of particulate biogenic silica was specified as 0.01 m d^{-1}.

Assignment to G Classes

Upon deposition in the sediments, state variables representing particulate organic matter in the water quality model required conversion into sediment model state variables. The water quality model considered two classes of particulate organic matter: labile and refractory. The sediment model was based on three classes of organic particles: labile (G1), refractory (G2), and inert (G3). Labile particles from the water quality model were transferred directly into the G1 class in the sediment model. Refractory particles from the water quality model had to be split into G2 and G3 fractions upon entering the sediments. Initial guidance for the splits was obtained from experiments (Westrich and Berner 1984) in which roughly even distribution between refractory and inert particulate organic carbon was noted. The final distribution (Table 13-2) was obtained from model calibration. Carbon and nitrogen were considered slightly more reactive than phosphorus. This treatment possibly reflected the presence of refractory mineral forms within the water column particulate phosphorus.

Algae settling directly to the sediments also required routing into sediment model state variables (Table 13-2). The algal fraction routed into G1 particles was adopted from the initial model calibration (Cerco and Cole 1994). Routing of refractory algae into G2 and G3 classes was equivalent to the split employed for refractory organic particles.

Table 13-2
Routing Organic Particles into Sediment Classes

WQM Variable	Carbon, Nitrogen			Phosphorus		
	% G1	% G2	% G3	% G1	% G2	% G3
Labile Particles	100			100		
Refractory Particles		86	14		73	27
Algae	65	30	5	65	25.5	9.5

Burial Rates

As part of the initial model effort (Cerco and Cole 1994), sedimentation rates were measured via a pollen-dating method (Brush 1989) at fifteen locations, primarily in the mainstem of the bay. Model sedimentation rates were specified based on these measures and on an additional assemblage (Officer et al. 1984). Sedimentation rates were 0.5 cm yr^{-1} near the fall line of the bay and tributaries, 0.25 cm yr^{-1} in the central bay and central and lower tributaries, and 0.37 cm yr^{-1} near the mouth

of the bay. The sedimentation rates from the initial study were retained in the present effort.

Sediment Model Parameters

With one exception, all parameters within the diagenesis model were exactly as derived for the original model application (DiToro and Fitzpatrick 1993). The exception was the phosphate partition coefficient in the surficial sediments. This value was increased from 300 L kg^{-1} to 3000 L kg^{-1} in freshwater sediments (salinity < 1 ppt). In applying the diagenesis model to multiple systems, DiToro (2001) noted the phosphorus partition coefficients frequently required revision. Low ionic strength of freshwater was suggested as the reason for employment of a higher partition coefficient in Lake Champlain. This explanation may hold, as well, for the use of a higher partition coefficient in the tidal fresh waters of the Chesapeake Bay system.

Sediment Model Results

Data Base

Sediment-water flux measures employed in model development, calibration, and performance evaluation were obtained from the SONE (sediment oxygen and nutrient exchange) program (Boynton et al. 1986). Observations of sediment oxygen demand, and ammonium, nitrate, phosphate, and silica exchange were conducted at ten stations in the upper Bay and Maryland tributaries (Figure 13-6). Measures were usually collected four times per year. The methodology employed intact sediment cores incubated in triplicate immediately upon collection. SONE data were obtained from the principal investigators by HydroQual Inc. and supplied to WES in March 2001.

Carbon, nitrogen, and phosphorus analyses of surficial sediments were conducted concurrent with the SONE measures. Mean values from the period of record, usually 10 years, were computed for comparison with the model.

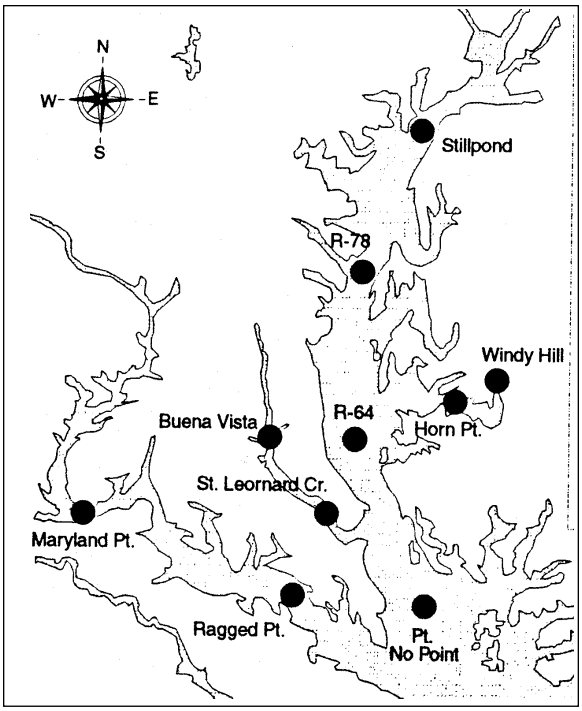

Figure 13-6. SONE observations stations.

Time Series

Time-series comparisons are presented for three stations: Still Pond, R- 64, and Point-No-Point (Figure 13-6). These stations are selected for their different bottom environments as characterized by dissolved oxygen concentration. Bottom dissolved oxygen at Still Pond rarely falls below 2 g m^{-3} (Figure 13-7). Complete anoxia is a regular occurrence during summer in bottom waters at R-64 (Figure 13-8). At Point-No-Point, intermittent bottom-water anoxia occurs but the duration is not so severe as at R-64 (Figure 13-9).

Peak sediment oxygen demand of 2 to 2.5 g m^{-2} d^{-1} is observed at Still Pond (Figure 13-10). The model matches these observations well and occasionally computes sediment oxygen demand as high as 3 g m^{-2} d^{-1}. Computed and observed

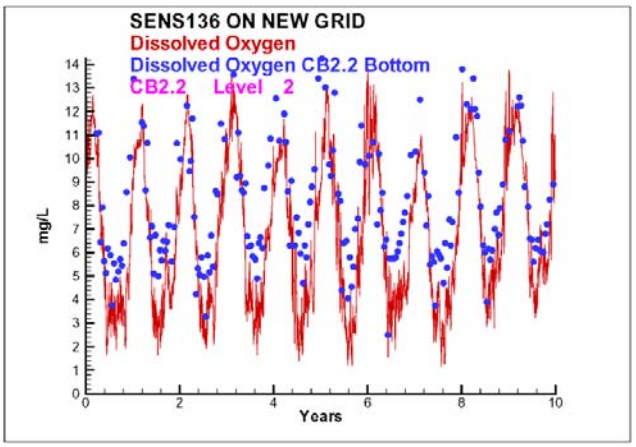

Figure 13-7. Computed and observed bottom dissolved oxygen at Station CB2.2, near Still Pond.

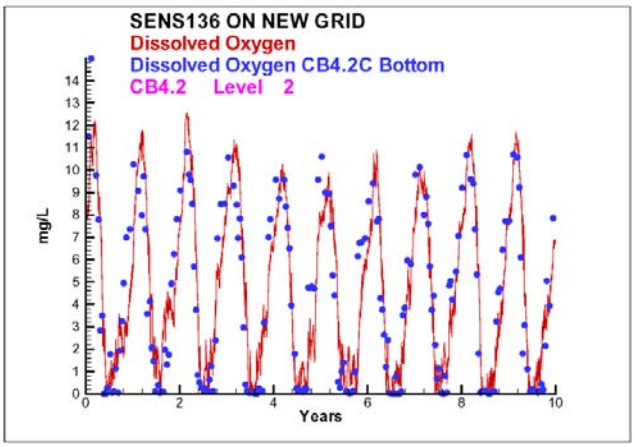

Figure 13-8. Computed and observed bottom dissolved oxygen at Station CB4.2C, near R-64.

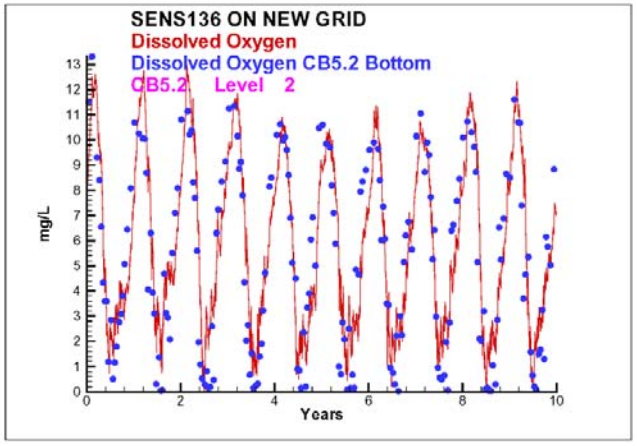

Figure 13-9. Computed and observed bottom dissolved oxygen at Station CB5.2, near Point-No-Point.

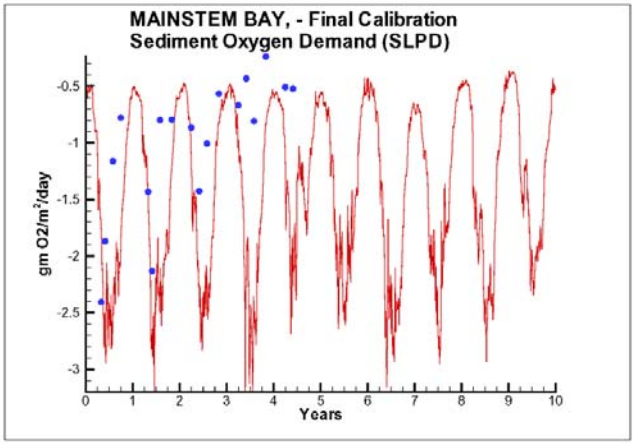

Figure 13-10. Computed (daily) and observed (instantaneous) sediment oxygen demand at Still Pond.

sediment oxygen demand in excess of 2 g m^{-2} d^{-1} occurs at R-64 but the preponderance of observations and computations are less than 1 g m^{-2} d^{-1} (Figure 13-11). At this location, sediment oxygen consumption is constrained by bottom-water anoxia and oxygen demand escapes from the sediments in the form of chemical oxygen demand (Figure 13-12). Observed sediment oxygen demand is also constrained by bottom-water anoxia at Point-No-Point (Figure 13-13). Computed sediment oxygen demand is higher, however. Careful examination of the computed bottom dissolved oxygen concentration indicates the model computes the presence of oxygen when none is observed (Figure 13-9). The availability of oxygen in the model allows sediment oxygen consumption when little actually occurs. This phenomenon does not imply more oxygen is consumed in the model than in reality at Point-No-Point. In the model, oxygen consumption occurs in surficial sediments. In reality, the sediments export chemical oxygen demand that consumes oxygen within the water column.

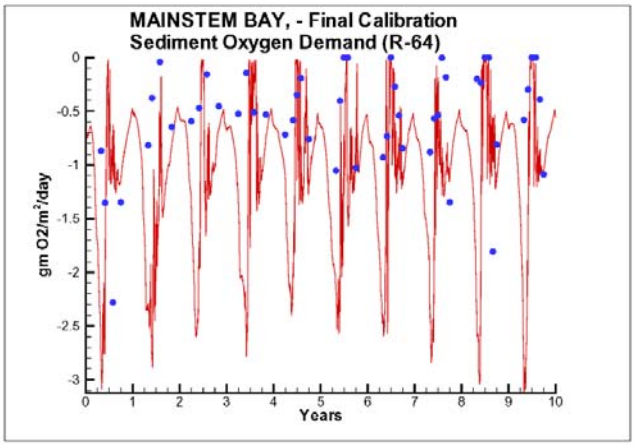

Figure 13-11. Computed (daily) and observed (instantaneous) sediment oxygen demand at R-64.

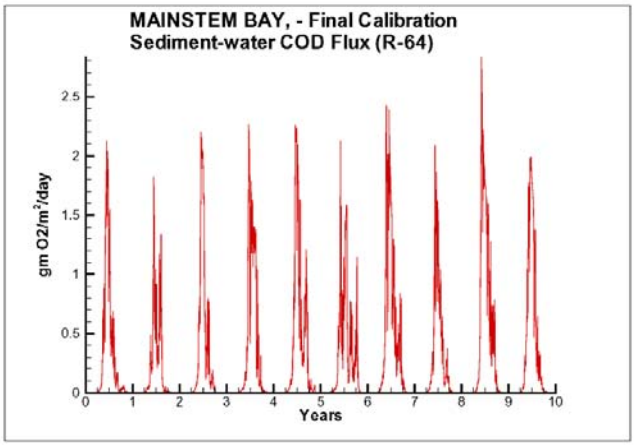

Figure 13-12. Computed sediment chemical oxygen demand release at R-64.

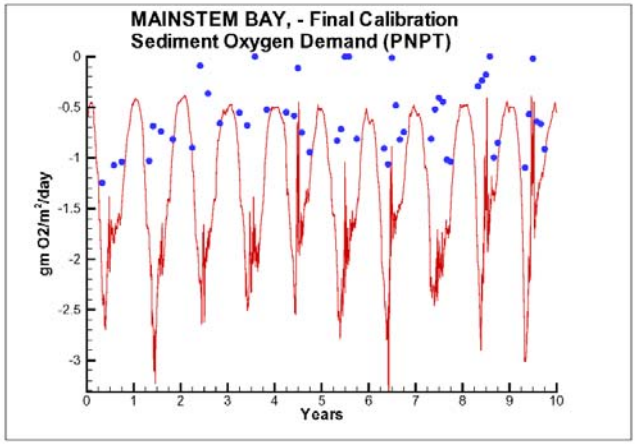

Figure 13-13. Computed (daily) and observed (instantaneous) sediment oxygen demand at Point-No-Point.

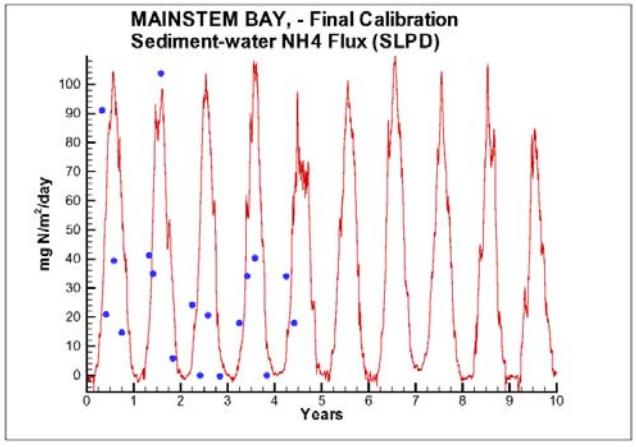

Figure 13-14. Computed (daily) and observed (instantaneous) sediment-water ammonium flux at Still Pond.

Of the three stations, observed sediment ammonium release is greatest at R-64, often in excess of 150 mg m^{-2} d^{-1} (Figure 13-15). Lesser releases occur at Point-No-Point (Figure 13-16) and Still Pond (Figure 13-17) respectively. The sequence of ammonium release corresponds to the occurrence of bottom-water anoxia. In the absence of oxygen, ammonium freely escapes from the sediments. In the presence of oxygen, ammonium is nitrified to nitrate which is denitrified in anoxic zones within the sediments (Jenkins and Kemp 1984). The model sequence of ammonium release is opposite the observed trend, however. Greatest releases occur in the aerobic waters at Still Pond. The nitrification/denitrification processes were carefully calibrated in the development of the sediment model (DiToro and Fitzpatrick 1993). The most likely explanation for the model behavior is that excess organic matter is deposited at Still Pond while a shortfall in deposition occurs at R-64.

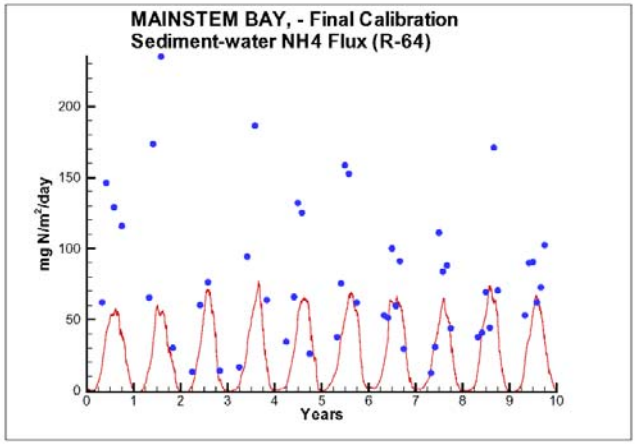

Figure 13-15. Computed (daily) and observed (instantaneous) sediment-water ammonium flux at R-64.

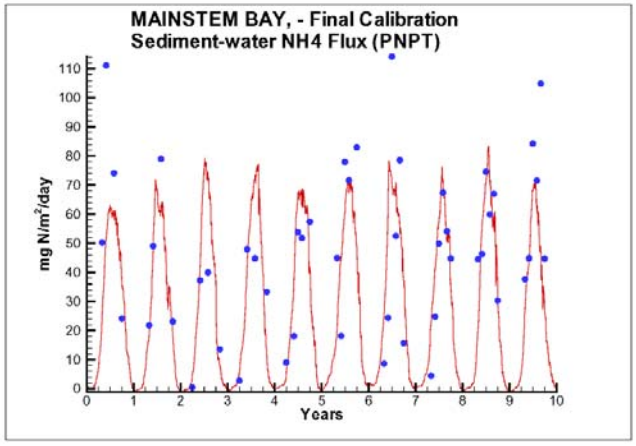

Figure 13-16. Computed (daily) and observed (instantaneous) sediment-water ammonium flux at Point-No-Point.

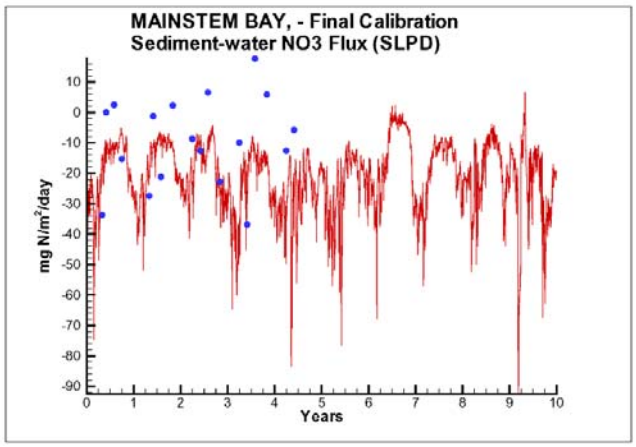

Figure 13-17. Computed (daily) and observed (instantaneous) sediment-water nitrate flux at Still Pond.

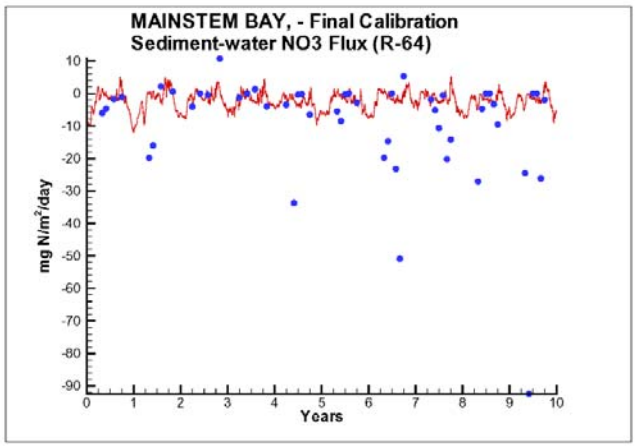

Figure 13-18. Computed (daily) and observed (instantaneous) sediment-water nitrate flux at R-64.

The observations show nitrate moves in both directions across the sediment-water interface (Figures 13-17 to 13-19). Sediment uptake predominates. Release is limited to 10 mg m^{-2} d^{-1} while uptake of 20 to 30 mg m^{-2} d^{-1} is common. In the model, uptake predominates at Still Pond (Figure 13-17). This uptake represents diffusive flux of nitrate-rich water from the Susquehanna River. Farther down the bay, bottom-water nitrate concentrations are much less and computed sediment-water nitrate flux is about evenly balanced between uptake and release. Observations show some extreme uptake rates that are not matched by the model. Otherwise, computed flux rates are in reasonable agreement with observations.

Observed sediment-water phosphate flux hovers in the interval ±5 mg m^{-2} d^{-1} when bottom dissolved oxygen remains above a critical concentration. (Figures 13-20 to 13-22). When dissolved oxygen falls below the critical concentration, phosphate release spikes up as high as 60 mg m^{-2} d^{-1}. The spiking is attributed to the reduction of iron oxides in the surficial sediments. Under oxygenated conditions, the oxides are in particulate form and sorb phosphorus liberated by diagenetic processes deeper in the sediments. As oxygen in the water is depleted, the iron oxides are reduced to soluble form and phosphate freely diffuses to the overlying water. The critical dissolved oxygen concentration is specified as 2 g m^{-3} in the model. Computed dissolved oxygen level seldom falls this low at Still Pond so release events are infrequent and of short duration. At Point-No-Point, release events occur more frequently although duration remains short. At R-64, which experiences lengthy intervals of complete anoxia, sediment phosphate release is a regular occurrence of substantial duration. The model correctly differentiates phosphate release among the stations and provides reasonable agreement with the magnitude of observed releases.

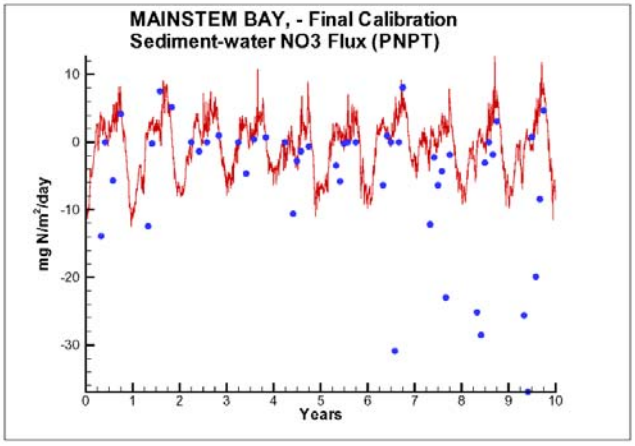

Figure 13-19. Computed (daily) and observed (instantaneous) sediment-water nitrate flux at Point-No-Point.

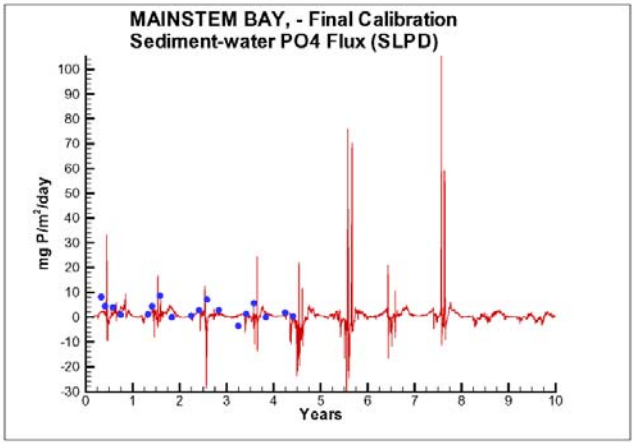

Figure 13-20. Computed (daily) and observed (instantaneous) sediment-water phosphate flux at Still Pond.

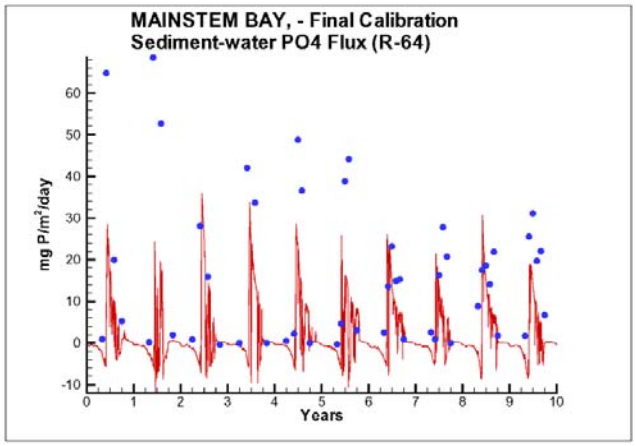

Figure 13-21. Computed (daily) and observed (instantaneous) sediment-water phosphate flux at R-64.

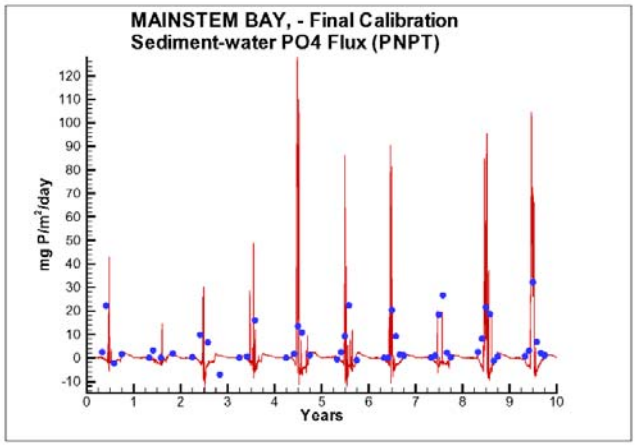

Figure 13-22. Computed (daily) and observed (instantaneous) sediment-water phosphate flux at Point-No-Point.

Observed silica flux is exclusively from sediments to water and regularly exceeds 300 mg m^{-2} d^{-1} (Figures 13-23 to 13-25). Computed silica fluxes occur in both directions across the sediment-water interface. Maximum release is 200 mg m^{-2} d^{-1} and most releases are much less. Shortfalls in computed silica release have been a property of the coupled model since its first application. In the initial application, the shortfall was attributed to omission of particulate biogenic silica from system-wide silica loads. Diagenesis of 100 mg m^{-2} d^{-1} was added to the sediments to account for the deficit in deposition. In the present model, biogenic silica was explicitly included in loads so the added sediment diagenesis was eliminated. Apparently, the added loading did not compensate for the diagenesis removed. The computed occurrence of sediment silica uptake suggests, also, that the modeled silica partition coefficients should be revisited. In view of management emphasis on nitrogen and phosphorus, minimal attention was devoted to silica in the present model effort. With a good deal of effort, the present silica results can, no doubt, be improved.

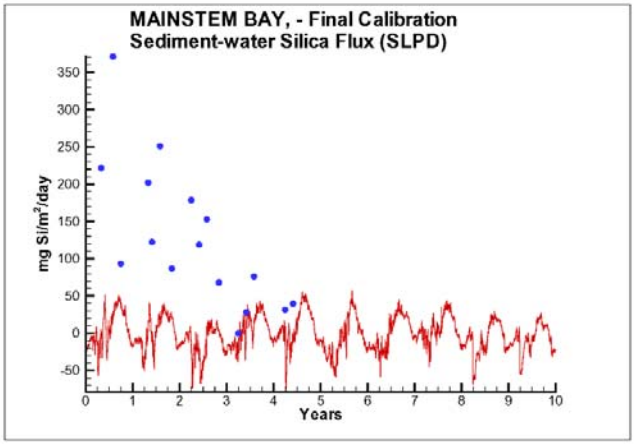

Figure 13-23. Computed (daily) and observed (instantaneous) sediment-water silica flux at Still Pond.

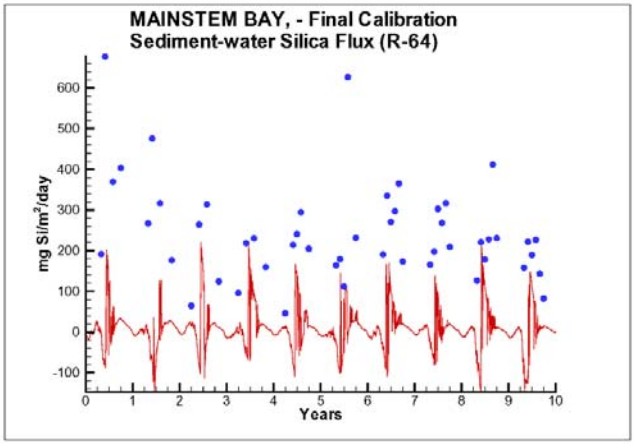

Figure 13-24. Computed (daily) and observed (instantaneous) sediment-water silica flux at R-64.

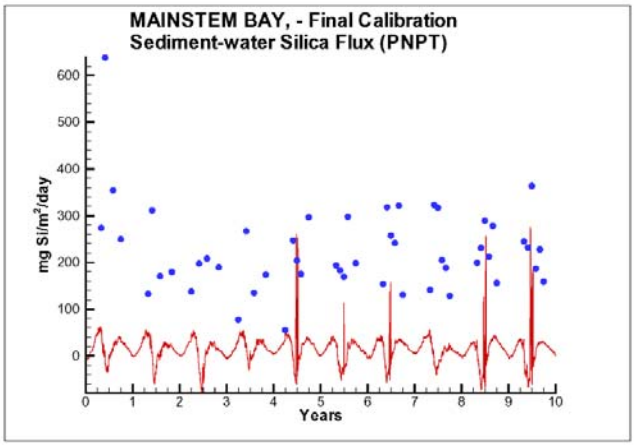

Figure 13-25. Computed (daily) and observed (instantaneous) sediment-water silica flux at Point-No-Point.

Cumulative Distribution

Cumulative distributions were created for the population of Chesapeake Bay sediment-water flux observations and for corresponding model computations. Computed sediment oxygen demand exceeded observed throughout the distribution (Figure 13-26). Median computed demand exceeded observed by more than 0.5 g m^{-2} d^{-1}. Observed sediment ammonium release exceeded computed throughout the distribution (Figure 13-27). Median observed release exceeded modeled by 10 mg m^{-2} d^{-1}. A number of explanations can be offered for these results. The excess of sediment oxygen demand may be attributed to computed bottom dissolved oxygen. Computed bottom water dissolved oxygen does not match the lowest observations (e.g. Figure 13-9) at all locations. As a result, computed sediment oxygen demand

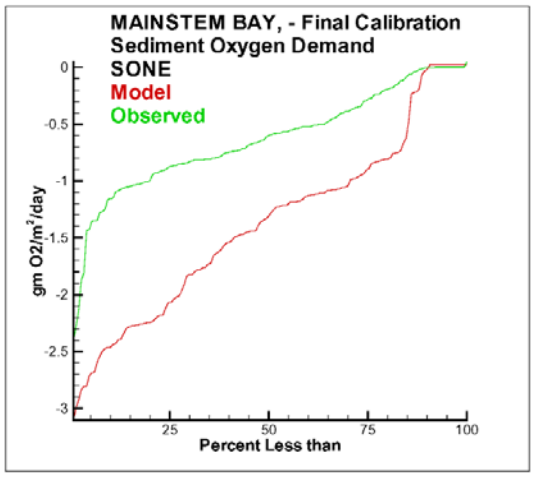

Figure 13-26. Cumulative distributions of observed and computed sediment oxygen demand at all Chesapeake Bay stations.

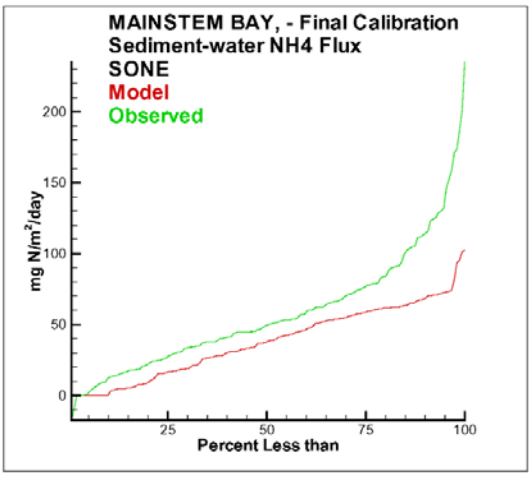

Figure 13-27. Cumulative distributions of observed and computed sediment-water ammonium flux at all Chesapeake Bay stations.

exceeds observed because the model allows consumption of oxygen where no oxygen is present in the bay. The excess of observed over computed ammonium release may indicate more nitrogen should be deposited on the bottom. Or the occasional excess of computed dissolved oxygen may be allowing more nitrification to take place in the modeled sediments than in the observations.

The preponderance of observed and computed sediment-water nitrate fluxes are essentially zero (Figure 13-28). At the lower end of the distribution, observed sediment uptake is greater than modeled although the magnitude of the excess is not great.

Half the observed and computed sediment-water phosphate fluxes are less than or effectively zero (Figure 13-29). In the upper half of the distribution, the observations show a gradual transition to sediment phosphorus release while the model shows a much steeper gradient. The model behavior may be attributable to the specification of a critical dissolved oxygen concentration and to the prescribed response of the sorption coefficient to dissolved oxygen less than the critical value. Maximum phosphorus releases agree in both model and observations.

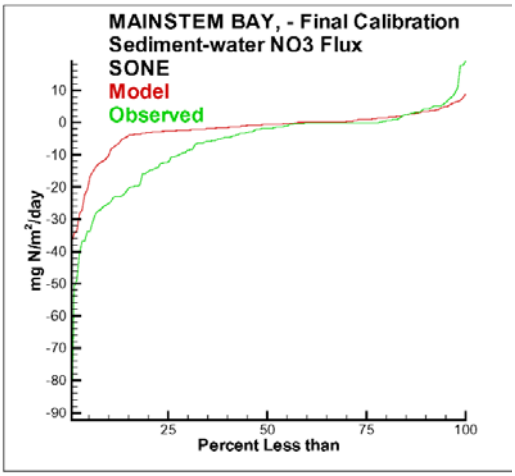

Figure 13-28. Cumulative distributions of observed and computed sediment-water nitrate flux at all Chesapeake Bay stations.

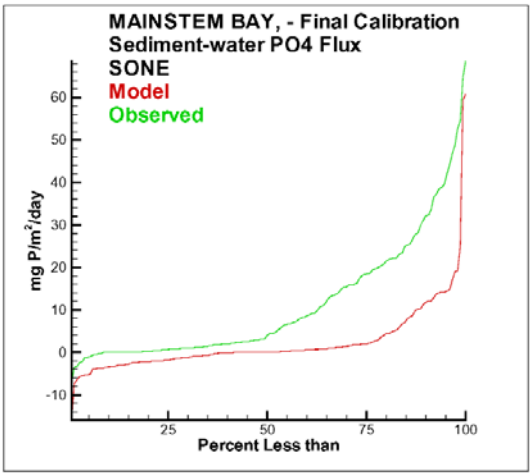

Figure 13-29. Cumulative distributions of observed and computed sediment-water phosphate flux at all Chesapeake Bay

As noted in the time series, observed sediment silica release greatly exceeds modeled (Figure 13-30). At the median, modeled release is essentially zero while median observed release is 175 mg m^{-2} d^{-1}. Maximum observed release exceeds 600 mg m^{-2} d^{-1} while the maximum modeled release is 100 mg m-2 d^{-1}.

One-to-one matching of observations with the model is an extremely demanding test. For highly-varying phenomenon such as sediment-water phosphorus flux, a small phase shift in the model can produce widely disparate pairs of observations and computations. We also produced distribution plots that considered the population of observations and the population of computations. In those comparisons, the distributions of nitrate flux matched almost perfectly. For the remaining substances, the computed distributions changed but the trends and conclusions noted above remained valid.

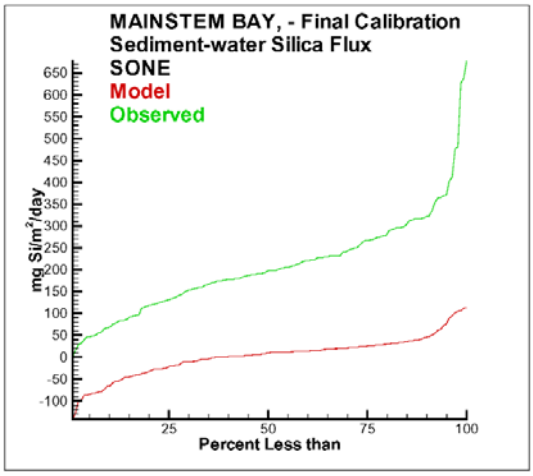

Figure 13-30. Cumulative distributions of observed and computed sediment-water silica flux at all Chesapeake Bay stations.

Sediment Composition

The author of the sediment diagenesis model describes particulate organic matter in the sediment as the "ashes" of the diagenesis process. That is, the majority of sediment organic matter is refractory or inert even though the majority of material deposited is labile (Figure 13-31). The labile material rapidly decays away leaving mostly ashes. Particulate carbon and nitrogen in the sediments is almost exclusively organic; the end products of diagenesis escape to the water in dissolved or gaseous form. For phosphorus, however, a substantial amount of diagenetically-produced phosphate is trapped in the sediments in mineral form. Consequently, sediment particulate phosphorus is a mixture of organic and mineral substances.

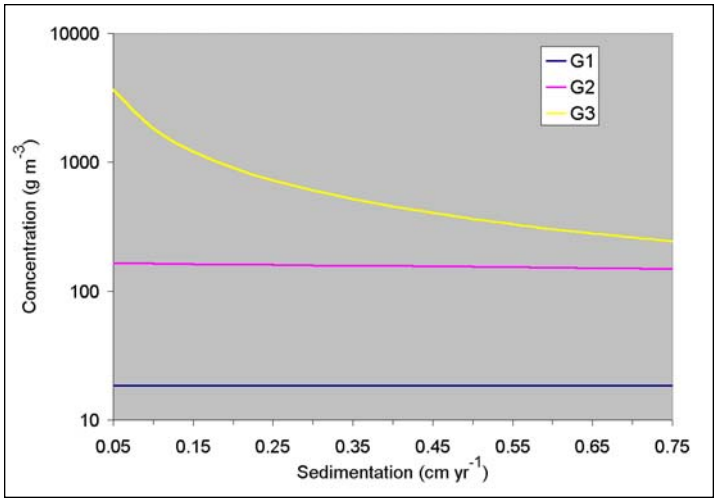

Figure 13-31. Effect of sedimentation (burial) rate on sediment organic matter. Calculations based on deposition of 1 g m^{-2} d^{-1} and G1, G2, G3 splits of 0.65, 0.3, 0.05 respectively.

Computed sediment composition is determined by computed deposition, by the specified splits into G1, G2, and G3 organic matter, and by the specified burial rate. Comparison of computed and observed composition provides a check that the modeled combination of deposition and burial are in balance with actual processes.

Observed sediment composition is on a percent basis by weight. Modeled composition is as mass per unit volume. Model units are readily converted, for comparison with the data, through division by the model sediment solids concentration, 0.5 L kg^{-1}. Results indicate the model sediments are largely deficient in carbon (Figure 13-32) and nitrogen (Figure 13-33). Model sediment phosphorus is in excess by a small amount (Figure 13-34). The computed carbon-to-nitrogen ratio in the sediments is correct (Figure 13-35) but the carbon-to-phosphorus ratio is low (Figure 13-36) indicating the sediments are enriched with phosphorus.

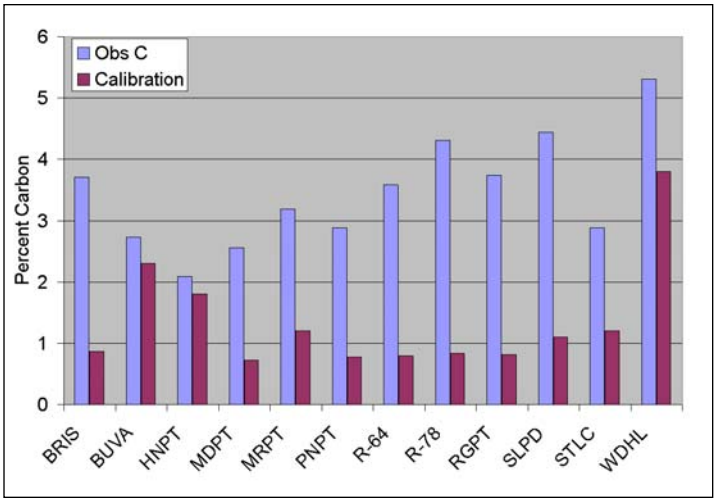

Figure 13-32. Observed and computed sediment carbon at stations in the upper Chesapeake Bay and Maryland tributaries.

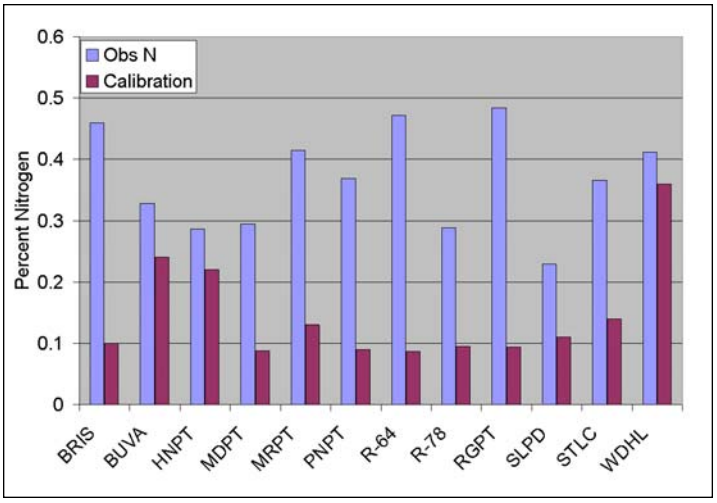

Figure 13-33. Observed and computed sediment nitrogen at stations in the upper Chesapeake Bay and Maryland tributaries.

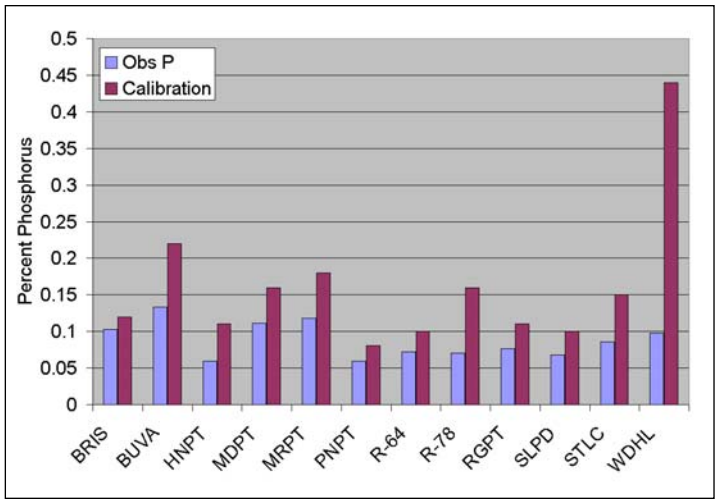

Figure 13-34. Observed and computed sediment phosphorus at stations in the upper Chesapeake Bay and Maryland tributaries.

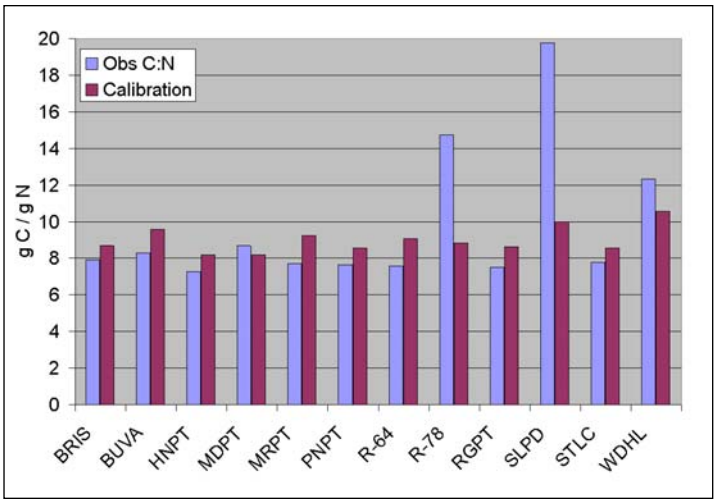

Figure 13-35. Observed and computed sediment carbon-to-nitrogen ratio at stations in the upper Chesapeake Bay and Maryland tributaries

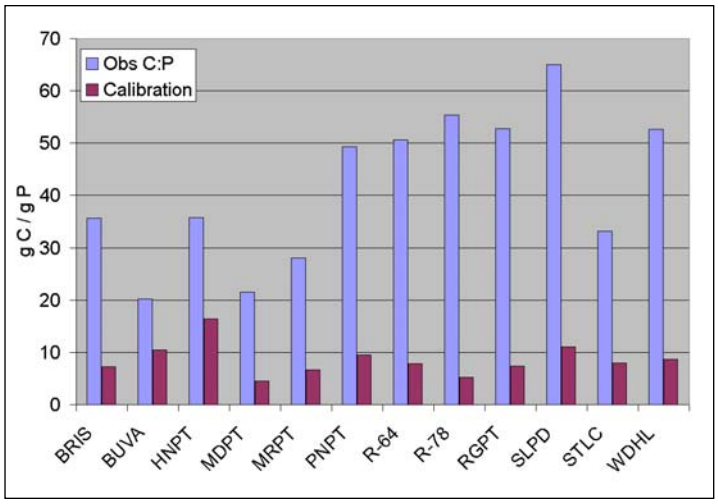

Figure 13-36. Observed and computed sediment carbon-to-phosphorus ratio at stations in the upper Chesapeake Bay and Maryland tributaries.

Computed sediment composition can be altered by three processes: deposition, burial, and fractionation. Deposition is computed dynamically while burial and splits into G fractions are specified parameters. Sediment composition is linearly proportional to deposition (Figure 13-37). Increasing deposition by a factor of two or three, necessary to bring about a proportional increase in sediment carbon and nitrogen, is impossible, however, without depleting the water column of these substances. Moreover, an increase in deposition of all substances would increase sediment phosphorus beyond observed concentrations. Balancing sediment composition through deposition requires simultaneous increases in carbon and nitrogen deposition and a decrease in phosphorus deposition. Deposition is likely not the origin of discrepancies in computed and observed concentrations nor is alteration of deposition likely to be the remedy.

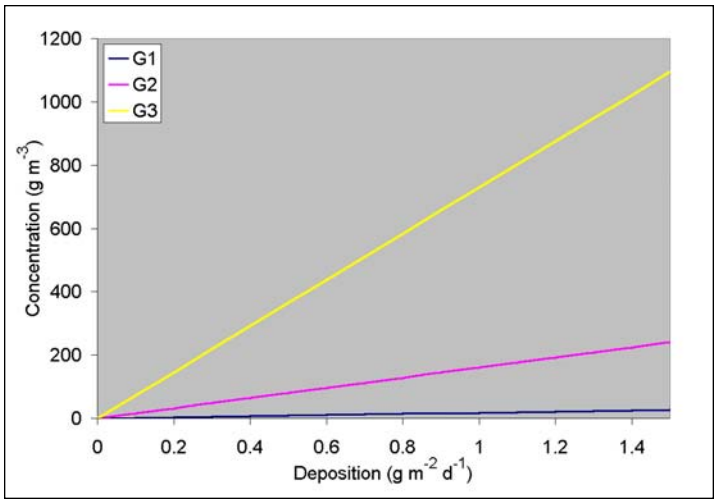

Figure 13-37. Effect of deposition rate on sediment organic matter. Calculations based on burial rate of 0.25 cm yr^{-1} and G1, G2, G3 splits of 0.65, 0.3, 0.05 respectively.

Sediment composition is inversely proportional to burial rate (Figure 13-31). Due to relatively rapid decay, concentrations of G1 and G2 organic matter show little sensitivity to burial rate while large alterations in the G3 fraction are possible. Uncertainties in specification of burial rate allow wide latitude to alter sediment composition through this process. Concentrations of carbon, nitrogen, and phosphorus will all change by the same percentage, however. Consequently, raising carbon and nitrogen concentration to observed levels will raise phosphorus well above the observations.

Concentration of sediment organic matter is roughly linearly proportional to specification of the G3 fraction of material deposited (Figure 13-38). In the present calibration, the G3 fraction of phosphorus is double the fraction of carbon and nitrogen (Table 13-2). Increasing the G3 fraction of carbon and nitrogen to the level specified for phosphorus appears to be the means to increase sediment carbon and nitrogen while minimizing change to sediment phosphorus.

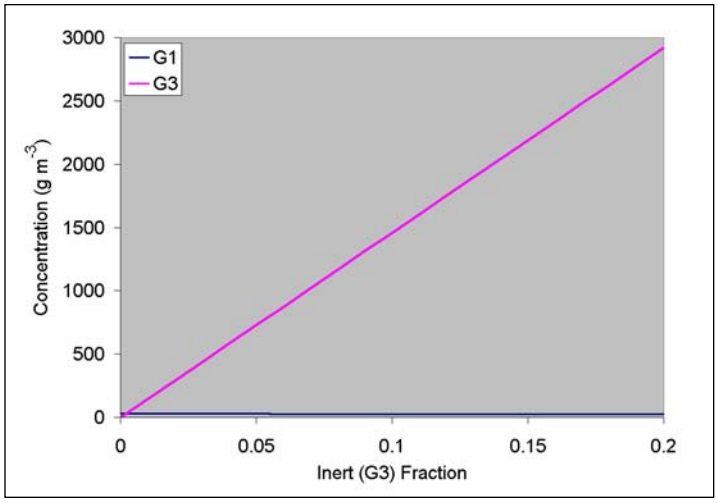

Figure 13-38. Effect of G3 fraction on sediment organic matter for a system comprised of labile and inert fractions. Calculations based on deposition of 1 g m^{-2} d^{-1} and burial of 0.25 cm yr^{-1}.

Sensitivity Analyses

More than 140 multi-year model runs were completed during the calibration process. In some of these runs, parameters were varied with the aim of improving model-data agreement. Other runs were classic sensitivity analyses aimed at examination of model behavior in response to parameter alteration. We have paired several of these runs to provide insight into the effects of parameter selection on model calibration. Some caution should be used in interpreting these comparisons. The paired runs are not always sequential and the parameters considered are not necessarily the only differences between the runs.

Net Settling. Net settling of inorganic solids was specified as 10% of settling through the water column to mimic the effects of resuspension. Net settling of organic solids was specified as equal to settling through the water column. In effect, no resuspension of organic matter was considered. In model run SENS85,

net settling of organic solids was set to 20% of settling through the water column. This specification increased and improved calculations of particulate organic matter near the bottom (Figure 13-39) but was detrimental in virtually all other respects. Computed sediment oxygen demand and ammonium release were vastly diminished and bottom-water dissolved oxygen increased by 1 to 2 g m^{-3} (Figures 13-40 to 13-42).

This run illustrates a paradox in the present model operation. Matching of observed suspended solids, inorganic and organic, requires a representation of resuspension while the diagenesis model requires the direct input of settling organic matter. Since computation of sediment diagenesis and its effects is far more important than the concentration of organic solids near the bottom, we have always specified net settling of organic matter equal to settling through the water column. The problem may be that our model does not truly represent resuspension. Rather, we inhibit settling. Inhibited settling prevents the deposition of fresh organic matter into the sediments and diminishes diagenesis. A possible solution is to incorporate true resuspension into the sediment model. Solids would settle directly into the sediments at the same rate as settling through the water column. Subsequently, the mixture of bed sediments would be resuspended at a specified resuspension velocity. This resuspension velocity could be calculated from first principles (e.g. shear velocity) or estimated through the calibration procedure. In this process, fresh organic matter would freely settle into the sediments while the resuspended material would be a mixture of fresh and aged solids. We cannot be certain this process would produce improved results but we see no other way out of the present paradox.

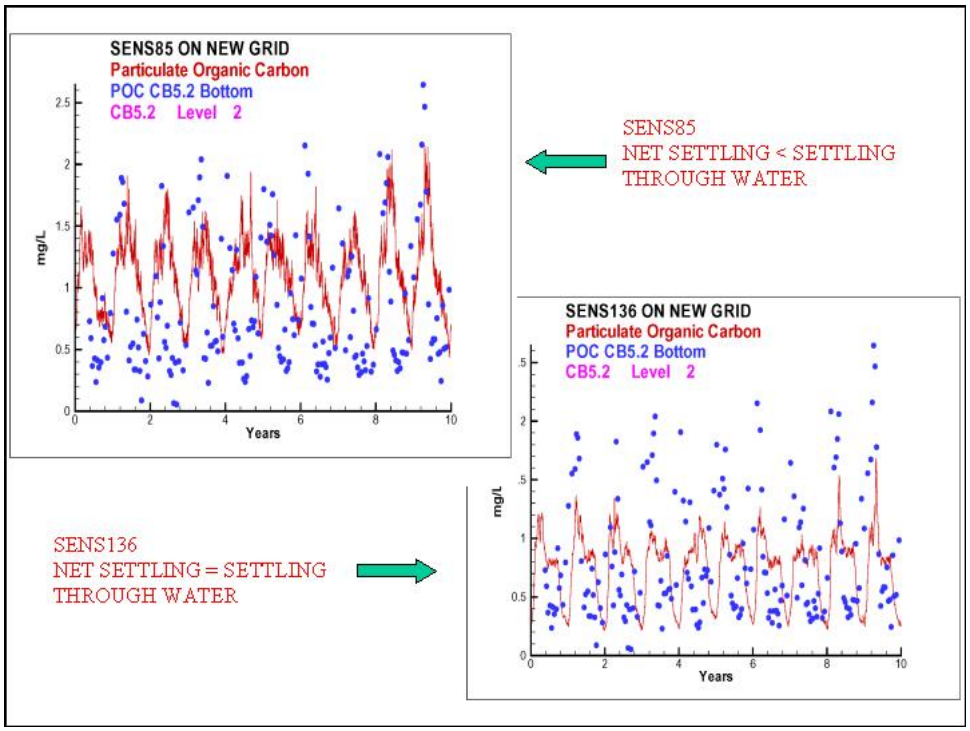

Figure 13-39. Effect of net settling on computed particulate organic carbon at the bottom of Station CB5.2 (near Point-No-Point).

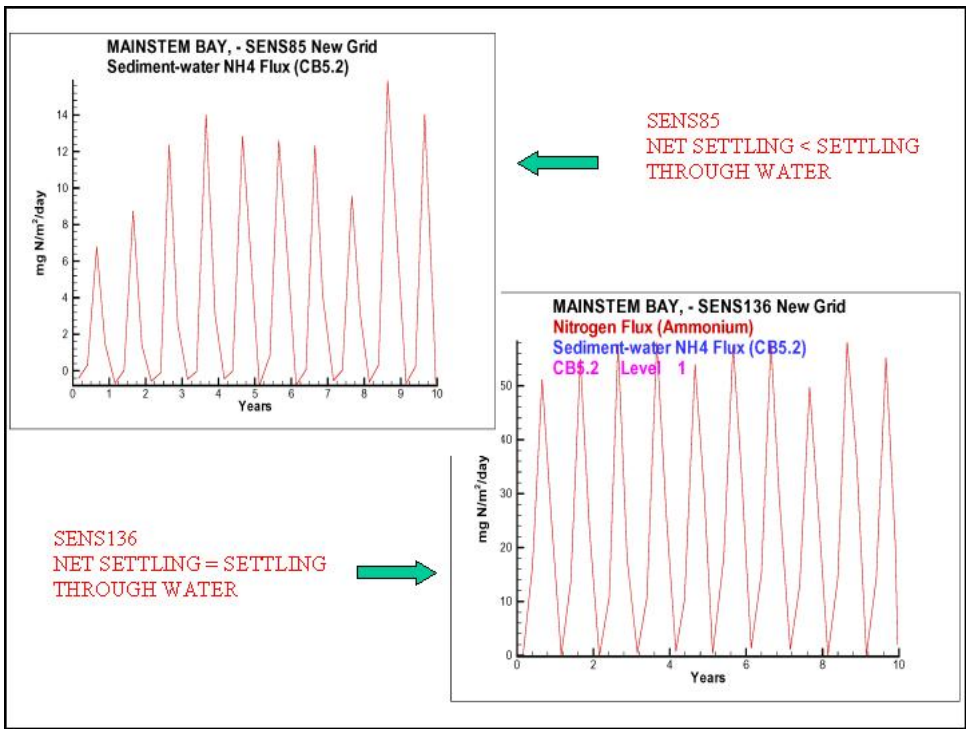

Figure 13-40. Effect of net settling on computed sediment-water ammonium flux (seasonally-averaged) at Station CB5.2 (near Point-No-Point).

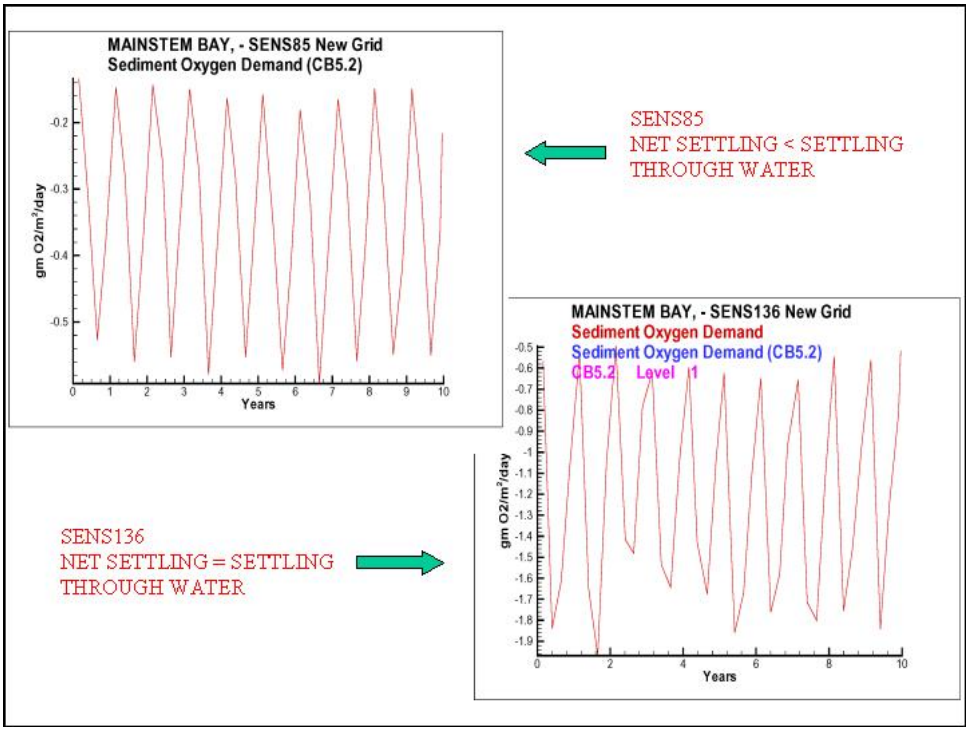

Figure 13-41. Effect of net settling on computed sediment oxygen demand (seasonally-averaged) at Station CB5.2 (near Point-No-Point).

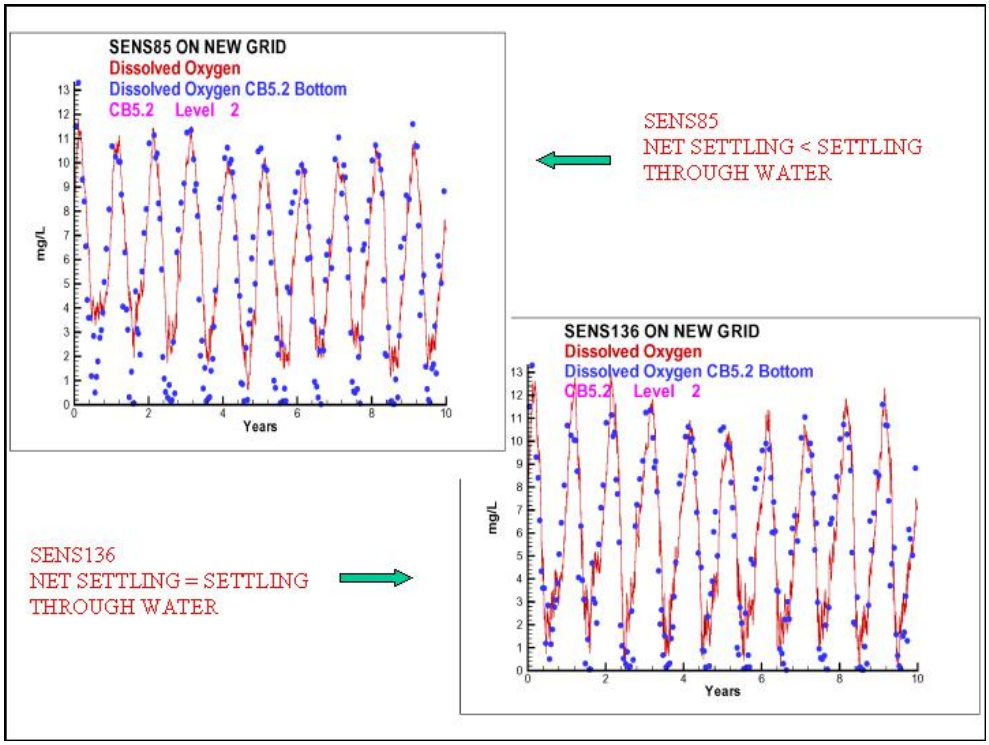

Figure 13-42. Effect of net settling on computed dissolved oxygen at the bottom of Station CB5.2 (near Point-No-Point).

Burial Rate. No spatial pattern was evident in the sedimentation rates collected as part of the original model study. Model sedimentation rates were specified based on the Brush data set and on other information. In SENS137, the median rate from the Brush data, 0.16 cm yr^{-1}, was employed throughout the system. This amounted to a reduction in burial since the rates employed in the calibration were 0.25 to 0.5 cm yr^{-1}.

As expected, reducing the burial rate increases the concentration of sediment organic matter although not by an amount sufficient to make up the deficit noted earlier (Figure 13-43). Reducing burial also increases sediment oxygen demand by 0.2 g m^{-2} d^{-1} (Figure 13-44), sediment ammonium release by 5 mg m^{-2} d^{-1} (Figure 13-45), and sediment phosphorus release by up to 5 mg m^{-2} d^{-1} (Figure 13-46). The impact of the increased sediment oxygen demand on bottom-water dissolved oxygen is less than 0.5 g m^{-3} at mid-bay (Figure 13-47). The major impact of reduced burial rate is not shown in any of these figures. The residence time in the sediments increases so that the time for the bay to respond to load changes, especially phosphorus, is increased.

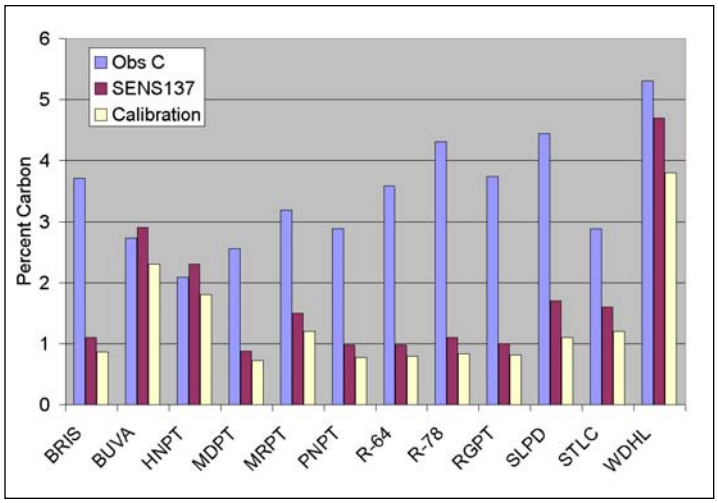

Figure 13-43. Effect of burial rate on computed sediment organic carbon at stations in upper Chesapeake Bay and Maryland tributaries.

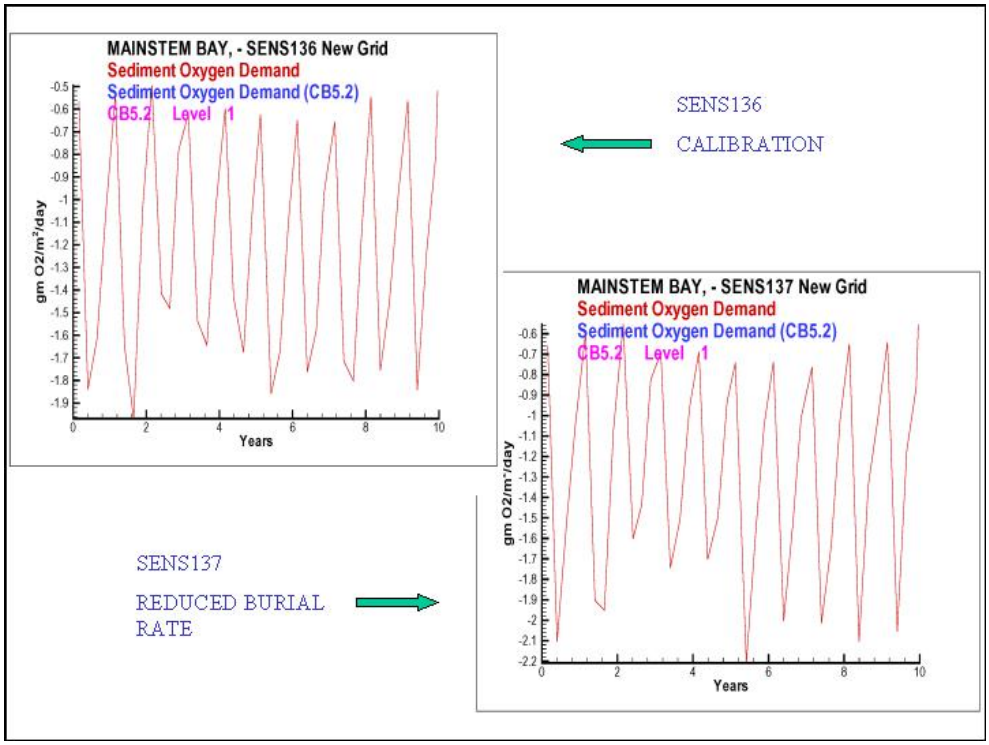

Figure 13-44. Effect of burial rate on computed sediment oxygen demand (seasonally-averaged) at Station CB5.2 (near Point-No-Point).

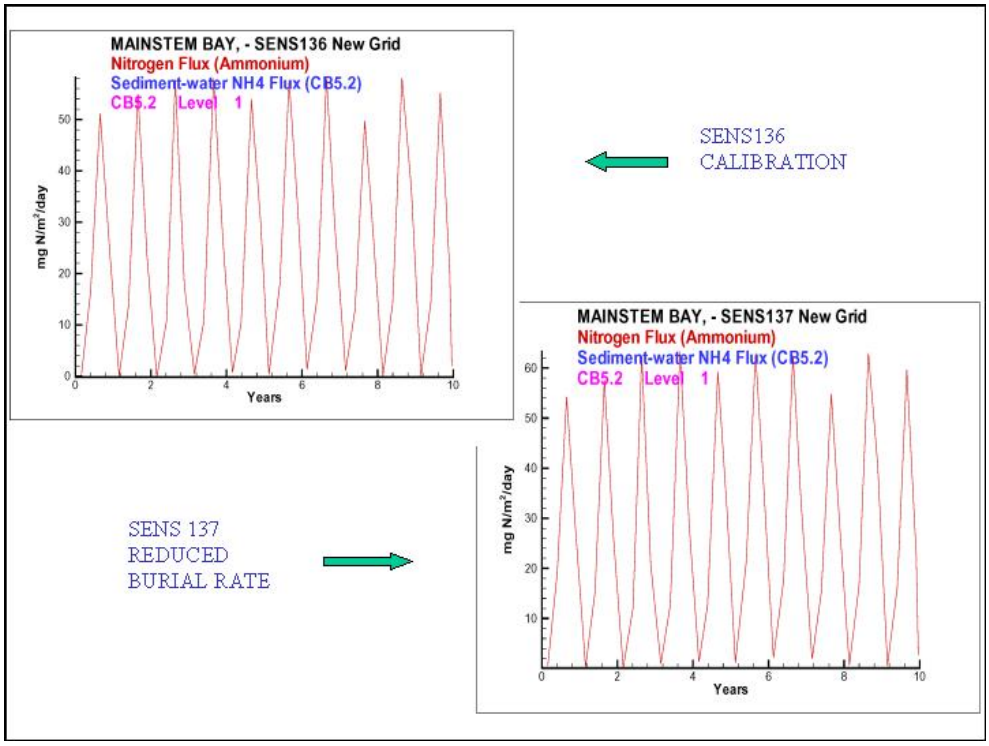

Figure 13-45. Effect of burial rate on computed sediment-water ammonium flux (seasonally-averaged) at Station CB5.2 (near Point-No-Point).

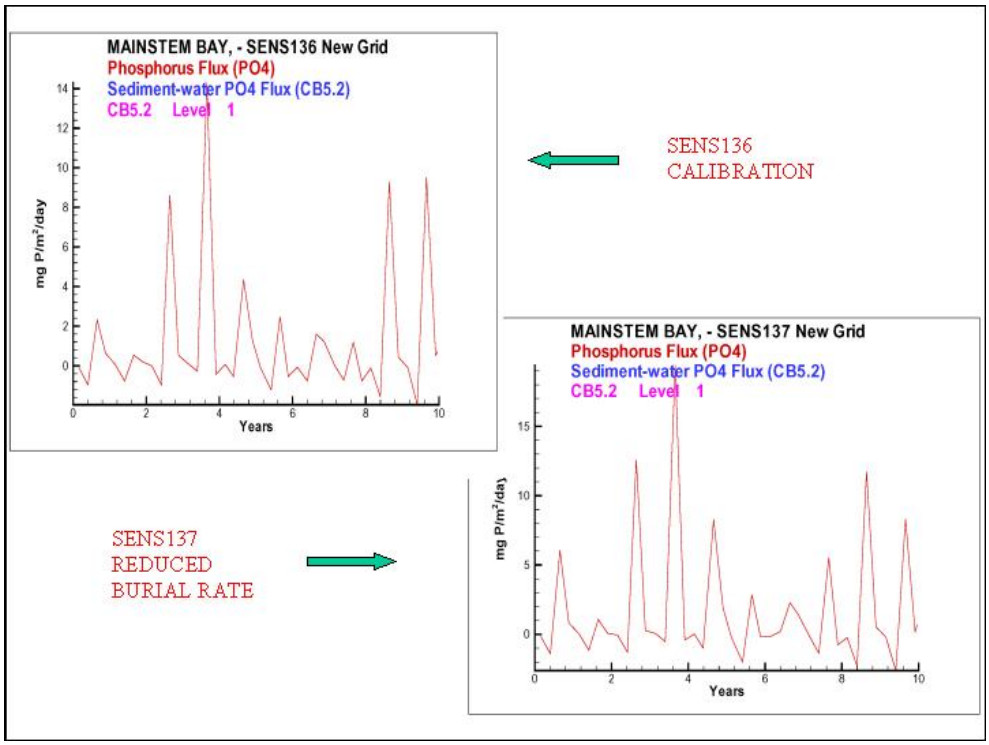

Figure 13-46. Effect of burial rate on computed sediment-water phosphate flux (seasonally-averaged) at Station CB5.2 (near Point-No-Point).

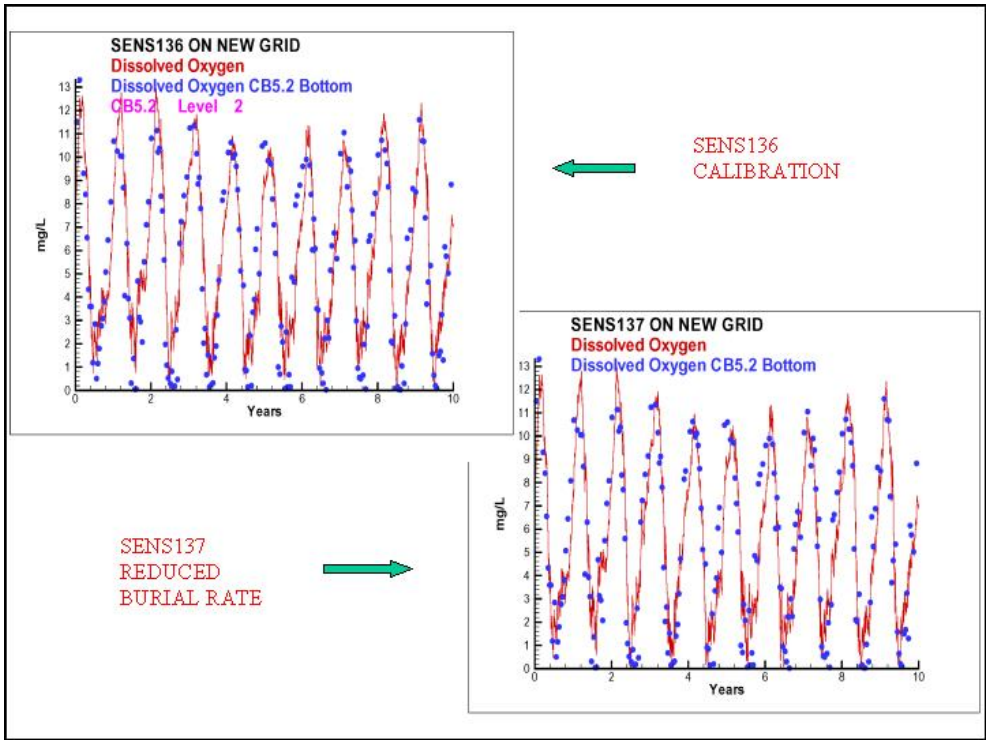

Figure 13-47. Effect of burial rate on computed dissolved oxygen at the bottom of Station CB5.2 (near Point-No-Point).

G3 Fractionation. In SENS104, the G3 fraction of settled organic carbon was increased from 5% to 9.5% at the expense of G2 carbon. This alteration had a large and usually beneficial effect on computed sediment carbon (Figure 13-48) although an even larger inert fraction is apparently required to match observations at many locations. (Or the SENS104 fractionation and the SENS137 burial rates.) Oddly, sediment carbon diminished at Still Pond. The odd behavior illustrates a caveat in these sensitivity analyses. SENS104 proceeded the final calibration by over 30 model runs. Other parameter changes took place as well as G3 fractionation. One of the other changes affected computed sediment carbon at Still Pond.

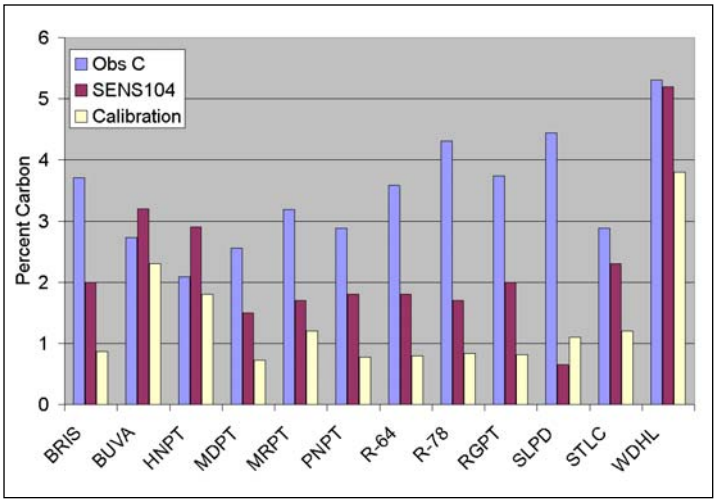

Figure 13-48. Effect of G3 fraction on computed sediment organic carbon at stations in upper Chesapeake Bay and Maryland tributaries.

Specification of a larger inert fraction diminished sediment oxygen demand by 0.1 g m^{-2} d^{-1} (Figure 13-49) which resulted in an increase in bottom dissolved oxygen of 0.5 g m^{-3} at mid-bay (Figure 13-50).

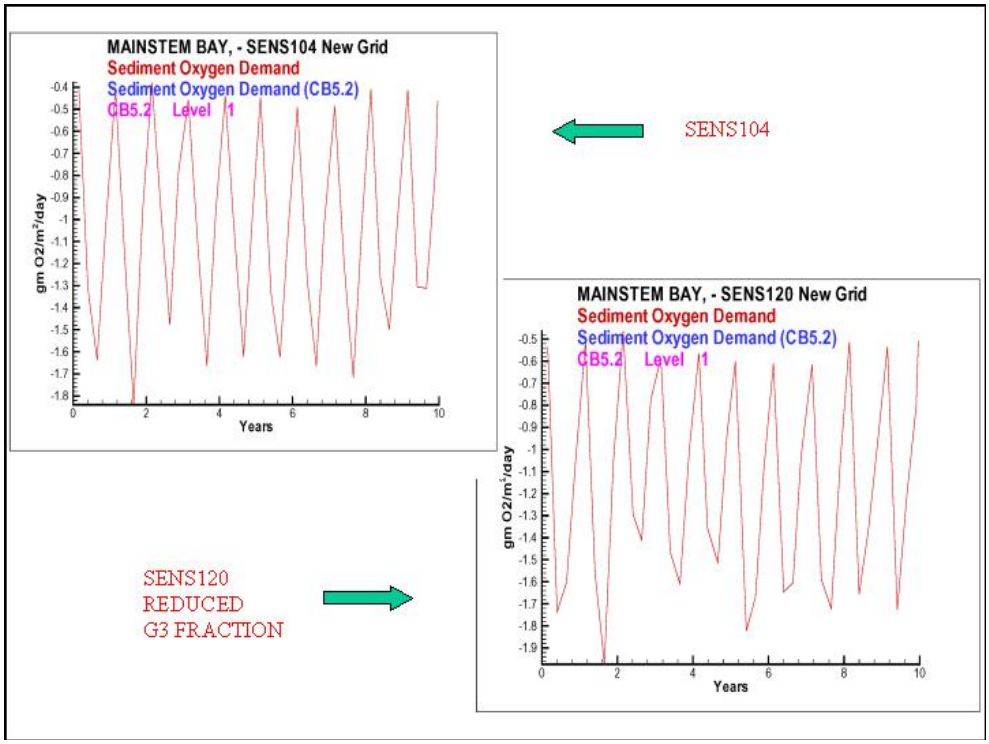

Figure 13-49. Effect of G3 fraction on computed sediment oxygen demand (seasonally-averaged) at Station CB5.2 (near Point-No-Point).

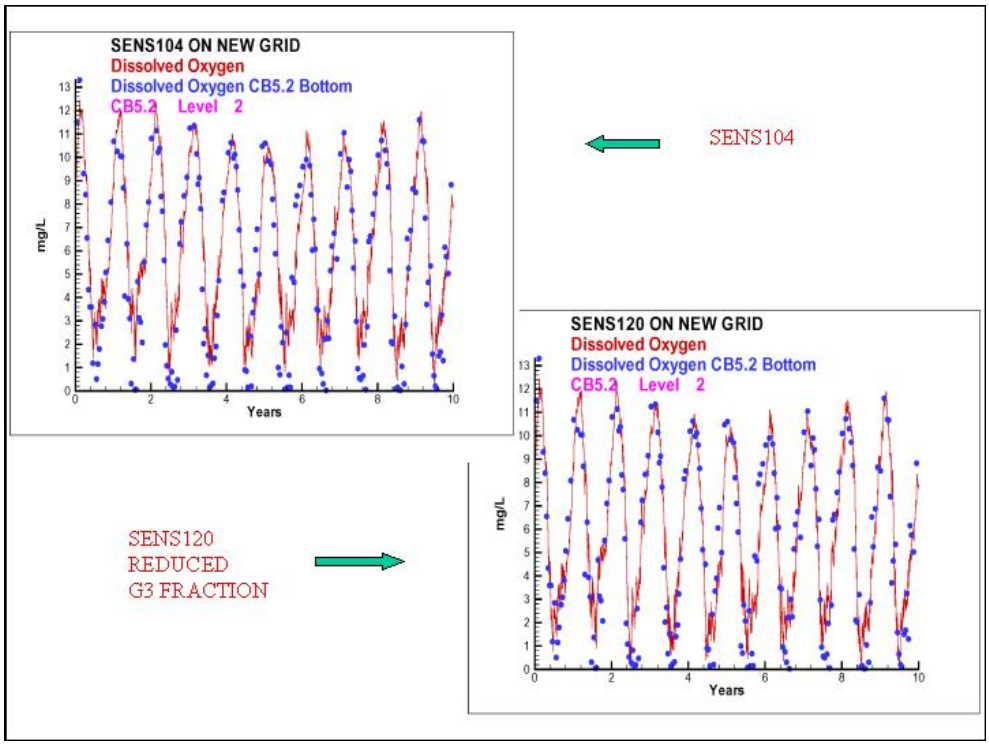

Figure 13-50. Effect of G3 fraction on computed dissolved oxygen at the bottom of Station CB5.2 (near Point-No-Point).

Benthos Model Results

The initial phase of the Chesapeake Bay model (Cerco and Cole 1994) relied on living-resource indicators. Living resources, including benthos, were introduced during the Virginia Tributary Refinements (Cerco et al. 2002) and living-resource responses to management actions were emphasized in interpreting model results. The present phase of the model activity has come full-circle. The living-resource indicators dissolved oxygen, chlorophyll, and clarity are once again the components emphasized in model computations. Living resources introduced earlier have barely been examined.

Complete results of the benthos model are provided in the CD-ROM that accompanies this report. Examination of present model results indicates the computation of filter feeders closely resembles the original application (Figures 13-51, 13-52). Computed deposit feeders have, perhaps, increased since the Virginia Tributaries application (Figures 13-53, 13-54). In view of the multiple orders-of-magnitude variation in observed deposit feeders, factor-of-two differences in computed biomass don't have major impacts on the calibration status. The role of deposit feeders in the model is minor; they enhance mixing in the bed sediments. The increase in deposit feeders is interpreted to have negligible impact on model computations.

Correct calculation of primary production was of fundamental interest in the present study. Improvement in the production calculation necessitated revisions in phytoplankton formulations and parameter values. Following initial improvements to the production calculation, the authors of the benthos model were invited to map

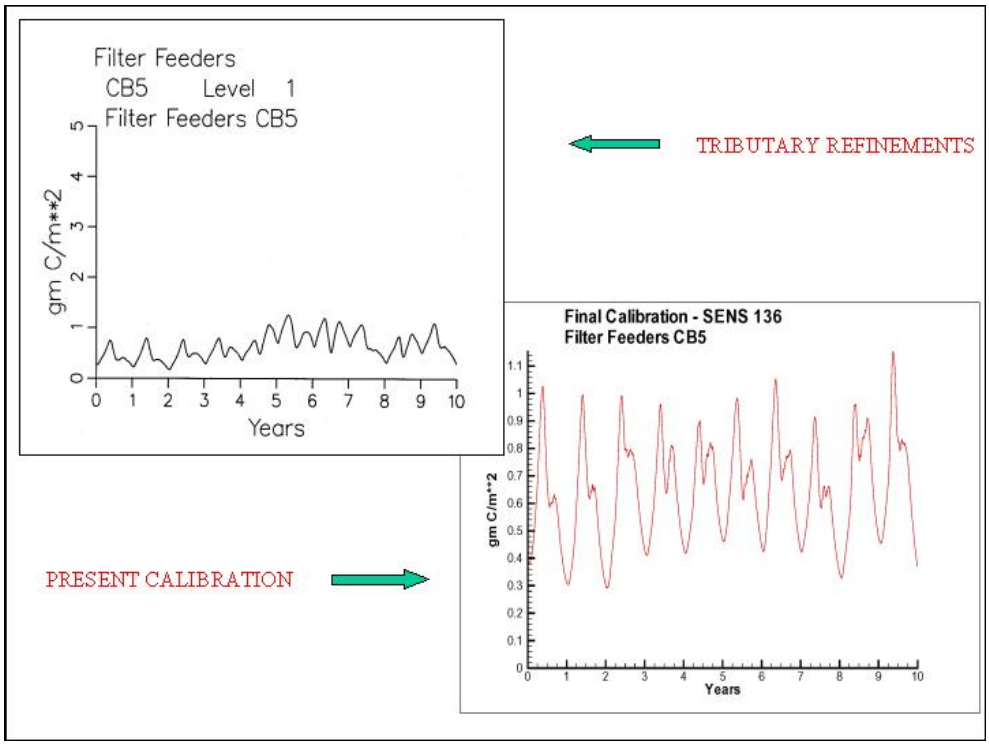

Figure 13-51. Computed filter feeders in central Chesapeake Bay (CB5): Virginia Tributary Refinements versus present calibration.

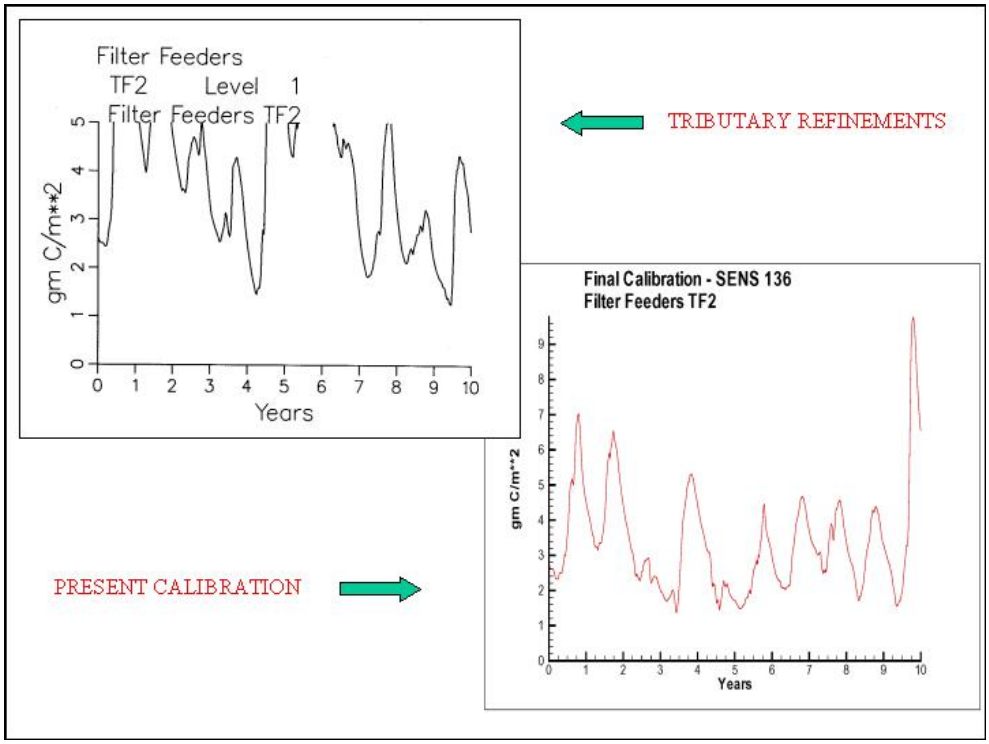

Figure 13-52. Computed filter feeders in the tidal fresh Potomac River (TF2): Virginia Tributary Refinements versus present calibration.

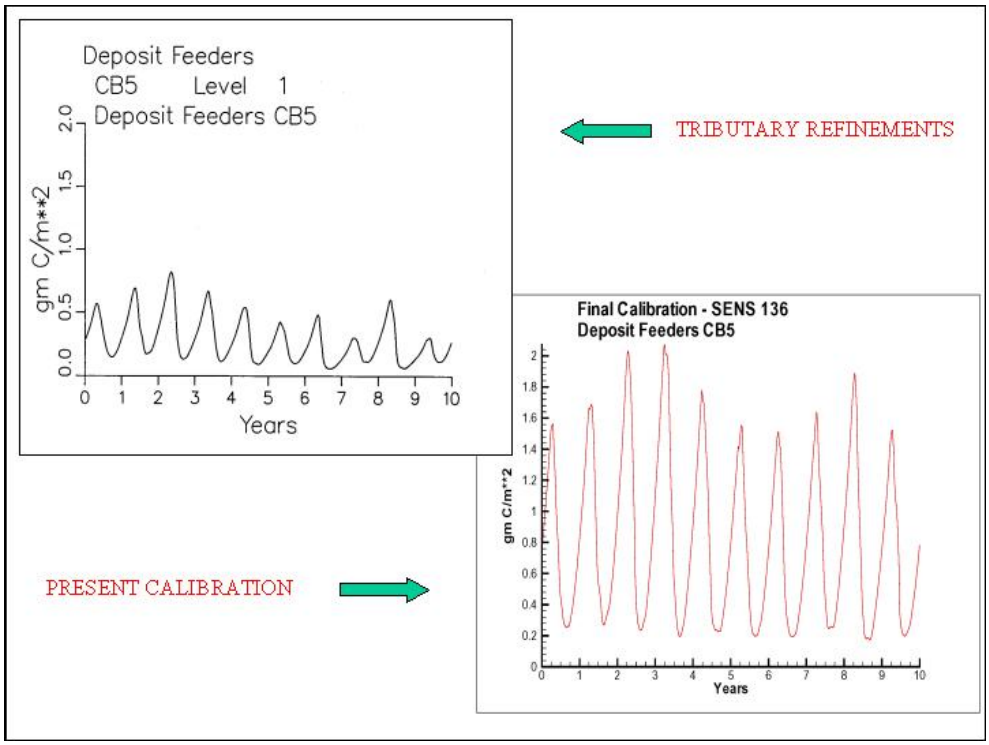

Figure 13-53. Computed deposit feeders in central Chesapeake Bay (CB5): Virginia Tributary Refinements versus present calibration.

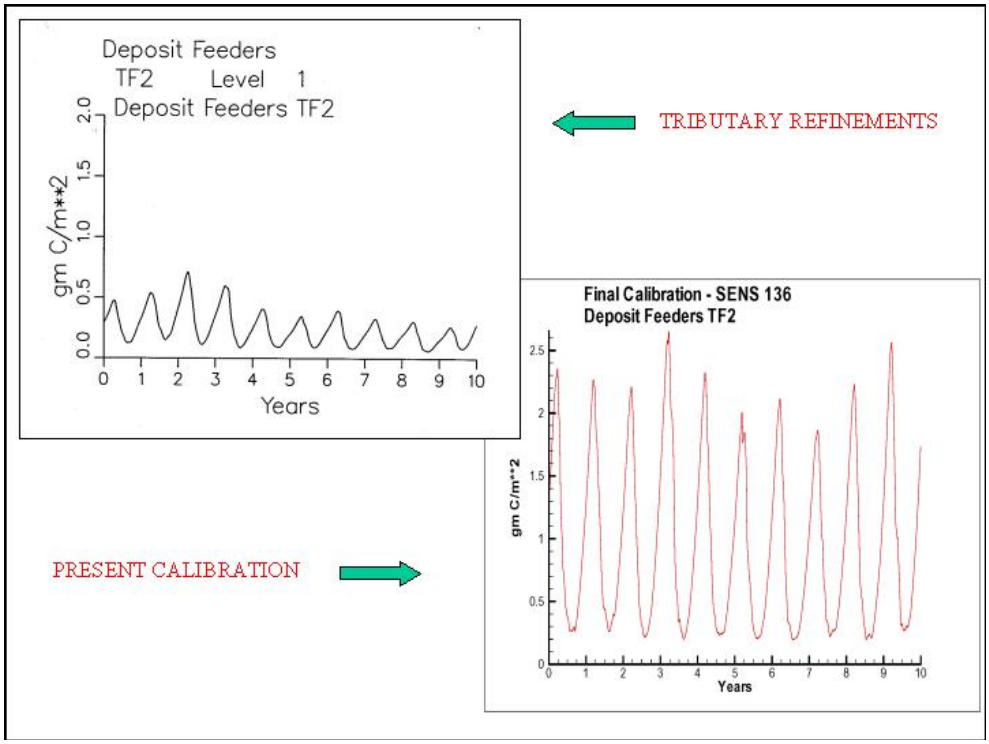

Figure 13-54. Computed deposit feeders in the tidal fresh Potomac River (TF2): Virginia Tributary Refinements versus present calibration.

the model to the new grid and to implement parameter revisions, if necessary. Since that time, no revisions were made to the benthos model. The stability of the benthos model through more than 100 water quality runs that succeeded the re-mapping indicates the benthos model is robust. The resemblance of results between the present model and the Virginia Tributaries model indicates the activity of the benthos, as originally calibrated, is maintained in the present model.

Results of the Submerged Aquatic Vegetation (SAV) Model

When the phytoplankton production relationships and parameters in the eutrophication model were revised, corresponding changes were made to the epiphyte component of the SAV model. One potentially significant alteration was a change from daily-average irradiance to sinusoidally-varying irradiance. Examination of the SAV component of the model revealed that these changes, and perhaps others, had a substantial, detrimental, effect on computed SAV. Computed epiphytes overwhelmed the vegetation. As a consequence, a re-calibration of the SAV model was completed. We endeavored to bring epiphytes and SAV back into calibration while minimizing revisions to the extensive model parameter suite. Changes were centered on the epiphyte loss terms and on the SAV production-irradiance relationships. Revised parameter sets are presented in Table 13-3 (SAV) and Table 13-4 (epiphytes).

Table 13-3. Parameters in SAV model

Parameter	Definition	Freshwater	Ruppia	Zostera	Potomac	Units
Acdw	carbon to dry weight ratio	0.37	0.37	0.37	0.37	
Acla	shoot carbon per unit leaf area	7.5	4.0	4.0	7.5	g shoot C m^{-2} leaf area
Fpsr	fraction of production transferred from shoots to roots	0.12 to 1.0	0.1 to 0.85	0.1 to 0.85	0.12 to 1.0	
Ksh	light attenuation by shoots	0.045	0.045	0.045	0.045	m^2 g^{-1} C
Khnw	half-saturation concentration for nitrogen uptake by shoots	0.19	0.19	0.1	0.19	g N m^{-3}
Khns	half-saturation concentration for nitrogen uptake by roots	0.95	0.95	0.4	0.95	g N m^{-3}
Khpw	half-saturation concentration for phosphorus uptake by shoots	0.028	0.028	0.02	0.028	g P m^{-3}
Khps	half-saturation concentration for phosphorus uptake by roots	0.14	0.14	0.1	0.14	g P m^{-3}
Pmax	maximum production at optimum temperature	0.1	0.09	0.06	0.1	g C g^{-1} DW d^{-1}
Rsh	shoot respiration	0.02	0.015	0.013	0.02	d^{-1}
Rrt	root respiration	0.02	0.015	0.013	0.02	d^{-1}
SL	sloughing	0.01 to 0.1	0.01 to 0.035	0.01 to 0.035	0.01 to 0.1	d^{-1}
Trs	transfer from root to shoot	0.0 to 0.05	0.0	0.0	0.0 to 0.05	d^{-1}
α	initial slope of PvsI curve	0.015	0.0036	0.0068	0.022	(g C g^{-1} DW) (E m^{-2})$^{-1}$

Table 13-4. Parameters in epiphyte model

Parameter	Definition	Value	Units
Acchl	carbon to chlorophyll ratio of viable epiphytes	75	g C g^{-1} Chl
Adwcep	ratio of epiphyte dry weight to viable epiphyte carbon	18	g DW g^{-1} C
Kep	light attenuation coefficient	0.06	m^2 leaf surface g^{-1} epiphyte C
Khep	density at which growth is halved	0.1	g epiphyte C g^{-1} shoot C
Khn	half-saturation concentration for nitrogen uptake	0.025	g N m^{-3}
Khp	half-saturation concentration for phosphorus uptake	0.0025	g P m^{-3}
Pep	maximum production at optimum temperature	350	g C g^{-1} Chl d^{-1}
PR	predation rate	5.0	g shoot C g^{-1} epiphyte C d^{-1}
Rep	respiration	0.02	d^{-1}
α	initial slope of PvsI curve	8	(g C g^{-1} Chl) (E m^{-2})$^{-1}$

Complete results of the SAV model are provided in the CD-ROM that accompanies this report. The computations are consistent with, but not identical to, the original application (e.g. Figures 13-55 to 13-57). The original application obeyed light attenuation criteria listed in the first SAV Technical Synthesis (Batuik et al. 1992). During the re-calibration we verified that the model remains consistent with these criteria.

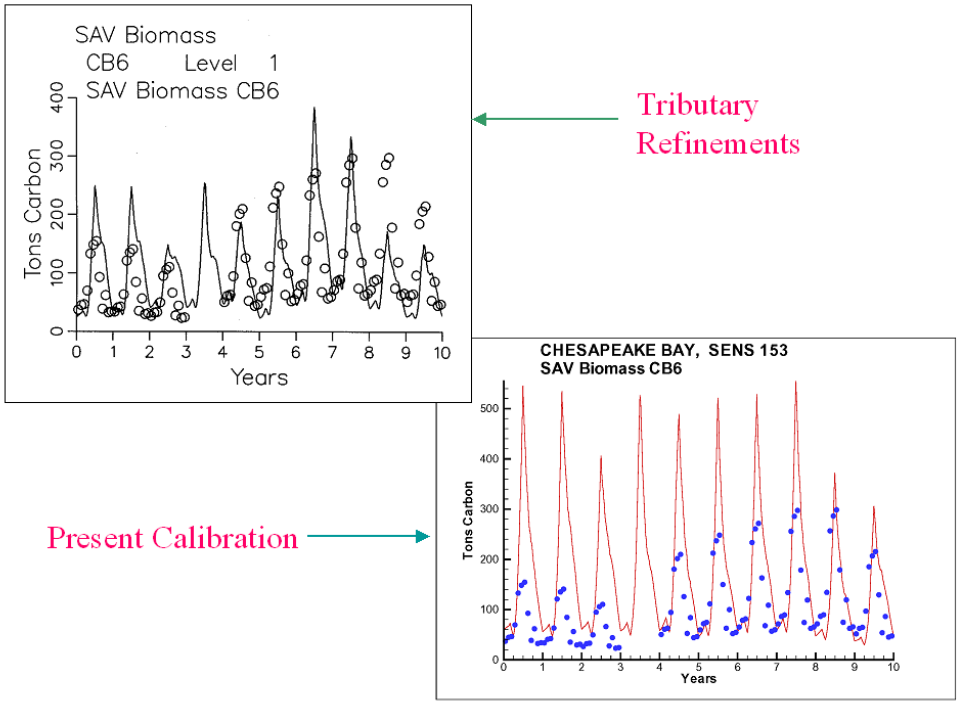

Figure 13-55. Submerged aquatic vegetation in the lower western shore of Chesapeake Bay (CB6): Virginia Tributary Refinements versus present calibration.

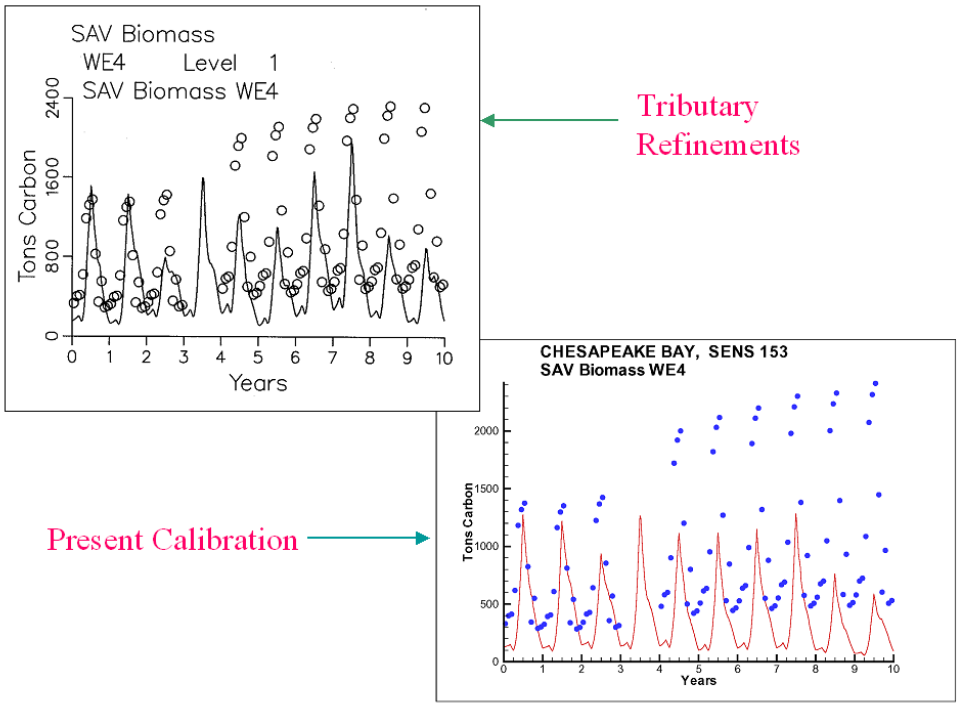

Figure 13-56. Submerged aquatic vegetation at the York River mouth (WE4): Virginia Tributary Refinements versus present calibration.

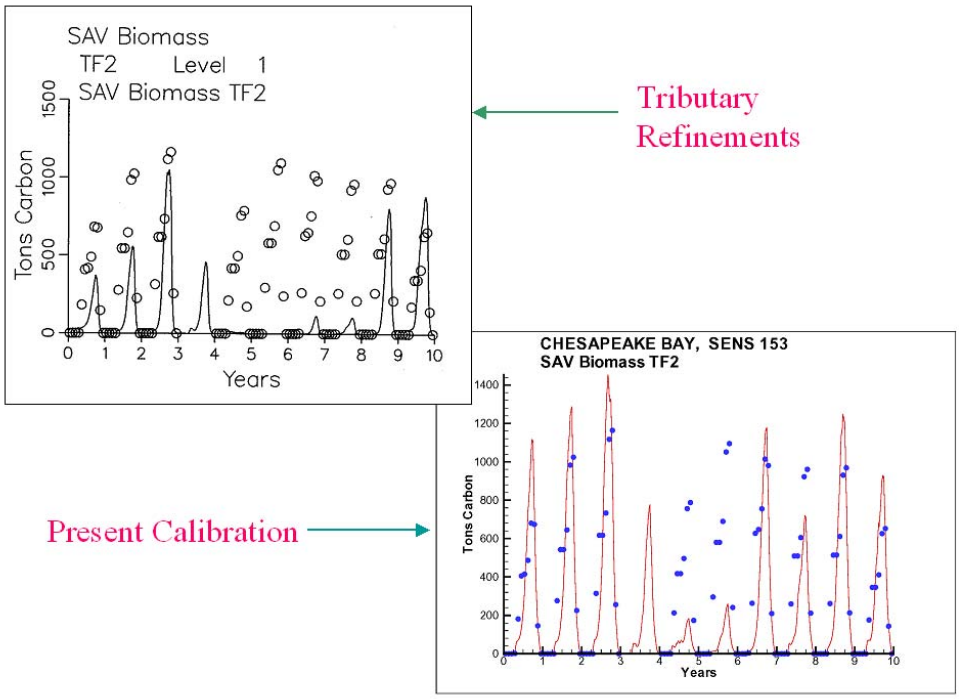

Figure 13-57. Submerged aquatic vegetation in the tidal fresh Potomac River (TF2): Virginia Tributary Refinements versus present calibration.

Results from the Benthic Algal Model

Benthic algae were introduced to the model as part of the Virginia Tributary Refinements (Cerco et al. 2002). At the time, their role in the model ecosystem was perceived as minor and little attention was devoted to them. Concurrent with the revisions to the phytoplankton kinetics in the present study, production relationships and parameters in the benthic algal model were revised for consistency with the phytoplankton model. During the model calibration, aberrant behavior of computed phosphorus was noted and attributed to the benthic algae. The revised relationships and parameters caused benthic algae to attain impossible biomass and sequester large quantities of nutrients in the sediments. Consequently, a recalibration of the benthic algal model was conducted. The primary goal of the recalibration was calculation of algal biomass comparable to measures in Chesapeake Bay and elsewhere. The resulting parameter set is presented in Table 13-5.

Table 13-5
Parameters in Benthic Algal Model

Symbol	Definition	Value	Units
PBm	maximum photosynthetic rate	300.	g C g^{-1} Chl d^{-1}
α	initial slope of production vs. irradiance relationship	8.	g C g^{-1} Chl $(E\ m^{-2})^{-1}$
CChl	carbon-to-chlorophyll ratio	100	g C g^{-1} Chl
Ancb	nitrogen-to-carbon ratio	0.167	g N g^{-1} C
Apcb	phosphorus-to-carbon ratio	0.0167	g P g^{-1} C
Khn	half-saturation concentration for nitrogen uptake	0.01	g N m^{-3}
Khp	half-saturation concentration for phosphorus uptake	0.001	g P m^{-3}
Topt	optimal temperature for algal growth	25	^{o}C
KTg1	effect of temperature below Topt on growth	0.003	$^{o}C^{-2}$
KTg2	effect of temperature above Topt on growth	0.010	$^{o}C^{-2}$
BMr	metabolic rate at reference temperature	0.02	d^{-1}
Tr	reference temperature for metabolism and predation	20	^{o}C
KTb	effect of temperature on metabolism and predation	0.032	$^{o}C^{-1}$
Phtl	rate of predation by planktivores	0.2	$m^{2}\ g^{-1}$ C d^{-1}
Kesed	light attenuation by sediment solids	0.5	
Kebalg	light attenuation by benthic algal self-shading	0.20	$m^{2}\ g^{-1}$ C

Computed benthic algal biomass ranges up to 3 g C m^{-2}, in agreement with measures conducted in a variety of systems (Table 13-6). The primary determinate of algal density is light. Algal biomass shows an inverse relationship to optical depth (total depth × light attenuation) at the sediment-water interface (Figure 13-58). No algae are computed above optical depth 5. The highest densities of computed benthic algae are found in shallow water near the mouths of the lower western tributaries, along the lower eastern shore, and in eastern embayments (Figure 13-59). Lesser densities occur in tidal fresh waters and in other shoal areas.

Table 13-6
Reported Benthic Algal Biomass

Biomass, g C m^{-2}	System	Citation	Comments
4	Delaware Inland Bays	Cerco and Seitzinger (1997)	Computed annual average.
2.1	Goodwin Islands, York River mouth	Buzzelli (1998)	Mean of 108 observations. Converted from mg Chl a m^{-2} using C:Chl ratio of 50 (Gould and Gallagher 1990).
2 to 4	North Inlet SC	Pinckney and Zingmark (1993)	Range over a year. Converted from mg Chl a m^{-2} using C:Chl ratio of 50 (Gould and Gallagher 1990).
1.6	Ems-Dollard Estuary	Admiraal et al. (1983)	Converted from cells cm^{-2} using 1 g C m^{-2} = 1.25 x 10^6 cells cm^{-2} found in text.
0.4 to 7.2	Laholm Bay	Sundbäck (1986)	Range over a year observed at 14 to 16 m. Converted from cells cm^{-2} as per Admiraal et al. (1983).
2.2 to 15	Savin Hill Cove, near Boston Harbor	Gould and Gallagher (1990)	Report C:Chl of 18.7 to 60.4.

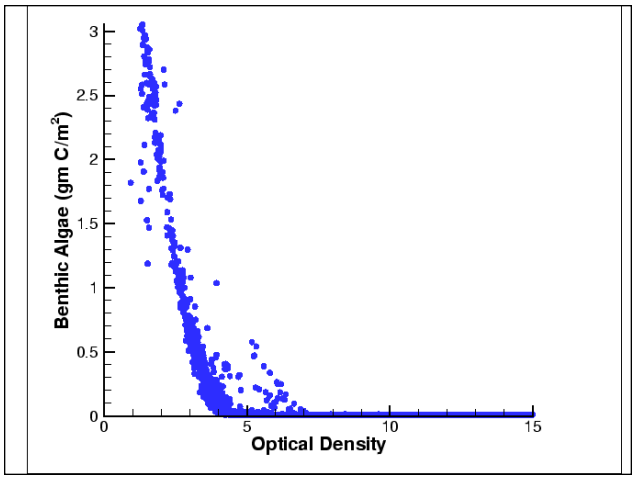

Figure 13-58. Summer-average benthic algal biomass versus optical density.

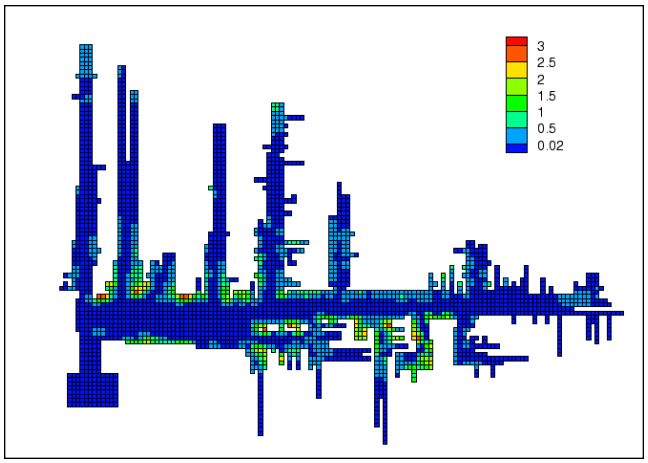

Figure 13-59. Computed summer-average benthic algal biomass, 1986.

Several investigators have extrapolated the results of experimental benthic flux measurements to describe whole ecosystem responses. For example, Rizzo et al. (1992) suggested an increase in water-column light attenuation would decrease benthic algal assimilation of nutrients, increase nutrient release to the overlying water, and thereby increase phytoplankton production. Other studies have suggested that increased nutrient loading would increase benthic algal production (Sundbäck et al. 1991).

To investigate the role of computed benthic algae in modulating sediment-water oxygen and nutrient flux, we isolated sediment-water fluxes in shoal areas likely to contain benthic algae. Shoals were defined as cells adjacent to the shoreline. The presence of 0.5 to 1.5 g algal C m^{-2} in shoal areas of CB5 (Figure 13-60) had little apparent effect on sediment-water fluxes compared to a deep station in the center of the segment. Peak sediment oxygen demand exceeded 3 g m^{-2} d^{-1} in shoals and deep water (Figure 13-61). Sediment ammonium (Figure 13-62) and phosphate (Figure 13-63) release were arguably higher in the shoals than in deep water, except for incidents of bottom-water anoxia at the deep station. Similar results were noted in other segments.

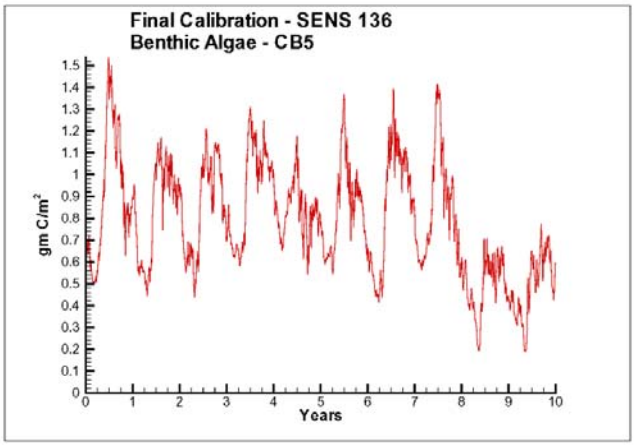

Figure 13-60. Spatially-averaged benthic algal biomass in shoal areas of Chesapeake Bay Program Segment CB5.

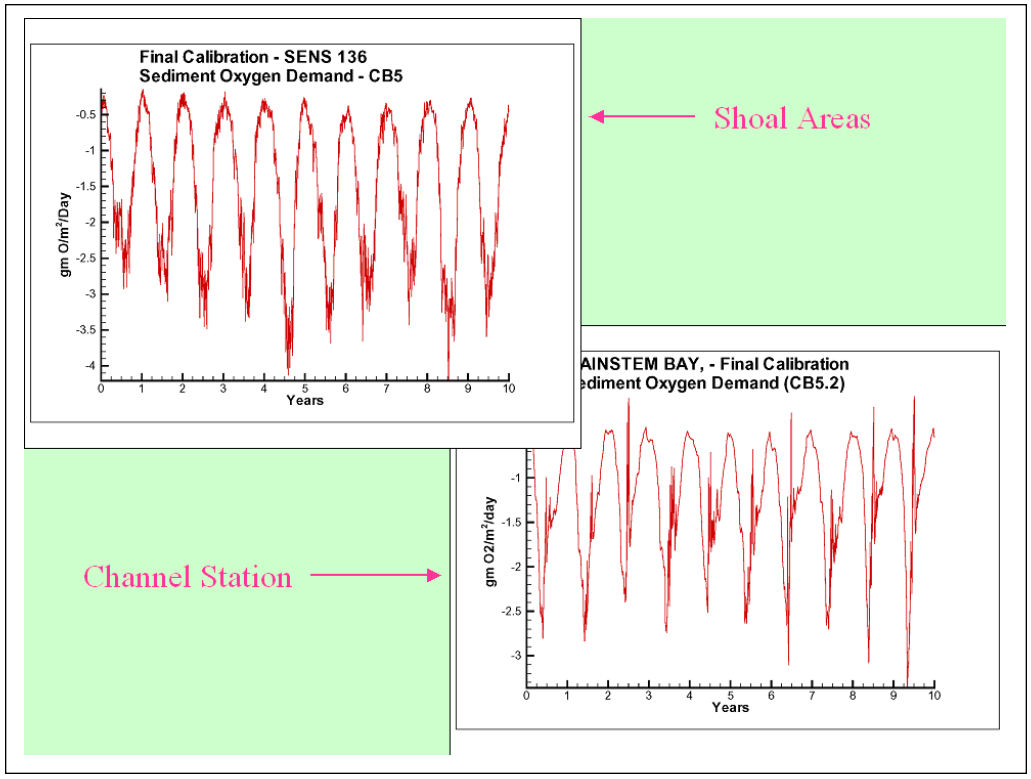

Figure 13-61. Daily-average sediment oxygen demand in shoal areas of CB5 and at deep station CB5.2.

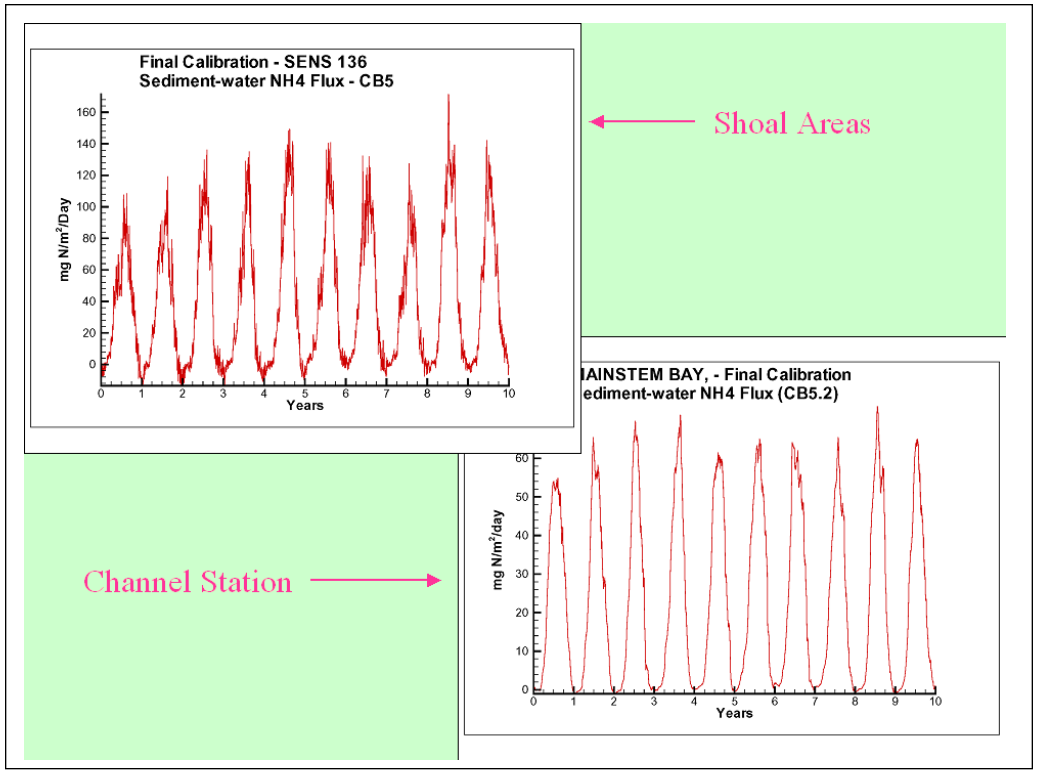

Figure 13-62. Daily-average sediment-water ammonium flux in shoal areas of CB5 and at deep station CB5.2.

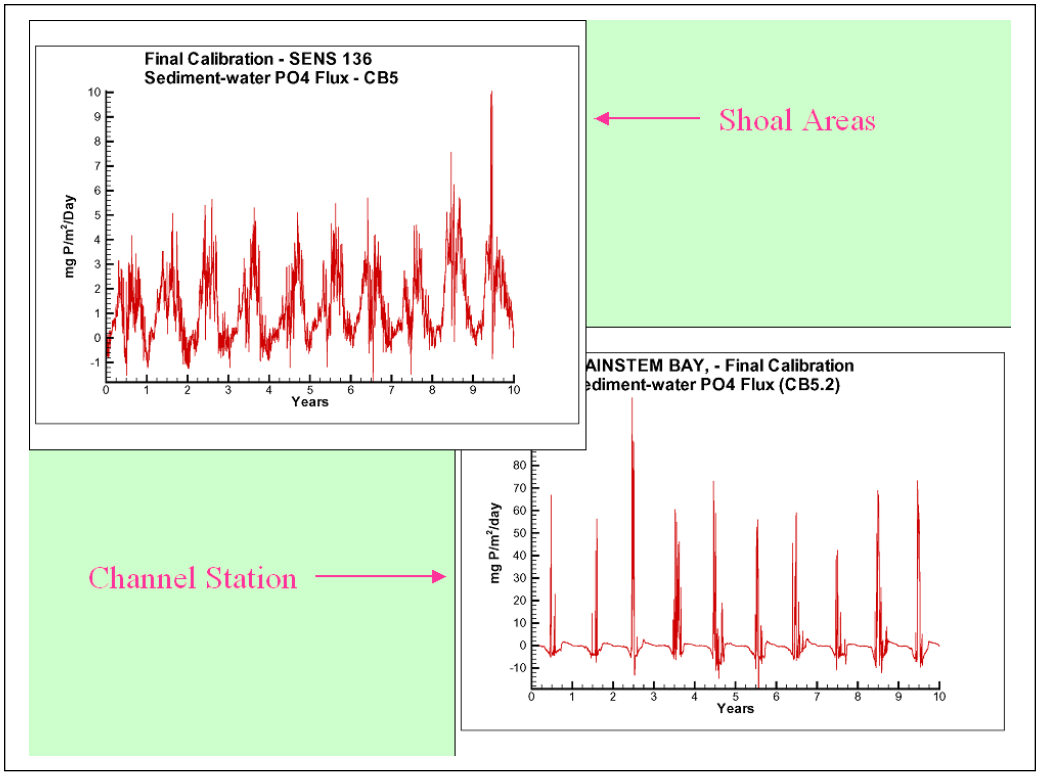

Figure 13-63. Daily-average sediment-water phosphate flux in shoal areas of CB5 and at deep station CB5.2.

These results appear contrary to numerous studies in which benthic algae were observed to trap nutrients in bottom sediments. Several factors contribute to our results. First, our fluxes are computed at model time steps (15 minutes) but reported as daily averages. Since daylight hours are only half the day, our daily average results will differ from studies that compare fluxes under light and dark conditions. Our regional averages include cells in which benthic algae are absent so that the effect of algal-rich areas is damped in the averaging process. Finally, the shoals receive direct loads from runoff and bank erosion. Consequently, deposition in these areas will differ from the channel reaches. Still, we must conclude that under present conditions, at time and spatial scales of regional significance, computed benthic algae do not exert major impact on sediment-water oxygen and nutrient fluxes.

Sensitivity Analysis

During the management scenarios conducted with the present model, positive responses of dissolved oxygen to reductions in bank loadings were noted. Experience suggested the dissolved oxygen response was one part of a system response to diminished light attenuation by solids and increased light availability at the sediment-water interface. Our hypothesis was that increased light stimulated benthic algae and enhanced algal nutrient trapping. Sequestration of nutrients in the sediments reduced nutrients available to phytoplankton, reduced phytoplankton production, and diminished carbon deposition to bottom waters. Diminished deposition led to diminished sediment oxygen demand and higher dissolved oxygen. To test this hypothesis, we conducted a sensitivity analysis in which bank solids loads, but not nutrient loads, were eliminated. The separation of solids and nutrient loads is not realistic but allows isolation of solids effects in the sensitivity analysis.

As expected, elimination of solids loads diminished suspended solids concentration (Figure 13-64) and light attenuation (Figure 13-65). Benthic algae increased in both abundance and distribution (Figure 13-66 compared to Figure 13-59). The sensitivity run confirmed a decrease in phytoplankton (Figure 13-67) despite the greater light availability. The diminished phytoplankton were brought about by decreased phosphate availability (Figure 13-69). Ammonium (Figure 13-70) and nitrate (Figure 13-71) increased due to diminished algal demand. The reduced phytoplankton resulted in increases of more than 0.5 g m^{-3} bottom dissolved oxygen in portions of the bay (Figure 13-71).

Response of benthic algal biomass to elimination of bank solids loads varied with location but doubling of computed biomass was characteristic (Figure 13-72). Benthic algal production responded in a non-linear fashion so that the proportional increase in net production exceeded the increase in biomass (Figure 13-73). Sediment oxygen demand decreased in shoal areas due to algal oxygen production (Figure 13-74). The demand was not diminished in all years, however. Years with lower algal biomass (years 4 to 5 and 8 to 10 on our scale, corresponding to 1989 and 1993-1994) had sediment oxygen demand comparable to the base run. Benthic algal uptake reduced sediment ammonium release (Figure 13-75). In the colder portions of the year, ammonium was removed from the water column. As with oxygen demand, however, the effect on ammonium was not uniform; years with lower algal biomass exhibited ammonium release similar to corresponding years in the base run. Except for two years with low algal biomass, nitrate was predominantly removed from the water column (Figure 13-76) as a result of reduction in bank solids loads. Under base conditions, sediment-water nitrate flux was roughly balanced between sediment uptake and release. The activity of benthic algae stripped phosphate from the water column in most years (Figure 13-77). In contrast, sediments almost exclusively released phosphorus under the base conditions.

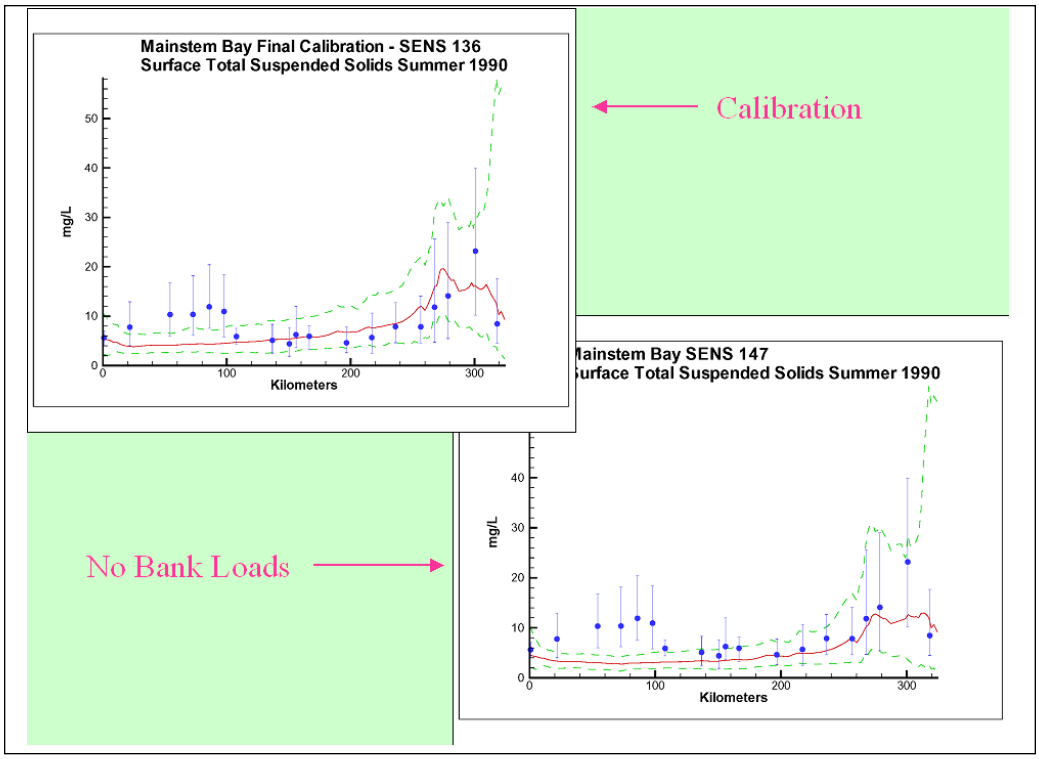

Figure 13-64. Surface total suspended solids along Chesapeake Bay axis with and without bank solids loads, summer 1990.

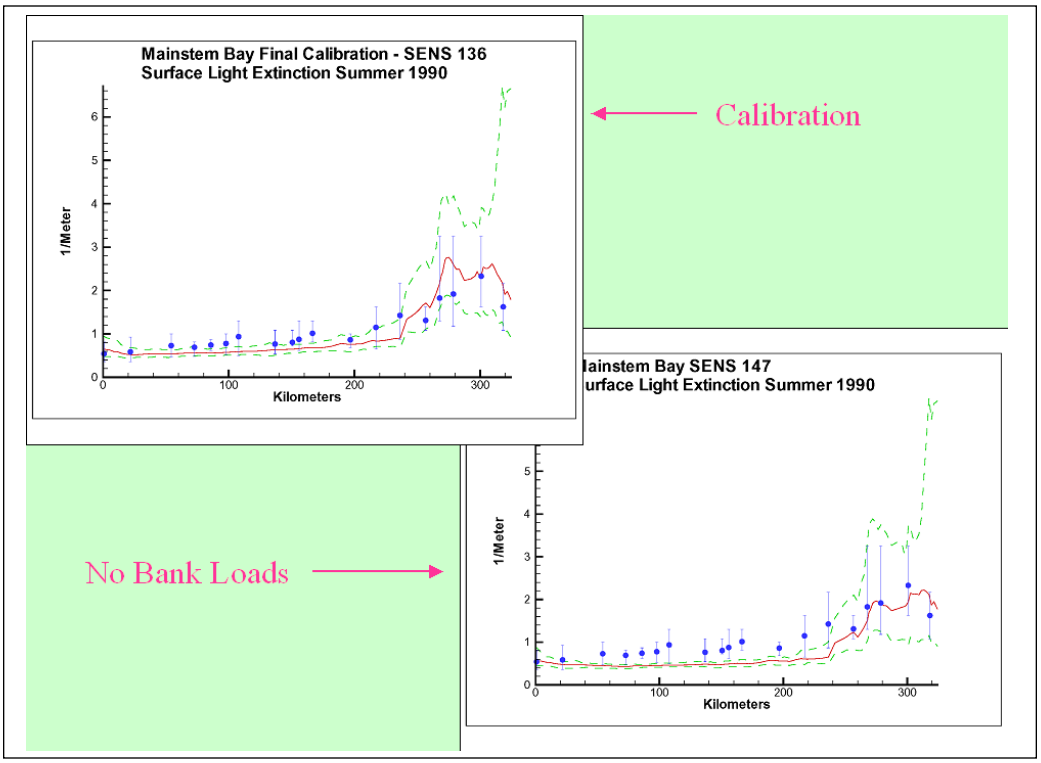

Figure 13-65. Light attenuation along Chesapeake Bay axis with and without bank solids loads, summer 1990.

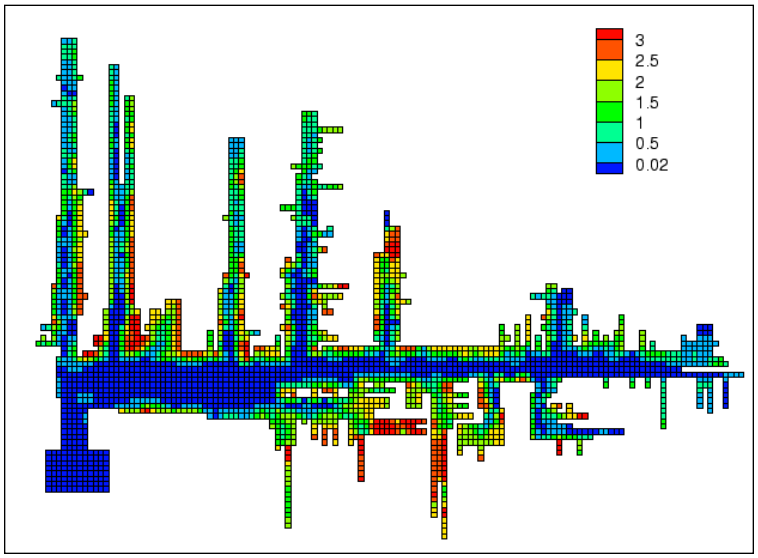

Figure 13-66. Computed summer-average benthic algal biomass without bank loads, 986.

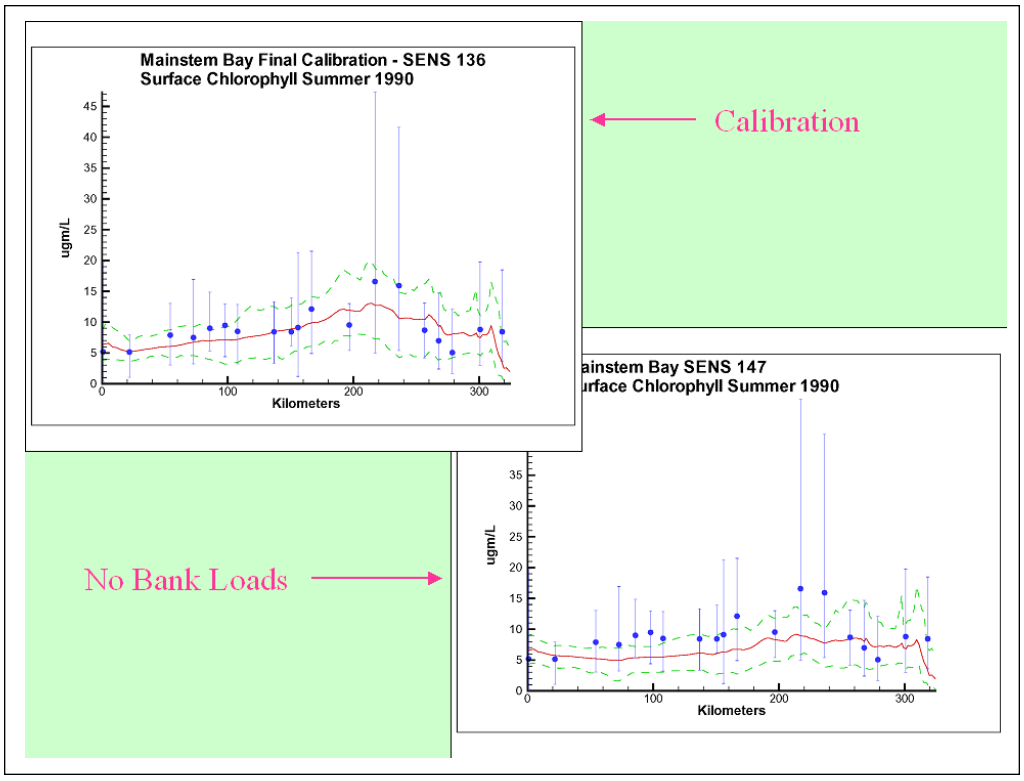

Figure 13-67. Surface dissolved chlorophyll along Chesapeake Bay axis with and without bank solids loads, summer 1990.

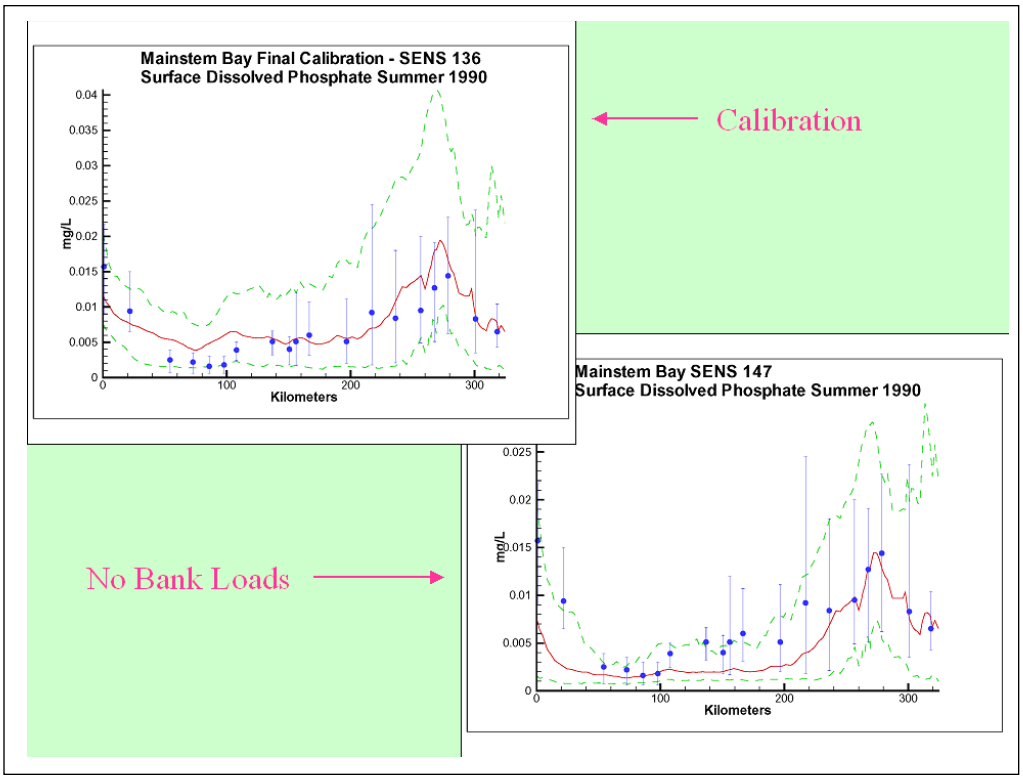

Figure 13-68. Surface dissolved phosphate along Chesapeake Bay axis with and without bank solids loads, summer 1990.

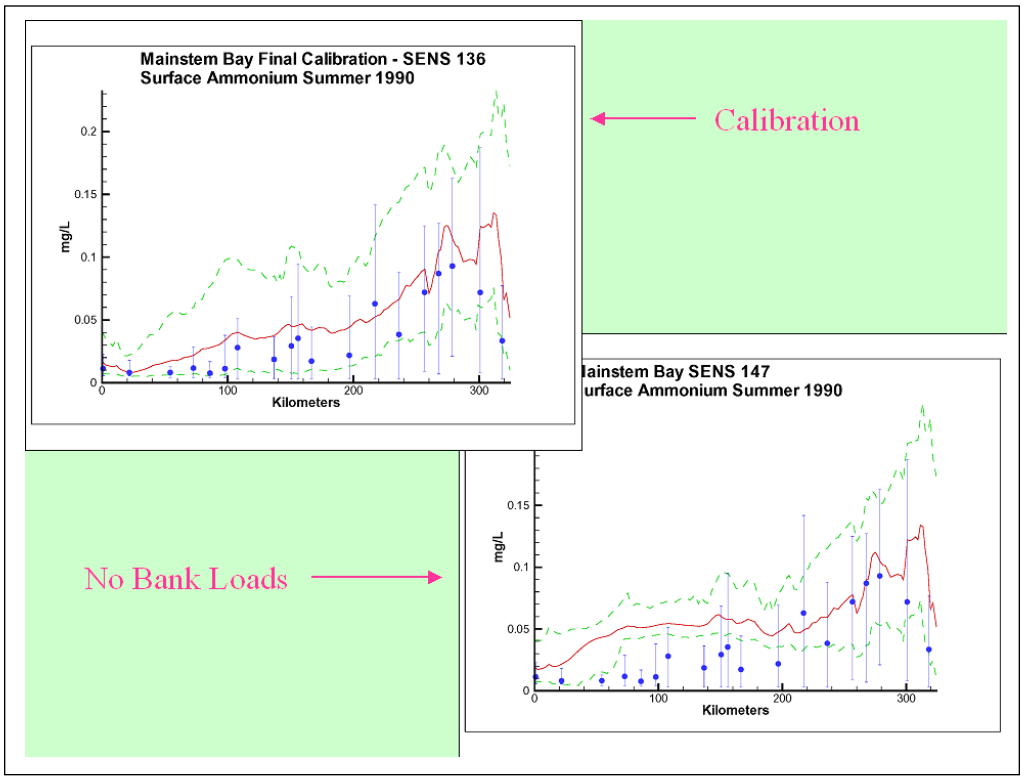

Figure 13-69. Surface ammonium along Chesapeake Bay axis with and without bank solids loads, summer 1990.

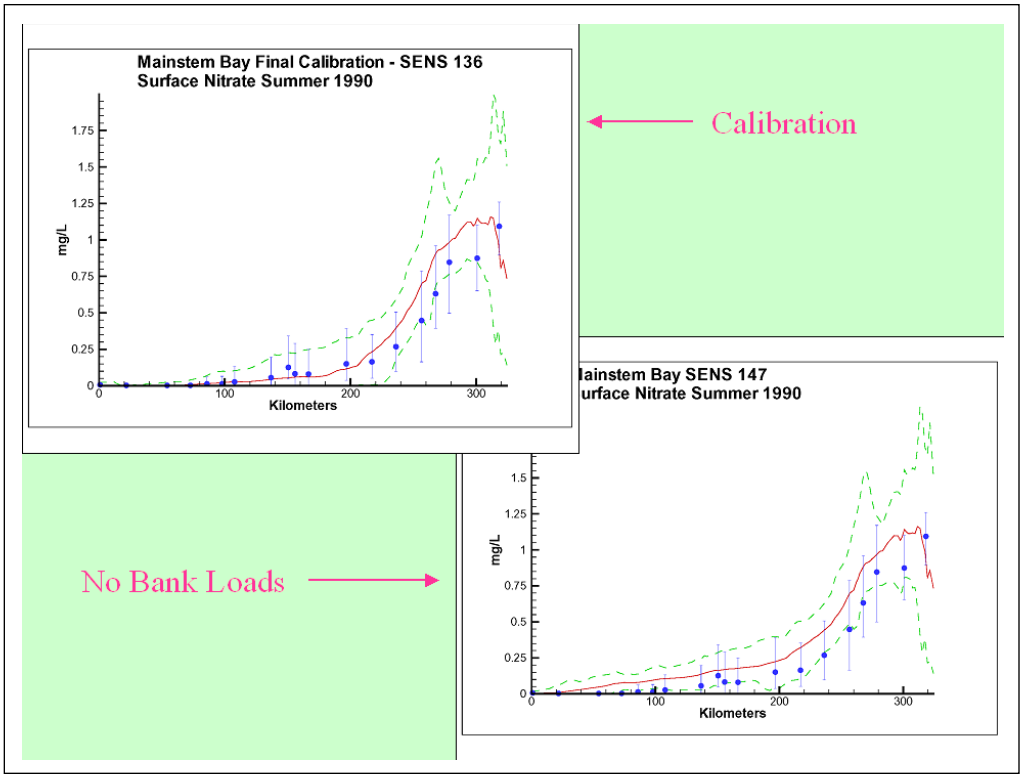

Figure 13-70. Surface nitrate along Chesapeake Bay axis with and without bank solids loads, summer 1990.

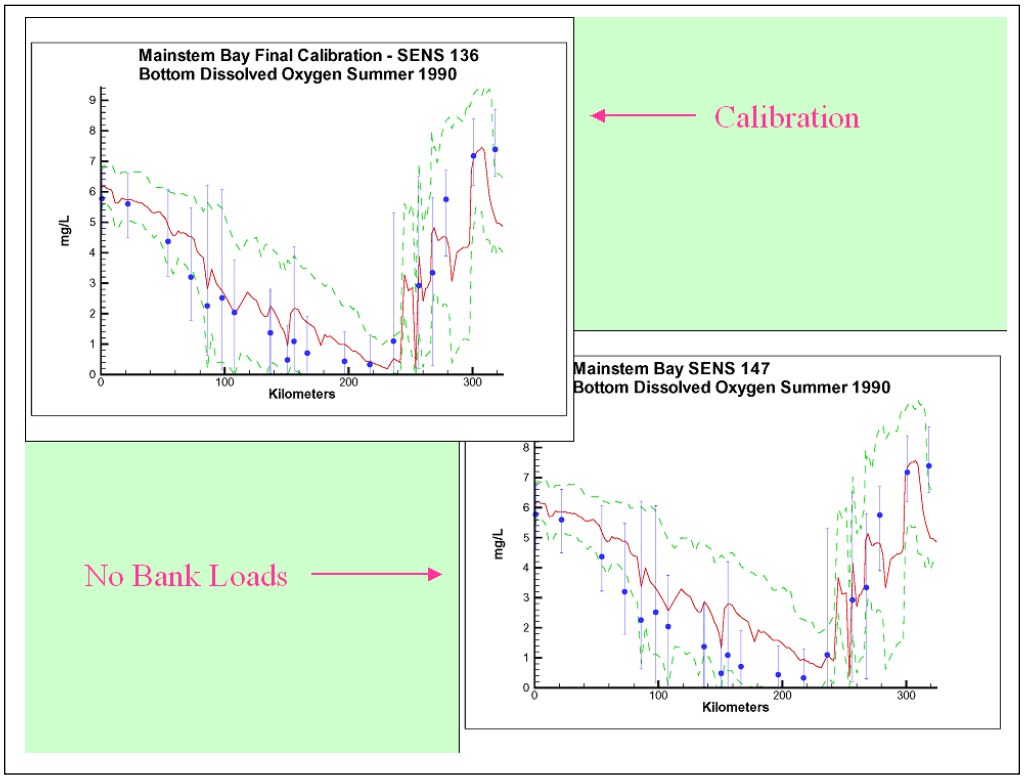

Figure 13-71. Bottom dissolved oxygen along Chesapeake Bay axis with and without bank solids loads, summer 1990.

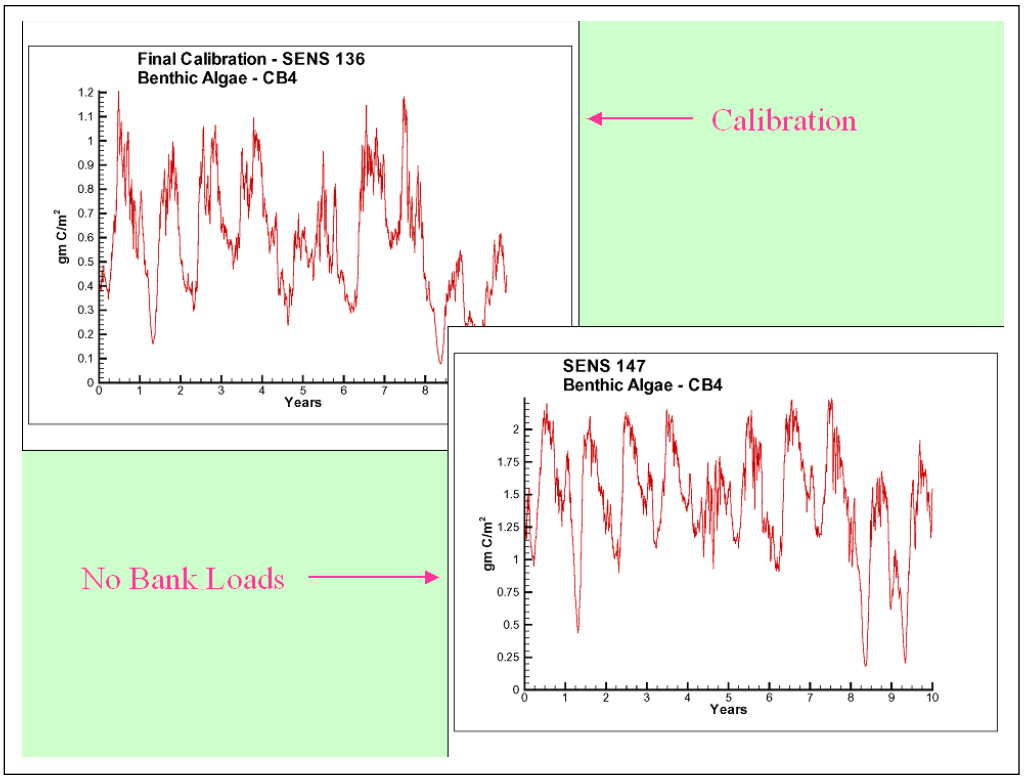

Figure 13-72. Spatially-averaged benthic algal biomass in shoal areas of Chesapeake Bay Program Segment CB4 with and without bank solids loads.

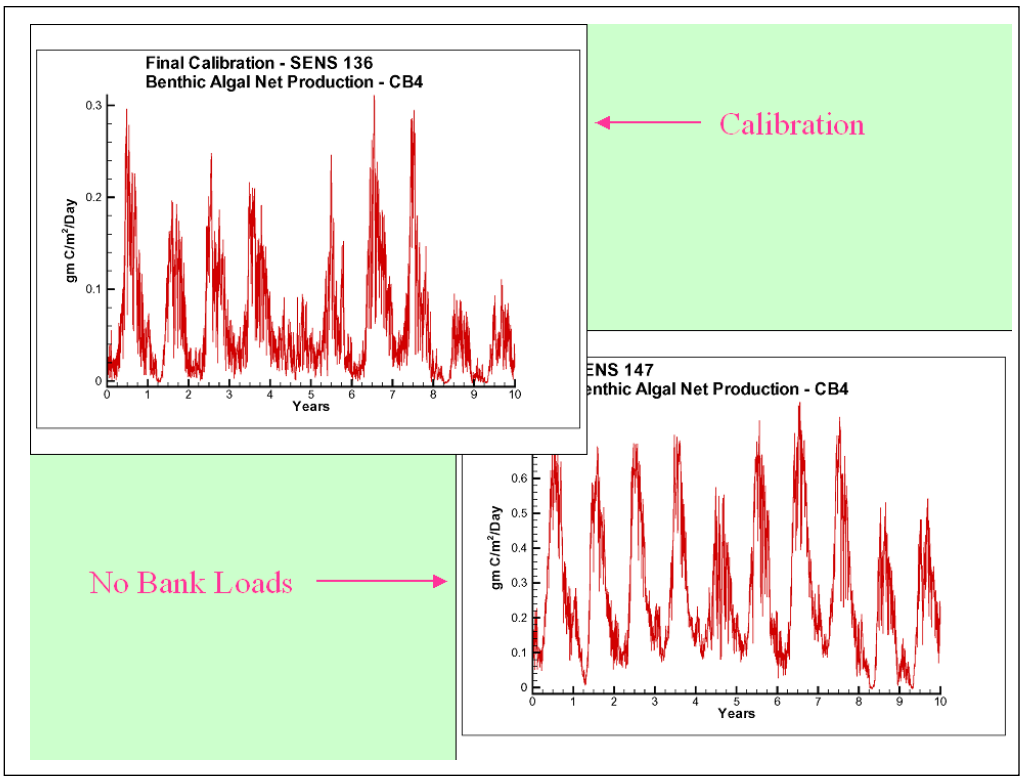

Figure 13-73. Spatially-averaged benthic algal net production in shoal areas of Chesapeake Bay Program Segment CB4 with and without bank solids loads.

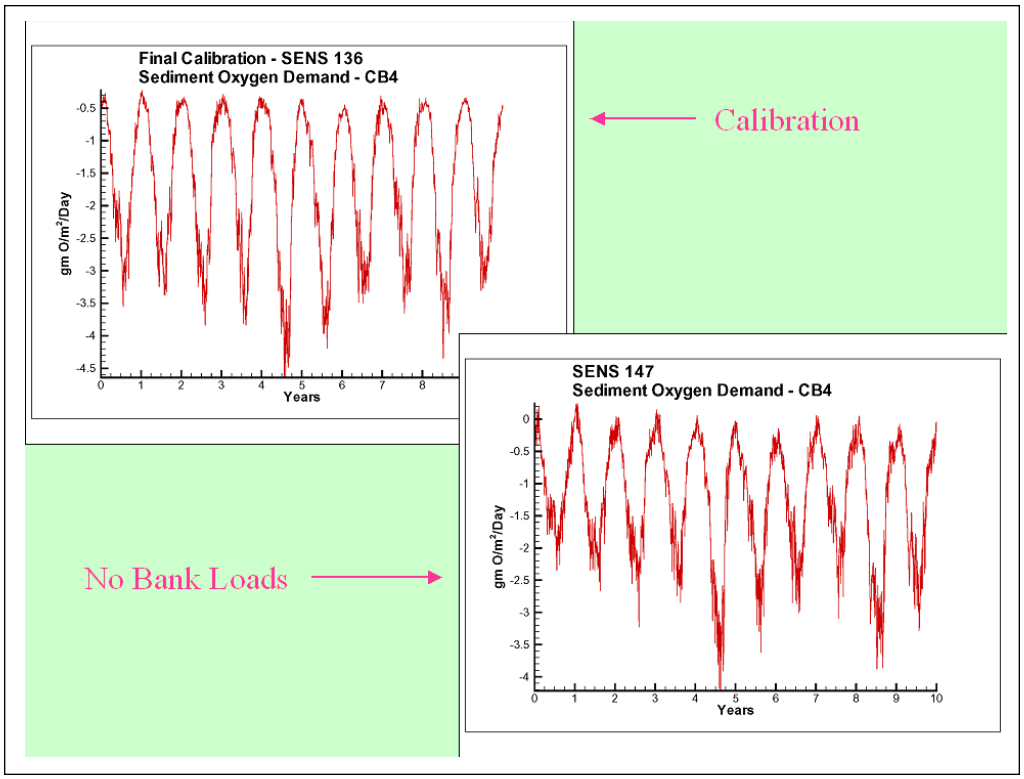

Figure 13-74. Daily-average sediment oxygen demand in shoal areas of Chesapeake Bay Program Segment CB4 with and without bank solids loads.

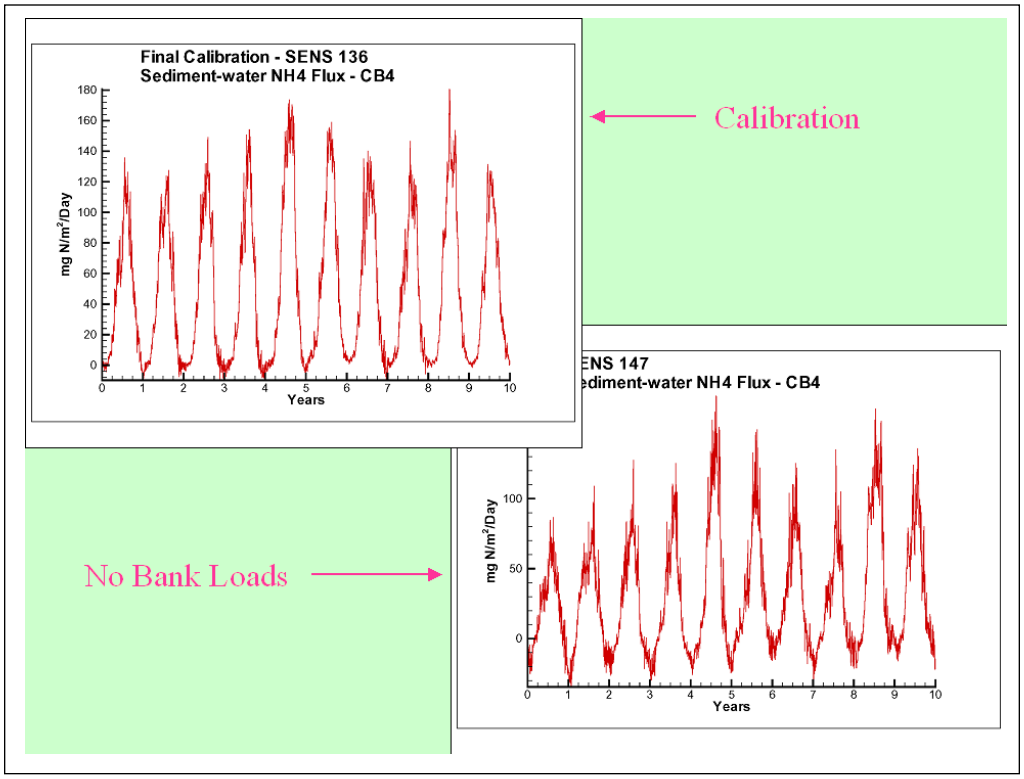

Figure 13-75. Daily-average sediment oxygen demand in shoal areas of Chesapeake Bay Program Segment CB4 with and without bank solids loads.

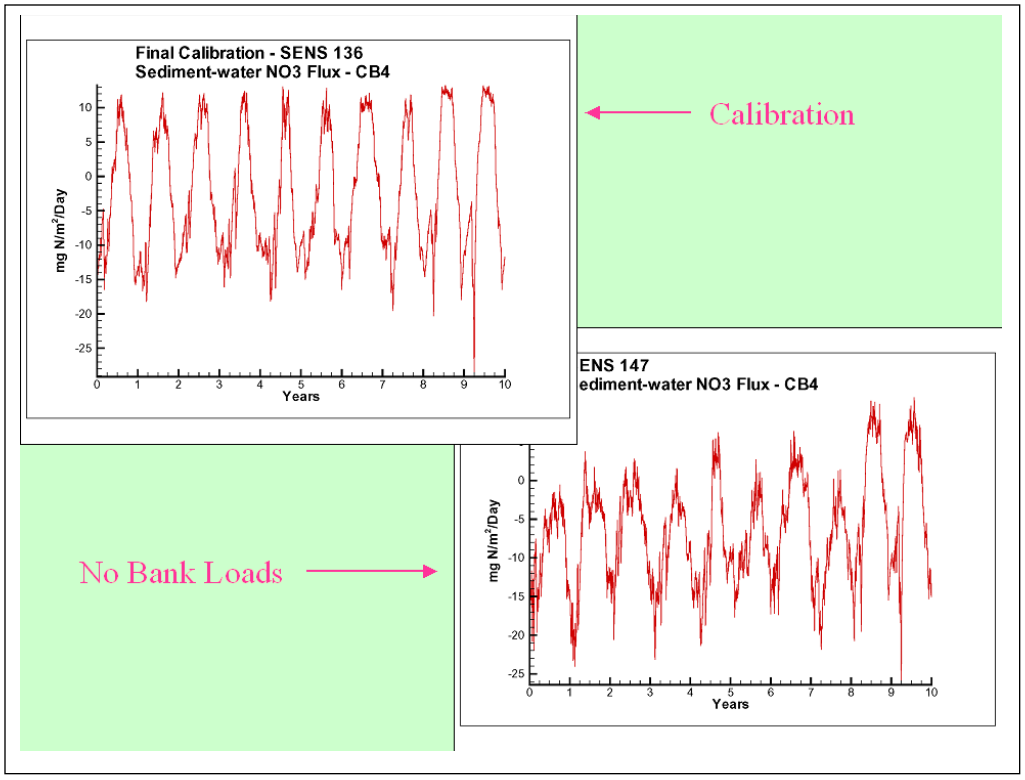

Figure 13-76. Daily-average sediment-water nitrate flux in shoal areas of Chesapeake Bay Program Segment CB4 with and without bank solids loads.

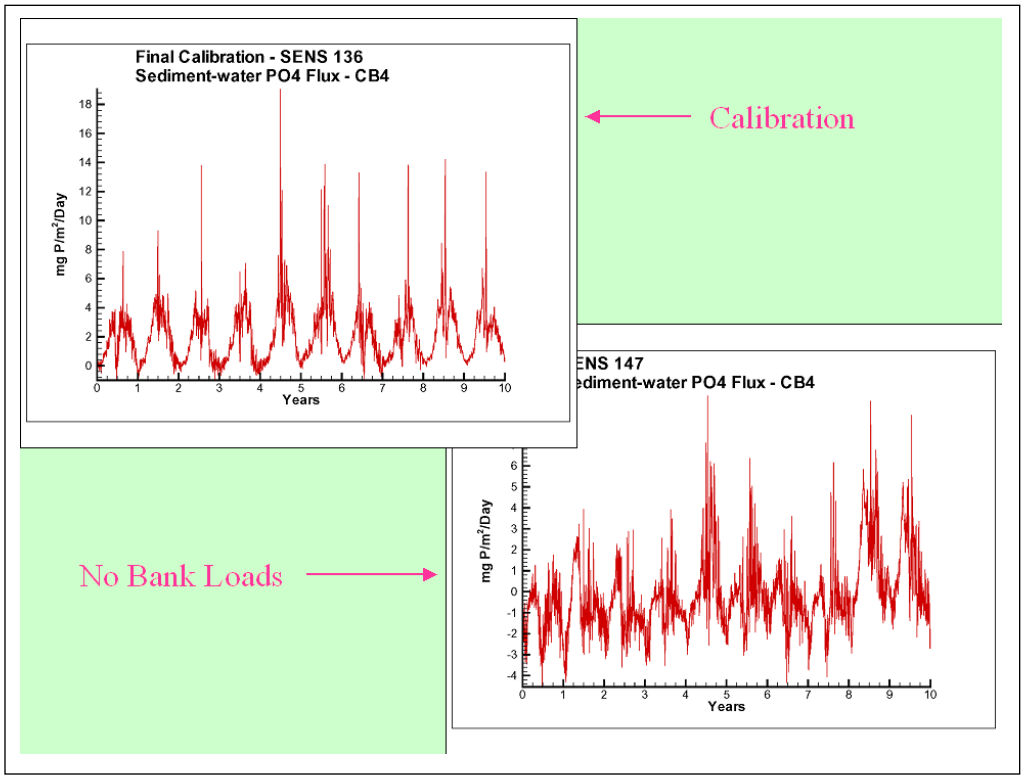

Figure 13-77. Daily-average sediment-water phosphate flux in shoal areas of Chesapeake Bay Program Segment CB4 with and without bank solids loads.

An entire volume could be written about this sensitivity run. Perhaps the best lesson is that water quality improvements analogous to those resulting from nutrient load reductions can potentially be gained through solids load reductions. It is also worthwhile to view the model behavior in light of historical reconstruction of the bay ecosystem (Cooper and Brush 1993). Analysis of sediment cores indicates sedimentation rates have increased significantly in Chesapeake Bay since European settlement. Increased sedimentation has been accompanied by a change from an evenly matched planktonic and benthic community to a predominantly planktonic community. Model results indicate reduction in solids loading will aid in restoration of the benthic community and drive the bay towards pre-settlement conditions.

References

Admiraal, W., Bouwman, L., Hoekstra, L., and Romeyn, K. (1983). "Qualitative and quantitative interactions between microphytobenthos and herbivorous meiofauna on a brackish intertidal mudflat," *Internationale Review of Gesamten Hydrobiologie*, 68, 175-101.

Batiuk, R., Orth, R., Moore, K., Dennison, W., Stevenson, J., Staver, L., Carter, V., Rybicki, N., Hickman, R., Kollar, S., Bieber, S., and Heasly, P. (1992). "Chesapeake Bay submerged aquatic vegetation habitat requirements and restoration targets: A technical synthesis," CBP/TRS 83/92, United States Environmental Protection Agency Chesapeake Bay Program, Annapolis MD.

Boynton, W., Kemp, W., Garber, J., and Barnes, J. (1986). "Ecosystem processes component (EPC) level I data report no. 3," UMCEES CBL Ref. No. 85-86, Univesity of Maryland System Center for Environmental and Estuarine Studies, Solomons MD.

Brush, G. (1989). "Rates and patterns of estuarine sediment accumulation," *Limnology and Oceanography*, 34(7), 1235-1246.

Buzzelli, C., (1998). "Dynamic simulation of littoral zone habitats in lower Chesapeake Bay. I. Ecosystem characterization related to model development," *Estuaries*, 21(4B), 659-672

Cerco, C., and Cole, T. (1994). "Three-dimensional eutrophication model of Chesapeake Bay," Technical Report El-94-4, US Army Engineer Waterways Experiment Station, Vicksburg, MS.

Cerco, C., and Seitzinger, S. (1997). "Measured and modeled effects of benthic algae on eutrophication in Indian River-Rehoboth Bay, Delaware," *Estuaries*, 20(1), 231-248.

Cerco, C., and Meyers, M. (2000). "Tributary refinements to the Chesapeake Bay Model," *Journal of Environmental Engineering*, 126(2), 164-174.

Cerco, C., and Moore, K. (2001). "System-wide submerged aquatic vegetation model for Chesapeake Bay," *Estuaries*, 24(4), 522-534.

Cerco, C., Johnson, B., and Wang, H. (2002). "Tributary refinements to the Chesapeake Bay model, ERDC TR-02-4, US Army Engineer Research and Development Center, Vicksburg, MS.

Cohen, R., Dresler, P., Phillips, E., and Cory, R. (1984). "The effect of the Asiatic clam, Corbicula Fluminea, on phytoplankton of the Potomac River, Maryland." Limnology and Oceanography, 29, 170-180.

Cooper, S., and Brush, G. (1993). "A 2,500-year history of anoxia and eutrophication in Chesapeake Bay," *Estuaries*, 16(3B), 617-626.

DiToro, D., and Fitzpatrick, J. (1993). "Chesapeake Bay sediment flux model," Contract Report EL-93-2, US Army Engineer Waterways Experiment Station, Vicksburg, MS.

DiToro, D. (2001). *Sediment Flux Modeling*, John Wiley and Sons, New York.

Fisher, T., Carlson, P., and Barber, R. (1982). "Sediment nutrient regeneration in three North Carolina estuaries," Estuarine, Coastal and Shelf Science, 4, 101- 116.

Gould, D., and Gallagher, E. (1990). "Field measurements of specific growth rate, biomass, and primary production of benthic diatoms of Savin Hill Cove, Boston," *Limnology and Oceanography*, 35, 1757-1770.

HydroQual. (1987). "A steady-state coupled hydrodynamic/water quality model of the eutrophication and anoxia process in Chesapeake Bay," Final Report, HydroQual Inc., Mahwah, NJ.

HydroQual. (2000). "Development of a suspension feeding and deposit feeding benthos model for Chesapeake Bay," produced by HydroQual Inc. under contract to the U.S. Army Engineer Research and Development Center, Vicksburg MS.

Jenkins, M., and Kemp, W., (1984). "The coupling of nitrification and denitrification in two estuarine sediments," *Limnology and Oceanography*, 29(3), 609-619.

Meyers, M., DiToro, D., and Lowe, S. (2000). "Coupling suspension feeders to the Chesapeake Bay eutrophication model," *Water Quality and Ecosystem Modeling*, 1, 123-140.

Moore, K., Wilcox, D., Orth, R. (2000). "Analysis and abundance of submersed aquatic vegetation communities in the Chesapeake Bay," *Estuaries*, 23, 115-127.

Officer, C., Lynch, D., Setlock, G., and Helz, G. (1984). "Recent sedimentation rates in Chesapeake Bay," *The estuary as a filter*. V. Kennedy, ed. Academic Press, Orlando FL, 131-157.

Newell, R. (1988). "Ecological Changes in Chesapeake Bay: Are They the Results of Overharvesting the American Oyster (Crassostrea Virginica)?" *Understanding the Estuary: Advances in Chesapeake Bay Research*. M Lynch and E Krome Eds., Chesapeake Bay Research Consortium Publication 129, Gloucester Point VA, 536-546

Orth, R., and Moore, K. (1984). "Distribution and abundance of submerged aquatic vegetation in Chesapeake Bay: An historical perspective." *Estuaries* (4B):531-540

Pinckney, J., and Zingmark, R. (1993). "Modeling the annual production of intertidal benthic microalgae in estuarine ecosystems," Journal of Phycology, 29, 396-407.

Rizzo, , W., Lackey, G., and Christian, R. (1992). "Significance of euphotic subtidal sediments to oxygen and nutrient cycling in a temperate estuary," *Marine Ecology Progress Series*, 85, 51-61.

Seitzinger, S., Nixon, S., and Pilson, M. (1984). "Denitrification and nitrous oxide production in a coastal marine ecosystem," Limnology and Oceanography, 29(1), 73-83.

Sundbäck, K. (1986). "What are the benthic microalgae doing on the bottom of Lanholm Bay?," *Ophelia* Supplement, 4, 273-286.

Sundbäck, K., Enoksson, V., Granéli, W., and Peterson, K. (1991). "Influence of sublittoral microphytobenthos on the oxygen and nutrient flux between sediment and water: A laboratory continuous flow study," *Marine Ecology Progress Series*, 74, 263-279

Westrich, J., and Berner, R. (1984). "The role of sedimentary organic matter in bacterial sulfate reduction: The G model tested," *Limnology and Oceanography*, 29, 236-249.

14 Dissolved Phosphate

Introduction

An excess of computed dissolved phosphate, especially during summer, has been a characteristic of the model since the earliest phase (Cerco and Cole 1994). While tuning the model to effect an overall reduction in computed dissolved phosphate presents no problem, reducing phosphate in summer while maintaining sufficient phosphate to support the spring phytoplankton bloom is precarious.

The first-phase model employed two processes to reduce excess phosphate. The first was variable algal stoichiometry. During periods of plentiful phosphate, the algal phosphorus-to-carbon ratio increased so that more phosphate was stored as algal biomass. During periods of phosphate depletion, the phosphorus-to-carbon ratio decreased so that less phosphate was required to support algal growth.

The second process was co-precipitation of phosphate with iron and manganese. Iron and manganese are released in dissolved form by Chesapeake Bay sediments under anoxic conditions. These metals precipitate at the interface between oxic and anoxic water and during the autumn aeration event. Dissolved phosphate is removed from the water by sorption to the fresh precipitates.

The variable algal stoichiometry relied on an iterative bisection algorithm. The algorithm was time-consuming and numerically unstable. Consequently, we reverted to constant algal composition in the Virginia Tributary Refinements study (Cerco et al. 2002). Iron and manganese (together referred to as Total Active Metal, TAM) occupied a slot in the model code originally intended for fixed solids. Since fixed solids were not modeled in the initial study, this variable was available for reprogramming as TAM. Fixed solids were modeled in the Virginia Tributary Refinements and in the present study so that TAM was dropped from the state variable suite. As a result, in this study, we reverted to the original problem of an excess of dissolved phosphate, especially during summer.

The present chapter outlines our efforts to bring dissolved phosphate into calibration. As with other sensitivity analyses, the runs compared are not necessarily sequential and may have multiple differences. Still, the results are illustrative of the magnitude and effects of various processes.

Dissolved Organic Phosphorus Mineralization

Dissolved phosphate is produced by multiple processes in the model ecosystem. A classic mechanism is the first-order mineralization of dissolved organic phosphorus to dissolved phosphate. The sensitivity of dissolved phosphate to mineralization was tested by setting this process to zero. This was a reduction in first-order rate from 0.15 d^{-1} to 0.0 d^{-1}. Results indicated mineralization of 0.15 d^{-1} was responsible for 0.005 g PO_4-P m^{-3} in surface waters of the bay during summer (Figure 14-1). Elimination of mineralization diminished phosphate uniformly except at the system boundaries. In the central bay (km 100 to 200), computed phosphate changed from an excess to agreement with observations. In the upper bay (> km 250) computed phosphate that agreed with observed decreased to below computed values. In portions of the lower bay (< km 100) computed phosphate was high and remained high following elimination of mineralization. This run illustrated the freedom the modeler has to alter phosphate via specification of mineralization. The run also illustrated that mineralization rate alone cannot be used to tune the model unless spatially-variable rates are employed.

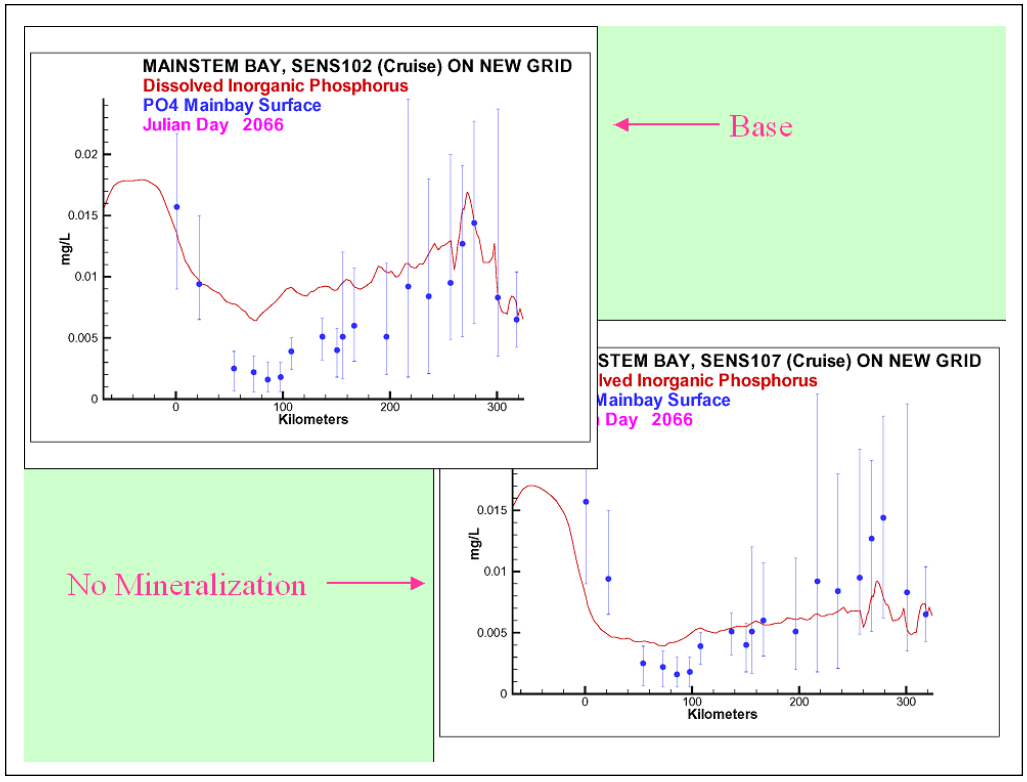

Figure 14-1. Effect of mineralization rate on surface dissolved phosphate. Results are shown for summer 1990 along Chesapeake Bay axis.

Sulfide Oxidizing Bacteria

Gavis and Grant (1986) noted that dissolved phosphate, transported upwards from anoxic bottom waters of the bay, was consumed by sulfide-oxidizing bacteria at the interface between the oxic and anoxic layers. We simulated this process in the model by relating phosphate uptake to oxidation of chemical oxygen demand:

$$\text{PUPBACT} = \text{PSBMAX} \bullet \frac{PO_4}{\text{KHPSB} + PO_4} \bullet \text{Kcod} \bullet \text{COD} \qquad (14\text{-}1)$$

in which:
PUPBACT = phosphate uptake by sulfide oxidizing bacteria (g P m^{-3} d^{-1})
PSBMAX = Stoichiometric relationship of phosphate uptake to bacterial COD oxidation (g P g^{-1} COD)
KHPSB = phosphate concentration at which bacterial COD oxidation is halved (g P m^{-3})
PO4 = dissolved phosphate (g P m^{-3})
Kcod = first-order COD oxidation rate, a function of dissolved oxygen and temperature (d^{-1})
COD = chemical oxygen demand (g O_2 equivalents m^{-3})

The quantity PUBACT was removed from the model phosphate pool. Since bacteria were not explicitly modeled, the quantity removed from the phosphate pool was transferred to the labile particulate organic phosphorus pool.

Parameters in the relationship were derived from Gavis and Grant (1986). The authors noted that consumption of 1 mol of phosphate requires oxidation of 60 mol of sulfide. This number was converted to model parameter PSBMAX through the relationship:

$$\frac{1 \text{ mol P}}{60 \text{ mol } HS^-} \bullet \frac{\text{mol } HS^-}{2 \text{ mol } O_2} \bullet \frac{\text{mol } O_2}{32 \text{ g } O_2} \bullet \frac{31 \text{ g P}}{\text{mol P}} = \frac{0.008 \text{ g P}}{\text{g oxygen exerted}} \qquad (14\text{-}2)$$

Due to phosphorus limitation on the bacteria, only a small fraction of chemical oxygen demand exertion is bacterially mediated. The phosphorus limitation is incorporated through parameter KHPSB. Inspection of Figure 6 in Gavis and Grant (1986) indicates phosphate is drawn down to 0.25 µmol. This value was taken as KHPSB, converted to model units as 0.008 g m^{-3}.

Model results (Figure 14-2) indicate sulfide oxidizing bacteria can diminish summer-average surface phosphate by up to 0.01 g P m^{-3}. The primary effect is at the upper end of the deep trench (km 250) where anoxia is prevalent and phosphorus is abundant. At mid-bay (km 150) phosphate removal is roughly 0.005 g P m^{-3} while in the lower bay, phosphate removed is perhaps 0.002 g P m^{-3}.

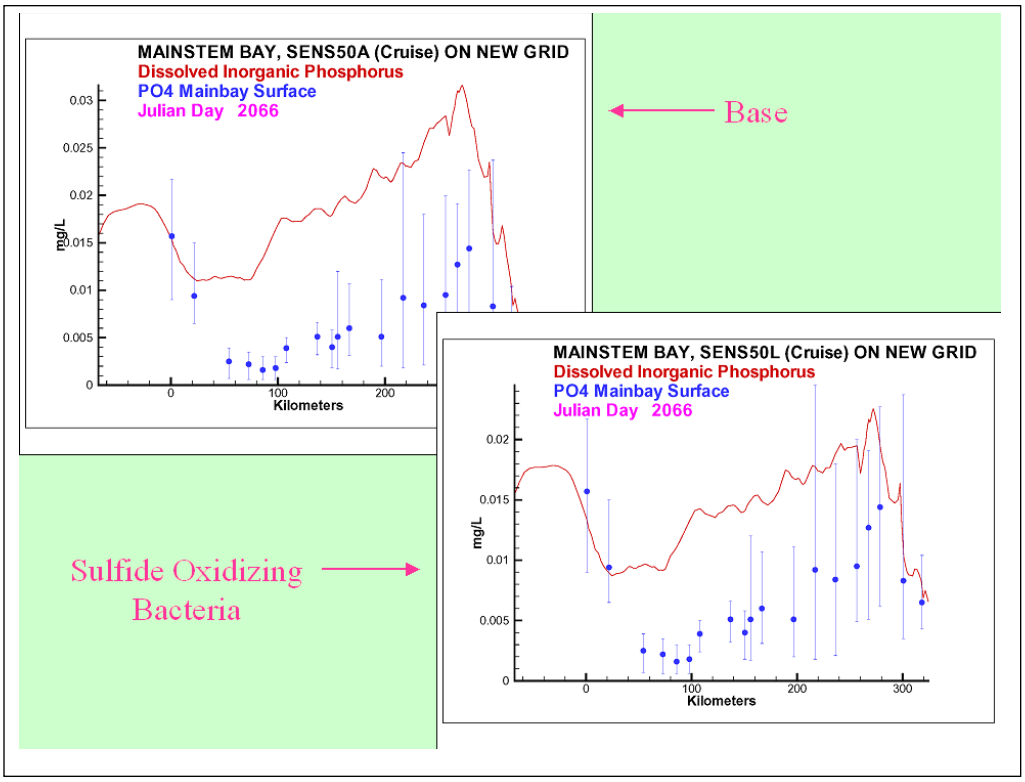

Figure 14-2. Effect of sulfide oxidizing bacteria on surface dissolved phosphate. Results are shown for summer 1990 along Chesapeake Bay axis. Note change of vertical scale.

Precipitation

We invoked precipitation in regions of the bay that experience anoxia (Table 14-1). Phosphorus was routed from the phosphate pool to the refractory particulate organic pool during the fall aeration period. Our relationship mimicked the results of precipitation although the approach was less mechanistic than the original formulation involving TAM:

$$PRECIP = PO_4 \bullet PCPMAX \bullet \frac{PO_4}{KHPCP + PO_4} \bullet PCPDAY \qquad (14\text{-}3)$$

in which:
PRECIP = precipitation rate (g P m^{-3} d^{-1})
PCPMAX = first-order precipitation rate (d^{-1})
KHPCP = phosphate concentration at which precipitation rate is halved (g P m^{-3})
PCPDAY = a binary variable indicating the reaeration period (0 or 1)

Experience and inspection suggested PCPMAX = 0.1 to 0.2 d^{-1}, KHPCP = 0.0025 g P m^{-3}, and a reaeration interval extending from mid-September to mid-December.

Results indicated daily precipitation of 10% to 20% of the phosphate pool effected a tremendous improvement in late-summer and autumn phosphate (Figure 14-3). Precipitation in late summer did little to impact summer-average phosphate concentration, however (Figure 14-4).

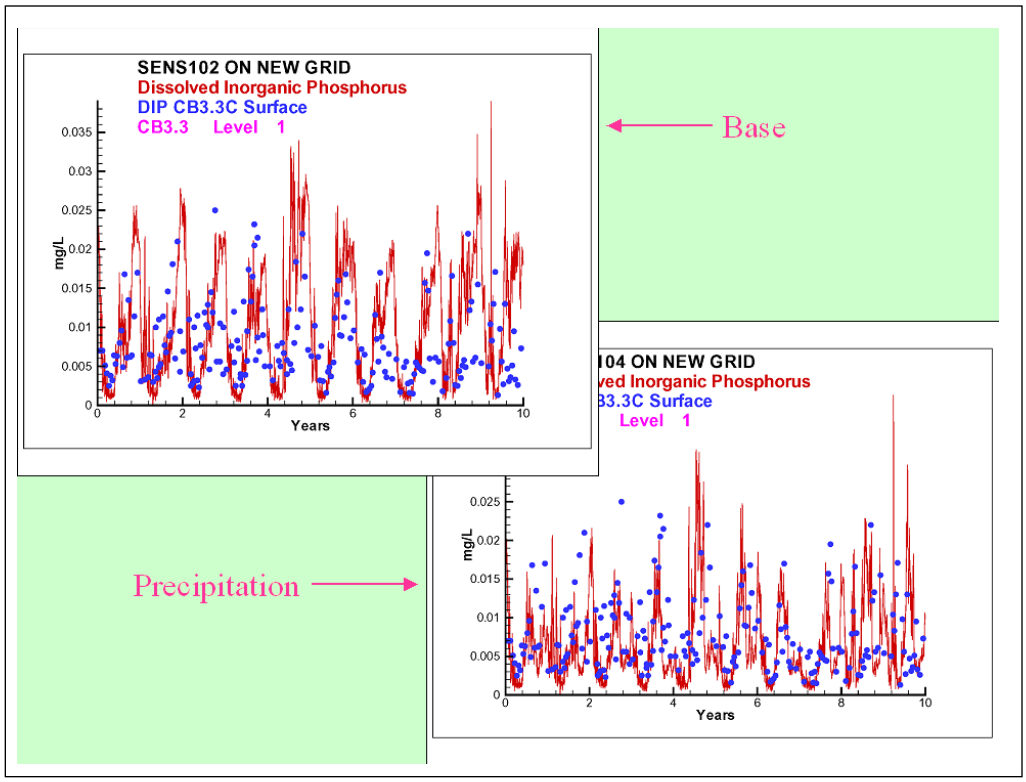

Figure 14-3. Effect of precipitation on surface dissolved phosphate at Chesapeake Bay station CB3.3C.

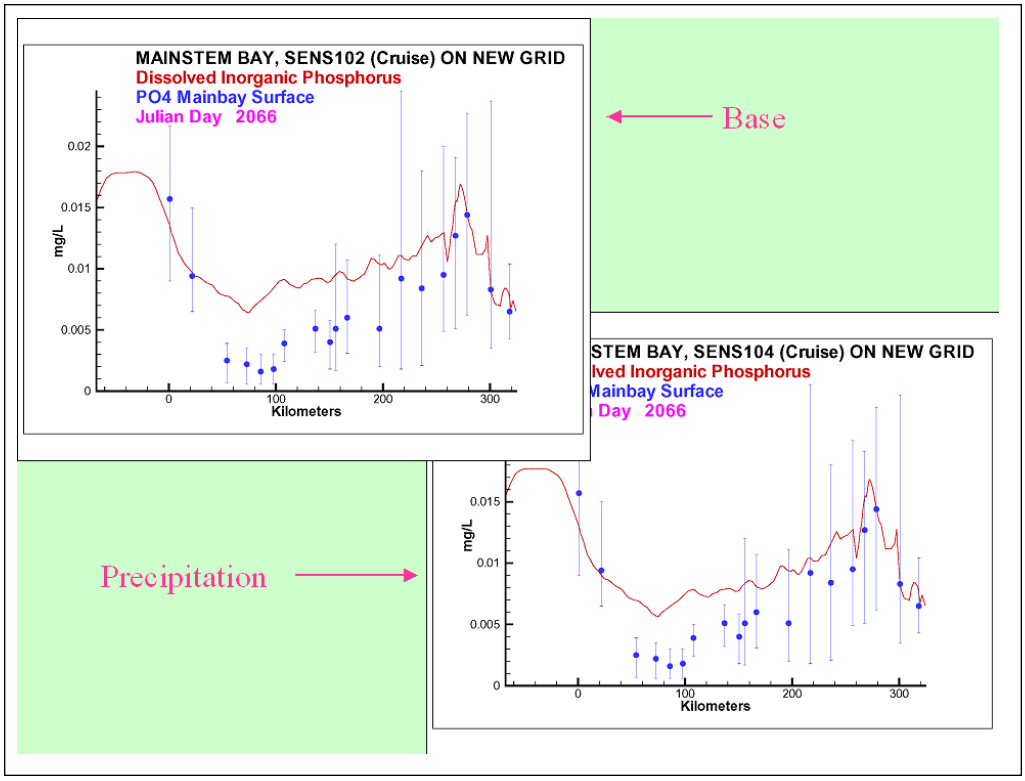

Figure 14-4. Effect of precipitation on surface dissolved phosphate. Results are shown for summer 1990 along Chesapeake Bay axis.

Table 14-1
Chesapeake Bay Program Segments with Phosphate precipitation

Segment	PCPMAX, d^{-1}	Segment	PCPMAX, d^{-1}
CB3	0.2	LE3	0.2
CB4	0.2	LE4	0.2
CB5	0.2	LE5	0.1
CB6	0.1	RET1	0.1
CB7	0.1	RET2	0.1
EE1	0.1	RET3	0.1
EE2	0.1	RET4	0.1
EE3	0.2	WE4	0.2
LE1	0.2	WT5	0.2
LE2	0.2		

Summary

The final model calibration incorporated dissolved organic phosphorus mineralization (KDP = 0.15 d^{-1}), uptake by sulfide oxidizing bacteria, and precipitation. Introduction of the two uptake mechanisms as well as alterations in multiple parameter values provided a reasonable representation of summer-average phosphorus in the surface of the bay, especially during years of dry (1985, Figure 14-5) to moderate hydrology (1990, Figure 14-6). Considerable excess of computed phosphate remained present in a wet year (1993, Figure 14-7).

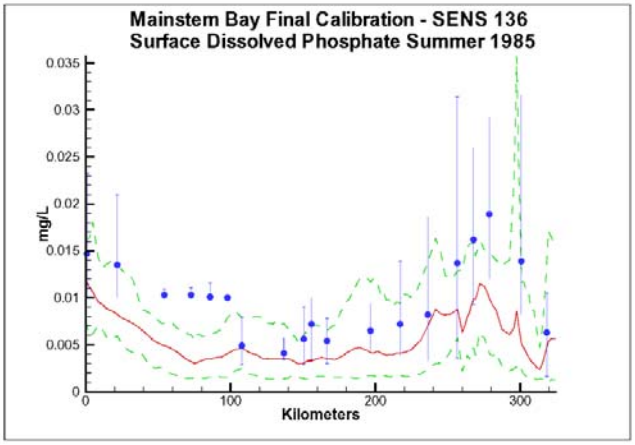

Figure 14-5. Surface dissolved phosphate along Chesapeake Bay axis in summer 1985. Final model calibration.

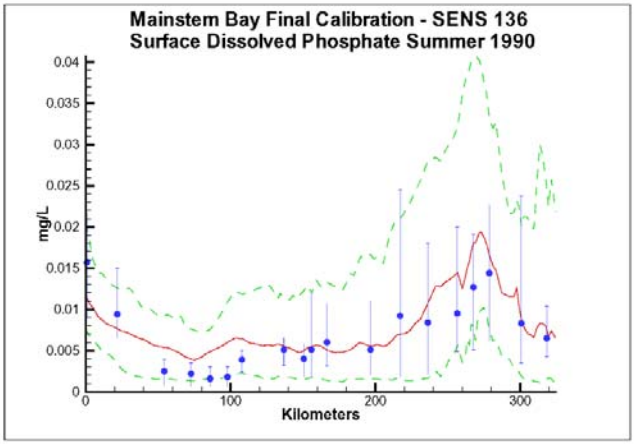

Figure 14-6. Surface dissolved phosphate along Chesapeake Bay axis in summer 1990. Final model calibration.

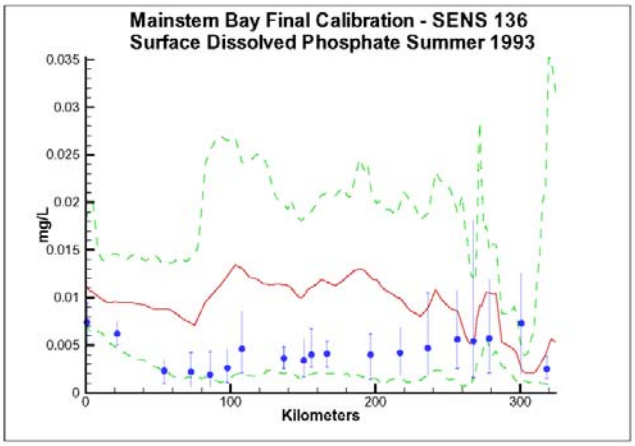

Figure 14-7. Surface dissolved phosphate along Chesapeake Bay axis in summer 1993. Final model calibration.

Phosphorus is a limiting nutrient in the mainstem bay in spring while nitrogen is the primary limiting nutrient in summer (Fisher et al. 1992, Malone et al. 1996, Fisher et al. 1999). Consequently, our rough approach to modeling dissolved phosphate in summer is acceptable. Still, a new phosphorus model seems appropriate, especially for management of freshwater segments where phosphorus is the more important nutrient.

Our model (and every other model we know of) ignores phosphate uptake by heterotrophic bacteria. A cursory search of extensive literature indicates, however, that bacteria compete with phytoplankton for phosphate (Thingstad et al. 1993) and may draw phosphate down to limiting levels (Zweifel et al. 1993). Bacterial utilization of phosphate in Chesapeake Bay itself has been recognized for decades (Faust and Correll, 1976). The first step in a new phosphate model is to explicitly recognize phosphate uptake by heterotrophic bacteria. Bacteria do not necessarily have to be incorporated into the model as a state variable. One reviewer suggested relating phosphate uptake to organic carbon respiration, which is a bacterial process.

Multiple studies have indicated that a substantial fraction of particulate phosphorus in the bay is of inorganic form (Keefe, 1994; Conley et al. 1995). The second step in an improved phosphorus model is to explicitly differentiate particulate inorganic phosphorus from particulate organic phosphorus through the addition of a particulate inorganic phosphorus state variable. Simple, linear partitioning of phosphate to inorganic solids is insufficient. Studies indicate that particulate matter in the bay has low capacity to adsorb additional phosphorus and that solids do not buffer the dissolved phosphate concentration (Conley et al. 1995).

In the Virginia Tributary Refinements, we approached the problem of particulate inorganic phosphorus by assigning a constant composition, 0.1% phosphorus, to fixed solids. This fraction was settled and resuspended as fixed solids rather than organic detritus. The approach showed promise in recognizing the distinct nature of the inorganic fraction and in reproducing the spatial phosphorus distribution (Figure 14-8). In the present study, we abandoned this approach when we were

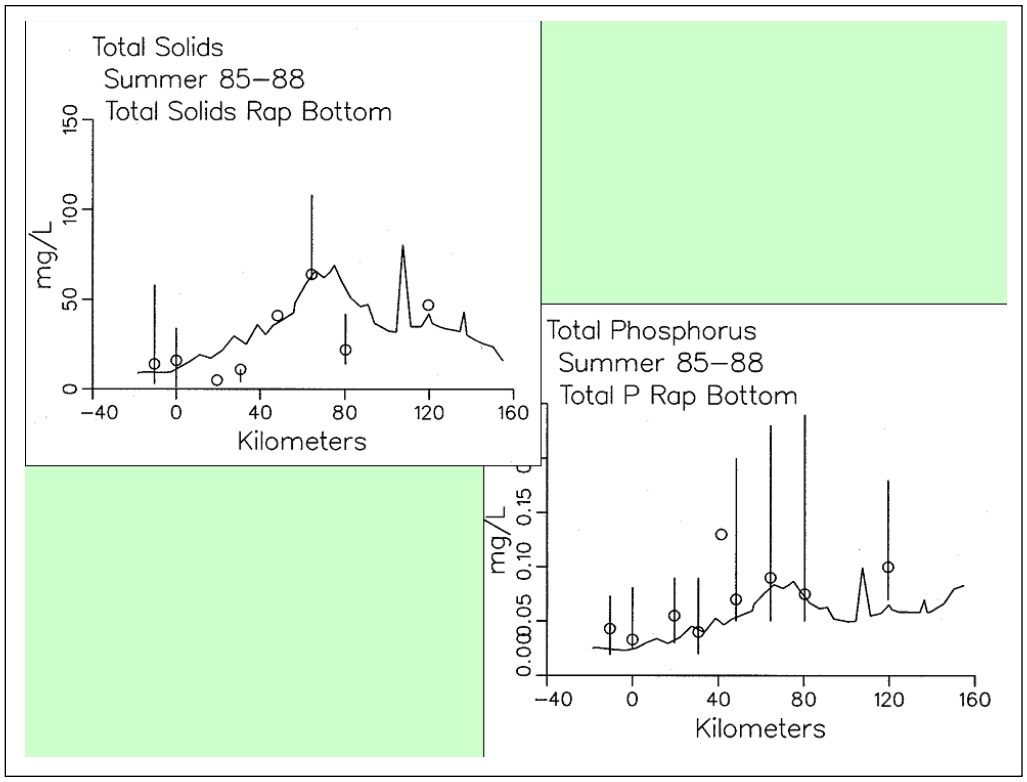

Figure 14-8. Median summer bottom total solids and total phosphorus along Rappahannock River axis 1985-1988. Results from Virginia Tributary Refinements with solids consisting of 0.1% phosphorus.

experiencing difficulty calibrating phosphorus. Time was unavailable to fully explore the implications of a new state variable so we fell back to a reliable, accepted phosphorus cycle.

A third step is to explore the utilization of dissolved organic phosphorus by bacteria and phytoplankton. From the start (Cerco and Cole 1994), this study has recognized that bacteria and phytoplankton enhance the mineralization of dissolved organic phosphorus to inorganic form (e.g. Chrost and Overbeck 1987). Our approach has been to enhance mineralization during periods of phosphate limitation. The modeled process increases the pool of dissolved phosphate in the water column. Although the process by which organisms enhance mineralization does not seem well documented, discussion with colleagues indicates the spatial scale of the process is limited. That is, mineralization takes place at the cell boundary and is immediately followed by uptake. From the model standpoint, this is equivalent to utilization of dissolved organic phosphorus. An approach worth exploring is to build in a preference function in which organisms utilize phosphate until it is exhausted and then utilize dissolved organic phosphorus.

A concluding modification is to implement realistic sediment transport processes. No doubt, a distinct particulate inorganic phosphorus form exists and is transported along with the solids with which it is associated. Our ability to simulate solids transport with the present model is limited, however. Consequently, correct representation of total phosphorus (Figure 14-9) is impossible when solids distributions cannot be reproduced (Figure 14-10).

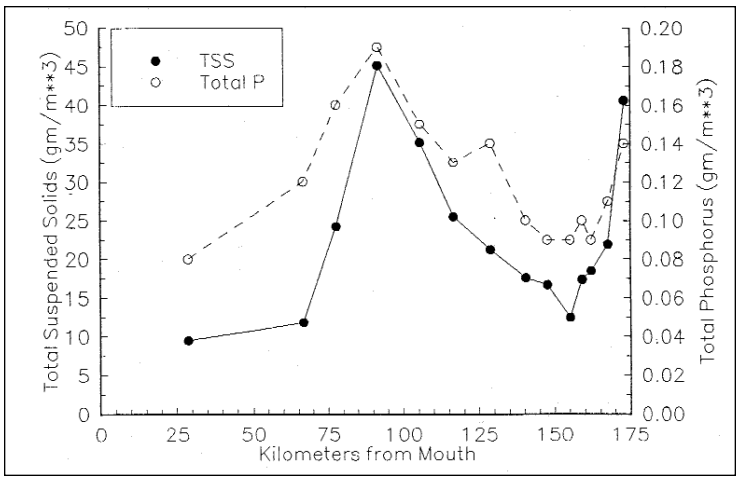

Figure 14-9. Observed surface total solids and total phosphorus along Potomac River axis, summer 1985.

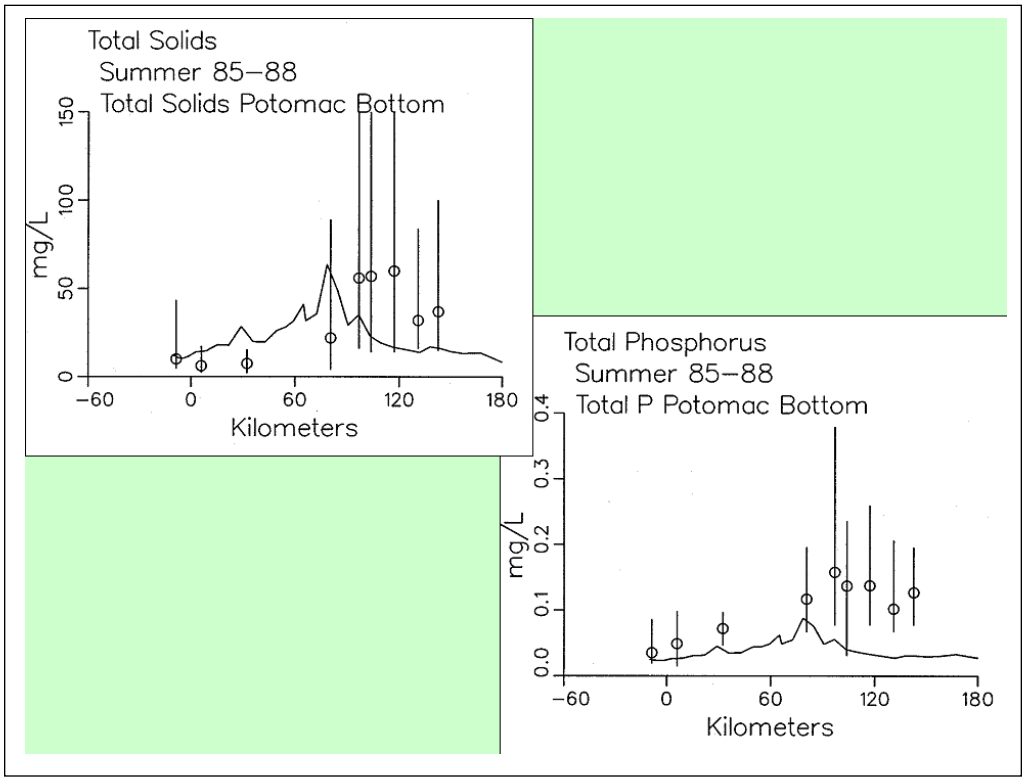

Figure 14-10. Median summer bottom total solids and total phosphorus along Potomac River axis 1985-1988. Results from Virginia Tributary Refinements with solids consisting of 0.1% phosphorus.

References

Cerco, C., Johnson, B., and Wang, H. (2002). "Tributary refinements to the Chesapeake Bay model," ERDC TR-02-4, U.S. Army Engineer Research and Development Center, Vicksburg, MS.

Cerco, C., and Cole, T. (1994). "Three-dimensional eutrophication model of Chesapeake Bay," Technical Report EL-94-4, U.S. Army Engineer Waterways Experiment Station, Vicksburg, MS.

Chrost, R., and Overbeck, J. (1987). "Kinetics of alkaline phosphatase activity and phosphorus availability for phytoplankton and bacterioplankton in Lake Plubsee (north German eutrophic lake), *Microbial Ecology*, 13, 229-248.

Conley, D., Smith, W., Cornwell, J., Fisher, T. (1995). "Transformation of particle-bound phosphorus at the land-sea interface," *Estuarine, Coastal and Shelf Science*, 40, 161-176.

Faust, M., and Correll, D. (1976). "Comparison of bacterial and algal utilization of orthophosphate in an estuarine environment," *Marine Biology*, 34, 151-162.

Fisher, T., Gustafson, A., Sellner, K., Lacouture, R., Haas, L., Wetzel, R., Magnien, R., Everitt, D., Michaels, B., and Karrh, R. (1999). "Spatial and temporal variation of resource limitation in Chesapeake Bay," *Marine Biology*, 133, 763-778.

Fisher, T., Peele, E., Ammerman, J., and harding, L. (1992). "Nutrient limitation of phytoplankton in Chesapeake Bay," *Marine Ecology Progress Series*, 82, 51- 63.

Gavis, J, and Grant, V. (1986). "Sulfide, iron, manganese, and phosphate in the deep water of the Chesapeake Bay during anoxia," *Estuarine, Coastal and Shelf Science*, 23, 451-462.

Keefe, C. (1994). "The contribution of inorganic compounds to the particulate carbon, nitrogen, and phosphorus in suspended matter and surface sediments of Chesapeake Bay," *Estuaries*, 17(1B), 122-130.

Malone, T., Conley, D., Fisher, T., Glibert, P., Harding, and Sellner, K. (1996). "Scales of nutrient-limited phytoplankton productivity in Chesapeake Bay," *Estuaries*, 19, 371-385.

Thingstad, T., Skjodal, E., and Bohne, R. (1993). "Phosphorus cycling and algal- bacterial competition in Sandsfjord, western Norway," *Marine Ecology Progress Series*, 99, 239-259.

Zweifel, U., Norrman, B., and Hagstrom, A. (1993). "Consumption of dissolved organic carbon by marine bacteria and demand for inorganic nutrients," *Marine Ecology Progress Series*, 101, 23-32.

Statistical Summary of Calibration 15

Introduction

The calibration of the model involved the comparison of hundreds of thousands of observations with model results in various formats. Comparisons involved conventional water quality data, process-oriented data, and living-resources observations. The graphical comparisons produced thousands of plots which cannot be assimilated in their entirety. Evaluation of model performance requires statistical and/or graphical summaries of results. We present summaries here for major water quality constituents in the mainstem bay and western tributaries. Additional graphical comparisons are available on the CD-ROM that accompanies this report.

Methods

No standard set of model performance statistics exists. We employ summary statistics that were developed as part of our initial Chesapeake Bay model study (Cerco and Cole 1994). Use of a consistent set of statistics facilitates comparisons with earlier model versions and with applications to other systems.

Statistics computed were mean error, absolute mean error, and relative error:

$$ME = \frac{\Sigma\ (O - P)}{N} \tag{15-1}$$

$$AME = \frac{\Sigma\ |O - P|}{N} \tag{15-2}$$

$$RE = \frac{\Sigma |O - P|}{\Sigma\ O} \tag{15-3}$$

in which
ME = mean error
AME = absolute mean error
RE = relative error
O = observation
P = prediction
N = number of observations.

The mean error describes whether the model over-estimates or under-estimates the observations, on average. The mean error can achieve its ideal value, zero, while large discrepancies exist between individual observations and computations. The absolute mean error is a measure of the characteristic difference between individual observations and computations. An absolute mean error of zero indicates the model perfectly reproduces each observation. The relative error is the absolute mean error normalized by the mean concentration. Relative error provides a statistic suitable for comparison between different variables or systems.

Quantitative statistics were determined through comparison of model computations with observations from 7 to 27 stations sampled at approximately monthly intervals. The number of model-data comparisons ranged from roughly 400 to 17,000 (Table 15-1). For salinity, total nitrogen, and total phosphorus, comparisons were made with surface and bottom samples. For chlorophyll and light attenuation, surface samples only were examined. Dissolved oxygen comparisons were restricted to bottom samples collected in summer. We formed this restriction for two reasons. First, summer, bottom dissolved oxygen is of primary interest to management. Second, dissolved oxygen at the surface during summer and throughout the water column during colder periods is near saturation. The predictive ability of the model is largely determined by the ability to calculate the

Table 15-1 Number of Stations and Observations in Statistical Summaries

	Mainstem Bay	James	York	Rappahannock	Potomac	Patuxent
# Stations	46	11	12	7	15	7
Chlorophyll	8216	2087	2188	1548	1971	1277
Dissolved Oxygen	2745	605	669	462	718	424
Light Attenuation	8351	1925	2108	1552	2223	1330
Salinity	17166	4300	4437	3233	4056	2690
Total Nitrogen	16700	4335	4480	3306	4184	1511
Total Phosphorus	17000	4331	4483	3296	4253	2663

saturation dissolved oxygen concentration. Computation of summer, bottom dissolved oxygen requires that the model correctly portray interactions of physical and biological processes. Statistics based on summer, bottom dissolved oxygen provide more realistic indication of model performance.

Our graphical summaries are in the form of cumulative distribution plots. Creation of the plots first requires pairing in space and time of observations and computations. These were from the same stations used in the statistical summaries. (The dissolved oxygen and chlorophyll graphical summaries include surface and bottom samples throughout the year.) Observations were paired with daily average computations in the cell corresponding to sample location and depth. Next, the observations and computations were individually sorted from smallest to largest. The sorted arrays were divided into quantiles and plotted as cumulative distributions. A point on the line in x-y space indicates the percentage of observations or computations (y-axis) less than the indicated concentration (x-axis). The 50^{th} percentile indicates the median value. Perfect correspondence is indicated when the cumulative distribution of modeled values exactly overlays the cumulative distribution of observed values.

Statistics of Present Calibration

Examination of statistical summaries (Table 15-2) requires a good deal of judgement and interpretation. Generalizations and distinctions are not always possible. One clear pattern is that the model overestimates, on average, surface chlorophyll. The overestimation ranges from less than 1 mg m^{-3} to more than 2 mg m^{-3}. The model consistently underestimates salinity although the mean error is always less than 1 ppt. For all systems except the Potomac, computed mean summer, bottom dissolved oxygen is within 1 g m^{-3} of the observed average. In the Potomac, computed mean summer bottom dissolved oxygen is almost 2 g m^{-3} higher than observed. Careful examination of model results indicates the region of greatest computed excess is in the tidal fresh portion of the river, where observed bottom dissolved oxygen exceeds 5 g m^{-3}. Excessive computed dissolved oxygen, surface and bottom, is a characteristics of the present model in most tidal freshwater regions. Except in the James, the model underestimates mean total phosphorus concentration. Underestimation of total phosphorus has been a characteristic of the model since the earliest application (Cerco and Cole 1994). We originally attributed the shortfall to omission of bankloads. In this version we include bankloads of phosphorus but they are difficult to estimate accurately. The model also omits resuspension of particulate phosphorus and has difficulty reproducing the concentration of particulate phosphorus in the turbidity maximums. In the James, we attribute the excess computed phosphorus to uncertainty in the large point-source and distributed loads to this tributary.

Examination of relative errors (Table 15-2, Figure 15-1) indicates that chlorophyll has the greatest error, salinity the least. Relative error in chlorophyll prediction is 60% to 80% while relative error in salinity prediction is 10% to 20%. The chlorophyll error reflects the difficulty in computing this dynamic biological component which can attain unlimited magnitude. In contrast, salinity is purely physical and is bounded at the upper end by oceanic concentration. The remaining components are in the mid-range, 30% to 50%, with total phosphorus, perhaps exhibiting slightly higher relative error. The higher error in phosphorus reflects the

Table 15-2 Statistical Summary of Calibration 1985-1994						
Surface Chlorophyll, ug/L	**Mainstem Bay**	**James**	**York**	**Rappahannock**	**Potomac**	**Patuxent**
Mean Error	-0.53	-2.05	-1.68	-2.55	-1.85	-1.53
Absolute Mean Error	5.01	9.29	4.71	8.22	7.45	8.15
Relative Error	58.4	75.7	60.1	81.4	80.2	65.4
Summer, Bottom Dissolved Oxygen, mg/L	Mainstem Bay	James	York	Rappahannock	Potomac	Patuxent
Mean Error	0.32	-0.09	0.37	0.62	-1.31	-0.92
Absolute Mean Error	1.47	2.43	1.18	1.93	2.13	1.74
Relative Error	35.7	36.6	22.8	35.4	40.5	39.3
Light Attenuation, 1/m	Mainstem Bay	James	York	Rappahannock	Potomac	Patuxent
Mean Error	0.02	-0.21	0.09	-0.17	-0.02	-0.20
Absolute Mean Error	0.36	0.97	0.84	0.89	1.03	0.84
Relative Error	35.3	43.7	41.9	42.3	45.2	38.4
Salinity, ppt	Mainstem Bay	James	York	Rappahannock	Potomac	Patuxent
Mean Error	0.71	0.11	0.95	0.01	0.45	0.16
Absolute Mean Error	1.97	2.01	1.84	1.49	0.97	1.69
Relative Error	11.8	31.2	14.5	18.3	22.5	17.5
Total Nitrogen, mg/L	Mainstem Bay	James	York	Rappahannock	Potomac	Patuxent
Mean Error	0.04	-0.16	0.01	0.14	0.32	-0.13
Absolute Mean Error	0.17	0.42	0.23	0.28	0.61	0.43
Relative Error	24.3	44.6	33.1	33.8	31.9	41.5
Total Phosphorus, mg/L	Mainstem Bay	James	York	Rappahannock	Potomac	Patuxent
Mean Error	0.005	-0.021	0.012	0.001	0.032	0.041
Absolute Mean Error	0.014	0.069	0.036	0.036	0.053	0.047
Relative Error	37.6	63.8	49.2	52.6	58.9	47.6

aforementioned difficulties in evaluating loads, in simulating resuspension, and in representing particulate phosphorus transport.

The mainstem bay is clearly superior in computations of salinity, total nitrogen, and total phosphorus. The James River stands out as demonstrating the highest relative error in these components. We partially attribute the greater accuracy in the mainstem to the relatively dense computational grid in this region. An additional, and probably more significant influence, is that the mainstem is dominated by internal processes while the tributaries are strongly influenced by point-source and distributed loads. The point-source loads are incompletely described, especially in the early years of the simulation and in the Virginia tributaries. Below-fall-line distributed loads cannot be measured; they can only be computed by the watershed

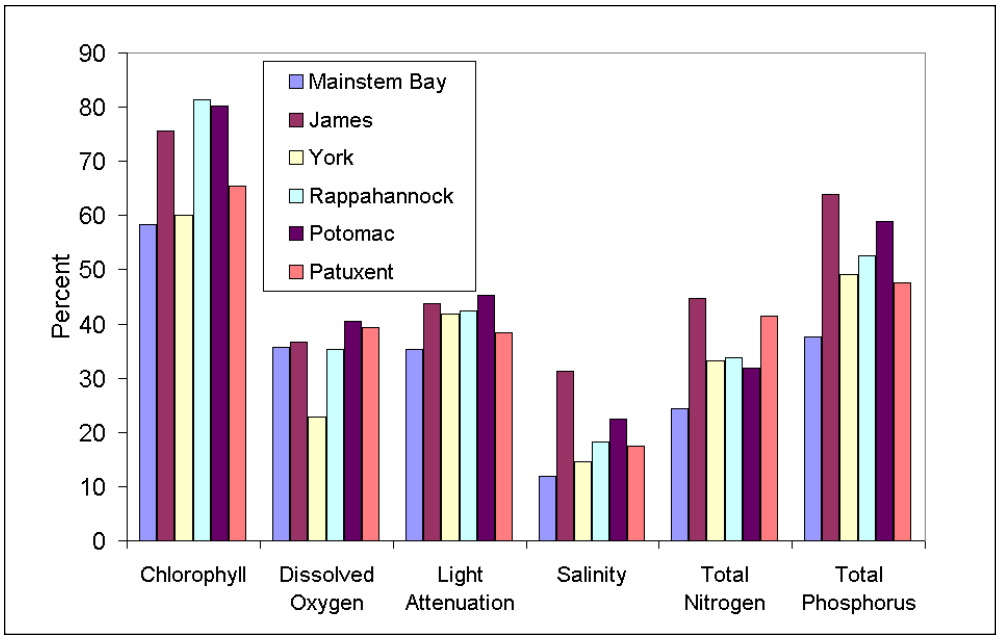

Figure 15-1. Relative Error in mainstem bay and western tributaries.

model. We believe the uncertain loads, discharged into the constrained volumes of the tributaries, are the major reason for higher relative error in the tributaries. The James River stands out in this regard.

Statistics of Model Improvements

The Chesapeake Bay model has gone through three stages. The first was the initial 4,000-cell model that was used in the 1992 re-evaluation (Cerco and Cole 1994). The second stage was the tributary refinements in which segmentation was substantially increased and living resources were introduced (Cerco et al. 2002). The present 2002 model is the third stage. This stage involved further re-segmentation and re-calibration. As part of the tributary refinements documentation, we summarized model performance at several stages in the mainstem bay and Virginia tributaries. We can now supplement that summary with the performance of the present model phase (Table 15-3, 15-4). This summary is based on the years 1985-1986 only. These years are common to the three simulations. Consequently, the summary statistics presented for the 2002 model differ from those presented earlier.

Statistics for summer, bottom dissolved oxygen are superior for the present model, especially when compared to the initial model application. Mean error is closer to the ideal value of zero everywhere and relative error is diminished everywhere except the James River.

Clear improvements are not apparent in the salinity statistics, which is interesting considering the two new grid resegmentations and the high level of attention devoted to the present effort. If anything, the salinity statistics show a decrease in performance in the mainstem bay. We suspect a trade-off has occurred between dissolved oxygen and salinity. In the initial model application, the hydrodynamic model was calibrated and the results were passed to the water quality team. In the

Table 15-3
Mean Errors in Three Model Phases

Salinity	Mainstem	James	Rappahannock	York
4000 Cell	-0.06	-0.95	2.43	0.08
VA Tribs	-0.62	0.55	-1.64	-0.94
2002 Model	1.69	0.32	1.14	1.68
Surface Chlorophyll	**Mainstem**	**James**	**Rappahannock**	**York**
4000 Cell	-1.59	0.24	0.54	-1.19
VA Tribs	-1.19	-4.84	2.25	-1.66
2002 Model	-0.32	-2.47	-0.14	-1.46
Light Attenuation	**Mainstem**	**James**	**Rappahannock**	**York**
4000 Cell	-0.146	-0.329	-0.169	0.021
VA Tribs	-0.206	-0.425	-0.599	0.222
2002 Model	0.065	0.009	0.135	0.125
Total Nitrogen	**Mainstem**	**James**	**Rappahannock**	**York**
4000 Cell	-0.003	0.108	0.197	0.057
VA Tribs	0.011	-0.174	0.128	0.092
2002 Model	0.025	-0.205	0.098	0.004
Total Phosphorus	**Mainstem**	**James**	**Rappahannock**	**York**
4000 Cell	0.012	-0.0077	0.0265	0.0146
VA Tribs	0.0091	-0.0456	0.0043	0.0149
2002 Model	0.0115	-0.0534	-0.0008	-0.0025
Summer, Bottom, Dissolved Oxygen	**Mainstem**	**James**	**Rappahannock**	**York**
4000 Cell	-0.89	-1.88	-2.96	-0.48
VA Tribs	0.58	0.26	0.81	-0.08
2002 Model	-0.03	-0.53	0.72	0.40

Table 15-4
Relative Error in Three Model Phases

Salinity	Mainstem	James	Rappahannock	York
4000 Cell	9.1	19.1	24.0	17.4
Step 2	9.5	19.4	18.3	11.6
2002 Model	13.1	25.4	16.5	15.6
Surface Chlorophyll	**Mainstem**	**James**	**Rappahannock**	**York**
4000 Cell	61.6	74.1	83.4	64.0
VA Tribs	57.6	78.6	64.8	66.2
2002 Model	59.2	66.4	70.8	49.1
Light Attenuation	**Mainstem**	**James**	**Rappahannock**	**York**
4000 Cell	36.5	32.6	32.8	39.9
VA Tribs	45.2	59.8	57.6	46.6
2002 Model	38.5	39.7	41.0	44.0
Total Nitrogen	**Mainstem**	**James**	**Rappahannock**	**York**
4000 Cell	22.1	31.9	32.5	20.8
VA Tribs	21.3	46.0	31.9	20.4
2002 Model	21.9	48.5	28.6	28.1
Total Phosphorus	**Mainstem**	**James**	**Rappahannock**	**York**
4000 Cell	42.5	49.3	53.4	41.0
VA Tribs	38.5	67.9	41.2	43.9
2002 Model	41.5	78.3	41.3	47.0
Summer, Bottom, Dissolved Oxygen	**Mainstem**	**James**	**Rappahannock**	**York**
4000 Cell	44.9	31.7	63.9	41.4
VA Tribs	31.6	38.1	46.6	25.9
2002 Model	27.9	40.5	32.2	22.7

present application, the hydrodynamic and water quality models were calibrated interactively. The salinity computation in the hydrodynamic model was weighed against the dissolved oxygen computation in the water quality model. We placed great emphasis on the dissolved oxygen computations. Apparently the devotion to dissolved oxygen diminished the performance of the model with regard to salinity.

The performance of the model with regard to light attenuation deteriorated from the initial application to the Virginia Tributary application. In the initial application, regression was used to specify attenuation as a function of location and runoff. (Runoff was used as a surrogate for sediment load). This specification was highly accurate, if not predictive. In the Virginia Tributaries phase, we made the first attempt to compute attenuation as a function of computed solids concentration. This model was intended to compute response to management control actions. The predictive model initially was less accurate than the regression model. In the present phase, we lavished attention on the solids calculation with the result that attenuation was computed at levels comparable to or better than a regression model.

Consistent montonic changes in chlorophyll, total nitrogen, and total phosphorus are difficult to discern. Mean and relative errors have varied but are now essentially where they were in the earlier model stages.

The statistical analysis that accompanied the Tributary Refinements examined multiple stages of model calibration. We noted then that clear, monotonic improvements in model representations of nitrogen, phosphorus, and chlorophyll were difficult to discern. We declared that model revisions contributed realism and confidence rather than quantitative improvements. Our conclusions then remain valid now. Improvements that have been made to the model over 15 years include:

- Increasing resolution from a grid of 4,000 cells to a grid of 13,000 cells
- Improved vertical resolution in shallow-water areas
- Incorporation of living resources including submerged aquatic vegetation, zooplankton, and benthos
- Accurate modeling of primary production
- Modeling of suspended solids
- Predictive modeling of light attenuation

We have no doubt the model is of more use to management than it has ever been although we may have reached a plateau in terms of quantitative model performance.

Comparison with Other Applications

No standard criteria exist for judging acceptable model performance. One approach is to compare performance with similar statistics from other model applications. Statistics comparable to other systems at least indicate the model is in the performance mainstream. We compared relative error in the 2002 Chesapeake Bay application with two recent model applications, Florida Bay (Cerco et al. 2000) and the lower St. Johns River, Florida (Tillman et al. 2003). Florida Bay is a shallow sub-tropical lagoon. The St. Johns is a partially- to well-mixed estuary with a substantial tidal freshwater extent.

All models indicate chlorophyll has the greatest relative error (Table 15-5, Figure 15-2). This finding is consistent with our earlier indication derived from the mainstem bay and tributaries (Figure 15-1). The Chesapeake Bay application is centrally located within the relative error in the other two systems. Relative errors for Chesapeake Bay total nitrogen and total phosphorus are also comparable to the other systems.

Table 15-5. Relative Error in Three Estuarine Applications

	Chesapeake Bay	Lower St. Johns River	Florida Bay
Chlorophyll, ug/L	58.4	49.3	72
Dissolved Oxygen, mg/L	35.7	9.3	7.7
Light Attenuation, 1/m	35.3	15.6	
Salinity, ppt	11.9	27.6	4.7
Total Nitrogen, mg/L	24.3	29	38.9
Total Phosphorus, mg/L	37.6	26.9	31.3

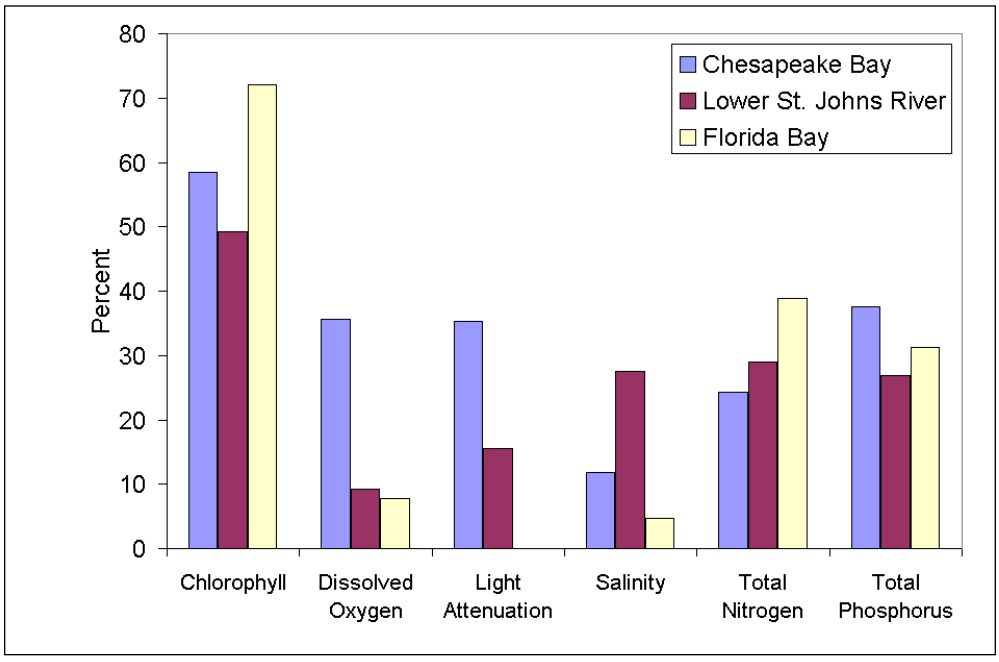

Figure 15-2. Relative error in three model applications.

Significant differences exist for dissolved oxygen, light attenuation, and salinity. The St. Johns River and Florida Bay have much lower relative error in computed dissolved oxygen. The discrepancy is due to the way the statistics were computed. Chesapeake Bay was restricted to summer, bottom dissolved oxygen while the other systems were not. Florida Bay is a shallow well-mixed lagoon in which dissolved oxygen occurs in the range 6 to 9 g m^{-3}. The preponderance of observations in the St. Johns were from the surface. The estuary demonstrates little dissolved-oxygen stratification so that the few subsurface observations showed minor departure from the surface observations. The performance in Florida Bay and the St. Johns validates our observation that dissolved oxygen statistics that include surface and cold-weather samples are biased by the tendency for dissolved oxygen to equilibrate with the atmosphere. The denominator in the relative error computation, essentially saturation concentration, is also larger than the mean bottom dissolved oxygen that forms the denominator in the Chesapeake Bay statistics.

The Chesapeake Bay and St. Johns applications use identical models for solids and light attenuation. The different statistics reflect the components that make up attenuation. In the St. Johns, the major component is color, represented in the model as refractory dissolved organic carbon. Computation of attenuation in the St. Johns relies on accurate observations of carbon loading and boundary conditions. Once the boundary conditions are specified, the refractory dissolved organic carbon passes through the system with little alteration except dilution. Consequently, computation of light attenuation is relatively simple. In Chesapeake Bay, the principle components of light attenuation are fixed and volatile solids. These components are highly dynamic and depend on loading, transport and internal kinetics. The higher relative error in Chesapeake Bay light attenuation reflects the greater difficulty in computing solids versus refractory dissolved organic carbon.

The salinity statistics are most interesting. Florida Bay has the least relative error yet we don't regard this application as particularly successful. The statistics are biased by a large number of samples in the perimeter of the bay in which salinity is nearly constant between 35 and 40 ppt. The St. Johns River has a well-validated hydrodynamic model yet relative error there is apparently the greatest of all. We cannot ascertain the origin of the higher error relative to Chesapeake Bay. Our opinion is that the St. Johns application (Sucsy and Morris 2001) is comparable in quality to the Chesapeake Bay application. The lesson here is that statistics can be deceptive and must be employed judiciously, in concert with other quantitative and qualitative performance measures.

Graphical Performance Summaries

Dissolved Oxygen

Computed and observed dissolved oxygen distributions in the mainstem bay virtually superimpose above 6 g m^{-3} (Figure 15-3). Computed dissolved oxygen in the range 2 to 6 g m^{-3} comprises a greater fraction of the population than observed while observations below 2 g m^{-3} out-number corresponding calculations. The James (Figure 15-4), Rappahannock (Figure 15-6) and Potomac (Figure 15-7) Rivers show an interesting crossover around 6 g m^{-3}. The crossover indicates the

fractions of computed and observed populations below 6 g m^{-3} (25%) and above 6 g m^{-3} (75%) are identical. When observations are below 6 g m^{-3}, the corresponding computation tends to be low. When observations are above 6 g m^{-3}, the corresponding computation tends to be high. The model tends to underestimate dissolved oxygen throughout the distribution in the York River (Figure 15-5). The opposite phenomenon occurs in the Patuxent; the model overestimates dissolved oxygen throughout the distribution (Figure 15-8).

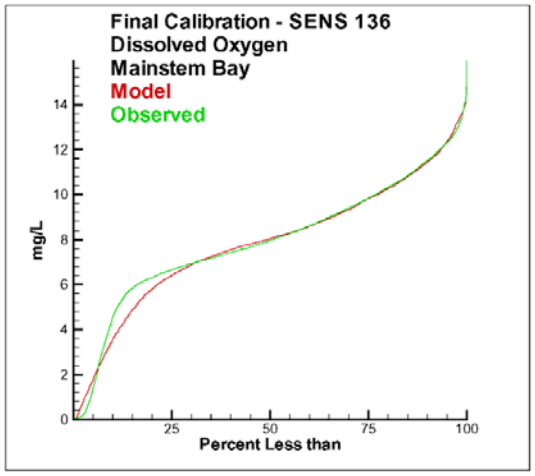

Figure 15-3. Cumulative distribution plot of dissolved oxygen in mainstem bay.

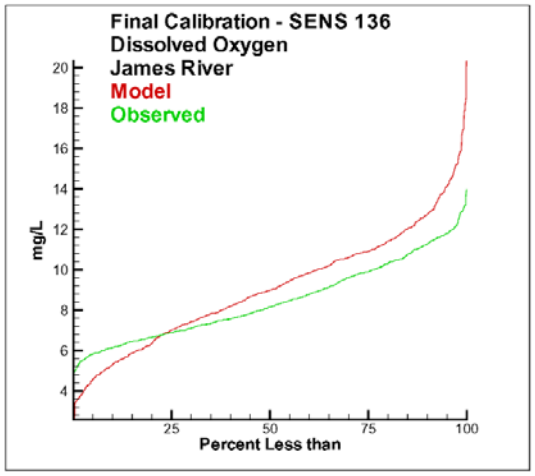

Figure 15-4. Cumulative distribution plot of dissolved oxygen in James River.

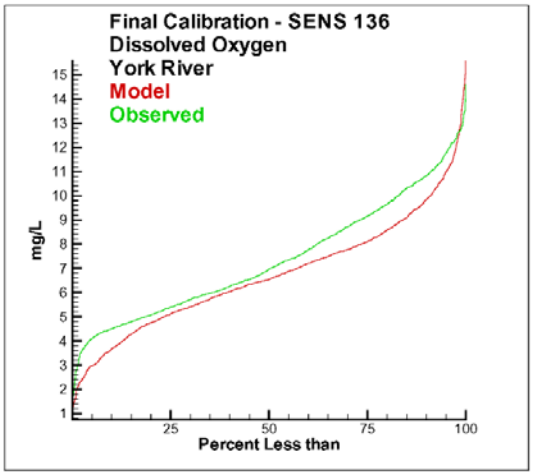

Figure 15-5. Cumulative distribution plot of dissolved oxygen in York River.

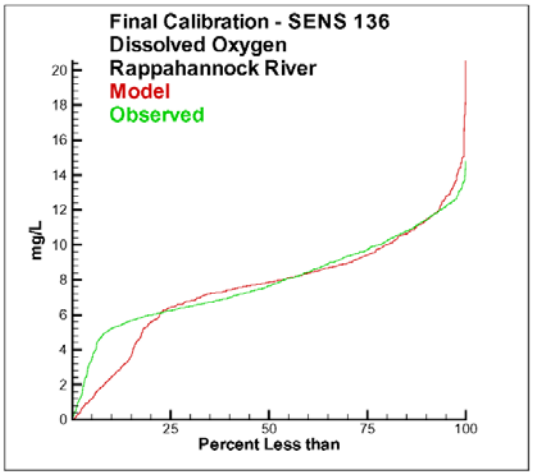

Figure 15-6. Cumulative distribution plot of dissolved oxygen in Rappahannock River.

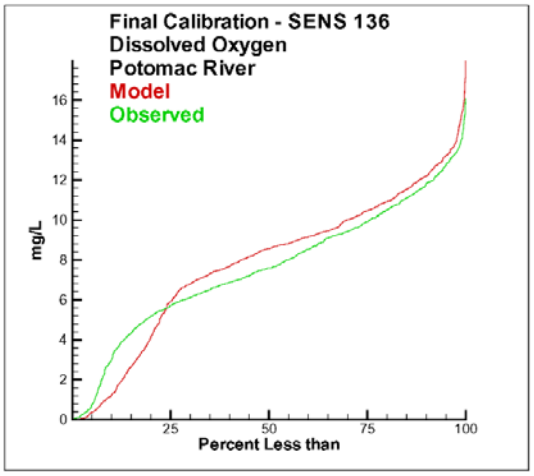

Figure 15-7. Cumulative distribution plot of dissolved oxygen in Potomac River.

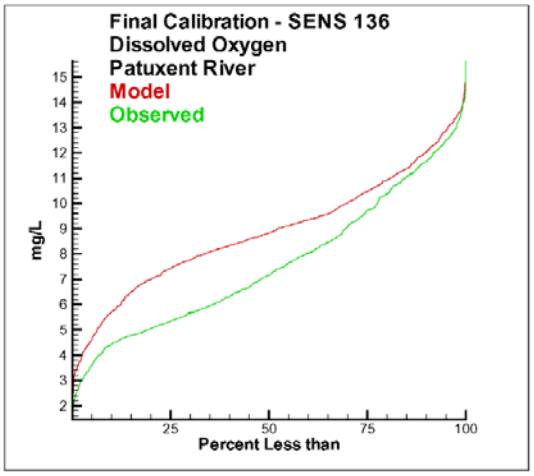

Figure 15-8. Cumulative distribution plot of dissolved oxygen in Patuxent River.

Salinity

The graphical distributions indicate excellent representations of salinity in the mainstem bay (Figure 15-9) and Potomac River (Figure 15-13). We believe the larger number of grid elements and major role of gauged runoff versus ungauged below-fall-line flow contribute to the computed accuracy in these systems. Salinity computations in the James (Figure 15-10), York (Figure 15-11), Rappahannock (Figure 15-12) and Patuxent Rivers are less accurate. This characteristic has been with the model since the earliest stages and remains after two grid re-segmentations. Further re-segmentation should be of benefit but we have to recognize the role of local processes and effects that may never be represented in a system-wide model.

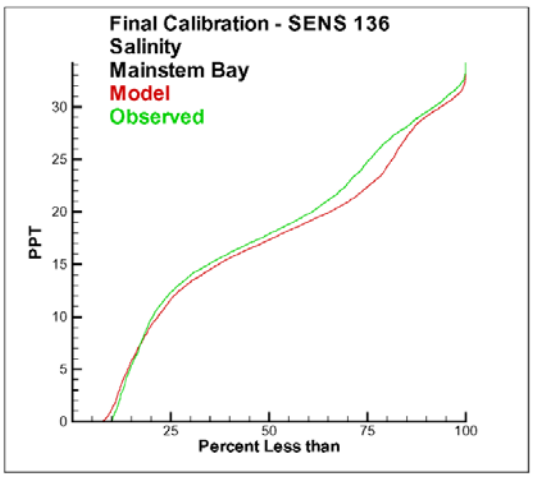

Figure 15-9. Cumulative distribution plot of salinity in mainstem bay.

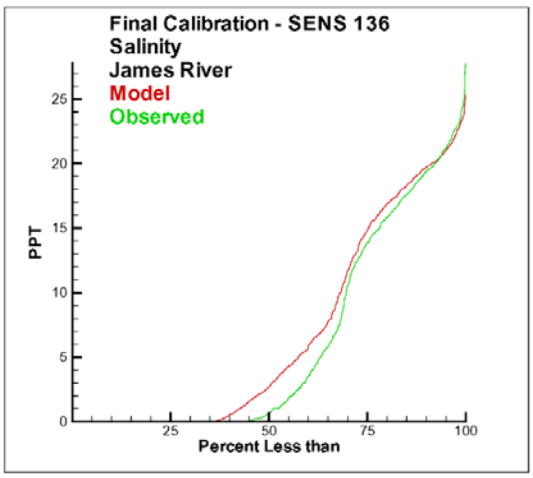

Figure 15-10. Cumulative distribution plot of salinity in James River.

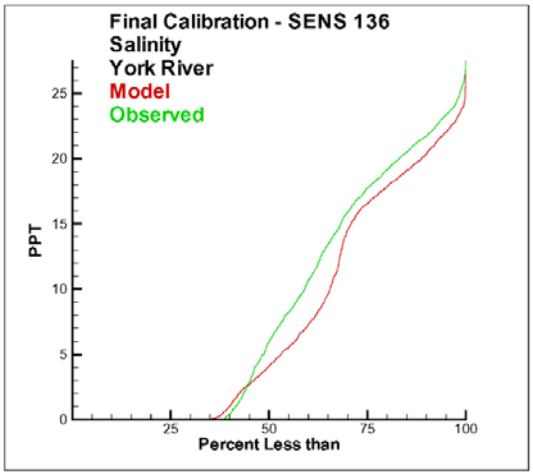

Figure 15-11. Cumulative distribution plot of salinity in York River.

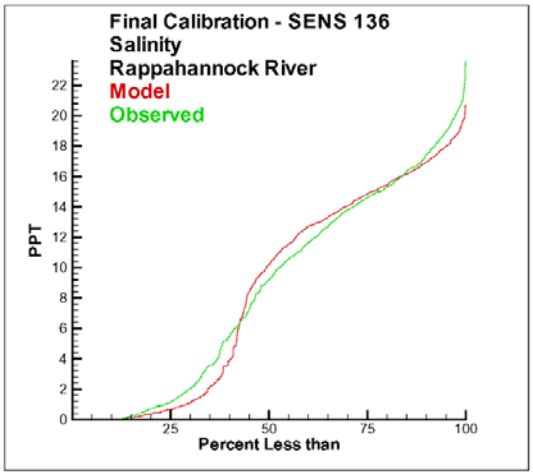

Figure 15-12. Cumulative distribution plot of salinity in Rappahannock River.

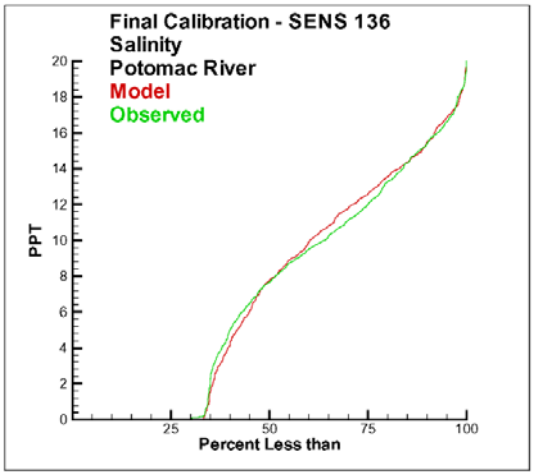

Figure 15-13. Cumulative distribution plot of salinity in Potomac River.

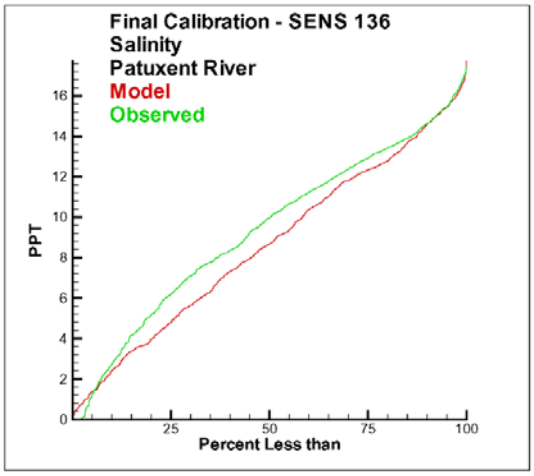

Figure 15-14. Cumulative distribution plot of salinity in Patuxent River.

Chlorophyll

Most of the chlorophyll distributions indicate a crossover around 10 to 20 mg m^{-3}. In the mainstem bay (Figure 15-15), James (Figure 15-16), Potomac (Figure 15-19) and Patuxent (Figure 15-20) Rivers, the model tends to underestimate the very highest chlorophyll concentrations. This property is characteristic of the model and is attributed to the unlimited extremes that observed chlorophyll observations can attain. The model is restricted to concentrations averaged over space (cell volume) and time (time step and averaging interval). The observations are subject to sub-grid scale processes that create local accumulations and are also affected by analytical variance. Except for the highest observations, the model tends to over-compute chlorophyll. In systems such as the mainstem bay and Potomac River, the overestimation is negligibly small while the overestimation is significant in the Rappahannock (Figure 15-18) and Patuxent Rivers (Figure 15-20).

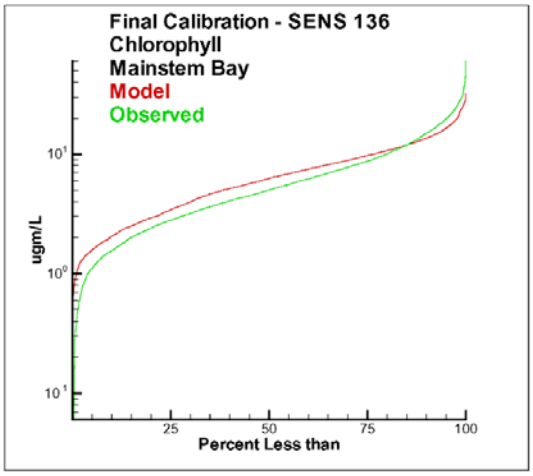

Figure 15-15. Cumulative distribution plot of chlorophyll in mainstem bay.

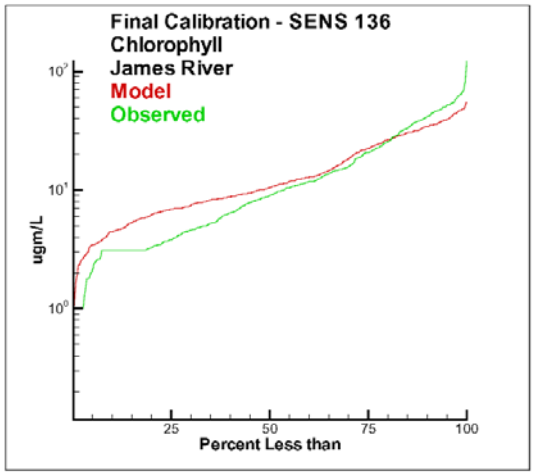

Figure 15-16. Cumulative distribution plot of chlorophyll in James River.

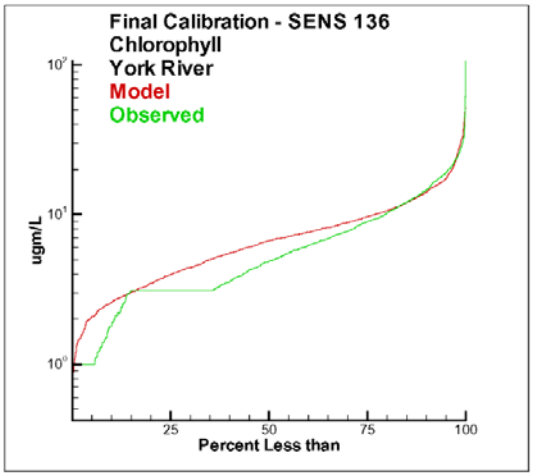

Figure 15-17. Cumulative distribution plot of chlorophyll in York River.

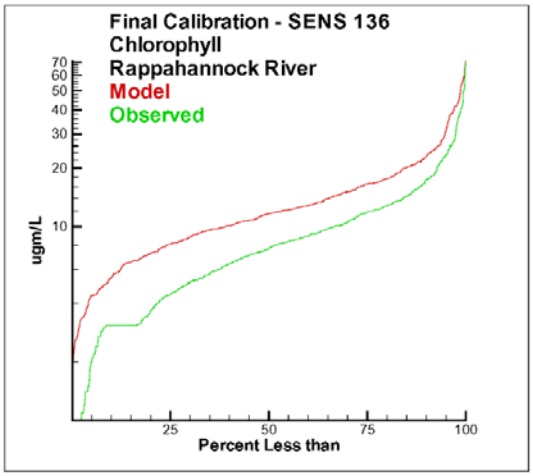

Figure 15-18. Cumulative distribution plot of chlorophyll in Rappahannock River.

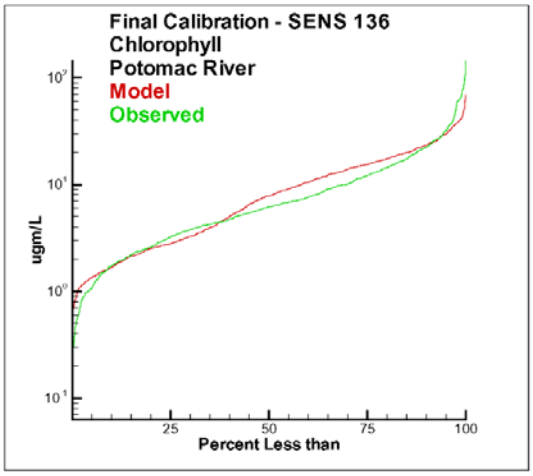

Figure 15-19. Cumulative distribution plot of chlorophyll in Potomac River.

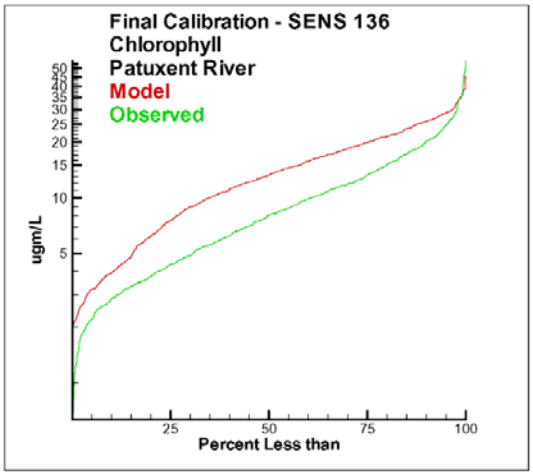

Figure 15-20. Cumulative distribution plot of chlorophyll in Patuxent River.

Light Attenuation

The light attenuation computations are remarkably successful, especially considering the relatively crude solids and attenuation algorithms in the model. The computed and observed distributions in the mainstem bay (Figure 15-21), James (Figure 15-22) and Potomac Rivers (Figure 15-25) are virtually congruent. In the York (Figure 15-23), Rappahannock (Figure 15-24) and Patuxent (Figure 15-26) Rivers, the upper halves of the computed and observed distributions tend to superimpose. In the lower portions of the distributions, below 1 to 2 m^{-1}, the model tends to overestimate observed attenuation.

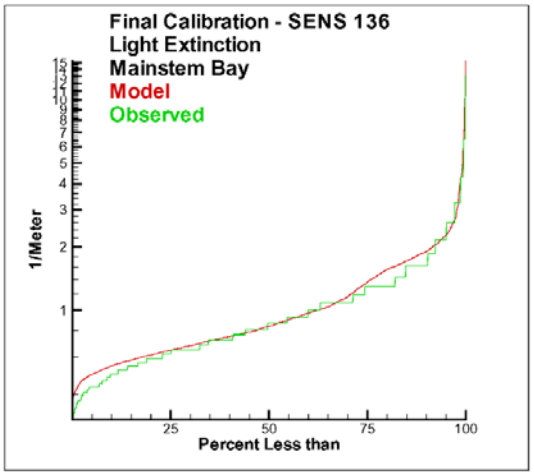

Figure 15-21. Cumulative distribution plot of light attenuation in mainstem bay.

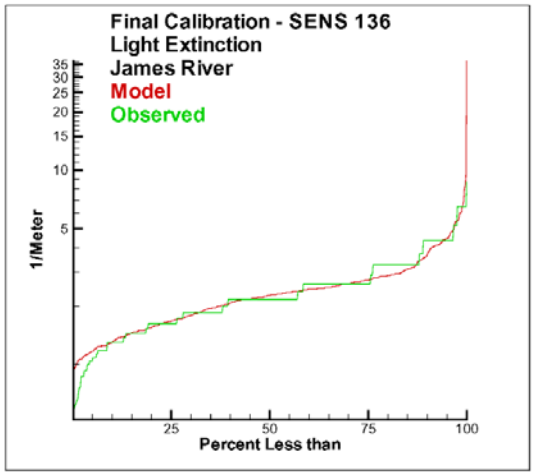

Figure 15-22. Cumulative distribution plot of light attenuation in James River.

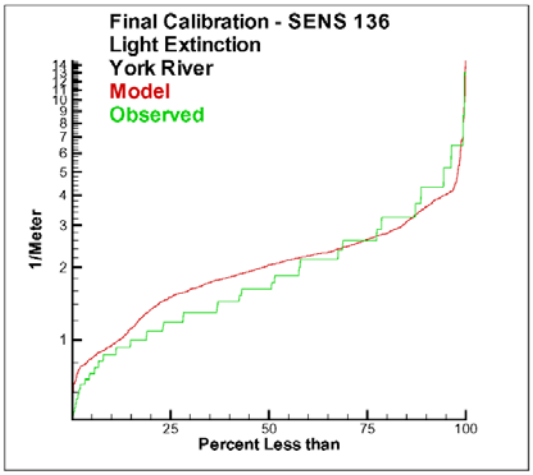

Figure 15-23. Cumulative distribution plot of light attenuation in York River

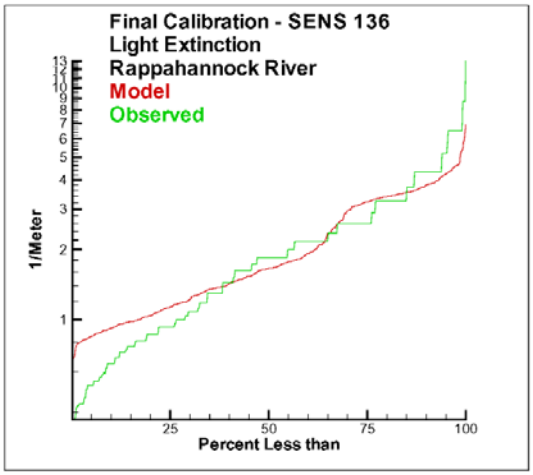

Figure 15-24. Cumulative distribution plot of light attenuation in Rappahannock River.

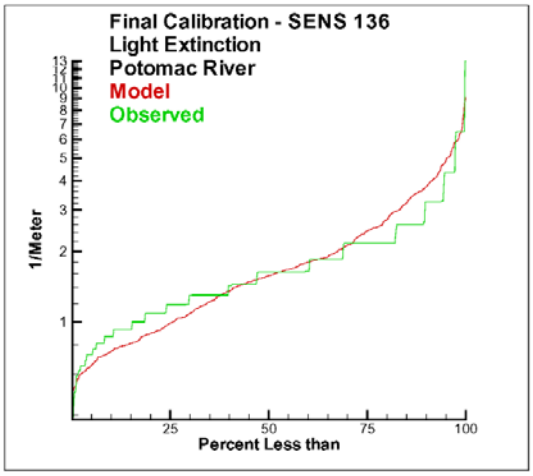

Figure 15-25. Cumulative distribution plot of light attenuation in Potomac River.

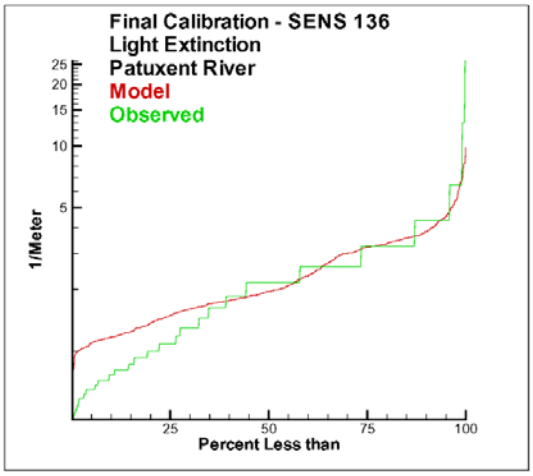

Figure 15-26. Cumulative distribution plot of light attenuation in Patuxent River.

Total Nitrogen

The James (Figure 15-28), York (Figure 15-29) and Patuxent (Figure 15-32) Rivers exhibit the familiar crossover pattern. In these tributaries, the model tends to overestimate the highest nitrogen concentrations and underestimate the lower concentrations. The crossover occurs around 0.8 g m^{-3}. We suspect this behavior is attributable to occasional enormous concentrations that are computed near the fall lines during storm events. The water quality and hydrodynamic models use gauged flows while the watershed model uses its own computed flow. Discrepancies between gauged and computed flows can cause wild fluctuations during the large loadings associated with storm events. The mainstem bay (Figure 15-27) and Potomac River (Figure 15-31) exhibit two crossovers. As with the preceding three tributaries, the model exceeds the very highest observed concentrations. The model also exceeds the lowest observations, less than about 0.6 g m^{-3}. In the portions of the distributions between the extremes, observations tend to exceed modeled concentrations. The Rappahannock River (Figure 15-30) stands out as one in which total nitrogen is under-computed throughout the distribution.

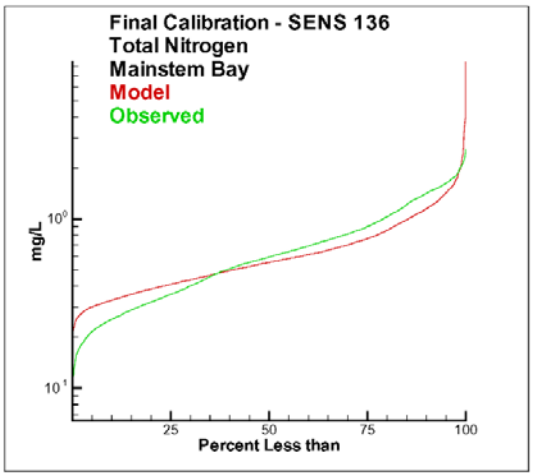

Figure 15-27. Cumulative distribution plot of total nitrogen in mainstem bay.

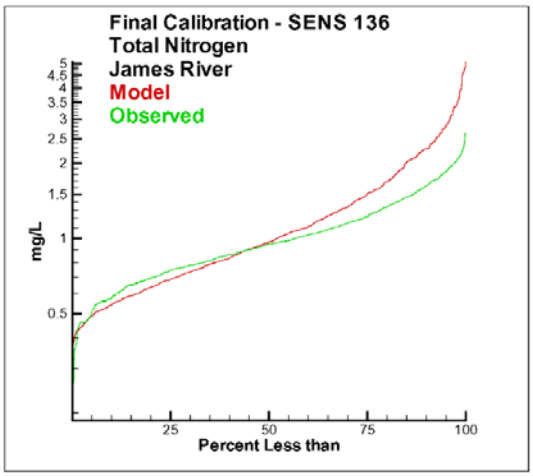

Figure 15-28. Cumulative distribution plot of total nitrogen in James River.

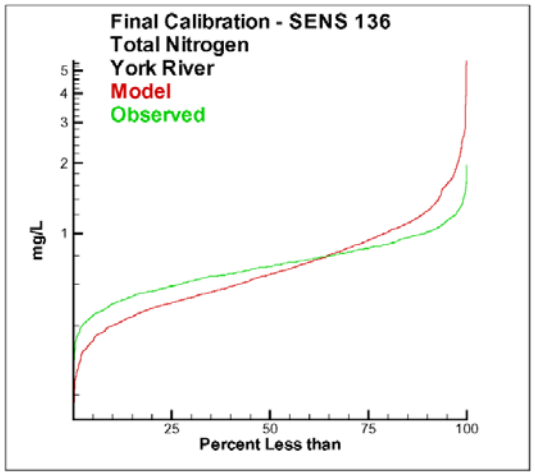

Figure 15-29. Cumulative distribution plot of total nitrogen in York River.

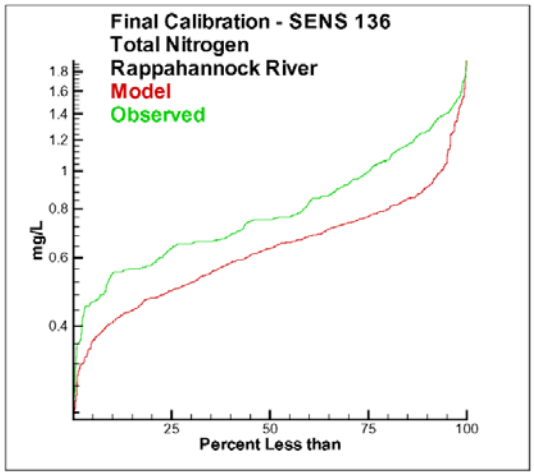

Figure 15-30. Cumulative distribution plot of total nitrogen in Rappahannock River.

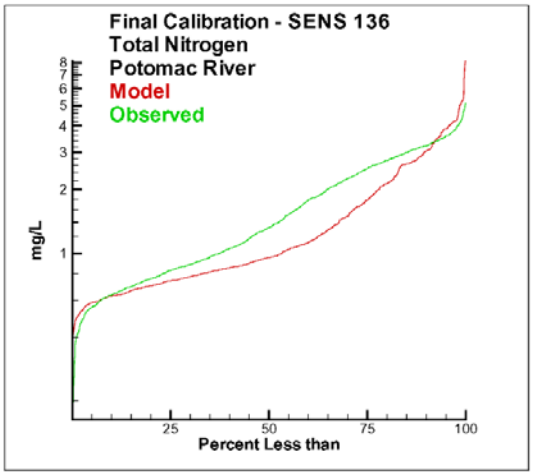

Figure 15-31. Cumulative distribution plot of total nitrogen in Potomac River.

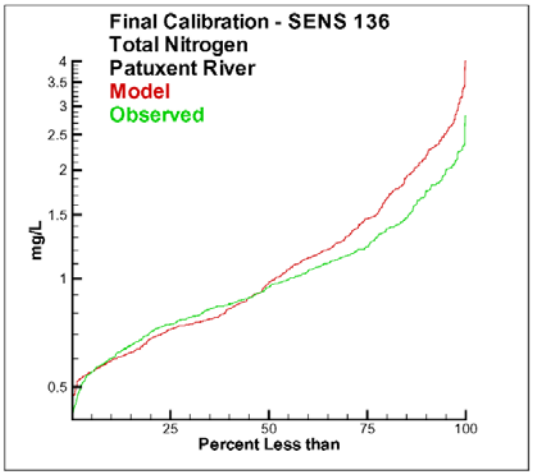

Figure 15-32. Cumulative distribution plot of total nitrogen in Patuxent River.

Total Phosphorus

As noted in the statistical summaries, the model usually underestimates total phosphorus. The graphs indicate the model matches the very highest 1 to 2% of the observations. The underestimation is almost universal in the lower 98% of the observed distribution. The mainstem bay (Figure 15-33) and the Rappahannock River (Figure 15-36) suggest that the model overestimates the lowest total phosphorus concentrations but interpretation is clouded in the Rappahannock by reporting increments and detection levels. We have attributed underestimation of computed total phosphorus to uncertainty in bank loading, to lack of a model resuspension mechanism, and to inability to represent concentration of particulate phosphorus in turbidity maximums.

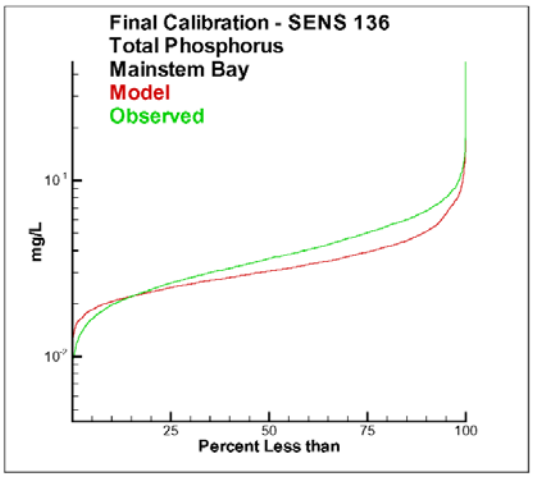

Figure 15-33. Cumulative distribution plot of total phosphorus in mainstem bay.

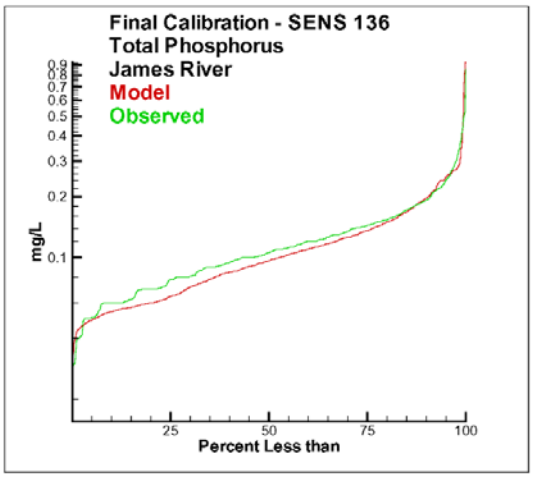

Figure 15-34. Cumulative distribution plot of total phosphorus in James River.

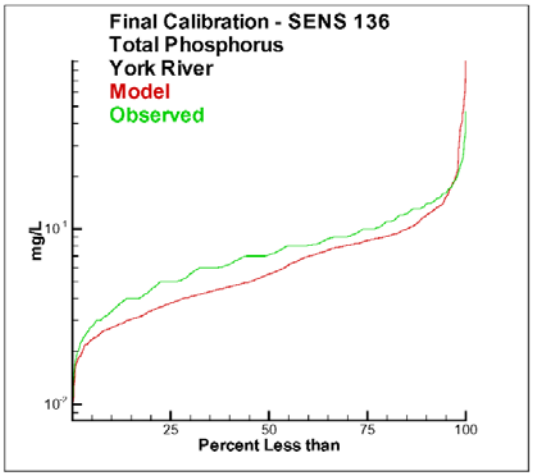

Figure 15-35. Cumulative distribution plot of total phosphorus in York River.

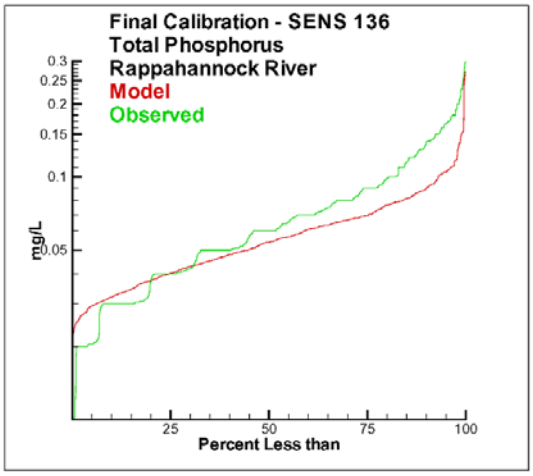

Figure 15-36. Cumulative distribution plot of total phosphorus in Rappahannock River.

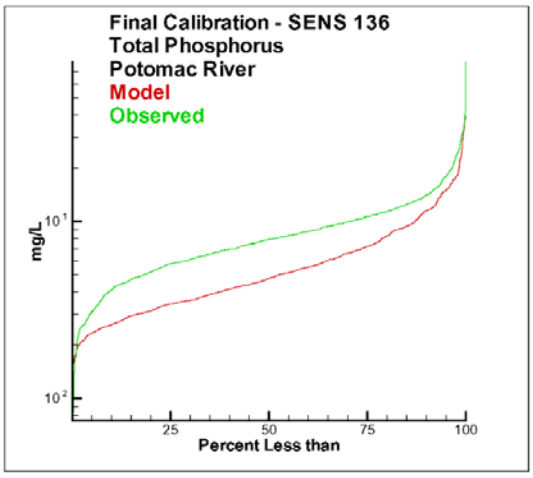

Figure 15-37. Cumulative distribution plot of total phosphorus in Potomac River.

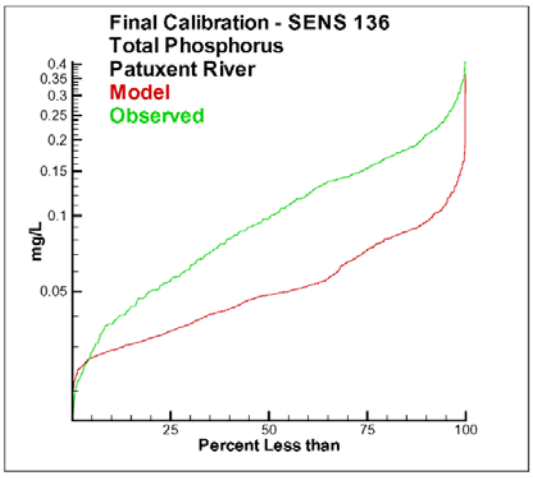

Figure 15-38. Cumulative distribution plot of total phosphorus in Patuxent River.

References

Cerco, C., and Cole, T. (1994). "Three-dimensional eutrophication model of Chesapeake Bay," TR EL-94-4, US Army Engineer Waterways Experiment Station, Vicksburg MS.

Cerco, C., Bunch, B., Teeter, A., and Dortch, M. (2000). "Water quality model of Florida Bay," ERDC TR-00-10, US Army Engineer Research and Development Center, Vicksburg MS.

Cerco, C., Johnson, B., and Wang, H. (2002). "Tributary refinements to the Chesapeake Bay model," ERDC TR-02-4, US Army Engineer Research and Development Center, Vicksburg MS.

Sucsy, P., and Morris, F. (2001). "Salinity intrusion in the St. Johns River, Florida." *Estuarine and Coastal Modeling, Proceedings of the Seventh International Conference*. M.L. Spaulding ed., American Society of Civil Engineers, Reston VA, 120-139.

Tillman, D., Cerco, C., Noel, M., Martin, J., and Hamrick, J. (2003). "Three-dimensional eutrophication model of the lower St. Johns River, Florida," ERDC TR-03EL353, US Army Engineer Research and Development Center, Vicksburg MS.